Spectroscopic and TDDFT-Based Electronic Structure Analysis of Porphyrin and Phthalocyanine Derivatives, and their Transition Metal Complexes

By

Dustin Eric Nevonen

A Thesis submitted to the Faculty of Graduate Studies of The University of Manitoba in partial fulfilment of the requirements of the degree of

Doctor of Philosophy

Department of Chemistry

University of Manitoba

Winnipeg

Abstract

The overarching theme of this thesis involves the investigation of the electronic structures of porphyrin and phthalocyanine derivatives and the predictable manipulation of their molecular orbital energy levels induced via changes in aromatic macrocyclic structure or peripheral substitution. Using both experimental spectroscopic (UV-vis, circular dichroism, magnetic circular dichroism) and theoretical (time-dependent density functional theory) techniques, the electronic structures of these macrocyclic systems were studied to provide tunable platforms to best suit their specific applications. Intended outcomes for these compounds include their use as photosensitizers for the photodynamic therapy of cancer, chemical sensors, and molecular wires.

The structural manipulations that took place involving the soft chromophoric porphyrin systems included extension of the π-system (chapters 2-4), symmetry loss due to rotated pyrrole ring (chapter 5), and microscale extension of the π-system via globular formation (also chapter 5). In all cases, extension of the π-system effectively destabilized the e_{gy} orbital and affected the magnitude of ΔLUMO; so much so in the case of the porphyrin tapes that an inverted ΔHOMO < ΔLUMO relationship was observed, which is not often seen in synthetically-prepared molecules. Rotation of a single pyrrole ring in porphyrin increased ΔHOMO through tandem a_{1u} orbital stabilization and a_{2u} orbital energetic destabilization. Once this system was allowed to aggregate, optically active microscale assemblies were observed which possessed a substantially extended π-system.

For the hard chromophoric phthalocyanine and triazatetrabenzcorrole (TBC) systems, the electronic structure manipulations were expectedly more difficult. The TBC chapter (6) demonstrated that removal of a *meso*-N atom from the phthalocyanine macrocycle destabilizes a_{2u} and slightly decreases ΔHOMO. The work presented in the axially-coordinated iron phthalocyanines chapters (8 and 9) employed a series of ligands which were coordinated to the iron center. The resulting effects on the electronic structure involved a strong dependence on the ΣE_L (L_{axial}) parameter, where either cationic radical (on the macrocycle) or iron(III) formation were observed under chemical and electrochemical oxidation conditions.

Acknowledgements

First, I would like to thank Prof. Victor Nemykin for allowing me the opportunity to study at the graduate level in his research group, and also for the excellent advice and advanced instruction that was provided over the years. Additionally, I would like to thank my advisory committee; the members of which include Dr. David Herbert (Chemistry), Dr. Christian Kuss (Chemistry), and Dr. Johan van Lierop (Physics and Astronomy), for taking the time to review and assess my progress in a realistically constructive manner. Lastly, I would like to thank the members (past and present) of both the Nemykin and van Lierop laboratories for providing a kind, professional, and productive work atmosphere.

Chapter three reproduced with permission from Belosludov, R. V.; Nevonen, D. E.; Nemykin, V. N. Accurate Prediction of the Excited States in the Fully Conjugated Porphyrin Tapes Across the Full Spectral Range: A Story of the Interplay Between π-π* and Intramolecular Charge-Transfer Transitions in Soft Chromophores. *J. Phys. Chem. A.* **2021**, *125*(12) 2480-2491. Copyright 2021 American Chemical Society.

Chapter four reproduced with permission from Dorazio, S. J.; Vogel, A.; Dechert, S.; Nevonen, D. E.; Nemykin, V. N.; Brueckner, C.; Meyer, F. Siamese-Twin Porphyrin Goes Platinum: Group 10 Monometallic, Homobimetallic, and Heterobimetallic Complexes. *Inorg. Chem.* **2020**, *59*(10), 7290-7305. Copyright 2020 American Chemical Society.

Chapter seven reproduced with permission from Nevonen, D. E.; Rohde, G. T.; Nemykin, V. N. New Insight into an Old Problem: Analysis, Interpretation, and Theoretical Modeling of the Absorption and Magnetic Circular Dichroism Spectra of Monomeric and Dimeric Zinc Phthalocyanine Cation Radical. *Inorg. Chem.* **2019**, *58*(20), 14120-14135. Copyright 2019 American Chemical Society.

Chapter eight reproduced with permission from Nemykin, V. N.; Nevonen, D. E.; Osterloh, R. W.; Ferch, L. S.; Harrison, L. A.; Marx, B. S.; Kadish, K. M. Application of Lever's E_L Parameter Scale Toward Fe(II)/Fe(III) versus Pc(2-)/Pc(1-) Oxidation Process Crossover Point in Axially Coordinated Iron(II) Phthalocyanine Complexes. *Inorg. Chem.* **2021**, *60*(21), 16626-16644. Copyright 2021 American Chemical Society.

Chapter nine reproduced with permission from Nevonen, D. E.; Ferch, L. S.; Schrage, B. R.; Nemykin, V. N. Charge-Transfer Spectroscopy of Bisaxially Coordinated Iron(II) Phthalocyanines through the Prism of the Lever's E_L Parameters Scale, MCD Spectroscopy, and TDDFT Calculations. *Inorg. Chem.* **2021**, 61(*21*), 8250-8266. Copyright 2022 American Chemical Society.

With regards to chapters 2-9, the contributions of the author (Dustin Nevonen) towards the work performed in those chapters is total, with the exception of synthesizing the studied compounds in three cases. Any previously published experimental work that was not completed by Dustin Nevonen was omitted from the bodies of chapters 2-9 of this thesis.

The compounds reported on in chapter two were synthesized by Austen Moss and Hong Wang (University of North Texas). The compounds included in chapter four were synthesized by Christian Brückner (University of Connecticut). Compound **6.1** of chapter six was synthesized by Basma Ghazal and Saad Makhseed (Kuwait University).

Table of Contents

List of Figures

List of Schemes and Charts

List of Tables

List of Abbreviations

CD: Circular dichroism

CV: Cyclic voltammetry

DCM: Dichloromethane

DMF: Dimethylformamide

ΔHOMO: $Energy_{HOMO} – Energy_{HOMO-1}$

ΔLUMO: $Energy_{LUMO+1} - Energy_{LUMO}$

DFT: Density functional theory

DLS: Dynamic light scattering

DMA: Dimethylacetamide

DmFc: Decamethylferrocene

DMSO: Dimethyl sulfoxide

DPV: Differential pulse voltammetry

EPR: Electron paramagnetic resonance

ESI: Electrospray ionization

ESR: Electron spin resonance

Fc: Ferrocene

GGA: Generalized gradient approximation

HOMO: Highest occupied molecular orbital

Im: Imidazole

ILCT: Interligand charge-transfer

InGaAs: Indium-Gallium-Arsenide

LCP: Left circularly-polarized

LMCT: Ligand to metal charge-transfer

LUMO: Lowest occupied molecular orbital

MAD: Mean average deviation

MCD: Magnetic Circular Dichroism

MLCT: Metal to ligand charge-transfer

MO: Molecular orbital

MTTP: Metalated tetraphenylporphyrin

NHE: Normal hydrogen electrode

NIR: Near infra-red

OLED: Organic light-emitting diode

PAHs: Polycyclic aromatic hydrocarbons

Pc: Phthalocyanine

PCM: Polarized continuum model

PDT: Photodynamic therapy

PEM: Photoelastic Modulator

PMT: Photomultiplier tube

PPP: Pariser-Parr-Pople

Py: Pyridine

RCP: Right circularly-polarized

SCE: Saturated calomel electrode

SEC: Spectroelectrochemistry

$\Sigma E_L(L_{ax})$: The sum of Lever's electrochemical parameters for all ligands on the compound

SOMO: Singly occupied molecular orbital

SOS: Sum-over-states

TBAP: Tetrabutylammonium perchlorate

TBC: Triazatetrabenzcorrole

TDDFT: Time-dependent density functional theory

TEABr: Triethylamine bromide

TEAP: Triethylammonium perchlorate

TFAB: Tetrakis(perfluoroaryl)borate tetrabutylammonium salt

TPP: Tetraphenylporphyrin

Tz: Triazole

UV: Ultraviolet

ZINDO/S: Zerner's Intermediate Neglect of Differential Overlap /(for Spectra)

1. Introduction

1.1 Characteristics of Porphyrins and Phthalocyanines

Porphyrins are fully-conjugated, tetrapyrrolic macrocycles which contain 26 π-electrons, 18 of which comprise a closed, continuous cycle that is best described as aromatic (Fig. 1.1a). There are many examples of naturally occurring porphyrins; the most common of which is the iron-centered heme, a cofactor of hemoglobin (Fig. 1.1b). Single benzannulation of the β-peripheral pyrrolic carbons of tetraazaporphyrin leads to the general phthalocyanine (Pc) structure (Fig. 1.1c). The increased π-conjugation imparts the molecule with greater rigidity compared to porphyrin and has a substantial effect on the optical properties of the macrocyclic core.

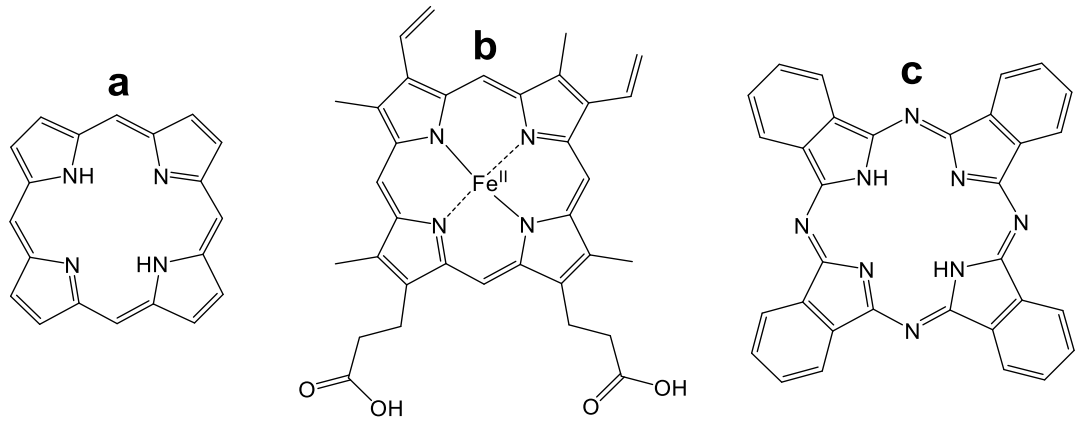

Figure 1.1. Structures of free-base porphyrin (a), heme B (b), and metal-free phthalocyanine (c).

1.2 A Brief History of Porphyrins and Phthalocyanines

Reported in the early 1840s, the first chemical manipulations of porphyrin involved the addition of concentrated sulfuric acid to hemoglobin to form metal-free hematin[1]; however, these reports were elementary and described inaccurately. In 1867, Thudichum[2] purified and crystallized this metal-free hematin which he referred to as cruentine, noting the blood-red colour with which it fluoresced. The term "porphyrin" was originally coined by Hoppe-Seyler in two separate reports in which he utilized the prefixes "haemato"[3] and "phyllo".[4] Finally, in 1883, Soret reported[5] his discovery of the intense, near-ultraviolet absorption band of hemoglobin, currently known as the Soret band.

The first report of phthalocyanine formation occurred in the early 1930s following an explosive industrial accident at a Scottish dye factory, involving the production of phthalimide from phthalic anhydride. The blue residue of iron(II) phthalocyanine ($PcFe^{II}$) was recovered and qualitatively analyzed following this incident. This $PcFe^{II}$ compound was soon after quantitatively characterized by Linstead[6] and Robertson[7] in the 1930's and extensive research on phthalocyanines and their substituted counterparts has been performed since.

1.3 Porphyrins in Nature

Porphyrins occur naturally in the form of chlorophylls, purple bacteria, and various bacteriochlorins, all of which are capable of harvesting light.

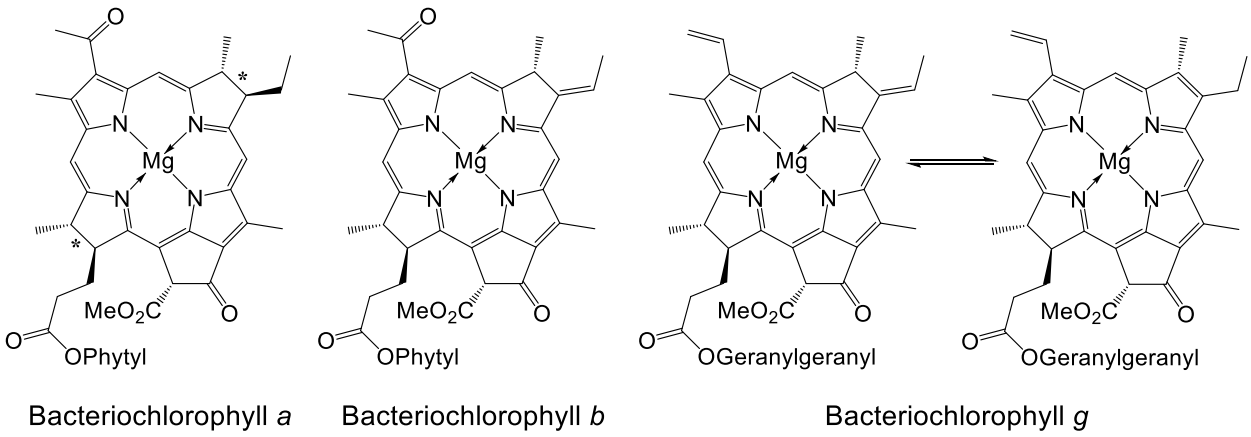

Bacteriochlorophyll *a* Bacteriochlorophyll *b* Bacteriochlorophyll *g*

Figure 1.2. Structures of select bacteriochlorophylls.

Bacteriochlorins (examples of which are shown in Fig. 1.2) are examples of naturally occurring reduced porphyrinoids; the term "reduced" will appear many times throughout this thesis and refers not to a chemical reduction but rather a reduction in the number of peripheral double bonds in one or more of the pyrrole rings. In the case of bacteriochlorophylls and as demonstrated in Fig. 1.2, two pyrrole rings, which are opposite in position from each other, are missing a double bond (the missing double bond locations are represented with stars for the bacteriochlorophyll *a* structure shown in Fig. 1.2). Naturally occurring reduced porphyrinoids such as bacteriochlorins possess a characteristic ΔHOMO < ΔLUMO relationship (where ΔHOMO is defined as the energy difference between HOMO and HOMO-1, while ΔLUMO is the energy difference between LUMO and LUMO+1) while most synthetic porphyrinoids exhibit the opposite ΔHOMO > ΔLUMO relationship.

1.4 Optical Properties and Current Applications of Porphyrins and Phthalocyanines

Due to their desirable and exploitable optical properties, porphyrins and phthalocyanines find current use in optical materials[8], antibacterial and antimicrobial phototherapy[9], as well as photochemotherapeutics[10].

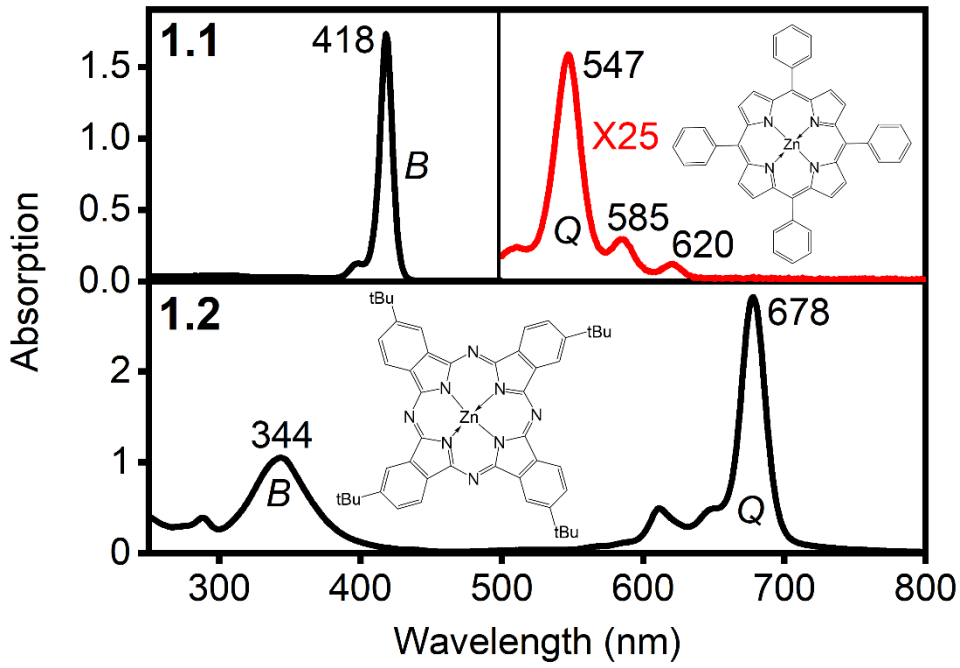

Figure 1.3. UV-Vis spectra of **1.1** (upper) and **1.2** (lower) in CH_2Cl_2.

In Fig. 1.3 above, the UV-vis spectra of two very general, zinc-centered porphyrin and phthalocyanine examples are shown. The upper spectrum is that of zinc tetraphenylporphyrin (**1.1**) and the lower spectrum is an enantiomerically pure zinc phthalocyanine (**1.2**) which has four *tert*-butyl groups at the β-positions on the phenyl rings. In the upper spectrum, the red

signal indicates that the concentration was increased (25 times in this case) so that the low energy *Q*-band ($Q_{0\text{-}0}$) and its vibronic satellites ($Q_{0\text{-}1}$ and $Q_{0\text{-}2}$) were near the intensity of the more prominent *B*-band (more commonly known as the Soret band in porphyrins) for improved visualization. In both cases, there are two main absorptions: one at a higher energy (*B*- or Soret band) and one at lower energy (*Q*-band). Since these structures are very generic and contain no additional moieties other than the non-chromophoric *tert*-butyl groups which were added to promote solubility, these spectra are excellent examples of the baseline optical absorption signals which these molecule types readily exhibit.

The solar energy directed at Earth, that passes through our atmosphere is comprised of substantial visible wavelengths. With regard to solar cells, in order to capture the source energy provided by the Sun, an efficient absorber material is required. Porphyrins and phthalocyanines are often used as such materials due to their desirable absorption profiles for this application. The strongly absorbing *B*- and *Q*-bands of the typical porphyrin or Pc UV-vis spectrum can be supplemented with signals either in between these two prominent bands and/or at a longer wavelength than the *Q*-band, often owing their nature to charge transfer events. This can be achieved by chemically fusing additional moieties to portions of the macrocycle, and many examples of this are presented within this thesis.

Porphyrins and phthalocyanines have also been recently recognized[10] as effective photochemotherapeutic agents used in the photodynamic therapy (PDT) of cancer. The attractiveness of these molecule classes for use in this particular application is due to the combination of their absorption profile and cytotoxic effects that they exhibit during and post-

irradiation. Specifically, porphyrins and Pcs, in general, possess the ability to strongly absorb light at long wavelengths and they produce cytotoxic singlet oxygen species upon photoexcitation. Using Fig. 3 as an example, the porphyrin sample (**1.1**) absorbs strongly at 547 nm while the phthalocyanine (**1.2**) has an intense signal at 678 nm. These relatively long-wavelength absorptions are critical for success in PDT as this cancer treatment technique relies on lasers or light sources that operate at wavelength ranges that are within what is known as the optical window of tissue (550-950 nm). Below or above these wavelengths, the light does not penetrate the tissue deeply enough to justify that particular photosensitizer as an adequate treatment strategy. Once adsorbed onto or injected into a tumor and radiated with specific wavelengths, the photochemotherapeutic material rapidly converts triplet oxygen into singlet oxygen, which destroys any cells in the immediate vicinity. This technique is minimally invasive and new photochemotherapeutic agents, many of which are porphyrins and Pcs, are currently being investigated.

1.5 Instrumental Techniques Utilized Herein

1.5.1 UV-Vis Spectroscopy. When chromophoric molecules are exposed to visible radiation, a number of excitations occur which involve the transfer of electrons from occupied to unoccupied molecular orbitals (MOs). These processes are stimulated by certain specific wavelengths of light and can be observed using a UV-visible absorption spectrum which functions as a visual representation of the intensity of light absorbed as a function of wavelength. Every observable peak in the UV-vis spectrum represents one or more of these electron-transfer processes. Within this body of work, the UV-vis technique is utilized quite

frequently, and a substantial effort has been made to identify the nature of many of the spectral transitions encountered herein, either by computational simulation, band deconvolution, or correlation with complimentary techniques.

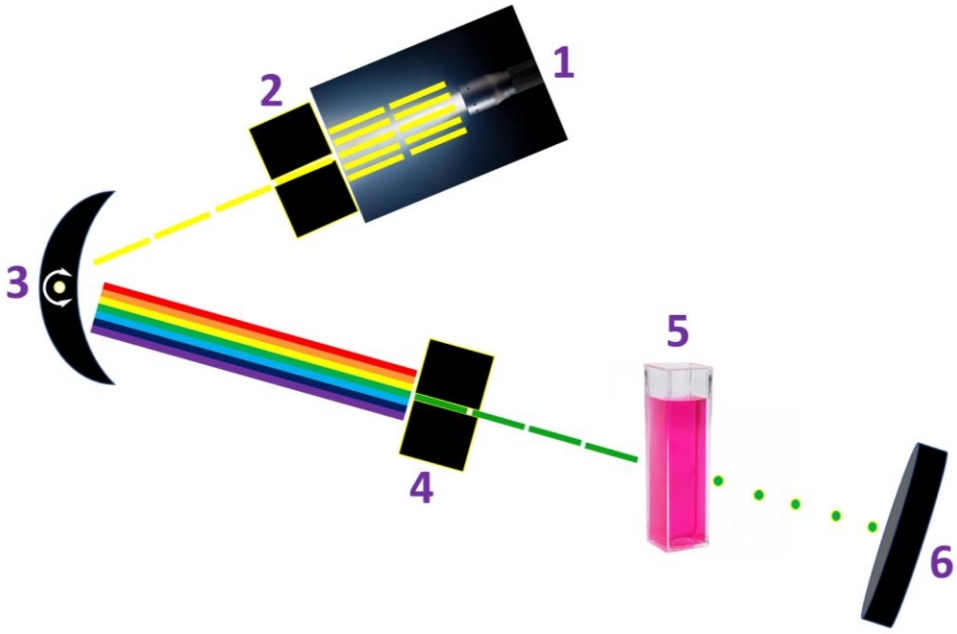

Figure 1.4. Block diagram of the UV-vis sample measurement process.

Shown above in Fig. 1.4 is a simplified block diagram of the inner workings of a typical UV-vis instrument labelled with numbers on each component. The UV-vis measurement process starts with the light source (1) which is a xenon lamp which emits white light containing all UV-vis-NIR wavelengths. The monochromator utilizes an entrance slit (2) which filters the initially scattered light into a narrow beam of focused light. This light beam simultaneously strikes and reflects off the rotatable diffraction grating (3) which converts the white light into an array of multicolored light that is separated by wavelength. It should be made clear that the entrance slit and diffraction grating are integrated into the monochromator and they exist as a single

component. The exit slit (4) filters, separates, and focuses the multicolored light into a single narrow beam of specific wavelength which is directed towards the sample (5). The sample itself is typically dissolved in a solvent, although solid samples can also be measured, and contained within a quartz cuvette. As the light passes through the solution, some of the light is absorbed and some is transmitted, and both events are measured by the detector (6).

1.5.2 Magnetic Circular Dichroism Spectroscopy. Magnetic circular dichroism (MCD) spectroscopy is an absorption technique that employs a strong magnetic field to split apart degenerate or closely spaced (in terms of energy) energy levels. This results in an optical absorption spectrum that exhibits much finer detail than can be achieved with other techniques, such as UV-vis, where overlapping peaks and transitions can often be difficult to deconvolute. In order to understand this relatively uncommon spectroscopic technique, MCD theory is discussed in relation to porphyrins and phthalocyanines below, starting with the simplified instrumental diagram presented in Fig. 1.5.

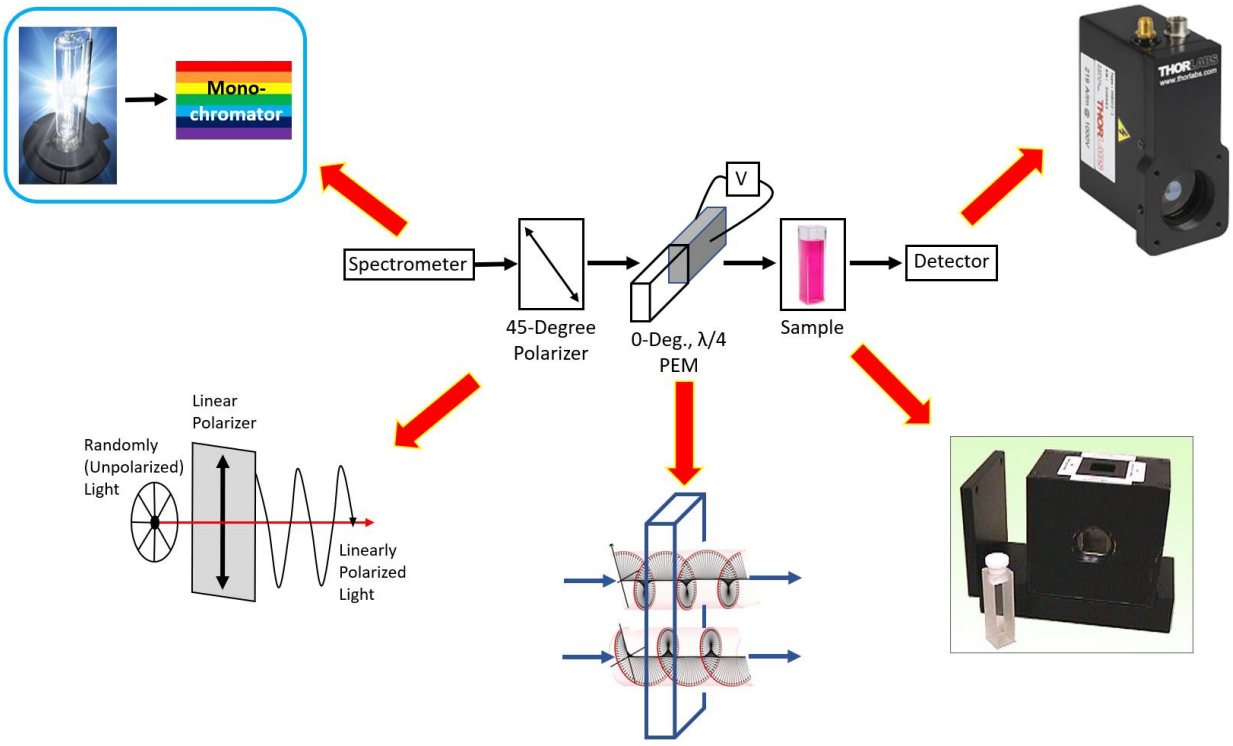

Figure 1.5. Typical components of the magnetic circular dichroism instrument[11].

Referring to Fig. 1.5 above, the magnetic circular dichroism instrumental process begins at the light source, which is typically a xenon lamp, producing scattered white light containing all UV-vis-NIR wavelengths. The light travels through a monochromator which is coupled to the entrance slit. This device filters, processes, and can separate the white light into specific wavelengths or ranges of monochromatized light. The 45° polarizer converts the randomly unpolarized light that exits the monochromator into linearly polarized light which is then further manipulated by the photoelastic modulator (PEM) which induces a ¼ wavelength shift in the light. Voltage pulses are applied to the PEM at a frequency of approximately 50 kHz which converts the linearly polarized light into equal distributions of left and right circularly polarized light that alternates with each voltage pulse. The light then passes through the

sample chamber where the sample itself is dissolved in solvent and placed into a quartz or glass cuvette. It is important to ensure that the direction of the cuvette is always oriented in the same configuration relative to the source and detector to avoid unwanted discrete signal distortions or spectral artifacts. There are two types of magnets that are typically used in magnetic circular dichroism. The type pictured in Fig. 1.5 is a permanent magnet which has a field of 1.4 T. In this configuration, the cuvette is placed into the center of the magnet and there are two holes on either side of the magnet which allows light to pass through. The other common option for an MCD magnet is an electromagnet. The advantage to these is that the field can be varied, allowing for variable field measurements; however, this type of magnet requires significant cooling of the power supply which can hamper efforts to run at higher fields if overheating occurs. The detector measures the amount of light transmitted through the sample and also the amount of light absorbed. Red photomultiplier tubes (PMTs) are conventionally used for the typical scanning ranges (250~850 nm); however, when wavelength ranges exceeding 850 nm are required, an InGaAs detector is typically employed and can be swapped out in a matter of a few minutes.

The origin of the magnetic circular dichroism signals that aromatic macrocycles produce is best described using the perimeter model[12-15]. Using this model, it is possible to directly correlate optical absorption spectroscopic signals with the molecular orbitals and magnetic quantum numbers of the molecule being instrumentally evaluated. A detailed description of such a perimeter model using benzene as an example is shown below in Fig. 1.6.

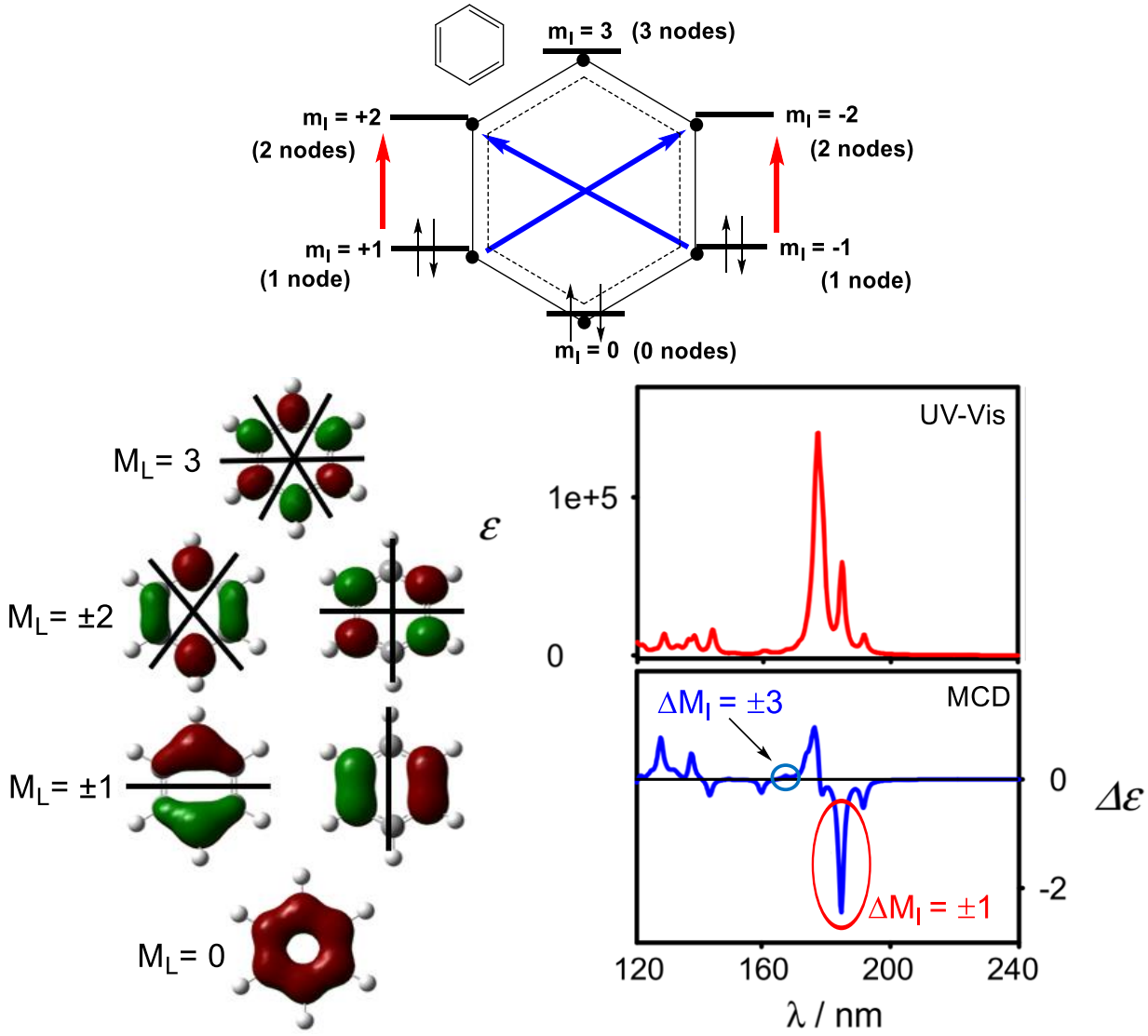

Figure 1.6. Perimeter model of benzene (top) with associated molecular orbitals (lower left) and simulated UV-vis/MCD spectra[16] (lower right); figure is partially adapted from Ref. 16.

The explanation of the perimeter model, with respect to Fig. 1.6 above, begins with the notion that the benzene molecule possesses six π-electrons. In Fig. 1.6 (top), a benzene molecule marked with six dots, representing the six π-electrons, is presented; these dots are closely accompanied with bars meant to represent molecular orbitals (MOs). In general terms,

the central four orbitals (m_L = ±1 and m_L = ±2) are the frontier orbitals of benzene and they represent the most likely regions on the molecule (dictated by applied energy) that a transfer of electrons will occur upon photoexcitation. In Fig. 1.6 (top), the smaller black arrows represent which molecular orbitals are occupied. Also, the magnetic quantum numbers are displayed next to the occupied and unoccupied MOs and are arranged with respect to energy, as indicated by the energy bar on the right. These magnetic quantum numbers are derived from the number of nodal planes present on the molecular orbitals of benzene (Fig. 1.6, lower left). Referring back to Fig. 1.6 (top), once benzene is photoexcited, some of the electrons in the occupied MOs will promote to the previously unoccupied orbitals; however, some of these transitions are more likely to occur than others. Due to the number of π-electrons that benzene possesses, there will be two primary electron transition events that are likely to occur: allowed and forbidden transitions. In the case of benzene, the allowed transitions are represented in Fig. 1.6 (top) with red arrows and they occur when an electron is transferred from the m_L = +1 to the m_L = +2 or the m_L = -1 to the m_L = -2 molecular orbitals. These allowed transitions are therefore represented spectroscopically in the absorption spectrum as intense signals. For benzene, the allowed transition is shown in Fig. 1.6 (bottom right) and is indicated with a red oval. Alternatively, forbidden electron transitions (which are forbidden by selection rules) can also occur and, in the case of benzene (Fig. 1.6, top), are represented with blue arrows which occur when an electron is transferred from the m_L = -1 to m_L = +2 or the m_L = +1 to m_L = -2 MOs. These forbidden transitions are manifested in the optical absorption spectrum as discrete, weak signals such as that circled in blue in Fig. 1.6 (lower right). For these electron promotion events, it can be consistently observed that larger differences in the magnetic quantum number (Δm_L)

will result in forbidden transitions and smaller differences in Δm_L leads to the allowed transitions. For benzene, the allowed transitions occur when $\Delta m_L = \pm 1$ while the forbidden transitions arise when $\Delta m_L = \pm 3$.

Taking this idea one step further, the perimeter model can then be applied to larger chromophoric species such as the fully conjugated macrocyclic porphyrins and phthalocyanines. For these particular systems, Gouterman's four-orbital model[17,18] and Michl's perimeter model are the most commonly used adequately reliable versions of the perimeter model, an example of which is briefly discussed below in Fig. 1.7.

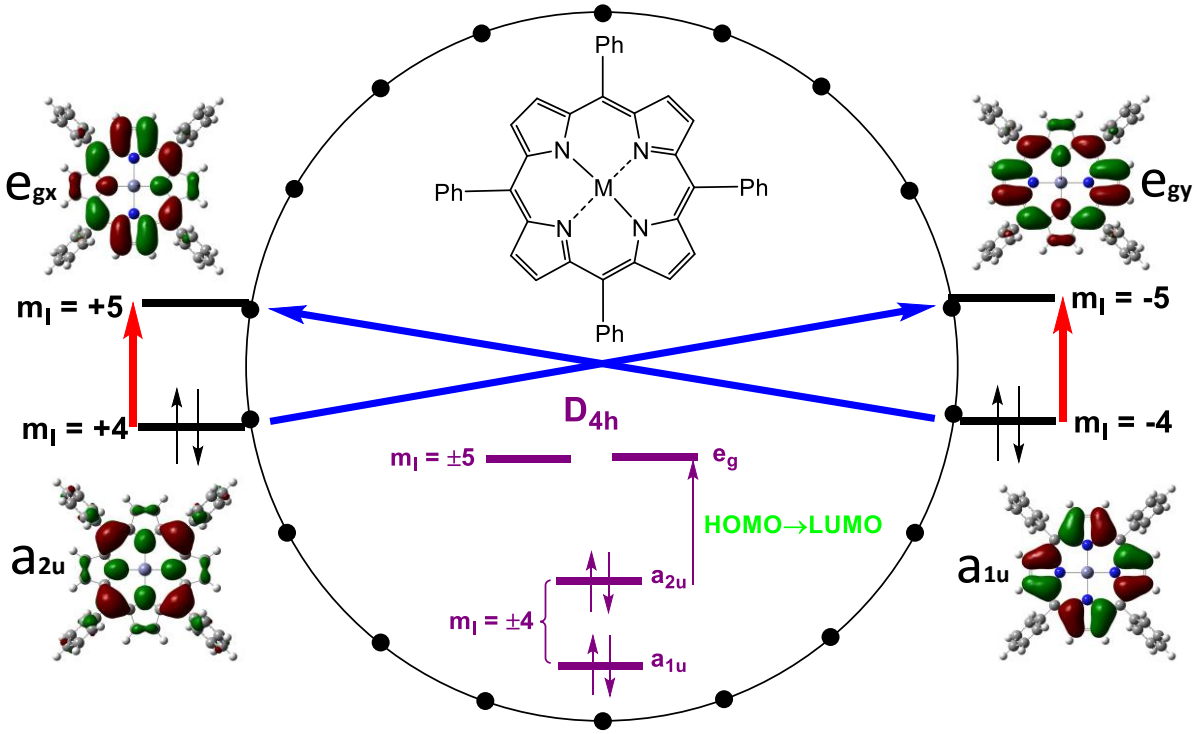

Figure 1.7. Visual representation of Gouterman's four-orbital model for metallated tetraphenylporphyrin.

Figure 1.7 above provides a visual demonstration of how the perimeter model can be expanded to include larger macrocyclic species such as the standard metallated tetraphenylporphyrin (MTPP). The arbitrary MTPP possesses 18 π-electrons, which are represented by dots along the perimeter of the large circle. Instead of placing molecular orbitals next to each dot such as was done for the benzene example of Fig. 1.6, only the frontier MOs are considered for simplicity. These four frontier orbitals are the HOMO-1 which is of a_{1u} orbital character and has a magnetic quantum number of -4, the HOMO which is of a_{2u} character and has an m_L value of +4, and the LUMO and LUMO+1 which are a degenerate pair of e_g orbitals with $m_L = \pm 5$. In this case, as illustrated with the red arrows, the allowed transitions, which will appear as an intense peak in the absorption and MCD spectrum, occur when there are electron promotions from the $m_L = +4$ to the $m_L = +5$ or the $m_L = -4$ to the $m_L = -5$ molecular orbitals and similarly, the forbidden transitions, which appear as discrete weak signals in the UV-vis and MCD spectrum will arise between transitions from the $m_L = -4$ to $m_L = +5$ or the $m_L = +4$ to $m_L = -5$ MOs. Note that similar to the previous case of benzene, the allowed transitions for a typical metallated tetrapheynlporphyrin favor a small change in the magnetic quantum number of the two molecular orbitals involved in the electronic transition ($\Delta m_L = \pm 1$) and the forbidden transition will occur when a greater Δm_L range is spanned ($\Delta m_L = \pm 9$). It should be acknowledged that the example porphyrin of Fig. 1.7 features highly localized orbitals, but when significant delocalization of the orbitals occurs, Gouterman's four-orbital model can break down and alternative descriptions are required. An example of this would be the systems presented in the following chapter (2).

The feature which separates the electronic structures of naturally occurring porphyrinoids from their synthetic counterparts has to do with the energetic spacing of their frontier molecular orbitals. To simplify this explanation, it can be assumed that the four frontier orbitals of interest in these systems are arbitrarily the HOMO-1, HOMO, LUMO, and LUMO+1. In the case of naturally occurring reduced porphyrinoid systems, the energy difference between HOMO-1 and HOMO (ΔHOMO) is less than that between the LUMO and LUMO+1 (ΔLUMO); therefore, naturally occurring reduced porphyrinoid systems possess a ΔHOMO < ΔLUMO relationship. Conversely, most synthetic porphyrinoids and many of the natural non-reduced porphyrins exhibit the opposite ΔHOMO > ΔLUMO relationship. Magnetic circular dichroism is the only experimental technique that can indicate whether ΔHOMO is less or greater than ΔLUMO. This can be elucidated by examining the splitting of the signals in the MCD spectrum where, relative to zero on the y-axis, negative-to-positive split signals in ascending energy indicate a ΔHOMO > ΔLUMO relationship (synthetic electronic structure) and positive-to-negative split signals represent a ΔHOMO < ΔLUMO relationship (natural electronic structure).

The final item that will be discussed is the general interpretation of magnetic circular dichroism signals. The intended purpose of magnetic circular dichroism is to provide a further resolved spectrum than one might obtain using the alternative and complementary technique of UV-vis spectroscopy. When overlapping signals or transitions occur in UV-vis, it is often the result of excited states which are degenerate or closely spaced, in terms of energy. When exposed to a magnetic field (H), these excited states which possess degeneracy split apart, in

terms of energy, resulting in a more resolved spectrum. Figure 8 below demonstrates the shape and origin of the MCD signal types.

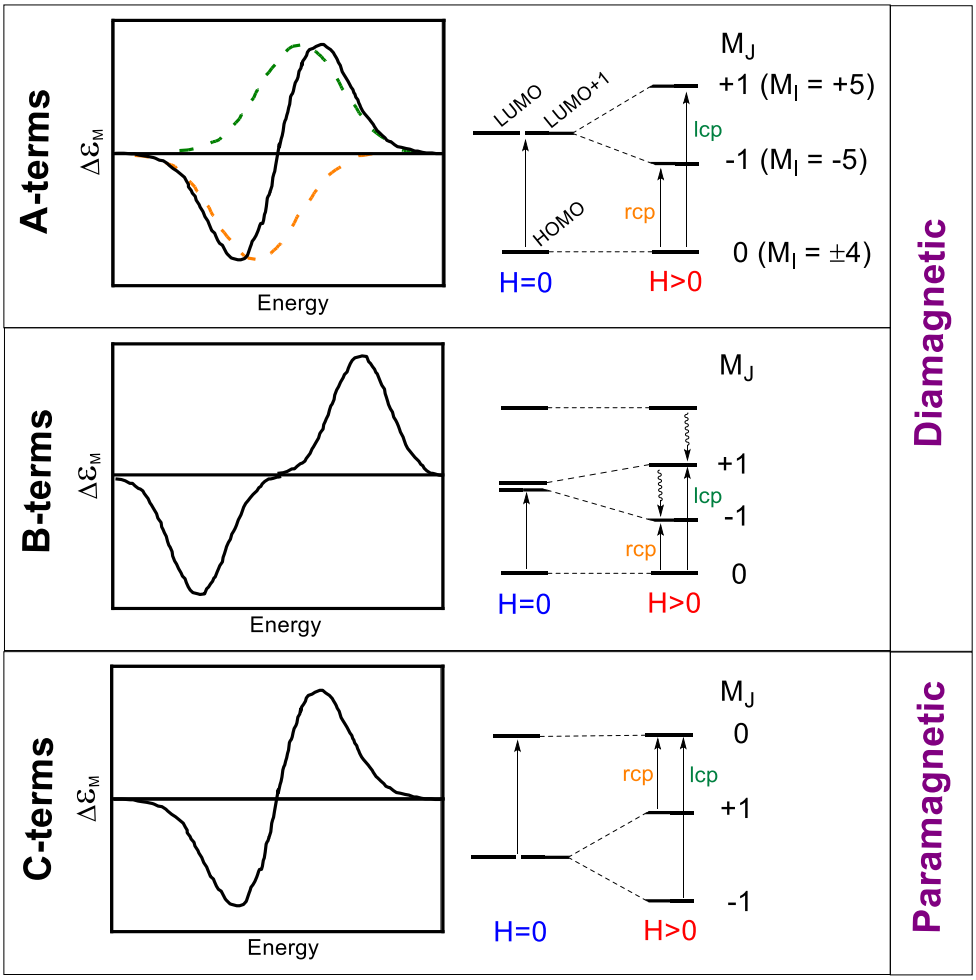

Figure 1.8. Visual representation of magnetic field-induced energy level splitting and resultant MCD signal types.

A description of the intensity of the MCD signals for fully allowed electronic transitions which utilizes the Franck-Condon and Born-Oppenheimer approximations is summarized in eqn. 1.1 below.[19]

$$\frac{\Delta A_{l-r}}{E} = 152.5Bcl\left[A\left(-\frac{df}{dE}\right) + \left(B + \frac{C}{kT}\right)f\right] \quad (1.1)$$

Within eqn. 1.1, $\Delta A_{l\text{-}r}$ represents the differential absorption of left circularly polarized (lcp) and right circularly polarized (rcp) light, *E* is the energy coordinate (in cm^{-1}), *B* is the field strength, c is concentration, l is the path length (in cm), *f* is the normalized Gaussian band shape function, k is the Boltzmann constant, and T is temperature. Finally, the *A*, *B*, and *C* variables represent the Farraday terms which are described below.

As indicated by Fig. 1.8, there are three types of signals which are referred to as Faraday terms; specifically, they are the Faraday *A*-, *B*-, and *C*-terms. The *A*-term, shown in the top row of Fig. 1.8, is the result of Zeeman splitting of an excited state which is orbitally degenerate. The *A*-term signal exhibits a characteristic derivative shape due to energetic separation of the lcp and rcp light-absorbing band centers. The formula[20] which describes the *A*-term and its intensity is summarized below in eqn. 1.2.

$$A = \frac{1}{d_A}\sum\langle J|\mu_z|J\rangle - \langle A|\mu_z|A\rangle\left(\left[m_{-1}^{AJ}\right]^2 - \left[m_{+1}^{AJ}\right]^2\right) \quad (1.2)$$

Within eqn. 1.2 above, d_A corresponds to the degree of degeneracy of excited states, *J* is the angular momenta of electrons in the excited state , μ_z is the value of the z-component of the magnetic moment which is aligned with the axis of light propagation, *A* is the angular momenta of electrons in the ground state, and $\left[m_{-1}^{AJ}\right]$ and $\left[m_{+1}^{AJ}\right]$ are the electric dipole matrix elements which are associated with lcp and rcp light absorption, respectively. Furthermore, the superscripted labels A and J represent an indication that the intensity of the *A*-term correlates

with the relative magnitudes of the spin and orbital angular momenta of ground and excited state electrons.

The Faraday *B*-term (Fig. 1.8, middle) signal manifests as a Gaussian-shaped peak and occurs as a result of second order effects of field-induced mixing of zero-field states by way of magnetic dipole transition moments. If the sample does not possess a three-fold or higher rotation axis, there will be no orbitally degenerate states which can be split apart via the Zeeman effect, and therefore, the spectrum would be completely dominated by *B*-terms. *B*-terms can also be present in the spectra of highly symmetrical compounds; however, their intensity is far lower than that of the *A*- or *C*-terms that will be present. Assuming that mixing between ground and excited states due to the magnetic field is absent, the formula[20] which describes the *B*-term and its intensity is presented below in eqn. 1.3.

$$B = \frac{2}{d_A}\mathcal{R}e\sum\frac{\langle J|\mu_z|J\rangle}{\Delta E_{KJ}}\left(\left[m_{-1}^{AJ}\right]\left[m_{+1}^{KA}\right] - \left[m_{+1}^{AJ}\right]\left[m_{-1}^{KA}\right]\right) \quad (1.3)$$

Within eqn. 1.3 above, $\mathcal{R}$ indicates the real part of the expression and ΔE_{KJ} represents the energetic separation between excited states J and K. Also, pseudo *A*-terms, where one of the lobes is more intense than the other, are also commonly observed, and they represent a situation where zero-field splitting occurs between orbitally degenerate π-π* excited states.

Lastly, *C*-terms (Fig. 1.8, bottom) demonstrate a strong temperature (1/*kT*) dependence as a result of the Boltzmann population distribution over a degenerate ground state. Since only the lowest split state will contribute to the MCD spectrum, a symmetric Gaussian-shaped *C*-term can be observed at very low temperatures. At temperatures higher than this point, the *C*-term

will appear asymmetric due to band-center separation of the transitions which are absorbing the rcp and lcp light. Increasing the temperature further will eventually lead to a symmetrical *A*-term-like derivative-shaped signal. Finally, the formula[20] used to describe the *C*-term and its intensity is listed below in eqn. 1.4.

$$C = -\frac{1}{d_A}\sum\langle A|\mu_z|A\rangle\left(\left[m_{-1}^{AJ}\right]^2 - \left[m_{+1}^{AJ}\right]^2\right) \quad (1.4)$$

1.5.3 Electrochemistry. Photoexcitation is one method of inducing electron transfer between a molecule's molecular orbitals; a process which can be examined using optical absorption spectroscopy. An alternative method of inducing electron transfer processes within a redox-active species is by electrical stimulation. Electrochemistry is thereby used to probe the electrical potentials at which oxidation and reduction events occur within a compound and a typical electrochemical apparatus is pictured below in Fig. 1.9 with a description to follow.

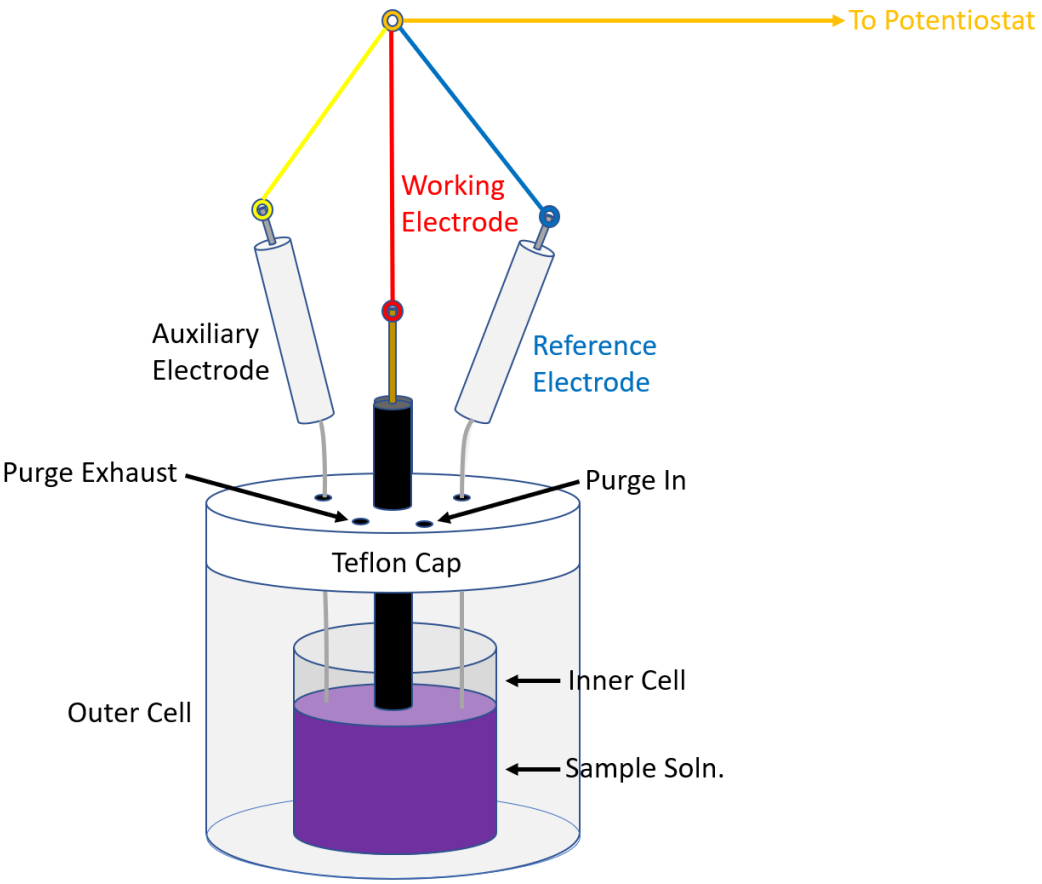

Figure 1.9. Electrochemical apparatus diagram.

Pictured above in Fig. 1.9 is the electrochemical apparatus used for the experiments presented in this thesis and a description and explanation of the data acquisition process follows. The outer cell is comprised of glass, is approximately 25 mL in volume, and has the primary function of sealing the atmosphere around the inner cell. The inner cell holds the sample solution, is comprised of glass as well, and has an approximate volume of 2 mL. The sample itself must be completely dissolved in a dry solvent which is optimally present in a relatively high concentration (~5mg/mL), and electrolyte is added such that its concentration is typically 0.1 M. The most commonly used electrolyte for the work presented in this thesis is

tetrabutylammonium perchlorate (TBAP); however, in cases where limiting the electrolyte interaction with the sample or improved resolution was required, the non-coordinating electrolyte tetrakis(perfluoroaryl)borate tetrabutylammonium salt (TFAB) was used. The preference for TBAP is a result of its relatively low cost and commercial availability. The atmosphere in the sample cell is completely sealed with a Teflon cap which contains a total of one large hole in the center and four additional small holes which can allow electrode and purge system access to the inner cell. To purge the system, either argon or nitrogen gas is bubbled into the sample solution for several seconds. The gas pressure generated within the cell needs to be relieved with the purge exhaust, which is required for effective purging when the system is completely sealed, as it should be.

The electrochemical experiments performed and described in this body of work utilized a three-electrode apparatus. Represented in Fig. 1.9, the working electrode provides a location at which the redox events can occur. For the electrochemical experiments described herein, two types of working electrode were used: platinum and glassy carbon; however, platinum was strongly preferred as sample deposition to the electrode occurred less frequently with the platinum electrode. An Ag/Ag^{+} reference electrode was used throughout, the purpose of which was to generate a constant potential which the other electrodes were compared and referenced to. The third electrode used in this three-electrode apparatus is the platinum auxiliary electrode which was used as an electron sink and/or source, allowing for the transfer of electrons from the external source throughout the sample solution[21]. Finally, all three

electrodes are attached via clamps to wires that lead back to the potentiostat which itself is controlled by a separate computer.

There are two electrochemical data acquisition methods that were routinely employed throughout portions of this thesis: cyclic voltammetry (CV) and differential pulse voltammetry (DPV). Within the field of electrochemistry, CV is the most commonly employed technique and it involves ramping the working electrode potential linearly with time (Fig. 1.10a).

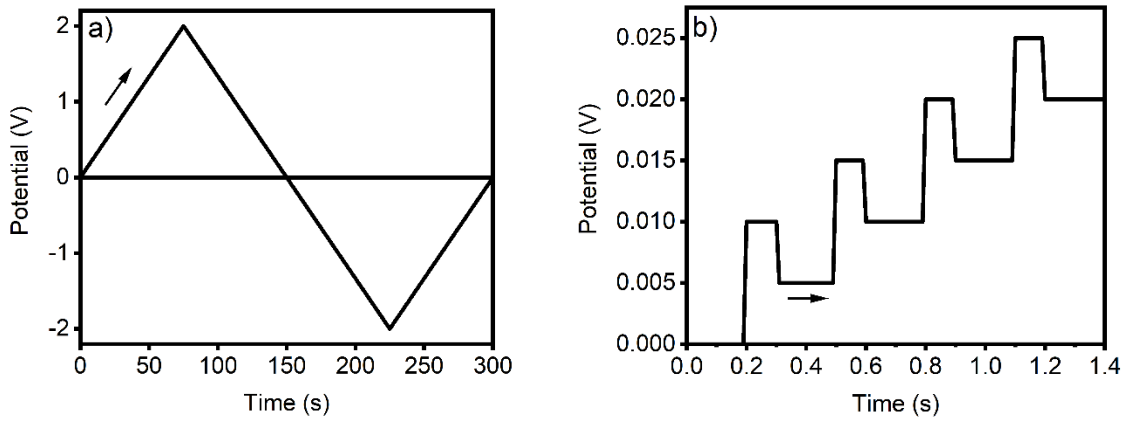

Figure 1.10. Typical (arbitrary) electrochemical potential behavior as a function of time for CV (a) and DPV (b) experiments.

Fig. 1.10a demonstrates how the voltage potential is applied to the system as a function of time for a typical CV experiment where oxidation and reduction potential ranges are probed. In this plot, the positive potential range is scanned from 0 to 150 seconds and the negative potential range is measure from 150 to 300 seconds. Alternatively, differential pulse voltammetry (Fig. 1.10b) employs a series of voltage pulses which follow a linear sweep pattern. Immediately before each potential change, the current is measured, and this current difference is then

plotted as a function of the potential. Figure 1.10b demonstrates how the plot of this application of electrical potential resembles a staircase as a function of time. DPV is typically performed to supplement CV experiments and can help to resolve overlapping redox signals. It should be noted that charge-build up was not accounted for and is assumed to be negligible in the example plots of Fig. 1.10.

1.5.4 Spectroelectrochemistry. Electrochemistry is useful for determining how many redox events and at what potentials they occur in redox-active species. In order to further probe the specific sites on the molecule at which these electron-transfer events occur, spectroelectrochemistry (SEC) is employed. This technique involves the UV-vis spectral measurement of a compound while simultaneously applying a constant electrical potential to the sample. A description of the sample chamber and simplified apparatus diagram is presented below in Fig. 1.11.

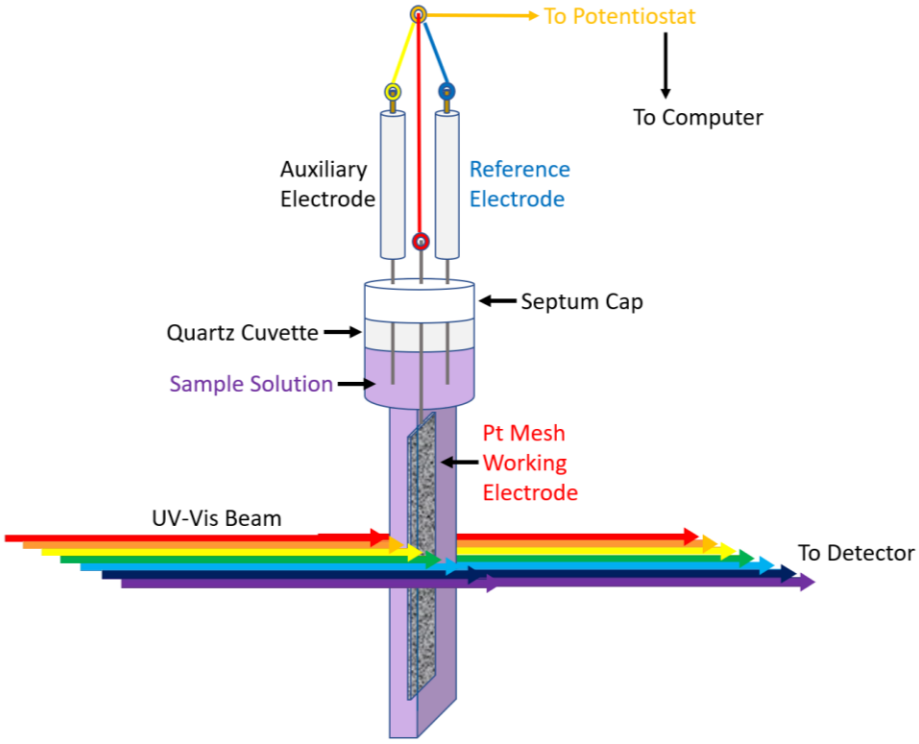

Figure 1.11. Spectroelectrochemical cuvette and simplified apparatus diagram.

Figure 1.11 above illustrates how the spectroelectrochemical cuvette and instrumental apparatus were configured for the associated data that were collected and presented in this thesis. The custom-made quartz cuvette itself holds approximately 2 mL of sample solution and has a 1 mm path length where the beam is directed. This cuvette is held in place by a specialized cuvette holder which fits into the standard cuvette slot in the UV-vis instrument. The sample itself is dissolved in a dry solvent-electrolyte mixture with a typical electrolyte concentration of 0.3 M. The sample chamber is sealed with a malleable, air-tight septum which prevents oxygen from reentering the system once purged. The sample solution is purged with nitrogen or argon gas using a long-needle attachment which reaches the bottom of the cuvette ensuring adequate purging, and a purge exhaust is required to let the excess purge gas escape.

Similar to the electrochemical apparatus presented earlier, the spectroelectrochemical arrangement utilizes the three-electrode apparatus. In this instrumental configuration, the working electrode is comprised of a semi-transparent platinum mesh which allows the redox events to occur near the entirety of the surface area of the mesh. Ag/Ag^{+} reference and platinum auxiliary wire electrodes are again utilized in this configuration. These three electrodes are clamped and attached to the potentiostat which is controlled by a separate computer. Finally, any portions of the UV-vis instrument that are not completely sealed from light are covered with appropriate materials.

Since the research described in this thesis focuses on the elucidation of electronic structures of various macrocyclic systems, SEC plays an important supplemental role to traditional spectroscopic and electrochemical experiments as well as the cutting-edge theoretical simulations that will be described later. The data acquisition process for SEC involves measuring the UV-vis spectrum several times while simultaneously applying a constant potential to the solution via the three-electrode apparatus. The obtained spectra are overlain, and from these plots, useful details may be uncovered. These include isosbestic points which are regions of the UV-vis spectrum where all of the signals converge to a single wavelength. These isosbestic points represent an equilibrium concentration between the two species in the solution: the oxidized and unoxidized components. Finally, isosbestic points will only be observed when there is a clean conversion of the two species, involving no side product formation. On either side of these isosbestic points, the existing signals will either increase or decrease in intensity. These intensity changes indicate the sites on the molecule where redox activity is occurring.

1.5.5 Computational Techniques. So far, all techniques described which assist in the investigation of electronic structures in macrocycles are instrumental physical methods. The use of computational chemistry allows for detailed theoretical-based investigations of electronic structure which directly supplements these physical methods described previously. Since the research included herein relies heavily on photonic excitation which involves the transfer of electrons, electron correlation must be considered in the computational approach used to simulate these systems and processes. For theoretical calculations of the excited states and electronic structures of macrocyclic species, it has been well-established that modern density functional theory (DFT) and time-dependent DFT (TDDFT) approaches are currently most suitable with respect to accuracy and computational cost.

To clarify, DFT and TDDFT calculations were employed in this body of work to theoretically analyze the electronic structure of macrocyclic compounds. Both of these types of calculations are run separately from each other for each compound but are still used in tandem, and the DFT calculations provide different valuable information from the TDDFT calculations, which are important in their own right. Specifically, the Density Functional Theory single-point calculations provide important electronic structural information such as the electron density distribution and energy of each molecular orbital. In cases where the MOs involved in the photoexcitation event are known, it is possible to examine where on the molecule the electron density is localized (or delocalized) prior to and just after photoexcitation in an effort to determine the nature of the electron transfer activity. To supplement the DFT calculations, Time-Dependent Density Functional Theory calculations are used herein to simulate the

absorption spectra of macrocycles. The TDDFT data also provides detailed theoretical predictions of the nature and probability of each absorption signal.

Whereas DFT methods are typically useful for exploring the energies and electronic density distributions of molecular orbitals as a snapshot in time, TDDFT methods provide a means of quantitatively calculating data involving excited states, which involves dynamic processes; therefore, TDDFT calculations are routinely utilized in spectroscopic simulations. The "time-dependent" prefix on the TDDFT term is derived from the equivalence of the wave function to the electronic density, both of which are time-dependent and accounted for in these types of calculations.

With regard to the specific calculations performed in this body of work, both DFT and TDDFT calculations were run in tandem for each project/chapter. These methods were utilized based on their ability to account for electron correlation effects, in addition to providing sufficient accuracy with reasonable/minimal computational cost. For the DFT and TDDFT calculations performed on the porphyrins and phthalocyanines in this thesis, the medium-sized 6-31G(d) basis set[22] was used in most cases. This is a result of previous calculations performed on similar systems by the Nemykin Research Group where smaller basis sets were found to provide less (unacceptably) accurate results and larger basis sets provided similar accuracies to 6-31G(d), but with a greater computational cost.[23]

Still within the context of DFT/TDDFT calculations, the use and mentioning of exchange correlation functionals (ECFs) is another subtopic that will emerge throughout chapters 2-9. An exchange correlation functional is a computational approach which accumulates all electronic

energy contributions as a functional of the electronic density. These energy terms include the exchange energy from the antisymmetric wavefunction, electron correlation effects on kinetic and potential energies, and the self-interaction energy. Given the large number of available exchange correlation functionals, the main thing to focus on (in our experience) is the amount of Hartree-Fock exchange that is accounted for in the ECF being considered. Hartree-Fock exchange correlates the extent to which electrons of like spin avoid each other. It is a term in the Hartree-Fock equations which approximates the wave function and energy of a quantum many-body system. Also, Hartree-Fock exchange has a large effect on geometrical displacement upon excitation. Previous work on this topic by Grimme,[24] where 40 conjugated small molecules were sampled, suggests that 30-40% of Hartree-Fock exchange is required within the utilized ECF to (on average) achieve the most accurate results for the simulation of UV-vis spectra. Our approach for most sample sets is to select one or two samples, and run multiple calculations on them using several different ECFs which span the range of Hartree-Fock exchange to identify the best-performing ECF for the particular sample set.

The only other types of calculations that will be encountered in future chapters are the semiempirical PPP and ZINDO/S methods. These methods are more primitive than DFT/TDDFT and historically allowed for the calculation of geometries, energies, and spectra while accounting for electron correlation effects. Semi-empirical methods are derived from vast empirical data sets and represent simplified versions of Hartree-Fock theory. Due to significant recent advances in computing hardware, the resources now exist to implement DFT/TDDFT calculations on systems which would have been too computationally demanding in the past;

therefore, in cases were semiempirical methods are mentioned, it is for comparison with our modern DFT/TDDFT data.

1.6 Description of Frontier Orbitals

In a general context, frontier orbitals represent the outermost orbitals of a molecule such as the HOMO and LUMO. In the case of porphyrins and phthalocyanines, the frontier orbitals are typically the HOMO-1, HOMO, LUMO, and LUMO+1. These four frontier orbitals are involved in the bulk of photonic excitations that occur within the optical window. Throughout this thesis, special attention will be paid to the ΔHOMO and ΔLUMO values, where ΔHOMO is defined as the energy difference between HOMO and HOMO-1, while ΔLUMO is the energy difference between LUMO and LUMO+1. Depending on the magnitude of ΔHOMO relative to ΔLUMO (whether or not ΔHOMO is greater than or less than ΔLUMO), macrocycles can essentially be classified into one of two possible electronic structure types: those being “naturally occurring” or synthetic. The “naturally occurring” designation is used as a very general descriptor which more accurately indicates that the electronic structure resembles those of naturally occurring reduced porphyrinoids, such as those discussed in section 1.3. Mentioned within that section was the fact that a ΔHOMO < ΔLUMO relationship will be observed for naturally occurring reduced porphyrinoids and the opposite ΔHOMO > ΔLUMO relationship can be expected for synthetic porphyrins and phthalocyanines.

The focus of this thesis involves the design and evaluation of synthetically prepared porphyrins, phthalocyanines, and triazacorroles where attempts were made to impart specific

structural modifications to the macrocyclic cores in an effort to manipulate the frontier orbital energies in a way that the molecules end up with a ΔHOMO < ΔLUMO relationship which would reflect the ordering of frontier orbitals in naturally occurring reduced porphyrinoids. The physical implications of a synthetic porphyrinoid having a "natural" (ΔHOMO < ΔLUMO) electronic structure are negligible; therefore, from a scientific standpoint, the goal of achieving this specific layout of the frontier orbitals is largely meant to be a demonstration of our understanding of how electronic structures and their subsequent optical absorption profiles can be manipulated in a targeted and specific manner through structural modification.

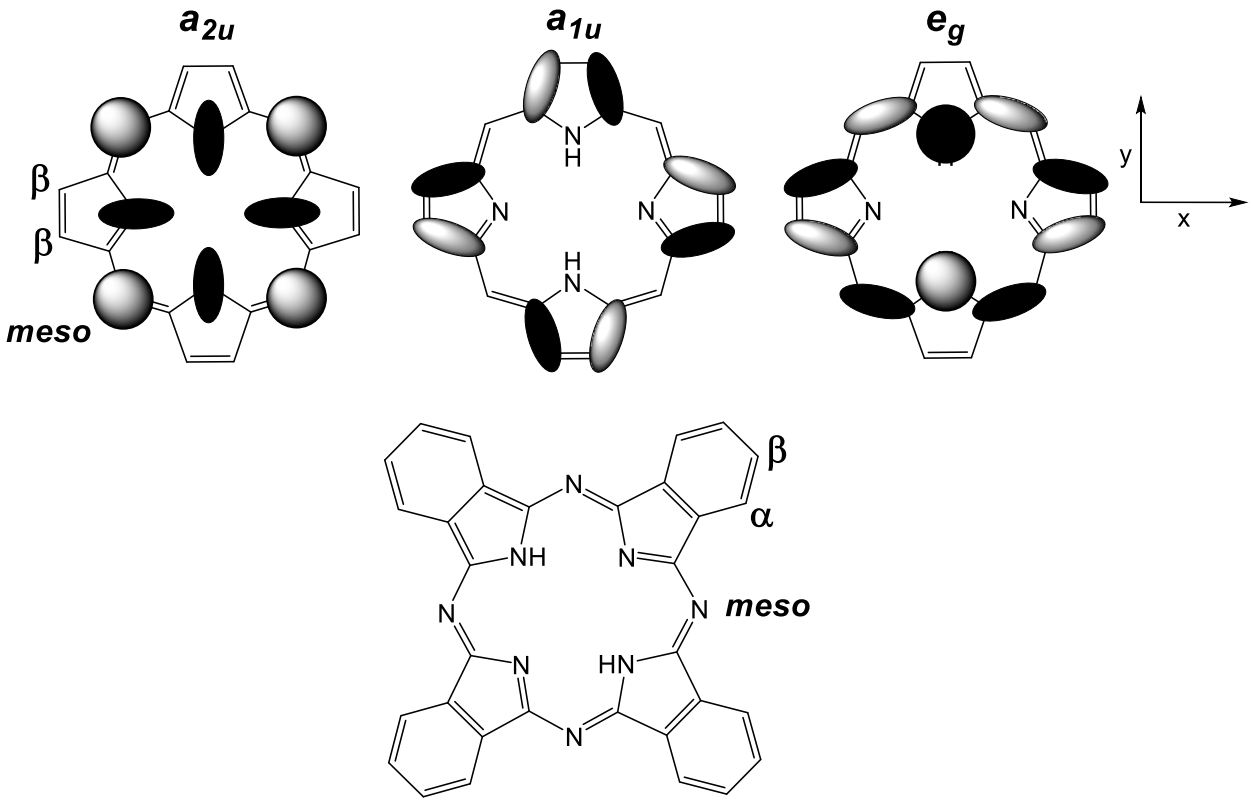

Figure 1.12. Gouterman's frontier molecular orbitals and atomic designations of metal-free porphyrin (upper row) and list of atomic designations for metal-free phthalocyanine (lower).

In order to influence the energetic ordering of frontier orbitals, structural modifications can be performed where, depending on where on the macrocycle the modification occurs and the electronic nature of the substituent, different results may be afforded. For porphyrin systems, if you were to add electron-withdrawing groups onto the *meso*-positions (Fig. 1.12), the resulting orbital overlap would stabilize the a_{2u} orbital, moving it to a lower energy. Depending on the nature of the considered porphyrin, the a_{2u} orbital is usually either the HOMO or the HOMO-1. Conversely, if you added electron donating groups onto the *meso*-positions, a_{2u} would be destabilized and move to a higher energy. The same can be said of the a_{1u} orbital and its energy, except to modify the energy of this orbital, the same structural manipulations would need to take part at the β-positions instead of the *meso*-positions. The spectral implications of this include being able to tune the energy of the λ_{max} band by adjusting the HOMO-LUMO gap by lowering or increasing the energy of either a_{1u} or a_{2u} (whichever is at a higher energy based on the particular system), since this transition is almost always dominated by HOMO→LUMO excitations. The doubly-degenerate e_g orbitals, which comprise ΔLUMO in most cases, can also be manipulated by extending the π-system in either the x- or y-direction, and this was the logic that I exploited in a few of the chapters included herein. Phthalocyanines have similar shaped frontier orbitals to porphyrin; however, their four extra benzene rings (relative to porphyrin) require an additional atomic designation, that being the α-positions which are non-peripheral (Fig. 1.12). For Pc systems, adding electron-donating groups to the α-positions lowers the band gap and shifts the *Q*-band to lower energy while adding electron-withdrawing groups to the α-positions has the opposite effect.

1.7 Research Goals

The overall goal of this thesis is to provide an investigative summary of how the electronic structures and absorption profiles of porphyrins, phthalocyanines, and their derivatives can be manipulated or tuned via structural modification including the addition of substituents, axial ligation of the central metal, or extension of the π-system (Fig. 1.13). Furthermore, the synthetic compounds that were investigated were purposely structurally manipulated in an attempt to shape their electronic structures to end up in a configuration which represents those of naturally occurring reduced porphyrinoids. Specifically, attempts were made to tune the energetic spacing of the four Gouterman's frontier orbitals such that a ΔHOMO < ΔLUMO relationship was achieved. As was mentioned in section 1.3, naturally occurring reduced porphyrinoids possess a ΔHOMO < ΔLUMO relationship while most synthetic porphyrinoids exhibit the ΔHOMO > ΔLUMO relationship. The ΔHOMO and ΔLUMO values can be obtained both experimentally and theoretically. Magnetic circular dichroism is the only experimental technique that allows for the determination of the ΔHOMO/ΔLUMO relationship. The numerical values of ΔHOMO and ΔLUMO cannot be elucidated from MCD; however, it is the signal pattern of the *Q*- and *B*-bands which reveal whether or not ΔHOMO is greater than or less than ΔLUMO. For example, a positive to negative MCD sign sequence (in ascending energy) reveals a ΔHOMO < ΔLUMO relationship, while a negative to positive MCD sign sequence indicates the opposite case. The ΔHOMO and ΔLUMO values can also be obtained from a combination of DFT and TDDFT calculations, all of which will be described in the following chapters.

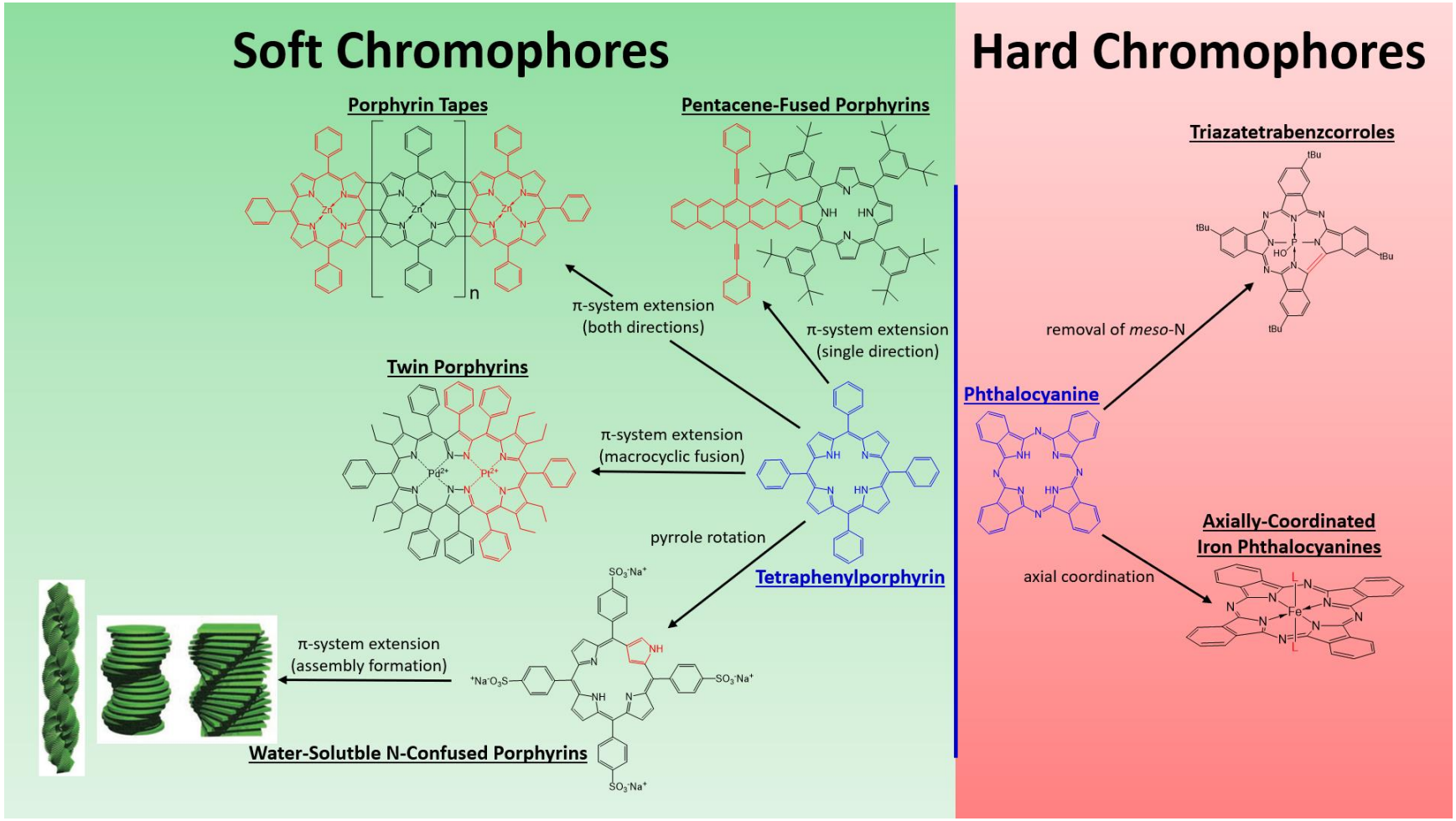

Figure 1.13. Strategic project overview for this thesis (*molecular assembly images adapted from reference 25).

1.7 References

1. a.) Berzelius, J. J. *Lehrbuch der Chemie*; Arnoldische Buckhandlung. Dresden & Leipzig, 1840; pp 67-79. b.) Scherer, J. Chemisch-physiologische Untersuchungen. *Liebigs Ann. Chem. Pharm.* **1841**, *40* (1-64), 30-31. c.) Mulder G. H. Über eisenfreises Hämatin. *J. Prakt. Chem.* **1844**, *32* (186), 197.

2. Thudichum, J. D. W. Report on Researches Intended to Promote an Improved Chemical Identification of Disease. In *Report of the Medical Officer, Privy Council Appendix 7*; H.M.S.O. London, 1867; pp 152-195, 200, and 227-233.

3. Hoppe-Seyler, F. Das Hämatin. *Tübinger Med.-Chem. Untersuchungen*. **1871**, *4*, 523-533.

4. Hoppe-Seyler, F. Über das Chlorophyll der Pflanzen. *Hoppe-Seyler's Z. Physiol. Chem.* **1879**, *4*, 193-203.

5. Soret, J. L. Recherches sur l'Absorption des Rayons Ultraviolets par Diverses Substances. *Arch. Sci. Phys. Nat.* **1883**, *10*, 430-485.

6. Linstead, R. P. Phthalocyanines. I. A New Type of Synthetic Coloring Matters. *J. Chem. Soc.* **1934**, 1016-17.

7. Robertson, J. M. An X-Ray Study of the Structure of the Phthalocyanines. I. The Metal-Free, Nickel, Copper, and Platinum Compounds. *J. Chem. Soc.* **1934**, 615-621.

8. (a) de la Torre, G.; Vazquez, P.; Agullo-Lopez, F.; Torres, T. Phthalocyanines and Related Compounds: Organic Targets for Nonlinear Applications. *J. Mater. Chem.* **1998**, *8*, 1671-

1683. (b) Chen, Y.; Hanack, M.; Blau, W. J.; Dini, D.; Liu, Y.; Lin, Y.; Bai, J. Soluble Axially Substituted Phthalocyanines : Synthesis and Nonlinear Optical Response. *J. Mater. Sci.* **2006**, *41*, 2169-2185. (c) Wrobel, D.; Dudkowiak, A. Porphyrins and Phthalocyanines – Functional Molecular Materials for Optoelectronics and Medicine. *Mol. Cryst. Liq. Cryst.* **2006**, *448*, 617-640.

9. (a) da Silva, R. N.; Cunha, A.; Tome, A. C. Phthalocyanine-Sulfonamide Conjugates: Synthesis and Photodynamic Inactivation of Gram-Negative and Gram-Positive Bacteria. *Eur. J. Med. Chem.* **2018**, *154*, 60-67. (b) George, L.; Hiltunen, A.; Santala, V.; Efimov, A. Photo-Antimicrobial Efficacy of Zinc Complexes of Porphyrin and Phthalocyanine Activated by Inexpensive Consumer LED Lamp. *J. Inorg. Biochem.* **2018**, *183*, 94-100. (c) Sindelo, A.; Osifeko, O. L.; Nyokong, T. Synthesis, Photophysicochemical and Photodynamic Antimicrobial Chemotherapy Studies of Indium Pyridyl Phthalocyanines: Charge Versus Bridging Atom. *Inorg. Chim. Acta* **2018**, *476*, 68-76.
10. (a) Juzenas, P. Lasers in Therapy of Human Diseases. *Trends Cancer Res.* **2005**, *1*, 93-110. (b) O'Riordan, K.; Akilov, O. E.; Hasan, T. The Potential for Photodynamic Therapy in the Treatment of Localized Infections. *Photodiagn. Photodyn. Ther.* **2005**, *2*, 247-262.
11. (a) Automotive Lighting Authority. https://lightheadz.com/xenon-lamp/ (accessed Sep 5, 2020). (b) Olis. Olis Magnet for MCD. https://olisweb.com/portfolio-item/desa-magnet-for-mcd-2/ (accessed Sep 5, 2020). (c) ThorLabs. Photomultiplier Modules. https://www.thorlabs.com/newgrouppage9.cfm?objectgroup_id=2909 (accessed Sep 5, 2020).

12. Waluk, J.; Michl, J. Perimeter Model and Magnetic Circular Dichroism of Porphyrin Analogs. *J.Org.Chem*. **1991**, *56*, 2729-2735.

13. Michl, J. Magnetic Circular Dichroism of Cyclic π-Electron Systems. 2. Algebraic Solution of the Perimeter Model for the *A* and *B* Terms of High-Symmetry Systems with a (4N + 2)-Electron [π]Annulene Perimeter. *J. Am. Chem. Soc*. **1978**, *100*, 6801-6811.

14. Michl, J. Magnetic Circular Dichroism of Cyclic π-Electron Systems. 2. Algebraic Solution of the Perimeter Model for the *B* Terms of Systems with a (4N + 2)-Electron [π]Annulene Perimeter. *J. Am. Chem. Soc*. **1978**, *100*, 6812-6818.

15. Michl, J. Magnetic Circular Dichroism of Cyclic π-Electron Systems. 3. Classification of Cyclic π Chromophores with a (4N + 2)-Electron [π]Annulene Perimeter and General Rules for Substituent Effects on the MCD Spectra of Soft Chromophores. *J. Am. Chem. Soc*. **1978**, *100*, 6819-6824.

16. Kaminsky, J.; Kriz, J.; Bour, P. On the Magnetic Circular Dichroism of Benzene. A Density-Functional Study. *J. Chem. Phys.* **2017**, *146*(14), 144301/1-144301/8.

17. Gouterman, M. J. In *The Porphyrins*; Dolphin, D., Ed.; Academic Press: New York, 1978; Vol. III, pp 1−165.

18. (a) Seybold, P. G.; Gouterman, M. J. Porphyrins. XIII. Fluorescence Spectra and Quantum Yields. *Mol. Spectrosc*. **1969**, *31*, 1−13. (b) Gouterman, M. J. Spectra of Porphyrins. *Mol. Spectrosc.* **1961**, *6*, 138−163.

19. Stephens, P. J. Magnetic Circular Dichroism. *Adv. Chem. Phys.* **1976**, *35*, 197-264.

20. Mack, J.; Stillman, M. J.; Kobayashi, N. Application of MCD Spectroscopy to Porphyrinoids. *Coord. Chem. Rev.* **2007**, *251*, 429-453.

21. Rieger, P.H. Electrochemistry, 2nd ed.; Chapman & Hall: New York, NY., 1993; pgs 1- 477.

22. Hehre, W. J; Ditchfield, R.; Pople, J. A. Self-Consistent Molecular Orbital Methods. 12. Further Extensions of Gaussian-type Basis Sets for Use in Molecular-Orbital Studies of Organic Molecules. *J. Chem. Phys.* **1972**, *56*, 2257-2261.

23. Beloslodov, R. V.; Nevonen, D. E.; Rhoda, H. M.; Sabin, J. R.; Nemykin, V. N. Simultaneous Prediction of the Energies of Q_x and Q_y Bands and Intramolecular Charge-Transfer Transitions in Benzoannulated and Non-Peripherally Substituted Metal-Free Phthalocyanines and Their Analogues: No Standard TDDFT Silver Bullet Yet. *J. Phys. Chem. A.* **2019**, *123*, 132-152.

24. Dierksen, M.; Grimme, S. The Vibronic Structure of Electronic Absorption Spectra of Large Molecules: A Time-Dependent Density Functional Study on the Influence of “Exact” Hartree-Fock Exchange. *J. Phys. Chem. A.* **2004**, *108*, 10225-10237.

25. Feng, X.; Liu, C.; Wang, X.; Jiang, Y.; Yang, G.; Wang, R.; Zheng, K.; Zhang, W.; Wang, T.; Jiang, J. Functional Supramolecular Gels Based on the Hierarchical Assembly of Porphyrins and Phthalocyanines. *Front. Chem. (Lausanne, Switz.)* **2019**, *7*, 336/1-336/20.

2. Unsymmetrical Pentacene- and Pentacenequinone-Fused Porphyrins: Understanding the Effect of Cross- and Linear-Conjugation

2.1 Chapter Preface

Through various implementations of structural design, the electronic structures and correspondingly, the optical absorption spectra of porphyrins can be significantly and purposefully influenced. Common porphyrin structural manipulations for such purposes include metalation and/or ligation to the metal center, addition of substituents to the *meso* or β-periphery (where the substituents may be electron-donating, electron-withdrawing, or sterically bulky), and extension of the π-system. Within this chapter, the macrocyclic cores are comprised of metal-free and transition-metal (Ni or Zn) tetraphenylporphyrin and the π-system of these cores was extended in a single direction through the addition of a pentacene moiety (in all, two different pentacene moieties were utilized).

Also, the magnitudes of ΔHOMO and ΔLUMO, with respect to each other, will be closely monitored experimentally (using magnetic circular dichroism) and theoretically (using TDDFT calculations). Since most naturally occurring reduced porphyrinoids possess a ΔHOMO < ΔLUMO relationship, it will be interesting to observe if the synthetically prepared compounds featured in this chapter demonstrate the ΔHOMO > ΔLUMO relationship of most other synthetic macrocycles or if the π-system extension in a single direction influences the

macrocycle in such a way that the inverse ΔHOMO < ΔLUMO relationship will be observed, such as with the naturally occurring reduced porphyrinoids. It was hypothesized that extension of the π-system in a single direction with the electron-donating pentacene fragment should stabilize the e_{gy} orbital (which corresponds to LUMO+1 in this case). This will surely increase the value of ΔLUMO which, prior to addition of the pentacene moieties, is comprised of the doubly degenerate e_{gx} and e_{gy} orbitals. Whether or not this increase in the magnitude of ΔLUMO will be large enough to overtake ΔHOMO was one of the focal points of this work.

2.2 Introduction

π-Extended structures have received intense attention due to their relevance to various topics in chemistry, physics and materials science.[1,2] π-Extended porphyrins fused with polycyclic aromatic hydrocarbons (PAHs) are especially attractive as they are reminiscent of "nanographenes" doped with heteroatoms. π- Extended porphyrins possess a unique combination of photophysical, optoelectronic, and physicochemical properties, which are of broad interest in various areas ranging from biomedicine to organic electronics.[3-14] π-Extended porphyrins can be classified into two categories: *meso*, β-fused and β, β-fused. A number of π-extended porphyrins fused with PAHs at *meso*, β-fused positions have been achieved.[15-26] These π-extended porphyrins display remarkable electronic and optical properties which have never been reported for other molecular systems. We are interested in fusing porphyrins with larger PAHs at porphyrin β, β-positions.[27-32] β, β-Fusion offers unique geometry and topology for PAHs not accessible through *meso*, β-fusion, which could serve as a powerful tool to construct novel π-extended systems with unprecedented electronic, optical and photophysical properties.

In similar previous work, a collaborating group prepared pentacenequinone- and pentacene-fused porphyrin dimers[30] (Fig. 2.1). Although the pentacenequinone- and pentacene-fused porphyrin dimers possess the same D_{2h} symmetry, their electronic and optical properties are strikingly different; yet, both are unprecedented and very interesting. In particular, the pentacene-fused nickel porphyrin dimer exhibited abnormally high stability, which was > 60 times more stable than the corresponding pentacene (Fig. 2.1). The unusual properties observed for these pentacenequinone- and pentacene-fused porphyrin dimers motivated us to investigate the underlying factors which determine the observed redox and optical behaviour. The first questions to be answered are: will other pentacenequinone- and pentacene-fused porphyrins possess similar properties? How does cross-conjugation (pentacenequinone-fused) and linear-conjugation (pentacene-fused) perturb the spectroscopy differently? Very importantly, stability issues have been one major challenge for longer acenes to overcome. Will fusion of Ni(II) porphyrin to acenes potentially become an effective strategy to tackle this challenge? Cross-conjugated chromophoric systems have been rarely investigated.[33-34] Through answering these questions, we hope to provide information on new principles for materials design. In this work, we introduce a new series of monopentacenequinone- and monopentacene-fused porphyrins (Fig. 2.1). Different from their dimer analogues which are of D_{2h} symmetry, monopentacenequinone- and monopentacene-fused porphyrins have effective C_{2v} symmetry.

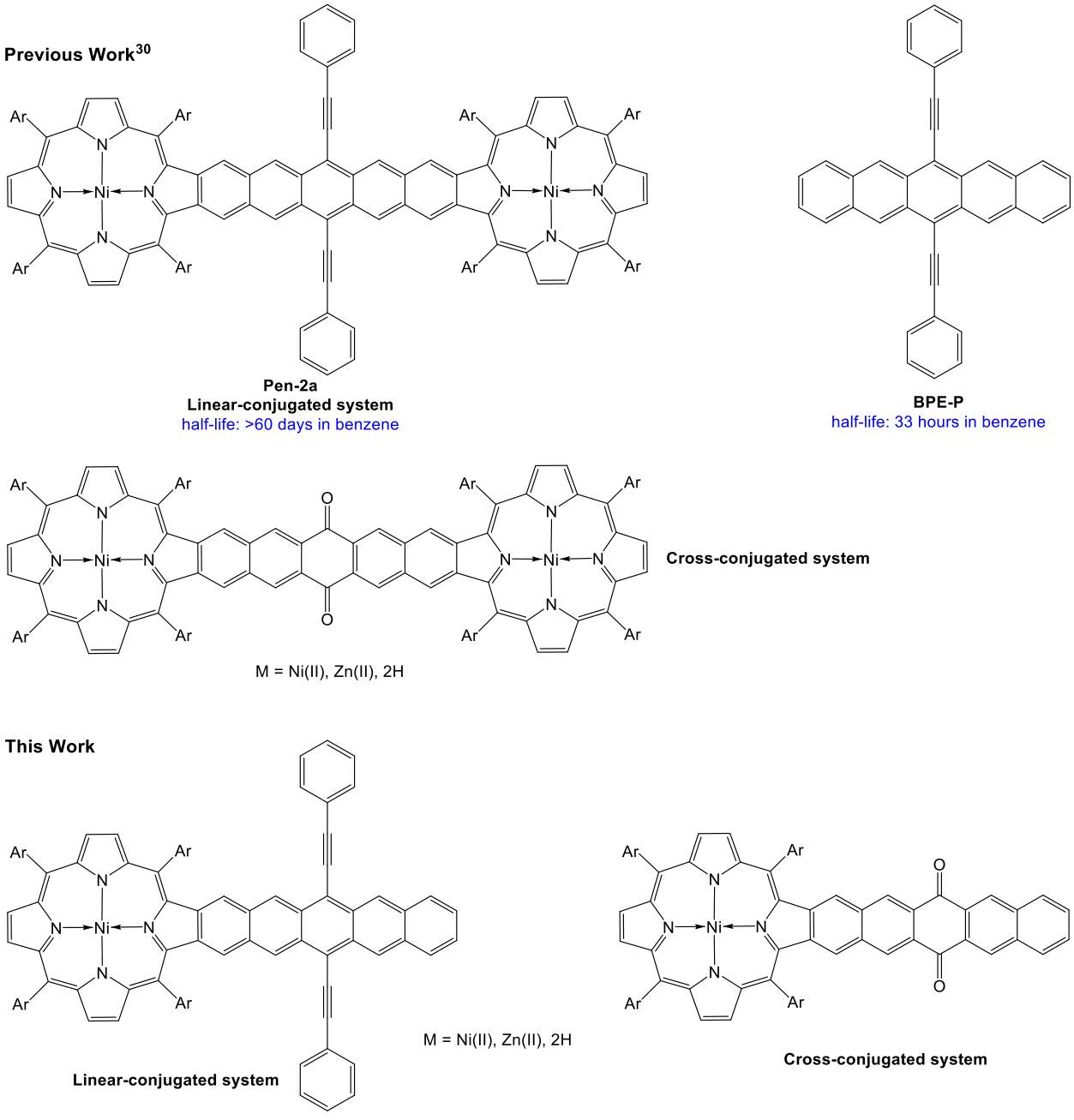

Figure 2.1 Pentacenequinone- and pentacene-fused porphyrins.

In this work, Zn(II)-, 2H- and Ni(II)-pentacene-fused porphyrins have also been made available to investigate the central metal effect with their structures presented below in Fig. 2.2. Nickel and zinc were chosen due to their abundance and low cost. These π-extended porphyrin systems were studied using UV-vis, florescence and magnetic circular dichroism (MCD) spectroscopies, cyclic voltammetry (CV), and spectroelectrochemistry. DFT and TDDFT calculations were carried out to further understand the electronic transitions of these compounds.

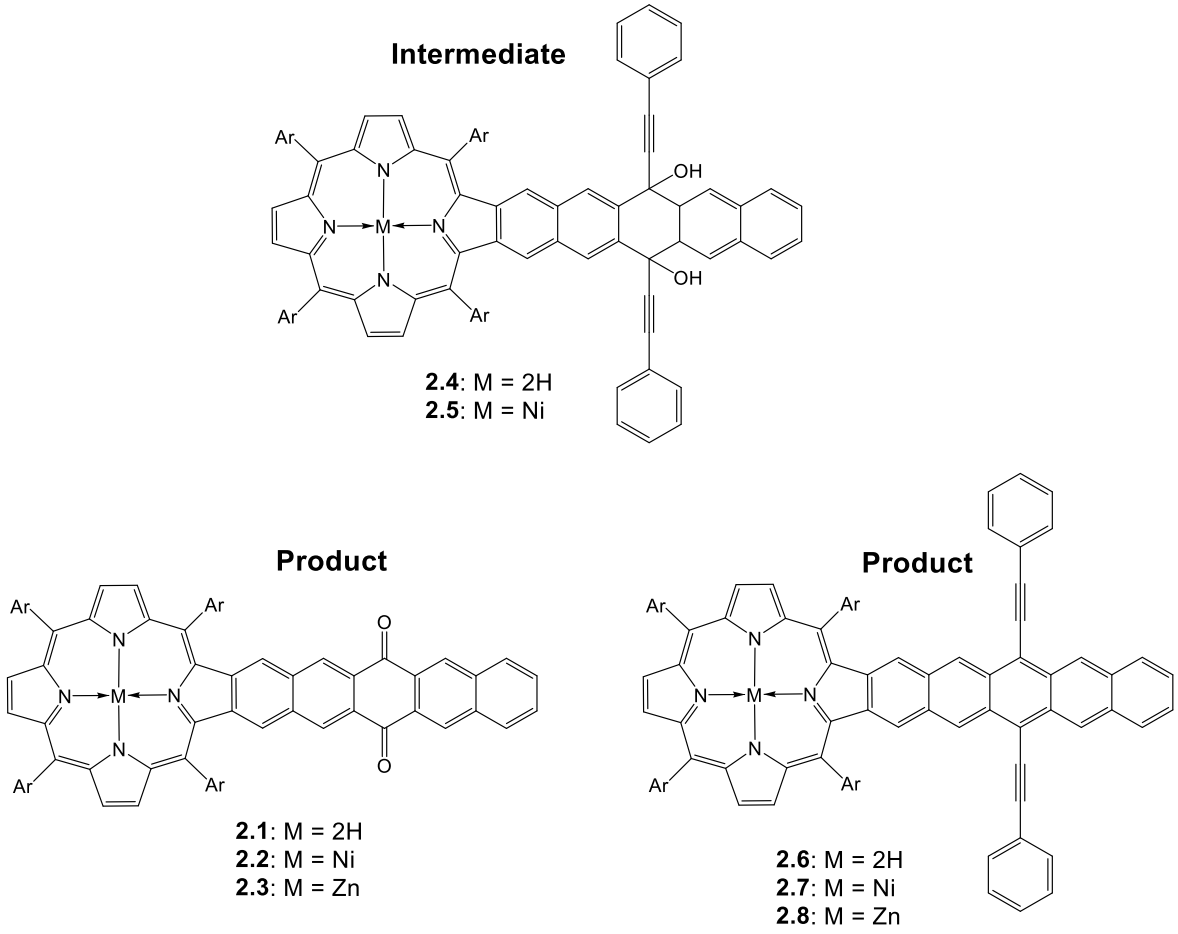

Figure 2.2. Structures of the pentacenequinone-fused porphyrins **2.1**-**2.3**, pentacene-fused porphyrin intermediates **2.4** and **2.5**, and pentacene-fused porphyrins **2.6**-**2.8**.

2.3 Results and Discussion

2.3.1 UV-Vis Spectroscopy. The UV-vis absorption spectra of pentacenequinone-fused porphyrins **2.1**-**2.3** and pentacene-fused porphyrins **2.6**-**2.8** are compiled in Figs. 2.3 and 2.4, respectively.

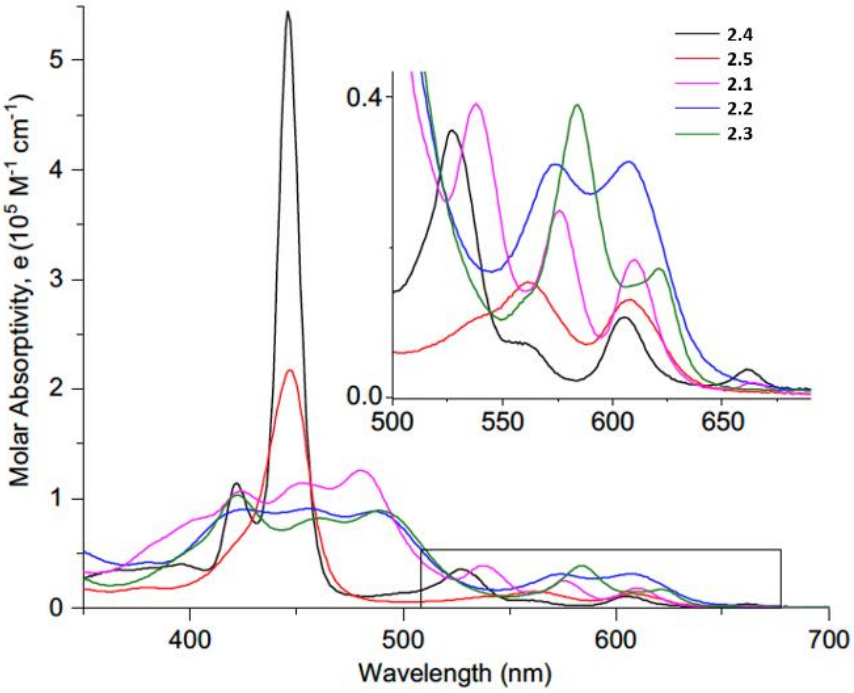

Figure 2.3 UV-Vis absorption spectra of **2.1**-**2.5** in DCM. Inset: Expanded *Q*-band region.

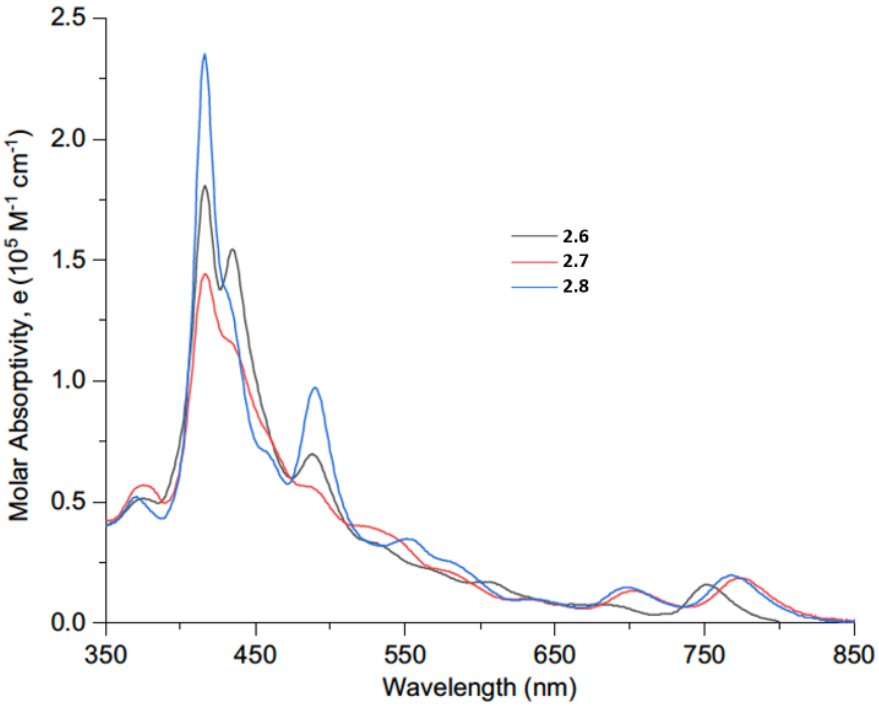

Figure 2.4. UV-Vis-NIR spectra of **2.6**-**2.8** in DCM.

All three monoporphyrin-fused pentacenequinones **2.1**-**2.3** displayed three prominent bands in the Soret-band region spanning from 320~550 nm. The intensities of these transitions are almost even, which is in sharp contrast to their pentacenequinone-fused porphyrin dimers which show non-typical porphyrin absorptions. This unusual splitting pattern has never been observed in any other porphyrins to our knowledge.[35] It is interesting to note that when phenylacetylide was added to the quinone groups of **2.1** and **2.2**, the absorption bands of the resulting porphyrins (**2.4** and **2.5**) reverted back to typical porphyrin absorptions with one sharp Soret-band and several weaker *Q*-bands. It is apparent that the abnormal spitting pattern observed for the Soret-bands of **2.1**-**2.3** can be mainly attributed to the cross-conjugation in **2.1**-**2.3**. The linear-conjugated pentacene-fused porphyrins **2.6**-**2.8** showed complex features of the Soret-bands which is not uncommon for porphyrins with reduced symmetry. Additionally,

the electronic interaction between the porphyrin and pentacene causes an absorption spanning across most of the visible portion and into the near-infrared (**2.6**: λmax = 753 nm, **2.7**: λmax= 773 nm, **2.8**: λmax = 770 nm) region of the electromagnetic spectrum, which is expected for π-extended systems. On the other hand, **2.6**-**2.8** exhibited many excessive absorption peaks compared to a normal π-extended porphyrin possessing C_{2v} symmetry,[3-13] suggesting the existence of complex electronic events in the molecular system. The sharp contrast in absorption spectra between the cross- and linear-conjugated system reflects different effects of electronic perturbations on the optical properties of these two systems. Further investigation of the electronic transitions present in these molecules was necessary to better understand their optical properties.

2.3.2 MCD Spectroscopy. Magnetic circular dichroism (MCD) spectroscopy was utilized to understand the unusual splitting pattern of the absorption bands of **2.1**-**2.3** and **2.6**-**2.8**. The UV-vis and MCD spectra of porphyrins **2.1**-**2.3** and **2.6**-**2.8** are shown in Figures 2.5 and 2.6. In the case of metal-free **2.1**, four MCD Faraday *B*-terms were observed at 666, 616, 580, and 549 nm in the *Q*-band region. The two lower energy bands have negative, and the two higher energy bands have positive amplitudes. These transitions correlate well with the absorption bands at 664, 610, 575, and 537 nm observed in the UV-vis spectrum of this compound. In the Soret-band region, the most intense transitions at 480, 453, and 423 nm observed in the UV-vis spectrum of **2.1** correlate well with the negative MCD transition at 474 nm, negative amplitude shoulder at 450 nm, and a positive amplitude *B*-term at 423 nm. In addition, the MCD pseudo *A*-term was observed between 392 and 376 nm (Figure 2.5). The *Q*-band region in the

transition-metal complexes **2.2** and **2.3** differs substantially from metal-free **2.1**. Indeed, in both cases, a pair of the MCD pseudo *A*-terms was observed in the *Q*-band region, with the lower energy pseudo *A*-term being about twice as intense as the higher energy one (Figure 2.5). Such behavior (the presence of two MCD pseudo *A*-terms in the *Q*-band region) has been observed in the case of bimetallic pentaquinone-fused porphyrins published by us.[29] Moreover, the energies of the main transitions observed in the *Q*-band region of porphyrins **2.2** and **2.3** are very close to those reported for their doubly fused analogs.[29] This observation suggests the similarity of the HOMO-LUMO gap in mononuclear porphyrins **2.2** and **2.3** and the binuclear analog, which might indicate the (at least partial) π-system interruption in the latter compounds caused by the pentaquinone bridge. The MCD signatures of porphyrins **2.2** and **2.3** in the Soret-band region resemble those in metal-free **2.1**. In particular, the two lower energy bands in the UV-vis spectra of **2.2** (486 and 456 nm) and **2.3** (489 and 460 nm) are associated with two *B*-terms of negative amplitude, while the intense higher energy band (424 nm for **2.2** and 422 nm for **2.3**) is associated with the positive amplitude *B*-term in the MCD spectra. In addition, an MCD pseudo *A*-term was observed for both transition-metal compounds between 395 and 369 nm. It is expected that elongation of the porphyrin conjugation using a pentaquinone substituent will significantly increase the energy difference between Gouterman's pair of $e_g(x)$ and $e_g(y)$ orbitals (in traditional D_{4h} point group notation).[36,37] The MCD spectra in the *Q*-band region, however, have a negative-to-positive amplitude sequence (in ascending energy), which is indicative of a ΔHOMO>ΔLUMO relationship (ΔHOMO is the energy difference between the a_{1u} and a_{2u} MOs in Gouterman's notation, and ΔLUMO is the energy difference between the $e_g(x)$ and $e_g(y)$ MOs in Gouterman's notation).[38-42]

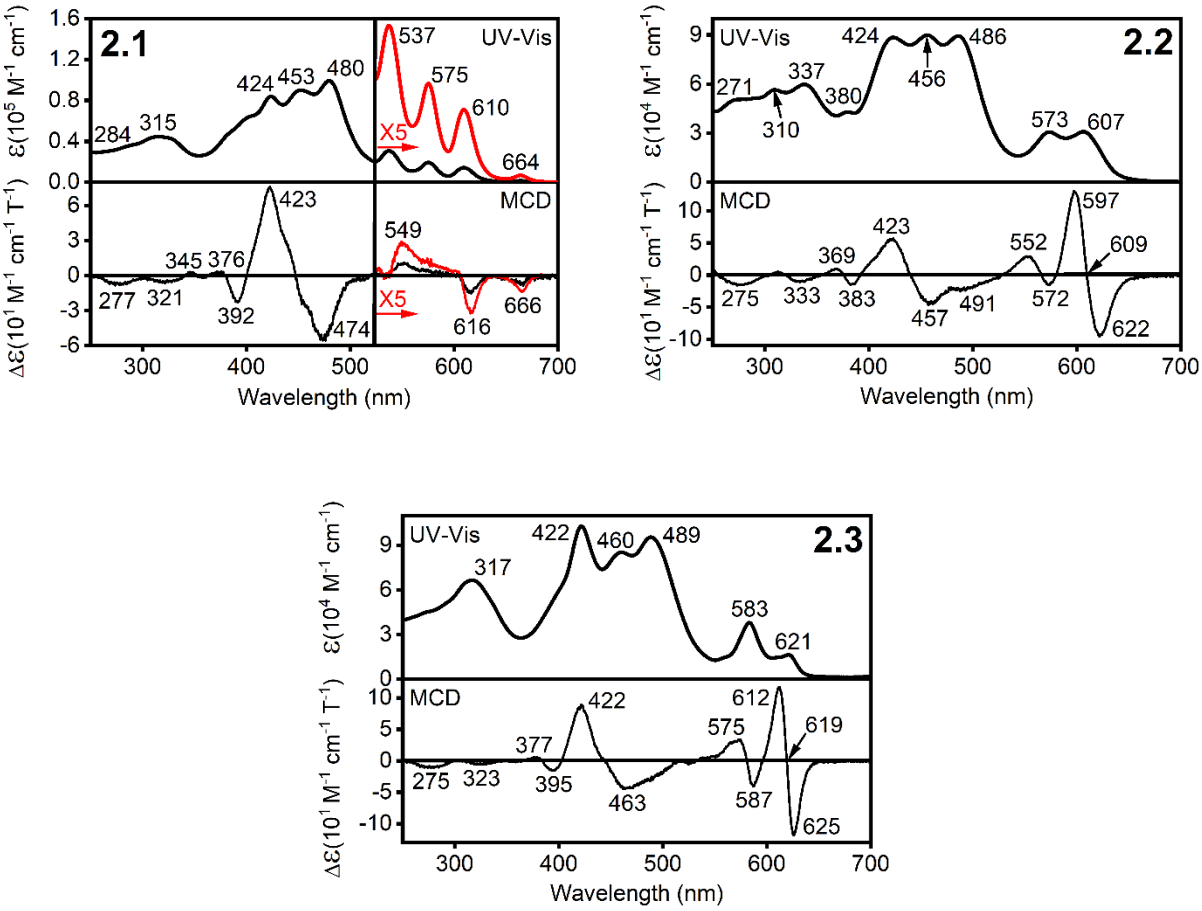

Figure 2.5. UV-Vis and MCD spectra of porphyrins **2.1**-**2.3** in DCM.

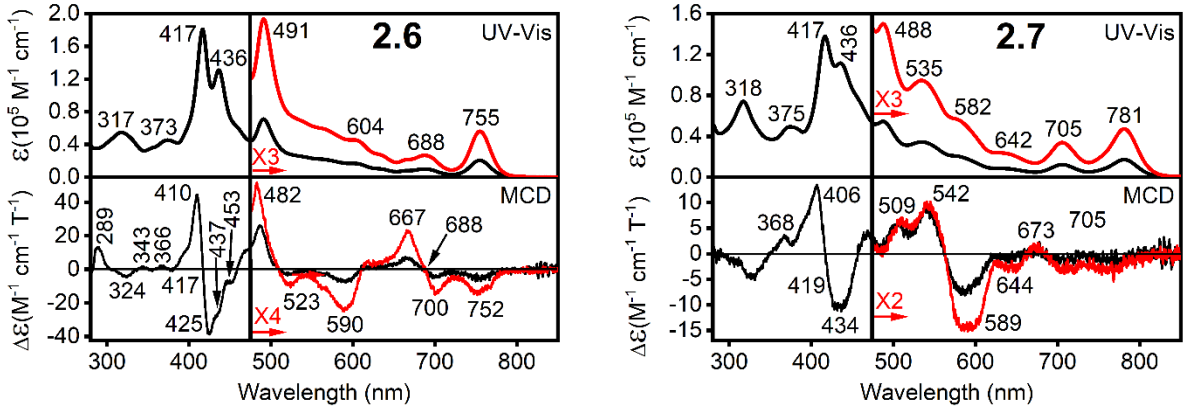

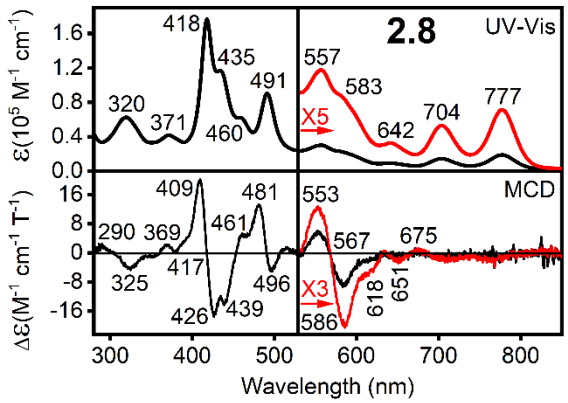

Figure 2.6. UV-Vis and MCD spectra of porphyrins **2.6**-**2.8** in DCM.

The *Q*-band region in the pentacene-fused porphyrins **2.6**-**2.8** is significantly more red-shifted compared to that in the pentaquinone-fused porphyrins **2.1**-**2.3** (Figure 2.6). For instance, the lowest energy transition in all compounds was observed between 755 and 781 nm. This band is associated with a very weak MCD *B*-term with negative amplitude. The energy of this weak MCD *B*-term correlates well with the position of the lowest energy transition observed in the UV-vis spectra of **2.6**-**2.7**. The next MCD signal belongs to the pseudo *A*-term centered around 690-705 nm. Unlike in the case of the pentaquinone-fused systems **2.1**-**2.3**, the pseudo *A*-term was observed for the metal-free and transition-metal complexes **2.6**-**2.8**. The center of this pseudo *A*-term correlates well with the UV-vis transitions observed at 688 (**2.6**), 705 (**2.7**), and 704 (**2.8**) nm. Another significantly stronger pseudo *A*-term was observed in the MCD spectra of porphyrins **2.6**-**2.8** between 500 and 560 nm.

In general, the intensity of the MCD signals in porphyrins **2.6**-**2.8** in the 600-800 spectral envelope is significantly lower compared to the intensity of the MCD bands observed for porphyrins **2.1**-**2.3** in the *Q*-band region. Such a dramatic decrease in intensity was also

observed in the doubly-fused pentacene bisporphyrins reported earlier.[29] Interestingly, the lowest energy band position in the porphyrins **2.6**-**2.8** is nearly constant (ΔE ~400 cm^{-1}) and correlates well with an absorption band at 730 nm observed in the UV-vis spectrum of the metal-free bisporphyrin fused by the pentacene bridge. That being said, the red-shifted low energy bands in the shorter π-systems of **2.6**-**2.8** (compared to the bisporphyrin analog) is unexpected. The most resolved MCD spectrum in the Soret-band region was observed for **2.8** (Figure 2.7). In this case, the four most prominent bands observed in the UV-vis spectrum at 491, 460, 435, and 418 nm correlate with two MCD pseudo *A*-terms centered at 489 and 417 nm, and two *B*-terms observed at 461 and 439 nm. Again, the MCD spectra in the *Q*-band region of porphyrins **2.6**-**2.8** have a negative-to-positive amplitude sequence (in ascending energy), which is indicative of a ΔHOMO > ΔLUMO relationship in these compounds.[38-42]

2.3.3 Electrochemistry and spectroelectrochemistry. Taking into consideration the potential redox activity of the pentacene or pentacenequinone fragments, it was interesting to investigate the redox properties of the **2.1**-**2.3** and **2.6**-**2.8** systems. The summary of the electrochemical data is shown in Table 2.1, with the representative examples outlined in Figure 2.7.

Table 2.1. Redox potentials of the studied compounds.

Sample	Redox Potential, V (FcH/FcH^+)
2.1	-1.65 (R_1); -1.84 (R_2); -2.09 (R_3); -2.19 (R_4)
	0.54 (Ox_1); 0.62 (Ox_2); 1.01 (Ox_3)
2.2	-1.60 (R_1); -1.75 (R_2); -1.98 (R_3)

0.43 (Ox_1); 0.60 (Ox_2)

2.3 -1.31 (R_1); -1.67 (R_2); -1.97 (R_3)

0.22 (Ox_1); 0.42 (Ox_2); 0.71 (Ox_3); 0.95 (Ox_4)

2.6 -1.44 (R_1); -1.81 (R_2)

0.19 (Ox_1); 0.64 (Ox_2); 1.04 (Ox_3); 1.49 (Ox_4)

2.7 -1.39 (R_1); -1.75 (R_2); -1.83 (R_3); -2.11 (R_4)

0.14 (Ox_1); 0.45 (Ox_2); 0.62 (Ox_3); 0.97 (Ox_4); 1.26 (Ox_5)

2.8 -1.45 (R_1); -1.85 (R_2)

0.08 (Ox_1); 0.36 (Ox_2); 0.61 (Ox_3); 0.93 (Ox_4); 1.08 (Ox_5); 1.36 (Ox_6)

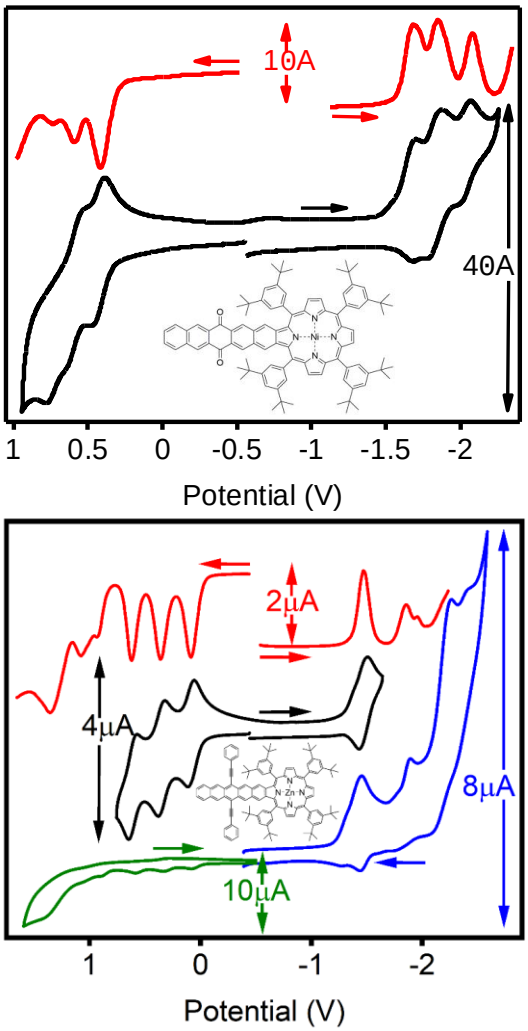

Figure 2.7. Representative examples of CV and DPV data for **2.2** (upper) and **2.8** (lower) in a DCM/0.1M TBAP system. All potentials are referenced to the Fc/Fc^{+} couple.

For each compound, multiple oxidation and reduction processes were observed. In the case of the pentacenequinone compounds, three reversible oxidation processes were observed for **2.1** and **2.2**, while two reversible and two irreversible processes were observed for **2.3**. The first oxidation potential for **2.1**-**2.3** spans over a 320 mV range. Three to four reduction processes

were observed in the **2.1**-**2.3** systems. Up to six oxidation processes were observed for the porphyrins **2.6**-**2.8**, with the first three being reversible. The first oxidation potential in **2.6**-**2.8** have a significantly smaller central ion dependency than **2.1**-**2.3**. Since our DFT calculations discussed below indicate that the HOMO in **2.6**-**2.8** is ~80% localized on the pentacene fragment, such a small dependency on the central metal ion is not surprising. Multiple reduction processes were also observed in **2.6**-**2.8**, with the first reduction potential being nearly constant.

The formation of a relatively stable charge-separated state upon the photoinduced electron transfer process is key for the performance of porphyrins **2.1**-**2.3** and **2.6**-**2.8** in light-harvesting modules of organic solar cells. Since these porphyrins are thought to be used as electron-donors, the formation and stability of their respective cation-radical forms generated under single-electron oxidation conditions using a controlled potential were realized under spectroelectrochemical conditions and investigated in detail. The single-electron oxidation of the transition-metal-centered **2.2** and **2.3** compounds results in a reduction of intensities in the Soret- and *Q*-band regions, in addition to the appearance of new bands at 664 and 901 nm (**2.2**) or 699, 753, 854, and 961 nm (**2.3**, Figure 2.8).

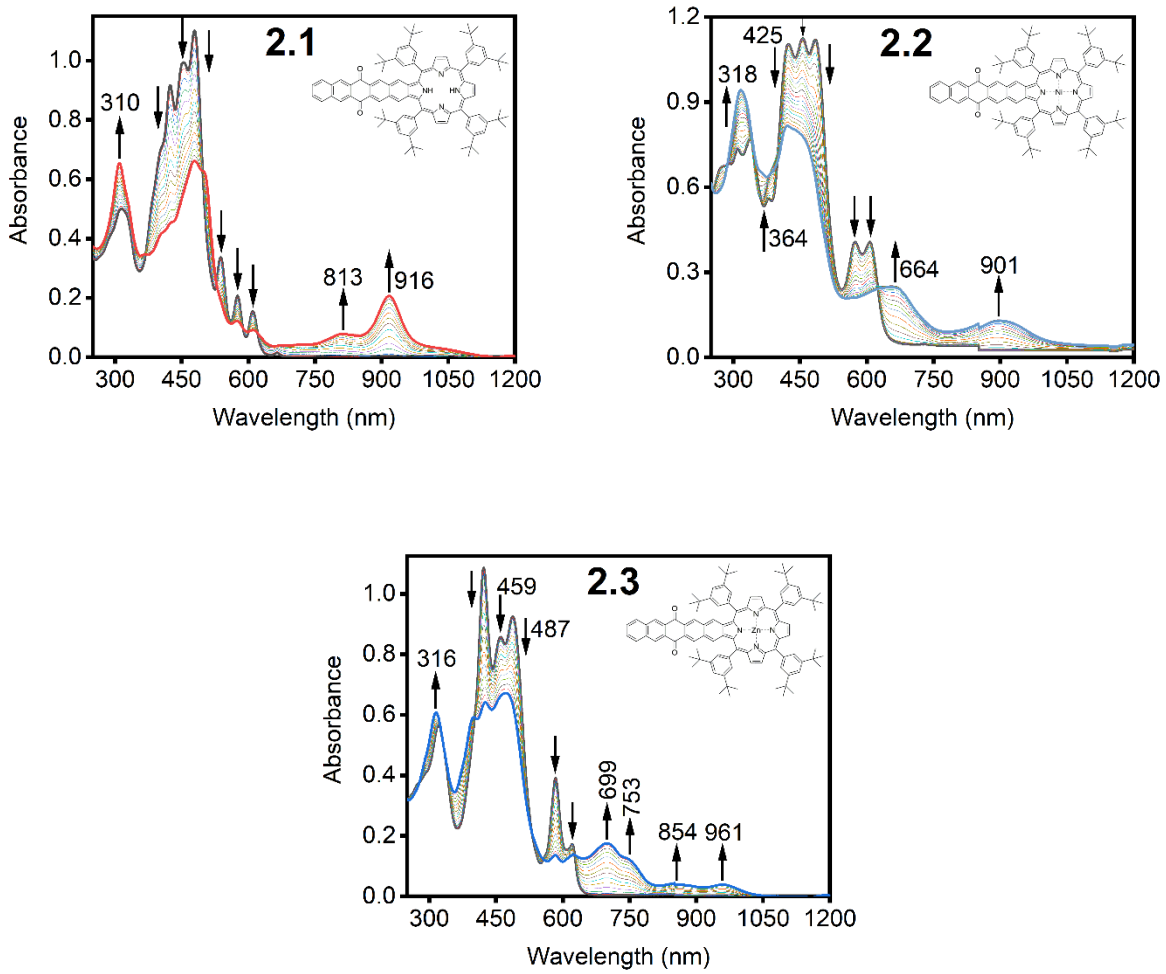

Figure 2.8. Oxidation of neutral **2.1**-**2.3** to **[2.1**-**2.3]**$^{+\bullet}$ cation-radicals under spectroelectrochemical conditions in a DCM/0.3M TBAP system.

The cation-radical species formed under spectroelectrochemical conditions are stable and can be almost quantitatively reduced back to the neutral compounds under spectroelectrochemical conditions (Fig. S2.1 in ESI). The oxidation of the metal-free porphyrin **2.1** under spectroelectrochemical conditions also results in the appearance of new NIR bands at 813 and 915 nm (Figure 2.8); however, reduction of the formed radical-cation species back to the

neutral porphyrin is not quantitative and regenerates only ~70% of the starting material (Fig S2.1 in ESI). The overall spectroscopic signatures of the cation-radical species [**2.1**-**2.3**]$^{+\bullet}$ are typical for cation-radicals of the traditional tetraarylporphyrins.[43-46] In agreement with the DFT calculations, this indicates a lack of interaction between the outer anthraquinone fragment and naphthalene-β,β-fused porphyrin. Thus, the quinone carbonyl fragment interrupts the π-conjugation, and the overall spectroscopy of **2.1**-**2.3** can be viewed as similar to the naphthalene- β,β -fused porphyrin.

On the contrary, the single-electron oxidation of the pentacene-fused porphyrins **2.6**-**2.8** reveals different spectroscopic signatures (Figure 2.9).

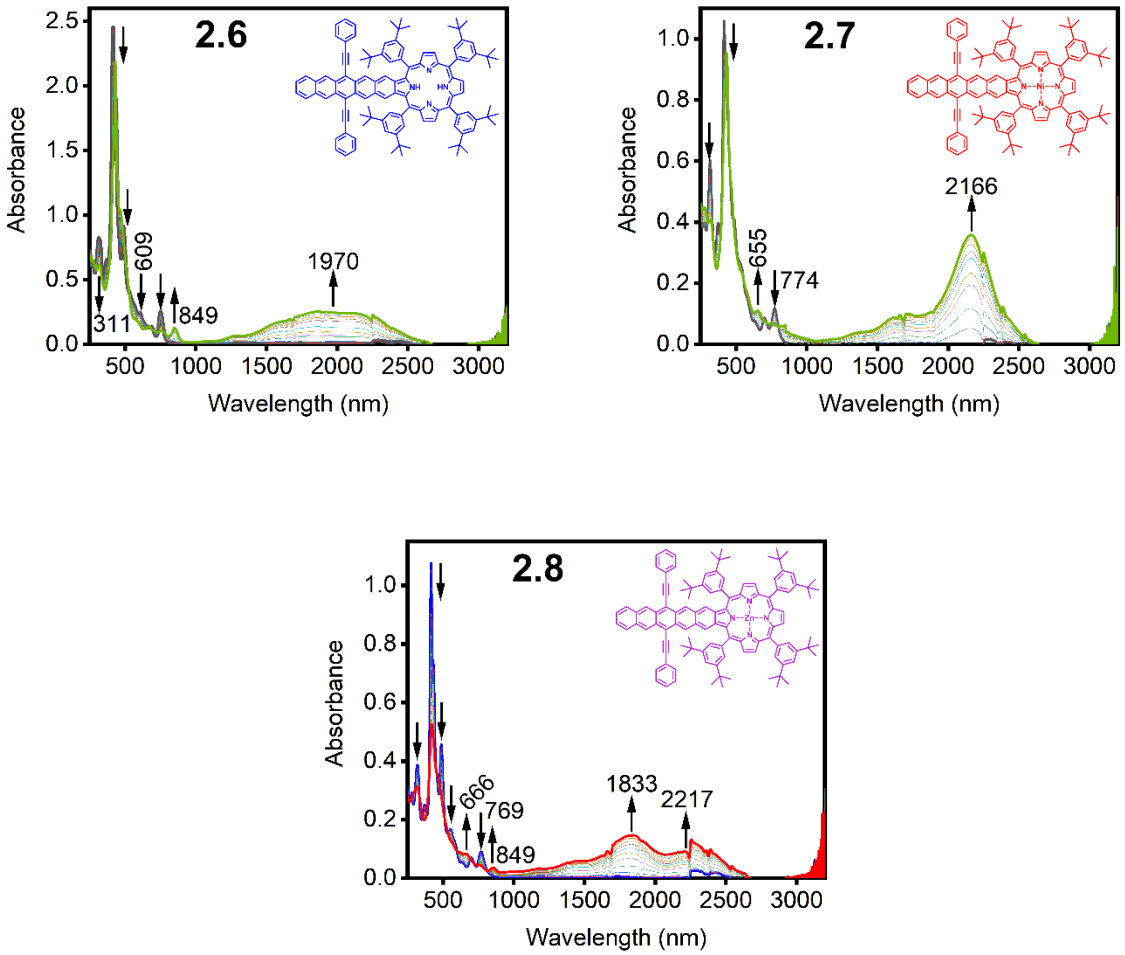

Figure 2.9. Oxidation of neutral **2.6**-**2.8** to **[2.6**-**2.8]**$^{+\bullet}$ cation-radicals under spectroelectrochemical conditions in a DCM/0.3M TBAP system.

In particular, a rise of two very intense (~20,000-50,000 $M^{-1}L^{-1}$) transitions between 1,500 and 2,500 nm was observed in each case. The relative intensities of these NIR bands have a clear central-metal dependency with approximately equal intensities observed for **2.6**, a significantly stronger lower energy transition for **2.7**, and the opposite trend for **2.8**. Based on our DFT calculations, the HOMO in **2.6**-**2.8** is delocalized over both the porphyrin (~20%) and pentacene (~80%) core, suggesting a significant degree of conjugation between the two chromophores.

Thus, it is not surprising to see lower energy transitions in the [**2.6**-**2.8**]$^{+\bullet}$ cation-radicals that have a larger degree of conjugation compared to [**2.1**-**2.3**]$^{+\bullet}$. However, the huge intensity of these bands needs to be carefully explored using modern computational approaches and is currently a subject undergoing a detailed investigation in our laboratories. Again, both transition-metal complexes can be quantitatively reduced from [**2.7**-**2.8**]$^{+\bullet}$ cation-radicals to the neutral **2.7**-**2.8** compounds (Fig S2.2 in ESI). However, similar to [**2.1**]$^{+\bullet}$, reduction of [**2.6**]$^{+\bullet}$ under spectroelectrochemical conditions does not lead to the quantitative recovery of neutral **2.6**. Indeed, in addition to the expected peaks at 755, 491, and 417 nm, we have observed a significant increase of the 431 nm peak that, unlike in the pure neutral **2.6** has a higher intensity than the 417 nm band.

2.3.4 DFT and TDDFT calculations. As mentioned above, the UV-vis and MCD spectra of the **2.1**-**2.3** and **2.6**-**2.8** porphyrins and the earlier reported dinuclear porphyrins bridged by pentacene of pentacenequinone are rather unusual. The complexity of their experimental spectra can be reflective of the presence of two NH tautomers in solution (metal-free compounds only),[47-51] simultaneous conformational isomerism,[52-58] or the non-traditional electronic structure of these compounds. In order to explain the optical and magnetooptical properties of the **2.1**-**2.3** and **2.6**-**2.8** porphyrins, we have conducted an extensive set of DFT and TDDFT calculations on the compounds of interest. First, we have optimized the geometries and calculated the energies of the conformational isomers as well as the NH tautomers using the B3LYP exchange-correlation functional coupled with either the 6-31G(d,p) or 6-311G(d) basis set. In addition, DFT and TDDFT calculations with the M06 exchange-correlation functional

were conducted for "twisted" and "bent" conformations of **2.2** and **2.7** to explore our computational protocol's validity in addition to general trends. It is found that the energies and nature of the frontier orbitals are similar for the two basis sets used. DFT calculations with both basis sets also indicate that the only one (the NH tautomer with two NH protons located on the short N-N axis) out of two possible NH tautomers in **2.1** and **2.6** is energetically favorable, and thus only this tautomer was considered. This is typical for metal-free extended porphyrins, phthalocyanines, and analogs.[59] Next, we found that both "twisted" (twisted porphyrin's π-system and planar pentacene/pentacenequinone fragment) and "bent" (both porphyrin and pentacene/pentacenequinone fragments are planar but have a small angle between them) conformations (Figure 2.10) are very close in energy and stable, while the expected classic fully planar conformation in **2.1**-**2.3** and **2.6**-**2.8** is the transition state (at least one small negative frequency was predicted by DFT).

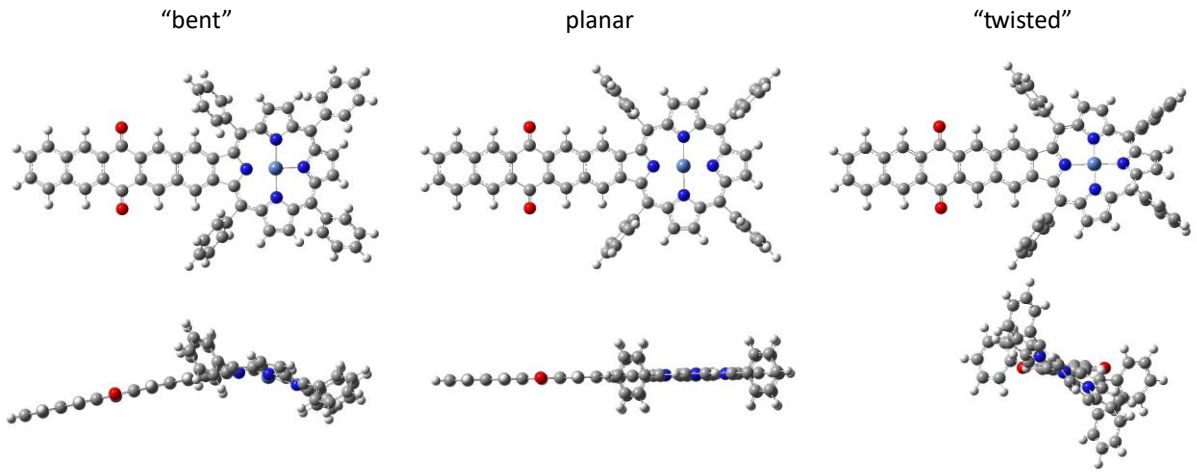

Figure 2.10. DFT-optimized conformations of **2.7**.

The HOMO in **2.1**-**2.3** resembles the classic Gouterman's a_{1u} (in standard D_{4h} symmetry notation) orbital that is coupled with the appended naphthalene fragment of pentacenequinone (Figure 2.11).

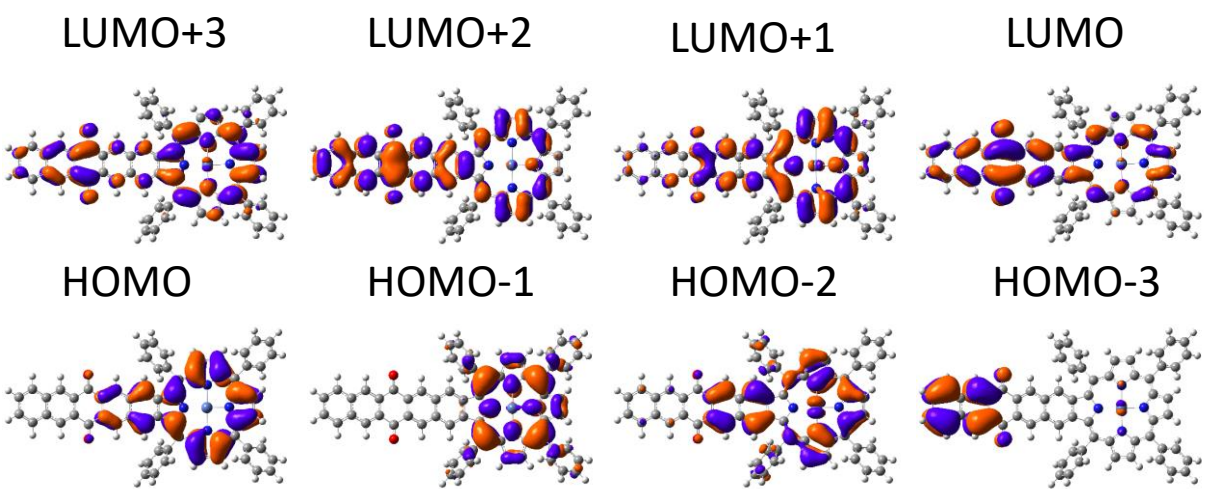

Figure 2.11. DFT-predicted frontier MOs for the "bent" conformation of **2.2** (M06 exchange-correlation functional)

The porphyrin ring contribution to the HOMO is ~80%. This is not typical for the tetra-(*meso*-aryl)porphyrins for which Gouterman's a_{2u}-type HOMO is expected.[60-62] However, taking into consideration the nearly degenerate energies of the a_{1u} and a_{2u} MOs in tetra-(*meso*-aryl)porphyrins and the conjugation of the additional π-system of the pentacenequinone at the β,β-position of the porphyrin ring, it is not surprising to see an a_{1u}-type MO as the HOMO in **2.1**-**2.3**. The HOMO-1 in **2.1**-**2.3** is localized entirely on the porphyrin π- system and resembles Gouterman's a_{2u} orbital. Taking into consideration the dominant contribution of the porphyrin π-system into the HOMO and HOMO-1 in **2.1**-**2.3**, it is safe to use the DFT-predicted energies of these two orbitals to define ΔHOMO, which is needed for MCD spectral analysis in these

compounds.[38-42] The LUMO region for porphyrins **2.1**-**2.3** is somewhat complicated by the interactions between the porphyrin and pentacenequinone π-systems. Indeed, two pairs of the orbitals (LUMO/LUMO+3 and LUMO+1/LUMO+2) emerge as a combination of the pentacenequinone MOs and porphyrin-centered Gouterman's $e_g(x)/e_g(y)$ pair. The first combination leads to a predominantly (~60%) pentacenequinone-centered LUMO and predominantly (~65%) porphyrin-centered LUMO+3. The second combination results in a predominantly (~75%) porphyrin-centered LUMO+1 and a predominantly (~60%) pentacenequinone-centered LUMO+2. If the simplistic way of calculating ΔLUMO is considered (i.e., the energy difference between the LUMO and LUMO+1), then ΔHOMO > ΔLUMO and the negative-to-positive MCD band sequence (in ascending energy) is expected in the MCD spectra of **2.1**-**2.3**, which, at first glance agrees with experiment. If the ΔLUMO is calculated using the energy difference between the LUMO+1 and LUMO+2 as two MOs that are dominated by the porphyrin contribution, then ΔHOMO < ΔLUMO and the positive-to-negative MCD band sequence (in ascending energy) is expected in the MCD spectra of **2.1**-**2.3**, which, at first glance disagrees with experiment. As discussed below, our TDDFT calculations reveal a significant deviation from such a simplistic description. The DFT-predicted occupied, predominantly pentacenequinone-centered MOs are significantly more stable compared to the frontier porphyrin-centered MOs, which, as expected, are reflective of the electron-deficient nature of the pentacenequinone. The difference between the energies of the frontier MOs for the "twisted" and "bent" conformations of **2.1**-**2.3** are negligibly small (Figure 2.12).

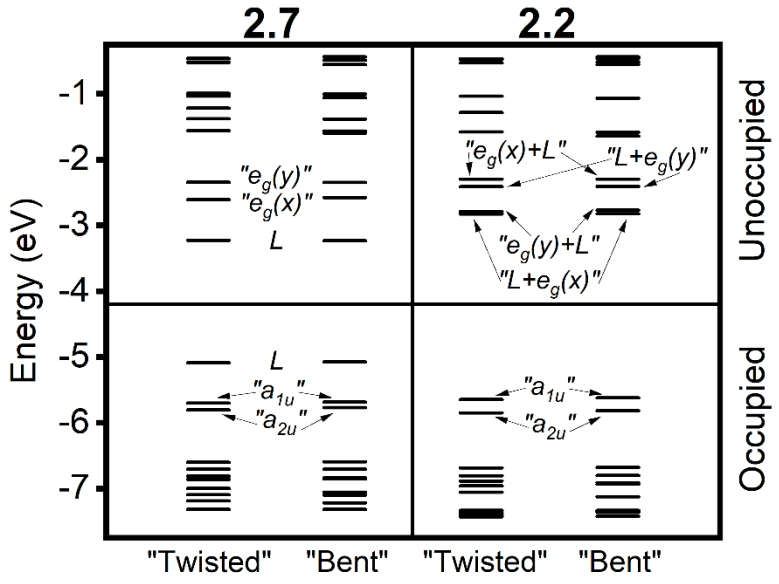

Figure 2.12. DFT-predicted energy level diagram using the M06 exchange correlation functional. Label "L" represents either the pentacenequinone or the pentacene fragment.

The DFT-predicted HOMO in the pentacene-fused porphyrins **2.6**-**2.8** is ~80% pentacene-centered with only ~20% contribution from the porphyrin's a_{1u}-type orbital, which is reflective of the strong electron-donating properties of the pentacene fragment (Figure 2.13).

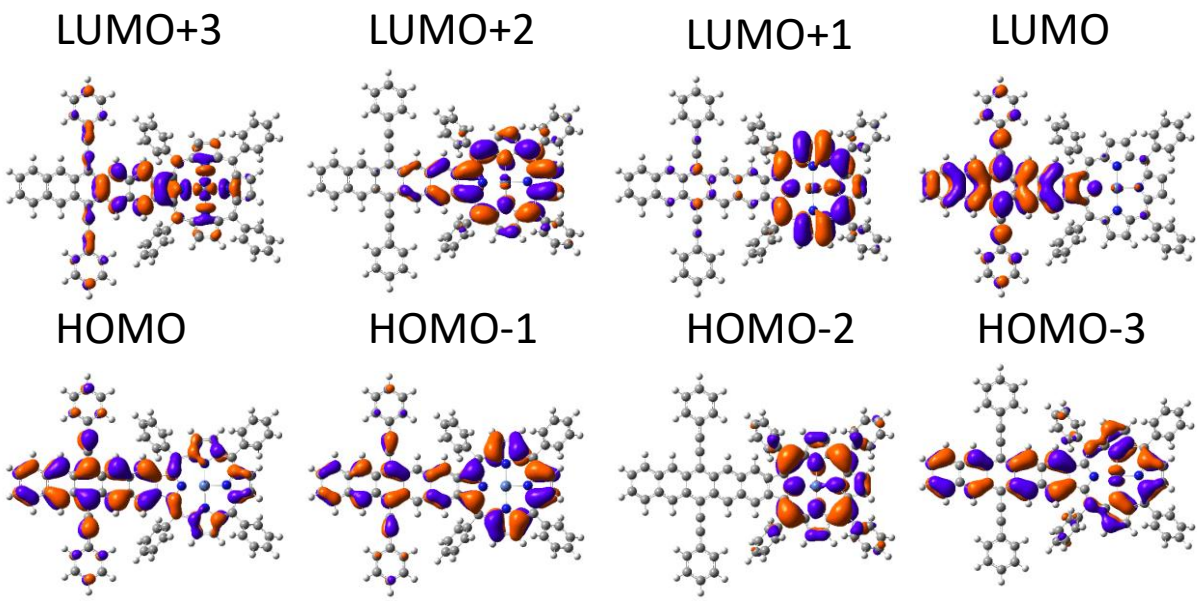

Figure 2.13. DFT-predicted frontier MOs for the "bent" conformation of **2.7** (M06 exchange-correlation functional).

The presence of a pentacene-centered MO in the HOMO region is also responsible for the richer redox properties observed for porphyrins **2.6**-**2.8** compared to **2.1**-**2.3**. The HOMO-1 in all complexes is predominantly porphyrin-centered and has a_{1u} character. The HOMO-2 is a localized a_{2u}-type porphyrin-centered orbital in all cases. The DFT-predicted nature of the LUMO in **2.6**-**2.8** is also ~90% localized on the pentacene fragment, while the LUMO+1 and LUMO+2 orbitals are ~90% localized at the porphyrin ring and resemble Gouterman's e_g pair of orbitals. The DFT-predicted energies of the a_{1u}/a_{2u} pair in **2.6**-**2.8** are close to those predicted in **2.1**-**2.3** (Figure 2.12). Again, if the simple approach for calculating the ΔHOMO/ΔLUMO ratio is used (HOMO-1/HOMO-2 for ΔHOMO and LUMO+1/LUMO+2 for ΔLUMO), the DFT calculations predict a ΔHOMO < ΔLUMO ratio that seemingly contradicts the experimental MCD data.

In order to get a deeper insight into the properties of the optical and magnetooptical transitions observed in porphyrins **2.1**-**2.3** and **2.6**-**2.8**, we have conducted TDDFT calculations on the nickel complexes **2.1** and **2.7** using the B3LYP and M06 exchange-correlation functionals on both "twisted" and "bent" conformations (Figure 2.14 and Fig S2.3 in ESI).

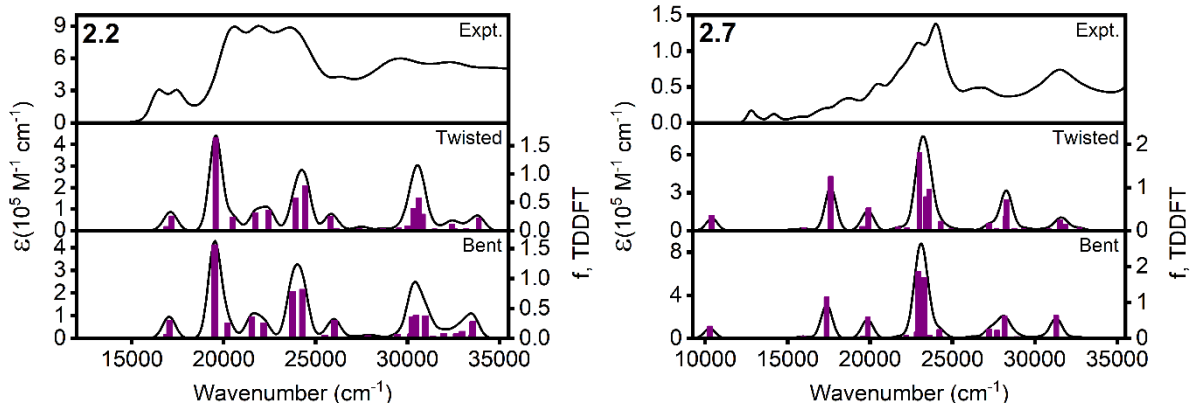

Figure 2.14. TDDFT-predicted UV-vis spectra of **2.2** and **2.7** using the M06 exchange correlation functional.

In general, the TDDFT-predicted spectra for porphyrin **2.2** correlates well with the experimental data. First, from the TDDFT calculations, it is clear that the conformational change between "twisted" and "bent" structures does not significantly alter the energies, intensities, and nature of the TDDFT-predicted spectra. This is not surprising as the energies of these two conformations are very close to each other. Next, the results for the TDDFT calculations using the B3LYP and M06 exchange-correlation functionals are close to each other with a small high-energy shift for the predicted vertical excitation energies observed in the M06 calculations, which is expected[63-64] as the latter functional has a higher percentage of Hartree-Fock exchange. Thus, in order to further simplify the discussion, only the M06 TDDFT results will be

discussed below. For **2.2**, the first two excitations predicted by TDDFT with significant intensity (excited states 5 and 6) are dominated by HOMO (~80% porphyrin-centered a_{1u}-type MO) → LUMO+1 (~75% porphyrin-centered $e_g(x)$-type MO) and HOMO (~80% porphyrin-centered a_{1u}-type MO) → LUMO (~40% porphyrin-centered $e_g(y)$-type MO) single-electron excitations, respectively. Since ~60% of the electron density in LUMO is pentacenequinone-centered, the latter one can be considered as substantially charge-transfer (porphyrin-to-pentacenequinone) in character (Table 2.2).

Table 2.2. TDDFT-predicted properties of selected excited states for **2.2** and **2.7** using the M06 exchange correlation functional and twisted geometry.

Excited State	Energy, cm^{-1}	λ, nm	Oscillator Strength, *f*	Contributions
				2.2
5	16886	592	0.0741	H→L+1 (66%), H-1→L (12%), H-24→L+5 (8%), H-1→L+3 (6%), H→L+2 (2%)
6	17165	583	0.2589	H→L (60%), H-1→L+1 (27%), H→L+3 (10%), H-1→L+2 (2%)
7	19564	511	1.6350	H-1→L+1 (52%), H→L (36%), H→L+3 (6%)
8	20478	488	0.2417	H-1→L (46%), H→L+2 (28%), H→L+1 (20%), H-1→L+3 (3%)
9	21734	460	0.3151	H→L+2 (55%), H-1→L (38%), H-1→L+3 (4%)
10	22432	446	0.3597	H→L+3 (50%), H-1→L+2 (26%), H-1→L+1 (19%)
12	23916	418	0.5698	H-1→L+2 (60%), H→L+3 (32%), H-2→L (3%)
13	24426	409	0.7892	H-1→L+3 (80%), H→L+2 (10%), H→L+1 (3%)
16	25814	387	0.2549	H-3→L (55%), H-4→L+1 (18%), H-2→L (6%), H-3→L+3 (5%), H-5→L (4%), H→L+5 (2%), H-4→L+2 (2%)
				2.7
1	10405	961	0.3551	H→L (100%)

5	15179	659	0.0265	H-1→L (54%), H→L+1 (37%), H-2→L+2 (4%), H-1→L+1 (4%)
6	15999	625	0.0609	H→L+1 (52%), H-1→L (42%), H-1→L+1 (3%), H-2→L+2 (3%)
9	17612	568	1.2570	H→L+2 (61%), H-2→L (32%), H-1→L+2 (3%), H-2→L+1 (3%)
10	19527	512	0.0983	H-1→L+1 (64%), H-2→L+2 (21%), H→L+1 (8%), H-3→L (3%)
11	19913	502	0.5291	H-2→L+1 (59%), H-1→L+2 (19%), H→L+2 (14%), H-2→L (3%)
12	21697	461	0.0817	H-3→L (50%), H-4→L (43%)
13	22243	450	0.0660	H-4→L (46%), H-3→L (28%), H→L+3 (9%), H-3→L+1 (7%), H-6→L+1 (5%)
14	22942	436	0.0303	H→L+3 (68%), H-6→L (9%), H-3→L+1 (6%), H-1→L+1 (4%), H-6→L+1 (4%), H-3→L (2%)
15	23014	435	1.8150	H-1→L+2 (44%), H-2→L+1 (19%), H-5→L (19%), H-9→L (14%)
16	23397	427	0.7892	H-6→L (36%), H→L+3 (19%), H-3→L+1 (14%), H-2→L+2 (12%), H-6→L+1 (5%), H-3→L (4%), H-4→L+1 (3%), H-4→L (3%), H-1→L+1 (2%)
17	23589	424	0.9630	H-2→L+2 (57%), H-1→L+1 (21%), H-6→L (12%), H-3→L+1 (4%), H-6→L+1 (3%)
20	24302	411	0.2199	H→L+4 (94%), H-1→L+4 (4%)
21	24896	402	0.0385	H→L+5 (65%), H-1→L+5 (31%)

However, both excited states resemble, to some extent, Gouterman's *Q*-band transitions.[36,37] More importantly, these excited states were predicted only ~280 cm^{-1} apart (592 and 583 nm) and thus, explains extremely well the observation of the MCD pseudo *A*-term observed at 609 nm. TDDFT calculations predict that three prominent bands in the Soret region (experimentally observed between 490 and 420 nm) can originate from six excited states. The experimentally

observed band at 486 nm in **2.2** correlates well with the strongly intense (f = 1.635) TDDFT-predicted (at 511 nm) excited state 7, which is dominated by a HOMO-1 (~100% porphyrin-centered a_{2u}-type MO) → LUMO+1 single-electron excitation. The experimental absorption at 456 nm correlates well with the energies of the TDDFT-predicted excited states 9 and 10 (460 and 446 nm, respectively). These are dominated by HOMO → LUMO+2 and HOMO → LUMO+3 single-electron excitations, respectively. Finally, the experimentally observed band at 424 nm correlates well with the TDDFT-predicted (418 and 409 nm) excited states 12 and 13, which are dominated by HOMO-1 → LUMO+2 and HOMO-1 → LUMO+3 single-electron excitations. The overall shape of the experimental UV-vis and MCD spectra of **2.2** is reflective of the "2+4" orbital active space which consists of two energetically closely spaced HOMO/HOMO-1 and four closely energy spaced LUMO-LUMO+3 orbitals, which form eight excited states that are dominated by the single-electron excitations from/to these orbitals (Table 2.2). HOMO and HOMO-1 resemble the classic Gouterman's a_{1u} and a_{2u} MOs, while the LUMO-LUMO+3 MOs are reflective of the linear combination of Gouterman's e_g set and two MOs of the pentacenequinone. Thus, the classic Gouterman's four-orbital model[36-37] is not applicable for the description of the UV-vis and MCD spectroscopy of the **2.2** porphyrin; however, the TDDFT calculations provide a very reasonable explanation of its spectroscopy.

The situation becomes more complex in the case of the reduced, pentacene-fused porphyrin **2.7** (Figure 2.14). In this case, for the description of the UV-vis and MCD spectra, one needs to consider "3+3" (HOMO-HOMO-2 and LUMO-LUMO+2) orbital active space. Moreover, since the HOMO and LUMO are heavily localized on the pentacene fragment, one would expect the

presence of the low-energy π−π* transition localized on the pentacene. Indeed, TDDFT predicts that the first excited state in **2.7** should have significant intensity and originates exclusively from the HOMO → LUMO single-electron excitation (Table 2.2). In agreement with this prediction, the MCD signal associated with the relatively strong band at ~780 nm in the UV-vis spectra of **2.7**-**2.8** porphyrins is very weak (Figure 7). The next two relatively weak transitions were predicted at 659 and 625 nm by TDDFT calculations and are dominated by HOMO-1 → LUMO and HOMO → LUMO+1 single-electron excitations making them heavily charge-transfer in nature. These two transitions can be responsible for a weak MCD pseudo *A*-term observed at ~680 nm in the spectra of **2.7** and **2.8**. A very strong band predicted by the TDDFT calculations at 568 nm is dominated by HOMO → LUMO+2 and HOMO-2 → LUMO single-electron excitations (Table 2.2). This excited state, again, has a predominant charge-transfer character and correlates well with the MCD *B*-term observed between 618 and 585 nm in the spectra of **2.7** and **2.8**. The next pair of relatively intense transitions was predicted at 512 and 502 nm. It is dominated by HOMO-1 → LUMO+1 and HOMO-2 → LUMO+1 single-electron excitations, respectively. These are centered at the porphyrin core and might be responsible for the MCD pseudo *A*-term centered at ~560 nm in the spectra of **2.7** and **2.8**. Finally, the TDDFT calculations predict that the 400-450 nm spectral envelope in the UV-vis and MCD spectra of **2.7** should be dominated by three excited states (excited states 15-17, Table 2.2). The excited states 15 and 17 have a clear porphyrin-centered π−π* excitation nature, while excited state 16 has significant charge-transfer character. More importantly, excited states 10 and 15, as well as 11 and 17 form two pairs (a_{1u} → $e_g(x)/e_g(y)$ for the excited states 10 and 15 and a_{2u} → $e_g(x)/e_g(y)$ for the excited states 11 and 17), which is characteristic for bacteriochlorins, thus

highlighting a strong perturbation of the porphyrin's π-system by conjugation with the pentacene fragment.

Overall, the classic Gouterman's four-orbital model is not applicable for the description of the UV-vis and MCD spectra of the pentacenequinone- or pentacene-fused porphyrins. To a large extent, the spectroscopy of the pentacenequinone-fused porphyrins can be explained using "2+4" active space, while the spectroscopy of the pentacene-fused porphyrins can be explained using "3+3" active space.

2.4 Conclusion

Largely π-extended systems represent one exciting research in frontier science. Conjugated systems incorporating two or more chromophores are challenging to achieve. Although possessing similar symmetry, the cross-conjugated (**2.1**-**2.3**) and linear-conjugated (**2.6**-**2.8**) macrocyclic systems displayed strikingly different electronic and optical properties, both of which are unusually complex and non-typical of porphyrins. While **2.1**-**2.3** showed an abnormal splitting pattern and large absorption range spanning from 250 to 550 nm for the "Soret" band, **2.6**-**2.8** displayed narrow and doubly split Soret bands with a large number of unexpected absorptions in the *Q*-band region (500-800 nm). CV revealed rich redox chemistry for both the cross-conjugated and linear-conjugated π-extended porphyrins with up to six oxidation processes observed for **2.6**-**2.8**. Both **2.1**-**2.3** and **2.6**-**2.8** formed stable radical cations under spectroelectrochemical conditions, suggesting the exceptional ability of these cross- and linear-conjugated π-extended systems to accommodate charges. The [**2.6**-**2.8**]$^{+\bullet}$ cation-radicals

exhibited exceptionally strong absorption bands in the IR region between 1,500 and 2,500 nm. While the low energy transition can be attributed to the large π-extension, the huge intensity of these bands remains elusive and is worthy of further investigation. MCD and TDDFT calculations suggest the existence of multiple charge-transfer state contributions to the complex spectra of **2.1**-**2.8**. The classical Gouterman's four-orbital model created for porphyrin systems was not suitable to interpret and understand the complex spectra of **2.1**-**2.8**. The UV-vis and MCD spectra of pentacenequinone- and pentacene-fused porphyrins were successfully resolved through "2+4" and "3+3" active spaces, respectively.

The Ni(II) pentacene-fused porphyrin (**2.7**) displayed unusually high stability and is significantly more stable than the relevant pentacene and hexacene derivatives. In contrast, when the central metal of the porphyrin was replaced with 2H or Zn(II), the stability of **2.6** and **2.8** dropped to a similar level to the pentacene derivatives. This work proves that incorporation of Ni(II) porphyrin is an effective strategy to stabilize longer acenes. The effects of the central metal of porphyrins and the substituent highlight the high turnability of these materials. This work has demonstrated that the fusion of acenes and other polycyclic aromatic hydrocarbons (PAHs) at porphyrin β,β-positions could become a powerful tool to construct novel classes of largely π-extended organic materials, providing new opportunities in basic science and applications.

Overall, it was confirmed experimentally (MCD) and theoretically (TDDFT) that extension of the π-system in a single direction using a pentacene derivative stabilizes the e_{gy} orbital as a result of the electron-donating nature of the pentacene moiety, causing a slight increase in the

ΔLUMO value; however, this increase was not enough to exceed ΔLUMO and therefore, these synthetically prepared porphyrins possess electronic structures that are similar to those of other synthetic macrocycles. Moreover, due to the extended conjugation offered by the pentacene group, the orbital character of the frontier orbitals is distorted from the classical Gouterman's four-orbital model; therefore, there are six frontier orbitals in these systems including the HOMO/HOMO-1 pair (which are very closely-spaced in energy) and the MO group of LUMO to LUMO+3, which feature similar electronic characteristics at similar energies.

2.5 Experimental Details

2.5.1 Materials. Dichloromethane solvent was purchased from commercial sources and distilled over sodium hydride to eliminated moisture and acid contamination. Tetrabutylammonium perchlorate (TBAP, for electrochemical analysis, ≥99.0%) was purchased from Sigma Aldrich and recrystallized prior to use. All compounds were synthesized by collaborating Prof. Hong Wang at University of North Texas where the procedures are not yet published at the time of writing.

2.5.2 UV-Vis and MCD Spectroscopy. All UV-vis spectra were collected on a Jasco V-770 spectrophotometer and MCD spectra were measured with a Jasco J-1500 CD spectrometer using a Jasco MCD-581 electromagnet operated at 1.0 T. The completed MCD spectra were measured at 10 °C in parallel and antiparallel orientations with respect to the magnetic field. The MCD spectra were recorded in terms of mDeg = [θ] on the y-axis and were converted to

molar ellipticity via $\Delta\varepsilon = \theta/(32980Blc)$, where B is the magnetic field, l is the path length (cm), and c is the concentration (M).[65]

2.5.3 Spectroscopy and electrochemistry. Electrochemical data were collected using a CH-620 analyzer. Cyclic voltametric measurements were performed using a three-electrode system consisting of a glassy carbon or platinum working electrode, platinum auxiliary electrode, and an Ag/AgCl wire pseudo-reference electrode. Decamethylferrocene (DmFc) or ferrocene (Fc) was used as an internal standard for the studied complexes and the reported potentials were corrected to the Fc/Fc^+ couple. For consistency purpose, all figures in this work are shown using the Fc/Fc^+ scale. All electrochemical experiments were conducted in a dichloromethane (DCM)/0.1M tetrabutylammonium perchlorate (TBAP) system. Spectroelectrochemical experiments were performed using a Jasco V-770 UV-vis-NIR spectrophotometer in tandem with a CH Instruments electrochemical analyzer which was operated using the bulk electrolysis mode. The data were collected using a custom-made 1 mm cell, a platinum mesh working electrode, platinum auxiliary electrode, and an Ag/AgCl wire pseudo-reference electrode. The spectroelectrochemical solutions consisted of 0.15 M TBAP in DCM.

2.5.4 Computational details. All calculations were run using Gaussian 16.[66] Either the B3LYP[67,68] or M06[69] exchange-correlation functional and the 6-311G(d) basis set[70] were used for all calculations. Vibrational frequencies were calculated to ensure all geometries were local minima. All computations were solution-phase calculations conducted using the PCM model[71] with dichloromethane (DCM) as the solvent. The QMForge program[72] was used for orbital analysis.

2.6 References

1. Stepien, M.; Gonka, E.; Zyla, M.; Sprutta, N., Heterocyclic Nanographenes and Other Polycyclic Heteroaromatic Compounds: Synthetic Routes, Properties, and Applications. *Chem Rev* **2017,** *117* (4), 3479-3716.
2. Narita, A.; Wang, X. Y.; Feng, X.; Mullen, K., New advances in nanographene chemistry. *Chem Soc Rev* **2015,** *44* (18), 6616-43.
3. Kobayashi, N., Ring-expanded porphyrins as an approach towards highly conductive molecular semiconductors. *Chem. Phys. Lett.* **1993,** *205*, 51-54.
4. Lash, T. D., Modification of the porphyrin chromophore by ring fusion: identifying trends due to annelation of the porphyrin nucleus. *J. Porphyrins Phthalocyanines* **2001,** *5*, 267-288.
5. Hayashi, S.; Tanaka, M.; Hayashi, H.; Eu, S.; Umeyama, T.; Matano, Y.; Araki, Y.; Imahori, H., Naphthyl-Fused π-Elongated Porphyrins for Dye-Sensitized TiO2 Cells. *J. Phys. Chem. C* **2008,** *112*, 15576-15585.
6. Cheprakov, A. V.; Filatov, M. A., The Dihydroisoindole Approach to Lineraly Annelated pi-Extended Porphyrins. *J. Porphyrins Phthalocyanines* **2009,** *13*, 291-303.
7. Ono, N.; Yamada, H.; Okujima, T., *Synthesis of Porphyrins Fused with Aromatic Rings* World Scientific: Singapore, 2010; Vol. 2.
8. Boerner, L. J. K.; Mazumder, S.; Pink, M.; Zaleski, J. M.; Baik, M.-H., Conformational and Electronic Consequences in Crafting Extended, pi-Conjugated, Light Harvesting Macrocycles. *Chem. Eur. J.* **2011,** *17*, 14539 – 14551.

9. Cheprakov, A. V., *The Synthesis of pi-Extended Porphyrins*. World Scientific Publ.: Singapore, 2011; Vol. 13.
10. Wang, C.-L.; Chang, Y.-C.; Lan, C.-M.; Lo, C.-F.; Wei-Guang Diau, E.; Lin, C.-Y., Enhanced light harvesting with π-conjugated cyclic aromatic hydrocarbons for porphyrin-sensitized solar cells. *Energy Environ. Sci.* **2011,** *4* (5), 1788.
11. Ball, J. M.; Davis, N. K. S.; Wilkinson, J. D.; Kirkpatrick, J.; Teuscher, J.; Gunning, R.; Anderson, H. L.; Snaith, H. J., A panchromatic anthracene-fused porphyrin sensitizer for dye-sensitized solar cells. *RSC Adv.* **2012,** *2* (17), 6846-6853.
12. Carvalho, C. M.; Brocksom, T. J.; de Oliveira, K. T., Tetrabenzoporphyrins: synthetic developments and applications. *Chem. Soc. Rev.* **2013,** *42* (8), 3302-17.
13. Roznyatovskiy, V. V.; Lee, C. H.; Sessler, J. L., pi-Extended isomeric and expanded porphyrins. *Chem. Soc. Rev.* **2013,** *42* (5), 1921-33.
14. Chaudhary, A.; Srinivasan, A.; Chandrashekar, T. K., *Handbook of Porphyrin Science* 2014; Vol. 32.
15. Yamada, H.; Kuzuhara, D.; Takahashi, T.; Shimizu, Y.; Uota, K.; Okujima, T.; Uno, H.; Ono, N., Synthesis and Characterization of Tetraanthroporphyrins. *Org Lett* **2008,** *10* (14), 2947-2950.
16. Davis, N. K. S.; Thompson, A. L.; Anderson, H. L., A Porphyrin Fused to Four Anthracenes. *J. Am. Chem. Soc.* **2011,** *133*, 30-31.
17. Lewtak, J. P.; Gryko, D. T., Synthesis of pi-extended porphyrins via intramolecular oxidative coupling. *Chem Commun (Camb)* **2012,** *48* (81), 10069-86.

18. Mysliwiec, D.; Donnio, B.; Chmielewski, P. J.; Heinrich, B.; Stepien, M., Peripherally fused porphyrins via the Scholl reaction: synthesis, self-assembly, and mesomorphism. *J Am Chem Soc* **2012,** *134* (10), 4822-33.

19. Chen, P.; Fang, Y.; Kadish, K. M.; Lewtak, J. P.; Koszelewski, D.; Janiga, A.; Gryko, D. T., Electrochemically driven intramolecular oxidative aromatic coupling as a pathway toward pi-extended porphyrins. *Inorg Chem* **2013,** *52* (16), 9532-8.

20. Koszelewski, D.; Nowak-Król, A.; Drobizhev, M.; Wilson, C. J.; Haley, J. E.; Cooper, T. M.; Romiszewski, J.; Górecka, E.; Anderson, H. L.; Rebane, A.; Gryko, D. T., Synthesis and linear and nonlinear optical properties of low-melting π-extended porphyrins. *J. Mater. Chem. C* **2013,** *1* (10), 2044-2053.

21. Fang, Y.; Koszelewski, D.; Kadish, K. M.; Gryko, D. T., Facile electrosynthesis of pi-extended porphyrins. *Chem Commun (Camb)* **2014,** *50* (64), 8864-7.

22. Fukui, N.; Yorimitsu, H.; Osuka, A., meso,beta-Oligohaloporphyrins as Useful Synthetic Intermediates of Diphenylamine-Fused Porphyrin and meso-to-meso beta-to-beta Doubly Butadiyne-Bridged Diporphyrin. *Angew Chem Int Ed Engl* **2015,** *54* (21), 6311-4.

23. Fukui, N.; Lee, S. K.; Kato, K.; Shimizu, D.; Tanaka, T.; Lee, S.; Yorimitsu, H.; Kim, D.; Osuka, A., Regioselective phenylene-fusion reactions of Ni(ii)-porphyrins controlled by an electron-withdrawing meso-substituent. *Chem Sci* **2016,** *7* (7), 4059-4066.

24. Fukui, N.; Osuka, A., Singly and Doubly 1,2-Phenylene-Inserted Porphyrin Arch-Tape Dimers: Synthesis and Highly Contorted Structures. *Angew Chem Int Ed Engl* **2018,** *57* (21), 6304-6308.

25. Hooper, R. W.; Zhang, A.; Koszelewski, D.; Lewtak, J. P.; Koszarna, B.; Levy, C. J.; Gryko, D. T.; Stillman, M. J., Differential quenching of the angular momentum of the B and Q bands of a porphyrin as a result of extended ring π-conjugation. *Journal of Porphyrins and Phthalocyanines* **2018,** *22* (12), 1111-1128.
26. Kato, K.; Furukawa, K.; Mori, T.; Osuka, A., Porphyrin-Based Air-Stable Helical Radicals. *Chemistry* **2018,** *24* (3), 572-575.
27. Deshpande, R.; Jiang, L.; Schmidt, G.; Rakovan, J.; Wang, X.; Wheeler, K.; Wang, H., A concise approach to the synthesis of opp- dibenzoporphyrins through the Heck reaction. *Org. Lett.* **2009,** *11*, 4251-4253.
28. Jiang, L.; Engle, J. T.; Sirk, L.; Hartley, C. S.; Ziegler, C. J.; Wang, H., Triphenylene-Fused Porphyrins. *Org. Lett.* **2011,** *13*, 3020-3023.
29. Jiang, L.; Engle, J. T.; Zaenglein, R. A.; Matus, A.; Ziegler, C. J.; Wang, H.; Stillman, M. J., Pentacene-fused diporphyrins. *Chem. Eur. J.* **2014,** *20* (43), 13865-70.
30. Hu, Y.; Thomas, M. B.; Webre, W. A.; Moss, A.; Jinadasa, R. G. W.; Nesterov, V. N.; DQSouza, F.; Wang, H., Nickel(II) Bisporphyrin-Fused Pentacenes Exhibiting Abnormal High Stability. *Angew. Chem. Int. Ed.* **2020,** *59*, 20075-20082.
31. Jiang, L.; Zaenglein, R. A.; Engle, J. T.; Mittal, C.; Hartley, C. S.; Ziegler, C. J.; Wang, H., Water-soluble ionic benzoporphyrins. *Chem Commun (Camb)* **2012,** *48* (55), 6927-9.
32. Jinadasa, R. G.; Fang, Y.; Kumar, S.; Osinski, A. J.; Jiang, X.; Ziegler, C. J.; Kadish, K. M.; Wang, H., beta-Functionalized Push-Pull opp-Dibenzoporphyrins. *J. Org. Chem.* **2015,** *80* (24), 12076-87.

33. Gholami, M.; Tykwinski, R. R., Oligomeric and Polymeric Systems with a Cross-conjugated ð-Framework. *Chem. Rev.* **2006,** *106*, 4997-5027.

34. Zucchero, A. J.; Mcgrier, P. L.; Bunz, U. H. F., Cross-Conjugated Cruciform Fluorophores. *Acc Chem Res* **2009,** *43* (3), 397-408.

35. Banala, S.; Ruhl, T.; Sintic, P.; Wurst, K.; Krautler, B., "Blackening" porphyrins by conjugation with quinones. *Angew Chem Int Ed Engl* **2009,** *48* (3), 599-603.

36. Gouterman, M. J., *The Porphyrins* Academic Press: New York, 1978.

37. Gouterman, M. J., Spectra of Porphyrins. *Mol. Spectrosc.* **1961,** *6*, 138-163.

38. Waluk, J.; Muller, M.; Swiderek, P.; Kocher, M.; Vogel, E.; Hohlneiche, G.; Michl, J., Monomeric (pentamethylcyclopentadienyl)iridium imido compounds: synthesis, structure, and reactivity. *J. Am. Chem. Soc.* **1991,** *113*, 551-5527.

39. Waluk, J.; Michl, J., Perimeter model and magnetic circular dichroism of porphyrin analogs. *J. Org. Chem.* **1991,** *56*, 2729-2735.

40. Michl, J., *Tetrahedron* **1984,** *40*, 3845-3934.

41. Michl, J., Magnetic circular dichroism of cyclic .pi.-electron systems. 2. Algebraic solution of the perimeter model for the B terms of systems with a (4N + 2)-electron [n]annulene perimeter. *J. Am. Chem. Soc.* **1978,** *100*, 6812-6818.

42. Michl, J., Magnetic circular dichroism of cyclic .pi.-electron systems. 1. Algebraic solution of the perimeter model for the A and B terms of high-symmetry systems with a (4N + 2)-electron [n]annulene perimeter*J. Am. Chem. Soc.* **1978,** *100*, 6801-6811.

43. Xue, S.; Ou, Z.; Ye, L.; Lu, G.; Fang, Y.; Jiang, X.; Kadish, K. M., Effect of Solvent and Protonation/Deprotonation on Electrochemistry, Spectroelectrochemistry and Electron-

Transfer Mechanisms of N-Confused Tetraarylporphyrins in Nonaqueous Media. *Chem. Eur. J.* **2015,** *21*, 2651-2661.

44. Sintic, P. J.; E, W.; Ou, Z.; Shao, J.; McDonald, J. A.; Cai, Z.-L.; Kadish, K. M.; Crossley, M. J.; Reimers, J. R., Control of the site and potential of reduction and oxidation processes in π-expanded quinoxalinoporphyrins. *Phys. Chem. Chem. Phys.* **2008,** *10*, 268-280.
45. Kadish, K. M.; Rhodes, R. K., Reactions of metalloporphyrin .pi. radicals. 2. Thin-layer spectroelectrochemistry of zinc tetraphenylporphyrin cation radicals and dications in the presence of nitrogenous bases. *Inorg. Chem.* **1981,** *20*, 2961-2966.
46. Kadish, K. M.; Cornillon, J. L.; Cocolios, P.; Tabard, A.; Guilard, R., Electrochemistry and spectroelectrochemistry in indium(III) porphyrins. Reactions of five-coordinate ionic complexes. *Inorg. Chem.* **1985,** *24*, 3645-3649.
47. Brueckner, C.; Chaudhri, N.; Nevonen, D. E.; Bhattacharya, S.; Graf, A.; Kaesmann, E.; Li, R.; Guberman-Pfeffer, M. J.; Mani, T.; Nimthong-Roldan, A.; Zeller, M.; Chauvet, A. A. P.; Nemykin, V., Structural and Photophysical Characterization of All Five Constitutional Isomers of the Octaethyl-β,β'-dioxo-bacterio- and -isobacteriochlorin Series. *Chem. Eur. J.* **2021,** *27*, 16189-16203.
48. Gao, S.; Li, C.; Baryshnikov, G.; Agren, H.; Li, Q.; Xie, Y., Stable thiophene-embedded N-confused homoporphyrins: Partial conjugation, fusion and fluoride binding. *Dyes Pigments* **2021,** *194*, 109612.
49. Koga, D.; Ono, T.; Shinjo, H.; Hisaeda, Y. J., Hydrogen Bond Engineering Visualized by Picometer-Level Distortion of Planar Porphyrin Isomers. *Phys. Chem. Lett.* **2021,** *12*, 10429-10436.

50. Listkowski, A.; Masiera, N.; Kijak, M.; Luboradzki, R.; Lesniewska, B.; Waluk, J., Controlling Emissive Properties by Intramolecular Hydrogen Bonds: Alkyl and Aryl meso-Substituted Porphycenes. *Chem. Eur. J.* **2021,** *27*, 6324-6333.

51. Nemykin, V. N.; Sabin, J. R., Profiling Energetics and Spectroscopic Signatures in Prototropic Tautomers of Asymmetric Phthalocyanine Analogues. *J. Phys. Chem. A* **2012,** *116*, 7364-7371.

52. Dyrda, G.; Broda, M. A.; Hnatejko, Z.; Pedzinski, T.; Slota, R., Adducts of free-base meso-tetraarylporphyrins with trihaloacetic acids: Structure and photostability. *J. Photochem. Photobiol A* **2020,** *393*, 112445.

53. Tang, M.; Yang, Y.; Zhang, S.; Chen, J.; Zhang, J.; Zhou, Z.; Liu, Q., Electron Transfer and Geometric Conversion of Co–NO Moiety in Saddled Porphyrins: Implications for Trigger Role of Tetrapyrrole Distortion. *Inorg. Chem.* **2018,** *57*, 277-287.

54. Roucan, M.; Flanagan, K. J.; O'Brien, J.; Senge, M. O., Nonplanar Porphyrins by N-Substitution: A Neglected Pathway. *Eur. J. Org. Chem.* **2018,** *2018*, 6432-6446.

55. Grover, N.; Kumar, R.; Chaudhri, N.; Butcher, R.; Sankar, M., β-Heptasubstituted Porphyrins: Synthesis, Structural, Spectral, and Electrochemical Properties. *Eur. J. Inorg. Chem.* **2018,** *2018*, 3338-3343.

56. Spyroulias, G. A.; Despotopoulos, A. P.; Raptopoulou, C. P.; Terzis, A.; de Montauzon, D.; Poilblanc, R.; Coutsolelos, A. G., Comparative Study of Structure−Properties Relationship for Novel β-Halogenated Lanthanide Porphyrins and Their Nickel and Free Bases Precursors, as a Function of Number and Nature of Halogens Atoms. *Inorg. Chem.* **2002,** *41*, 2648-2659.

57. Jia, S.-L.; Jentzen, W.; Shang, M.; Song, X.-Z.; Ma, J.-G.; Scheidt, W. R.; Shelnutt, J. A., Axial Coordination and Conformational Heterogeneity of Nickel(II) Tetraphenylporphyrin Complexes with Nitrogenous Bases. *Inorg. Chem.* **1998,** *37*, 4402-4412.

58. Song, X.-Z.; Jentzen, W.; Jaquinod, L.; Khoury, R. G.; Medforth, C. J.; Jia, S.-L.; Ma, J.-G.; Smith, K. M.; Shelnutt, J. A., Substituent-Induced Perturbation Symmetries and Distortions of meso-tert-Butylporphyrins. *Inorg. Chem.* **1998,** *37*, 2117-2128.

59. Belosludov, R. V.; Nevonen, D.; Rhoda, H. M.; Sabin, J. R.; Nemykin, V. N., Simultaneous Prediction of the Energies of Qx and Qy Bands and Intramolecular Charge-Transfer Transitions in Benzoannulated and Non-Peripherally Substituted Metal-Free Phthalocyanines and Their Analogues: No Standard TDDFT Silver Bullet Yet. *J. Phys. Chem. A* **2019,** *123*, 132-152.

60. Mack, J.; Bunya, M.; Shimizu, Y.; Uoyama, H.; Komobuchi, N.; Okujima, T.; Uno, H.; Ito, S.; Stillman, M. J.; Ono, N., Application of MCD Spectroscopy and TD-DFT to Nonplanar Core-Modified Tetrabenzoporphyrins: Effect of Reduced Symmetry on Nonplanar Porphyrinoids. *Chem. Eur. J.* **2008,** *14*, 5001-5020.

61. Mack, J.; Stillman, M. J.; Kobayashi, N., Application of MCD spectroscopy to porphyrinoids. *Coord. Chem. Rev.* **2007,** *251*, 429-453.

62. Mack, J.; Asano, Y.; Kobayashi, N.; Stillman, M. J., Application of MCD Spectroscopy and TD−DFT to a Highly Non-Planar Porphyrinoid Ring System. New Insights on Red−Shifted Porphyrinoid Spectral Bands. *J. Am. Chem. Soc.* **2005,** *127*, 17697-17711.

63. Martynov, A. G.; Mack, J.; May, A. K.; Nyokong, T.; Gorbunova, Y. G.; Tsivadze, A. Y., Methodological Survey of Simplified TD-DFT Methods for Fast and Accurate

Interpretation of UV–Vis–NIR Spectra of Phthalocyanines. *ACS Omega* **2019,** *4*, 7265-7284.

64. Nemykin, V. N.; Hadt, R. G.; Belosludov, R. V.; Mizuseki, H.; Kawazoe, Y., Influence of Molecular Geometry, Exchange-Correlation Functional, and Solvent Effects in the Modeling of Vertical Excitation Energies in Phthalocyanines Using Time-Dependent Density Functional Theory (TDDFT) and Polarized Continuum Model TDDFT Methods: Can Modern Computational Chemistry Methods Explain Experimental Controversies?. *J. Phys. Chem. A* **2007,** *111*, 12901-12913.
65. Galinato, M. G. I.; Spolitak, T.; Ballou, D. P.; Lehnert, N. Elucidating the Role of the Proximal Cysteine Hydrogen-Bonding Network in Ferric Cytochrome P450cam and Corresponding Mutants Using Magnetic Circular Dichroism Spectroscopy. *Biochemistry* **2011**, *50*(6), 1053-1069.
66. Gaussian 16, Revision B.01, Frisch, M. J.; Trucks, G. W.; Schlegel, H. B.; Scuseria, G. E.; Robb, M. A.; Cheeseman, J. R.; Scalmani, G.; Barone, V.; Petersson, G. A.; Nakatsuji, H.; Li, X.; Caricato, M.; Marenich, A. V.; Bloino, J.; Janesko, B. G.; Gomperts, R.; Mennucci, B.; Hratchian, H. P.; Ortiz, J. V.; Izmaylov, A. F.; Sonnenberg, J. L.; Williams-Young, D.; Ding, F.; Lipparini, F.; Egidi, F.; Goings, J.; Peng, B.; Petrone, A.; Henderson, T.; Ranasinghe, D.; Zakrzewski, V. G.; Gao, J.; Rega, N.; Zheng, G.; Liang, W.; Hada, M.; Ehara, M.; Toyota, K.; Fukuda, R.; Hasegawa, J.; Ishida, M.; Nakajima, T.; Honda, Y.; Kitao, O.; Nakai, H.; Vreven, T.; Throssell, K.; Montgomery, J. A., Jr.; Peralta, J. E.; Ogliaro, F.; Bearpark, M. J.; Heyd, J. J.; Brothers, E. N.; Kudin, K. N.; Staroverov, V. N.; Keith, T. A.; Kobayashi, R.; Normand, J.; Raghavachari, K.; Rendell, A. P.; Burant, J. C.; Iyengar, S. S.;

Tomasi, J.; Cossi, M.; Millam, J. M.; Klene, M.; Adamo, C.; Cammi, R.; Ochterski, J. W.; Martin, R. L.; Morokuma, K.; Farkas, O.; Foresman, J. B.; Fox, D. J. Gaussian, Inc., Wallingford CT, 2016.

67. Becke, A. D. "Density-Functional Thermochemistry. III. The Role of Exact Exchange" *J. Chem. Phys.* **1993**, *98*, 5648-5652.

68. Lee, C.; Yang, W.; Parr, R. G. "Development of the Colle-Salvetti correlation-energy formula into a functional of the electron density" *Phys. Rev. B.* **1988**, *37*, 785-789.

69. Zhao, Y.; Truhlar, D. G. The M06 Suite of Density Functionals for Main Group Thermochemistry, Thermochemical Kinetics, Noncovalent Interactions, Excited States, and Transition Elements: Two New Functionals and Systematic Testing of Four M06-Class Functionals and 12 Other Functionals. *Theor. Chem. Acc.* **2008**, 120(*1-3*), 215-241.

70. McLean, A. D.; Chandler, G. S. Contracted Gaussian basis sets for molecular calculations. 1. Second row atoms, Z = 11-18. *J. Chem. Phys.* **1980**, *72*, 5639-5648.

71. Tomasi, J.; Mennucci, B.; Cammi, R. Quantum mechanical continuum solvation models. *Chem. Rev.* **2005**, *105*, 2999-3093.

72. Tenderholt, A. L. QMForge, version 2.1; Standord University: Stanford, CA, 2011. https://qmforge.net/.

3 Accurate Prediction of the Excited States in the Fully Conjugated Porphyrin Tapes Across the Full Spectral Range: A Story of the Interplay Between π-π* and Intramolecular Charge-Transfer Transitions in Soft Chromophores

3.1 Chapter Preface

In the previous chapter, the π-system of *meso*-tetraphenylporphyrin was extended in a single direction with the intention of destabilizing the e_{gy} orbital, which was meant to increase the value of ΔLUMO. This structural design strategy did in fact increase the energy of e_{gy} and therefore increased the magnitude of ΔLUMO; however, it was not enough of an energetic shift to overtake the magnitude of ΔHOMO, leading to the commonly encountered (for synthetic molecules) ΔHOMO > ΔLUMO relationship.

The structural design strategy of this chapter is similar to the last but grander, as we will now extend the π-system in both directions (along the arbitrarily assigned y-axis) by linking several zinc-centered tetraphenylporphyrin subunits together. Several lengths of porphyrin tapes ranging from dimer to dodecamer (12 sequentially bound porphyrin units) will be theoretically (DFT and TDDFT) explored. Similar to the last chapter, the expectations are that the e_{gy} orbital will be destabilized after π-system extension, and its energy will increase as the porphyrin chain is lengthened. This is hypothesized to increase the magnitude of ΔLUMO; hopefully to the point that it exceeds ΔHOMO.

3.2 Introduction

Porphyrins are well-known compounds that have attracted research interest for many years due to their relevance in biology,[1–10] catalysis,[11–17] and medicine.[18–24] The application of porphyrins and similar functional dyes in the textile industry,[25] chemo- and electrochromic devices,[26–29] photodynamic cancer therapy,[30–36] optical recording,[37,38] and light harvesting[39–50] relies on their photophysical properties. Thus, accurate prediction of the energies and intensities of excited states in such systems is crucial for the *in silico* design of new synthetic porphyrins with predefined optical properties. In the last several decades, Osuka and co-workers as well as several other research groups have developed a variety of synthetic procedures for the preparation and purification of conjugated oligoporphyrins.[51–63] Such oligoporphyrins, especially two-dimensional fully conjugated members of this family, were sought for potential applications as organic semiconductors, materials for nonlinear optics, molecular wires, and near-infrared dyes.[51]

When considering oligoporphyrins that are fully conjugated through *meso–meso* β–β β–β triple linkage, Osuka and coauthors have demonstrated a systematic red-shift of the λ_{max} band which, in some cases, goes all the way into the infrared region.[63] Such a systematic and controllable shift of this low-energy absorption can potentially be used in the photodynamic therapy (PDT) of cancer.[63,64] In general, these oligomers have three optical windows identified by Kim, Osuka, and coauthors.[63,64] The third transition region is dominated by the lowest energy near-infrared or infrared transitions. The second transition region consists of a broad and ill-defined absorption in the low-energy visible range, while the third transition region is better

defined and located on the edge of the ultraviolet region. When molecular electronics and biomedical applications of fully conjugated systems are desired, the accurate assignment and theoretical prediction of the major optical transitions are critical in order to elucidate the nature of these absorption bands.

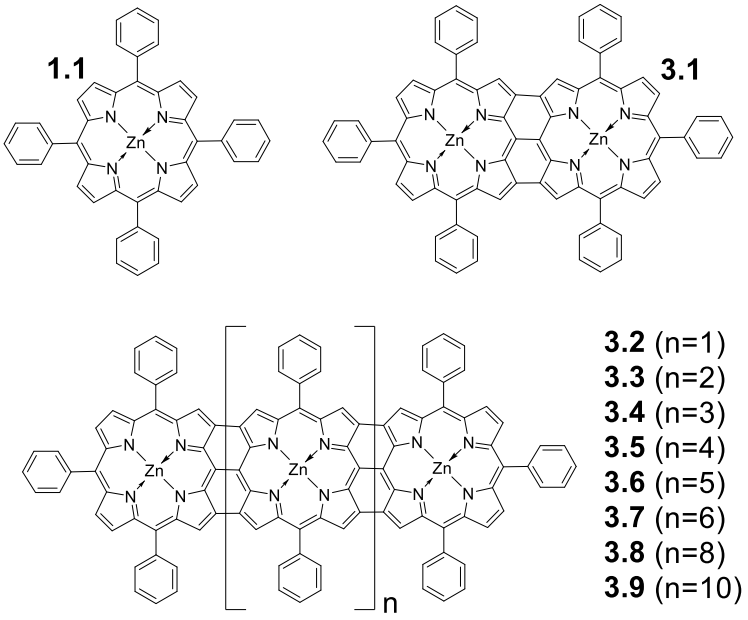

Figure 3.1. Structure of the parent porphyrin **1.1** and porphyrin tapes **3.1**-**3.9**.

To date, there were two attempts[64,65] made to calculate absorption profiles of fully conjugated triple-linked *meso*−*meso* β-β β-β porphyrin oligomers (Figure 3.1). The first attempt reported by Kim, Osuka, and coauthors[64] was based on simple semiempirical PPP calculations and idealized geometries for the porphyrin tapes **3.1**-**3.9**. The second attempt[65] was based on the semiempirical ZINDO/S Hamiltonian and ZINDO/1 optimized geometries for the porphyrin tapes **3.1**–**3.3**. Although in both cases the experimental trends of the spectral envelopes were reproduced reasonably well, the quantitative uncertainties were rather high and were between

0.25 and 0.7 eV. Such large uncertainties do not allow for the assignment of optical transitions in the fully conjugated two-dimensional porphyrin tapes with a high degree of confidence. In addition, the ZINDO/S calculations on the porphyrin tapes **3.1**–**3.3** are indicative of only one intensive transition in the spectral region II,[65] which does not correlate well with the experimental data.

Time-dependent density functional theory (TDDFT) methodology offers a reasonable computational cost, a variety of specifically tuned exchange-correlation functionals, and good accuracy for the large π-extended systems.[66−76] The TDDFT approach was successfully applied for the accurate prediction of the vertical excitation energies in porphyrins, phthalocyanines, and their structural analogues. Two research groups have recently attempted to find the best TDDFT methodology for a large group of phthalocyanines and their analogues substituted with electron-donating groups.[66,71] These systems have UV−vis spectra that are composed of the combination of the macrocycle-centered π−π* transitions and interligand charge-transfer bands. Although the best exchange-correlation functionals still result in ∼0.1 to 0.15 eV uncertainties in comparison with the experimental data, these uncertainties are applicable to the whole range of the UV−vis−NIR spectral region and provide a much better agreement between theory and experiment compared to the PPP and ZINDO/S methods. Thus, in this paper, results of the TDDFT calculations are reported for the series of fully conjugated two-dimensional porphyrin systems. Specifically, we address the influence of the exchange-correlation functional on the predicted energies and oscillator strengths and find a computational protocol that allows for the prediction of the UV−vis−NIR spectra of the fully

conjugated porphyrin oligomers with a high degree of accuracy. Such a protocol affords not only the accurate simulation of absorption spectra but also provides a high level of confidence toward the optical band assignments of these systems.

3.3 Results and Discussion

The influence of the exchange-correlation functional on the TDDFT-predicted energies and oscillator strengths in porphyrins, phthalocyanines, and their analogues is well described in the literature.[66,70,71] In general, one would expect that, for the types of fully conjugated porphyrins that are of interest in this chapter, there will be some degree of intramolecular charge-transfer transitions originating from different porphyrin subunits in these tapes. Indeed, according to the earlier PPP/SCI semiempirical calculations reported by Osuka, Kim, and co-workers,[64] region II contains a number of such charge-transfer transitions. Since intramolecular charge-transfer processes are expected in the fully conjugated porphyrin tapes, the choice of the pure GGA or meta GGA exchange-correlation functionals might lead to the well-known low-energy ghost states.[77] In order to avoid these states, the long-range corrected LC-wPBE exchange-correlation functional along with two hybrid exchange-correlation functionals (standard B3LYP and the long-range separated CAM-B3LYP) were tested. Both gas-phase and solvated model calculations were considered.

Independent of the utilized exchange-correlation functional and environment (i.e., gas-phase or solvation model), the DFT-predicted geometries in porphyrin **1.1** and porphyrin oligomers **3.1**–**3.9** differ from those used in the previous reports. First, the preliminary geometry

optimizations on the planar porphyrin **1.1** (D_{4h} symmetry), dimer **3.1** (D_{2h} symmetry), and trimer **3.2** (D_{2h} symmetry) with the phenyl groups being perpendicular to the macrocyclic core using LC-wPBE, B3LYP, and CAM-B3LYP exchange-correlation functionals resulted in geometries with a nonplanar chromophore core and non-perpendicular phenyl groups. For instance, in the case of parent porphyrin **1.1**, all geometry optimizations in the gas phase and solution resulted in a stable structure of the D_4 point group with a nearly (but not exactly) planar macrocycle and phenyl groups that were tilted from the perpendicular position by ∼20°. Such a D_4 point group geometry is in agreement with the previous reports on MTPP complexes optimized by the DFT method.[67] When the geometry of ZnTPP **1.1** was forced into the D_{4h} point group during geometry optimizations, the frequency calculations on converged geometries were suggestive of the transition state (negative predicted frequencies) rather than local or global minima and this was also the case for the ZINDO/1 optimized geometry of **1.1**. The transition state is necessary to achieve when optimizing geometries as it represents the lowest energy geometrical configuration which closely resembles the structure of the modelled compound in reality. In the case of porphyrin tapes **3.1**–**3.9**, with the DFT calculations, we found that the highest symmetry that converged to the stationary point belongs to the D_2 point group. In this case, (i) the phenyl groups are not perpendicular to the porphyrin core, and (ii) the porphyrin tapes undergo the size-dependent twist described in Figure 3.2.

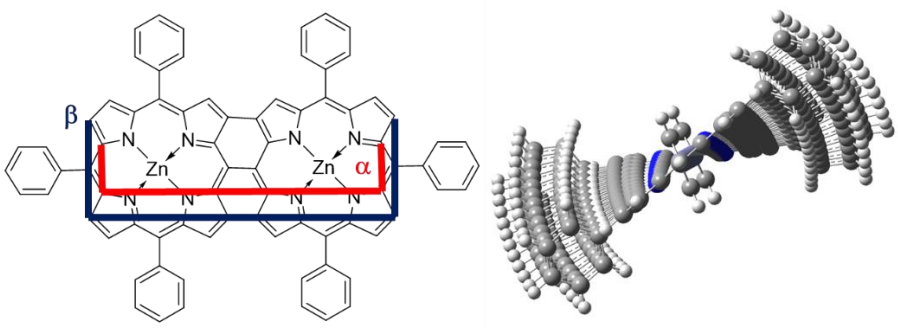

Figure 3.2. Left: definition of the torsion angles α and β. Right: side-view of the optimized (CAM-B3LYP, gas-phase) structure of oligomer **3.9** (on the right, the blue atoms correspond to nitrogens).

Although the DFT-predicted twist angle in oligomers **3.1**–**3.9** depends on the specific exchange-correlation functional and environment (i.e., gas-phase versus solution), it tends to increase with the size of the porphyrin tape (Supporting Information Figure S3.1). The solution calculations also tend to have a "saturation" behavior for the predicted twist angles, while the gas-phase DFT predictions appear more linear. The lack of inversion center in the DFT-optimized structures of compounds **1.1** and **3.1**–**3.9** complicates the interpretation of the TDDFT and TDDFT/SOS data due to the increase of a large number of low-intensity transitions and more complex expansion coefficients.

The results for all the test TDDFT calculations for the systems of interest are shown in the supporting information Figs. S3.2-S3.7. From these results, it was clear that the B3LYP exchange-correlation functional, coupled with the solvation model represented the best agreement between theory and experiment. Both pure (LC-wPBE) and hybrid (CAM-B3LYP) long-range corrected functionals provided reasonable agreement between theory and

experiment for the region III spectral area (defined ahead in Fig. 3.7); however, the long-range corrected exchange correlation functionals predicted a much larger than experimentally observed gap between spectral regions III and II for the fully conjugated porphyrin tapes. Thus, only a detailed analysis of the B3LYP-PCM calculations will be provided below.

The molecular orbital energy diagram for the frontier orbitals of systems **1.1** and **3.1**-**3.5** is shown in Fig. 3.3 (systems **1.1** and **3.1**-**3.8** are shown in Fig. S3.8) with the orbital composition diagrams shown in Figure 3.4 and supporting information Figs. S3.9-S3.13. Representative examples of the frontier orbitals of porphyrin tapes **1.1**, **3.1**, and **3.2** are listed in Fig. 3.5 with those of the larger tape sizes included in supporting information Figs. S3.14-S3.18.

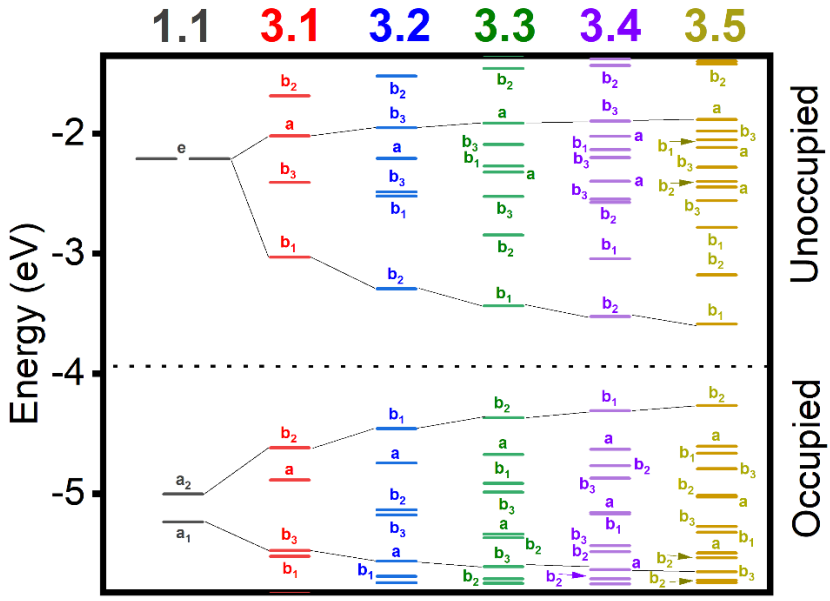

Figure 3.3. DFT-predicted energy level diagram for porphyrin tapes **1.1** and **3.1**-**3.5**. Defined by Osuka, Kobayashi and co-workers in ref. 65 (the ΔHOMO and ΔLUMO orbitals are connected by thin lines across the diagram).

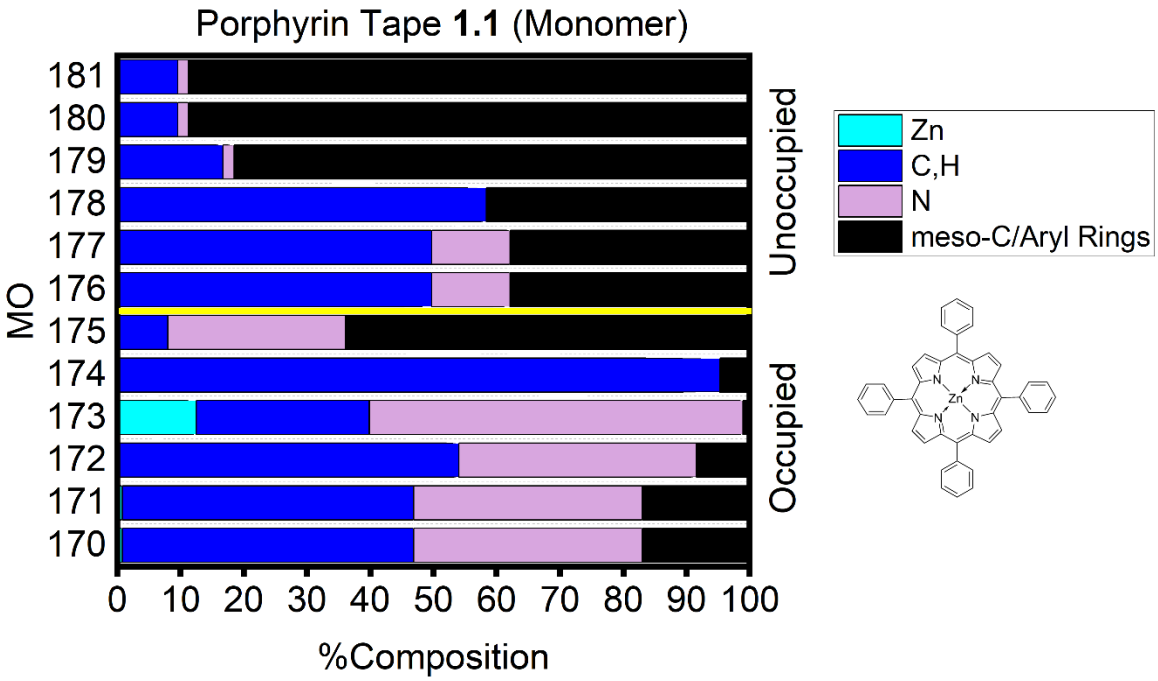
Porphyrin Tape 1.1 (Monomer)
MO
181
180
179
178
177
176
175
174
173
172
171
170
Unoccupied
Occupied
0 10 20 30 40 50 60 70 80 90 100
%Composition
Zn
C,H
N
meso-C/Aryl Rings

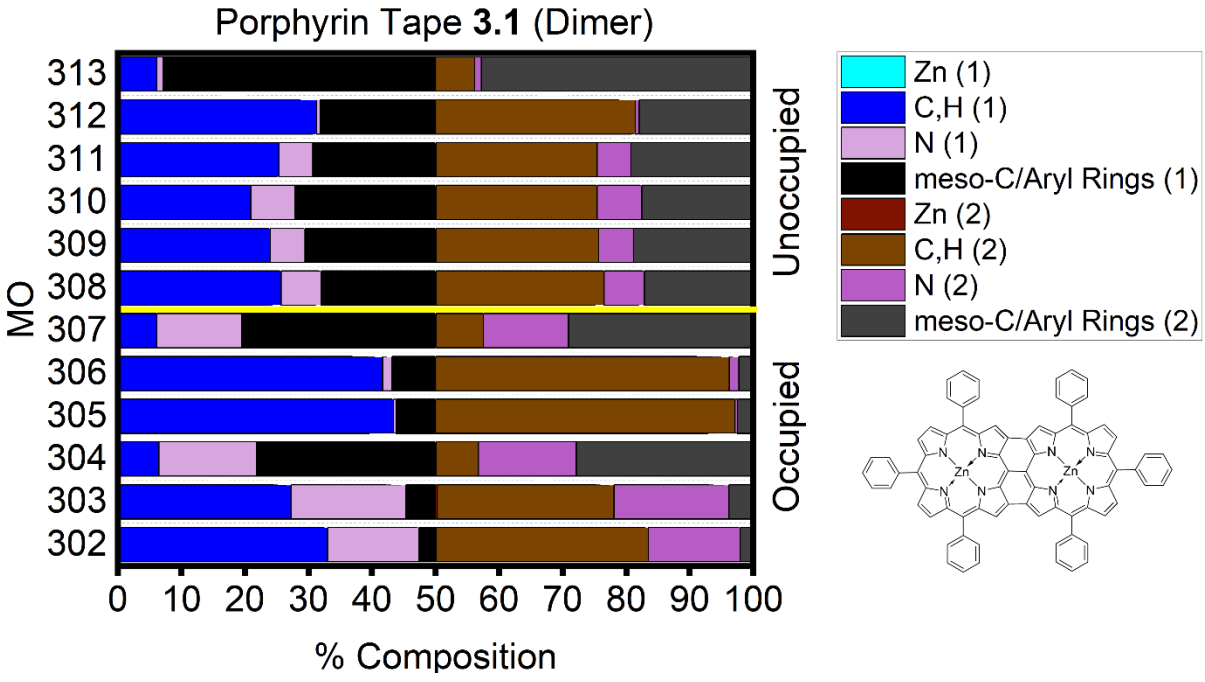
Porphyrin Tape 3.1 (Dimer)
MO
313
312
311
310
309
308
307
306
305
304
303
302
Unoccupied
Occupied
0 10 20 30 40 50 60 70 80 90 100
% Composition
Zn (1)
C,H (1)
N (1)
meso-C/Aryl Rings (1)
Zn (2)
C,H (2)
N (2)
meso-C/Aryl Rings (2)

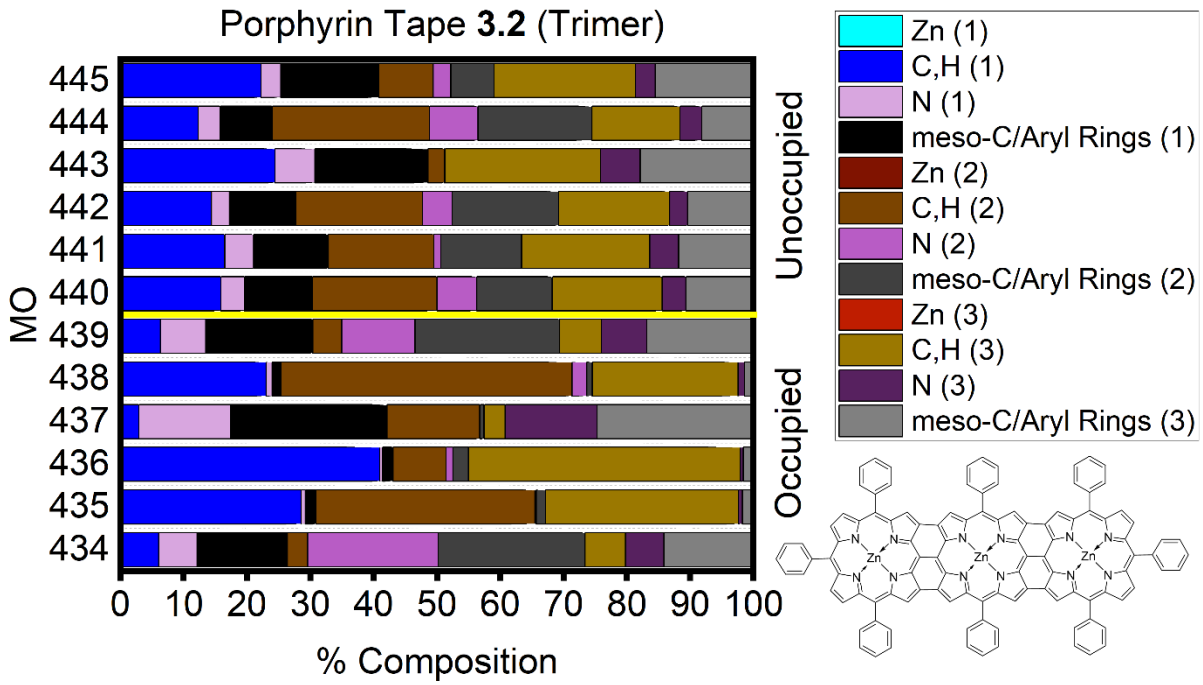

Figure 3.4. Molecular orbital vs. percent composition diagrams for **1.1** (top), **3.1** (middle), and **3.2** (bottom).

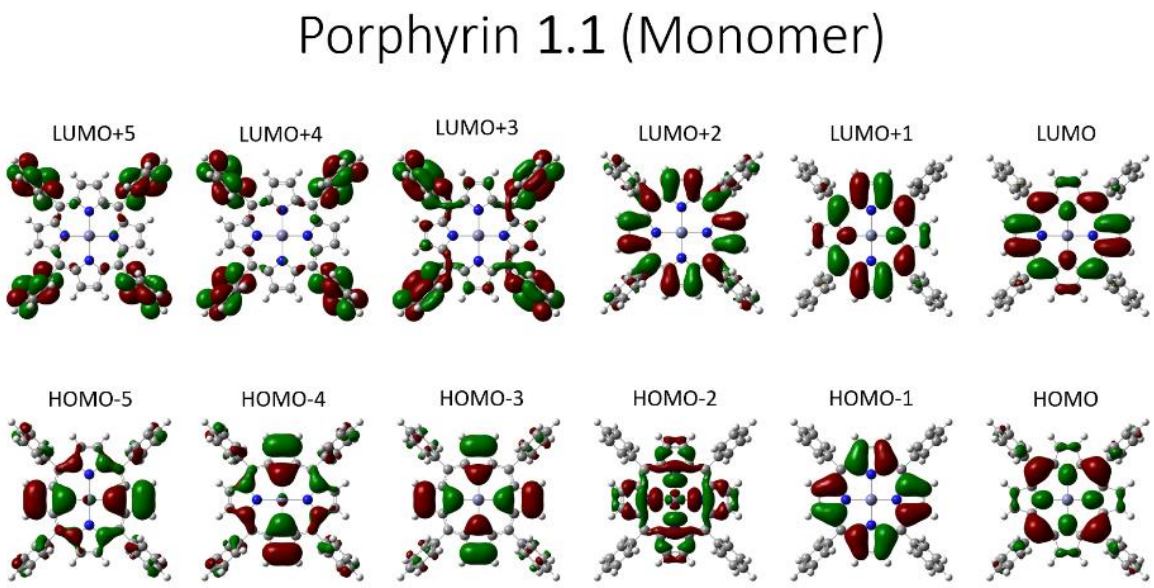

Porphyrin 3.1 (Dimer)

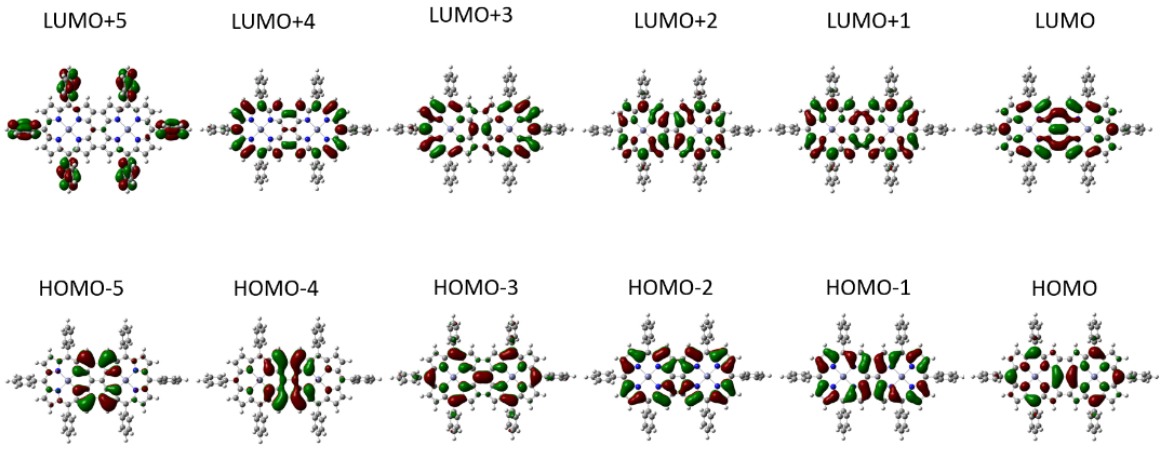

Porphyrin 3.2 (Trimer)

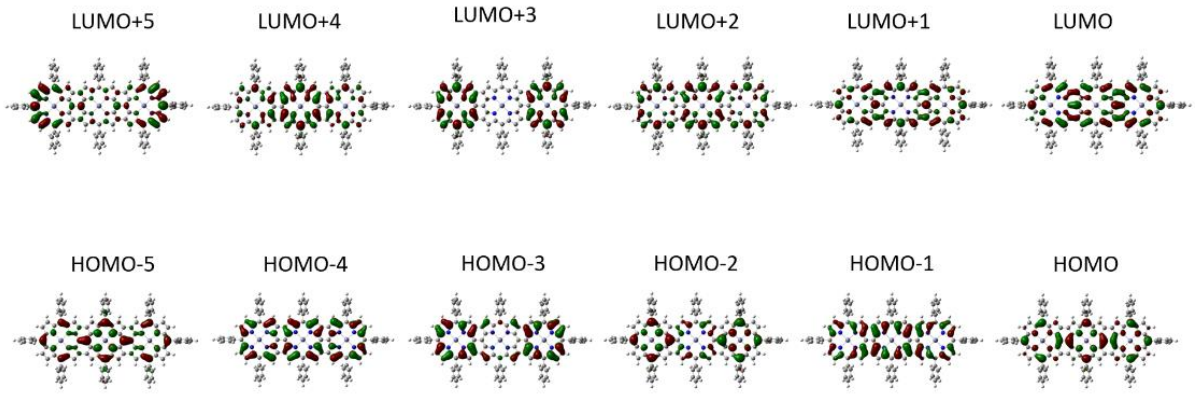

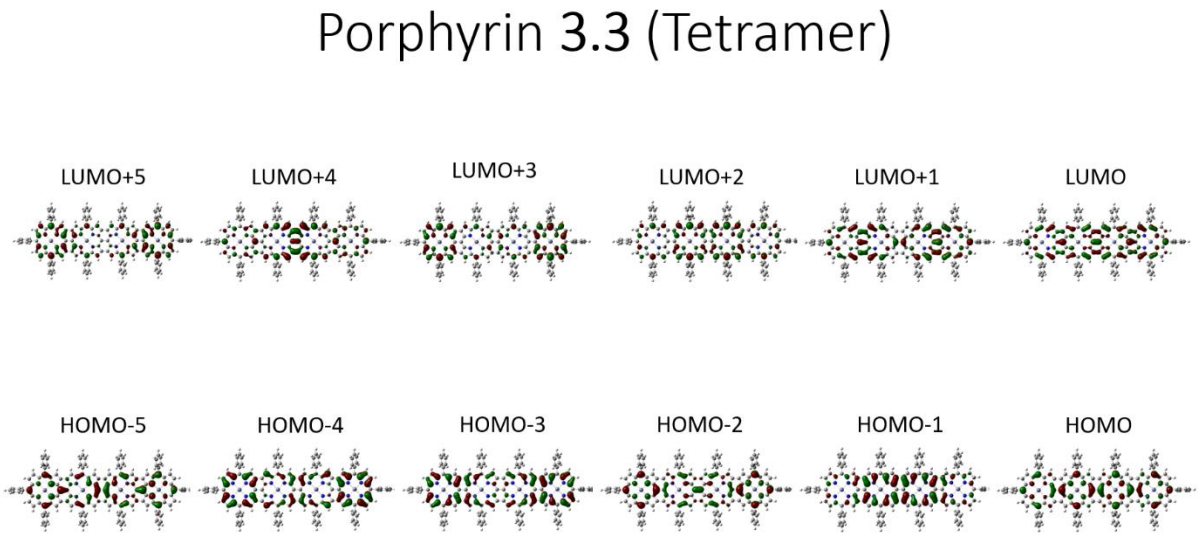

Figure 3.5. Selected DFT-predicted molecular orbitals for porphyrin tapes **1.1** (top) to **3.3** (bottom).

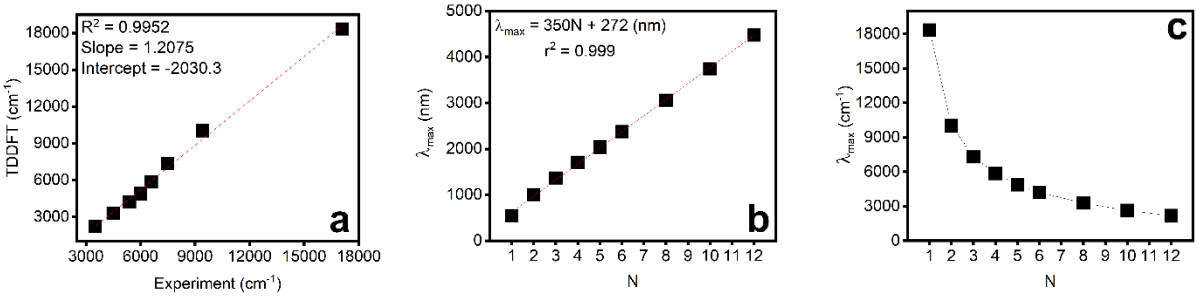

Figure 3.6 (a.) Linear correlation between the theoretical and experimental energies of the λ_{max} (region III) band. **(b.)** Linear correlation between the TDDFT-predicted wavelength of the λ_{max} (region III) band versus number of porphyrin subunits in the chain. For the similar experimental correlation see ref. 63. **(c.)** Exponential-type decay (or power law distribution) behavior of the TDDFT-predicted wavenumber of the λ_{max} (region III) band versus the number of porphyrin subunits in the chain (N).

First, an excellent agreement was observed between the experimental and TDDFT-predicted energies for the lowest energy band in the spectral region III transition, although the slope and intercept deviate slightly from the ideal values (Fig. 3.6a). Our calculations also agree with the previous experimental observation by Osuka and coworkers[63] for the linear dependency observed between the position of this band (in the nanometer scale) and the number of porphyrin subunits present in the fully conjugated porphyrin tapes (Fig. 3.6b). In an energy scale, the TDDFT predicted energies for the most prominent band in spectral region III follows an exponential-type decay model (Fig. 3.6c).

In the case of monomeric ZnTPP (**1.1**), the classic Gouterman's four-orbital model[78-80] predicts an a_{2u}-type HOMO and an a_{1u}-type HOMO-1 with two doubly degenerate e_g-type LUMO and LUMO+1 orbitals (Figure 3.3). Density functional theory predicted an a_{2u}-type HOMO which correlates well with previous calculations and experimental data[63-65], and contrasts the ZINDO/S calculations which predicted an a_{1u}-type orbital as the HOMO. Because of the small energy separation between HOMO and HOMO-1, both single electron transitions from HOMO to LUMO/LUMO+1 and from HOMO-1 to LUMO+1 contribute to the *Q*-band spectral region (Fig. 3.7a and Table S3.1). The predicted energies of the *Q*- and Soret-bands fit well with the experimental data.

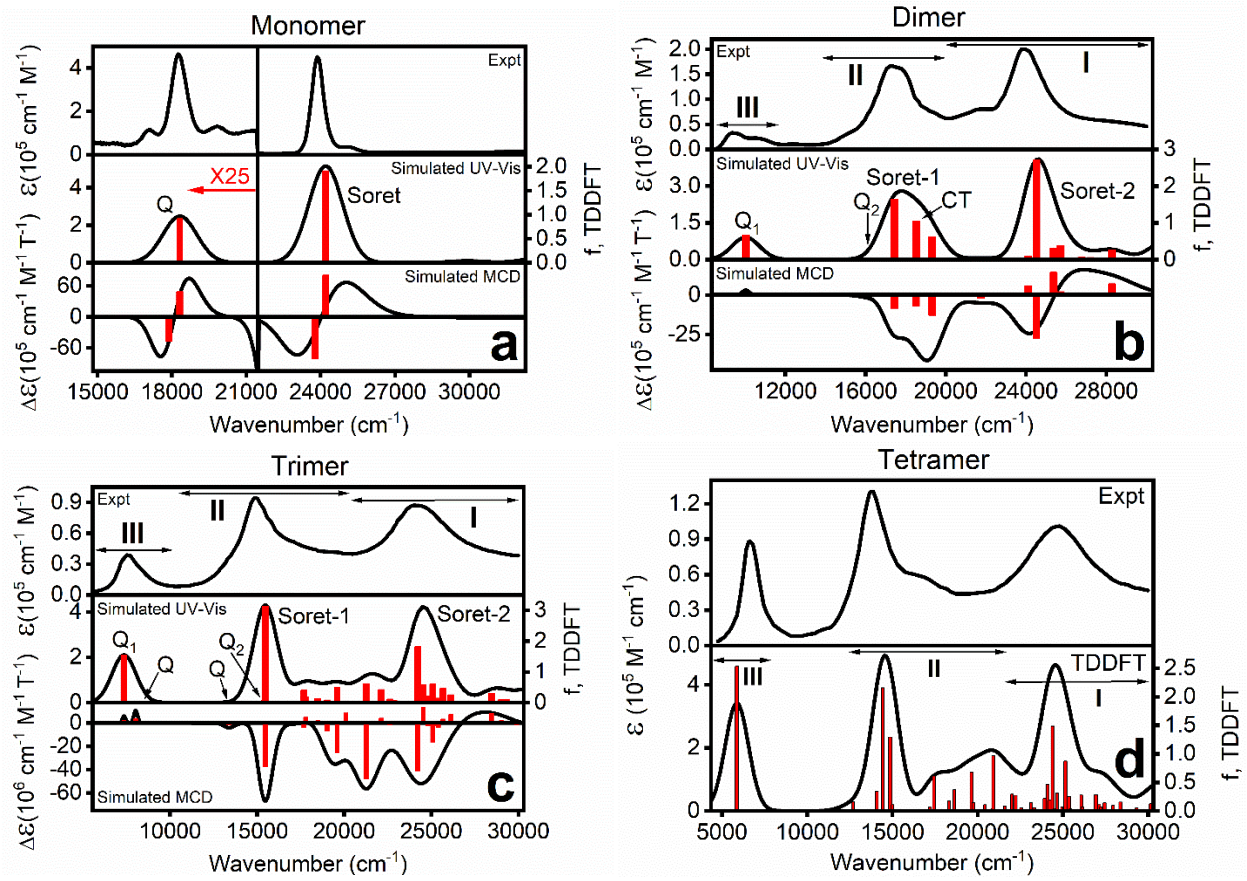

Figure 3.7. Experimental (top) and TDDFT-predicted (bottom) UV-vis and MCD spectra of (a.) monomer **1.1**, (b.) dimer **3.1**, (c.) trimer **3.2**, and (d.) tetramer **3.3**. Experimental data are adapted from ref. 63 with the permission from The American Association for the Advancement of Science.

Developed by Michl, the perimeter model[81-83] allows for the prediction of the sign sequence of MCD signals that are associated with the *Q*-bands of porphyrins. When ΔHOMO > ΔLUMO (ΔHOMO is the energy difference between the two highest in energy occupied orbitals localized at the porphyrin core and ΔLUMO is the energy difference between the two lowest in energy unoccupied orbitals localized at the porphyrin core), a negative-to-positive sign sequence (in

ascending energy) of the *A*- or *B*-terms that are associated with the *Q*-bands is observed. When ΔHOMO < ΔLUMO, the opposite sign sequence is predicted. In the case of porphyrin tapes **3.1**-**3.9**, the MOs that contribute to the ΔHOMO and ΔLUMO energies were defined by Osuka, Kobayashi, and co-workers and used in this paper without changes.[65] The density functional theory-predicted ΔHOMO > ΔLUMO for **1.1** (Table S3.1 and Fig. 3.8) correlates well with its magnetic circular dichroism spectrum which has a negative to positive sign sequence (in ascending energy) in the *Q*-band region. Not surprisingly, TDDFT SOS calculations correctly predicted the sign sequence and relative amplitudes of the MCD spectrum for this compound (Fig. 3.7a). Indeed, both *Q*- and Soret bands of **1.1** are represented by two MCD *A*-terms with their negative components having lower energies.

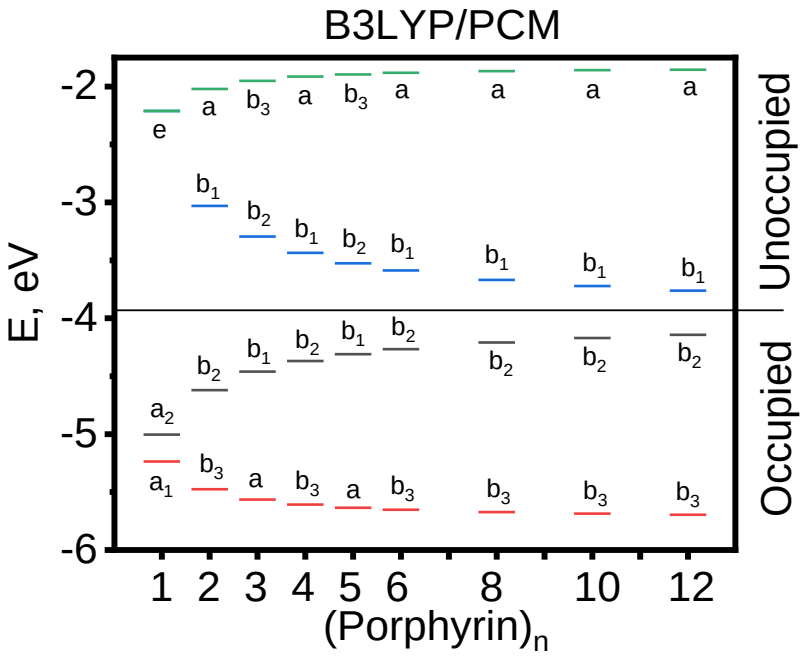

Figure 3.8. DFT-predicted energies of the ΔHOMO and ΔLUMO orbitals in **1.1** and **3.1**-**3.9**.

Table 3.1. DFT (B3LYP/PCM) predicted energies (eV) of ΔHOMO and ΔLUMO orbitals.

n	"$HOMO_1$"	"$HOMO_2$"	ΔHOMO	"$LUMO_1$"	"$LUMO_2$"	ΔLUMO	ΔLUMO-ΔHOMO
1	-5.004	-5.236	0.232	-2.211	-2.211	0.000	-0.232
2	-4.620	-5.475	0.856	-3.030	-2.020	1.009	0.154
3	-4.460	-5.564	1.104	-3.295	-1.951	1.344	0.240
4	-4.369	-5.608	1.239	-3.435	-1.914	1.521	0.282
5	-4.310	-5.635	1.325	-3.525	-1.895	1.630	0.305
6	-4.267	-5.652	1.385	-3.587	-1.881	1.705	0.320
8	-4.209	-5.673	1.464	-3.669	-1.867	-1.802	0.338
10	-4.170	-5.686	1.516	-3.722	-1.859	-1.863	0.347
12	-4.142	-5.696	1.554	-3.761	-1.855	-1.906	0.352

The frontier orbitals of the dimer **3.1** can be viewed as linear combinations of the a_{2u}/a_{1u} and e_{gx}/e_{gy} orbitals (Fig. 3.5). In particular, the HOMO and HOMO-3 in **3.1** are formed as the antibonding and bonding combinations of the a_{2u} orbital of ZnTPP (**1.1**) while HOMO-1 and HOMO-2 in **3.1** are formed as the linear combination of antibonding and bonding interactions between two a_{1u} type orbitals of ZnTPP **(1.1)**. Similaraly, the LUMO and LUMO+3 in **3.1** are formed as the bonding and antibonding combinations of the e_{gx} orbitals of ZnTPP (**1.1**) while

LUMO and LUMO+2 in **3.1** are formed by bonding and antibonding combinations of e_{gy}-type orbitals of the ZnTPP (**1.1**) core. Our DFT results for the frontier orbitals of **3.1** correlate well with the PPP and ZINDO/S calculations reported earlier.[64,65]

Following previous reports by Osuka and co-workers, the UV-vis-NIR spectrum of the dimer **3.1** was separated into spectral regions III (E < 17,000 cm^{-1}), II (E = 17,000 – 24,000 cm^{-1}), and I (E > 24,000 cm^{-1}). Overall, the TDDFT calculations predicted 26 excited states with oscillator strengths higher than 0.01 from 1000-300 nm. Out of these, 11 excited states have high intensity (f > 0.1) and form the absorption profile of the UV-vis-NIR spectrum of **3.1**. On a qualitative level, our TDDFT calculations for the dimer **3.1** as well as porphyrin tapes **3.2**-**3.9** correlate well with the earlier PPP results. When the porphyrin dimer **3.1** was considered, TDDFT calculations predicted five excited states within spectral region III. The lowest energy transitions for the dimeric compound **3.1** are predicted to have ~94% contribution from the HOMO → LUMO single electron excitation which is complemented by a ~5% contribution from the HOMO-1 → LUMO+1 transition (Table S3.1). This transition is defined as Q_1 in the previous work and has high intensity.[64] TDDFT also predicted a second excited state in the band III region at ~10700 cm^{-1} (934 nm). This transition originates from a HOMO-1 to LUMO single electron excitation (98%) but has zero intensity according to TDDFT calculations. Thus, the experimentally observed shoulders in region III can be attributed to the vibronic components of the Q_1 band (Fig. 3.7b). The only other excited state with appreciable intensity predicted for spectral region III has an oscillator strength of 0.017 and is located at 620 nm. It is dominated by HOMO-2 → LUMO (~64%) and HOMO → LUMO+2 (~33%) single electron transitions. This

excited state has y-polarization and was suggested by Osuka, Kobayashi, and co-workers as the excited state for the Q_2 transition.[65] A similar y-polarized transition has been predicted by the PPP SCI calculations performed by Osuka, Kim, and coworkers.[64] Again, our TDDFT predictions for these low intensity excited states are within 0.1 eV uncertainty between theory and magnetic circular dichroism (MCD) experiment.

According to TDDFT results, the region II envelope in the UV-vis spectrum of the dimer should be dominated by three excited states (excited states 6, 7, and 8) out of the ten predicted by calculations. The nature of excited states 6 and 8 can be considered as localized porphyrin π-π transitions. These excited states are dominated by the HOMO-1 → LUMO+1 (~91%) single electron excitation (excited state 6) or HOMO → LUMO+2 (~58%) and HOMO-2 → LUMO (~27%) single electron excitations (excited state 8, Table S3.1). In addition, the strong band associated with excited state 7 is dominated (~93%) by the single electron excitation from HOMO-4 to LUMO. The HOMO-4 orbital mostly consists of bridging atoms that are connected to porphyrin subunits while the LUMO is the bonding linear combination of two e_{gx} orbitals localized over two porphyrins. Thus, excited state 8 can be viewed as intramolecular charge transfer which moves electron density from the triply linked portion of the dimer to the periphery. Such charge transfer transitions were suggested on the basis of PPP SCI calculations by Osuka, Kim, and coworkers.[64] Osuka and Kim proposed that the two very intense x- and y-polarized bands observed in regions II and I of the spectrum of the dimer can be assigned as Soret-x and Soret-y bands (labeled as Soret-type bands in this paper).[64] In our TDDFT calculations, these bands were predicted to be excited states 6 and 17. In both of these excited

states, HOMO-1/HOMO-3 → LUMO+1/LUMO+3 single electron transitions dominate the configurational interaction. Again, the TDDFT-predicted energy of the Soret-type band (17434 cm^{-1}) correlates well with the 17285 cm^{-1} maximum, observed experimentally in region II, while the TDDFT-predicted energy for the Soret-type band (24518 cm^{-1}) correlates well with the strong peak observed at 23873 cm^{-1} in region I of the experimental spectrum of the dimer. Again, several excited states that contribute to region I of the spectral envelope of the dimer (excited states 22, f = 0.303 and 23, f = 0.377 in particular) possess intramolecular charge-transfer character that is associated with the HOMO → LUMO+4, and HOMO-5 → LUMO+1 single electron excitations. Finally, DFT-predicted excited states 42, 49, 50, and 53 also have relatively high intensities and (except excited state 42) have predominant intramolecular charge-transfer character (Table S3.1).

Following the definitions of the ΔHOMO and ΔLUMO orbitals reported by Osuka, Kobayashi, and co-workers, the ΔHOMO of dimer **3.1** is smaller than the ΔLUMO (Fig. 3.8 and Table 3.1). According to the perimeter model, the ΔHOMO < ΔLUMO relationship should result in a positive-to-negative (in ascending energy) sign sequence in the *Q*-band region of the MCD spectrum of **3.1**, which correlates well with the experimental data. Our TDDFT SOS calculations also predicted that the lowest energy band in the MCD spectrum of **3.1** (~1000 nm) has a positive amplitude of its *B*-term, while the transition at ~620 nm (assigned as the Q_2 band) should have a negative amplitude of its MCD *B*-term (Figure 3.7b). Also noteworthy, is the agreement with the experimental data, as the TDDFT SOS calculations predicted similar absolute magnitudes for the MCD signals associated with the Q_1 and Q_2 bands, while their

oscillator strengths (that are reflective of the Q_1 and Q_2 band intensities in their UV-vis-NIR spectra) differ by more than an order of magnitude.

In the case of the trimer **3.2**, the linear combinations of Gouterman's a_{1u}, a_{2u}, and e_g type orbitals result in several interesting spectral features. In particular, the HOMO-3, HOMO-2, and LUMO+3 orbitals have depleted electron density at the central subunit. Again, similar to the dimer, the HOMO and HOMO-1 in the trimer tape are fully antibonding linear combinations of a_{2u} and a_{1u} Gouterman-type orbitals (Fig. 3.5). For the trimer **3.2**, the Q_1-band again consists of almost pure single electron excitation from the HOMO to the LUMO and correlates well with the experimentally observed intense band in region III. In agreement with the previous PPP calculations, this is the only intense transition predicted for spectral region III of **3.2**. There were two y-polarized low intensity bands predicted by TDDFT calculations in the low-energy envelope of the visible spectrum (excited states 6 and 8). Excited state 6 consists of almost pure single electron excitation from the HOMO to the LUMO+2 while excited state 8 has two major contributions originating from HOMO-4 → LUMO (~76%) and HOMO → LUMO+4 (~20%) single electron excitations. TDDFT-predicted excited state 6 also correlates very well with the position of the Q_2 band (Table S3.1), which was experimentally proposed on the basis of MCD spectroscopy. The most intense TDDFT-predicted transition in spectral region II belongs to the Soret-type band (excited state 9). This band possesses the greatest intensity in the entire predicted spectrum and correlates with the experimental data extremely well with respect to region II, and has ~90% contribution from the HOMO-1 → LUMO+2 single electron excitation. The second most intense transition was predicted in spectral region I and has Soret-type

character. It was computationally predicted as excited state 40 and fits nicely with the most intense peak in experimental region I. It has high oscillator strength and is mostly defined by a single electron contribution from HOMO-1 → LUMO+5 (46%) which is complimented by several other single electron excitations. In agreement with the experimental data,[63] TDDFT predicted 17 other intense (f > 0.1) transitions in spectral regions II and I, with many of them having intramolecular charge transfer character (Table S3.1 and Fig. 3.7c).

Again, DFT predicted ΔHOMO < ΔLUMO for the trimer **3.2** (Fig. 3.8 and Table 3.1), which should result in positive-to-negative (in ascending energy) amplitude of the *B*-terms in the *Q*-band region. Indeed, our TDDFT SOS calculations (Fig. 3.7c) predict positive amplitude for the *B*-term at 1358 nm (Q_1 band) and a negative amplitude for the *B*-term at 649 nm (Q_2 band). The former *B*-term corresponds to the intense absorption of the trimer **3.2** in spectral region III. In addition, the TDDFT SOS calculations suggest the presence of the other pair of opposite sign and intensity *B*-terms at 1245 (positive amplitude) and 747 (negative amplitude) nm, which are associated with very low intensity absorption bands in the UV-vis-NIR spectrum of **3.2**. The *B*-term at 1245 nm correlates well with the second positive MCD signal observed experimentally for trimer **3.2**.

In the case of the tetramer **3.3**, the HOMO represents the fully antibonding combination of the a_{2u} Gouterman-type orbital while the HOMO-1 is the fully antibonding combination of the Gouterman a_{1u} type orbital; however, unlike in the case of the dimer and trimer tapes, the outermost subunits of the tetramer's HOMO-1 have depleted electron density compared to the two inner units (Fig. 3.5). Similar to the HOMO, the LUMO and LUMO+1 are fully bonding

combinations of the e_x and e_y orbitals delocalized over the entire tetramer core. The TDDFT-predicted energy and intensity of the Q_1 transition in the tetramer correlates well with the strong absorption experimentally observed in the near-infrared region III. This transition has x-polarization and consists almost purely of a single electron HOMO to LUMO excitation. There are two candidates for the Q_2 band based on the TDDFT calculations (excited states 6 and 11) and both of these excited states have y-polarization. The first one is dominated (~86%) by single electron excitation from the HOMO-1 to the LUMO+2 while the second is dominated (~92%) by single electron excitation from HOMO to LUMO+3. TDDFT predicted two strong x-polarized bands at 693 and 672 nm which contribute the most to the intensity of spectral region II (excited states 13 and 14, Table S3.1). The first one is dominated by single electron excitations from HOMO-1 to LUMO+2 (~43%) and HOMO to LUMO+4 (~39%), while the latter one is dominated by single electron contributions from HOMO-1 to LUMO+2 (~45%) and HOMO-2 to LUMO+1 (~39%). The most intense y-polarized Soret-type band was predicted in spectral envelop I (excited state 75) and is consistent with those of smaller porphyrin tape lengths described so far. This transition is dominated by the HOMO-1 to LUMO+7 (~30%) single electron excitation which is complemented by several other single electron transitions. Time-dependent density functional theory also predicted a large number of π-π and intramolecular charge transfer events which occur between the Soret-type x- and y-polarized transitions that were experimentally observed between the most intense spectral regions II and I (Fig. 3.7d).

Again, DFT calculations predicted a ΔHOMO < ΔLUMO relationship for the tetramer **3.3**, which is indicative of the positive-to-negative (in ascending energy) amplitudes of the Q_1 and Q_2

bands. It correlates well with the positive signal observed in spectral region III of this compound.[65] Unfortunately, our TDDFT SOS code cannot handle porphyrin tapes larger than a trimer **3.2** and thus, it is not clear if the second positive MCD signal observed as a shoulder around 1200 nm corresponds to the separate MCD-active excited state (similar to that predicted for trimer **3.2**) or if it is a vibronic component of the Q_1 band.

The general trends of porphyrin tapes **3.4**-**3.9** (Figs. S3.19-S3.23) in spectral regions III and II follow the trends established for the porphyrin tapes **3.1**-**3.3**. In particular, region III is dominated by the first excited state which, in all cases, originates almost purely from a HOMO to LUMO single electron excitation. In all of the longer tapes, spectral region II is also dominated by the x-polarized Soret-type transition which correlates well with the position of the experimental peak in spectral region II. Starting from the pentamer **3.4**, the spectral envelope is mainly defined as a superposition of lower intensity π-π* and charge-transfer transitions. For all longer porphyrin tapes (**3.4**-**3.9**), there is a large number of intramolecular charge transfer transitions that were predicted by the TDDFT calculations in spectral envelopes I and II. This agrees well on a qualitative level with the previous PPP calculations[64] and contrasts the ZINDO/S data[65] according to which spectral region II is dominated by a single excited state. In addition, the ΔHOMO < ΔLUMO relationship was predicted by the DFT calculations for the porphyrin tapes **3.4**-**3.9** (Table 3.1 and Fig. 3.8), which is indicative of the positive-to-negative (in ascending energy) amplitudes of the *B*-terms for the Q_1 and Q_2 bands in their respective MCD spectra (no experimental data are available for these systems). In general, the ΔLUMO - ΔHOMO value increases with the size of the porphyrin tape (Table 3.1).

The TDDFT-predicted intensity of the lowest energy transition was observed to have a linear dependency on the number of units in the porphyrin tape (Fig. 3.9a) and, conversely, exponential decay behavior vs. its energy (Fig. 3.9b). Since its energy also follows a pseudo-exponential decay trend as the number of units increases, it was not surprising to observe the same trend in the HOMO-LUMO gap (Fig. 3.9c).

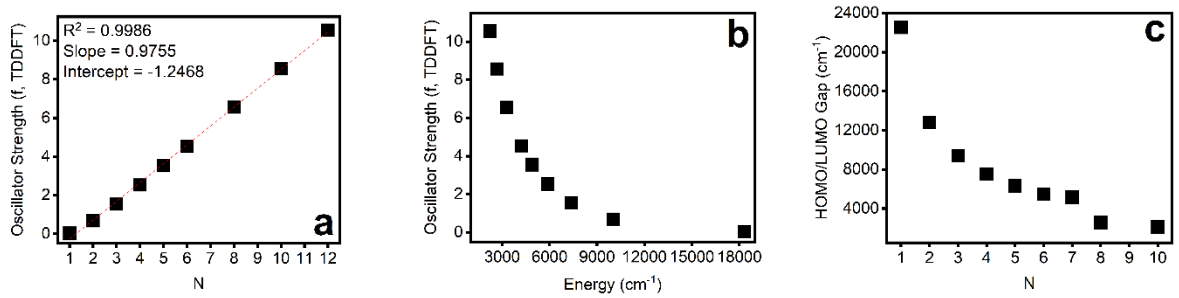

Figure 3.9 (a.) TDDFT-predicted intensity (*f*) of the λ_{max} band versus porphyrin tape length. **(b.)** TDDFT-predicted intensity (*f*) of the λ_{max} band versus its predicted energy. **(c.)** Energy of the HOMO-LUMO gap versus porphyrin tape length.

3.4 Conclusions

Overall, our TDDFT calculations correlate well on a qualitative level, with the PPP SCI calculations reported by Kim, Osuka, and coworkers;[64] however, unlike with the previous calculations, our time-dependent density functional theory work provided a significant improvement in accuracy with regards to the agreement achieved between theoretical and experimental data, with respect to the transition energies and intensities which afforded band assignments that are more reliable than anything reported previously. We can confirm that with increasing size of the porphyrin tape, there is an increase in intramolecular charge-transfer

states between spectral regions II and I. We can also confirm that spectral region III is dominated by a single transition state which originates almost exclusively from a HOMO to LUMO excitation. We observed quantitative correlation between the x-polarized Soret-type transition and the most intense band that was experimentally observed in region II. We have also demonstrated, at least for the shorter tapes (**3.1**-**3.3**), that spectral region I is dominated by the y-polarized Soret-type transition. In the cases of porphyrins **1.1** and **3.1**-**3.9**, where the ΔHOMO and ΔLUMO values were defined following the method reported by Osuka, Kobayashi, and co-workers, our calculations agree well with the semiempirical ZINDO/S spectral predictions and available experimental MCD data reported previously for systems **1.1** and **3.1**-**3.3**.[65] In particular, the TDDFT SOS calculations correctly predicted the signs of the MCD *A*- and *B*-terms in the *Q*-band region.

Interestingly, for compounds **3.1**-**3.9**, a ΔHOMO < ΔLUMO relationship was observed, indicating that extension of the π-system in both directions along the y-axis was enough to influence this result. As the porphyrin tape length increased, the orbital initially labelled as e_{gy} (for the monomer) became more destabilized in a linear fashion. This caused the ΔLUMO value to increase with each additional porphyrin subunit present in the chain. The significance here being that these are rare example of synthetically prepared porphyrin-based structures that possesses a ΔHOMO < ΔLUMO relationship, which is typically only observed for naturally occurring reduced porphyrinoid species.

3.5 Experimental Section

3.5.1 Materials and Instrumentation. Dichloromethane (DCM) used in the experiments was purchased from commercial sources and dried by distillation before use. Compound **1.1** was obtained from Boulder Scientific Company. All UV−vis spectra were collected on a Jasco V-770 spectrophotometer. Experimental data for **3.1**−**3.9** are adapted from reference 63 with permission from the publisher.

3.5.2 Computational Aspects. All TDDFT calculations were performed using the Gaussian 09 software package.[84] The starting geometries of the target compounds were optimized using the LC-wPBE,[85] B3LYP,[86,87] and CAM-B3LYP[88] exchange-correlation functionals both in the gas phase and with chloroform as solution media. In the latter case, the PCM approach was used.[89] The equilibrium geometries were confirmed with frequency calculations and, more specifically, by the absence of imaginary frequencies. Taking into consideration the size of the oligomers, Wachters full-electron basis set was used for zinc[90] and the 6-31G(d) basis set[91] was used for all other atoms. GaussView was used to visualize the orbitals and the TDDFT-predicted spectra. The QMForge[92] DFT analysis program was used to compile molecular orbital contributions from single-point calculations. Magnetic circular dichroism (MCD) spectra were simulated using the sum-over-state (SOS) approach as described previously.[92-96] This approach uses the TDDFT-predicted wavefunction and expansion coefficients to determine the intensities of the MCD *A*- and *B*-terms. The semiempirical ZINDO/1[97] geometry optimization and frequency calculation of the monomeric porphyrin **1.1** in the D_{4h} symmetry point group were done using HyperChem 8.0.10 software.[98]

3.6 References

1. Weitz, A. C.; Biswas, S.; Rizzolo, K.; Elliott, S.; Bominaar, E. L.; Hendrich, M. P. Electronic State of the His/Tyr-Ligated Heme of BthA by Mössbauer and DFT Analysis. *Inorg. Chem.* **2020**, *59*, 10223-10233.

2. Ehudin, M. A.; Gee, L. B.; Sabuncu, S.; Braun, A.; Moenne-Loccoz, P.; Hedman, B.; Hodgson, K. O.; Solomon, E. I.; Karlin, K. D. Tuning the Geometric and Electronic Structure of Synthetic High-Valent Heme Iron(IV)-Oxo Models in the Presence of a Lewis Acid and Various Axial Ligands. *J. Am. Chem. Soc.* **2019**, *141*, 5942-5960.

3. Chang, H.-C.; Mondal, B.; Fang, H.; Neese, F.; Bill, E.; Ye, S. Electron Paramagnetic Resonance Signature of Tetragonal Low Spin Iron(V)-Nitrido and -Oxo Complexes Derived from the Electronic Structure Analysis of Heme and Non-Heme Archetypes. *J. Am. Chem. Soc.* **2019**, *141*, 2421-2434.

4. Peng, Q.; Sage, J. T.; Liu, Y.; Wang, Z.; Hu, M. Y.; Zhao, J.; Alp, E. E.; Scheidt, W. R.; Li, J. How Does a Heme Carbene Differ from Diatomic Ligated (NO, CO, and CN^-) Analogues in the Axial Bond? *Inorg. Chem.* **2018**, *57*, 8788-8795.

5. Alenkina, I. V.; Kumar, A.; Berkovsky, A. L.; Oshtrakh, M. I. Comparative Analysis of the Heme Iron Electronic Structure and Stereochemistry in Tetrameric Rabbit Hemoglobin and Monomeric Soybean Leghemoglobin α using Mössbauer Spectroscopy with a High Velocity Resolution. *Spectrochim. Acta*, **2018**, *191A*, 547-557.

6. Gorski, A.; Starukhin, A.; Stavrov, S. S. Mössbauer Spectroscopy as a Probe of Electric Field in Heme Pocket of Deoxyheme Proteins: Theoretical Approach. *J. Radioanalyt. Nucl. Chem.* **2017**, *313*, 141-144.

7. Yosca, T. H.; Langston, M. C.; Krest, C. M.; Onderko, E. L.; Grove, T. L.; Livada, J.; Green, M. T. Spectroscopic Investigations of Catalase Compound II: Characterization of an Iron(IV) Hydroxide Intermediate in a Non-thiolate-Ligated Heme Enzyme. *J. Am. Chem. Soc.* **2016**, *138*, 16016-16023.

8. Khade, R. L.; Fan, W.; Ling, Y.; Yang, L.; Oldfield, E.; Zhang, Y. Iron Porphyrin Carbenes as Catalytic Intermediates: Structures, Mössbauer and NMR Spectroscopic Properties, and Bonding. *Angew. Chem., Int. Ed.* **2014**, *53*, 7574-7578.

9. Nakamura, M.; Takahashi, M. Basics and Applications of Mössbauer Spectrometry Methodology to Determine Heme Electronic Structure by means of Mössbauer Spectrometry. *Radioisotopes* **2013**, *62*, 609-622.

10. Kepp, K. P.; Dasmeh, P. Effect of Distal Interactions on O_2 Binding to Heme. *J. Phys. Chem. B* **2013**, *117*, 3755-3770.

11. Lascu, A. Platinic Metal Porphyrins and Hybrid Nanomaterials Embedding Them as Catalysts in Chemical Transformations. *ARKIVOC* **2020**, (*i*), 272-296.

12. Beyene, B. B.; Hung, C.-H. Recent Progress on Metalloporphyrin-based Hydrogen Evolution Catalysis. *Coord. Chem. Rev.* **2020**, *410*, 213234.

13. Smith, P. T.; Nichols, E. M.; Cao, Z.; Chang, C. J. Hybrid Catalysts for Artificial Photosynthesis: Merging Approaches from Molecular, Materials, and Biological Catalysis *Acc. Chem. Res.* **2020**, *53*, 575-587.

14. Weissenborn, M. J.; Koenigs, R. M. Iron-porphyrin Catalyzed Carbene Transfer Reactions - an Evolution from Biomimetic Catalysis towards Chemistry-inspired Non-natural Reactivities of Enzymes. *ChemCatChem* **2020**, *12*, 2171-2179.

15. Gotico, P.; Halime, Z.; Aukauloo, A. Recent Advances in Metalloporphyrin-based Catalyst Design towards Carbon Dioxide Reduction: From Bio-inspired Second Coordination Sphere Modifications to Hierarchical Architectures. *Dalton Trans.* **2020**, *49*, 2381-2396.

16. Longevial, J.-F.; Clement, S.; Wytko, J. A.; Ruppert, R.; Weiss, J.; Richeter, S. Peripherally Metalated Porphyrins with Applications in Catalysis, Molecular Electronics and Biomedicine. *Chem. Eur. J.* **2018**, *24*, 15442-15460.

17. Dogutan, D. K.; Bediako, D. K.; Graham, D. J.; Lemon, C. M.; Nocera, D. G. Proton-coupled Electron Transfer Chemistry of Hangman Macrocycles: Hydrogen and Oxygen Evolution Reactions. *J. Porphyrins Phthalocyanines* **2015**, *19*, 1-8.

18. Santoro, A. M.; Lo Giudice, M. C.; D'Urso, A.; Lauceri, R.; Purrello, R.; Milardi, D. Cationic Porphyrins are Reversible Proteasome Inhibitors. *J. Am. Chem. Soc.* **2012**, *134*, 10451-10457.

19. Ohshima, T.; Hirata, M.; Oda, T.; Sasaki, A.; Shiratsuchi, M. Pheophorbide A, A Potent Endothelin Receptor Antagonist for Both ETA and ETB Subtypes. *Chem. Pharm. Bull.* **1994**, *42*, 2174-2176.

20. Mody, T. D. Pharmaceutical Development and Medical Applications of Porphyrin-Type Macrocycles. *J. Porphyrins Phthalocyanines* **2000**, *4*, 362-367.

21. Guo, C. C.; Tong, R. B.; Li, K. L. Chloroalkyl Piperazine and Nitrogen Mustard Porphyrins: Synthesis and Anticancer Activity. *Bioorg. Med. Chem.* **2004**, *12*, 2469-2475.

22. Amirshani, N.; Alyautdin, R. N.; Sarkar, S.; Rezayat, S. M.; Orlova, M. A.; Trushkov, I. V.; Buchachenko, A. L.; Kuznetsov, D. A. New Porphyrin Adduct of Fullerene-C_{60}: A Promising Nanotool for Medicinal Use in the Heart Muscle Hypoxia Cases. *Int. J. Nanosci.* **2008**, *7*, 113-135.

23. McCoy, C. P; Craig, R. A.; McGlinchey, S. M.; Carson, L.; Jones, D. S.; Gorman, S. P. Surface Localization of Photosensitizers on Intraocular Lens Biomaterials for Prevention of Infectious Endophthalmitis and Retinal Protection. *Biomaterials* **2012**, *33*, 7952-7958.

24. Gomes, M. L.; DeFreitas-Silva, G.; dos Reis, P. G.; Melo, M. N.; Frezard, F.; Demicheli, C.; Idemori, Y. M. Synthesis and Characterization of Bismuth(III) and Antimony(V) Porphryins: High Antileishmanial Activity Against Antimony-Resistant Parasite. *JBIC, J. Biol. Inorg. Chem.* **2015**, *20*, 771-779.

25. Afzal, S.; Daoud, W. A.; Langford, S. J. Photostable Self-Cleaning Cotton By a Copper(II) Porphyrin/TiO_2 Visible-Light Photocatalytic System. *ACS Appl. Mater. Interfaces* **2013**, *5*, 4753−4759.

26. Isik-Buyukeksi, S.; Karatay, A.; Orman, E. B.; Acar-Selcuki, S.; Ozkaya, A. R.; Salih, B.; Elmali, A.; Sengul, A. A Novel AB3-Type Trimeric Zinc(II)-Phthalocyanine as an Electrochromic and Optical Limiting Material. *Dalton Trans.* **2020**, *49*, 14068-14080.

27. Silver, J.; Lukes, A.; Houlton, A.; Howe, S.; Hey, P.; Ahmet, M. T. Electrochromism in the Transition-Metal Phthalocyanines. Part 3. Molecular Organization, Reorganization and Assembly Under the Influence of an Applied Electric Field. Response of [Fe(pc)] and [Fe(pc)Cl] *J. Mater. Chem.* **1992**, *2*, 849-855.

28. Nicholson, M. M.; Pizzarello, F. A. Cathodic Electrochromism of Lutetium Diphthalocyanine Films. *J. Electrochem. Soc.* **1981**, *128*, 1740-1743.

29. Karadag, S.; Bozoglu, C.; Kasim-Sener, M.; Koca, A. Synthesis and Electrochemical Properties of a Double-Decker Lutetium(III) Phthalocyanine Bearing Electropolymerizable Substituents on Non-Peripheral Positions. *Dyes Pigments* **2014**, *100*, 168-176.

30. McRae, E. K. S.; Nevonen, D. E.; McKenna, S. A.; Nemykin, V. N. Binding and Photodynamic Action of the Cationic Zinc Phthalocyanines with Different Types of DNA Toward Understanding of their Cancer Therapy Activity. *J. Inorg. Biochem.* **2019**, *199*, 110793/1-110793/9.

31. Agostinis, P.; Berg, K.; Cengel, K. A.; Foster, T. H.; Girotti, A. W.; Gollnick, S. O.; Hahn, S. M.; Hamblin, M. R.; Juzeniene, A.; Kessel, D.; Korbelik, M.; Moan, J.; Mroz, P.; Nowis, D.; Piette, J.; Wilson, B. C.; Golab, J. Photodynamic Therapy of Cancer: An Update. *Ca-Cancer J. Clin.* **2011**, *61*, 250– 281.

32. Ethirajan, M.; Chen, Y.; Joshi, P.; Pandey, R. K. The Role of Porphyrin Chemistry in Tumor Imaging and Photodynamic Therapy. *Chem. Soc. Rev.* **2011**, *40*, 340–362.

33. Singh, S.; Aggarwal, A.; Bhupathiraju, N. D. K.; Arianna, G.; Tiwari, K.; Drain, C. M. Glycosylated Porphyrins, Phthalocyanines, and Other Porphyrinoids for Diagnostics and Therapeutics. *Chem. Rev.* **2015**, *115*, 10261–10306.

34. Ziessel, R.; Hissler, M.; El-Ghayoury, A.; Harriman, A. Multifunctional Transition Metal Complexes: Information Transfer at the Molecular Level. *Coord. Chem. Rev.* **1998**, *178*, 1251–1298.

35. Li, X.; Zheng, B.-D.; Peng, X.-H.; Li, S.-Z.; Ying, J.-W.; Zhao, Y.; Huang, J.-D.; Yoon, J. Phthalocyanines as Medicinal Photosensitizers: Developments in the Last Five Years. *Coord. Chem. Rev.* **2019**, *379*, 147–160.

36. Li, X.; Lee, S.; Yoon, J. Supramolecular Photosensitizers Rejuvenate Photodynamic Therapy. *Chem. Soc. Rev.* **2018**, *47*, 1174–1188.

37. Mathew, S.; Yella, A.; Gao, P.; Humphry-Baker, R.; Curchod, B. F. E.; Ashari-Astani, N.; Tavernelli, I.; Rothlisberger, U.; Nazeeruddin, M. K.; Grätzel, M. Dye-Sensitized Solar Cells

With 13% Efficiency Achieved Through the Molecular Engineering of Porphyrin Sensitizers. *Nat. Chem.* **2014**, *6*, 242–247.

38. Urbani, M.; Grätzel, M.; Nazeeruddin, M. K.; Torres, T. Meso-Substituted Porphyrins for Dye-Sensitized Solar Cells. *Chem. Rev.* **2014**, *114*, 12330– 12396.

39. Tang, Y.; Wang, Y.; Li, X.; Agren, H.; Zhu, W.-H.; Xie, Y. Porphyrins Containing a Triphenylamine Donor and up to Eight Alkoxy Chains for Dye-Sensitized Solar Cells: A High Efficiency of 10.9%. *ACS Appl. Mater. Interfaces* **2015**, *7*, 27976– 27985.

40. Ragoussi, M.-E.; Torres, T. New Generation Solar Cells: Concepts, Trends and Perspectives. *Chem. Commun.* **2015**, *51*, 3957– 3972.

41. Song, H.; Liu, Q.; Xie, Y. Porphyrin-Sensitized Solar Cells: Systematic Molecular Optimization, Coadsorption and Cosensitization. *Chem. Commun.* **2018**, *54*, 1811–1824.

42. Kurumisawa, Y.; Higashino, T.; Nimura, S.; Tsuji, Y.; Iiyama, H.; Imahori, H. Renaissance of Fused Porphyrins: Substituted Methylene-Bridged Thiophene-Fused Strategy for High-Performance Dye-Sensitized Solar Cells. *J. Am. Chem. Soc.* **2019**, *141*, 9910–9919.

43. Auwärter, W.; Écija, D.; Klappenberger, F.; Barth, J. V. Porphyrins at Interfaces. *Nat. Chem.* **2015**, *7*, 105–120.

44. Li, X. Y.; Sinks, L. E.; Rybtchinski, B.; Wasielewski, M. R. Ultrafast Aggregate-to-Aggregate Energy Transfer Within Self-Assembled Light-Harvesting Columns of Zinc Phthalocyanine Tetrakis(Perylenediimide) *J. Am. Chem. Soc.* **2004**, *126*, 10810–10811.

45. Lindsey, J. S.; Brown, P. A.; Siesel, D. A. Visible Light-Harvesting in Covalently-Linked Porphyrin-Cyanine Dyes. *Tetrahedron* **1989**, *45*, 4845-4866.

46. Prathapan, S.; Johnson, T. E.; Lindsey, J. S. Building-Block Synthesis of Porphyrin Light-Harvesting Arrays. *J. Am. Chem. Soc.* **1993**, *115*, 7519-7520.

47. Gregg, B. A.; Resch, U. Design of an Artificial Light Harvesting System that may Spontaneously Evolve Toward Greater Efficiency. *J. Photochem. Photobiol., A* **1995**, *87*, 157-162.

48. Kodis, G.; Herrero, C.; Palacios, R.; Marino-Ochoa, E.; Gould, S.; De la Garza, L.; Van Grondelle, R.; Gust, D.; Moore, T. A.; Moore, A. L. Light Harvesting and Photoprotective Functions of Carotenoids in Compact Artificial Photosynthetic Antenna Designs. *J. Phys. Chem. B.* **2004**, *108*, 414-425.

49. Rhoda, H. M.; Kayser, M. P.; Wang, Y.; Nazarenko, A. Y.; Belosludov, R. V.; Kiprof, P.; Blank, D. A.; Nemykin, V. N. Tuning Up an Electronic Structure of the Subphthalocyanine Derivatives toward Electron-Transfer Process in Noncovalent Complexes with C_{60} and C_{70} Fullerenes: Experimental and Theoretical Studies. *Inorg. Chem.* **2016**, *55*, 9549-9563.

50. Li, Y.; Rhoda, H. M.; Wertish, A. M.; Nemykin, V. N. Organometallic Pyrene-containing Porphyrins: Synthesis, Characterization, and Non-covalent Interactions with C_{60} Fullerenes. *J. Porphyrins Phthalocyanines* **2016**, *20*, 1098-1113.

51. Tanaka, T.; Osuka, A. Triply Linked Porphyrinoids. *Chem. Eur. J.* **2018**, *24*, 17188-17200.

52. Fukui, N.; Kim, T.; Kim, D.; Osuka, A. Porphyrin Arch-Tapes: Synthesis, Contorted Structures, and Full Conjugation. *J. Am. Chem. Soc.* **2017**, *139*, 9075-9088.

53. Mori, H.; Kim, T.; Kim, D.; Osuka, A. Trimeric and Tetrameric Electron-Deficient Porphyrin Tapes. *Chem. Asian J.* **2016**, *11*, 1454-1463

54. Mori, H.; Tanaka, T.; Lee, S.; Lim, J. M.; Kim, D.; Osuka, A. *meso-meso* Linked Porphyrin-[26] Hexaphyrin-Porphyrin Hybrid Arrays and Their Triply Linked Tapes Exhibiting Strong Absorption Bands in the NIR Region. *J. Am. Chem. Soc.* **2015**, *137*, 2097-2106.

55. Mori, H.; Tanaka, T.; Osuka, A. Fused Porphyrinoids as Promising Near-infrared Absorbing Dyes. *J. Mater. Chem. C* **2013**, *1*, 2500-2519.

56. Mori, H.; Tanaka, T.; Aratani, N.; Lee, B. S.; Kim, P.; Kim, D.; Osuka, A. An Electron-Deficient Porphyrin Tape. *Chem. Asian J.* **2012**, *7*, 1811-1816.

57. Tanaka, T.; Lee, B. S.; Aratani, N.; Yoon, M.-C.; Kim, D.; Osuka, A. Synthesis and Properties of Hybrid Porphyrin Tapes. *Chem. Eur. J.* **2011**, *17*, 14400-14412.

58. Ikeda, T.; Aratani, N.; Osuka, A. Synthesis of Extremely π-Extended Porphyrin Tapes from Hybrid meso-meso Linked Porphyrin Arrays: An Approach Towards the Conjugation Length. *Chem. Asian J.* **2009**, *4*, 1248-1256

59. Nakamura, Y.; Jang, S. Y.; Tanaka, T.; Aratani, N.; Lim, J. M.; Kim, K. S.; Kim, D.; Osuka, A. Two-dimensionally Extended Porphyrin Tapes: Synthesis and Shape-dependent Two-photon Absorption Properties. *Chem. Eur. J.* **2008**, *14*, 8279-8289

60. Ikeda, T.; Lintuluoto, J. M.; Aratani, N.; Yoon, Z. S.; Kim, D.; Osuka, A. Synthesis of Doubly Strapped meso-meso-linked Porphyrin Arrays and Triply Linked Conjugated Porphyrin tapes. *Eur. J. Org. Chem.* **2006**, 3193-3204.

61. Aratani, N.; Osuka, A. Directly Linked Porphyrin Arrays. *Chem. Record* **2003**, *3*, 225-234.

62. Tsuda, A.; Nakamura, Y.; Osuka, A. Synthesis of meso-β Doubly Linked Porphyrin Tapes. *Chem. Commun.* **2003**, 1096-1097.

63. Tsuda, A.; Osuka, A. Fully Conjugal Porphyrin Tapes with Electronic Absorption Bands that Reach into Infrared. *Science* **2001**, *293*, 79-82.

64. Cho, H. S.; Jeong, D. H.; Cho, S.; Kim, D.; Matsuzaki, Y.; Tanaka, K.; Tsuda, A.; Osuka, A. Photophysical Properties of Porphyrin Tapes. *J. Am. Chem. Soc.* **2002**, *124*, 14642-14654.

65. Muranaka, A.; Yokoyama, M.; Matsumoto, Y.; Uchiyama, M.; Tsuda, A.; Osuka, A.; Kobayashi, N. Magnetic Circular Dichroism Study of Directly Fused Porphyrins. *ChemPhysChem* **2005**, *6*, 171-179.

66. Belosludov, R. V.; Nevonen, D.; Rhoda, H. M.; Sabin, J. R.; Nemykin, V. N. Simultaneous Prediction of the Energies of Qx and Qy Bands and Intramolecular Charge-Transfer Transitions in Benzoannulated and Non-Peripherally Substituted Metal-Free Phthalocyanines and Their Analogues: No Standard TDDFT Silver Bullet Yet. *J. Phys. Chem. A* **2019**, *123*, 132-152.

67. Doble, S.; Osinski, A. J.; Holland, S. M.; Fisher, J. M.; Geier, G. R.; Belosludov, R. V.; Ziegler, C. J.; Nemykin, V. N. Magnetic Circular Dichroism of Transition-Metal Complexes of Perfluorophenyl-N-Confused Porphyrins: Inverting Electronic Structure through a Proton. *J. Phys. Chem. A* **2017**, *121*, 3689-3698.

68. Belosludov, R. V.; Rhoda, H. M.; Zhdanov, R. K.; Belosludov, V. R.; Kawazoe, Y.; Nemykin, V. N. Conceptual Design of Tetraazaporphyrin- and Subtetraazaporphyrin-based Functional Nanocarbon Materials: Electronic Structures, Topologies, Optical Properties, and Methane Storage Capacities. *Phys. Chem. Chem. Phys.* **2016**, *18*, 13503-13518.

69. Nemykin, V. N.; Dudkin, S. V.; Fathi-Rasekh, M.; Spaeth, A. D.; Rhoda, H. M.; Belosludov, R. V.; Barybin, M. V. Probing Electronic Communications in Heterotrinuclear Fe-Ru-Fe Molecular Wires Formed by Ruthenium(II) Tetraphenylporphyrin and Isocyanoferrocene or 1,1'-Diisocyanoferrocene Ligands. *Inorg. Chem.* **2015**, *54*, 10711-10724.

70. Nemykin, V. N.; Hadt, R. G.; Belosludov, R. V.; Mizuseki, H.; Kawazoe, Y. Influence of Molecular Geometry, Exchange-Correlation Functional, and Solvent Effects in the Modeling of Vertical Excitation Energies in Phthalocyanines Using Time-Dependent Density Functional Theory (TDDFT) and Polarized Continuum Model TDDFT Methods: Can Modern Computational Chemistry Methods Explain Experimental Controversies? *J. Phys. Chem. A* **2007**, *111*, 12901-12913.

71. Martynov, A. G.; Mack, J.; May, A. K.; Nyokong, T.; Gorbunova, Y. G.; Tsivadze, A. Yu Methodological Survey of Simplified TD-DFT Methods for Fast and Accurate Interpretation of UV-Vis-NIR Spectra of Phthalocyanines. *ACS Omega* **2019**, *4*, 7265-7284.

72. Gorski, A.; Kijak, M.; Zenkevich, E.; Knyukshto, V.; Starukhin, A.; Semeikin, A.; Lyubimova, T.; Rolinski, T.; Waluk, J. Magnetic Circular Dichroism of *meso*-Phenyl-Substituted Pd-Octaethylporphyrins. *J. Phys. Chem. A* **2020**, *124*, 8144-8158.

73. Ortega-Guerrero, A.; Fumanal, M.; Capano, G.; Smit, B. From Isolated Porphyrin Ligands to Periodic Al-PMOF: A Comparative Study of the Optical Properties Using DFT/TDDFT. *J. Phys. Chem. C* **2020**, *124*, 21751−21760.

74. Alberto, M. E.; Mazzone, G.; Regina, C.; Russo, N.; Sicilia, E. Theoretical Exploration of the Photophysical Properties of Two-Component RuII-Porphyrin Dyes as Promising Assemblies for a Combined Antitumor Effect. *Dalton Trans.* **2020**, *49*, 12653-12661.

75. Du, J.; Feng, S.; Qin, P.; Zhang, Y.; Zhang, Z.; Xu, L. Theoretical Calculation on the Substituent Effect of Strontium Para-Tetraphenyl Porphyrins. *Struct. Chem.* **2020**, *31*, 1785-1792.

76. Dorazio, S. J.; Vogel, A.; Dechert, S.; Nevonen, D. E.; Nemykin, V. N.; Brueckner, C.; Meyer, F. Siamese-Twin Porphyrin Goes Platinum: Group 10 Monometallic, Homobimetallic, and Heterobimetallic Complexes. *Inorg. Chem.* **2020**, *59*, 7290-7305.

77. Dreuw, A.; Weisman, J. L.; Head-Gordon, M. Long-Range Charge-Transfer Excited States in Time-Dependent Density Functional Theory Require Non-Local Exchange. *J. Chem. Phys.* **2003**, *119*, 2943-2946.

78. Zerner, M.; Gouterman, M. Porphyrins. IV. Extended Hueckel Calculations on Transition Metal Complexes. *Theor. Chim. Acta* **1966**, *4*, 44-63.

79. Zerner, M.; Gouterman, M. Porphyrins. V. Extended Hueckel Calculations on Vanadyl (VO2+) and Vanadium(II) Complexes. *Inorg. Chem.* **1966**, *5*, 1699-1706.

80. Zerner, M.; Gouterman, M. Porphyrins. X. Extended Hueckel Calculations on Alkaline Earth Complexes. *Theor. Chim. Acta* **1967**, *8*, 26-34.

81. Waluk, J.; Michl, J. Perimeter Model and Magnetic Circular Dichroism of Porphyrin Analogs. *J. Org. Chem*. **1991**, *56*, 2729-2735.

82. Michl, J. Magnetic Circular Dichroism of Cyclic π-Electron Systems. 1. Algebraic Solution of the Perimeter Model for the *A* and *B* Terms of High-Symmetry Systems with a (4N + 2)-Electron [n]Annulene Perimeter. *J. Am. Chem. Soc.* **1978**, *100*, 6801-6811.

83. Michl, J. Magnetic Circular Dichroism of Cyclic π-Electron Systems. 2. Algebraic Solution of the Perimeter Model for the *B* Terms of Systems with a (4N + 2)-Electron [n]Annulene Perimeter. *J. Am. Chem. Soc.* **1978**, *100*, 6812-6818.

84. Frisch, M. J.; Trucks, G. W.; Schlegel, H. B.; Scuseria, G. E.; Robb, M. A.; Cheeseman, J. R.; Scalmani, G.; Barone, V.; Mennucci, B.; Petersson, G. A. *et al.* Gaussian 09, revision D.01; Gaussian, Inc.: Wallingford, CT, **2009**. (see Supporting Information for full citation)

85. Vydrov, O. A.; Scuseria, G. E. Assessment of a Long-Range Corrected Hybrid Functional. *J. Chem. Phys.* **2006**, *125*, 234109.

86. Becke, A. D. Density-functional Thermochemistry. III. The Role of Exact Exchange. *J. Chem. Phys.* **1993**, *98*, 5648−5652.

87. Lee, C.; Yang, W.; Parr, R. G. Development of the Colle-Salvetti Correlation-Energy Formula into a Functional of the Electron Density. *Phys. Rev. B* **1988**, *37*, 785-789.

88. Yanai, T.; Tew, D.; Handy, N. A New Hybrid Exchange Correlation Functional Using the Coulomb-Attenuating Method (CAM-B3LYP). *Chem. Phys. Lett.* **2004**, *393*, 51−57.

89. Tomasi, J.; Mennucci, B.; Cammi, R. Quantum Mechanical Continuum Solvation Models *Chem Rev*. **2005**, 105, 2999-3093.

90. Wachters, A. J. H. Gaussian Basis Set for Molecular Wavefunctions Containing Third-Row Atoms. *J. Chem. Phys.* **1970**, *52*, 1033-1036.

91. Petersson, G. A.; Bennett, A.; Tensfeldt, T. G.; Al-Laham, M. A.; Shirley, W. A.; Mantzaris, J. A Complete Basis Set Model Chemistry. I. The Total Energies of Closed-Shell Atoms and Hydrides of the First-Row Atoms. *J. Chem. Phys.* **1988**, *89*, 2193-218.

92. Tenderholt, A. L. *QMForge, version 2.1*; Stanford University: Stanford, CA, 2011.

93. Andrushchenko, V.; Padula, D.; Zhivotova, E.; Yamamoto, S.; Bouř, P. Magnetic Circular Dichroism of Porphyrin Lanthanide M^{3+} Complexes. *Chirality* **2014**, *26*, 655−662.

94. Štěpánek, P.; Bouř, P. Computation of Magnetic Circular Dichroism by Sum over States Summations. *J. Comput. Chem.* **2013**, *34*, 1531−1539.

95. Štěpánek, P.; Andrushchenko, V.; Ruud, K.; Bouř, P. Porphyrin Protonation Studied by Magnetic Circular Dichroism. *J. Phys. Chem. A* **2012**, *116*, 778−783.

96. Štěpánek, P.; Bouř, P. Origin-independent Sum over States Simulations of Magnetic and Electronic Circular Dichroism Spectra via the Localized Orbital/local Origin Method. *J. Comput. Chem.* **2015**, *36*, 723−730.

97. Bacon, A. D.; Zerner, M. C. An Intermediate Neglect of Differential Overlap Theory for Transition Metal Complexes: Fe, Co and Cu Chlorides *Theor. Chim. Acta* **1979**, *53*, 21–54.

98. HyperChem Professional, version 8.0; MakoLab, HyperCube Inc.: Gainesville, FL, 2007.

4 Siamese-Twin Porphyrin Goes Platinum: Group 10 Monometallic, Homobimetallic, and Heterobimetallic Complexes

4.1 Chapter Preface

In the last chapter, the π-system of zinc *meso*-tetraphenylporphyrin was extended in both directions through triple-linkages. This fashion of linkage allowed the porphyrin tapes to remain structurally rigid where full aromaticity was maintained (although minor structural flexing was observed/simulated). This extension of the π-system in both directions resulted in the rarely observed (within synthetic systems) ΔHOMO < ΔLUMO relationship for porphyrin tapes ranging in length from dimer to dodecamer (12 sequentially bound porphyrin units). Following our

success with the triply-linked porphyrin tapes, we then chose to examine the electronic structure of "twin" metalated (Ni, Pd, Pt) *meso*-tetraphenylporphyrins where the π-system was again extended along the arbitrary y-axis; however, the linkage for these systems was different and featured two porphyrins which are directly fused together. The monomeric units of these dimers are each missing one pyrrole ring and one *meso*-carbon/hydrogen in the final fused form. For these twin porphyrin systems, it is hypothesized that the e_{gy} orbital of the monomers will become destabilized following macrocyclic fusion, resulting in a larger ΔLUMO value. The focus here was to again, observe whether or not the ΔLUMO value exceeds ΔHOMO.

4.2 Introduction

Expanded porphyrins are porphyrin-inspired oligopyrrolic macrocycles of at least seventeen internal ring atoms.[1-6] Such expansion may introduce, inter alia, conformational flexibility into the macrocycle, enlarge its metal binding cavity, or increase the number of donor atoms for the complexation of one or more metal ions. Most expanded porphyrins rely on increasing the number of pyrrolic building blocks linked either directly via α-α linkages or through one carbon atom, such as the classic sapphyrin,[7-8] hexaphyrin **$H_2$1**,[9-13] octaphyrins **$H_4$2**,[14-16] or even larger architectures (Figure 4.1).[5-6] Non-pyrrolic heterocycles (e.g., thiophene, furan, pyridine, or pyrazole)[8, 17-23] or conjugated spacers such as phenylene[24] or ferrocene[25] may be incorporated into the macrocycle, illustrating the broad diversity of molecules categorized as expanded porphyrins.

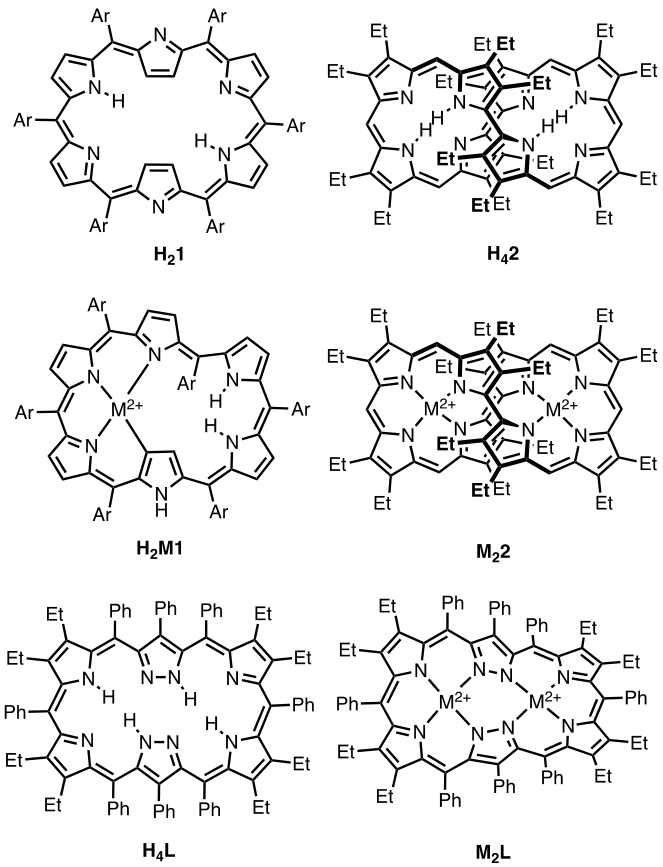

Figure 4.1. Representative expanded porphyrins and their metal complexes: A hexaphyrin **$H_2$1** and its metal complexes **H_2M1**, an octaphyrin **$H_4$2** and its metal complexes **$M_2$2**, and the Siamese-twin porphyrin H_4L (**4.1**) and its metal complexes **M_2L**.

An abundance of main group, d-block, and f-block metal ions coordinate to expanded porphyrins,[26-27] mirroring the versatility of porphyrinic ligands while providing further insight into aromaticity, morphology, and electronic communication.[5, 28-31] Changes in macrocycle topology upon metal ion complexation are reflected in the frequently much altered electronic properties of the macrocycle, as measured by, for instance, UV-vis spectroscopy, NMR spectroscopy, and electrochemistry.[5, 28-31]

We previously introduced Siamese-twin porphyrin H_4L (**4.1**) as a nonaromatic, nonplanar expanded porphyrin incorporating two pyrazole moieties that bridge two porphyrin-like N_4 binding pockets,[19, 32] shown to be suitable for the coordination to one or two metal ions.[19, 32-34] The periphery of **4.1** is decorated with phenyl and ethyl groups, enforcing a helimeric twist that is rigidified and modulated upon metal ion complexation. The structure of **4.1** is reminiscent of hexaphyrin $\mathbf{H_21}$ due to the arrangement of six heterocycles with aryl groups at each *meso*-position,[12, 35-36] but more closely resembles octaphyrin $\mathbf{H_42}^1$ in its mode of all-N coordination to metal ions ($\mathbf{M_22}$ and $\mathbf{M_2L}$).[37-39] Metalation of both octaphyrin $\mathbf{H_42}$ and twin porphyrin **4.1** is facilitated by the steric constraints imposed by the peripheral substituents that force all coordinating nitrogen atoms toward the center of the cavity.[19, 32]

Variation of the *meso*-aryl groups in twin porphyrin **4.1** only negligibly altered the optical absorbance and redox properties, reflecting the orthogonality of the aryl π-system and the macrocycle mean plane.[33] Efforts to oxidize the macrocycle to achieve a fully aromatic system resulted instead in fused and folded "origami" structures.[40] The use of different metal ions produced more spectral and electrochemical changes than aryl substitution,[33, 41-42] leading to studies of monometallic and bimetallic complexes of twin porphyrin **4.1** (i.e., H_2NiL (**4.2**), H_2PdL (**4.3**), Ni_2L (**4.5**), $\mathbf{Cu_2L}$, and **NiCuL** complexes),[19, 32-34, 41-42] establishing the twin porphyrin macrocycle as a non-innocent ligand capable of undergoing ligand-centered oxidations.[41-42] The remarkable stability of monometallic H_2PdL (**4.3**) toward oxidation and reduction allowed for electrochemical, spectroelectrochemical, and EPR studies of the oxidized/reduced species as

well as investigations into its acid-base properties, providing further insight into the conjugated, yet electronically distinct, halves of the macrocycle.[34]

Platinum(II) and palladium(II) porphyrinoids have found utility as optical oxygen sensors related to technical and biological applications,[43-48] as photosensitizers for isomerization processes[49] and photodynamic therapy,[50-51] as photocatalysts for CH activation,[52] and as luminophores with high quantum yield (sometimes also emitting in the NIR).[53-55] In this contribution we expand the investigation of the twin porphyrin metal complexes to Pt^{II}-based monometallic and bimetallic complexes of the group 10 metals (H_2PtL (**4.4**), Pt_2L (**4.7**), NiPtL (**4.9**), and PdPtL (**4.10**)), as well as the new heterobimetallic complex NiPdL (**4.8**). Thus, in combination with the H_2NiL (**4.2**),[42] H_2PdL (**4.3**),[34] Ni_2L (**4.5**),[42] and Pd_2L (**4.6**)[34] complexes prepared previously, the entire series (Chart 4.1) of monometallic and bimetallic complexes of the group 10 metals with all possible combinations of Ni^{II}, Pd^{II}, and Pt^{II} are now available to further probe structure-function relationships of the twin porphyrins, particularly their optical and redox properties as a function of the chelated metal ions. The diamagnetic nature of the square planar geometry of these low spin d^8 metal ions lend themselves to probe their solution-state structures using NMR spectroscopy. The series of complexes prepared also proved suitable for magnetic circular dichroism (MCD) spectral analysis combined with TD-DFT computations to illuminate in greater detail the origins of their optical spectra.

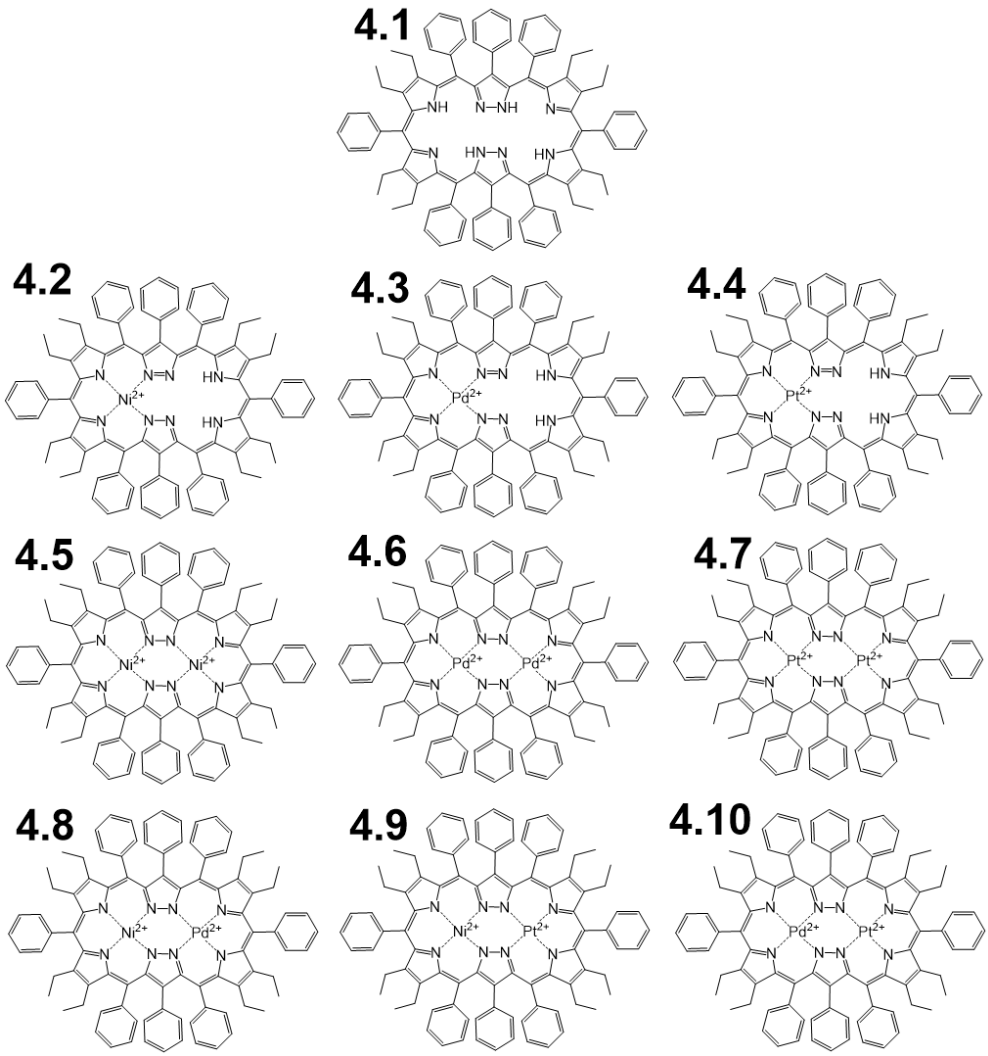

Chart 4.1 Structures of the studied twin-porphyrin compounds.

4.3 Results and Discussion

4.3.1 UV-vis Spectra. As is characteristic for the nonaromatic macrocyclic twin porphyrins and their metal complexes,[19, 32-34, 40-42] the UV-vis spectra of the group 10 twin porphyrin complexes resemble more those of linear tetrapyrroles, with extinction values (ε) between 6 and 8 $\times$ 10^4 $cm^{-1}M^{-1}$. The absence of any significant extension of the UV-vis absorbance into the NIR, as

frequently observed in aromatic expanded porphyrins,[2] also reflects the lack of continuous macrocycle π-conjugation of the group 10 metal complexes of the twin porphyrin (Figure 4.2).

The UV-vis spectrum of the free-base ligand **4.1** exhibits two intense bands at λ_{max} = 390 and 638 nm with a shoulder on the longest wavelength band. Upon complexation with one metal ion, three primary bands arise with some additional minor features present. The monometallic species **4.4** absorbs well into the NIR, with the λ_{max} band tailing past 1000 nm. The spectrum of the homobimetallic complex **4.6** possesses three intense and sharpened bands, similar to that observed for the corresponding complex **4.5**. The UV-vis spectrum of **4.7** is much different and most striking in its complexity in the range between 250 and 550 nm. Furthermore, its *Q*-like band peaks at 768 nm; the longest wavelength of all twin porphyrin complexes thus prepared. The heterobimetallic complexes exhibit UV-vis absorbances that are intermediate between the parent homobimetallic species. The Pt-based complexes **4.9** and **4.10**, for example, reflect the complexities seen in the spectrum of **4.7**, albeit much less pronounced.

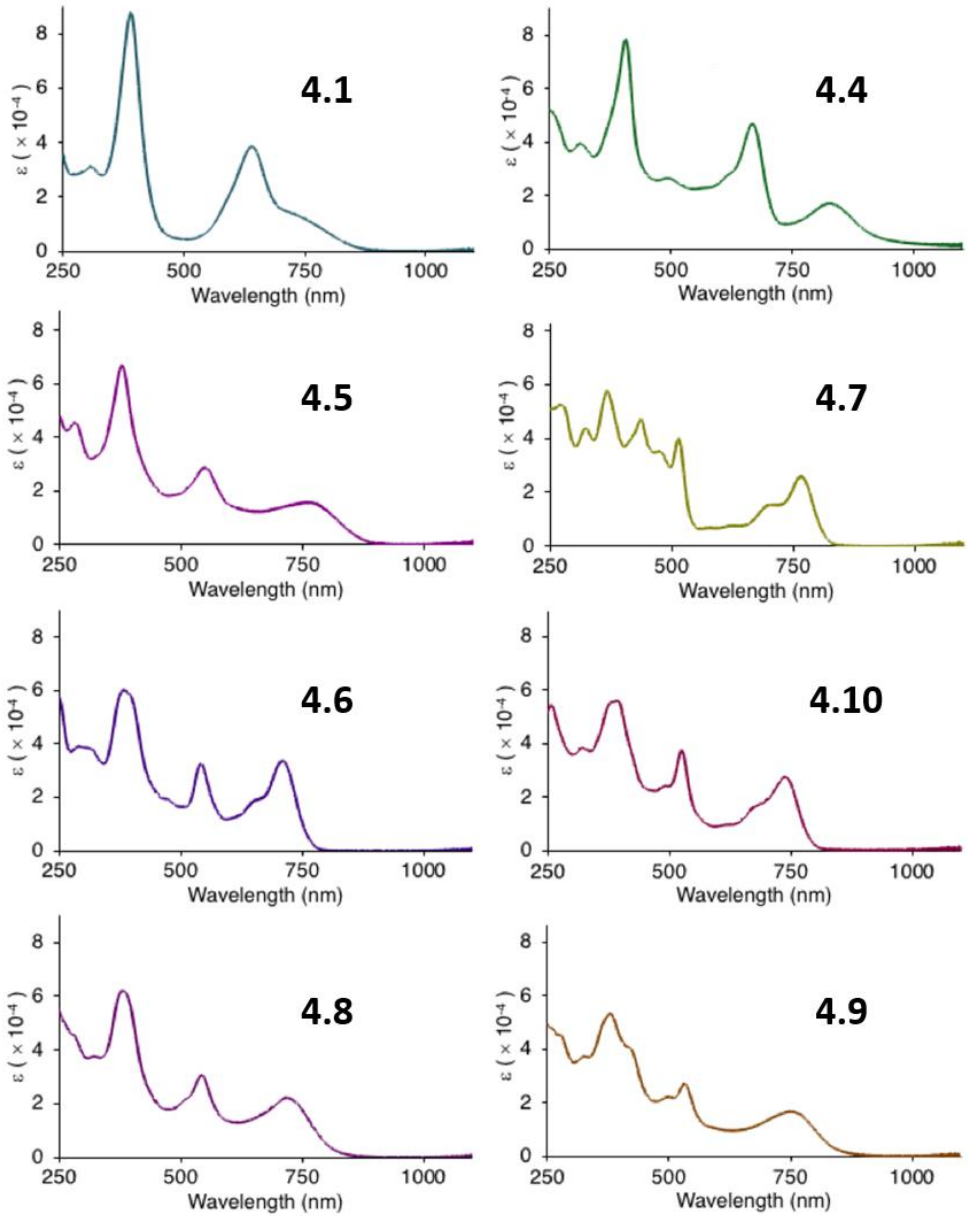

Figure 4.2. UV-vis spectra (CH_2Cl_2) of the compounds indicated.

4.3.2 Magnetic Circular Dichroism. The magnetic circular dichroism (MCD) and corresponding UV-vis spectra of the compounds investigated are shown in Figure 4.3 (cf. also to Figure 4.2). The MCD spectrum of the **4.1** free-base ligand consists of rather weak Faraday *B*-terms, with the most intense negative signal in the visible region centered at 686 nm, which does not

correlate to any of the major absorption peaks in the UV-vis spectrum. In the higher energy region, the MCD spectrum revealed three negative signals at 533, 421, and 365 nm, and two positive Faraday MCD *B*-terms observed at 459 and 327 nm, which again do not correlate with the energy of the intense absorption band observed at 390 nm in the UV-vis spectrum of **4.1**.

For the monometallic **H_2ML** complexes, the relatively strong band at 683 (**4.2**), 662 (**4.3**), and 664 nm (**4.4**) in the visible region is complemented by a fingerprint NIR band between 797 and 829 nm unique to the monometallic twin porphyrin complexes. Unlike in the case of **4.1**, no spectral absorption gap was observed between the UV and visible portions of their optical spectra. The MCD spectra of the monometallic derivatives are dominated by a negative signal centered between 481 and 566 nm for **4.2** and a broad band around 550 nm, observed for both **4.3** and **4.4**. The NIR fingerprint bands of the monometallic twin porphyrins are associated with weak and positive Faraday *B*-terms: one for **4.2** and two each for **4.3** and **4.4**. Similar to the metal-free twin porphyrin, the two most intense absorption bands in the UV-vis spectra of the monometallic derivatives do not show much MCD intensity. The NIR band observed in the absorption spectra for the monometallic derivatives disappears in the case of both homo- and hetero-bimetallic complexes. Indeed, in the case of the bimetallic compounds, the low energy spectral envelope is dominated by a prominent band observed between 709 and 767 nm; the bimetallic complexes possess a fingerprint band located between 514 and 548 nm. In all bimetallic complexes, the low energy visible or NIR MCD signals have negative intensities and do not correlate with the most intense bands observed in the UV-vis spectra of these compounds.

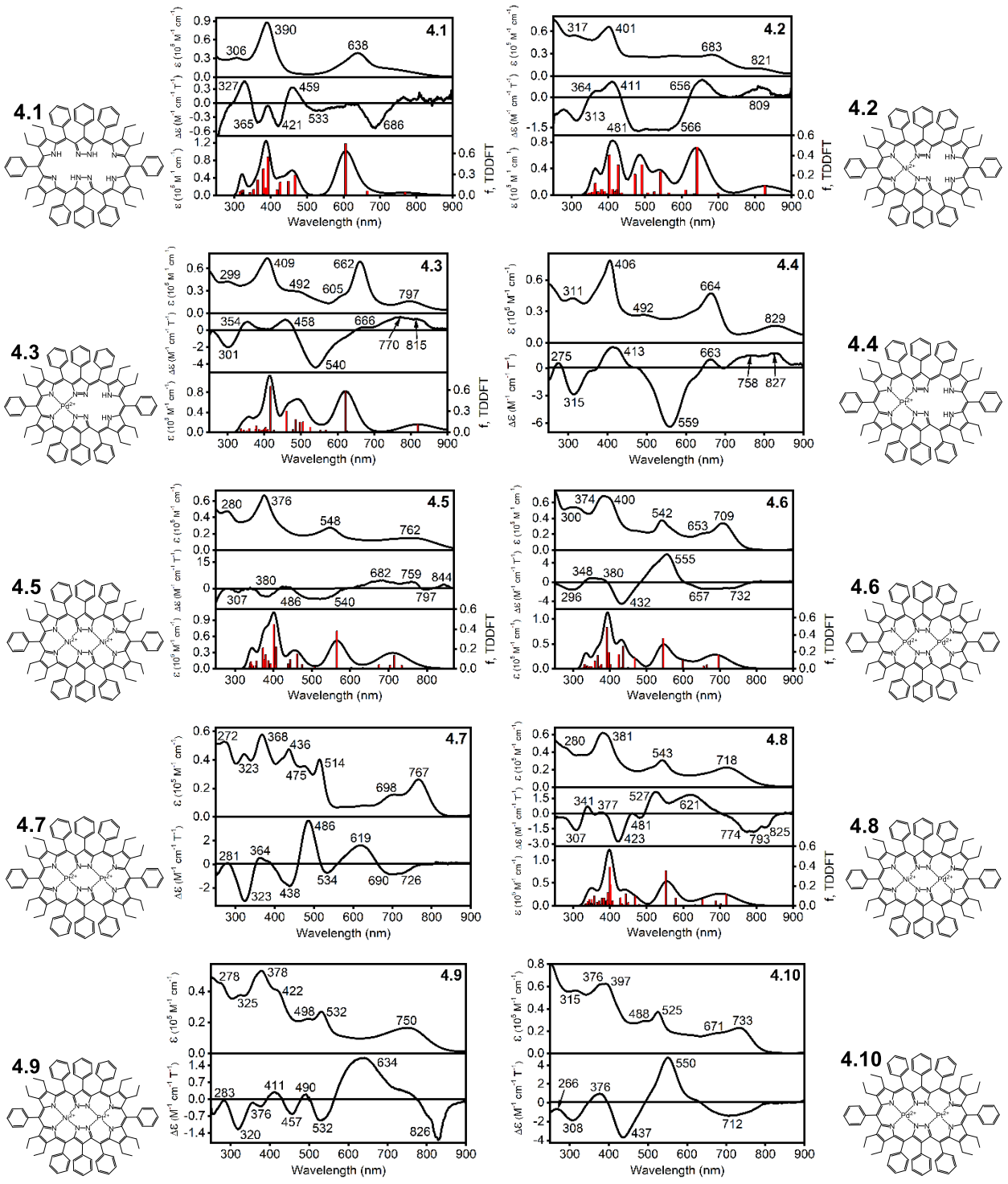

Figure 4.3. UV-vis (top), MCD (middle), and TDDFT-predicted (bottom) spectra of target compounds (all in CH_2Cl_2). In the case of the Pt^{II} complexes, only the UV-vis (top) and MCD (bottom) spectra are provided.

Thus, in all cases observed, the most intense absorption bands in the UV-vis spectra of the metal-free, monometallic, and bimetallic twin porphyrins do not possess much MCD intensity. This is in strong contrast to the intense MCD signals that are observed for the *Q*- and Soret-bands of metal-free and transition metal metalloporphyrins and many of their analogs.[57-61] The low intensity of the MCD signals in the compounds of interest reflects their twisted geometries and lack of strong and delocalized macrocyclic ring current. Thus, their low intensity MCD transitions indicate that the twin porphyrin π-system behaves more like an open-chain tetrapyrrole and not like an aromatic macrocyclic porphyrinic compound. Indeed, the highly nonplanar structures of the twin porphyrins incorporating two nearly independent π-systems are one of their defining characteristics.[32, 34, 42] Low intensity MCD spectra were also observed for other macrocyclic porphyrinoids with compromised/localized π-aromatic systems.[62]

4.3.3 Density Functional Theory and Time-Dependent DFT Calculations. To better correlate the spectroscopic properties observed for the metal-free twin porphyrin, monometallic, and bimetallic twin porphyrin complexes, the electronic structures of selected examples were evaluated using density functional theory (DFT) and time-dependent DFT (TDDFT) calculations. The resulting molecular orbital (MO) energy diagram is shown in Figure 4.4.

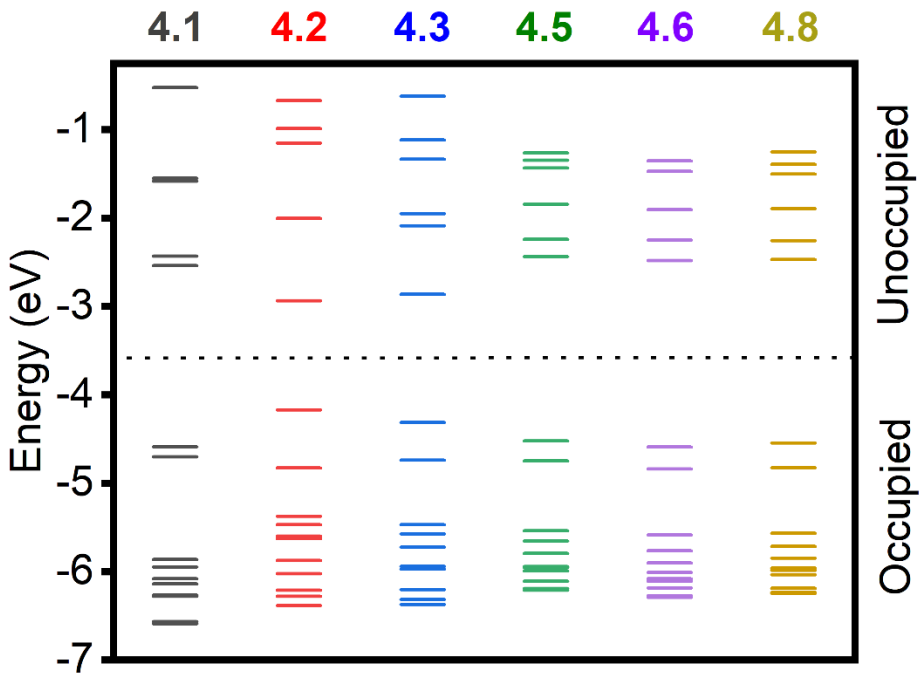

Figure 4.4. DFT-predicted frontier orbitals energy diagram for the compounds indicated.

In all compounds, the HOMO and HOMO-1 orbitals as well as the LUMO and LUMO+1 orbitals are energetically well-separated from the remaining filled or empty orbitals, respectively. The HOMO to HOMO-1 as well as LUMO to LUMO+1 energy gaps decrease in the order of **4.2** > **4.3** > **4.1**, while similar gaps for the binuclear **4.5**, **4.6**, and **4.8** complexes were predicted to be close to each other.

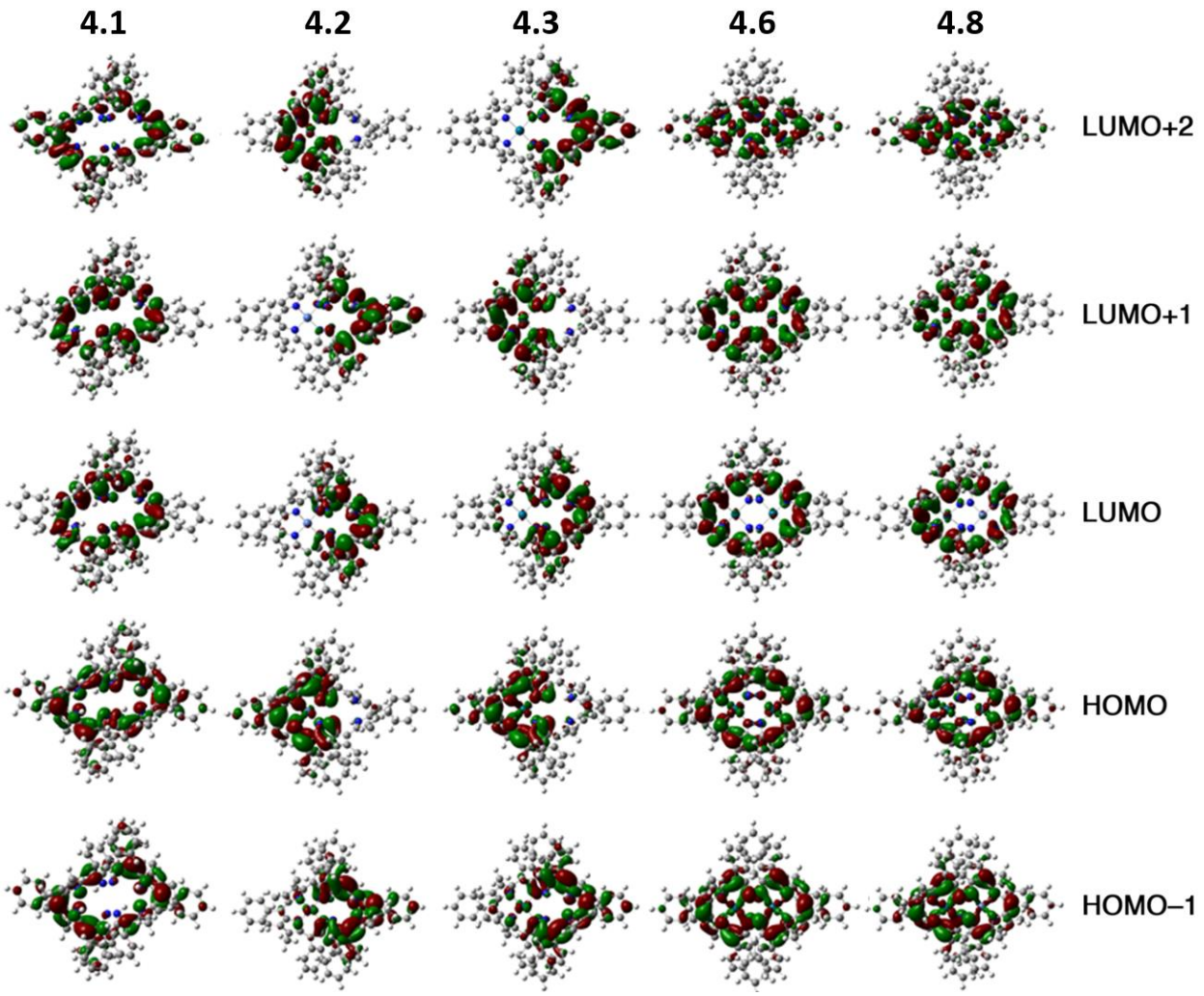

Figure 4.5. DFT-predicted frontier orbitals for the compounds indicated. See the Supporting Information for the frontier orbitals of the full set of compounds investigated.

While the HOMO orbitals of the free-base as well as the homo- and heterobimetallic complexes are evenly distributed over the macrocycle, they are mostly centered on the metalated halves of the molecule in the monometallic species (Figure 4.5 and Supporting Information). The LUMO orbitals in **4.2** and **4.3** are localized on the metal-free part of the macrocycle. The LUMO+1 and LUMO+2 orbitals of **4.2** are close in energy, with the former

localized over the metal-free part and the latter over the metal-containing part of the macrocycle. In comparison, the LUMO+1 and LUMO+2 orbitals of **4.3** are better separated and feature an inverse localization.

A molecular orbitals composition analysis further refines this picture (Figure 4.6), revealing that the contribution of the pyrazole fragments to the frontier orbitals of all compounds does not exceed 25% while the contributions from the pyrrolic fragments to the HOMO-1 to LUMO+1 MOs play a dominant role. In the case of the monometallic and bimetallic compounds, the contribution from the transition metal orbitals to the frontier MOs does not exceed 10%.

The nature of the excited states in all target compounds was probed by TDDFT calculations (Figure 4.3). In all cases, reasonable agreement between theory and experiment was observed. Specifically in the case of the metal-free twin porphyrin **4.1**, the energy of the experimentally observed features between 700 and 800 nm in the UV-vis spectrum correlates well with the energy of the first excited state, predicted at 769 nm, and characterized as a pure HOMO → LUMO single-electron transition that is predominantly centered at pyrrolic fragments of the twin porphyrin core. The TDDFT calculations suggest that the relatively intense MCD signal observed at 686 nm represents the third excited state predicted at 666 nm, which is dominated by the HOMO-1 → LUMO+1 single-electron excitation. TDDFT calculations also predict that the most intense transition, experimentally observed at 638 nm, is associated with the HOMO-1 → LUMO and the HOMO → LUMO+1 single electron excitations (fourth excited state). The most intense transition in the higher energy region observed at 390 nm is associated with nearly

equal HOMO-3 → LUMO+1 and HOMO-6 → LUMO single electron excitations (excited state 14). The latter single electron excitation has distinct pyrazole (π) → pyrrole (π*) charge-transfer character.

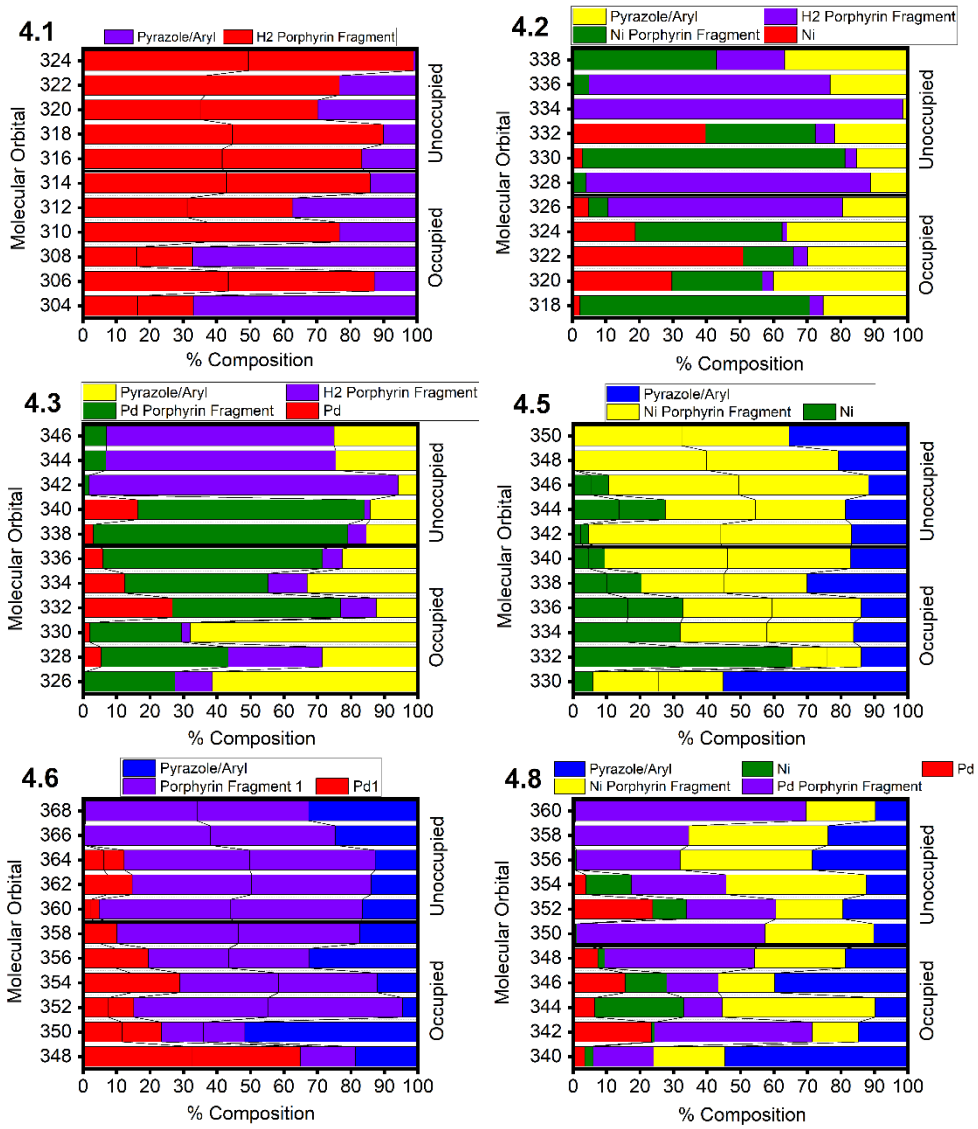

Figure 4.6. DFT-predicted frontier orbital compositions for the compounds indicated.

In the case of the monometallic **4.2** and **4.3** complexes, TDDFT calculations correctly predicted a hypsochromic shift of the lowest energy NIR band going from the lighter to the

heavier metal ion, as well as a hypsochromic shift of the most prominent visible band (observed at 683 nm in **4.2** and 662 nm in **4.3**) and a bathochromic shift of the most prominent band observed at ~400 nm. The first NIR band, observed at ~800 nm, is predominantly associated with the HOMO-1 → LUMO single-electron excitation while the intense band in the visible region observed between 660 and 680 nm for these compounds is predicted to be dominated by the HOMO → LUMO+2 (**4.2** or the HOMO → LUMO+1 (**4.3**) single-electron excitations. Similar to the metal-free twin porphyrin **4.1**, the intense transition observed at ~400 nm was predicted to have a substantial pyrazole (π) → pyrrole (π*) intramolecular charge-transfer character. Importantly, the TDDFT calculations correctly predicted an energy gap at ~480 nm, which was experimentally observed in the UV-vis spectrum of **4.1**, but is filled with numerous excited states in **4.2** and **4.3** complexes.

Three distinct absorption envelopes were predicted for the bimetallic **4.5**, **4.6**, and **4.8** twin porphyrin complexes without any spectral gap between the UV and visible parts in the spectra of these compounds, in full agreement with experimental observations. In all cases, the intense NIR absorption is dominated by a HOMO → LUMO single-electron excitation centered at the pyrrolic π and π* orbitals. The most intense absorption band in the visible region of the absorption spectrum for these compounds observed around 545 nm correlates well with the TDDFT-predicted excited state at 550 nm, which is dominated by the HOMO-1 → LUMO+1 single-electron excitations centered at the pyrrolic π and π* orbitals. Parallel to the free base and mono-metallic cases, the most intense absorption band in the higher energy region (~400

nm) correlates well with the excited state dominated by a single-electron transition with significant pyrazole (π) → pyrrole (π*) intra-molecular charge-transfer character.

Overall, it seems that the TDDFT calculations correctly predicted the broad spectral nature of the monometallic and bimetallic twin porphyrin complexes and accurately predicted general trends observed in the UV-vis spectra of these compounds to within ~0.1 eV uncertainty, which is typical for modern TDDFT methods.[63-65] A large number of TDDFT transitions in all target compounds correlate well with the complex MCD spectra of these systems, which are indicative of several excited states observed in the UV-vis to NIR spectral envelope.

4.4 Conclusions

A comprehensive series of group 10 complexes of the twin porphyrin **4.1** is reported, including the first Pt^{II}-containing complexes **4.4** and **4.7** as well as the novel heterobimetallic complexes **4.8**, **4.9**, and **4.10**. Structurally, the bimetallic complexes do not differ considerably from each other or from related twin porphyrin complexes reported previously.[19, 32-34] Their optical spectra are distinctly different from each other, indicative of a mixing of the d-orbitals with the π-system of the ligands. The low MCD intensity of the group 10 metal complexes of twin porphyrin **4.1** stands in contrast to the generally intense MCD signals for the *Q*- and Soret-bands of transition metal metalloporphyrins, but the finding is in line with the absence of a strong macrocyclic ring current. This confirms previous notions that the highly twisted twin porphyrin does not possess macrocycle aromatic character but features two nearly independent conjugated π-systems that are separated by the central pyrazolate units.[19, 32]

(TD)DFT calculations allowed an analysis of the rich UV-vis to NIR spectral features of the monometallic and bimetallic twin porphyrin complexes. The frontier MOs involved in the lowest energy transitions are predominantly located at the pyrrolic fragments of the twin porphyrin core, with only minor contributions of the pyrazole units (< 25%) and the group 10 metal ions (< 10%). While in case of the homo- and heterobimetallic complexes, these frontier orbitals extend over the entire macrocycle. Monometalation leads to the HOMO being confined to the metalated half and the LUMO being confined to the free base half. The panchromatic absorbance of the twin porphyrin complexes suggests that these systems may find utility in optoelectronic or electrochromic applications.

As opposed to the triply-linked porphyrin tapes of chapter three, the twin porphyrins reported on in this chapter demonstrated the resultant electronic structure profiles following the alternative mode of binding for two or more (in this case two) porphyrins where one pyrrole ring and one *meso*-nitrogen/hydrogen of each of the monomeric units were omitted from the fused dimer. As was determined by a collaborating research group[70] via x-ray crystallography, this type of side-by-side porphyrin binding resulted in a significant twisting of the dimer, leading to a loss in overall macrocyclic aromaticity. This overall aromaticity was deemed broken, and the two dimer halves maintained their own nearly independent conjugated π-systems. This severe twisting (and subsequent loss of overall aromaticity) resulted in weak MCD signals and also a ΔHOMO > ΔLUMO relationship, indicating that extension of the π-system along the y-axis through the mode of macrocyclic binding featured within this chapter ("macrocyclic fusion") leads to an electronic structure that can be generally characterized as synthetic. Based on the results from this chapter and those from the previous porphyrin tapes

chapter (3), extension of the π-system along the y-axis will lead to an electronic structure that resembles those of naturally-occurring reduced porphyrinoids as long as the target structure maintains its relatively planar shape through structural rigidity, which can be achieved through triple linkages.

4.5 Experimental Section

4.5.1 Materials. Solvents were of reagent grade or better and used as received. **4.1**,[19, 32, 40] **4.2**,[42] **4.3**, and **4.5**[32, 42] were prepared by Prof. Christian Brückner according to literature procedures with slight modifications. All samples were shielded from light by covering the sample vials with aluminum foil.

4.5.2 UV-vis/MCD spectroscopy. All UV-vis spectra were collected on a Jasco V-770 spectrophotometer (CH_2Cl_2) and MCD spectra were measured (CH_2Cl_2) with a Jasco J-1500 CD spectrometer using a Jasco MCD-581 electromagnet operated at 1.0 T. The MCD spectra were recorded in mdeg = [θ] and converted to molar ellipticity as $\Delta\varepsilon = \theta/(32980 \times Blc)$; where B is the magnetic field (T), l is the path length (cm), and c is the concentration (M).[66] The completed MCD spectra were measured at 10 °C in parallel and antiparallel orientations with respect to the magnetic field.

4.5.3 DFT and TDDFT methods. All calculations were performed using the Gaussian 09 software package[67] on UNIX OS. The geometries of all twin porphyrins were optimized using the hybrid B3LYP exchange-correlation functional[68] and full-electron DGDZVP basis set[69] in the gas phase. Frequency calculations were run to ensure that a global energetic minimum on the

potential energy surface was obtained. The optimized geometries were used for single-point and TDDFT calculations. The lowest energy 60 excited states were considered for TDDFT calculations. Only nickel and palladium complexes were modeled using DFT and TDDFT methods due to lack of a DGDZVP basis set for the platinum ion.

4.6 References

1. Sessler, J. L.; Weghorn, S., *Expanded, Contracted & Isomeric Porphyrins*. Pergamon Press: New York, NY, 1997.

2. Saito, S.; Osuka, A., Expanded porphyrins: Intriguing structures, electronic properties, and reactivities. *Angew. Chem. Int. Ed.* **2011,** *50* (19), 4342–4373.

3. Roznyatovskiy, V. V.; Lee, C.-H.; Sessler, J. L., p-Extended isomeric and expanded porphyrins. *Chem. Soc. Rev.* **2013,** *42* (5), 1921–1933.

4. Szyszko, B.; Latos-Grażyński L., Core chemistry and skeletal rearrangements of porphyrinoids and metalloporphyrinoids. *Chem. Soc. Rev.* **2015,** *44* (11), 3588–3616.

5. Tanaka, T.; Osuka, A., Chemistry of *meso*-aryl-substituted expanded porphyrins: Aromaticity and molecular twist. *Chem. Rev.* **2017,** *117* (4), 2584–2640.

6. Szyszko, B.; Białek, M. J.; Pacholska-Dudziak, E.; Latos-Grażyński L., Flexible porphyrinoids. *Chem. Rev.* **2017,** *117* (4), 2839–2909.

7. Bauer, V. J.; Clive, D. L. J.; Dolphin, D.; Paine, J. B., III; Harris, F. L.; King, M. M.; Loder, J.; Wang, S. W. C.; Woodward, R. B., Sapphyrins: Novel aromatic pentapyrrolic macrocycles. *J. Am. Chem. Soc.* **1983,** *105* (21), 6429–6436.

8. Chatterjee, T.; Srinivasan, A.; Ravikanth, M.; Chandrashekar, T. K., Smaragdyrins and sapphyrins analogues. *Chem. Rev.* **2017,** *117* (4), 3329–3376.

9. Neves, M. G. P. M. S.; Martins, R. M.; Tome, A. C.; Silvestre, A. J. D.; Silva, A. M. S.; Felix, V.; Cavaleiro, J. A. S.; Drew, M. G. B., *meso*-Substituted expanded porphyrins: New and stable hexaphyrins. *Chem. Commun.* **1999,** (4), 385–386.

10. Sessler, J. L.; Seidel, D.; Bucher, C.; Lynch, V., [26]Hexaphyrin(1.1.1.1.0.0): An all-aza isomer of rubyrin with an inverted pyrrole subunit. *Chem. Commun.* **2000,** (16), 1473–1474.

11. Sessler, J. L.; Seidel, D.; Vivian, A. E.; Lynch, V.; Scott, B. L.; Keogh, D. W., Hexaphyrin(1.0.1.0.0.0): An expanded porphyrin ligand for the actinide cations uranyl (UO_2^{2+}) and neptunyl (NpO^{2+}). *Angew. Chem., Int. Ed. Engl.* **2001,** *40* (3), 591–594.

12. Suzuki, M.; Osuka, A., Improved synthesis of *meso*-aryl-substituted [26]hexaphyrins. *Org. Lett.* **2003,** *5* (21), 39433946.

13. Mori, S.; Shimizu, S.; Taniguchi, R.; Osuka, A., Group 10 metal complexes of *meso*-aryl-substituted [26]hexaphyrins with a metal-carbon bond. *Inorg. Chem.* **2005,** *44* (12), 4127–4129.

14. Sessler, J. L.; Seidel, D.; Lynch, V., Synthesis of [28]heptaphyrin(1.0.0.1.0.0.0) and [32]octaphyrin(1.0.0.0.1.0.0.0) via a directed oxidative ring closure: The first expanded porphyrins containing a quaterpyrrole subunit. *J. Am. Chem. Soc.* **1999,** *121* (48), 11257–11258.

15. Geier, G. R., III; Grindrod, S. C., *meso*-Substituted [34]octaphyrin(1.1.1.0.1.1.1.0) and corrole formation in reactions of a dipyrromethanedicarbinol with 2,2'-bipyrrole. *J. Org. Chem.* **2004,** *69* (19), 6404–6412.

16. Kido, H.; Shin, J.-Y.; Shinokubo, H., Selective synthesis of a [32]octaphyrin(1.0.1.0.1.0.1.0) bis(palladium) complex by a metal-templated strategy. *Angew. Chem., Int. Ed.* **2013,** *52* (51), 13727–13730.

17. Misra, R.; Chandrashekar, T. K., Structural diversity in expanded porphyrins. *Acc. Chem. Res.* **2008,** *41* (2), 265–279.

18. Stępień, M.; Szyszko, B.; Latos-Grażyński L., Three-level topology switching in a molecular Möbius band. *J. Am. Chem. Soc.* **2010,** *132* (9), 3140–3152.

19. Frensch, L. K.; Proepper, K.; John, M.; Demeshko, S.; Brückner, C.; Meyer, F., Siamese-twin porphyrin: A pyrazole-based expanded porphyrin providing a bimetallic cavity. *Angew. Chem., Int. Ed.* **2011,** *50* (6), 1420–1424.

20. Ho, I. T.; Zhang, Z.; Ishida, M.; Lynch, V. M.; Cha, W.-Y.; Sung, Y. M.; Kim, D.; Sessler, J. L., A hybrid macrocycle with a pyridine subunit displays aromatic character upon uranyl cation complexation. *J. Am. Chem. Soc.* **2014,** *136* (11), 4281–4286.

21. Oh, J.; Mori, H.; Sung, Y. M.; Kim, W.; Osuka, A.; Kim, D., Switchable π-electronic network of bis(α-oligothienyl)-substituted hexaphyrins between helical versus rectangular circuit. *Chem. Sci.* **2016,** *7* (3), 2239–2245.

22. Abebayehu, A.; Dutta, R.; Lee, C.-H., Synthesis, characterization and properties of expanded pyriporphyrins: A new family of alkylidenyl porphyrin homologues bearing *meso*-exocyclic double bonds. *Chem.—Eur. J.* **2016,** *22* (39), 13850–13856.

23. Cha, W.-Y.; Kim, T.; Ghosh, A.; Zhang, Z.; Ke, X.-S.; Ali, R.; Lynch, V. M.; Jung, J.; Kim, W.; Lee, S.; Fukuzumi, S.; Park, J. S.; Sessler, J. L.; Chandrashekar, T. K.; Kim, D., Bicyclic Baird-type aromaticity. *Nat. Chem.* **2017,** *9*, 1243-1248.

24. Setsune, J.-i.; Toda, M.; Yoshida, T.; Imamura, K.; Watanabe, K., The synthesis and dynamic structures of multinuclear complexes of large porphyrinoids expanded by phenylene and thienylene spacers. *Chem.—Eur. J.* **2015,** *21* (36), 12715–12727.

25. Chatterjee, T.; Theophall, G. G.; Silva, K. I.; Lakshmi, K. V.; Ravikanth, M., Synthesis and quantum mechanical studies of a highly stable ferrocene-incorporated expanded porphyrin. *Inorg. Chem.* **2016,** *55* (14), 6873–6881.

26. Sessler, J. L.; Vivian, A. E.; Seidel, D.; Burrell, A. K.; Hoehner, M.; Mody, T. D.; Gebauer, A.; Weghorn, S. J.; Lynch, V., Actinide expanded porphyrin complexes. *Coord. Chem. Rev.* **2001,** *216-217*, 411–434.

27. Brewster, J. T.; Mangel, D. N.; Gaunt, A. J.; Saunders, D. P.; Zafar, H.; Lynch, V. M.; Boreen, M. A.; Garner, M. E.; Goodwin, C. A. P.; Settineri, N. S.; Arnold, J.; Sessler, J. L., In-plane

thorium(IV), uranium(IV), and neptunium(IV) expanded porphyrin complexes. *J. Am. Chem. Soc.* **2019,** *141* (44), 17867–17874.

28. Gisselbrecht, J. P.; Gross, M.; Vogel, E.; Scholz, P.; Bröring, M.; Sessler, J. L., Redox properties of hemiporphycene and isoporphycene. Comparison with those of porphyrin and other porphyrin isomers, porphycene and corrphycene. *J. Electroanal. Chem.* **2001,** *507* (1-2), 244–249.

29. Bley-Escrich, J.; Gisselbrecht, J.-P.; Michels, M.; Zander, L.; Vogel, E.; Gross, M., Electrochemical and spectroelectrochemical investigations of mono- and binuclear cobalt(II) complexes of "figure-eight" octapyrrolic macrocycles. *Eur. J. Inorg. Chem.* **2004,** (3), 492–499.

30. Tanaka, Y.; Saito, S.; Mori, S.; Aratani, N.; Shinokubo, H.; Shibata, N.; Higuchi, Y.; Yoon, Z. S.; Kim, K. S.; Noh, S. B.; Park, J. K.; Kim, D.; Osuka, A., Metalation of expanded porphyrins: A chemical trigger used to produce molecular twisting and Möbius aromaticity. *Angew. Chem., Int. Ed. Engl.* **2008,** *47* (4), 681–684.

31. Anguera, G.; Cha, W.-Y.; Moore, M. D.; Lee, J.; Guo, S.; Lynch, V. M.; Kim, D.; Sessler, J. L., Hexadecaphyrin-(1.0.0.0.1.1.0.1.1.0.0.0.1.1.0.1): A dual site ligand that supports thermal conformational changes. *J. Am. Chem. Soc.* **2018,** *140* (11), 4028–4034.

32. Blusch, L. K.; Hemberger, Y.; Pröpper, K.; Dittrich, B.; Witterauf, F.; John, M.; Bringmann, G.; Brückner, C.; Meyer, F., Siamese-twin porphyrin: A pyrazole-based expanded porphyrin of persistent helical conformation. *Chem.—Eur. J.* **2013,** *19* (19), 5868–5880.

33. Mitevski, O.; Dechert, S.; Brückner, C.; Meyer, F., Siamese-twin porphyrins: Variation of two *meso*-aryl groups. *Eur. J. Inorg. Chem.* **2016**, 4814–4819.

34. Vogel, A.; Dechert, S.; Brückner, C.; Meyer, F., Reaching across the divide: How monometalation of one binding pocket affects the empty binding pocket in a Siamese-twin porphyrin palladium complex. *Inorg. Chem.* **2017,** *56* (4), 2221–2232.

35. Ahn Tae, K.; Kwon Jung, H.; Kim Deok, Y.; Cho Dae, W.; Jeong Dae, H.; Kim Seong, K.; Suzuki, M.; Shimizu, S.; Osuka, A.; Kim, D., Comparative photophysics of [26]- and [28]hexaphyrins(1.1.1.1.1.1): Large two-photon absorption cross section of aromatic [26]hexaphyrins(1.1.1.1.1.1). *J. Am. Chem. Soc.* **2005,** *127* (37), 12856–12861.

36. Yoon, Z. S.; Osuka, A.; Kim, D., Möbius aromaticity and antiaromaticity in expanded porphyrins. *Nat. Chem.* **2009,** *1* (2), 113–122.

37. Latos-Grażyński, Bimetallic figure-eight octaphyrins split into four-pyrrolic macrocycles. *Angew. Chem. Int. Ed.* **2004,** *43* (39), 5124–5128.

38. Tanaka, Y.; Hoshino, W.; Shimizu, S.; Youfu, K.; Aratani, N.; Maruyama, N.; Fujita, S.; Osuka, A., Thermal splitting of bis-Cu(II) octaphyrin(1.1.1.1.1.1.1.1) into two Cu(II) porphyrins. *J. Am. Chem. Soc.* **2004,** *126* (10), 3046–3047.

39. Shimizu, S.; Tanaka, Y.; Youfu, K.; Osuka, A., Dicopper and disilver complexes of octaphyrin(1.1.1.1.1.1.1.1): Reversible hydrolytic cleavage of the pyrrolic ring to a keto-imine. *Angew. Chem. Int. Ed.* **2005,** *44* (24), 3726–3729.

40. Vogel, A.; Dechert, S.; John, M.; Brückner, C.; Meyer, F., Siamese-twin porphyrin origami: Oxidative fusing and folding. *Chem.—Eur. J.* **2016,** *22* (7), 2307–2316.

41. Blusch, L. K.; Craigo, K. E.; Martin-Diaconescu, V.; McQuarters, A. B.; Bill, E.; Dechert, S.; DeBeer, S.; Lehnert, N.; Meyer, F., Hidden non-innocence in an expanded porphyrin: Electronic structure of the Siamese-twin porphyrin's dicopper complex in different oxidation states. *J. Am. Chem. Soc.* **2013,** *135* (37), 13892–13899.

42. Blusch, L. K.; Mitevski, O.; Martin-Diaconescu, V.; Propper, K.; DeBeer, S.; Dechert, S.; Meyer, F., Selective synthesis and redox sequence of a heterobimetallic nickel/copper complex of the noninnocent Siamese-twin porphyrin. *Inorg. Chem.* **2014,** *53* (15), 7876–7885.

43. Lee, W. W. S.; Wong, K. Y.; Li, X. M.; Leung, Y. B.; Chan, C. S.; Chan, K. S., Halogenated platinum porphyrins as sensing materials for luminescence-based oxygen sensors. *J. Mater. Chem.* **1993,** *3* (10), 1031–1035.

44. Papkovsky, D. B.; Ponomarev, G. V.; Wolfbeis, O. S., Longwave luminescent porphyrin probes. *Spectrochi. Acta A: Mol. Biomol. Spectrosc.* **1996,** *52A* (12), 1629–1638.

45. Grenoble, S.; Gouterman, M.; Khalil, G.; Callis, J.; Dalton, L., Pressure-sensitive paint (PSP): Concentration quenching of platinum and magnesium porphyrin dyes in polymeric films. *J. Lumin.* **2005,** *113* (1-2), 33–44.

46. Amao, Y.; Okura, I., Optical oxygen sensor devices using metalloporphyrins. *J. Porphyrins Phthalocyanines* **2009,** *13* (11), 1111–1122.

47. Spencer, J. A.; Ferraro, F.; Roussakis, E.; Klein, A.; Wu, J.; Runnels, J. M.; Zaher, W.; Mortensen, L. J.; Alt, C.; Turcotte, R.; Yusuf, R.; Cote, D.; Vinogradov, S. A.; Scadden, D. T.; Lin, C. P., Direct measurement of local oxygen concentration in the bone marrow of live animals. *Nature* **2014,** *508* (7495), 269–273.

48. Pandey, G.; Chaudhari, R.; Joshi, B.; Choudhary, S.; Kaur, J.; Joshi, A., Fluorescent biocompatible platinum-porphyrin–doped polymeric hybrid particles for oxygen and glucose biosensing. *Sci. Rep.* **2019,** *9* (1), 5029–5039.

49. Mercer-Smith, J. A.; Whitten, D. G., Photosensitization of stilbene isomerization by palladium and platinum porphyrins, an intermolecular quantum chain process. *J. Am. Chem. Soc.* **1978,** *100* (9), 2620–2625.

50. Vakrat-Haglili, Y.; Weiner, L.; Brumfeld, V.; Brandis, A.; Salomon, Y.; McLlroy, B.; Wilson, B. C.; Pawlak, A.; Rozanowska, M.; Sarna, T.; Scherz, A., The microenvironment effect on the generation of reactive oxygen species by Pd-bacteriopheophorbide. *J. Am. Chem. Soc.* **2005,** *127* (17), 6487–6497.

51. Huang, Y.-Y.; Balasubramanian, T.; Yang, E.; Luo, D.; Diers, J. R.; Bocian, D. F.; Lindsey, J. S.; Holten, D.; Hamblin, M. R., Stable synthetic bacteriochlorins for photodynamic therapy: Role of dicyano peripheral groups, central metal substitution (2H, Zn, Pd), and Cremophor EL delivery. *ChemMedChem* **2012,** *7* (12), 2155–2167.

52. To, W.-P.; Liu, Y.; Lau, T.-C.; Che, C.-M., A robust palladium(II)–porphyrin complex as catalyst for visible light induced oxidative C-H functionalization. *Chem.—Eur. J.* **2013,** *19* (18), 5654–5664.

53. Lau, K. S. F.; Zhao, S.; Ryppa, C.; Jockusch, S.; Turro, N. J.; Zeller, M.; Gouterman, M.; Khalil, G. E.; Brückner, C., Synthesis, structure, and optical properties of the platinum(II) complexes of indaphyrin and thiaindaphyrin. *Inorg. Chem.* **2009,** *48* (9), 4067–4074.

54. Sommer, J. R.; Shelton, A. H.; Parthasarathy, A.; Ghiviriga, I.; Reynolds, J. R.; Schanze, K. S., Photophysical properties of near-infrared phosphorescent π-extended platinum porphyrins. *Chem. Mater.* **2011,** *23* (24), 5296–5304.

55. Akhigbe, J.; Luciano, M.; Atoyebi, A. O.; Jockusch, S.; Brückner, C., Quinoline-annulated porphyrin platinum complexes as NIR emitters. *J. Porphyrins Phthalocyanines* **2020**, *24* (1-3), 386–393.

56. Arumugam, K.; Shaw, M. C.; Chandrasekaran, P.; Villagrán, D.; Gray, T. G.; Mague, J. T.; Donahue, J. P., Synthesis, structures, and properties of 1,2,4,5-benzenetetrathiolate linked group 10 metal complexes. *Inorg. Chem.* **2009,** *48* (22), 10591–10607.

57. Mack, J.; Stillman, M. J., Electronic structures of metal phthalocyanine and porphyrin complexes from analysis of the UV-visible absorption and magnetic circular dichroism spectra and molecular orbital calculations. In *The Porphyrin Handbook*, Kadish, K. M.; Smith, K. M.; Guilard, R., Eds. Academic Press: San Diego, 2003; Vol. 16, pp 43–116.

58. Stillman, M.; Mack, J.; Kobayashi, N., Theoretical aspects of the spectroscopy of porphyrins and phthalocyanines. *J. Porphyrins Phthalocyanines* **2002,** *6* (4), 296–300.

59. Rhoda, H. M.; Crandall, L. A.; Geier, G. R.; Ziegler, C. J.; Nemykin, V. N., Combined MCD/DFT/TDDFT study of the electronic structure of axially pyridine coordinated metallocorroles. *Inorg. Chem.* **2015,** *54* (10), 4652–4662.

60. Rhoda, H. M.; Akhigbe, J.; Ogikubo, J.; Sabin, J. R.; Ziegler, C. J.; Brückner, C.; Nemykin, V. N., Magnetic circular dichroism spectroscopy of *meso*-tetraphenylporphyrin-derived hydroporphyrins and pyrrole-modified porphyrins. *J. Phys. Chem. A* **2016,** *120* (29), 5805–5815.

61. Mack, J., Expanded, contracted, and isomeric porphyrins: Theoretical aspects. *Chem. Rev.* **2017,** *117* (4), 3444–3478.

62. Kobayashi, N.; Inagaki, S.; Nemykin, V. N.; Nonomura, T., A novel hemiporphyrazine comprising three isoindolediimine and three thiadiazole units. *Angew. Chem. Int. Ed.* **2001,** *40* (14), 2710–2712.

63. Nemykin, V. N.; Hadt, R. G.; Belosludov, R. V.; Mizuseki, H.; Kawazoe, Y., Influence of molecular geometry, exchange-correlation functional, and solvent effects in the modeling of vertical excitation energies in phthalocyanines using time-dependent density functional theory (TDDFT) and polarized continuum model TDDFT methods: Can modern computational chemistry methods explain experimental controversies? *J. Phys. Chem. A* **2007,** *111* (50), 12901–12913.

64. Belosludov, R. V.; Nevonen, D. E.; Rhoda, H. M.; Sabin, J. R.; Nemykin, V. N., Simultaneous prediction of the energies of Q_x and Q_y bands and intramolecular charge-transfer transitions in benzoannulated and non-peripherally substituted metal-free phthalocyanines and their analogues: No standard TDDFT silver bullet yet. *J. Phys. Chem. A* **2019,** *123* (1), 132–152.

65. Martynov, A. G.; Mack, J.; May, A. K.; Nyokong, T.; Gorbunova, Y. G.; Tsivadze, A. Y., Methodological survey of simplified TD-DFT methods for fast and accurate interpretation of UV–vis–NIR spectra of phthalocyanines. *ACS Omega* **2019,** *4* (4), 7265–7284.

66. Galinato, M. G. I.; Spolitak, T.; Ballou, D. P.; Lehnert, N., Elucidating the role of the proximal cysteine hydrogen-bonding network in ferric cytochrome P450cam and corresponding mutants using magnetic circular dichroism spectroscopy. *Biochemistry* **2011,** *50* (6), 1053–1069.

67. Frisch, M. J.; Trucks, G. W.; Schlegel, H. B.; Scuseria, G. E.; Robb, M. A.; Cheeseman, J. R.; Scalmani, G.; Barone, V.; Mennucci, B.; Petersson, G. A.; Nakatsuji, H.; Caricato, M.; Li, X.; Hratchian, H. P.; Izmaylov, A. F.; Bloino, J.; Zheng, G.; Sonnenberg, J. L.; Hada, M.; Ehara, M.; Toyota, K.; Fukuda, R.; Hasegawa, J.; Ishida, M.; Nakajima, T.; Honda, Y.; Kitao, O.; Nakai, H.; Vreven, T.; Montgomery Jr., J. A.; Peralta, J. E.; Ogliaro, F.; Bearpark, M. J.; Heyd, J.; Brothers, E. N.; Kudin, K. N.; Staroverov, V. N.; Kobayashi, R.; Normand, J.; Raghavachari, K.; Rendell, A. P.; Burant, J. C.; Iyengar, S. S.; Tomasi, J.; Cossi, M.; Rega, N.; Millam, N. J.; Klene, M.; Knox, J. E.; Cross, J. B.; Bakken, V.; Adamo, C.; Jaramillo, J.; Gomperts, R.; Stratmann, R. E.; Yazyev, O.; Austin, A. J.; Cammi, R.; Pomelli, C.; Ochterski, J. W.; Martin, R. L.; Morokuma, K.; Zakrzewski, V. G.; Voth, G. A.; Salvador, P.; Dannenberg, J. J.; Dapprich, S.; Daniels, A. D.; Farkas, Ö.; Foresman, J. B.; Ortiz, J. V.; Cioslowski, J.; Fox, D. J. *Gaussian 09*, Gaussian, Inc.: Wallingford, CT, USA, 2009.

68. Becke, A. D., Density-functional thermochemistry. III. The role of exact exchange. *J. Chem. Phys.* **1993,** *98* (7), 5648–5652.

69. Godbout, N.; Salahub, D. R.; Andzelm, J.; Wimmer, E., Optimization of Gaussian-type basis sets for local spin density functional calculations. Part I. Boron through neon, optimization technique and validation. *Can. J. Chem.* **1992,** *70* (2), 560–571.

70. Dorazio, S. J.; Vogel, A.; Dechert, S.; Nevonen, D. E.; Nemykin, V. N.; Bruckner, C.; Meyer, F. Siamese-Twin Porphyrin Goes Platinum: Group 10 Monometallic, Homobimetallic, and Heterobimetallic Complexes. *Inorg. Chem.* **2020**, *59*(10), 7290-7305.

5 Formation and Spectroscopic Evaluation of N-Confused Porphyrin-Based Microscale Architectures in Aqueous Media

5.1 Chapter Preface

In chapters 2-4, the electronic structures of soft chromophoric systems were investigated experimentally (UV-vis, MCD, electrochemistry, spectroelectrochemistry) and theoretically (DFT, TDDFT) to determine the effects of various methods of π-system extension. This included extension of the π-system in a single direction (Ch. 2), both directions through triple linkages (Ch. 3), and along the arbitrary y-axis through the fusion of two macrocycles (Ch. 4). This chapter will be the last to focus on soft chromophores, and will introduce a novel alternative method of extending the π-system.

The soft chromophore featured in this chapter is a metal-free *N*-confused *meso*-tetraphenylporphyrin where, relative to standard *meso*-tetraphenylporphyrin, one of the four pyrrole rings is rotated and has a carbon atom facing the molecule center. Sulfonyl groups were incorporated onto the *meso*-phenyl (para) positions to impart this molecule with the property of water solubility. The focus of this chapter is the unconventional method of π-system extension, where observed aggregation of this compound in a water solution was exploited to form large globules which consist of thousands or possibly, millions of porphyrin subunits. Their optical absorption spectra, optical activity, and particle size will be evaluated to provide a detailed picture of the electronic structure of this system.

5.2 Introduction

Originally isolated as an impurity following the synthesis and chromatographic purification of metal-free tetraphenylporphyrin, *N*-confused porphyrin, which is also known as "inverted porphyrin" and 2-aza-21-carbaporphyrin, is currently one of the most commonly investigated isomers of normal porphyrin.[1,2] The structural configuration of this macrocycle features one inverted pyrrole ring relative to normal porphyrin where the pyrrolic nitrogen atom is positioned on the periphery of the porphyrinoid and the β-pyrrolic carbon atom occupies the core of the macrocycle (Fig. 5.1a).

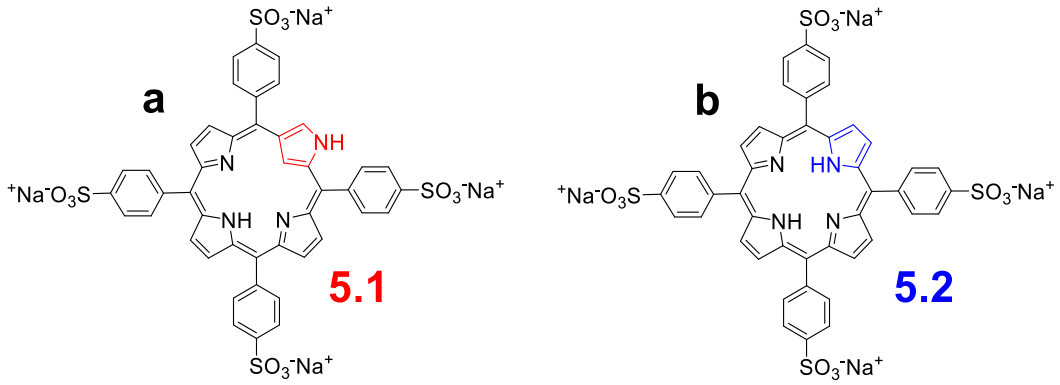

Figure 5.1. Structures of (a) sulfonated *N*-confused tetraphenylporphyrin (**5.1**) and (b) sulfonated tetraphenylporphyrin (**5.2**).

Although the physical structure of isomer **5.1** is quite similar to that of **5.2** (Fig. 5.1b), the rotated pyrrole ring significantly affects the macrocyclic electronic structure which imparts **5.1** with unique physical and chemical properties.[3-10] Despite these differences in their electronic structures compared to normal porphyrins, free-base and metalated *N*-confused porphyrins have only been investigated in a limited quantity up to this point.[12-18]

The formation of supramolecular optically active architectures comprised of achiral molecules such as porphyrins has been accomplished using chiral director molecules.[19-21] These assemblies are held together by the noncovalent electrostatic interactions between monomers; however, these weak bonding interactions can only be achieved and maintained in organic solvents or mixtures of organic solvents with water.[22-25] To date, only a handful of reports on the self-assembly of helical architectures formed exclusively in water exist.[26-28] The importance of using water media, as opposed to organic solvents or mixtures, to form these nanoscale assemblies lies in the potential applications for these helical particles with respect to chemical

biology and the important role that water plays in such biological systems; not to mention to provide insights into naturally-occurring self-assembly processes.[29,30]

The focus of this report is to prepare self-assembled architectures from sulfonated *N*-confused tetraphenylporphyrin (**5.1**) using tartaric acid as the chiral directing molecules in water. As a comparison, sulfonated tetraphenylporphyrin (**5.2**) will also be used in separate self-assembly experiments as a "normal porphyrin" reference. Following the optimization of the preparation protocol, these assemblies will be structurally confirmed using high-resolution ESI mass spectrometry and spectroscopically assessed using UV-vis, circular dicroism (CD), and magnetic circular dichroism (MCD). In order to provide insight into the nature of the aggregation of these particles as well as to simulate their UV-vis spectra and provide band assignments, DFT and TDDFT calculations will be performed. Finally, the particle size will be assessed using the dynamic light scattering (DLS) technique.

5.3 Results and Discussion

The self-assembled architectures were formed in water (brine specifically) over a period of several minutes to hours. These assemblies were comprised of either protonated **5.1** or **5.2** subunits which aggregated and stacked via four-fold hydrogen bonding interactions and were held together by electrostatic attraction. The ordered nature of the stacking of these particles originated from the use of tartaric acid which functioned as a chiral director molecule, thereby imparting these assemblies, which are constructed using achiral **5.1** or **5.2** building blocks, with optical activity. Their formation was monitored by UV-vis spectroscopy and was primarily

represented by a red-shifted Soret-band. In the case of the UV-vis spectrum of the particles derived from **5.1** (Fig. 5.2a upper), the Soret-band at 465 nm decreased in intensity and a newly formed peak grew at 501 nm, while for the particles formed from **5.2** (Fig. 5.2b upper), the Soret-band at 440 nm lost intensity and a new peak at 492 nm was observed to increase in intensity. The evolution of these two peaks in the Soret-band region did reach a limit after a few hours; however, the initial Soret-band was never observed to entirely disappear, indicating that monomers still existed in solution. The purity of the **5.1** monomers and the presence of higher ordered assemblies was confirmed using high-resolution ESI mass spectrometry (Fig. S5.1)

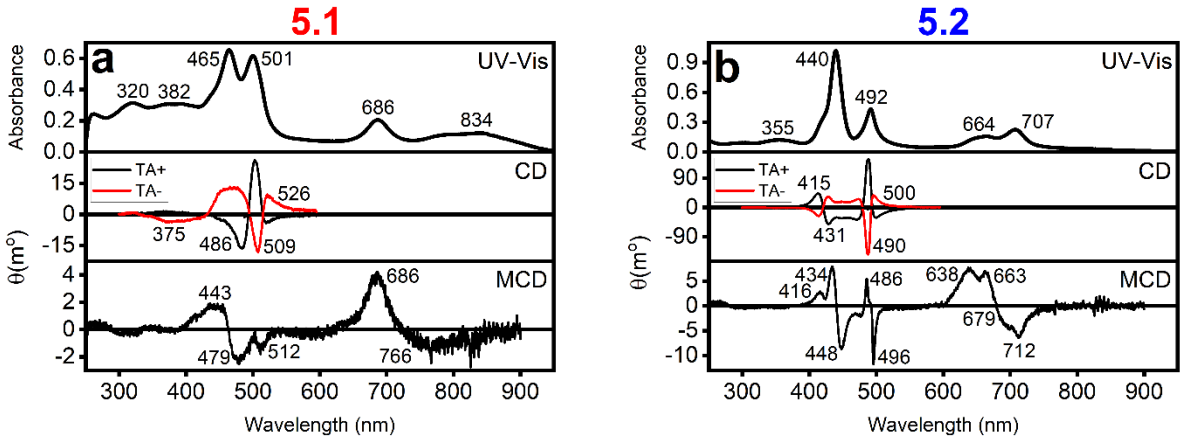

Figure 5.2. UV-Vis (upper), CD (middle), and MCD (lower) spectra of protonated (a) **5.1** and (b) **5.2** in brine.

Both the **5.1** and **5.2** monomers are achiral; however, upon introduction of either (+)- or (-)-tartaric acid, which functions as a chiral directing molecule, to a solution of the monomers in brine results in the protonation and self-aggregation of particles that possess overall optical activity as demonstrated by their CD spectra (Fig. 5.2 middle). In both cases, it is apparent that

the opposing CD signals derived from the (+)- and (-)-tartaric acids are not exactly symmetrical in terms of intensity with respect to each other despite our best efforts to quantitatively achieve this spectral symmetry. This was hypothesized to be the case due to the nature in which the (+)- and (-)-tartaric acids are prepared, where (+)-tartaric acid occurs naturally and the (-)-tartaric acid enantiomer is synthetically[31] produced.

The magnetic circular dichroism spectroscopy of *N*-confused porphyrins has gained increasing amounts of interest over the last few decades.[32-44] Due to the absence of reports on the MCD spectroscopy of N-confused porphyrin-based architectures in water, their spectra are reported herein (Fig. 5.2 bottom). For the **5.1** particles, its MCD spectrum (Fig. 5.2a bottom) is of rather low intensity which lead to a significant amount of signal noise; nonetheless, the MCD spectrum of the **5.1** assemblies possesses a Faraday *A*-term centered at 463 nm which is associated with the Soret band of the excess monomer in solution and a *B*-term at 512 nm which corresponds to the newly evolved signal which represents the formation of the self-assembled architectures. The CD spectrum, as well as the MCD spectrum of the **5.2** architectures (Fig. 5.2b bottom) both possess much higher intensities than its **5.1** counterpart. This is possibly due to the more ordered stacking achieved by **5.2** since it is more symmetric than **5.1** as the rotated pyrrole ring breaks the two-fold macrocyclic symmetry of **5.1** relative to **5.2**. Within the MCD spectrum of the **5.1** particles, a Faraday *A*-term is present and centered at 441 nm which is associated with the Soret-band of the still present monomers in solution, and this signal possesses single vibronic satellites on either side. Due to the higher degree of symmetry of **5.2** relative to **5.1**, a pseudo-*A*-term is presently centered at 492 nm is corresponds to the peak formed by the

particles in the UV-vis spectrum. Between 600-750 nm, the MCD spectrum of the **5.2** assemblies is comprised of an *A*-term centered at 679 nm which is surrounded on either side by *B*-terms at 638 and 712 nm. The presence of *A*-terms within the MCD spectrum of the **5.2** architectures, as well as the significantly higher intensity of its CD and MCD signals, suggests that these self-assembled architectures possess more structural uniformity than those formed from **5.1**. This increased level of structural uniformity of the particles derived from **5.2** originates from the highly symmetric nature of the sulfonated *meso*-tetralphenylporphyrin which possesses d_{4h} symmetry compared to a complete lack of symmetry in **5.2**.

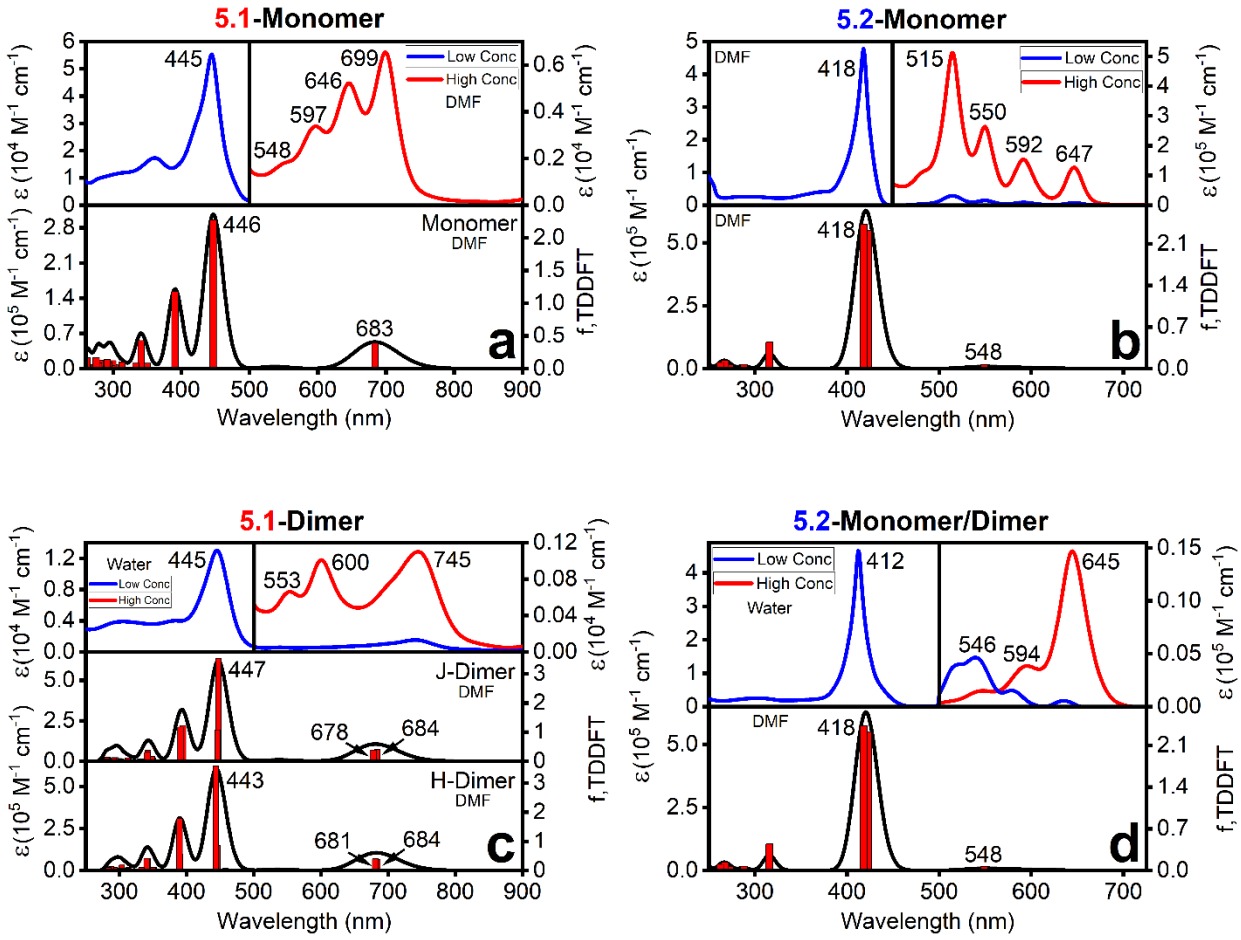

Figure 5.3. TDDFT-predicted UV-vis spectra of the monomer and dimer for **5.1** and **5.2** using the CAM-B3LYP exchange correlation functional. In each case, the upper spectrum is experimental and the lower spectrum/spectra are simulated. In the case of plot d, the experimental (upper) UV-vis spectrum is the dimer in water; however, since the dimer of **5.2** was not simulated, the calculated spectrum (lower) is that of the monomer in DMF for comparison.

TDDFT calculations were performed to simulate the UV-vis spectra of the monomers and dimer, as well as to potentially provide theoretical support to identify the primary mode of aggregation. Two commonly used exchange correlation functionals (CAM-B3LYP and TPSSh)

were utilized for the calculations, and the peak energies predicted by CAM-B3LYP (Fig. 5.3) were found to be more accurate than those from TPSSh (Fig. S5.2). All calculations simulated DMF solvent effects. In the case of the simulated UV-vis spectrum of the **5.1** dimer (Fig. 5.3c), the geometries of the J- and H-aggregated dimeric systems were accounted for prior to running the calculation, rather than simulating particle interaction between monomers. In the case of the monomer/dimer spectrum of Fig. 5.3d, the upper experimental spectrum was measured in water and was assigned to the dimer species, while the lower simulated spectrum was calculated in DMF for qualitative comparison. In the case of the **5.1** and **5.2** monomers of Figs. 5.3a and 5.3b, the Soret-band was predicted at the correct energy and the *Q*-band was also well-represented in the correct energetic spectral region, both relative to their corresponding experimental spectra. With regard to the type of aggregation that fuels this self-assembly behavior, the experimental UV-vis spectra are strongly suggestive of J-type aggregation due to the red-shifting of the Soret-band. Our theoretical modelling of the UV-vis spectra are in agreement with this assumption as the Soret-band is red-shifted by 2 nm for the calculated J-dimer and blue-shifted by 2 nm for the H-dimer.

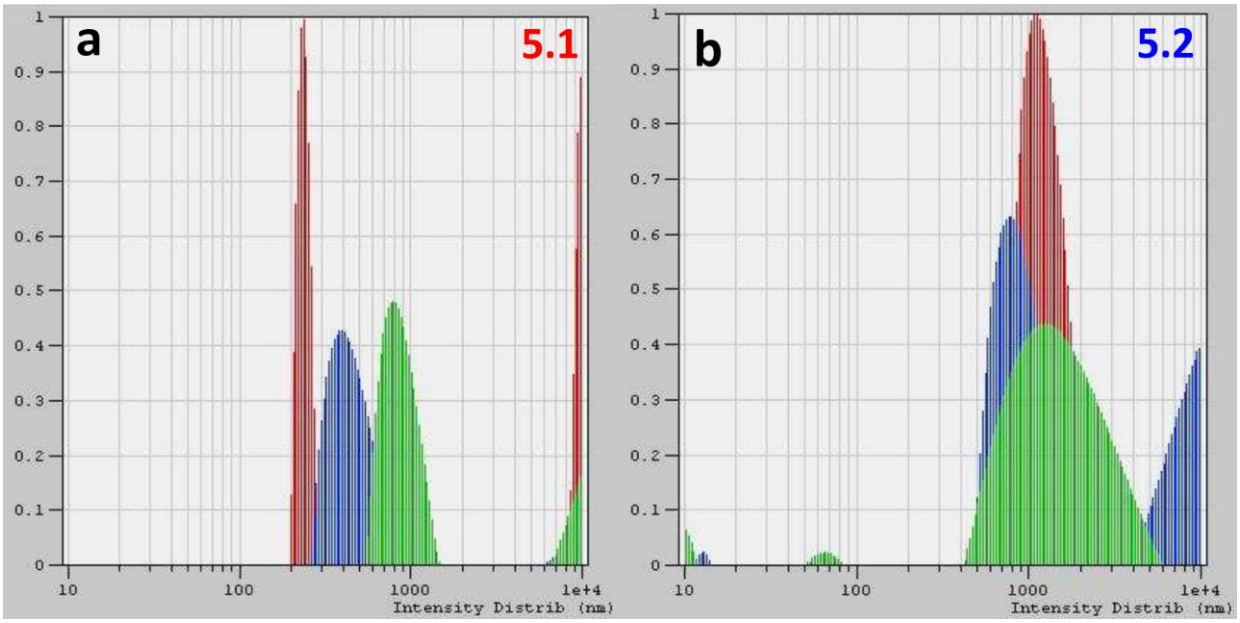

Figure 5.4. DLS size distribution profiles of (a) **5.1** and (b) **5.2** particles (the red, blue, and green peaks are associated with detector angles of 75˚, 60˚, and 90˚, respectively).

Finally, the dynamic light scattering (DLS) technique was employed to evaluate the average hydrodynamic diameter of the particles in solution (Fig. 5.4). DLS was run on several batches of **5.1** and **5.2** assemblies, and the particle sizes were found to vary from 0.4-9.0 µm for the **5.1** particles and 1.0-9.0 µm for the **5.2** particles depending on how long the assemblies were allowed to aggregate. Overall, the average **5.1** particle size for all measured batches was found to be 3.9 µm and that for the **5.2** particles was 5.6 µm (additional DLS plots present in Fig. S5.3). Since the peaks of Fig. 5.4, which represent different laser angles relative to the detector, are not completely overlapping, this indicates particles which are not of uniform size and are perhaps elongated as opposed to spherical. Also present in the plots of Fig. 5.4 are peaks that exceed the intensity distribution range of 10 µm, which suggest that very large particles (outside the range of detection) are present and were not factored into the average sizes

presented. The larger particle size of the **5.2** assemblies confirms the suspicion that the higher degree of symmetry possessed by **5.2** results in more ordered and subsequently larger particles as was interpreted from the larger CD and MCD signal intensities observed for the **5.2** assemblies compared to those formed from **5.1**.

5.4 Conclusions

Self-assembled architectures were prepared in aqueous (brine) media from achiral sulfonated tetraphenylporphyrin and N-confused tetraphenylporphyrin, which were held together by four-fold hydrogen bonding electrostatic interactions and their formation was monitored by UV-vis. The use of tartaric acid as a chiral directing molecule facilitated the assemblies to aggregate in an ordered fashion which resulted in overall optical activity of the microscale assemblies as was confirmed by circular dichroism. Magnetic circular dichroism experiments suggested that the *B*-term at 512 nm (Fig. 2a), which was associated with the newly formed **5.1** assemblies, involves transitions between non-degenerate ground and excited states. For the **5.2** microscale architectures (Fig. 2b), a pseudo-*A*-term was observed at 492 nm which corresponded to the signal formed by the self-assembled particles, and indicated that the formed particles themselves maintain a high degree of symmetry. The TDDFT UV-vis spectral simulations provided excellent agreement with the corresponding experimental spectra with respect to the predicted energies of the Soret-bands and signals present in the *Q*-band region. The TDDFT calculations also supported the idea of J-type aggregation by these particles as the UV-vis spectra displayed a red-shifted Soret-band which is indicative of J-aggregates in these systems.

Finally, DLS size distribution data provided an overall average **5.1** particle size of 3.9 μm and **5.2** particle size of 5.6 μm for all measured batches.

This work was able to conclude that extension of the π-system of water-soluble N-confused *meso*-tetraphenylporphyrin through aggregation leads to the formation of large optically active architectures. The tartaric acid likely played a strong role in influencing the optical activity and ordered stacking of these monomeric subunits. The mode of stacking was determined from UV-vis spectroscopy to be J-type where red-shifting of the Soret band was observed. The microscale size of these particles, as suggested by DLS, was observed to be in excess of one micron. The results of the electronic structure analysis of this system uncovered a ΔHOMO > ΔLUMO relationship, as was determined experimentally (MCD) and theoretically (DFT). This indicates that these soft chromophoric *N*-confused porphyrin globules possess a commonly encountered electronic structure that generally represents those of other synthetically prepared molecules.

5.5 Experimental Section

5.5.1 Particle Preparation. On a spectroscopic scale, the particles were qualitatively prepared by adding a small amount of highly concentrated solution of **5.1** or **5.2** in water (5mg/0.5mL) to 3.0 mL of brine (until the absorption intensity of the Soret-band was decidedly nominal). 50 mg of either (+)- or (-)- tartaric acid was then added to the sample solution to begin the self-assembly process. After 12 hours, approximately 85% of the monomers became aggregated into the target particles as was determined by UV-vis spectroscopy.

5.5.2 UV-Vis, CD, and MCD Spectroscopy. All UV-vis spectra were collected on a Jasco V-770 spectrophotometer and the CD spectra were collected using a Jasco J-1500 CD spectrometer. The MCD spectra were measured with a Jasco J-1500 CD spectrometer coupled to a Jasco MCD-581 electromagnet operated at 1.0 T. The completed MCD spectra were measured at 10 °C in parallel and antiparallel orientations with respect to the magnetic field.

5.5.3 Computational Aspects. All calculations were run using Gaussian 16.[45] The starting geometries of all compounds were optimized using the TPSSh[46,47] exchange correlation functional with the 6-311 G(d) basis set.[48] Vibrational frequencies were calculated to ensure all geometries were local minima. Time-dependent density functional theory (TDDFT) with CAM-B3LYP[49] and TPSSh was used to calculate the first 40 excited states for each compound. The 6-31 G(d) basis set[48] was used for the TDDFT calculations. All calculations were run in solution using the PCM model[50] with dimethylformamide (DMF) as the solvent.

5.5.4 DLS Measurements. The DLS measurements were performed with Rachel Nickel in the laboratory of Prof. Johan van Lierop (University of Manitoba – Dept. of Physics and Astronomy). The average hydrodynamic diameters of the assemblies created from **5.1** and **5.2** were determined using the dynamic light scattering technique. The DLS measurements were performed on a suspension of particles (the particles were naturally suspended in their original solutions and were either shaken or sonicated) in water/brine at room temperature using a Photocor Complex system equipped with a 638 nm laser with an intensity of 25 mW. The detector angle was positioned at 60˚, 75˚, or 90˚ relative to the laser source for each

measurement. A built-in photon correlation spectroscopy function was utilized by the Photocor Complex hardware/software to process the data.

5.6 References

1. Furuta, H.; Asano, T,; Ogawa, T. "N-Confused Porphyrin": A New Isomer of Tetraphenylporphyrin. *J. Am. Chem. Soc.* **1994**, *116* (2), 767-768.
2. Chmielewski, P. J.; Latos-Grazynski, L.; Rachlewics, K.; Glowiak, T. Monoinverted Tetra-*p*-tolylporphyrin: A Novel Porphyrin Isomer. *Angew. Chem. Int. Ed. Engl.* **1994**, *33* (7), 779-781.
3. Latos-Grazynski, L. Core-Modified Heteroanalogues of Porphyrins and Metalloporphyrins. In *The Porphyrin Handbook*; Kadish, K. M., Smith, K. M., Guilard, R., Eds.; Academic Press: New York, 2000; pp 361-416.
4. Furuta, H.; Maeda, H.; Osuka, A. Confusion, Inversion, and Creation-A New Spring from Porphyrin Chemistry. *Chem. Commun.* **2002**, *17*, 1795-1804.
5. Harvey, J. D.; Ziegler, C. J. Developments in the Metal Chemistry of N-Confused Porphyrin. *Coord. Chem. Rev.* **2003**, *247* (1-2), 1-19.
6. Chmielewski, P. J.; Latos-Grazynski, L. Core Modified Porphyrins – A Macrocyclic Platform for Organometallic Chemistry. *Coord. Chem. Rev.* **2005**, *249* (21-22), 2510-2533.
7. Srinivasan, A.; Furuta, H. Confusion Approach to Porphyrinoid Chemistry. *Acc. Chem. Res.* **2005**, *38* (1), 10-20.

8. Pawlicki, M.; Latos-Grazynski, L. O-Confusion Approach in Construction of Carbaporphyrinoids. *Chem. Rec.* **2006**, *6* (2), 64-78.

9. Maeda, H.; Furuta, H. A Dozen Years of N-Confusion: From Synthesis to Supramolecular Chemistry. *Pure Appl. Chem.* **2006**, *78* (1), 29-44.

10. Harvey, J. D.; Ziegler, C. J. The Metal Complexes of N-Confused Porphyrin as Heme Model Compounds. *Inorg. Biochem.* **2006**, *100* (4), 869-880.

11. Zandler, M. E.; D'Souza, F. Electronic and Structural Properties of the Metalloporphyrin Structural Isomers: Semiempirical AM1 and PM3 Calculations. *J. Mol. Struct.* (THEOCHEM) **1997**, *401* (3), 301-314.

12. Szterenberg, L.; Latos-Grazynski, L. Structure and Stability of 2-Aza-21-carbaporphyrin Tautomers Prearranged for Coordination. *Inorg. Chem.* **1997**, *36* (27), 6287-6291.

13. Ghosh, A.; Wondimagegn, T.; Nilsen, H. Molecular Structures, Tautomerism, and Carbon Nucleophilicity of Free-Base Inverted Porphyrins and Carbaporphyrins: A Density Functional Theoretical Study. *J. Phys. Chem. B* **1998**, *102* (50), 10459-10467.

14. Parusel, A. B. J.; Ghosh, A. Density Functional Theory Based Configuration Interaction Calculations on the Electronic Spectra of Free-Base Porphyrin, Chlorin, Bacteriochlorin, and cis- and trans-Isobacteriochlorin. *J. Phys. Chem. A* **2000**, *104* (11), 2504-2507.

15. Belair, J. P.; Ziegler, C. S.; Rajesh, C. S.; Modarelli, D. A. Photophysical Characterization of Free-Base N-Confused Tetraphenylporphyrins. *J. Phys. Chem. A* **2002**, *106* (27), 6445-6451.

16. Shaw, J. L.; Garrison, S. A.; Aleman, E. A.; Ziegler, C. J.; Modarelli, D. A. Synthesis and Spectroscopy of a Series of Substituted N-Confused Tetraphenylporphyrins. *J. Org. Chem.* **2004**, *69* (22), 7423-7427.

17. Aleman, E. A.; Rajesh, C. S.; Ziegler, C. S.; Modarelli, D. A. Ultrafast Spectroscopy of Free-Base N-Confused Tetraphenylporphyrins. *J. Phys. Chem.* **2006**, *110* (28), 8605-8612.

18. Vyas, S.; Hadad, C. M.; Modarelli, D. A. A Computational Study of the Ground and Excited State Structure and Absorption Spectra of Free-Base N-Confused Porphine and Free-Base N-Confused Tetraphenylporphyrin. *J. Phys. Chem. A* **2008**, *112* (29), 6533-6549.

19. Oda, R.; Huc, I.; Schmutz, M.; Canau, S.; MacKintosh, F. Tuning Bilayer Twist Using Chiral Counterions. *Nature* **1999**, *399* (6736), 566-569.

20. Xiao, J.; Xu, J.; Cui, S.; Liu, H.; Wang, S.; Li, Y. Supramolecular Helix of an Amphiphilic Pyrene Derivative Induced by Chiral Tryptophan Through Electrostatic Interactions. *Org. Lett.* **2008**, *10* (4), 645-648.

21. Huang, Y.; Yan, Y.; Smarsly, B. M.; Wei, Z.; Faul, C. F. Helical Supramolecular Aggregates, Mesoscopic Organization and Nanofibers of a Perylenebisimide – Chrial Surfactant Complex via Ionic Self-Assembly. *J. Mater. Chem.* **2009**, *19* (16), 2356-2362.

22. Kumar, M.; Jonnalagadda, N.; George, S. J. Molecular Recognition Driven Self-Assembly and Chiral Induction in Naphthalene Diimide Amphiphiles. *Chem. Commun.* **2012**, *48* (89), 10948-10950.

23. George, S. J.; de Bruijn, R.; Tomovic, Z. E.; Van Averbeke, B.; Beljonne, D.; Lazzaroni, R.; Schenning, A. P. H. J.; Meijer, E. Asymmetric Noncovalent Synthesis of Self-Assembled One-Dimensional Stacks by a Chiral Supramolecular Auxiliary Approach. *J. Am. Chem. Soc.* **2012**, *134* (42), 17789-17796.

24. Sobczuk, A. A.; Tsuchiya, Y.; Shiraki, T.; Tamaru, S. I.; Shinkai, S. Creation of Chiral Thixotropic Gels Through a Crown-Ammonium Interaction and Their Application to a Memory-Erasing Recycle System. *Chem.-Eur. J.* **2012**, *18* (10), 2832-2838.

25. Yashima, E.; Ousaka, N.; Taura, D.; Shimomura, K.; Ikai, T.; Maeda, K. Supramolecular Helical Systems: Helical Assemblies of Small Molecules, Foldamers, and Polymers with Chiral Amplification and Their Functions. *Chem. Rev.* **2016**, *116* (22), 13752-13990.

26. Kumar, M.; Brocorens, P.; Tonnele, C.; Beljonne, D.; Surin, M.; George, S. J. A Dynamic Supramolecular Polymer with Stimuli-Responsive Handedness for *in situ* Probing of Enzymatic ATP Hydrolysis. *Nat. Commun.* **2014**, *5*, 5793/1-5793/8.

27. Dhiman, S.; Jain, A.; George, S. J.; Transient Helicity: Fuel-Driven Temporal Control Over Conformational Switching in a Supramolecular Polymer. *Angew. Chem., Int. Ed.* **2017**, *56* (5), 1329-1333.

28. Dhiman, S.; Jain, A.; Kumar, M.; George, S. J. Adenosine-Phosphate-Fueled, Temporally Programed Supramolecular Polymers with Multiple Transient States. *J. Am. Chem. Soc.* **2017**, *139* (46), 16568-16575.

29. Ball, P. Water as an Active Constituent in Cell Biology. *Chem. Rev.* **2008**, *108* (1), 74-108.

30. Wei, P.; Yan, X.; Huang, F. Supramolecular Polymers Constructed by Orthogonal Self-Assembly Based on Host-Guest and Metal-Ligand Interactions. *Chem. Soc. Rev.* **2015**, *44* (3), 815-832.

31. Church, J. M.; Blumberg, R. Synthesis of Tartaric Acid – By the Hydroxylation of Maleic Acid. *Ind. Eng. Chem.* **1951**, *43*, 1780-1786.

32. Nemykin, V. N.; Kobayashi, N. A Tetraazaporphyrin with an Intense, Broad Near-IR Band. *Chem. Commun.* **2001**, *2*, 165-166.

33. Gorski, A.; Vogel, E.; Sessler, J. L.; Waluk, J. Magnetic Circular Dichroism of Octaethylcorrphycene and Its Doubly Protonated and Deprotonated Forms. *J. Phys. Chem. A* **2002**, *106* (35), 8139-8145.

34. Stillman, M. J.; Mack, J.; Kobayashi, N. Theoretical Aspects of the Spectroscopy of Porphyrins and Phthalocyanines. *J. Porphyrins Phthalocyanines* **2002**, *6* (4), 296-300.

35. Nakamura, Y.; Aratani, N.; Shinokubo, H.; Takagi, A.; Kawai, T.; Matsumoto, T.; Yoon. Z. S.; Kim, D. Y.; Ahn, T. K.; Kim, D.; Kobayashi, N. A Directly Fused Tetrameric Porphyrin Sheet and Its Anomalous Electronic Properties That Arise from the Planar Cyclooctatetraene Core. *J. Am. Chem. Soc.* **2006**, *128* (12), 4119-4127.

36. Kobayashi, N.; Nakai, K. Applications of Magnetic Circular Dichroism Spectroscopy to Porphyrins and Phthalocyanines. *Chem. Commun.* **2007**, *40*,4077-4092.

37. Mack, J.; Stillman, M. J.; Kobayashi, N. Application of MCD Spectroscopy to Porphyrinoids. *Coord. Chem. Rev.* **2007**, *251* (3+4), 429-453.

38. Nemykin, V. N.; Galloni, P.; Floris, B.; Barrett, C. D.; Hadt, R. G.; Subbotin, R. I.; Marrani, A. G.; Zanoni, R.; Loim, N. M. Metal-Free and Transition-Metal Tetraferrocenylporphyrins Part 1: Synthesis, Characterization, Electronic Structure, and Conformational Flexibility of Neutral Compounds. *Dalton Trans.* **2008**, *32*, 4233-4246.

39. Mack, J.; Bunya, M.; Lansky, D.; Goldberg, D. P.; Kobayashi, N. The MCD Spectroscopy of Corrolazines and Triazatetrabenzcorroles. *Heterocycles* **2008**, *76*, 1369-1380.

40. Xue, Z.-L.; Shen, Z.; Mack, J.; Kuzuhara, D.; Yamada, H.; Okujima, T.; Ono, N.; You, X.-Z.; Kobayashi, N. A Facile One-Pot Synthesis of *meso*-Aryl-Substituted [14]Triphyrin(2.1.1). *J. Am. Chem. Soc.* **2008**, *130*, 16478-16479.

41. Kuzuhara, D.; Mack, J.; Yamada, H.; Okujima, T.; Ono, N.; Kobayashi, N. Synthesis, Structures, and Optical and Electrochemical Properties of Benzoporphycenes *Chem.-Eur. J.* **2009**, *15*, 10060-10069.

42. Nemykin, V. N; Rohde, G. T.; Barrett, C. D.; Hadt, R. G.; Sabin, J. R.; Reina, G.; Galloni, P.; Floris, B. Long-Range Electronic Communication in Free-Base *meso*-Poly(ferrocenyl)-Containing Porphyrins. *Inorg. Chem.* **2010**, *49*, 7497-7509.

43. Lukyanets, E. A.; Nemykin, V. N. The Key Role of Peripheral Substituents in the Chemistry of Phthalocyanines and Their Analogues. *J. Porphyrins Phthalocyanines* **2010**, *14* (1), 1-40.

44. Sripothongnak, S.; Ziegler, C. J.; Dahlby, M. R.; Nemykin, V. N. Controllable and Reversible Inversion of the Electronic Structure in Nickel N-Confused Porphyrin: A Case When MCD Matters. *Inorg. Chem.* **2011**, *50*, 6902-6909.

45. Gaussian 16, Revision B.01, Frisch, M. J.; Trucks, G. W.; Schlegel, H. B.; Scuseria, G. E.; Robb, M. A.; Cheeseman, J. R.; Scalmani, G.; Barone, V.; Petersson, G. A.; Nakatsuji, H.; Li, X.; Caricato, M.; Marenich, A. V.; Bloino, J.; Janesko, B. G.; Gomperts, R.; Mennucci, B.; Hratchian, H. P.; Ortiz, J. V.; Izmaylov, A. F.; Sonnenberg, J. L.; Williams-Young, D.; Ding, F.; Lipparini, F.; Egidi, F.; Goings, J.; Peng, B.; Petrone, A.; Henderson, T.; Ranasinghe, D.; Zakrzewski, V. G.; Gao, J.; Rega, N.; Zheng, G.; Liang, W.; Hada, M.; Ehara, M.; Toyota, K.; Fukuda, R.; Hasegawa, J.; Ishida, M.; Nakajima, T.; Honda, Y.; Kitao, O.; Nakai, H.; Vreven, T.; Throssell, K.; Montgomery, J. A., Jr.; Peralta, J. E.; Ogliaro, F.; Bearpark, M. J.; Heyd, J. J.; Brothers, E. N.; Kudin, K. N.; Staroverov, V. N.; Keith, T. A.; Kobayashi, R.; Normand, J.; Raghavachari, K.; Rendell, A. P.; Burant, J. C.; Iyengar, S. S.; Tomasi, J.; Cossi, M.; Millam, J. M.; Klene, M.; Adamo, C.; Cammi, R.; Ochterski, J. W.; Martin, R. L.; Morokuma, K.; Farkas, O.; Foresman, J. B.; Fox, D. J. Gaussian, Inc., Wallingford CT, 2016.

46. Tao, J. M.; Perdew, J. P.; Staroverov, V. N.; Scuseria, G. E. Climbing the Density Functional Ladder: Nonempirical Meta-Generalized Gradient Approximation Designed for Molecules and Solids. *Phys. Rev. Lett.* **2003**, *91*, 146401/1-146401/4.

47. Staroverov, V. N.; Scuseria, G. N.; Tao, J.; Perdew, J. P. Comparative Assessment of a New Nonempirical Density Functional: Molecules and Hydrogen-Bonded Complexes. *J. Chem. Phys.* **2003**, *119*, 12129-12137.

48. McLean, A. D.; Chandler, G. S. Contracted Gaussian Basis Sets for Molecular Calculations. I. Second Row Atoms, Z=11-18. *J. Chem. Phys.* **1980**, *72*, 5639-5648.

49. Yanai, T.; Tew, D.; Handy, N. A New Hybrid Exchange-Correlation Functional Using the Coulomb-Attenuating Method (CAM-B3LYP). *Chem. Phys. Lett.* **2004**, *393*, 51-57.

50. Tomasi, J.; Mennucci, B.; Cammi, R. Quantum Mechanical Continuum Solvation Models. *Chem. Rev.* **2005**, *105*, 2999-3093.

6. Systematic Investigation of the Electronic Structures of Triazatetrabenzcorroles Decorated with Peripheral Carbazole Moieties

6.1 Chapter Preface

In Chapters 2-5, the electronic structures of various π-extended soft chromophoric porphyrins were investigated. In addition to observing the spectral changes associated with extending these π-systems, our other simultaneous goal was to impart structural modifications in a way that manipulated the electronic structures to resemble their natural reduced porphyrinoid

counterparts. This involved an understanding of how (where and what type) a structural modification would affect the energy of certain specific frontier molecular orbitals. Since naturally occurring reduced porphyrinoids possess a ΔHOMO < ΔLUMO relationship, the focus was on increasing the value of ΔLUMO so that it exceeded that of ΔHOMO. This was attempted by the previously mentioned π-system extension where the e_{gy} orbital becomes more destabilized as the π-system becomes more extended. Of the four major attempts on soft chromophoric systems documented in this thesis, only the π-system extension in both directions through triple-linkages produced the target ΔHOMO < ΔLUMO relationship. This is due to the robust structural rigidity that the triple-linkages provide in porphyrin systems which assists in avoiding significant twisting which would disrupt the aromaticity of the macrocycle.

From this chapter onwards, the molecule types will now fall under the category of hard chromophores. This (hard chromophores) term refers to the energetic spacing of frontier orbitals in these systems where the ΔLUMO ($E_{LUMO+1} – E_{LUMO}$) consists of a doubly degenerate pair of orbitals and the ΔHOMO ($E_{HOMO} – E_{HOMO-1}$) is comprised of the a_{1u} orbital and the a_{2u} orbital which is very far apart (in terms of energy) from a_{1u}. This naturally leads to a large ΔHOMO value which cannot easily be reduced or overcome by the magnitude of ΔLUMO. This difficulty in rearranging these frontier orbitals as well as their energetic robustness (in terms of stability) contributes to their designation as hard chromophores.

This first chapter in the hard chromophores section (Ch. 6) features the triazatetrabenzcorrole (TBC) system which is similar in structure to metal-free porphyrin; however, the *meso*-carbon atoms are replaced with nitrogens and one of these *meso*-atoms has been eliminated from the

macrocycle itself (Scheme 6.1). Therefore, these TBC molecules only possess a total of three *meso*-atoms instead of the typically encountered four found in porphyrin and phthalocyanine systems. From a structural design perspective, since the goal was to decrease the value of ΔHOMO as much as possible, it was hypothesized that removal of one of the *meso*-nitrogen atoms will destabilize the a_{2u} orbital and decrease the value of ΔHOMO; the extent to which will be determined in this chapter.

6.2 Introduction

Within the last several years, the synthesis of contracted, expanded, and isomeric porphyrin analogues has been actively pursued.[1] As of late, corroles, which are contracted porphyrin analogues, have been commonly targeted.[2-5] Corroles are classified as contracted porphyrins due to their single missing *meso*-carbon atom; however, they still possess the tetrapyrrolic aromatic structure as a classic porphyrin macrocycle. The initial synthetic reports[6] on corroles date back to the cobalamin chemistry investigations of 1965, but their low yielding and tedious synthetic routes led many chemists in the field to focus on porphyrins and phthalocyanines instead. Currently, several modern reports[7-11] on the synthesis of *meso*-aryl-substituted corroles have brought this molecule class back into the spotlight in some circles. Nonetheless, corroles, which do not possess *meso*-phenyl substituents, remain difficult to prepare.

Some relatively recent reports[12-14] present a synthetic method for the preparation of a triazacorrole species, which are corrole structures that possess *meso*-nitrogen atoms instead of carbons. Interestingly, previous reports suggest that corroles and triazacorroles are able to

stabilize high oxidation states on the metal center.[12] A similar phthalocyanine (Pc) analogue, the triazatetrabenzcorrole (TBC) was initially prepared via ring contraction involving $NaBH_4$ and this germanium-centered compound was first reported[15] in 1986. Shortly thereafter, two more synthetic TBC reports[17,18] were published which utilized PBr_3 and Si_2Cl_6 to initiate ring contraction. In 1981, Gouterman reported[19] on phosphorus(III) and phosphorus(V) Pcs which were prepared in a similar manner; however, it was later discovered[17] that Gouterman had actually synthesized a phosphorus(V)-centered TBC compound in that report. Following these early studies, research has been quite limited on these triazatetrabenzcorrole species.

Carbazole derivatives are a useful class of heterocyclic aromatic compounds due to their excellent electrochemical and photophysical properties. They are commonly used as active components in medicine such as psychotropic, anti-inflammatory, antioxidative, antihistaminic, antimicrobial, and antitumor drugs.[20-24] A prominent example are the carbazomycins which are a carbazole-containing antibiotic class of drugs.[25-27] The carbazomycins A and B were found to possess antibacterial and antiyeast activities, and were found to inhibit the propagation of phytopathogenic fungi. Due to their excellent charge-transport ability and large emission yield, carbazoles have been recently used as building blocks for optoelectronic materials.[28-32] They have also been utilized in photovoltaic/display devices[33-36], OLEDs[37,38], charge/hole transport materials[39-42], and light-emitting photosensitizers.[43,44]

Currently, there are no existing reports on the synthesis of a carbazole-containing triazatetrabenzcorrole species. For this report, a TBC core was decorated with eight peripheral

carbazole substituents (**6.1**) and, for comparison, an alternative sample containing four peripheral *tert*-butyl substituents (**6.2**) was also prepared and reported on (Scheme 6.1).

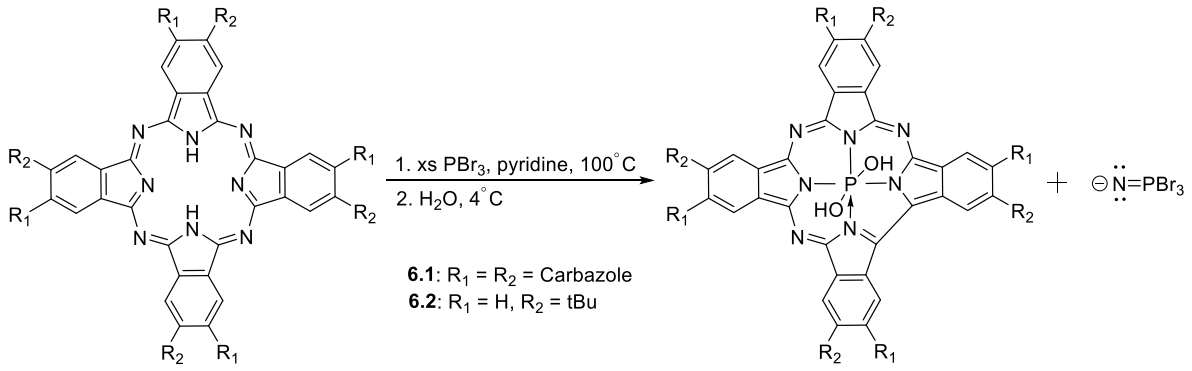

Scheme 6.1. Reaction conditions for the generation of triazatetrabenzcorroles **6.1** and **6.2** from phthalocyanine (the carbazole groups are bonded to the β-carbons through covalent C-N bonds).

In this report, we provide the first study on the electronic structures, absorption spectra, and redox profiles of the octacarbazole-decorated triazatetrabenzcorrole (**6.1**) systems. For comparison, the *tert*-butylated analogue (**6.2**) was also prepared to examine the effects of which the chromophoric carbazole substituents have on the electronic structure.

For this report, several methods were utilized including UV-vis, magnetic circular dichroism (MCD), electrochemistry, and spectroelectrochemistry, as well as density functional theory (DFT) and time-dependent DFT (TDDFT) calculations. The UV-vis and MCD spectral profiles of both samples were quite similar to each other; however, compound **6.1** possessed a more intense and red-shifted *Q*-band than compound **6.2**. The redox profiles showed a mixture of reversible and irreversible oxidation and reduction processes. The spectroelectrochemical

oxidation was found to be completely reversible for **6.1**; however, this experiment was completely irreversible for **6.2**, indicating that the octacarbazole substituents contribute strongly to the redox profile of **6.1**. Also, a cationic radical signature was observed during the spectroelectrochemical experiments performed on **6.1**, which was represented by the propagation and evolution of a broad signal at ~950 nm. Through TDDFT simulations, excellent agreement was achieved between the calculated spectrum and that obtained from experimentation when the B3LYP exchange correlation functional was utilized. The subsequently performed DFT calculations uncovered energy levels of the frontier orbitals that were mixed with those of the carbazole substituents for **6.1**; for **6.2**, the frontier orbitals were found to be energetically sequential.

6.3 Results and Discussion

6.3.1 UV-Vis and MCD Spectroscopy. The UV-vis and MCD spectra of **6.1** and **6.2** in DCM are shown in Fig. 6.1. For both compounds, their UV-vis spectra are dominated by the classic *B*- and *Q*-bands.

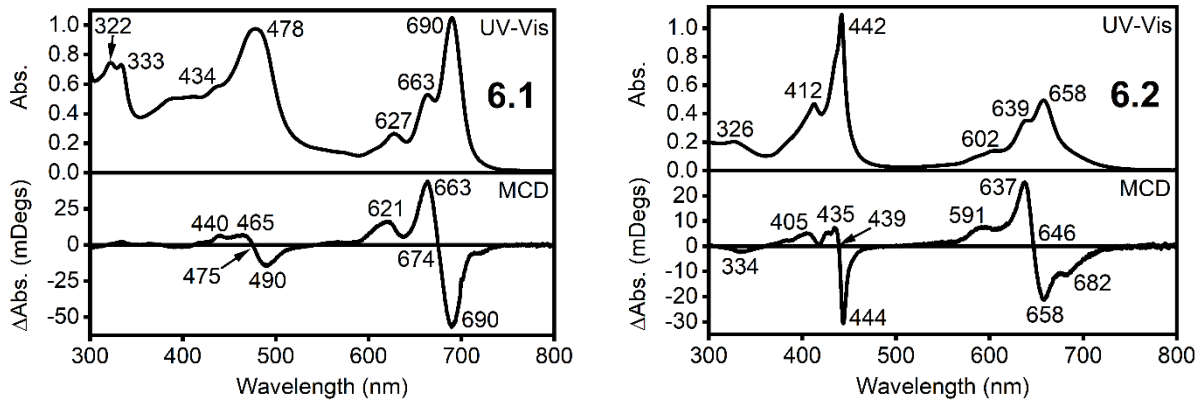

Figure 6.1. UV-vis and MCD spectra of **6.1** and **6.2**.

The *Q*-band in **6.2** (658 nm) is slightly shifted to a lower energy compared to that of the unsubstituted phosphorus-centered triazatetrabenzcorrole[45] (654 nm) and is dramatically red-shifted to 690 nm in the case of **6.1**. This significant red-shifting of the *Q*-band in **6.1** is strongly influenced by the electron-donating nature of the eight peripheral carbazole groups. The *Q*-bands of both compounds possess two vibronic satellites located at higher energies in their UV-vis spectra. The *B*-band of **6.1** is rather broad and consists of several overlapping transitions centered at 478 nm, while the *B*-band of **6.2** (442 nm) is much sharper and well-defined in the UV-vis spectrum, and this definition in the *B*-band region carries over to its respective MCD spectrum. Finally, a broad and low intensity band was observed in the UV-vis spectrum at ~580 nm for **6.1**, which is absent in the unsubstituted phosphorus-centered triazatetrabenzcorrole[45] (TBC) UV-vis spectrum. The carbazole groups in **6.1** are electron-donating in nature; therefore, it could be expected that the energies of the carbazole-centered molecular orbitals (MOs) could be near the energy of the triazatetrabenzcorrole-centered highest occupied molecular orbital (HOMO) which is a π-orbital. In the case of **6.1**, low-energy carbazole-to-TBC interligand charge-

transfer (ILCT) transitions are expected to appear at larger than *Q*-band energies; therefore, the broad band observed in the UV-vis spectrum of **6.1** at ~580 nm can tentatively be assigned as an ILCT transition. This tentative assignment was further supported by magnetic circular dichroism (MCD) spectroscopy. The *Q*-band region in the MCD spectra of **6.1** and **6.2** is dominated by intense Faraday MCD pseudo *A*-terms centered at 674 nm (**6.1**) or 646 nm (**6.2**). In both cases, this *A*-term is accompanied by one negative (at lower than *Q*-band energy) and one positive (higher than *Q*-band energy) MCD signals which are not centered around the vibronic satellites of the *Q*-band, and these spectroscopic signatures have been observed for a previously reported phosphorus-centered β-octasubstituted triazatetrabenzcorrole species[46]. Similar to previously reported MCD spectra of phosphorus-centered triazatetrabenzcorroles[46,47], the *B*-band region is at a comparable intensity to the *Q*-band region. Furthermore, MCD Faraday pseudo *A*-terms are clearly present in the *B*-band region which indicates twofold effective symmetry of the triazatetrabenzcorrole chromophore. The intensity of the MCD spectra of TBCs **6.1** and **6.2** in the 525-580 nm region is quite low, which further supports the tentative ILCT assignment of the ~580 nm transition in **6.1**, and a similar spectroscopic profile was observed in previously reported phosphorus-centered triazatetrabenzcorrole compounds.[46,47]

6.3.2 Redox Properties of Triazatetrabenzcorroles 6.1 and 6.2. The electrochemical behavior of triazatetrabenzcorroles **6.1** and **6.2** was investigated with cyclic voltammetry (CV) and differential pulse voltammetry (DPV) methods using a DCM/0.1M tetrabutylammonium perchlorate (TBAP) system (Fig. 6.2).

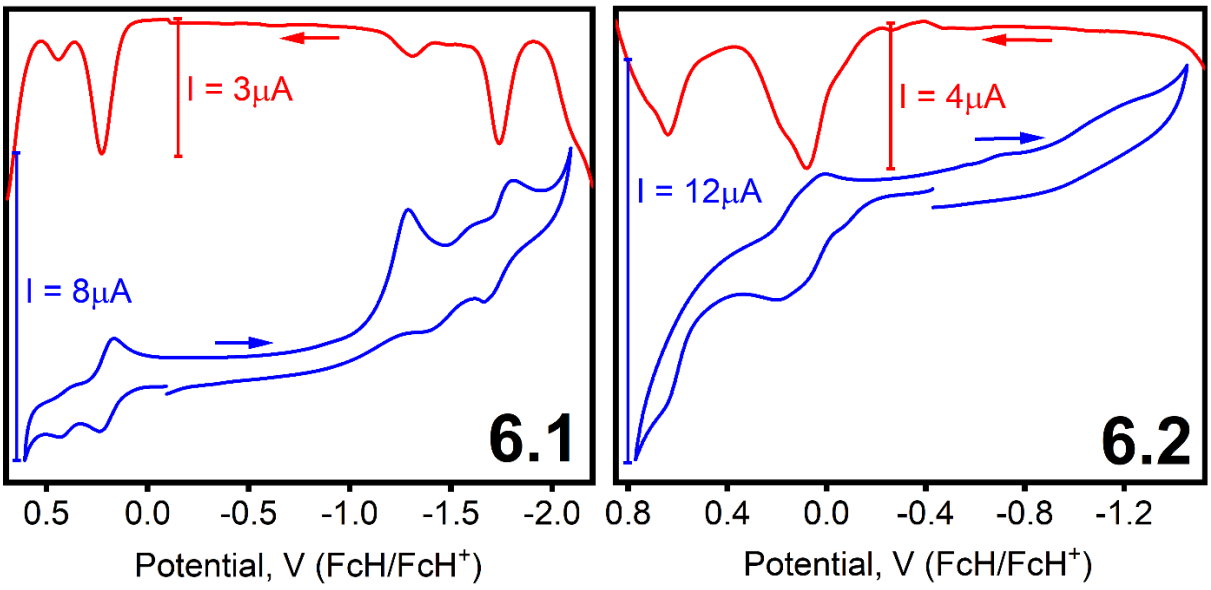

Figure 6.2. Electrochemical CV (blue) and DPV (red) voltammograms for **6.1** and **6.2** in a DCM/0.1M TBAP system.

Regarding compound **6.1**, two fully-reversible oxidation processes were observed within the electrochemical window where the oxidation event at higher potential is approximately half the intensity of its lower-energy counterpart. The reduction window of **6.1** shows two partially-reversible reduction processes with another relatively strong irreversible reduction event appearing at a less negative reduction potential. All redox events were assigned to oxidation and reduction of the triazatetrabenzcorrole core. Interestingly, the octacarbazole-based multielectron oxidation event typically observed at higher potentials in metalated phthalocyanines (Pcs) bearing eight peripheral octacarbazole substituents[48,49] was not observed in **6.1** (Fig. S6.1). For compound **6.2**, two closely spaced overlapping partially-reversible oxidation events were observed at slightly lower potentials than were observed for **6.1**,

followed by an irreversible oxidation event at a higher oxidation potential. The reduction window of **6.2** is largely featureless, and arguably does not possess any substantial signals which could be clearly identified as redox events.

In support of this hypothesis, spectroelectrochemical oxidation of triazatetrabenzcorroles **6.1** and **6.2** was performed using a DCM/0.3M TBAP system (Fig. 6.3).

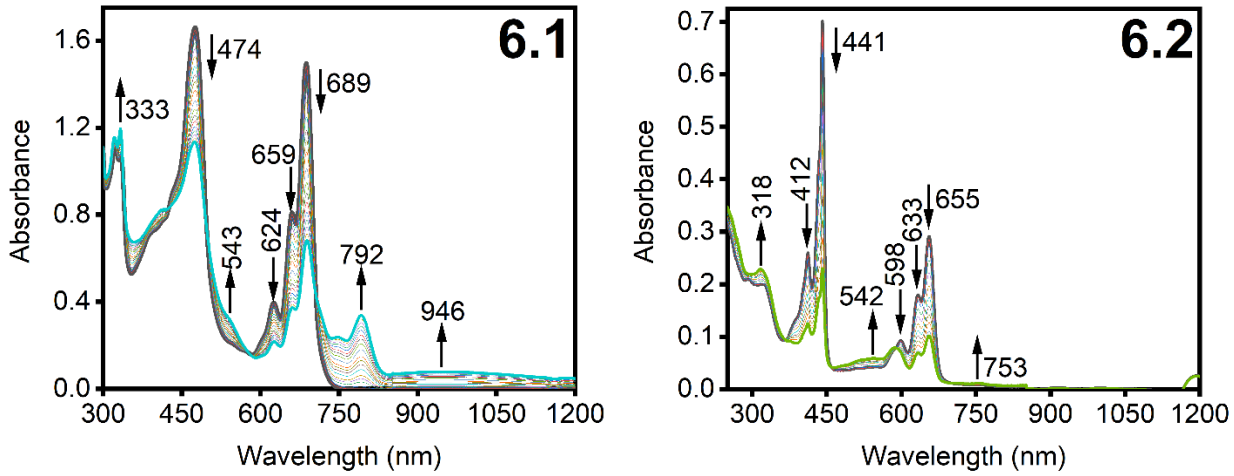

Figure 6.3. Spectro-electrochemical oxidation of **6.1** and **6.2** using a DCM/0.3M TBAP system.

Within the optical range of 300-750 nm, **6.1** and **6.2** showed similar transformation of their UV-vis spectra under spectroelectrochemical oxidation conditions. Specifically, the *Q*-band intensity of **6.1** and **6.2** decreases and the increasing signal of **6.1** at 792 nm was not as intensely present for **6.2**. Also for **6.1**, the broad increasing signal at 946 nm was entirely absent in the spectroelectrochemical UV-vis-NIR plot of **6.2**. Additionally, a broad ILCT band in **6.1** and **6.2** evolves into stronger-intensity transitions which are centered at 543 and 542, respectively. These types of transformations are characteristic of triazatetrabenzcorrole-centered cationic radical formation and have been previously reported in analogous phthalocyanine systems,[50-53]

confirming that the first oxidation is macrocycle-centered. Reciprocating the well-defined literature on the oxidation of analogous phthalocyanine systems, the near-infrared (NIR) band observed in the case of [**6.1**]$^{\cdot+}$ at 946 nm is assigned to monomeric units, while the observed transitions between 710 and 800 nm for both [**6.1**]$^{\cdot+}$ and [**6.2**]$^{\cdot+}$ indicate aggregation of the cationic radical species.[54] Interestingly, the triazatetrabenzcorrole macrocyclic oxidation was fully reversible for **6.1** via reduction; however, the spectroelectrochemical oxidation of **6.2** was completely irreversible upon attempted reduction of the oxidized species (Fig. S6.2).

6.3.3 DFT and TDDFT Calculations. The vertical excitation energies and electronic structures of triazatetrabenzcorroles **6.1** and **6.2** were investigated with DFT and TDDFT calculations. In order to correlate the DFT and TDDFT results with experimental redox properties and UV-vis spectra, the polarized continuum model (PCM) was utilized to account for solvent effects where chloroform was used as the solvent for all calculations. The energy level diagrams for **6.1** and **6.2** as predicted by DFT-PCM are shown in Fig. 6.4, and the selected frontier molecular orbital (MO) profiles are depicted in Figs. 6.5, S6.3 and S6.4.

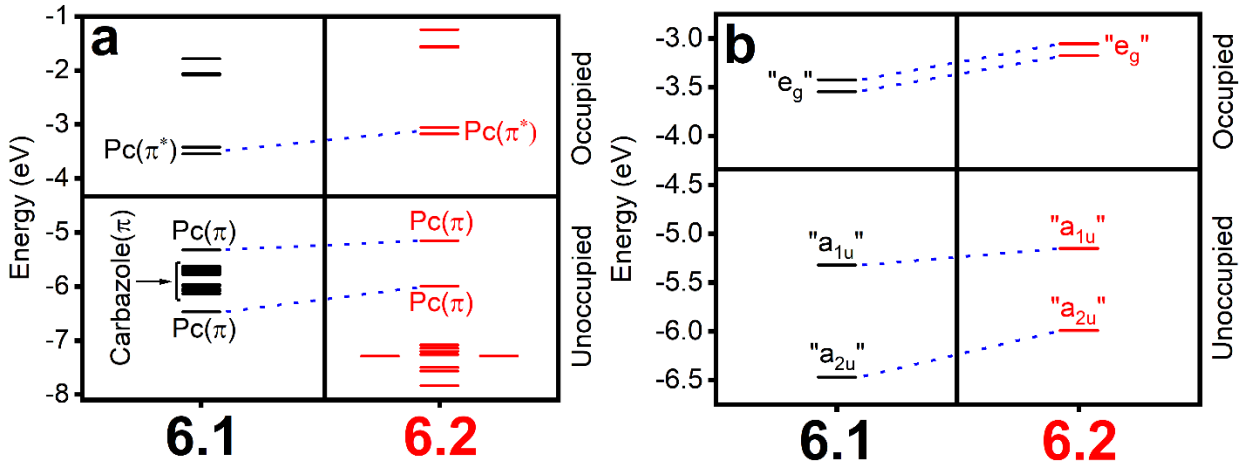

Figure 6.4. DFT-PCM predicted energy level diagram for (a) select frontier molecular orbitals and (b) Gouterman's classical frontier orbitals.

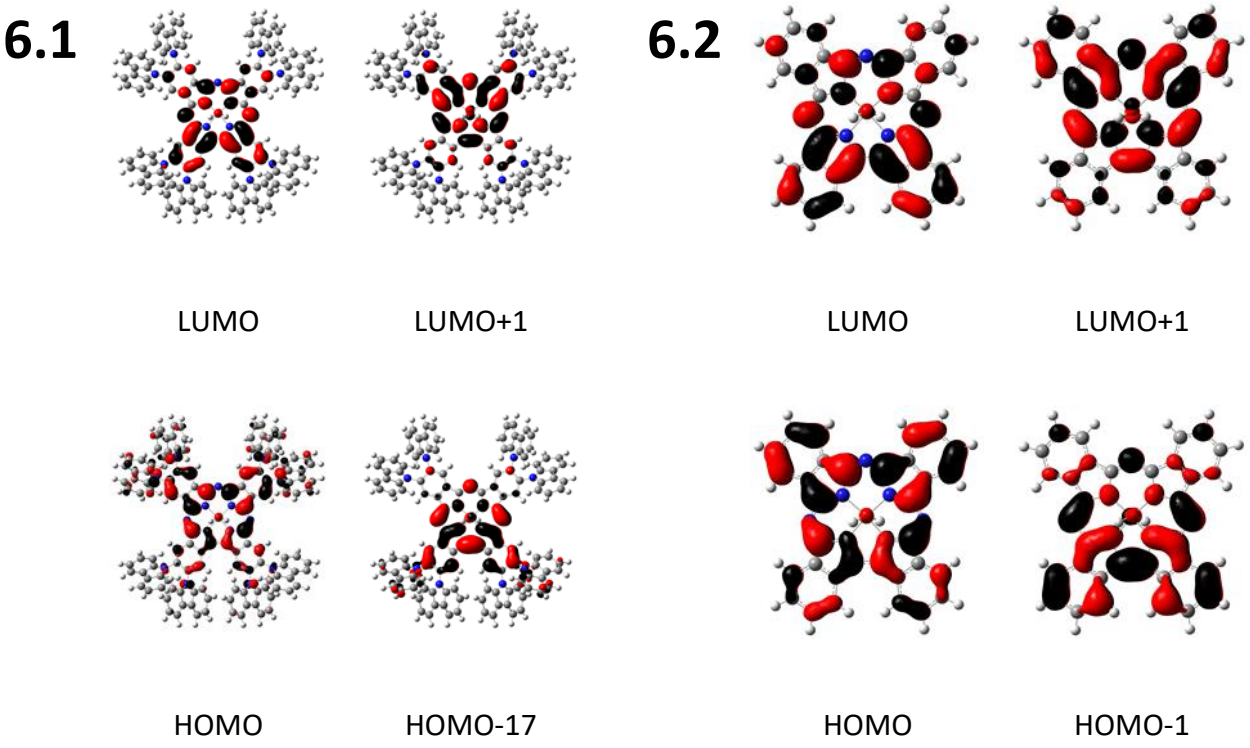

Figure 6.5. DFT-PCM predicted images of Gouterman's classic frontier orbitals of **6.1** (left) and **6.2** (right).

In both compounds **6.1** and **6.2**, the DFT-predicted HOMO takes the form of Gouterman's a_{1u} orbital,[55,56] with significant electron density contributions from the pyrrolic α- and β-carbon atoms. In the case of **6.1**, DFT predicts that the electron density distributions on HOMO-1 to HOMO-16 remain largely localized on the carbazole moieties, while HOMO-17 resembles Gouterman's a_{2u} orbital with additional electron density present on the inner- and *meso*-nitrogen atoms of the triazatetrabenzcorrole core. The energy differences between Gouterman's a_{1u} and a_{2u} orbitals that were predicted by DFT are about half that of typical phthalocyanines at about 1.2 and 0.8 eV for **6.1** and **6.2**, respectively, and the carbazole-based HOMO-1 to HOMO-16 orbitals are also energetically closely spaced (~0.5 eV, Fig. 6.4). This indicates energetic stabilization of the a_{2u} orbital as a result of the removal of one *meso*-nitrogen atom in these triazatetrabenzcorroles compared to the four *meso*-nitrogen atoms that phthalocyanines possess. The LUMO and LUMO+1 as predicted by DFT in compounds **6.1** and **6.2** also resemble the classical Gouterman's pair of e_g orbitals, which are dominated by electron density contributions from α- and β-pyrrolic carbons, inner- and *meso*-nitrogen atoms, and the benzene ring of the triazatetrabenzcorrole core (Fig. 6.5). Overall, the electronic structures of compounds **6.1** and **6.2** that were predicted by DFT correlate well with the electrochemical and spectroscopic data that were collected. To be more specific, based on the DFT calculations, it is expected that the first two oxidations will be centered on the triazatetrabenzcorrole core and this notion is well-correlated with the spectro-electrochemical and electrochemical data collected on **6.1** and **6.2**. Additionally, the DFT calculations are indicative of a triazatetrabenzcorrole-centered lowest-energy excited state, while many of the ILCT transitions can be expected in the spectral envelope containing energies higher than that of the *Q*-band.

The TDDFT-predicted UV-vis spectra of **6.1** and **6.2** are presented in Figs. 6.6 and S6.5, while the summary of excited state contributions for the most intense excited states is listed in Table S6.1.

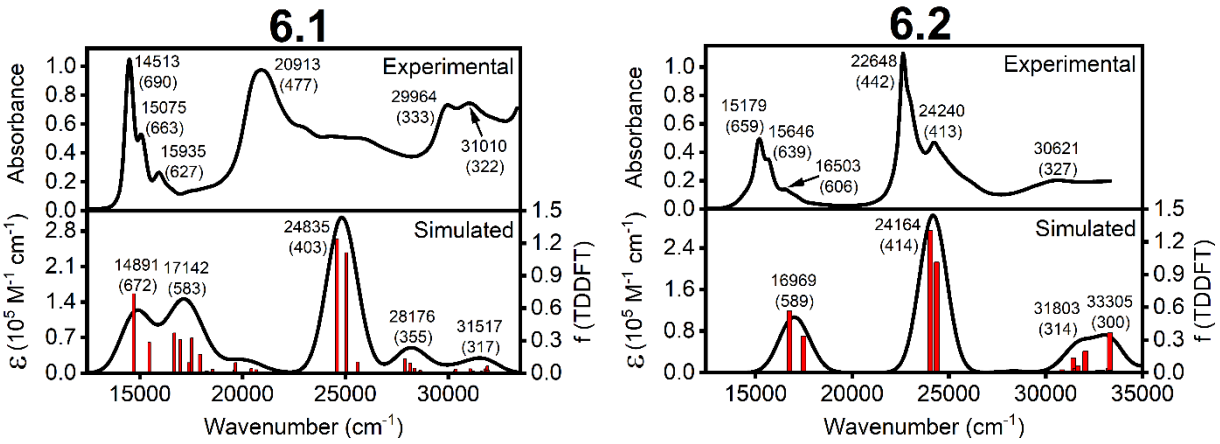

Figure 6.6. Experimental (upper) and TDDFT-predicted (lower) UV-vis spectra of **6.1** and **6.2** using the HSEH1PBE/LANL2DZ-PCM method.

Generally, the TDDFT results agree well with both the experimental UV-vis spectra and electronic structures of compounds **6.1** and **6.2**. Particularly, the first few excited states of **6.1** and **6.2** that were predicted by TDDFT and comprise the *Q*-band region are singly-degenerate transitions of moderate intensity which are dominated by H → L, H → L+1, and H-1 → L excitations. The non-degeneracy of these excited states differs from those of analogous phthalocyanine compounds due to the lower degree of molecular symmetry which is a result of the "missing" *meso*-nitrogen atom on the triazatetrabenzcorrole framework relative to the Pc structure. In the case of **6.1** and absent from **6.2** are the several TDDFT-predicted ILCT bands, which are largely dominated by carbazole-based single-electron excitations of the HOMO-1 to HOMO-16 orbitals to higher-energy carbazole-centered and unoccupied triazatetrabenzcorrole

(LUMO and LUMO+1) orbitals. Also, the TDDFT results indicate large HOMO-17→LUMO, LUMO+1 (for **6.1**) and HOMO-1→LUMO, LUMO+1 (for **6.2**) contributions to the most intense *B*-band region transitions. Overall, the TDDFT results indicate TBC-centered excited states at low energy, followed by the expected ILCT transitions.

6.4 Conclusions

In all, two phosphorus-centered triazatetrabenzcorrole samples were prepared and investigated from an electronic structure standpoint where structure **6.1** possessed eight peripheral carbazole substituents and **6.2** was decorated with four peripheral *tert*-butyl groups. Overall, the UV-vis and MCD spectra for **6.1** and **6.2** appeared quite similar with the exception of the red-shifted and more intense *Q*-band for **6.1**. The UV-vis spectra were accurately simulated for both compounds using the B3LYP exchange correlation functional and the LanL2DZ basis set. For **6.1**, the electrochemical experiments detected two reversible oxidation and reduction processes, with the first oxidation appearing to be multielectron in nature and the second oxidation being characteristic of a single electron process. The electrochemical analysis of **6.2** uncovered two fully reversible, partially overlapping oxidation processes and one irreversible reduction. It was found that for **6.2**, addition of methanol to the electrolyte/sample solution caused the two oxidation processes to shift closer together as a result of the axial hydroxy groups being replaced by methoxy groups. The spectroelectrochemical oxidation performed on **6.2** was found to be completely irreversible but fully reversible for **6.1**. Also for **6.1**, the spectroelectrochemical data showed the characteristic feature of a cationic radical species via the broad low-energy signal at ~950 nm; this feature was not observed for **6.2**.

Finally, the DFT-predicted energy level diagram of **6.1** showed several carbazole-centered molecular orbitals that were energetically intermixed with the Gouterman's frontier a_{1u} and a_{2u} orbitals; however, for **6.2**, the four Gouterman's frontier orbitals were predicted to be energetically sequential as the *tert*-butyl substituents behaved quite innocently with negligible contribution to the electronic structure.

Since the triazatetrabenzcorroles examined within this thesis are hard chromophores, the energetic spacing of the a_{1u} and a_{2u} orbitals, which are responsible for ΔHOMO, is quite large. The goal was to manipulate the TBC structure in such a way that ΔLUMO would end up having a larger magnitude than ΔHOMO, which would be expected of naturally occurring porphyrinoids. The structural manipulation used in this attempt was the omission of a single *meso*-nitrogen atom from the phthalocyanine structure, which was expected to destabilize the a_{2u} orbital to some degree. This destabilization turned out not to be enough to decrease ΔHOMO to a point where it was exceeded by ΔLUMO; therefore, these synthetic TBC systems possess an electronic structure that can be generally characterized as synthetic.

6.5 Experimental Section

6.5.1 Synthesis. Compound **6.1** was prepared in the collaborating lab of Prof. Saad Makhseed at University of Kuwait according to a not-yet-published procedure. **6.2** was prepared as follows: 25 eq. of PBr_3 was added to metal-free tetra-*tert*-butylated phthalocyanine in pyridine under an argon atmosphere and was stirred at 95℃ for 75 minutes. The product was

precipitated in ice water and purified via (silica gel) column chromatography using an 85% DCM: 15% THF system.

6.5.2 UV-Vis/MCD Spectroscopy. All UV-vis spectra were collected on a Jasco V-770 spectrophotometer and MCD spectra were measured with a Jasco J-1500 CD spectrometer using a Jasco MCD-581 electromagnet operated at 1.0 T. The completed MCD spectra were measured at 10 °C in parallel and antiparallel orientations with respect to the magnetic field.

6.5.3 Electrochemical Measurements. The electrochemical data were collected using a CH-620 analyzer with either glassy carbon or platinum working, platinum auxiliary, and Ag/AgCl pseudo-reference electrodes. Decamethylferrocene was used as an internal standard for the studied complexes and the reported potentials were corrected to the FcH/FcH^+ couple. All electrochemical experiments were conducted in a CH_2Cl_2/0.1M tetrabutylammonium perchlorate (TBAP) system.

6.5.4 Spectroelectrochemical Measurements. The spectroelectrochemical experiments were performed using a Jasco V-770 UV-vis-NIR spectrophotometer in tandem with a CH Instruments electrochemical analyzer which was operated using the bulk electrolysis mode. The data were collected using a custom-made 1 mm cell, a platinum mesh working electrode, platinum auxiliary electrode, Ag/AgCl pseudo-reference electrode, and a 0.3 M solution of TBAP in CH_2Cl_2.

6.5.5 Computational Details. All calculations were run using Gaussian 16.[57] The B3LYP[58,59], HSEH1PBE[60,61], or MN12SX[62] exchange-correlation functional with the LANL2DZ basis set[63] were

used for all calculations. Vibrational frequencies were calculated to ensure all geometries were local minima. All calculations were conducted in solution using the PCM model,[64] with chloroform as the solvent. For all TDDFT-PCM calculations, 100 excited states were predicted for each compound. The QMForge program[65] was used for the orbital analysis.

6.6 References

1. Sessler, J. L.; Weghorn, S. J. *Expanded, Contracted, & Isomeric Porphyrins*; Elsevier Science Inc.: New York, 1997; Vol. 15.

2. Gross, Z. High-Valent Corrole Metal Complexes. *J. Biol. Inorg. Chem.* **2001**, *6*, 733-738.

3. Ghosh, A.; Steene, E. High-Valent Transition Metal Centers Versus Noninnocent Ligands in Metallocorroles: Insights from Electrochemistry and Implications for High-Valent Heme Protein Intermediates. *J. Inorg. Biochem.* **2002**, *91*, 423-436.

4. Erben, C.; Will, S.; Kadish, K. M. In *The Porphyrin Handbook*; Kadish, K. M., Smith, K. M., Guilard, R., Eds.; Academic Press: New York, 2000; Vol. 2, pp 233-300.

5. Gryko, D. T. Recent Advances in the Synthesis of Corroles and Core-Modified Corroles. *Eur. J. Org. Chem.* **2002**, 1735-1743.

6. Johnson, A. W.; Kay, I. T. Corroles. I. Synthesis. *J. Chem. Soc.* **1965**, 1620-1629.

7. Gryko, D. T.; Jadach, K. A Simple and Versatile One-Pot Synthesis of *meso*-Substituted trans-A2B-Corroles. *J. Org. Chem.* **2001**, *66*, 4267-4275.

8. Decreau, R. A.; Collman, J. P. Corrole Synthesis by Dipyrromethane-Dicarbinol and 2,2'-Bipyrrole Condensation. *Tetrahedron Lett.* **2003**, *44*, 3323-3327.

9. Paolesse, R.; Jaquinod, L.; Nurco, D. J.; Mini, S.; Sagone, F.; Boschi, T.; Smith, K. M. 5,10,15-Triphenylcorrole: A Product from a Modified Rothemund Reaction. *Chem. Commun.* **1999**, 1307-1308.

10. Gross, Z.; Galili, N.; Simkhovich, L.; Saltsman, I.; Botoshansky, M.; Blaser, D.; Boese, R.; Goldberg, I. Solvent-Free Condensation of Pyrrole and Pentafluorobenzaldehyde: A Novel Synthetic Pathway to Corrole and Oligopyrromethenes. *Org. Lett.* **1999**, *1*, 599-602.

11. Gross, Z.; Galili, N.; Saltsman, I. The First Direct Synthesis of Corroles from Pyrrole. *Angew. Chem. Int. Ed.* **1999**, *38*, 1427-1429.

12. Mandimutsira, B. S.; Ramdhanie, B.; Todd, R. C.; Wang, H. L.; Zareba, A. A.; Czernuszewicz, R. S.; Goldberg, D. P. A Stable Manganese(V)-Oxo Corrolazine Complex. *J. Am. Chem. Soc.* **2002**, *124*, 15170-15171.

13. Ramdhanie, B.; Stern. C. L.; Goldberg, D. P. Synthesis of the First Corrolazine: A New Member of the Porphyrinoid Family. *J. Am. Chem. Soc.* **2001**, *123*, 9447-9448.

14. Ramdhanie, B.; Zakharov, L. N,; Rheingold, A. L.; Goldberg, D. P. Synthesis, Structures, and Properties of a Series of Four-, Five-, and Six-Coordinate Cobalt(III) Triazacorrole Complexes: The First Examples of Transition Metal Corrolazines. *Inorg. Chem*. **2002**, *41*, 4105-4107.

15. Fujiki, M.; Tabei, H.; Isa, K. New Tetrapyrrolic Macrocycle: α,β,γ-Triazatetrabenzcorrole. *J. Am. Chem. Soc.* **1986**, *108*, 1532-1536.

16. Liu, J.; Zhang, F.; Zhao, F.; Tang, Y.; Song, X.; Yao, G. Complexation of Phosphorus(III) with a Novel Tetrapyrrolic Phthalocyanine-Like Macrocyclic Compound. *J. Photochem. Photobiol.* **1995**, *91*, 99-104.

17. Li, J.; Subramanian, L. R.; Hanack, M. Studies on Phosphorus Phthalocyanines and Triazatetrabenzcorroles. *Eur. J. Org. Chem.* **1998**, 2759-2767.

18. Li, J.; Subramanian, L. R.; Hanack, M. Substituted α,β,γ-Triazatetrabenzcorrole: An Unusual Reduction Product of a Phthalocyanine. *Chem. Commun.* **1997**, 679-680.

19. Gouterman, M.; Sayer, P.; Shankland, E.; Smith, J. P. Porphyrins. 41. Phosphorus Mesoporphyrin and Phthalocyanine. *Inorg. Chem*. **1981**, *20*, 87-92.

20. Nyokong, T.; Isago H. The Renaissance in Optical Spectroscopy of Phthalocyanines and Other Tetraazaporphyrins. *J. Porphyrins Phthalocyanines* **2004**, *8*, 1083-1090.

21. Taube, H. Rates and Mechanisms of Substitution in Inorganic Complexes in Solution. *Chem. Rev.* **1952**, *50*, 69-126.

22. Thomson, A. J.; Gadsby, P. M. A. A Theoretical Model of the Intensity of the Near-Infrared Porphyrin-to-Iron Charge-Transfer Transitions in Low-Spin Iron(III) Hemoproteins. A Correlation Between the Intensity of the Magnetic Circular Dichroism Bands and the Rhombic Distortion Parameter of Iron. *Dalton Trans.* **1990**, 1921-1928.

23. Yamamoto, T.; Nozawa, T.; Kobayashi, N.; Hatano, M. Origins and Spin Dependence of Near Infrared Magnetic Circular Dichroism of Iron(III) Hemoproteins. *Bull. Chem. Soc. Jpn.* **1982**, *55*, 3059-3063.

24. Kobayashi, N; Nozawa, T.; Hatano, M. Near-Infrared Magnetic Circular Dichroism Studies on Iron(III) Horse Heart Cytochrome C. *Bull. Chem. Soc. Jpn.* **1981**, *54*, 919-924.

25. Lei, H.; Han, A.; Li, F.; Zhang, M.; Han, Y.; Du, P.; Lai, W.; Cao, R. Electrochemical, Spectroscopic, and Theoretical Studies of a Simple Bifunctional Cobalt Corrole Catalyst for Oxygen Evolution and Hydrogen Production. *Phys. Chem. Chem. Phys.* **2014**, *16*, 1883-1893.

26. Nardis S.; Cicero, D. O.; Licoccia, S.; Pomarico, G.; Berionni, Berna, B.; Sette, M.; Ricciardi, G.; Rosa, A.; Fronczek, F. R.; Smith, K. M.; Paolesse, R. Phenyl Derivative of Iron 5,10,15-Tritolylcorrole. *Inorg. Chem*. **2014**, *53*, 4215-4227.

27. Conradie, J.; Ghosh, A. Correlation Between the FeNO Angle and d-p Mixing in {FeNO}7 Complexes. *Inorg. Chem.* **2011**, *50*, 4223-4225.

28. Ghosh, A.; Wondimagegn, T.; Parusel, A. B. J. Electronic Structure of Gallium, Copper, and Nickel Complexes of Corrole. High-Valent Transition Metal Centers versus Noninnocent Ligands. *J. Am. Chem. Soc.* **2000**, *122*, 5100-5104.

29. Bendix, J.; Dmochowski, I. J.; Gray, H. B.; Mahammed, A.; Simkhovich, L. ; Gross, Z. Structural, Electrochemical, and Photophysical Properties of Gallium(III) 5,10,15-Tris(pentafluorophenyl)corrole. *Angew. Chem., Int. Ed.* **2000**, *39*, 4048-4051.

30. Rovira, C.; Kunc, K.; Hutter, J.; Parrinello, M. Structural and Electronic Properties of Co-corrole, Co-corrin, and Co-porphyrin. *Inorg. Chem*. **2001**, *40*, 11-17.

31. Hocking, R. K.; DeBeer, G. S.; Gross, Z.; Walker, F. A.; Hodgson, K. O.; Hedman, B.; Solomon, E. I. Fe L- and K-edge XAS of Low-Spin Ferric Corrole: Bonding and Reactivity Relative to Low-Spin Ferric Porphyrin. *Inorg. Chem.* **2009**, *48*, 1678-1688.

32. Ye, S.; Tuttle, T.; Bill, E.; Simkhovich, L.; Gross, Z.; Thiel, W.; Neese, F. The Electronic Structure of Iron Corroles: A Combined Experimental and Quantum Chemical Study. *Chem.-Eur. J.* **2008**, *14*, 10839-10851.

33. Qu, B.; Wu, H.; Zhao, B.; Liu, H.; Gao, C.; Qi, X.; Zhao, Y.; Xuan, L.; Wei, W. An Alternating Polymer with Fluorinated Quinoxaline and 2,7-Carbazolel Segments for Photovoltaic Devices. *RSC Adv.* **2017**, *7*, 16041-16048.

34. Li, J.; Grimsdale, A. C. Carbazole-Based Polymers for Organic Photovoltaic Devices. *Chem. Soc. Rev.* **2010**, *39*, 2399-2410.

35. Lin, S. L.; Chan, L. H.; Lee, R. H.; Yen, M. Y.; Kuo, W. J.; Chen, C. T.; Jeng, R. J. Highly Efficient Carbazole-π-Dimesitylborane Bipolar Fluorophores for Nondoped Blue Organic Light-Emitting Diodes. *Adv. Mater.* **2008**, *20*, 3947-3952.

36. Tang, S.; Liu, M.; Lu, P.; Xia, H.; Li, M.; Xie, Z.; Shen, F.; Gu, C.; Wang, H.; Yang, B.; Ma, Y. A Molecular Glass for Deep-Blue Organic Light-Emitting Diodes Comprising a 9,9'-Spirofluorene Core and Peripheral Carbazole Groups. *Adv. Funct. Mater.* **2007**, *17*, 2869-2877.

37. Dumur, F.; Beouch, L.; Peralta, S.; Wantz, G.; Goubard, F.; Gigmes, D. Solution-Processed Blue Phosphorescent OLEDs with Carbazole-Based Polymeric Host Materials. *Org. Electron.* **2015**, *25*, 21-30.

38. Chang, C. H.; Griniene, R.; Su, Y. D.; Yeh, C. C.; Kao, H. C.; Grazulevicius, J. V.; Volyniuk, D.; Grigalevicius, S. Efficient Red Phosphorescent OLEDs Employing Carbazole-Based Materials as the Emitting Host. *Dyes Pigm.* **2015**, *122*, 257-263.

39. Rimkus, R.; Tumkevicius, S.; Serevicius, T.; Komskis, R.; Adomenas, P.; Gruodis, A.; Jankauskas, V.; Kazlauskas, K.; Jursenas, S. Heterocyclic Heptacene Analogs – 8*H*-16,17-Epoxydinaphto[2,3-*c*:2',3'-*g*]Carbazoles as Charge Transport Materials. *Dyes Pigm.* **2016**, *214*, 133-144.

40. Huang, P.; Manju.; Kazim, S.; Sivakumar, G.; Salado, M.; Misra, R.; Ahmad, S. Pyridine Bridging Diphenylamine-Carbazole with Linking Topology as Rational Hole Transporter for Perovskite Solar Cells Fabrication. *ACS Appl. Mater. Interfaces* **2020**, *12*, 22881-22890.

41. Liu, X.; Shi, X.; Liu, C.; Ren, Y.; Wu, Y.; Yang, W.; Alsaedi, A.; Hayat, T.; Kong, F.; Liu, X.; Ding, Y.; Yao, J.; Dai, S. A Simple Carbazole-Triphenylamine Hole Transport Material for Perovskite Solar Cells. *J. Phys. Chem. C* **2018**, *122*, 26337-26343.

42. Yin, X.; Guan, L.; Yu, J.; Zhao, D.; Wang, C.; Shrestha, N.; Han, Y.; An, Q.; Zhou, J.; Zhou, B.; Yu, Y.; Grice, C. R.; Awni, R. A.; Zhang, F.; Wang, J.; Ellingson, R. J.; Yan, Y.; Tang, W.

One-Step Facile Synthesis of a Simple Carbazole-Cored Hole Transport Material for High-Performance Perovskite Solar Cells. *Nano Energy* **2017**, *40*, 163-169.

43. Adhikari, R. M.; Mondal, R.; Shah, B. K.; Neckers, D. C. Synthesis and Photophysical Properties of Carbazole-Based Blue Light-Emitting Dendrimers. *J. Org. Chem.* **2007**, *72*, 4727-4732.

44. Ledwon, P. Recent Advances of Donor-Acceptor Type Carbazole-Based Molecules for Light Emitting Applications. *Org. Electron.* **2019**, *75*, 105422/1-105422/15.

45. Zhang, X. F.; Huang, J.; Zhao, H.; Zheng, X.; Zhu, J. Photophysical Properties of Nonperipherally and Peripherally Substituted Triazatetrabenzcorrole Phosphorus Dihydroxy and Singlet Oxygen Generation. *J. Photochem. Photobiol., A* **2010**, 215(*1*), 96-102.

46. Shi, M.; Tian, J.; Mkhize, C.; Kubheka, G.; Zhou, J.; Mack, J.; Nyokong, T.; Shen, Z.; Synthesis, Characterization and Photodynamic Therapy Properties of an Octa-4-tert-butylphenoxy-Substituted Phosphorus(V) Triazatetrabenzcorrole. *J. Porphyrins Phthalocyanines* **2014**, 18(*8-9*), 698-707.

47. Mkhize, C.; Britton, J.; Mack, J.; Nyokong, T. Optical Limiting and Singlet Oxygen Generation Properties of Phosphorus Triazatetrabenzcorroles. *J. Porphyrins Phthalocyanines* **2015**, 19(*1/3*), 192-204.

48. Majeed, S. A.; Ghazal, B.; Nevonen, D. E.; Goff, P. C.; Blank, D. A.; Nemykin, V. N.; Makhseed, S. Evaluation of the Intramolecular Charge-Transfer Properties in

Solvatochromic and Electrochromic Zinc Octa(carbazolyl)phthalocyanines. *Inorg. Chem.* **2017**, *56*, 11640-11653.

49. Majeed, S. A.; Ghazal, B.; Nevonen, D. E.; Nemykin, V. N.; Makhseed, S. Spectroscopic and TDDFT Studies on the Charge-Transfer Properties of Metallated Octa(carbazolyl)phthalocyanines. *Dyes Pigm.* **2019**, *170*, 107593/1-107593/13.

50. Nemykin, V. N.; Chernii, V. Y.; Volkov, S. V. Synthesis and Characterization of New Mixed-Ligand Lanthanide-Phthalocyanine Cation Radical Complexes. *J. Chem. Soc., Dalton Trans.* **1998**, *18*, 2995-3000.

51. Rosa, A.; Ricciardi, G. A Time-Dependent Density Functional Theory (TDDFT) Interpretation of the Optical Spectra of Zinc Phthalocyanine π-cation and π-anion radicals. *Can. J. Chem.* **2009**, *87*(7), 994-1005.

52. Mack, J.; Kobayashi, N.; Stillman, M. J. Magnetic Circular Dichroism Spectroscopy and TD-DFT Calculations of Metal Phthalocyanine Anion and Cation Radical Species. *J. Porphyrins Phthalocyanines* **2006**, *10*(10), 1219-1237.

53. Nyokong, T.; Gasyna, Z.; Stillman, M. J. Phthalocyanine π-Cation-Radical Species: Photochemical and Electrochemical Preparation of $[ZnPc(-1)^{\cdot+}$ in Solution. *Inorg. Chem.* **1987**, *26*(4), 548-553.

54. Yamasaki, K.; Kaneda, M.; Watanabe, K.; Ueki, Y.; Ishimaru, K.; Nakamura, S.; Nomi, R.; Yoshida, N.; Nakajima, T. New Antibiotics, Carbazomycins A and B. III. Taxonomy and Biosynthesis. *J. Antibiot.* **1983**, *36*(5), 552-558.

55. Gouterman, M. Spectra of Porphyrins. *J. Mol. Spectrosc.* **1961**, *26*(4), 548-553.

56. Seybold, P. G.; Gouterman, M. Porphyrins. *J. Mol. Spectrosc.* **1969**, *31*(1), 1-13.

57. Gaussian 16, Revision B.01, Frisch, M. J.; Trucks, G. W.; Schlegel, H. B.; Scuseria, G. E.; Robb, M. A.; Cheeseman, J. R.; Scalmani, G.; Barone, V.; Petersson, G. A.; Nakatsuji, H. Gaussian, Inc., Wallingford CT, 2016.

58. Becke, A. D. "Density-Functional Thermochemistry. III. The Role of Exact Exchange" *J. Chem. Phys.* **1993**, *98*, 5648-5652.

59. Lee, C.; Yang, W.; Parr, R. G. "Development of the Colle-Salvetti correlation-energy formula into a functional of the electron density" *Phys. Rev. B.* **1988**, *37*, 785-789.

60. Heyd, J.; Scuseria, G. E. Efficient Hybrid Density Functional Calculations in Solids: The HS-Ernzerhof Screened Coulomb Hybrid Functional. *J. Chem. Phys.* **2004**, *121*, 1187-1192.

61. Heyd, J.; Scuseria, G. E. Assessment and Validation of a Screened Coulomb Hybrid Density Functional. *J. Chem. Phys.* **2004**, *120*, 7274-7280.

62. Peverati, R.; Truhlar, D. G. Screened-Exchange Density Functionals With Broad Accuracy for Chemistry and Solidstate Physics. *Phys. Chem. Chem. Phys. 2012,* ***14*****(47)**, 16187-16191.

63. Schaefer, H. F., Ed. Modern Theoretical Chemistry; Plenum: New York, NY, 1976; Vol. 3.

64. Tomasi, J.; Mennucci, B.; Cammi, R. Quantum Mechanical Continuum Solvation Models. *Chem. Rev*. **2005**, *105*(8), 2999−3093.

65. Tenderholt, A. L. QMForge, Version 2.1; Stanford University: Stanford, CA, 2011. https://qmforge.net/.

7. New Insight into an Old Problem: Analysis, Interpretation, and Theoretical Modeling of the Absorption and Magnetic Circular Dichroism Spectra of Monomeric and Dimeric Zinc Phthalocyanine Cation Radical

7.1 Chapter Preface

In the last chapter (6), the electronic structures of two triazatetrabenzcorrole hard chromophoric systems were analyzed. These systems were structurally analogous to phthalocyanines; however, they were missing a single *meso*-nitrogen atom which resulted in a lower a_{2u} orbital energy. We will now transition to phthalocyanine molecules for the next two closely related chapters, which are still classified as hard chromophores. The work summarized in this chapter (7) is a necessary precursor to the more substantial project which will be presented in the next chapter (8). Specifically, this chapter features an experimental (UV-vis, MCD) and theoretical (DFT, TDDFT) based analysis of the cation-radical of zinc phthalocyanine, which was generated chemically (using an oxidant) and spectroelectrochemically (using an applied potential). The work presented within this chapter (7) will provide a thorough

evaluation of the occurrence and characteristic properties of metal-centered phthalocyanine cation-radicals.

7.2 Introduction

Phthalocyanines (Pcs) are well-known, robust platforms that have been used during the last century as industrial textile colorants,[1] photosensitizers for photodynamic therapy (PDT) of cancer,[2–10] antibacterial agents,[11–13] prospective models in data recording devices,[14,15] molecular electronics materials and imaging,[16–18] and more recently as catalysts for C–H bond activation.[19–25] Phthalocyanines possess rich redox properties that have been well investigated by electrochemical and chemical methods. In particular, up to two successful oxidation processes and four successful reduction processes have been identified in some transition-metal Pcs.[26–28] The first single-electron oxidation of the phthalocyanine macrocycle has been used in prospective electrochromic and chemiochromic devices[29–34] and is associated with a clear, blue (neutral Pc form) to red (single-electron oxidized Pc cation-radical form) transformation, which can be monitored even with the naked eye. Such a transition can be observed both in solution and in the solid state. Formation and understanding of the spectroscopic signatures of the phthalocyanine-centered cation radicals are also important when electron transfer, and specifically formation of the charge-separated states, in the phthalocyanine-containing supramolecular systems are needed for solar cell applications.[35–42] Typically, upon oxidation of main group and transition-metal phthalocyanines to their respective cation radical forms, both the monomeric cation radical $[MPc]^{+\bullet}$ and the dimeric $[MPc]_2^{2+}$ species (M is a divalent metal) can be formed in solution.[43] The monomeric cation

radical is paramagnetic and can be easily identified by electron paramagnetic resonance (EPR) spectroscopy (classic signal observed at g ≈ 2, which is characteristic for delocalized organic radical cations).[43] In contrast, the dimeric form is EPR silent because of the antiferromagnetic coupling between two singly oxidized phthalocyanine macrocycles.[43] These two forms have been shown to possess different absorption spectra in the near-infrared (NIR) region. In particular, it has been demonstrated that the monomeric phthalocyanine cation radical has a *Q*-band centered at around 820−840 nm, while the diamagnetic dimer is associated with a *Q*-band centered around 715−730 nm[43] and a broad NIR band observed at ∼1000 nm.[44,45] In addition, both the monomer and dimer have an absorption at ∼500 nm (fingerprint band) and a set of transitions identified by UV−vis spectroscopy for $[(Im)\text{-}ZnPc]^{+\bullet}$ at ∼420, ∼380, ∼330, and ∼286 nm.[43−56]

In a set of elegant studies,[57] Stillman and co-workers have shown that UV−vis transitions observed for $[(Im)ZnPc]^{+\bullet}$ and $[(Im)ZnPc]_2^{2+}$ at ∼830, ∼720, ∼430, ∼330, and ∼286 nm are associated with magnetic circular dichroism (MCD) Faraday *A*-terms, while the fingerprint band at ∼500 nm is associated with a very strong MCD Faraday *B*-term. The nature of this transition has been debated for more than 30 years, and the following assignments have been proposed so far: (i) z-polarized transition to the half-empty a_{1u} orbital of the phthalocyanine cation radical from the nondegenerate doubly occupied orbital of lower energy.[57−59] This transition, as discussed below in the Results and Discussion section, is symmetry allowed for the $a_{2g} \rightarrow a_{1u}$ single-electron excitations in the D_{4h} point group. If the geometry of the phthalocyanine cation radical relaxes to either the C_{4v} or C_4 point group via axial ligand coordination, the other single-

electron transitions could also contribute to such an excited state. The main problem with such a band assignment is the intensity of the fingerprint band, which was not supported by semiempirical ZINDO,[59] time-dependent density functional theory (TDDFT),[58,59] or ab initio calculations.[60] Indeed, all of these calculations are suggestive of rather weak, much higher energy z-polarized transitions. (ii) Assignment to the ^2E_g excited state, which mainly originates from a single-electron excitation from occupied, closely spaced in energy pairs of $6e_g$ and $5e_g$ orbitals to the half occupied $2a_{1u}$ orbital. The main problem with this assignment is the presence of a strong and symmetric (Gaussian-shaped) MCD *B*-term in the fingerprint region, which is usually associated with nondegenerate excited states, although Ishikawa and co-workers provided a reasonable explanation for the disappearance of the MCD *A*-term of the fingerprint band.[60−62] (iii) n → π* transition centered at the phthalocyanine cation radical core.[63] Again, the main problem with such an assignment is the lack of explanation of the large intensity of the fingerprint band.

The crystal structures for some of the monomeric transition-metal phthalocyanine cation radicals are known; however, until the recent work of Leznoff and co-workers,[44] there was no crystallographic evidence available regarding the formation and geometry of antiferromagnetically coupled phthalocyanine cation radical dimers. Moreover, the nature and degeneracy of the associated dimeric species NIR transition at ∼1000 nm has never been discussed in the literature. Finally, to the best of our knowledge, no explanation is provided in the literature of a strong similarity between the UV−vis and MCD spectra of monomeric and dimeric phthalocyanine cation radicals between 280 and 550 nm.

Theoretical methods such as semiempirical ZINDO/S,[59] density functional theory (DFT) using the BP86[58] and B3LYP[59,63] exchange-correlation functionals, as well as ab initio methods[60–62] were used to correlate experimental observations for the monomeric phthalocyanine cation radical with their optical spectra. Although some calculations reproduce the *Q*-band in the monomeric phthalocyanine cation radical reasonably well, the general agreement for the energies and especially intensities of the excited states between theory and experiment have been poor so far, with typical uncertainties between 0.5∼1.0 eV for the *B*- and fingerprint-band regions. More importantly, only one report[60] by Ishikawa and co-workers is present in the literature regarding lanthanide-phthalocyanine double-decker cations which resemble, to some extent, transition metal and main group antiferromagnetically coupled phthalocyanine cation radical dimers. Building further on the earlier work by Stillman, Ishikawa, and the other researchers by refining theoretical calculations and extending the discussion to dimeric species, this report addresses the following key questions associated with the phthalocyanine cation radical optical and magneto-optical spectroscopy: (i) what is the assignment of the NIR band which is experimentally observed at ∼1000 nm? (ii) What are the spectroscopic signatures of the phthalocyanine cation radical-aggregates besides the dimer? (iii) Can modern TDDFT methods accurately (within ∼0.1 eV uncertainty) predict the energies and intensities of the major optical transitions observed in the NIR-UV−vis and MCD spectra of the phthalocyanine cation radical monomer and dimer, and provide better confidence on the assignment of the fingerprint cation radical band experimentally observed at ∼500 nm?

7.3 Results and Discussion

7.3.1 NIR-UV−vis and MCD Spectra. In order to avoid any complications associated with the open shell configuration at the central metal ion, maintain the highest possible effective point group framework, and avoid solubility problems, the highly soluble zinc(II) tetra-*tert*-butylphthalocyanine ($ZnPc^{tBu}$, **7.1**) was used as a model compound in this report. Although this compound consists of a mixture of positional isomers with respect to the location of the tert-butyl substituents, its effective spectroscopic symmetry is D_{4h}. It has been shown by Stillman,[43,57] Leznoff,[44] and other researchers[47] that zinc(II) phthalocyanine (ZnPc) and its axially coordinated complexes (LZnPc) can be selectively oxidized to the respective cation radical using a variety of oxidants such as bromine, nitric acid, NO_2, and $[AdAdBr]^+[BArF]^-$. In addition, spectroelectrochemical oxidation as well as photochemical oxidation via CBr_4 as an electron-acceptor were also proposed for the effective formation of the phthalocyanine cation radicals.[43,57,64] In our hands, during the oxidation of **7.1** in DCM with Br_2, NO_2, $NO^+BF_4^-$, or under spectroelectrochemical oxidation conditions in a DCM/0.15M TFAB system (TFAB is a non-coordinating tetrabutylammonium tetrakis(pentafluorophenyl) borate electrolyte, $NBu_4^+[B(C_6F_5)_4]^-$), clean transformation into the classic phthalocyanine-centered cation radical mixture of monomeric and dimeric species has been observed at room temperature (Figure 7.1).

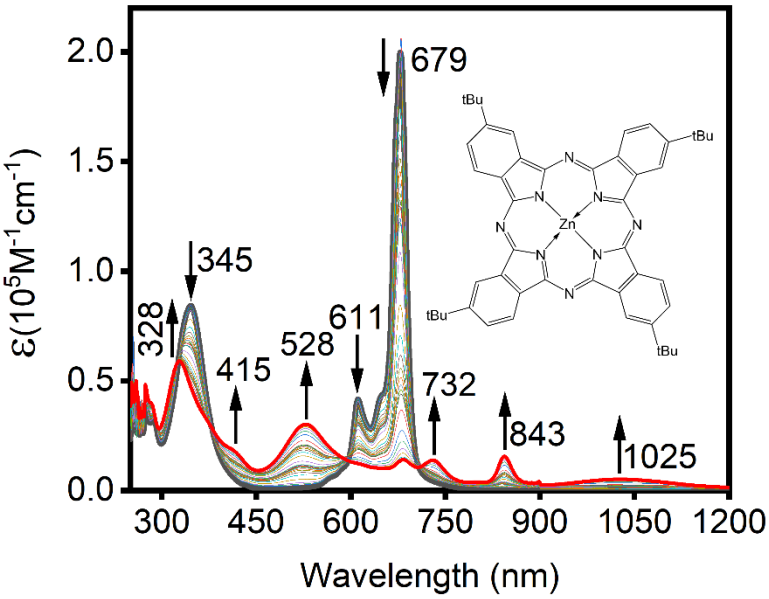

Figure 7.1. Oxidation of **7.1** under spectroelectrochemical conditions in a DCM/0.15M TFAB system at room temperature.

The MCD spectrum of such a mixture of monomeric and dimeric phthalocyanine cation radicals is shown in Figure 7.2 and correlates well with the MCD spectra on the $[(Im)ZnPc]^{+\cdot}$ (Im = imidazole) cation radical reported by Stillman and co-workers.[57]

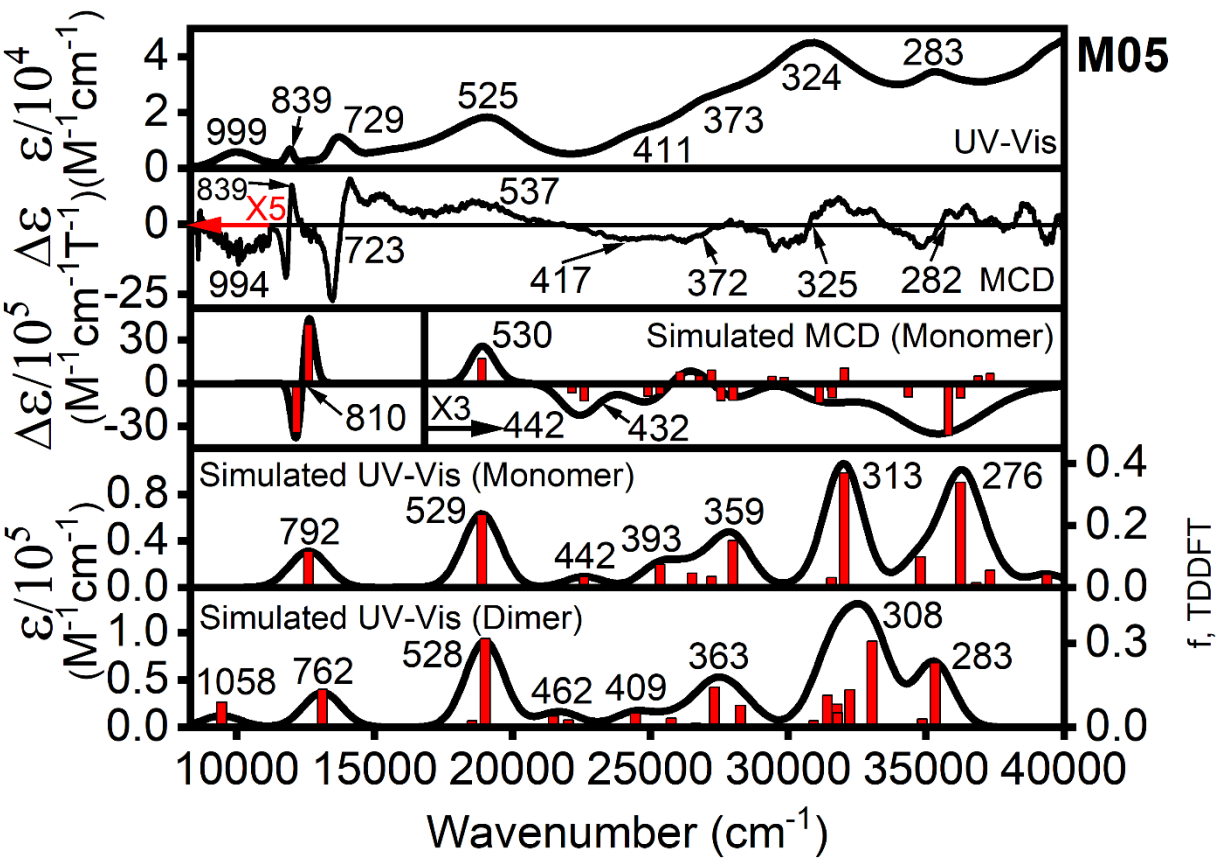

Figure 7.2. Experimental (top two) and theoretical (bottom three) UV-vis and MCD spectra of [**7.1**]$^{+\bullet}$/[**7.1**]$_2^{2+}$. Experimental spectra were recorded on the chemically oxidized by NO_2 vapors **7.1** complex in DCM at room temperature. Theoretical spectra for monomeric [**7.1**]$^{+\bullet}$ and dimeric [**7.1**]$_2^{2+}$ are based on TDDFT calculations using the M05 exchange-correlation functional and DCM as a solvent. For dimeric [**7.1**]$_2^{2+}$, the TDDFT calculations only cover transitions up to 36000 cm^{-1}.

In particular, the *Q*-band of the cation radical monomer at 838 nm and the *Q*-band of the dimer at 723 nm are associated with MCD Faraday *A*-terms in their respective MCD spectra, while the fingerprint band observed at 514 nm has Faraday *B*-term character. As can be seen, the NIR

band at ~1000 nm is associated with a rather weak MCD *B*-term and has negative intensity (the nature of this signal was confirmed using both Jasco and OLIS instruments). In agreement with the previous reports on magnesium and zinc phthalocyanine cation radicals,[43,44,57] the spectroscopic signatures of the monomeric, [**7.1**]$^{+\bullet}$ and dimeric [**7.1**]$_2^{2+}$ cation radical species have low sensitivity to the nature of the oxidant. Indeed, use of chemical oxidants or oxidation under spectroelectrochemical conditions leads to very close spectra of the cation radical species. This observation is important because the formation of the [**7.1**]$^{+\bullet}$ and dimeric [**7.1**]$_2^{2+}$ species under spectroelectrochemical conditions in the presence of noncoordinating electrolyte is indicative of the rather negligible influence of the axial ligand or counterion on the [**7.1**]$^{+\bullet}$ and dimeric [**7.1**]$_2^{2+}$ spectra.

Leznoff and co-workers[44] have shown that the monomer to dimer ratio in oxidized ZnPc has a clear concentration dependency, as upon an increase in concentration, the *Q*-band of the monomeric cation radical reduces in intensity while the *Q*- and NIR-bands associated with the dimer increase in intensity. Similarly, Stillman and co-workers[43] have shown that the concentration of the monomer in the magnesium phthalocyanine [L$_n$MgPc]$^{+\bullet}$ cation radical in DCM solution decreases with a decrease in temperature. In our case, a decrease of temperature from ambient to −40 °C also resulted in prominent dimerization of the oxidized phthalocyanine cation radical, as is evident from Figure 7.3.

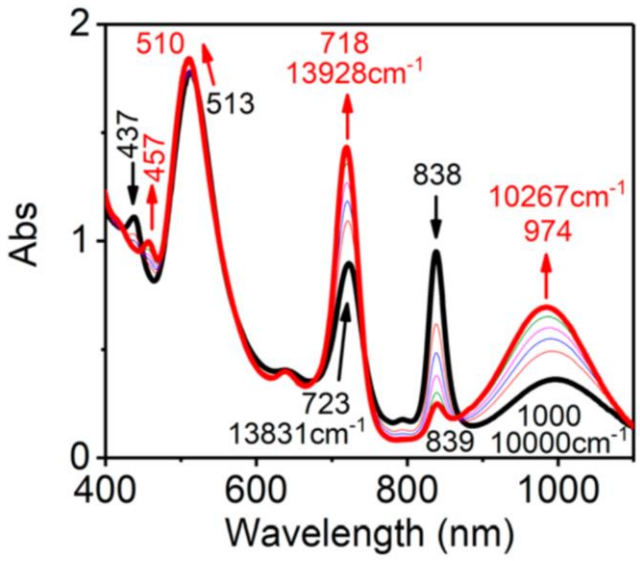

Figure 7.3. Variable-temperature UV-vis spectra of the [**7.1**]$^{+\bullet}$/[**7.1**]$_2^{2+}$ mixture in DCM recorded between +20 (black line) and -40℃ (red line). Oxidized species were generated upon chemical oxidation of the **7.1** complex in DCM with Br_2 vapors.

As has been shown by Leznoff[44] and co-workers, the fingerprint band intensity decreases with increasing concentration of the cation radical of [**7.1**]$^{+\bullet}$, while Stillman's report[43] on the [L_nMgPc]$^{+\bullet}$ cation radical was suggestive of the rather constant intensity of this fingerprint band. In our case, the intensity of the band at 513 nm in [**7.1**]$^{+\bullet}$ does not change much upon decrease of the temperature from +20 to −40 °C. The low-temperature shift of the NIR band at ~1000 nm upon lowering the temperature (~250 cm^{-1}) is larger than that for the *Q*-band of the dimer at ~720 nm (~100 cm^{-1}). In addition to temperature, the dimerization of the highly hydrophobic *tert*-butyl phthalocyanine cation radical can be facilitated via the addition of polar solvent into the solution. Indeed, a stepwise increase of the nitromethane content has a clear effect on the aggregation in a DCM solution of the [**7.1**]$^{+\bullet}$ cation radical (Figure 7.4).

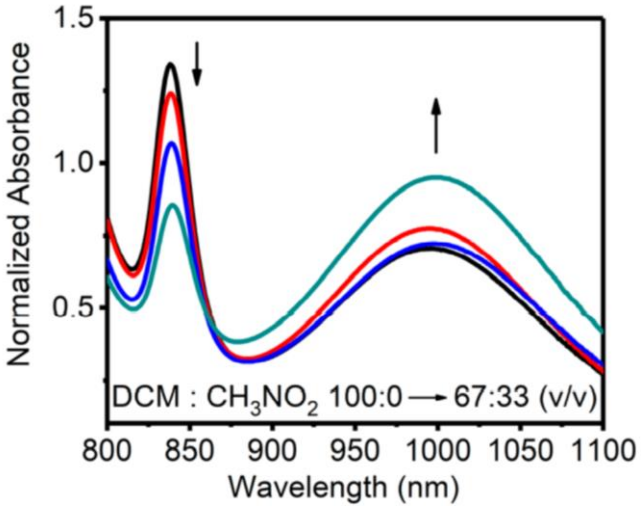

Figure 7.4. Room temperature solvent-dependent spectral changes in the UV-vis spectra of the [**7.1**]$^{+\bullet}$/[**7.1**]$_2^{2+}$ mixture in the NIR region as the concentration of the nitromethane is increased from 0% (v/v) to 33% (v/v). The oxidized species were generated upon chemical oxidation of the **7.1** complex in DCM with Br_2 vapors.

To facilitate a higher degree of aggregation in solution, a high concentration solution of **7.1** was oxidized using bromine in perfluorobenzene as a solvent. In this case, the formation of a rather unusual UV−vis spectrum was observed and consisted of a broad and complex NIR band centered at ∼700 nm, which is associated with a broad MCD Faraday *A*-term centered at ∼700 nm (Figure 7.5).

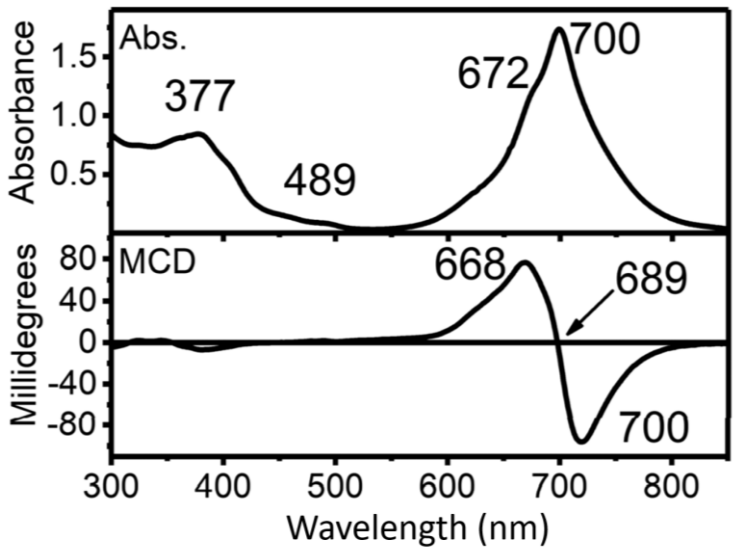

Figure 7.5. Room-temperature UV-vis and MCD spectra of the {[**7.1**]$^{+\bullet}$}$_n$ oligomer in C_6F_6. Oxidized species were generated upon chemical oxidation of the **7.1** complex in C_6F_6 with Br_2 vapors.

It is interesting to note that the fingerprint band in the perfluorobenzene solution is dramatically reduced in intensity and is shifted to 489 nm.

Similarly, oxidation of a higher concentration solution of **7.1** in DCM also suggests the initial formation of monomeric and dimeric species which, upon prolonged standing, transforms into the broad and complex band centered at ~710 nm in the UV−vis spectrum. This band is associated with an MCD *A*-term centered at 720 nm; however, in this case, the fingerprint band in the UV−vis and MCD spectra can still be seen (Figure 7.6).

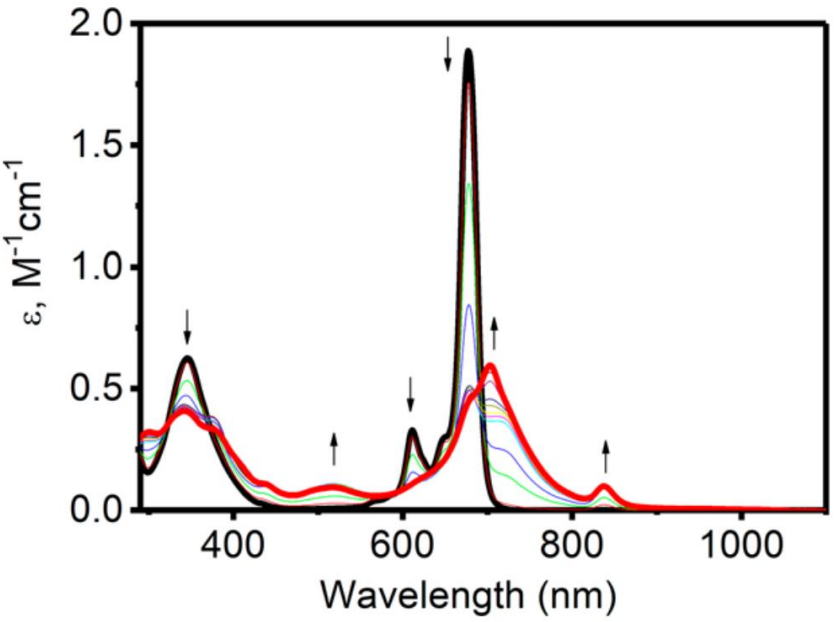

Figure 7.6. Room-temperature UV-vis spectra of the {[**7.1**]$^{+\bullet}$}$_n$ oligomer in DCM. Oxidized species were generated upon chemical oxidation of the **7.1** complex (2 x 10^{-4} M) in DCM with Br_2 vapors in 1 mm UV-vis cell.

The energy of the fingerprint band of the monomer, dimer, and oligomer (518 nm) in the same solvent (DCM) is very similar; however, this band is blue-shifted to 489 nm in C_6F_6, probably because of the solvent polarity. Close energies for the fingerprint band in the monomer and dimer were also predicted by the TDDFT calculations discussed below. Overall, it seems that besides the monomeric and dimeric phthalocyanine cation radicals, higher diamagnetic aggregates can be formed using either high concentration of the starting **7.1** compound or perfluorobenzene as a solvent. During this process, the unique NIR band observed at ~1000 nm for [**7.1**]$_2^{2+}$ loses its intensity, while the *Q*-band of the dimer observed at ~723 nm transforms into a single rather broad transition, which still is associated with the MCD Faraday *A*-term.

7.3.2 Theoretical Background. Optimization of all monomeric [**7.1**]$^{+\bullet}$ species converged to D_{4h} symmetry. The ground state of [**7.1**]$^{+\bullet}$ is $^2A_{1u}$. The selection rules for the D_{4h} point group allow $^2A_{1u} \rightarrow {}^2E_g$ (x,y-polarization) and $^2A_{1u} \rightarrow {}^2A_{2g}$ (z-polarization) transitions. In a simplified view, the first transition should result in MCD *A*- and *B*-terms, while the second one should give rise to MCD *B*-terms.[43] On the molecular orbital level, single-electron transitions from the SOMO (a_{1u} symmetry), as well as other a_{1u}, a_{2u}, b_{1u}, and b_{2u} symmetry orbitals to the doubly degenerate LUMO and LUMO+1 (e_g symmetry) as well as single-electron transitions from the fully occupied e_g molecular orbitals to the SOMO, should contribute to the MCD *A*-term's intensity, while transitions from doubly occupied a_{2g} MOs to the SOMO and from the SOMO to unoccupied a_{2g} MOs should contribute to z-polarized transitions associated with MCD *B*-terms. DFT-optimized cation radical dimers, [**7.1**]$_2^{2+}$ converged to the C_{4v} point group. For the antiferromagnetically coupled singlet state, the ground state in this case is $^1A_1$, and the allowed transitions are $^1A_1 \rightarrow {}^1E$ (x,y-polarized) and $^1A_1 \rightarrow {}^1A_1$ (z-polarized). The former should give an increase to the MCD *A*- and *B*-terms, while the latter should result in the appearance of MCD *B*-terms. Again, on the molecular orbital level, single-electron transitions from a_1, a_2, b_1, and b_2 orbitals to empty e orbitals or from occupied e symmetry orbitals to the SOMO of a_2 symmetry should contribute towards the MCD *A*- and *B*-terms.

7.3.3 DFT and TDDFT Calculations. To correlate the spectroscopic signatures of the monomeric and dimeric phthalocyanine cation radicals with their electronic structures and to gain, with high confidence, insight into the nature of the experimentally observed (by UV−vis and MCD spectroscopy) transitions, DFT and TDDFT calculations were conducted using an array

of exchange-correlation functionals. When geometry optimization is considered, it was found that, although resulting in slightly different geometries for the monomeric phthalocyanine cation radical, both generalized gradient approximation (GGA) based and hybrid-based exchange-correlation functionals provided a reasonable agreement between theory and experiment (thus, B3LYP geometry was used in all TDDFT calculations); however, for the reasonable optimization of the inter-phthalocyanine distances in the antiferromagnetically coupled phthalocyanine radical dimer, the inclusion of dispersion correction was found to be critical. Indeed, when such a dimer was optimized using the B3LYP[65] or CAM-B3LYP[66] exchange-correlation functional without dispersion correction, the optimized distance between two Pc macrocycles was found to be unacceptably large (∼4 Å), which does not correlate with the recent X-ray crystal structure published by Leznoff and co-workers[44] in which the interligand distance was found to be ∼3.14−3.18 Å. In contrast, when dispersion correction was utilized during optimization, the geometry of the antiferromagnetically coupled dimer was found to be in good agreement with the experimental data; thus, B3LYP-D3 geometry was used in all TDDFT calculations. Having both geometries of the monomer and dimer cation radical in good agreement with experimental data, the influence of different exchange-correlation functionals on the predicted vertical excitation energies was tested.

It has been shown numerous times that the use of GGA based and meta-GGA based exchange-correlation functionals allow the accurate prediction of the energies and intensities of the phthalocyanine centered π−π transitions in the neutral unsubstituted and substituted metal-free and transition metal Pcs;[67−69] however, it was also shown that for phthalocyanine

compounds substituted with electron-donating groups at the α-positions of the Pc core, the energies of the intramolecular charge-transfer transitions can only be predicted accurately if a substantial amount of Hartree−Fock exchange is present in the hybrid exchange-correlation functional.[70,71] Since it was not clear for us whether or not pure GGA or meta-GGA based exchange-correlation functionals would be superior over the variety of available hybrid exchange-correlation functionals for the accurate modeling of the vertical excitation energies and intensities of the transitions in the phthalocyanine cation radical and its dimer, a large array of exchange-correlation functionals which vary between pure functionals to the hybrids with about 50% of Hartree−Fock exchange were explored. First, it was found that the use of GGA (BP86)[72,73] and meta-GGA (TPSS)[74] exchange-correlation functionals result in a strong underestimation of the vertical excitation energies in the monomeric phthalocyanine cation radical as well as the appearance of well-known ghost charge-transfer states in the diamagnetic phthalocyanine cation radical dimer. Although a better agreement between theory and experiment was observed in the case of the hybrid TPSSh[74] (10% of Hartree−Fock exchange) and B3LYP[65] (20% of Hartree−Fock exchange) exchange-correlation functionals, the most stable wave function obtained using these two functionals for the phthalocyanine cation radical dimer is indicative of complete delocalization of the spin density over two macrocycles, which again results in ghost charge-transfer bands that were not observed experimentally. The usage of hybrid exchange-correlation functionals with 25% of Hartree−Fock exchange (PBE0[75] and HS1PBE[76]) allowed, for the first time, spin localization (±0.32 e^-) between two antiferromagnetically coupled phthalocyanine cation radicals (Table 7.1). The presence of spin localization in all considered exchange correlation functionals was important as it provided

well-separated spin densities of the stable antiferromagnetically coupled wave function in the dimer.

Table 7.1. DFT-predicted spin localization in the antiferromagnetically coupled [**7.1**]$_2^{2+}$ dimer as a function of exchange-correlation functional.

Functional	*Spin Localization, e$^-$*
B3LYP	±0.00 (delocalized)
MN12SX	±0.00 (delocalized)
PBE0	±0.32
HSEh1PBE	±0.32
M05	±0.81
M06	±0.56
M06HF	±0.84
MPW1B95	±0.50
SOGGA11X	±0.66
MPWKCIS1K	±0.78
BMK	±0.49
M11	±0.91
CAM-B3LYP	±0.83
wB97X	±0.90
wB97XD	±0.85

Starting from Minnesota hybrid exchange-correlation functionals M06[77] (27% Hartree−Fock exchange) and M05[78] (28% Hartree−Fock exchange), the spin localization between the

antiferromagnetically coupled phthalocyanines for the ligands on the dimer became more prominent (Table 7.1). Encouraged by these results, we have added the following hybrid exchange correlation functionals to our test set: MPW1B95[79] (31% Hartree−Fock exchange), SOGGA11X[80] (40% Hartree−Fock exchange), MPWKCIS1K[81] (41% Hartree−Fock exchange), BMK[82] (42% Hartree−Fock exchange), as well as the long-range corrected M11,[83] CAM-B3LYP,[66] wB97X,[84] wB97XD,[84] and M06-HF[77] functionals. It was found that for all of these exchange-correlation functionals, the spin densities of the stable antiferromagnetically coupled wave function in the dicationic phthalocyanine dimer are well separated and are in agreement with experimental data (Table 7.1).

Next, having a variety of exchange-correlation functionals that correctly reproduced spin density in the antiferromagnetically coupled phthalocyanine dication, we tested these in TDDFT calculations on the monomeric phthalocyanine cation radical and its dimer. In the case of the M11, M06-HF, and wB97X exchange-correlation functionals, the TDDFT calculations on the phthalocyanine cation radical dimer predicted degeneracy of the NIR band observed at ∼1000 nm and nondegeneracy of the excited state which is associated with the *Q*-band observed at 723 nm. This prediction does not correlate well with experimental data and thus, these functionals were not further considered. Although the wB97XD range-separated exchange-correlation functional provided reasonable agreement for the nondegenerate NIR band observed at ∼1000 nm and the degenerate *Q*-band observed at 723 nm for the diamagnetic dimer, this functional was found to significantly overestimate the vertical excitation energies of the excited states of the monomer and dimer in the fingerprint and *B*-band spectral envelope,

and thus, it was not further considered. The TDDFT-predicted vertical excitation energies and oscillator strengths of the [**7.1**]$^{+\bullet}$ and [**7.1**]$_2^{2+}$ systems using the CAMB3LYP, M05, M06, BMK, MPW1B95, MPWKICS1K, and SOGGA11X exchange-correlation functionals were found to be in significantly better agreement with the experimental data (Figures 7.2 and 7.7 and Supporting Information).

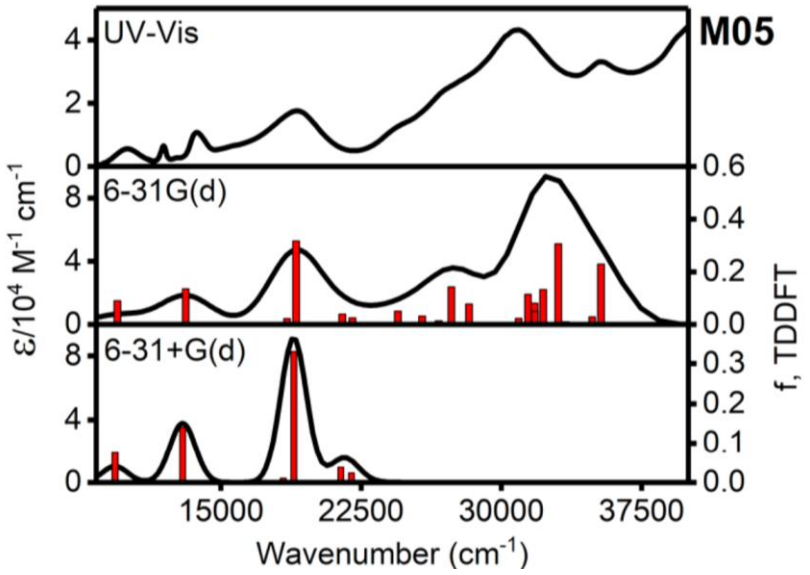

Figure 7.7. Comparison between the experimental UV-vis spectrum of the [**7.1**]$^{+\bullet}$/[**7.1**]$_2^{2+}$ mixture (top) and the TDDFT-predicted UV-vis spectra of the [**7.1**]$_2^{2+}$ dimer in DCM. The 6-31G(d) (middle) or 6-31+G(d) (bottom) basis sets were used for carbon, nitrogen, and hydrogen atoms. Only the first 60 states were calculated for the 6-31+G(d) basis set.

Thus, these exchange-correlation functionals were further compared to investigate the influence of diffuse basis functions on the calculated vertical excitation energies and oscillator strengths in the phthalocyanine cation radical dimer as one can assume that diffuse basis functions can play a significant role in weakly coupled antiferromagnetically arranged systems

positioned at distances of more than 3 Å. To our surprise (Figure 7.7 and Supporting Information), only a very small influence of the diffuse functions on the TDDFT-predicted vertical excitation energies, intensities, and oscillator strengths of the phthalocyanine cation radical dimer, was observed. Thus, taking into consideration the enormous increase in computational cost for calculations that involve diffuse basis functions, we did not consider those in our final set of calculations. We also compared the TDDFT data obtained with the Wachters full electron basis set used for Zn and the 6-311G(d) basis set for all other atoms with the data produced from our "regular" calculations (6-31G for zinc and 6-31G(d) for all other atoms). The results for the monomeric cation radical were found to be almost identical (Supporting Information). The elimination of diffuse functions and use of the double-ζ quality basis set for the TDDFT calculations on the dimer allowed us to consider up to the first 280 excited states for the dimer, which is necessary to cover the experimental spectral range in the NIR, visible, and ultraviolet (UV) spectral envelopes to a large extent (Figures 7.2 and 7.7). The resulting functionals were then further compared for their accuracy in predicting the NIR band, the *Q*-band in the monomer and dimer, the fingerprint band observed at ∼500 nm, and the other degenerate transitions identified from the analysis of the MCD spectra of the zinc phthalocyanine cation radical by Stillman and co-workers (Table 7.2).[43,57]

Table 7.2. Experimental and DFT-predicted energies for ^2E_g excited states with high intensity for the $[LMPc^R]^{+\bullet}$ cation radicals using different exchange-correlation functionals.

		CT_{dimer}	$Q_{monomer}$	Q_{dimer}	*fingerprint*	B_1	B_2	B_3	B_4	B_5	B_6
					$[(Im)ZnPc]^{+\bullet}/[(Im)ZnPc]_2^{2+b}$						
exp	cm^{-1}		12165	14006	19569	23585	27027	31546	35971		
	eV		1.51	1.74	2.43	2.92	3.35	3.91	4.46		
	nm		822	714	511	424	370	317	278		
					$[(Im)_nMgPc]^{+\bullet}/[(Im)_nMgPc]_2^{2+c}$						
exp	cm^{-1}		12121	13947	19724	23697	26882	31348	36232	37594	39216
	eV		1.50	1.73	2.45	2.94	3.33	3.89	4.49	4.66	4.86
	nm		825	717	507	422	372	319	276	266	255
					$[(THF)ZnPc]^{+\bullet}/[(THF)ZnPc]_2^{2+d}$						
exp	cm^{-1}	10030	12019	13831							
	eV	1.24	1.49	1.71							
	nm	997	832	723							
					$[\mathbf{7.1}]^{+\bullet}/[\mathbf{7.1}]_2^{2+e}$						
exp	cm^{-1}	10060	11933	13831	19455	22779	26247	30303	35336		
	eV	1.25	1.48	1.71	2.41	2.82	3.25	3.76	4.38		
	nm	994	838	723	514	439	381	330	283		
					$[\mathbf{7.1}]^{+\bullet}/[\mathbf{7.1}]_2^{2+}$						
M05											
monomer	cm^{-1}		12626		18904	22624	25381	32051	36232	37324	39385
	eV		1.57		2.34	2.81	3.15	3.97	4.49	4.63	4.88
	nm		792		529	442	394	312	276	268	254
dimer	cm^{-1}	9470		13123	19011	21505	27322	33003	35336		
	eV	1.17		1.63	2.36	2.67	3.39	4.09	4.38		
	nm	1056		762	526	465	366	303	283		
M06											
monomer	cm^{-1}		12626		18248	23474	27027	30769	35842		
	eV		1.57		2.26	2.91	3.35	3.82	4.44		
	nm		792		548	426	370	325	279		
dimer	cm^{-1}	8937		13643	18657						
	eV	1.11		1.69	2.31						
					$[\mathbf{7.1}]^{+\bullet}/[\mathbf{7.1}]_2^{2+}$						
	nm	1119		733	536						
BMK											
monomer	cm^{-1}		13755		20121	25707	27548	30864	34722		
	eV		1.71		2.49	3.19	3.42	3.83	4.31		
	nm		727		497	389	363	324	288		

		CT_{dimer}	$Q_{monomer}$	Q_{dimer}	*fingerprint*	B_1	B_2	B_3	B_4	B_5	B_6
dimer	cm^{-1}	9372		15106	20619						
	eV	1.16		1.87	2.56						
	nm	1067		662	485						
MPW1B95											
monomer	cm^{-1}		13387		18692	24450	28571	31949	36900		
	eV		1.66		2.32	3.03	3.54	3.96	4.57		
	nm		747		535	409	350	313	271		
dimer	cm^{-1}	8673		14472	19231						
	eV	1.08		1.79	2.38						
	nm	1153		691	520						
MPWKCIS1K											
monomer	cm^{-1}		13055		20921	24938	26738	31250	35461		
	eV		1.62		2.59	3.09	3.32	3.87	4.40		
	nm		766		478	401	374	320	282		
dimer	cm^{-1}	10352		13870	21053						
	eV	1.28		1.72	2.61						
	nm	966		721	475						
SOGGA11X											
monomer	cm^{-1}		13228		20790	25773	27624	30675	35088		
	eV		1.64		2.58	3.20	3.43	3.80	4.35		
	nm		756		481	388	362	326	285		
dimer	cm^{-1}	9728		14388	21186						
	eV	1.21		1.78	2.63						
	nm	1028		695	472						
CAM-B3LYP											
					$[\mathbf{7.1}]^{+\bullet}/[\mathbf{7.1}]_2^{2+}$						
monomer	cm^{-1}		12453		21786	25510	27473	32468	35587		
	eV		1.54		2.70	3.16	3.41	4.02	4.41		
	nm		803		459	392	364	308	281		
dimer	cm^{-1}	11468		13280	21930						
	eV	1.42		1.64	2.72						
	nm	872		753	456						

[a]All experiments and TDDFT calculations were conducted using DCM as a solvent. For all monomers, the 80 lowest energy excited states and, for all dimers, the first 60 excited states were calculated except for the M05 calculations; the numerical values are listed in cm^{-1}/eV/nm format; "B_1-B_6" labels are used to indicate the main transitions in the *B*-band region. [b]Reference 57. [c]Reference 43. [d]Reference 44. [e]This work.

As it can be seen, all of the utilized exchange-correlation functionals predicted that the energy of the *Q*-band of the phthalocyanine cation radical monomer would be located in between the vertical excitation energy of the nondegenerate NIR band and *Q*-band of the dimer, which is in good agreement with experiment. Moreover, all of these exchange-correlation functionals correctly predicted that the energy difference for the fingerprint band in the monomer and dimer was negligibly small and agrees well with the experimental data. Assuming that the positions of the *A*- and *B*-terms, as well as the *B*-terms' assignment to the third E_g excited state (following the discussion below), the mean average deviation (MAD) uncertainties for the degenerate excited states, were found to be the lowest for the M05 exchange-correlation functional (Table 7.2), and thus, further discussion will be focused on these data (Figures 7.8, 7.9, 7.10, and 7.11 and Tables 7.3, 7.4, and 7.5).

	α		**β**	
LUMO+6	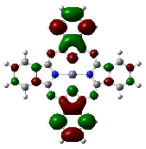	$8e_g$	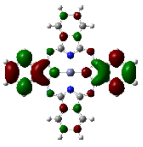	$8e_g$
LUMO+5	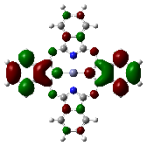	$8e_g$	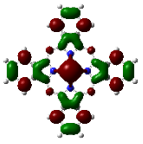	$7a_{2u}$
LUMO+4	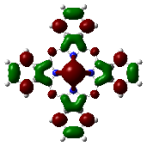	$7a_{2u}$	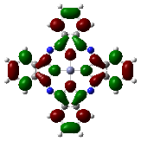	$4b_{2u}$

LUMO+3	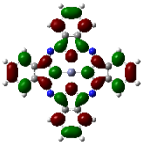	$4b_{2u}$	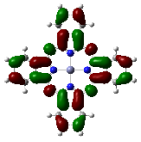	$3b_{1u}$
LUMO+2	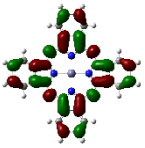	$3b_{1u}$	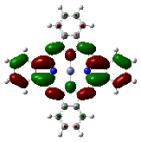	$7e_g$
LUMO+1	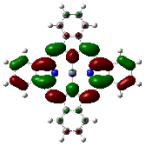	$7e_g$	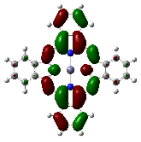	$7e_g$
LUMO	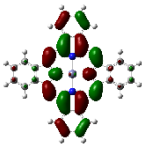	$7e_g$	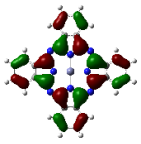	$2a_{1u}$
HOMO	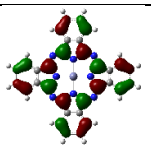	$2a_{1u}$	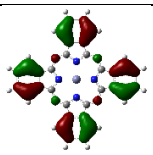	$2b_{1u}$
HOMO-1	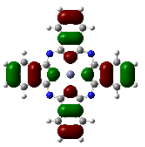	$3b_{2u}$	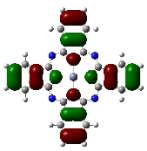	$3b_{2u}$
HOMO-2	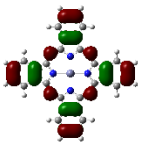	$6a_{2u}$	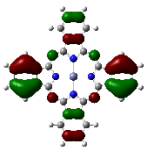	$6e_g$
HOMO-3	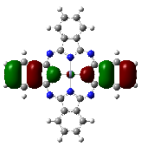	$6e_g$	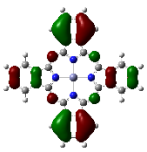	$6e_g$
HOMO-4	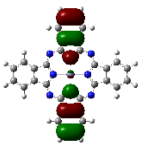	$6e_g$	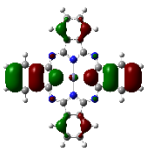	$5e_g$

HOMO-5	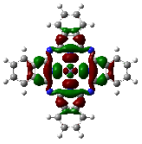	$16b_{1g}$	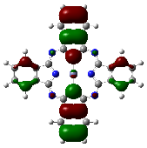	$5e_g$
HOMO-6	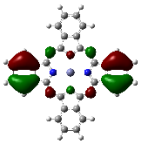	$5e_g$	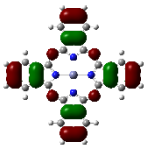	$6a_{2u}$
HOMO-7	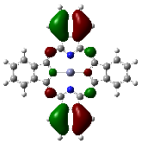	$5e_g$	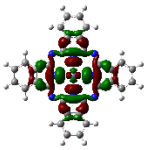	$16b_{1g}$
HOMO-8	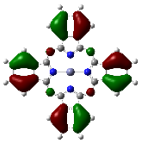	$2b_{1u}$	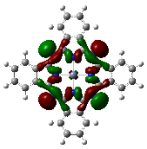	$14b_{2g}$
HOMO-9	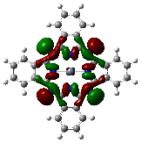	$14b_{2g}$	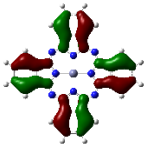	$1a_{1u}$
HOMO-10	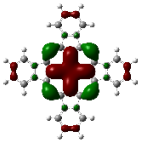	$5a_{2u}$	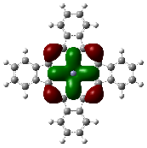	$5a_{2u}$

Figure 7.8. DFT-predicted frontier orbitals for the [**7.1**]$^{+\bullet}$ monomer.

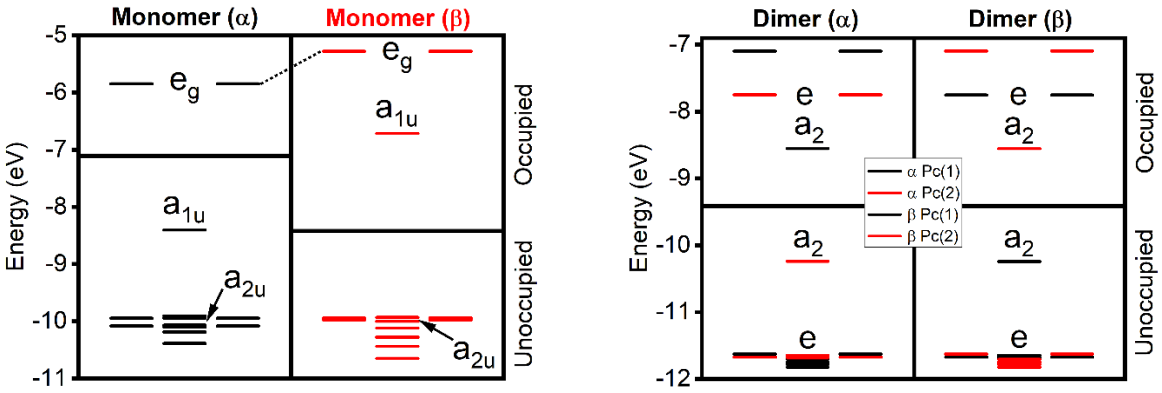

Figure 7.9. DFT-predicted frontier orbitals energy diagram for the [**7.1**]$^{+\bullet}$ monomer and [**7.1**]$_2^{2+}$ dimer. *Pc*(1) and *Pc*(2) denote the two different phthalocyanine fragments of the dimer.

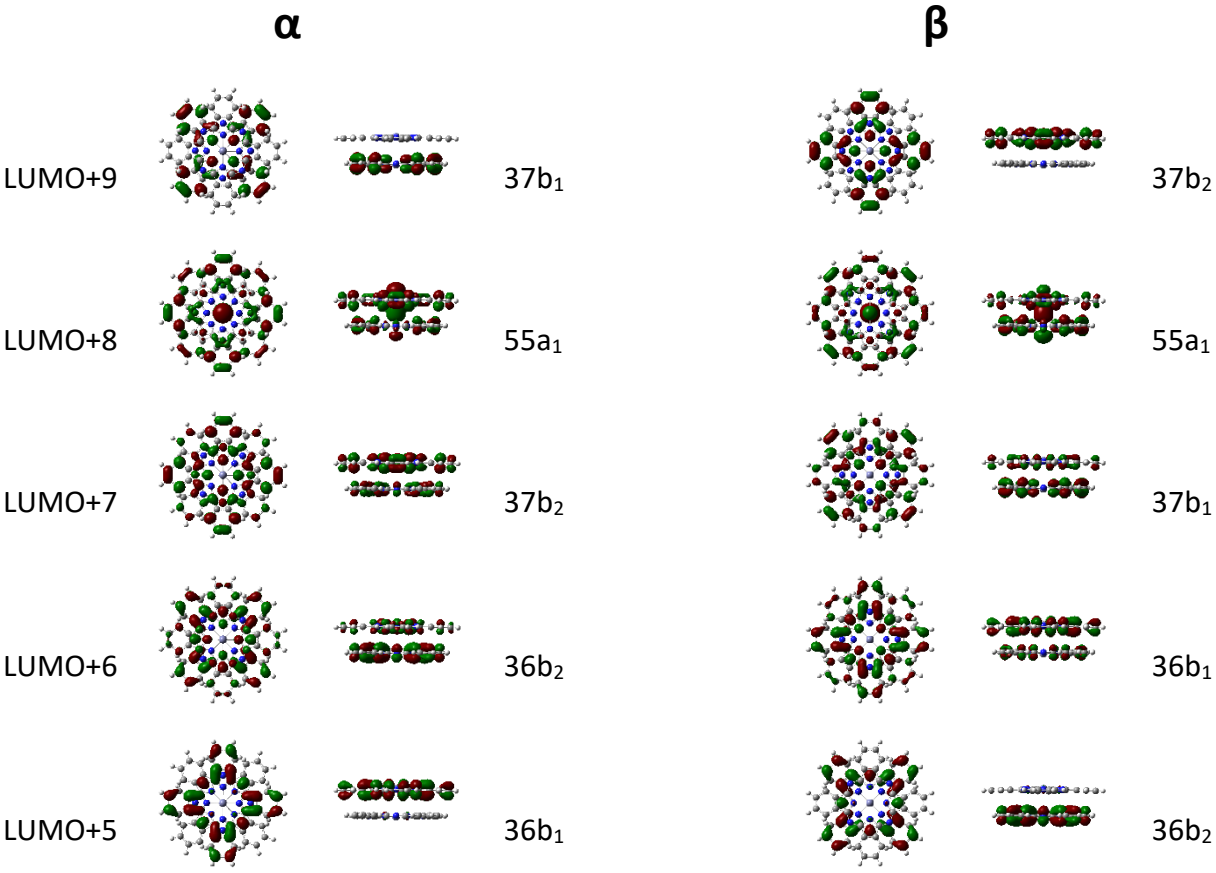

LUMO+4	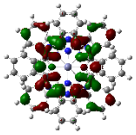	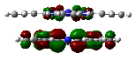	74e	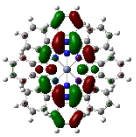	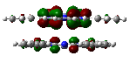	74e
LUMO+3	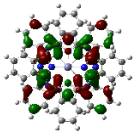	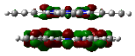	74e	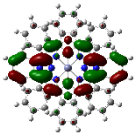	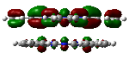	74e
LUMO+2	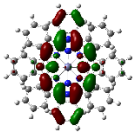	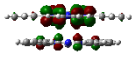	73e	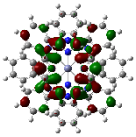	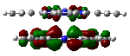	73e
LUMO+1	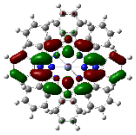	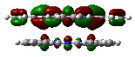	73e	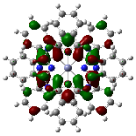	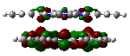	73e
LUMO	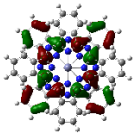	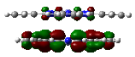	$26a_2$	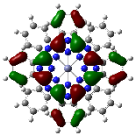	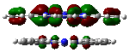	$26a_2$
HOMO	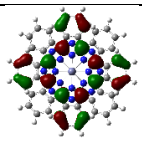	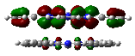	$25a_2$	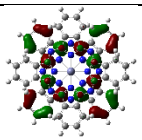	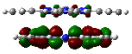	$25a_2$
HOMO-1	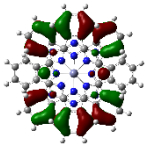	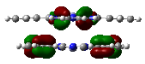	72e	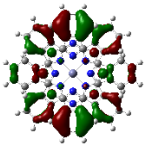	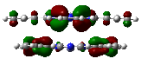	72e
HOMO-2	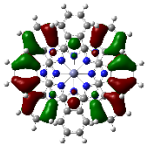	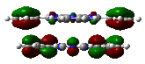	72e	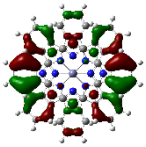	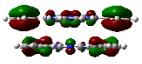	72e
HOMO-3	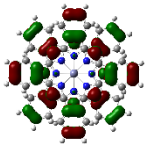	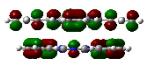	$54a_1$	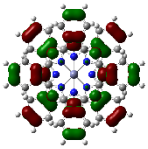	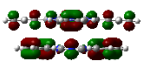	$54a_1$
HOMO-4	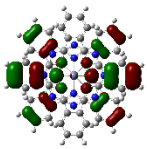	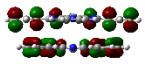	71e	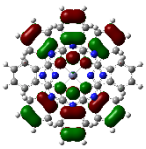		71e

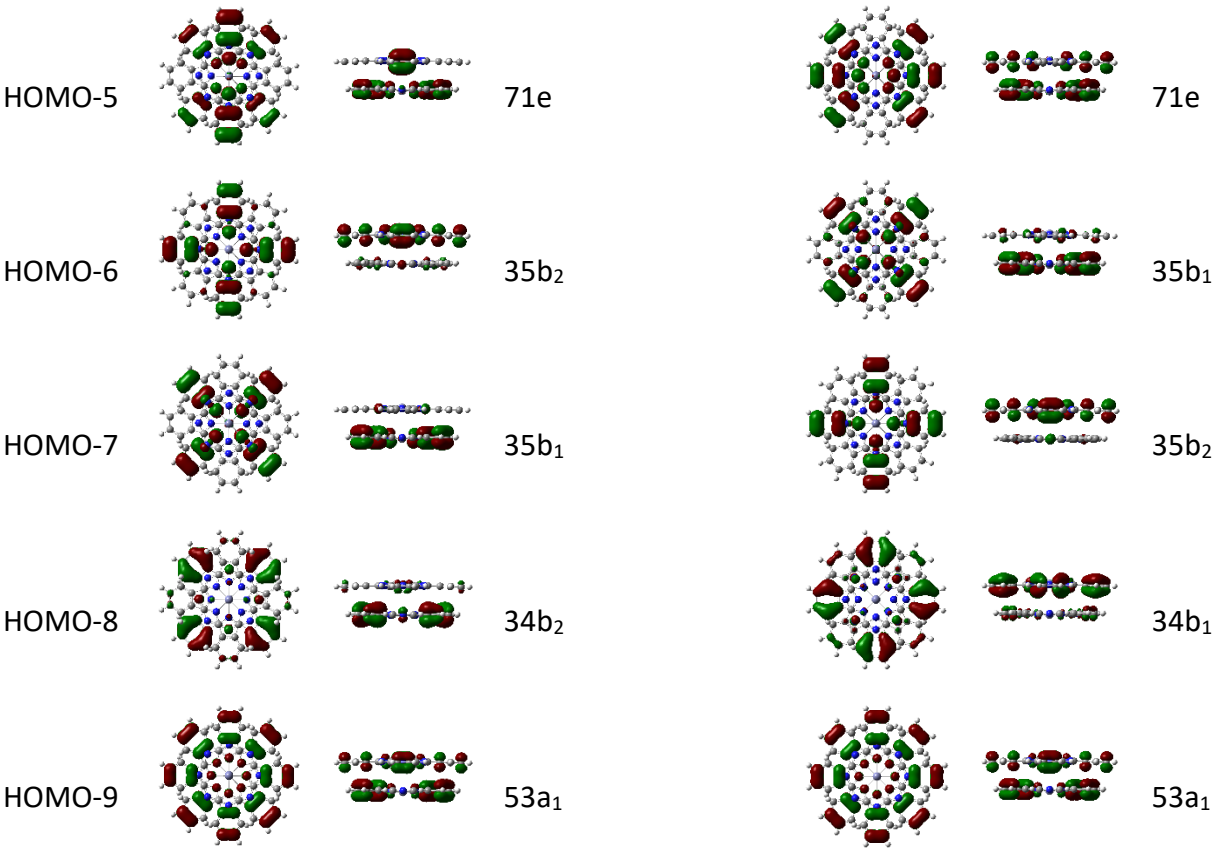

Figure 7.10. DFT-predicted frontier orbitals (top and side views) for the $[\mathbf{7.1}]_2^{2+}$ dimer.

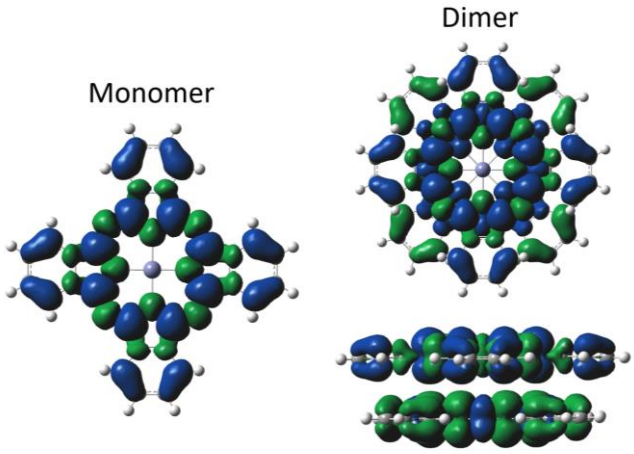

Figure 7.11. DFT-predicted total spin densities for the monomeric $[\mathbf{7.1}]^{+\bullet}$ (left) and antiferromagnetically coupled $[\mathbf{7.1}]_2^{2+}$ dimer (right).

Table 7.3. Analysis of TDDFT-predicted selected excited state energies, expansion coefficients, and oscillator strengths for monomeric [**7.1**]$^{+\bullet}$ (M05 exchange-correlation functional).[a]

State	*Energy/cm^{-1}*	*λ/nm*	*f* [b]	*Character* [c]
$1E_g$	12620	792	0.1159	90% $2a_{1u}(\alpha) \rightarrow 7e_g(\alpha)$
$2E_g$	16238	616	0.0004	55% $6e_g(\beta) \rightarrow 2a_{1u}(\beta)$, 13% $5e_g(\beta) \rightarrow 2a_{1u}(\beta)$
$3E_g$	18897	529	0.2345	66% $5e_g(\beta) \rightarrow 2a_{1u}(\beta)$, 19% $6e_g(\beta) \rightarrow 2a_{1u}(\beta)$
$4E_g$	22604	442	0.0348	29% $3b_{2u}(\alpha) \rightarrow 7e_g(\alpha)$, 18% $6a_{2u}(\alpha) \rightarrow 7e_g(\alpha)$, 16% $6e_g(\beta) \rightarrow 2a_{1u}(\beta)$
$5E_g$	25363	394	0.0735	31% $6a_{2u}(\alpha) \rightarrow 7e_g(\alpha)$, 22% $5a_{2u}(\alpha) \rightarrow 7e_g(\alpha)$, 20% $3b_{2u}(\alpha) \rightarrow 7e_g(\alpha)$
$6E_g$	26525	377	0.0455	37% $3b_{2u}(\alpha) \rightarrow 7e_g(\alpha)$, 20% $2b_{1u}(\alpha) \rightarrow 7e_g(\alpha)$
$7E_g$	27223	367	0.0348	52% $5a_{2u}(\alpha) \rightarrow 7e_g(\alpha)$, 26% $2b_{1u}(\alpha) \rightarrow 7e_g(\alpha)$
$8E_g$	28008	357	0.1509	25% $6a_{2u}(\alpha) \rightarrow 7e_g(\alpha)$, 22% $2b_{1u}(\alpha) \rightarrow 7e_g(\alpha)$
$1A_{2g}$	28435	352	0.0011	88% $30e_u(\alpha) \rightarrow 7e_g(\alpha)$
$9E_g$	29853	335	0.0033	29% $3b_{2u}(\beta) \rightarrow 7e_g(\beta)$, 21% $1a_{1u}(\alpha) \rightarrow 7e_g(\alpha)$
$10E_g$	30577	327	0.0060	32% $2b_{1u}(\beta) \rightarrow 7e_g(\beta)$, 22% $3b_{2u}(\beta) \rightarrow 7e_g(\beta)$, 14% $2b_{1u}(\alpha) \rightarrow 7e_g(\alpha)$
$11E_g$	31572	317	0.0314	35% $6a_{2u}(\beta) \rightarrow 7e_g(\beta)$, 23% $3b_{2u}(\beta) \rightarrow 7e_g(\beta)$, 15% $2b_{1u}(\beta) \rightarrow 7e_g(\beta)$
$12E_g$	32040	312	0.3688	30% $6a_{2u}(\beta) \rightarrow 7e_g(\beta)$, 25% $2b_{1u}(\beta) \rightarrow 7e_g(\beta)$, 12% $1a_{1u}(\alpha) \rightarrow 7e_g(\alpha)$, 11% $4e_g(\beta) \rightarrow 2a_{2u}(\beta)$
$13E_g$	34262	292	0.0002	31% $5a_{2u}(\beta) \rightarrow 7e_g(\beta)$, 24% $1a_{1u}(\beta) \rightarrow 7e_g(\beta)$, 22% $1a_{1u}(\alpha) \rightarrow 7e_g(\alpha)$, 15% $4e_g(\beta) \rightarrow 2a_{1u}(\beta)$
$2A_{2g}$	34521	290	0.0021	84% $30e_u(\beta) \rightarrow 7e_g(\beta)$

$14E_g$	34801	287	0.0988	45% $4e_g(\beta) \rightarrow 2a_{1u}(\beta)$, 30% $1a_{1u}(\beta) \rightarrow 7e_g(\beta)$
$15E_g$	36255	276	0.3380	26% $5a_{2u}(\beta) \rightarrow 7e_g(\beta)$, 11% $1a_{1u}(\alpha) \rightarrow 7e_g(\alpha)$
$16E_g$	36818	272	0.0152	59% $2a_{1u}(\alpha) \rightarrow 8e_g(\alpha)$
$17E_g$	37324	268	0.0554	20% $5a_{2u}(\beta) \rightarrow 7e_g(\beta)$, 10% $1a_{1u}(\beta) \rightarrow 7e_g(\beta)$
$18E_g$	39385	254	0.0424	22% $6e_g(\alpha) \rightarrow 3b_{1u}(\alpha)$, 13% $3e_g(\beta) \rightarrow 2a_{1u}(\beta)$
$3A_{2g}$	39961	250	0.0004	72% $11a_{2g}(\beta) \rightarrow 2a_{1u}(\beta)$

[a] E_g states have x,y-polarization and A_{2g} states have z-polarization; see Supporting Information for complete list of the excited states. [b] *f* is the TDDFT-predicted oscillator strength. [c] Only contributions with >10% are listed, for complete character of excited states, see Supporting Information.

Table 7.4. DFT-predicted compositions for the frontier MOs (MO5 exchange-correlation functional)[a]

MO	*Energy/eV*	*Zn*	*N*	*C, H*
		Monomer (α)		
158	-1.862	0.03	2.29	97.68
157	-1.862	0.03	2.29	97.68
156	-1.872	64.9	8.47	26.63
155	-1.897	0	0.04	99.96
154	-3.167	0.08	10.56	89.36
153	-3.167	0.08	10.56	89.36
152	-3.326	8.73	7.55	83.72
151	-3.624	0	24.15	75.85
150	-3.823	0	28.31	71.69

149	-5.845	0.32	34.8	64.88
148	**-5.845**	**0.32**	**34.8**	**64.88**
147	**-8.404**	**0**	**0.21**	**99.79**
146	-9.907	0	22.19	77.81
145	-9.943	0.01	23.61	76.38
144	-9.946	0.84	22.68	76.48
143	-9.946	0.84	22.68	76.48
142	-10.067	17.61	55.98	26.42
141	-10.083	0.08	12.03	87.89
140	-10.083	0.08	12.03	87.89
139	-10.100	0	4.79	95.21
138	-10.186	0.53	76.36	23.12
137	-10.388	1.98	86.11	11.91
		Monomer (β)		
157	-1.701	0	0.06	99.94
156	-1.719	77.49	13.72	8.79
155	-1.828	67.01	9.21	23.78
154	-3.016	0.07	9.05	90.88
153	-3.016	0.07	9.05	90.88
152	-3.165	9.13	6.1	84.77
151	-3.351	0	18.69	81.31
150	-3.672	0	22.81	77.19
149	-5.28	0.21	25.25	74.54
148	-5.28	0.21	25.25	74.54
147	**-6.715**	**0**	**0.24**	**99.76**

146	**-9.931**	**0**	**5.67**	**94.33**
145	-9.935	0	21.31	78.69
144	-9.942	0	9.25	90.75
143	-9.942	0	9.25	90.75
142	-9.977	0.85	24.94	74.21
141	-9.977	0.85	24.94	74.21
140	-10.001	0.13	12.57	87.3
139	-10.119	17.94	56.16	25.9
138	-10.279	0.53	76.24	23.23
137	-10.438	0	0.04	99.96
136	-10.65	1.59	94.75	3.66

MO	*Energy/eV*	*Zn (1)*	*N (1)*	*C, H (1)*	*Zn (2)*	*N (2)*	*C, H (2)*
			Dimer (α)				
304	-5.049	0.21	3.22	26.65	0.08	7.78	62.06
303	-5.179	0.01	18.45	77.24	0	0.75	3.55
302	-5.315	3.71	3.3	29.91	6.21	5.68	51.2
301	-5.365	0	5.54	21.5	0.01	16.31	56.65
300	-5.59	0	17.51	53	0	8.27	21.21
299	-5.668	0	1.38	3.75	0	27.15	67.72
298	-7.096	0.19	20.71	62.78	0.1	4.2	12.01
297	-7.096	0.19	20.71	62.78	0.1	4.2	12.01
296	-7.749	0.23	4.46	9.81	0.45	29.56	55.48
295	-7.749	0.23	4.46	9.81	0.45	29.56	55.48
294	**-8.556**	**0**	**0.21**	**88.38**	**0**	**0.05**	**11.36**
293	**-10.24**	**0**	**0.04**	**9.16**	**0**	**0.21**	**90.59**

292	-11.628	0.03	7.31	57.66	0.03	4.2	30.77
291	-11.628	0.03	7.31	57.66	0.03	4.2	30.77
290	-11.648	0.04	9.55	29.93	0.1	18.59	41.79
289	-11.672	0.4	10.19	30.3	0.52	13.05	45.55
288	-11.672	0.4	10.19	30.3	0.52	13.05	45.55
287	-11.68	0.02	3.73	9.14	0.28	19.97	66.86
286	-11.704	0.56	20.22	69.81	0.03	5.7	3.68
285	-11.747	0	5.4	84.68	0.1	1.78	8.04
284	-11.781	0.32	6.15	48.83	0.34	6.07	38.29
283	-11.824	0.44	11.88	46.1	0.34	9.36	31.88
			Dimer (β)				
304	-5.05	0.09	7.88	62.63	0.18	3.13	26.08
303	-5.179	0	0.57	3.22	0.01	18.61	77.59
302	-5.315	6.29	5.69	51.34	3.63	3.29	29.77
301	-5.36	0.01	15.83	55.27	0	6.1	22.8
300	-5.594	0	8.74	22.62	0	16.97	51.67
299	-5.668	0	27.3	68.03	0	1.26	3.41
298	-7.094	0.11	4.12	11.88	0.2	20.8	62.9
297	-7.094	0.11	4.12	11.88	0.2	20.8	62.9
296	-7.751	0.44	29.64	55.58	0.24	4.4	9.71
295	-7.751	0.44	29.64	55.58	0.24	4.4	9.71
294	**-8.554**	**0**	**0.05**	**11.32**	**0**	**0.21**	**88.43**
293	**-10.243**	**0**	**0.21**	**90.61**	**0**	**0.04**	**9.14**
292	-11.626	0.06	5	29.1	0.01	6.59	59.23
291	-11.626	0.06	5	29.1	0.01	6.59	59.23

290	-11.647	0.11	19.01	39.05	0.04	9.38	32.41
289	-11.674	0.47	12.01	46.1	0.43	11.2	29.79
288	-11.674	0.47	12.01	46.1	0.43	11.2	29.79
287	-11.676	0.53	19.66	63.68	0.02	3.79	12.32
286	-11.707	0.03	5.53	3.36	0.29	19.9	70.89
285	-11.747	0.2	2.78	10.84	0	5.46	80.72
284	-11.781	0.33	6.13	41.4	0.32	6	45.82
283	-11.823	0.35	9.17	32.49	0.43	11.98	45.58

[a]HOMO and LUMO are in bold, "(1)" and "(2)" for the dimer is reference to the first and second phthalocyanine macrocycle, respectively. Orbital symmetries are given in Figs. 7.8 and 7.10.

Table 7.5. Analysis of the TDDFT-predicted selected excited state energies, expansion coefficients, and oscillator strengths for dimeric [**7.1**]$_2^{2+}$ (M05 exchange-correlation functional).[a]

State	*Energy/cm^{-1}*	*λ/nm*	*f*	*Character*
A_1	9469	1056	0.09	51% 25a_2 (β, Pc2) → 26a_2 (β, Pc1)
				49% 25a_2 (α, Pc1) → 26a_2 (β, Pc2)
E	13119	762	0.14	40% 25a_2 (α, Pc1) → 73e (α, Pc1)
				39% 25a_2 (β, Pc2) → 73e (β, Pc2)
E	18540	539	0.02	37% 25a_2 (α, Pc1) → 74e (α, Pc2)
				35% 25a_2 (β, Pc2) → 74e (β, Pc1)
E	19023	526	0.32	22% 72e (α, Pc2) → 26a_2 (α, Pc2)
				22% 72e (β, Pc1) → 26a_2 (β, Pc1)
E	21494	465	0.04	31% 69e (α, Pc2) → 26a_2 (α, Pc2)
				29% 69e (β, Pc1) → 26a_2 (β, Pc1)

				13% 72e (β, Pc2) → 26a_2 (β, Pc1)
				13% 72e (α, Pc1) → 26a_2 (α, Pc2)
E	22037	454	0.03	11% 35b_2 (α, Pc1) → 73e (α, Pc1)
				11% 35b_1 (β, Pc2) → 73e (β, Pc2)
				10% 54a_1 (α, Pc2) → 73e (α, Pc1)
				10% 54a_1 (β, Pc1) → 73e (β, Pc2)
E	24464	409	0.05	20% 54a_1 (β, Pc1) → 73e (β, Pc2)
				18% 54a_1 (α, Pc2) → 73e (α, Pc1)
				13% 35b_2 (α, Pc1) → 73e (α, Pc1)
				13% 35b_1 (β, Pc2) → 73e (β, Pc2)
E	25759	388	0.03	14% 35b_2 (α, Pc1) → 73e (α, Pc1)
				14% 34b_1 (α, Pc2) → 73e (α, Pc1)
				14% 35b_1 (β, Pc2) → 73e (β, Pc2)
				11% 34b_2 (β, Pc1) → 73e (β, Pc2)
E	26649	375	0.01	42% 33b_1 (α, Pc1) → 73e (α, Pc1)
				13% 33b_2 (β, Pc2) → 73e (β, Pc2)
E	27327	366	0.14	18% 34b_2 (α, Pc2) → 73e (α, Pc1)
				16% 34b_1 (β, Pc1) → 73e (β, Pc2)
				10% 24a_2 (β, Pc2) → 73e (β, Pc2)
E	28276	354	0.08	*All contributions under 10%
E	30926	323	0.02	18% 35b_1 (α, Pc2) → 74e (α, Pc2)
				17% 35b_2 (β, Pc1) → 74e (β, Pc1)
				10% 35b_1 (β, Pc2) → 74e (β, Pc1)
E	31426	318	0.11	15% 34b_2 (α, Pc1) → 74e (α, Pc1)

				15% $34b_1$ (β, Pc1) → 74e (β, Pc1)
				12% $54a_1$ (α, Pc2) → 74e (α, Pc2)
				12% $54a_1$ (β, Pc1) → 74e (β, Pc1)
E	31775	315	0.08	21% $34b_1$ (β, Pc1) → 74e (β, Pc1)
				20% $54a_1$ (α, Pc2) → 74e (α, Pc2)
				12% $53a_1$ (α, Pc1) → 74e (α, Pc2)
				10% $54a_1$ (β, Pc1) → 74e (β, Pc1)
E	31797	314	0.05	27% $34b_2$ (α, Pc2) → 74e (α, Pc2)
				13% $54a_1$ (β, Pc1) → 74e (β, Pc1)
				11% 66e (α, Pc1) → $26a_2$ (α, Pc2)
E	32240	310	0.13	23% $51a_1$ (β, Pc2) → 73e (β, Pc2)
				22% $51a_1$ (α, Pc1) → 73e (α, Pc1)
				20% $53a_1$ (β, Pc2) → 74e (β, Pc1)
				13% $53a_1$ (α, Pc1) → 74e (α, Pc2)
E	33045	303	0.31	18% $23a_2$ (β, Pc1) → 73e (β, Pc2)
				18% $23a_2$ (α, Pc2) → 73e (α, Pc1)
				10% 66e (β, Pc2) → $26a_2$ (β, Pc1)
				10% 66e (α, Pc1) → $26a_2$ (α, Pc2)
E	33438	299	0.01	81% $34b_2$ (β, Pc1) → 74e (β, Pc1)
E	34861	287	0.03	27% $52a_1$ (α, Pc2) → 74e (α, Pc2)
				25% $52a_1$ (β, Pc1) → 74e (β, Pc1)
				11% $24a_2$ (α, Pc1) → 74e (α, Pc2)
				10% $24a_2$ (β, Pc2) → 74e (β, Pc1)
E	35328	283	0.23	19% $23a_2$ (α, Pc2) → 73e (α, Pc1)

18% $23a_2$ (β, Pc1) → 73e (β, Pc2)

11% 66e (β, Pc2) → $26a_2$ (β, Pc1)

11% 66e (α, Pc1) → $26a_2$ (α, Pc2)

---

[a]E states have x,y-polarization and A_1 states have z-polarization, see Supporting Information for complete list of the excited states; [b]*f* is the TDDFT-predicted oscillator strength; [c]Only contributions with >10% are listed, for complete character of excited states; see Supporting Information.

In the case of the monomeric phthalocyanine cation radical, the M05 TDDFT calculations predicted 18 degenerate excited states of E_g symmetry between 800 and 250 nm (Table 7.3). Out of these allowed x,y-polarized transitions, five ($22E_g$, $92E_g$, $102E_g$, $132E_g$, and $162E_g$) were predicted with negligible intensity, while six ($12E_g$, $32E_g$, $82E_g$, $122E_g$, $142E_g$, and $152E_g$) were predicted with high intensity ($f \geq 0.1$). TDDFT calculations predicted three z-polarized transitions of low intensity (Table 7.3) in the 350−250 nm spectral envelope. Thus, the TDDFT data indicates that such z-polarized transitions should not contribute significantly to the fingerprint spectroscopic range at ~500 nm.

The first TDDFT-predicted excited state of E_g symmetry at 792 nm is dominated by the α-HOMO → α-LUMO, LUMO+1 ($2a_{1u}$ → $7e_g$) single electron excitations, which is similar to the *Q*-band of neutral Pc (Table 3). The energy and the intensity of this TDDFT-predicted band correlates very well with the experimentally observed MCD *A*-term representing the *Q*-band at 836 nm for [**7.1**]$^{+\bullet}$, 822 nm for [(Im)ZnPc]$^{+\bullet}$,[57] and 826 nm for [(Im)$_n$MgPc]$^{+\bullet}$.[43] More importantly, the sum-over-states (SOS) simulated MCD spectroscopic signature for this *Q*-band

has a clear MCD *A*-term shape (Figure 7.2), which correlates well with the experimental data. The second degenerate excited state ($22E_g$) was predicted at 616 nm and is dominated by the β-HOMO-4, HOMO-5 → β-LUMO ($6e_g \rightarrow 2a_{1u}$) single-electron transitions complemented by a significant contribution from the β-HOMO-2, HOMO-3 → βLUMO ($5e_g \rightarrow 2a_{1u}$) single-electron excitations. This excited state was predicted to have a small oscillator strength and correlates well with the second degenerate excited state predicted by Ishikawa and co-workers.[60] The third doubly degenerate $32E_g$ excited state was predicted at 529 nm (Table 7.3) and correlates perfectly well with the fingerprint band observed at 514 nm in [**7.1**]$^{+\bullet}$, 511 nm in [(Im)ZnPc]$^{+\bullet}$,[57] and 507 nm in [(Im)$_n$MgPc]$^{+\bullet}$.[43] This excited state has high intensity and is dominated (66%) by β-HOMO-2, HOMO-3 → β-LUMO ($5e_g \rightarrow 2a_{1u}$) single-electron excitations to the hole which is heavily complemented (19%) by the β-HOMO-4, HOMO-5 → β-LUMO ($6e_g \rightarrow 2a_{1u}$) single-electron excitations. This TDDFT prediction aligns very well to the proposed description by Ishikawa and coauthors of the fingerprint band that should consist of two allowed excited state configurations originating from closely spaced in energy $6e_g \rightarrow 2a_{1u}$ and $5e_g \rightarrow 2a_{1u}$ single-electron excitations. According to Ishikawa's model,[60–62] the orbital angular momenta of these two electronic configurations are similar in magnitude but opposite in sign because of the heavy configurational interaction. The magnitude of the L_z value then is expected to be significantly reduced, which, in turn, should reduce the *A*-term contribution to this excited state. In agreement with Ishikawa's model, the SOS-predicted MCD spectrum in the fingerprint region has an MCD *B*-term shape and a large positive amplitude, which is in perfect agreement with the experimental data (Figure 7.2). Although our TDDFT and SOS MCD calculations fit well with Ishikawa's model, which is supports the $5e_g$, $6e_g \rightarrow 2a_{1u}$ single electron excitations to the

half-empty $2a_{1u}$ orbital, we still cannot clearly conclude that the fingerprint region band assignment problem is resolved. Indeed, MCD spectral band deconvolution analysis reported by Stillman and co-workers[43,57] is indicative of the rather perfectly symmetric Gaussian-shape of the experimentally observed MCD *B*-term at ~500 nm. Formation of the Gaussian-shaped *B*-term at ~500 nm would then require a nearly perfect cancellation of two opposite-signed MCD *A*-terms originating from the $6e_g \rightarrow 2a_{1u}$ and $5e_g \rightarrow 2a_{1u}$ single electron excitations.

The next degenerate excited state was experimentally observed at 438 nm in [**7.1**]$^{+\bullet}$, 424 nm in [(Im)ZnPc]$^{+\bullet}$,[57] and 413 nm in [(Im)$_n$MgPc]$^{+\bullet}$.[43] The M05 TDDFT calculations predicted two potential candidates for this band. The first one is the $42E_g$ state predicted at 442 nm (*f* = 0.035). This excited state has three major contributions from α-HOMO−1→ α-LUMO, LUMO+1 ($3b_{2u} \rightarrow 7e_g$, 29%), α-HOMO−2→ α-LUMO, LUMO+1 ($6a_{2u} \rightarrow 7e_g$, 18%), and β-HOMO−4, HOMO−5→ β-LUMO ($6e_g \rightarrow 2a_{1u}$, 16%) single-electron excitations, which resembles to some extent, the first weak degenerate transition in the neutral **7.1**. The second candidate is the more intense (*f* = 0.074) $52E_g$ state, which was predicted at 394 nm and is dominated by the α-HOMO−2→ α-LUMO, LUMO+1 ($6a_{2u} \rightarrow 7e_g$, 31%), α-HOMO−10→ α-LUMO, LUMO+1 ($5a_{2u} \rightarrow 7e_g$, 22%), and α-HOMO−1→ α-LUMO, LUMO+1 ($3b_{2u} \rightarrow 7e_g$, 20%) single-electron excitations. The next degenerate transition identified by Stillman and co-workers in the [(Im)ZnPc]$^{+\bullet}$ [57] and [(Im)$_n$MgPc]$^{+\bullet}$ [43] compounds is located at ~370 nm (Table 7.3). The TDDFT results are indicative of three excited states as the potential candidates for this band. Excited states $62E_g$ and $72E_g$ were predicted with much lower intensity than excited state $82E_g$ (Table 7.3). The $82E_g$ state is dominated by the α-HOMO−2→ α-LUMO, LUMO+1 ($6a_{2u} \rightarrow 7e_g$, 25%) and α HOMO−8→ α-

LUMO, LUMO+1 ($2b_{1u} \rightarrow 7e_g$, 22%) single-electron excitations. The most intense degenerate transition in the Soret-band region was identified for $[(Im)ZnPc]^{+\bullet}$ [49] and $[(Im)_nMgPc]^{+\bullet}$ [35] compounds at 317 and 319 nm, respectively. Only one very intense excited state is predicted by TDDFT in this region ($122E_g$, 312 nm, Table 7.3). This excited state is dominated by the β-HOMO-6→ β-LUMO+1, LUMO+2 ($6a_{2u} \rightarrow 7e_g$, 30%) and β-HOMO → β-LUMO+1, LUMO+2 ($2b_{1u} \rightarrow 7e_g$, 25%) single-electron excitations. Similarly, there is one excited state ($152E_g$, 276 nm, Table 7.3) which correlates well with the intense band observed at ~277 nm for $[(Im)ZnPc]^{+\bullet}$ [57] and $[(Im)_nMgPc]^{+\bullet}$.[43] This excited state is dominated by the β-HOMO-10→ β-LUMO+1, LUMO+2 ($5a_{2u} \rightarrow 7e_g$, 26%) and α-HOMO-13→ α-LUMO, LUMO+1 ($1a_{1u} \rightarrow 7e_g$, 11%) single-electron excitations. Finally, the degenerate excited states that were experimentally observed at 266 and 255 nm correlate well with the low-intensity degenerate excited states $172E_g$ and $182E_g$, which are predicted at 268 and 254 nm, respectively (Table 7.3). Overall, the TDDFT-predicted UV−vis and MCD spectra of the monomeric phthalocyanine cation radical are in excellent agreement with experimental data, both in energies of the excited states and predicted oscillator strengths. The discrepancy between the larger number of doubly degenerate excited states predicted by TDDFT and extracted from the band deconvolution analysis can be easily explained because: (i) a number of low-intensity degenerate MCD *A*-terms can be hardly detected in the band deconvolution analysis; (ii) the experimental data are typically fitted using the lowest possible number of bands, and, in most cases, room-temperature and frozen-solution UV−vis and MCD spectra can be fitted with a larger number of transitions. If only the aforementioned assignments are considered, the TDDFT data using the M05 exchange-

correlation functional provided a better than 0.1 eV agreement between theory and experiment, making us quite confident with our band assignment (Table 7.2).

Regarding the TDDFT calculations on the Pc cation radical dimer, the first predicted 280 excited states were not enough to cover the entire spectral range (the last excited state energy was predicted at 279 nm); however, it was enough to cover the majority of the NIR, visible, and UV spectral envelopes to account for all MCD *A*-term-derived spectroscopic signatures for the dimer. Overall, 19 degenerate transitions of E symmetry for the C_{4v} symmetry $[\mathbf{7.1}]_2^{2+}$ dimer with an oscillator strength higher than 0.01 were predicted by the broken-symmetry TDDFT calculations (Table 7.4). Out of these, only seven of the ^{2}E symmetry excited states were predicted to have higher than 0.1 oscillator strength. More interestingly, the first two z-polarized transitions in the $[\mathbf{7.1}]_2^{2+}$ dimer were predicted at lower energy than the lowest energy x,y-polarized E symmetry excited state (Table 7.5 and Supporting Information).

The first excited state with nonzero intensity was predicted to be z-polarized and located at 1056 nm. This excited state consists of the contribution from two almost equal single-electron configurations originating from β-HOMO → β-LUMO (51%) and α-HOMO → α-LUMO (49%) (a_2 → a_2) excitations that have clear intermolecular charge-transfer character as the LUMO of the $[\mathbf{7.1}]_2^{2+}$ dimer is localized on the opposing phthalocyanine fragment, while LUMO+1 and LUMO+2 are localized on the same macrocycle as the HOMO (Figure 7.10). On a physical level, this excited state represents an electron-transfer from the half-occupied MO at one macrocycle to a second macrocycle (SOMO → SOMO, Pc(1) → Pc(2) and Pc(2) → Pc(1) transition). It is important to note that this z-polarized excited state is nondegenerate, which explains the

experimental observation of the *B*-term in the MCD spectrum of the dimeric species in the low-energy NIR region. In agreement with the experimental data, excited states four and five were predicted to be x,y-polarized doubly degenerate ^{2}E-symmetry states. These were predicted at 762 nm and are in excellent agreement with experiment (723 nm for [**7.1**]$_2^{2+}$, 714 nm for [(Im)ZnPc]$_2^{2+}$,[57] and 717 nm for [MgPc]$_2^{2+}$).[43] This excited state is dominated by an almost equal contribution from the α,β-HOMO → α,β-LUMO+1 and LUMO+2 ($a_2 \rightarrow e_g$) single-electron excitations localized at the same macrocycle in the dimer, which should result in the observation of an MCD *A*-term than can be assigned as the *Q*-band of the dimer. Similar to the phthalocyanine cation radical monomer, TDDFT predicted a strong absorption at 526 nm (11^{2}E state with f = 0.32). This transition is dominated by a α,β-HOMO−1, HOMO−2 → LUMO ($e_g \rightarrow a_2$) excitations (44% total) but heavily complemented by the other single-electron excitations (Figure 7.2 and Table 7.5). The closeness of the TDDFT predicted and experimental fingerprint bands for monomeric [**7.1**]$^{+\bullet}$ and dimeric [**7.1**]$_2^{2+}$ is in excellent agreement with the experimental data,[43,44,57] which are indicative of the similarity of the fingerprint spectral region for the monomer and dimer. Moreover, the energetic closeness of the fingerprint band for the monomer and dimer fits also well with the "fingerprint" band observed for the oligomer in DCM (518 nm). Similar to the monomeric cation radical, there are two TDDFT-predicted candidates for the experimentally observed *A*-term at 422 nm. These were predicted at 454 nm (f = 0.03) and 409 nm (f = 0.05, Figure 7.2, Table 7.5). For the dimer, the experimentally observed transitions at 372, 319, and 276 nm correlate well with the TDDFT-calculated intense excited states predicted at 366 (f = 0.14), 303 (f = 0.31), and 283 (f = 0.23) nm (Table 7.5 and Figure 7.2). All of these transitions are localized on the same phthalocyanine macrocycle and have no

interligand charge-transfer character. Overall, the TDDFT results predicted for the dimer regarding the excited state energies and intensities which are responsible for the UV−vis and MCD spectral profile are very close to those observed for the monomeric [**7.1**]$^{+\bullet}$ compound in the UV-to-fingerprint band spectral envelope and are in good agreement with the experimental data. Thus, the use of hybrid exchange-correlation functionals, and in particular M05 and M06, allows for the accurate prediction of the UV−vis and MCD spectra of the phthalocyanine cation radical and its dimer and explains all of the major features that were experimentally observed in their UV−vis and MCD spectra.

7.4 Conclusions

In this report, the formation and aggregation of a chemically or spectroelectrochemically generated phthalocyanine cation radical was investigated using UV−vis and MCD spectroscopies. According to MCD spectroscopy, the NIR band at ∼1000 nm observed for the [**7.1**]$_2^{2+}$ dimer has no degeneracy, the monomer−dimeric equilibrium is temperature dependent, and higher degree aggregates can be formed at specific conditions. Sixteen different exchange-correlation functionals were tested to accurately predict the energies, intensities, and profiles of the UV−vis and MCD spectra of the phthalocyanine cation radical and its dimer. It was found that the M05 exchange-correlation functional provided an excellent agreement between theory and experiment for the phthalocyanine cation radical monomer and antiferromagnetically coupled dimer. Not only did this method correctly predict the nondegenerate excited states, monomer and dimer energies, and oscillator strengths, but it also correctly described the nature of the experimentally observed MCD *B*-term occurring in the

fingerprint region for both the monomeric and dimeric phthalocyanine cation radicals. The TDDFT data explains the similarities in the UV−vis and MCD spectra of the monomeric and dimeric species observed between the UV and fingerprint spectral envelopes, and correctly predicted the antiferromagnetic coupling between the two singly oxidized phthalocyanine macrocycles.

This work involved the spectral and theoretical evaluation of the zinc phthalocyanine cationic radical system and provided the preparation necessary to understand the phthalocyanine-based cationic radical systems that were expected to occur in the next two chapters (8 and 9). This [**7.1**]$^{+\bullet}$ system was purposefully prepared and observed using both a chemical oxidant and an electrochemical oxidation; therefore, phthalocyanine systems that are subjected to oxidation conditions may exhibit cationic radical formation which can generally be spectroscopically identified (via UV-vis) as a broad signal between the *B*- and *Q*-bands (between 450~550 nm) and/or a broad signal in the NIR region (between 950~1100 nm).

7.5 Experimental Section

7.5.1 Materials and Methods. All commercial reagents were ACS grade and were used without further purification. Tetrabutylammonium tetrakis(pentafluorophenyl)borate (TFAB, $(NBu_4)^+[B\text{-}(C_6F_5)_4]^-$)[85] was prepared according to the published procedure. The cationic radical monomer and neutral dimer mixture were chemically prepared on a spectroscopic scale by adding ~2mg of nitrosonium tetrafluoroborate to a solution of tetra-*tert*-butylated zinc(II) phthalocyanine in DCM, which was obtained from Sigma-Aldrich. All UV−vis data were obtained

on a JASCO-720 spectrophotometer at room temperature. A Jasco V-1500 and OLIS DCM 17 CD spectropolarimeter with a 1.2 T electro- or 1.4 T permanent magnet were used to obtain all magnetic circular dichroism (MCD) data. Spectroelectrochemical data were collected using a custom-made 1 mm cell, a working electrode made of platinum mesh, and a 0.15 M solution of TFAB in CH_2Cl_2.

7.5.2 Computational Details. All computations were performed using the Gaussian 09 software package running under the UNIX OS.[86] The molecular orbital contributions were compiled from single point calculations using the QMForge program.[87] The geometries were optimized using the B3LYP-D3 exchange-correlation functional and 6-31G basis set for zinc,[88] and 6-31G(d)[89] basis set for all other atoms. In a set of separate calculations, TDDFT was conducted using Wachters full-electron basis set for zinc[90] and 6-311G(d)[91] basis set for all other atoms. The frequencies were calculated for all optimized geometries in order to ensure that the final geometries represent minima on the potential energy surface. TDDFT calculations were conducted for the first 100 (monomer) or 200 (dimer) excited states, except only 80 excited states were considered for the dimer calculations with the 6-31+G(d) basis set used for carbon, nitrogen, and hydrogen atoms. For the final M05 calculations on the dimer, the first 280 states were considered. Solvent effects were modeled using a polarized continuum model (PCM) approach with DCM as a solvent. MCD spectra were simulated using the SOS approach.[92–95]

7.6 References

1. Gregory, P. Industrial applications of phthalocyanines. *J. Porphyrins Phthalocyanines* **2000**, *4*, 432−437.

2. Abrahamse, H.; Hamblin, M. R. New photosensitizers for photodynamic therapy. *Biochem. J.* **2016**, *473*, 347−364.

3. Nyokong, T. Desired properties of new phthalocyanines for photodynamic therapy. *Pure Appl. Chem.* **2011**, *83*, 1763−1779.

4. Garland, M. J.; Cassidy, C. M.; Woolfson, D.; Donnelly, R. F. Designing photosensitizers for photodynamic therapy: strategies, challenges and promising developments. *Future Med. Chem.* **2009**, *1*, 667−691.

5. Moreira, L. M.; dos Santos, F. V.; Lyon, J. P.; Maftoum-Costa, M.; Pacheco-Soares, C.; da Silva, N. S. Photodynamic Therapy: Porphyrins and Phthalocyanines as Photosensitizers. *Aust. J. Chem.* **2008**, *61*, 741−754.

6. Miller, J. D.; Baron, E. D.; Scull, H.; Hsia, A.; Berlin, J. C.; McCormick, T.; Colussi, V.; Kenney, M. E.; Cooper, K. D.; Oleinick, N. L. Photodynamic therapy with the phthalocyanine photosensitizer Pc 4: The case experience with preclinical mechanistic and early clinical-translational studies. *Toxicol. Appl. Pharmacol.* **2007**, *224*, 290−299.

7. Makarov, V. I.; Vasil'chenko, S. Yu.; Ryabova, A. V.; Konov, V. I.; Shevchenko, E. N.; Lukyanets, E. A.; Ermakov, A. E.; Loschenov, V. B. Photodynamic effect of iron(III) oxide nanoparticles coated with zinc phthalocyanine. *Russ. J. Gen. Chem.* **2015**, *85*, 338−340.

8. Lukyanets, E. A. Phthalocyanines as photosensitizers in the photodynamic therapy of cancer. *J. Porphyrins Phthalocyanines* **1999**, *3*, 424−432.

9. Singh, S.; Aggarwal, A.; Bhupathiraju, N. V. S. D. K.; Arianna, G.; Tiwari, K.; Drain, C. M. Glycosylated Porphyrins, Phthalocyanines, and Other Porphyrinoids for Diagnostics and Therapeutics. *Chem. Rev.* **2015**, *115*, 10261−10306.

10. Ogura, S.-I.; Tabata, K.; Fukushima, K.; Kamachi, T.; Okura, I. Development of phthalocyanines for photodynamic therapy. *J. Porphyrins Phthalocyanines* **2006**, *10*, 1116−1124.

11. Anaya-Plaza, E.; van de Winckel, E.; Mikkilae, J.; Malho, J.-M.; Ikkala, O.; Gulias, O.; Bresoli-Obach, R.; Agut, M.; Nonell, S.; Torres, T.; Kostiainen, M. A.; de la Escosura, A. Photoantimicrobial Biohybrids by Supramolecular Immobilization of Cationic Phthalocyanines onto Cellulose Nanocrystals. *Chem. - Eur. J.* **2017**, *23*, 4320−4326.

12. Biyiklioglu, Z.; Ozturk, I.; Arslan, T.; Tuncel, A.; Ocakoglu, K.; Hosgor-Limoncu, M.; Yurt, F. Synthesis and antimicrobial photodynamic activities of axially {4-[(1E)-3-oxo-3-(2-thienyl)prop-1-en-1- yl]phenoxy} groups substituted silicon phthalocyanine, subphthalocyanine on Gram-positive and Gram-negative bacteria. *Dyes Pigm.* **2019**, *166*, 149−158.

13. Chen, X.; Wu, S.; Ma, D.; Chen, J.; Guo, Q.; Han, X.; Chen, K.; Yang, H.; Huang, Y.; Peng, Y. A polyfluoroalkyl substituted phthalocyanine based supramolecular light switch for photothermal and photodynamic antibacterial activity against Escherichia coli. *Chem. Commun.* **2018**, *54*, 13279−13282.

14. Li, Z.; Li, B.; Yang, J.; Hou, J. G. Single-Molecule Chemistry of Metal Phthalocyanine on Noble Metal Surfaces. *Acc. Chem. Res.* **2010**, *43*, 954−962.

15. Gao, P.; Konrad, D.; Aghazada, S.; Nazeeruddin, M. K. Molecular engineering of functional materials for energy and optoelectronic applications. *Chimia* **2015**, *69*, 253−263.

16. Hasobe, T. Phthalocyanine-Nanocarbon Ensembles: Supramolecular assemblies of porphyrin and phthalocyanine derivatives for solar energy conversion and molecular electronics. In Handbook of Porphyrin Science: Kadish, K. M.; Smith, K. M.; Guilard, R., Eds.; World Scientific: Singapore, 2014; Vol. 34, pp 147−194.

17. Bottari, G.; de la Torre, G.; Guldi, D. M.; Torres, T. Covalent and Noncovalent Phthalocyanine-Carbon Nanostructure Systems: Synthesis, Photoinduced Electron Transfer, and Application to Molecular Photovoltaics. *Chem. Rev.* **2010**, *110*, 6768−6816.

18. McKeown, N. B. Out of the blue. *Chemistry & Industry* **1999**, *No. 3*, 92−98.

19. Afanasiev, P.; Sorokin, A. B. μ-NitridoDiiron Macrocyclic Platform: Particular Structure for Particular Catalysis. *Acc. Chem. Res.* **2016**, *49*, 583−593.

20. Sorokin, A. B. Phthalocyanine Metal Complexes in Catalysis. *Chem. Rev.* **2013**, *113*, 8152−8191.

21. Woehrle, D.; Suvorova, O.; Gerdes, R.; Bartels, O.; Lapok, L.; Baziakina, N.; Makarov, S.; Slodek, A. Efficient oxidations and photooxidations with molecular oxygen using metal phthalocyanines as catalysts and photocatalysts. *J. Porphyrins Phthalocyanines* **2004**, *8*, 1020−1041.

22. Zagal, J. H. Metallophthalocyanines as catalysts in electrochemical reactions. *Coord. Chem. Rev.* **1992**, *119*, 89−136.

23. Kudrik, E. V.; Sorokin, A. B. Oxidation of aliphatic and aromatic C-H bonds by t-BuOOH catalyzed by μ-nitridodiironphthalocyanine. *J. Mol. Catal. A: Chem.* **2017**, *426*, 499−505.

24. Geraskin, I. M.; Pavlova, O.; Neu, H. M.; Yusubov, M. S.; Nemykin, V. N.; Zhdankin, V. V. Comparative reactivity of hypervalent iodine oxidants in metalloporphyrin-catalyzed oxygenation of hydrocarbons: iodosylbenzene sulfate and 2-iodylbenzoic acid ester as safe and convenient alternatives to iodosylbenzene. *Adv. Synth. Catal.* **2009**, *351*, 733−737.

25. Neu, H. M.; Zhdankin, V. V.; Nemykin, V. N. Binuclear iron(III) phthalocyanine(μ-oxodimer)/tetrabutylammoniumoxone: a powerful catalytic system for oxidation of hydrocarbons in organic solution. *Tetrahedron Lett.* **2010**, *51*, 6545−6548.

26. Minor, P. C.; Gouterman, M.; Lever, A. B. P. Electronic spectra of phthalocyanine radical anions and cations. *Inorg. Chem.* **1985**, *24*, 1894−1900.

27. Silver, J.; Lukes, P.; Houlton, A.; Howe, S.; Hey, P.; Ahmet, M. T. Electrochromism in the transition-metal phthalocyanines. Part 3. Molecular organization, reorganization and assembly under the influence of an applied electric field. Response of [Fe(pc)] and [Fe(pc)Cl]. *J. Mater. Chem.* **1992**, *2*, 849−855.

28. Alexiou, C.; Lever, A. B. P. Tuning metalloporphyrin and metallophthalocyanine redox potentials using ligand electrochemical (E_L) and Hammett (σ_p) parametrization. *Coord. Chem. Rev.* **2001**, *216−217*, 45−54.

29. Homborg, H. Preparation and characterization of phthalocyanine π-cation radicals of hydrogen ion, magnesium(2+), and copper(2+). *Z. Anorg. Allg. Chem.* **1983**, *507*, 35−50.

30. Homborg, H.; Kalz, W. Phthalocyanines of cobalt(III): preparation and resonance-Raman, infrared, and electronic absorption spectra of [CoX2Pc(1-)] (X = Cl, Br) and [CoX2Pc(2-)]- (X = OH, F, Cl, Br). Z. *Naturforsch., B: J. Chem. Sci.* **1984**, *39B*, 1490−1499.

31. Nyokong, T.; Gasyna, Z.; Stillman, M. J. Photochemical formation of ruthenium phthalocyanine π-cation radical species. *Inorg. Chim. Acta* **1986**, *112*, 11−15.

32. Moubaraki, B.; Ley, M.; Benlian, D.; Sorbier, J. P. Structure and single-crystal conductivity measurements of oxidized 3d metal phthalocyanines: bis-chloro derivatives of chromium(III), Iron(III) and cobalt(III). *Acta Crystallogr., Sect. C: Cryst. Struct. Commun.* **1990**, *46*, 379−385.

33. Pakhomov, G. L.; Pokhomov, L. G.; Bagrov, A. M. Interaction of NO2 with thin films of cobalt phthalocyanines. *KhimicheskayaFizika* **1995**, *14*, 108−117.

34. Doppagne, B.; Chong, M. C.; Bulou, H.; Boeglin, A.; Scheurer, F.; Schull, G. Electrofluorochromism at the single-molecule level. *Science* **2018**, *361*, 251−255.

35. Liu, Y.; He, B.; Duan, J.; Zhao, Y.; Ding, Y.; Tang, M.; Chen, H.; Tang, Q. Poly(3-hexylthiophene)/zinc phthalocyanine composites for advanced interface engineering of 10.03%-efficiency $CsPbBr_3$ perovskite solar cells. *J. Mater. Chem. A* **2019**, *7*, 12635−12644.

36. Gobeze, H. B.; Tram, T.; Kc, C. B.; Cantu, R. R.; Karr, P. A.; D'Souza, F. Singlet Oxygen Generation and Photoinduced Charge Separation of Tetra Polyethyleneglycol Functionalized Zinc Phthalocyanine-Fullerene Dyad. *Chin. J. Chem.* **2016**, *34*, 969−974.

37. Sekita, M.; Ballesteros, B.; Diederich, F.; Guldi, D. M.; Bottari, G.; Torres, T. Intense Ground-State Charge-Transfer Interactions in Low-Bandgap, Panchromatic Phthalocyanine-Tetracyanobuta-1,3- diene Conjugates. *Angew. Chem., Int. Ed.* **2016**, *55*, 5560−5564.

38. Lederer, M.; Hahn, U.; Strub, J.-M.; Cianferani, S.; Van Dorsselaer, A.; Nierengarten, J.-F.; Torres, T.; Guldi, D. M. Probing Supramolecular Interactions between a Crown Ether-Appended Zinc Phthalocyanine and an Ammonium Group Appended to a C60 Derivative. *Chem. - Eur. J.* **2016**, *22*, 2051−2059.

39. Kirner, S. V.; Henkel, C.; Guldi, D. M.; Megiatto, J. D., Jr.; Schuster, D. I. Multistep energy and electron transfer processes in novel rotaxane donor-acceptor hybrids generating microsecond-lived charge separated states. *Chem. Sci.* **2015**, *6*, 7293−7304.

40. Arero, J.; Kodis, G.; Schmitz, R. A.; Mendez-Hernandez, D. D.; Moore, T. A.; Moore, A. L.; Gust, D. Design, synthesis and photophysical studies of phenylethynyl-bridged phthalocyanine-fullerene dyads. *J. Porphyrins Phthalocyanines* **2015**, *19*, 934−945.

41. Ikeuchi, T.; Agrawal, S.; Ezoe, M.; Mori, S.; Kimura, M. Enhanced Charge Separation Efficiency in Pyridine-Anchored Phthalocyanine-Sensitized Solar Cells by Linker Elongation. *Chem. - Asian J.* **2015**, *10*, 2347−2351.

42. Kawashima, Y.; Ohkubo, K.; Blas-Ferrando, V. M.; Sakai, H.; Font-Sanchis, E.; Ortiz, J.; Fernandez-Lazaro, F.; Hasobe, T.; Sastre-Santos, A.; Fukuzumi, S. Near-Infrared Photoelectrochemical Conversion via Photoinduced Charge Separation in Supramolecular Complexes of Anionic Phthalocyanines with Li+@C60. *J. Phys. Chem. B* **2015**, *119*, 7690−7697.

43. Ough, E.; Gasyna, Z.; Stillman, M. J. Photochemical, electrochemical, and chemical formation of the π-cation-radical species of magnesium phthalocyanine. Analysis of the absorption and MCD spectra of $[MgPc(-1)]^{\bullet+}$. *Inorg. Chem.* **1991**, *30*, 2301− 2310.

44. McKearney, D.; Choua, S.; Zhou, W.; Ganga-Sah, Y.; Ruppert, R.; Wytko, J. A.; Weiss, J.; Leznoff, D. B. Ring-Oxidized Zinc(II) Phthalocyanine Cations: Structure, Spectroscopy, and Decomposition Behavior. *Inorg. Chem.* **2018**, *57*, 9644−9655.

45. Homborg, H.; Teske, C. L. Lithium phthalocyanines: preparation and characterization of the monoclinic and tetragonal modifications of LiPc(1-) and the halogen adducts LiPc(1-)X (X = Cl, Br, I). *Z. Anorg. Allg. Chem.* **1985**, *527*, 45−61.

46. Nemykin, V. N.; Chernii, V. Y.; Volkov, S. V. Synthesis and characterization of new mixed-ligand lanthanide-phthalocyanine cation radical complexes. *J. Chem. Soc., Dalton Trans.* **1998**, *No. 18*, 2995−3000.

47. Majeed, S. A.; Ghazal, B.; Nevonen, D. E.; Goff, P. C.; Blank, D. A.; Nemykin, V. N.; Makhseed, S. Evaluation of the Intramolecular Charge-Transfer Properties in Solvatochromic and Electrochromic Zinc Octa(carbazolyl)phthalocyanines. *Inorg. Chem.* **2017**, *56*, 11640−11653.

48. Ou, Z.; Zhan, R.; Tomachynski, L. A.; Chernii, V. Ya.; Kadish, K. M. Electrochemistry and spectroelectrochemistry of zirconium(IV) and hafnium(IV) phthalocyanines with β-diketone axial ligands in nonaqueous media. *Makrogeterotsikly* **2011**, *4*, 164−170.

49. Ou, Z.; Jiang, Z.; Chen, N.; Huang, J.; Shen, J.; Kadish, K. M. Electrochemistry and spectroelectrochemistry of tetra-α-substituted metallophthalocyanines. *J. Porphyrins Phthalocyanines* **2008**, *12*, 1123−1133.

50. Stillman, M.; Mack, J.; Kobayashi, N. Theoretical aspects of the spectroscopy of porphyrins and phthalocyanines. *J. Porphyrins Phthalocyanines* **2002**, *6*, 296−300.

51. Mack, J.; Stillman, M. J. Transition Assignments in the Ultraviolet-Visible Absorption and Magnetic Circular Dichroism Spectra of Phthalocyanines. *Inorg. Chem.* **2001**, *40*, 812−814.

52. Stillman, M. Formation and electronic properties of ring-oxidized and ring-reduced radical species of the phthalocyanines and porphyrins. *J. Porphyrins Phthalocyanines* **2000**, *4*, 374−376.

53. Banfi, S.; Cavazzini, M.; Pozzi, G.; Barkanova, S. V.; Kaliya, O. L. Kinetic studies on the interactions of manganese-porphyrins with peracetic acid. Part 2. The influence of acetic acid and porphyrin substituents. *J. Chem. Soc. Perkin Trans 2* **2000**, *No. 4*, 879−885.

54. Nyokong, T. Cyclic voltammetry and spectroelectrochemistry of rhodium phthalocyanines. *J. Chem. Soc., Dalton Trans.* **1994**, *No. 9*, 1359−1365.

55. Manivannan, V.; Nevin, W. A.; Leznoff, C. C.; Lever, A. B. P. Electrochemistry and spectroelectrochemistry of polynuclear zinc phthalocyanines: formation of mixed valence cation radical species. *J. Coord. Chem.* **1988**, *19*, 139−158.

56. Nyokong, T.; Gasyna, Z.; Stillman, M. J. Phthalocyanine π cation-radical species: photochemical and electrochemical preparation of $[ZnPc(-1)]^{\bullet+}$ in solution. *Inorg. Chem.* **1987**, *26*, 548−553.

57. Nyokong, T.; Gasyna, Z.; Stillman, M. J. Analysis of the absorption and magnetic circular dichroism spectra of zinc phthalocyanine and the π-cation-radical species $[ZnPc(1-)]^{\bullet+}$. *Inorg. Chem.* **1987**, *26*, 1087−1095.

58. Rosa, A.; Ricciardi, G. A time-dependent density functional theory (TDDFT) interpretation of the optical spectra of zinc phthalocyanine π-cation and π-anion radicals. *Can. J. Chem.* **2009**, *87*, 994−1005.

59. Mack, J.; Kobayashi, N.; Stillman, M. J. Magnetic circular dichroism spectroscopy and TD-DFT calculations of metal phthalocyanine anion and cation radical species. *J. Porphyrins Phthalocyanines* **2006**, *10*, 1219−1237.

60. Ishikawa, N.; Ohno, O.; Kaizu, Y. Electronic states of bis(phthalocyaninato)lutetium radical and its related compounds: the application of localized orbital basis set to open-shell phthalocyanine dimers. *J. Phys. Chem.* **1993**, *97*, 1004−1010.

61. Ishikawa, N.; Kaizu, Y. Disappearance of MCD *A* term in the fingerprint band of cation radicals of phthalocyanine metal complexes. *Chem. Phys. Lett.* **2001**, *339*, 125−132.

62. Ishikawa, N.; Maurice, D.; Head-Gordon, M. An ab initio study of excited states of the phthalocyanine magnesium complex and its cation radical. *Chem. Phys. Lett.* **1996**, *260*, 178−185.

63. Tiedemann, M. T.; Stillman, M. J. Application of magnetic circular dichroism spectroscopy to porphyrins, phthalocyanines and hemes. *J. Porphyrins Phthalocyanines* **2011**, *15*, 1134−1149.

64. Gasyna, Z.; Nyokong, T.; Stillman, M. J. Photooxidation of phthalocyanines. Photoinduced reactivity of the triplet state. *ACS Symp. Ser.* **1986**, *321*, 309−327.

65. Becke, A. D. Density-functional thermochemistry. III. The role of exact exchange. *J. Chem. Phys.* **1993**, *98*, 5648−5652.

66. Yanai, T.; Tew, D.; Handy, N. A new hybrid exchange-correlation functional using the Coulomb-attenuating method (CAM-B3LYP). *Chem. Phys. Lett.* **2004**, *393*, 51−57.

67. Nemykin, V. N.; Hadt, R. G.; Belosludov, R. V.; Mizuseki, H.; Kawazoe, Y. Influence of Molecular Geometry, Exchange-Correlation Functional, and Solvent Effects in the Modeling

of Vertical Excitation Energies in Phthalocyanines Using Time-Dependent Density Functional Theory (TDDFT) and Polarized Continuum Model TDDFT Methods: Can Modern Computational Chemistry Methods Explain Experimental Controversies? *J. Phys. Chem. A* **2007**, *111*, 12901− 12913.

68. Nemykin, V. N.; Sabin, J. R. Profiling Energetics and Spectroscopic Signatures in PrototropicTautomers of Asymmetric Phthalocyanine Analogues. *J. Phys. Chem. A* **2012**, *116*, 7364−7371.

69. Gao, Y.; Nemykin, V. N. Modeling of the energies and splitting of the Qx and Qy bands in positional isomers of zinc pyridinoporphyrazines by TDDFT approach: Can TDDFT help distinguishing the structural isomers? *J. Mol. Graphics Modell.* **2013**, *42*, 73−80.

70. Belosludov, R. V.; Nevonen, D. E.; Rhoda, H. M.; Sabin, J. R.; Nemykin, V. N. Simultaneous Prediction of the Energies of Qx and Qy Bands and Intramolecular Charge-Transfer Transitions in Benzoannulated and Non-Peripherally Substituted Metal-Free Phthalocyanines and Their Analogues: No Standard TDDFT Silver Bullet Yet. *J. Phys. Chem. A* **2019**, *123*, 132−152.

71. Martynov, A. G.; Mack, J.; May, A. K.; Nyokong, T.; Gorbunova, Y. G.; Tsivadze, A. Y. Methodological Survey of Simplified TD-DFT Methods for Fast and Accurate Interpretation of UV-Vis-NIR Spectra of Phthalocyanines. *ACS Omega* **2019**, *4*, 7265−7284.

72. Becke, A. D. Density-functional exchange-energy approximation with correct asymptotic-behavior. *Phys. Rev. A: At., Mol., Opt. Phys.* **1988**, *38*, 3098−3100.

73. Perdew, J. P. Density-functional approximation for the correlation energy of the inhomogeneous electron gas. *Phys. Rev. B: Condens. Matter Mater. Phys.* **1986**, *33*, 8822−8824.

74. Tao, J. M.; Perdew, J. P.; Staroverov, V. N.; Scuseria, G. E. Climbing the density functional ladder: Nonempirical meta-generalized gradient approximation designed for molecules and solids. *Phys. Rev. Lett.* **2003**, *91*, 146401/1-146401/4.

75. Adamo, C.; Barone, V. Toward reliable density functional methods without adjustable parameters: The PBE0 model. *J. Chem. Phys.* **1999**, *110*, 6158−6169.

76. Heyd, J.; Scuseria, G. Efficient hybrid density functional calculations in solids: The HS-Ernzerhof screened Coulomb hybrid functional. *J. Chem. Phys.* **2004**, *121*, 1187−1192.

77. Zhao, Y.; Truhlar, D. G. The M06 suite of density functionals for main group thermochemistry, thermochemical kinetics, non-covalent interactions, excited states, and transition elements: two new functionals and systematic testing of four M06-class functionals and 12 other functionals. *Theor. Chem. Acc.* **2008**, *120*, 215−241.

78. Zhao, Y.; Schultz, N. E.; Truhlar, D. G. Exchange-Correlation Functionals with Broad Accuracy for Metallic and Nonmetallic Compounds, Kinetics, and Noncovalent Interactions. *J. Chem. Phys.* **2005**, *123*, 161103/1-161103/4.

79. Zhao, Y.; Truhlar, D. G. Hybrid Meta Density Functional Theory Methods for Thermochemistry, Thermochemical Kinetics, and Noncovalent Interactions: The MPW1B95

and MPWB1K Models and Comparative Assessments for Hydrogen Bonding and van der Waals Interactions. *J. Phys. Chem. A* **2004**, *108*, 6908−6918.

80. Peverati, R.; Truhlar, D. G. Communication: A Global Hybrid Generalized Gradient Approximation to the Exchange-Correlation Functional that Satisfies the Second-Order Density-Gradient Constraint and Has Broad Applicability in Chemistry. *J. Chem. Phys.* **2011**, *135*, 191102/1-191102/4.

81. Zhao, Y.; Gonzalez-García, N.; Truhlar, D. G. Benchmarḱ Database of Barrier Heights for Heavy Atom Transfer, Nucleophilic Substitution, Association, and Unimolecular Reactions and Their Use to Test Density Functional Theory. *J. Phys. Chem. A* **2005**, *109*, 2012−2018.

82. Boese, A. D.; Martin, J. M. L. Development of Density Functionals for Thermochemical Kinetics. *J. Chem. Phys*. **2004**, *121*, 3405−3416.

83. Peverati, R.; Truhlar, D. G. Improving the Accuracy of Hybrid Meta-GGA Density Functionals by Range Separation. *J. Phys. Chem. Lett.* **2011**, *2*, 2810−2817.

84. Chai, J.-D.; Head-Gordon, M. Long-range corrected hybrid density functionals with damped atom-atom dispersion corrections. *Phys. Chem. Chem. Phys.* **2008**, *10*, 6615−6620.

85. Barriere, F.; Geiger, W. E. Use of Weakly Coordinating Anions to Develop an Integrated Approach to the Tuning of ΔE1/2 Values by Medium Effects. *J. Am. Chem. Soc.* **2006**, *128*, 3980−3989.

86. Frisch, M. J.; Trucks, G. W.; Schlegel, H. B.; Scuseria, G. E. et al. Gaussian 09, Revision D.1; Gaussian, Inc.: Wallingford, CT, 2009. For full citation, see Supporting Information.

87. Tenderholt, A. L. QMForge, Version 2.1; Stanford University: Stanford, CA, USA.

88. Rassolov, V. A.; Pople, J. A.; Ratner, M. A.; Windus, T. L. 6- 31G* Basis Set for Atoms K Through Zn. *J. Chem. Phys.* **1998**, *109*, 1223−1229.

89. Ditchfield, R.; Hehre, W. J.; Pople, J. A. Self-Consistent Molecular Orbital Methods. 9. Extended Gaussian-Type Basis for Molecular-Orbital Studies of Organic Molecules. *J. Chem. Phys.* **1971**, *54*, 724−728.

90. Wachters, A. J. H. Gaussian Basis Set for Molecular Wavefunctions Containing Third-Row Atoms. *J. Chem. Phys.* **1970**, *52*, 1033−1036.

91. Godbout, N.; Salahub, D. R.; Andzelm, J.; Wimmer, E. Optimization of Gaussian-type basis sets for local spin density functional calculations. Part I. Boron through neon, optimization technique and validation. *Can. J. Chem.* **1992**, *70*, 560−571.

92. Andrushchenko, V.; Padula, D.; Zhivotova, E.; Yamamoto, S.; Bour, P. Magnetic Circular Dichroism of Porphyrin Lanthanide M3+ Complexes. *Chirality* **2014**, *26*, 655−662.

93. Stepanek, P.; Bour, P. Computation of magnetic circular dichroism by sum over states summations. *J. Comput. Chem.* **2013**, *34*, 1531−1539.

94. Stepanek, P.; Andrushchenko, V.; Ruud, K.; Bour, P. Porphyrin protonation studied by magnetic circular dichroism. *J. Phys. Chem. A* **2012**, *116*, 778−783.

95. Stepanek, P.; Bour, P. Origin-independent sum over states simulations of magnetic and electronic circular dichroism spectra via the localized orbital/local origin method. *J. Comput. Chem.* **2015**, *36*, 723−730.

8. Application of Lever's E_L Parameters Scale Toward Fe(II)/Fe(III) Versus Pc(2-)/Pc(1-) Oxidation Process Crossover Point in Axially Coordinated Iron(II) Phthalocyanine Complexes

8.1 Chapter Preface

This chapter maintains the electronic structure investigation of hard chromophoric systems; specifically, the iron(II) phthalocyanine system where the central iron atom will be axially coordinated with two ligands (one on each of the two open iron coordination sites). This work involves the manipulation of both the iron d-orbitals and the phthalocyanine (Pc) frontier core orbitals which is achieved by varying the electronic and steric nature of the coordinated ligands. The rational here is that ligation of the central metal atom could possibly introduce charge transfer states which would influence the ΔHOMO and ΔLUMO values. As indicated by the chapter title, oxidation of these systems results in various outcomes where, depending on the electronic and steric nature of the coordinated ligands, either the central iron atom will be oxidized or the Pc core will undergo the oxidation. An additional focus herein is to consider

Lever's E_L parameter scale and to identify some previously unidentified correlations such as the "crossover point" where, relative to the value of $\Sigma E_L(L_{ax})$ for each system, this would represent the $\Sigma E_L(L_{ax})$ value which separates the preference for Fe(II)/Fe(III) vs. Pc(2-)/Pc(1-) oxidation. The work involving the cationic zinc phthalocyanine radical system presented in the previous chapter (7) provides a prime example of what to spectroscopically expect when the phthalocyanine core becomes oxidized.

8.2 Introduction

In 1990, Lever introduced the electrochemistry-based additive E_L scale, which was established using the metal-centered oxidation or reduction potentials of transition-metal complexes.[1-4] In this scale, the E_L values for each ligand reflect their cumulative σ-donor, π-acceptor/donor and steric properties that stabilize or destabilize the metal-centered orbitals in an additive way. The tabulated E_L parameters then allow for the prediction of oxidation potentials for metal-centered processes using equation 8.1 where S_M and I_M are metal- and spin-state dependent scaling and offset factors, respectively.[1]

$$E_{1/2} = S_M \Sigma E_L(L) + I_M \quad (8.1)$$

Lever also later demonstrated that the electrochemical potential for the Fe^{II}/Fe^{III} oxidation couple could be predicted for a limited number of six-coordinate iron phthalocyanine ($PcFe^{II}$) complexes, with the general formula $PcFe^{II}L_2$ and $[PcFe^{II}X_2]^{2-}$, using equation 8.2:[4]

$$E_{1/2} = S_M \Sigma E_L(L_{ax}) + I_M \quad (8.2)$$

where only the E_L values of the axial ligands ($E_L(L_{ax})$) were needed.

In light of Lever's work and the considerable academic and industrial interest surrounding iron phthalocyanine ($PcFe^{II}$) derivatives[5-11] this work focuses on expanding the already rich chemistry of these complexes. Indeed, iron phthalocyanine complexes have been studied as catalysts for C-H bond activation,[12-22] electrocatalysts for the oxygen reduction reaction,[23-25] active components for catalytic cancer therapy,[26,27] platforms for optical detection of small molecules,[28-32] and composite materials for electrochemical detection of biologically relevant species.[33-36] The axial coordination of nitrogen bases,[37-58] phosphines and phosphites,[59-63] nitroso compounds,[61] sulfoxides and sulfides,[64-66] carbon monoxide,[65-67] and isonitriles[68-74] to iron(II) phthalocyanine was studied by UV-visible, NMR, and Mössbauer spectroscopies as well as by crystallography. Based on early electrochemical,[75] spectroelectrochemical,[76] chemical,[76,77] and photochemical[76] oxidation data, it was always assumed that the highest occupied molecular orbital (HOMO) in the six-coordinate $PcFe^{II}L_2$, $PcFe^{II}L'L''$ and $[PcFe^{II}X_2]^{2-}$ complexes (where L, L', and L'' are neutral and X^- are anionic axial ligands) is comprised of the iron(II)-centered d_π or d_{xy} orbital and, thus, it was also assumed that the first oxidation process led to formation of the respective iron(III) products; however, we have recently shown[69] that the spectroelectrochemical or chemical oxidation of the six-coordinate isonitrile complexes, $PcFe^{II}(CNR)_2$ where R = *t*-Bu or ferrocene (Fc), results in the formation of the $[Pc(1-)Fe^{II}(CNR)_2]^{+\bullet}$ species which have UV-vis and EPR spectra that are characteristic of a phthalocyanine cation-radical. This observation then leads to several interesting questions. First, can the energies of the occupied phthalocyanine-centered a_{1u} (in traditional Gouterman's notation for the D_{4h}

point group) and iron-centered d_π/d_{xy} orbitals in $PcFe^{II}L_2$, $PcFe^{II}L'L''$, and $[PcFe^{II}X_2]^{2-}$ complexes intercross? If this is the case, can Lever's E_L parameters scale[1-4] explain the experimental observations and predict an intercrossing point? Indeed, it is expected that the strong σ-donor axial ligands, which have low values of E_L, will destabilize the energies of the Fe(II) orbitals, while axial ligands with significant π-accepting character will stabilize the Fe(II) orbitals making the first oxidation process more prone to occur at the phthalocyanine macrocycle as opposed to metal-centered electron abstraction. A simple diagram depicting the effect of σ-donating and π-accepting axial ligands on the metal-centered (d_π/d_{xy}) and phthalocyanine centered (a_{1u}) HOMO/HOMO-1 orbitals is shown in Scheme 8.1 where the possible intercrossing point (*i.e.* change in site of electron transfer) is labeled.

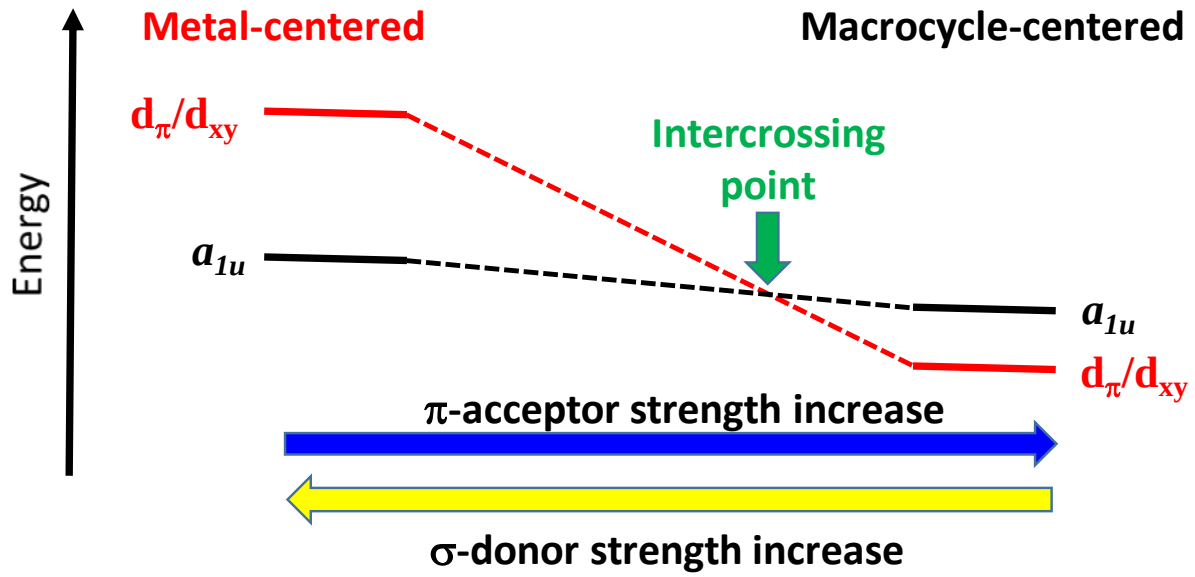

Scheme 8.1. Schematic energy diagram showing the effect of σ-donor and π-acceptor axial ligands on the HOMO/HOMO-n of the phthalocyanine/macrocycle (a_{1u}) and metal-centered (d_π/d_{xy}) orbitals.

In order to answer the above mentioned questions, we have conducted a systematic analysis of the electrochemical and spectroelectrochemical data on a large range of the $PcFe^{II}L_2$, $PcFe^{II}L'L''$, and $[PcFe^{II}X_2]^{2-}$ complexes with a wide variety of axial ligands ranging from pure σ-donors to strong π-acceptors (Chart 8.1, Table 8.1) and provide detailed density functional theory (DFT) predictions which support the experimental results. Such a systematic analysis allows for the first-time rationalization of the spectroscopic and redox behavior of these systems with respect to the scale of Lever's E_L ligand parameters.

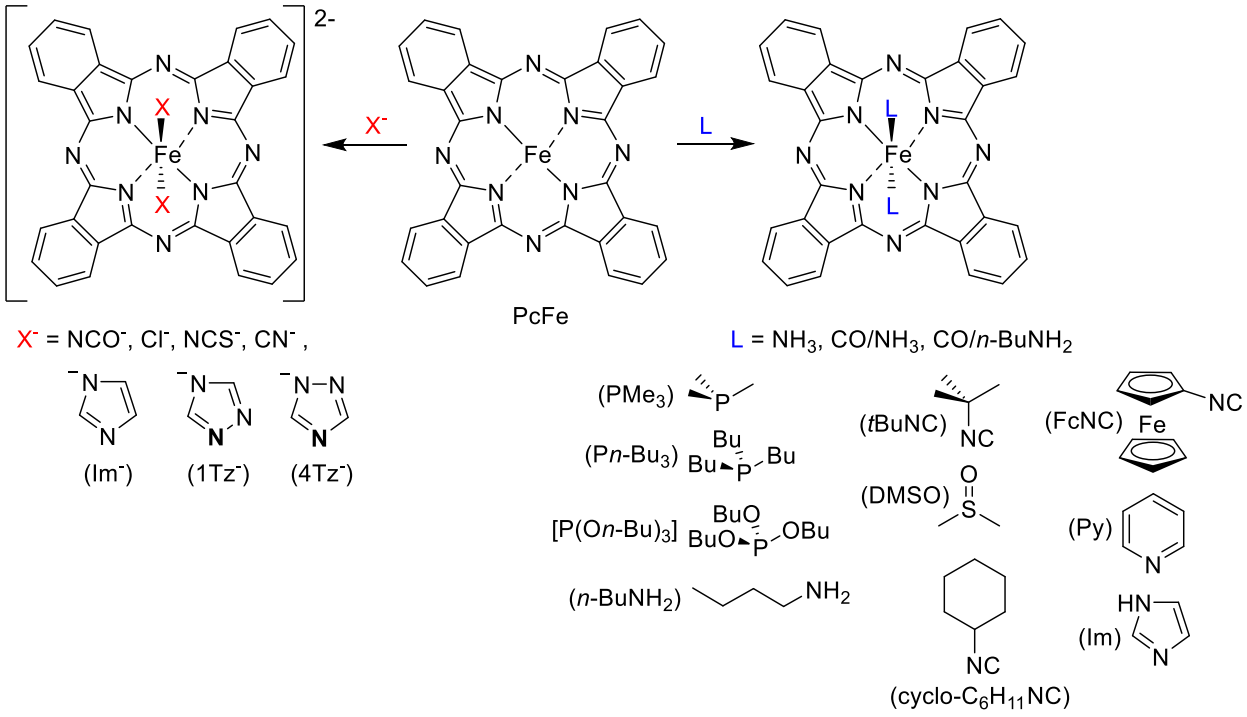

Chart 8.1. Structures of the phthalocyanine complexes discussed in this report.

Table 8.1. Compound abbreviation/numbering scheme.

Compound abbreviation	*Compound number*
$[PcFe^{II}(NCO)_2]^{2-}$	**8.1**
$[PcFe^{II}(Im)_2]^{2-}$	**8.2**
$[PcFe^{II}(Tz)_2]^{2-}$	**8.3**
$[PcFe^{II}(1\text{-}Tz)_2]^{2-}$	**8.3.1**
$[PcFe^{II}(4\text{-}Tz)_2]^{2-}$	**8.3.2**
$[PcFe^{II}(NCS)_2]^{2-}$	**8.4**
$[PcFe^{II}(CN)_2]^{2-}$	**8.5**
$PcFe^{II}Im_2$	**8.6**
$PcFe^{II}(n\text{-}BuNH_2)_2$	**8.7**
$PcFe^{II}Py_2$	**8.8**
$PcFe^{II}(Pn\text{-}Bu_3)_2$	**8.9**
$PcFe^{II}(PMe_3)_2$	**8.10**
$PcFe^{II}[P(On\text{-}Bu)_3]_2$	**8.11**
$PcFe^{II}(DMSO)_2$	**8.12**
$PcFe^{II}(CO)(n\text{-}BuNH_2)$	**8.13**
$[PcFe^{II}(Cl)_2]^{2-}$	**8.14**
$PcFe^{II}(NH_3)_2$	**8.15**
$PcFe^{II}(t\text{BuNC})_2$	**8.16**
$PcFe^{II}[P(OMe)_3]_2$	**8.17**
$PcFe^{II}(CO)(NH_3)$	**8.18**

8.3 Results and Discussion

8.3.1 Electrochemistry. The multifaceted electrochemical approach for the reported $PcFe^{II}L_2$, $PcFe^{II}L'L''$, and $[PcFe^{II}X_2]^{2-}$ complexes includes expanding the established relationship between Lever's E_L scale (*vide supra*) and the Fe^{II}/Fe^{III} oxidation couple[4] given by equation 8.2 where the relevant E_L parameters for the various ligands of interest in this study are listed in Table 8.2. The more negative the E_L value, the more destabilized the occupied iron-centered d_π and d_{xy} orbitals in $PcFe^{II}L_2$, $PcFe^{II}L'L''$, and $[PcFe^{II}X_2]^{2-}$ complexes should be while more positive E_L values should result in more stabilized iron-centered orbitals (Scheme 8.1). Although Lever reported the first oxidation potential for iron(II) phthalocyanine in pyridine and DMSO (which effectively belongs to the $PcFe^{II}Py_2$ and $PcFe^{II}(DMSO)_2$ complexes) back in 1978,[75] to the best of our knowledge, a limited number of oxidation potentials for $PcFe^{II}L_2$, $PcFe^{II}L'L''$, and $[PcFe^{II}X_2]^{2-}$ have been reported to date (see summary in Table 8.3) and many classes of axial ligands with these type of macrocycles remain completely unexplored *via* systematic electrochemical studies.

Table 8.2. E_L values for the axial ligands of interest.

$L/L'/X^-$	E_L	$L/L'/X^-$	E_L
NCO^-	-0.25[a]	*n*-$BuNH_2$	0.13[a]
Cl^-	-0.24[a]	Py	0.25[a]
Im^-	-0.23[b]	PBu_3	0.29[a]
Br^-	-0.22[a]	cyclo-$C_6H_{11}NC$	0.32[a]
Tz^-	-0.17[a]	PMe_3	0.33[a]
SCN^-	-0.06[a]	*t*-BuNC	0.36[a]

CN^-	0.02[a]	FcNC	0.41[e]
DMF	0.03[c]	$P(OBu)_3$	0.42[a,f]
DMA	0.03[d]	DMSO	0.47[a]
NH_3	0.07[a]	CO	0.99[a]
Im	0.12[a]		

[a] Ref. 1; [b] estimated on the basis of constant difference in Tz/Tz^- and $BzIm/BzIm^-$ (benzimidazole/benzimidazolate) pairs from Ref. 1; [c] Ref. 3; [d] assumed to be equal to the E_L value of DMF (Ref. 4); [e] estimated based on the redox properties in the series of chromium compounds from Ref. 1, 78, 79, and 80; [f] assumed to be equal to the E_L value in $P(OMe)_3$ (Ref. 1).

Table 8.3. Oxidation potentials (vs SCE)[a] of $PcFe^{II}L_2$, $PcFe^{II}L'L''$, and $[PcFe^{II}X_2]^{2-}$ complexes.

L/L'/X^-	Σ E_L	Redox Potential, V (SCE)			Solvent	Electrolyte[a]	Ref.
		Ox₁	*Ox₂*	*Ox₃*			
NCO^-	-0.5	-0.09[b,c]	0.07[d]		DMF	$KNCO_{(sat.)}$	*tw*[k]
		-0.10[b,c]			DMF	$KNCO_{(sat.)}$	*tw*[l]
Cl^- [e]	-0.48	-0.15[b]			DMA	LiCl	75
Im^-	-0.46	-0.06[c]	0.43		DMF	TBAP/NaH	*tw*
Tz^-	-0.34	-0.05[c]	0.06	0.16	DMF	TBAP	*tw*
Br^-/DMA[d]	-0.16	0.17[b]			DMA	TEABr	75
SCN^-	-0.12	0.20[b,c]			DMF	KSCN	*tw*
CN^-	0.04	0.30[c]	1.00		DMSO	TBAP	*tw*
		0.14[c]	0.93		acetone	TBAP	84
		0.14[b]	0.85		DCM	TBAP	85
		0.36[c]	1.16		ACN		86
DMF	0.06	0.24[b]			DMF	TBAP	87
DMA	0.06	0.38[b]			DMA	TEAP	75
DMSO/Cl^- [g]	0.23	0.35[b]			DMSO	LiCl	75
Im	0.24	0.32[c]	1.05	1.74[i]	DCM	TBAP	*tw*
		0.37[c]	1.06[i]		DMF	TBAP	*tw*
		0.60[c]	1.19		DMA	TPAP	76
dmso/Br^- [h]	0.25	0.39[b]			DMSO	TBABr	75
n-$BuNH_2$	0.26	0.48[c]	1.02		DCM	TBAP	*tw*

		0.47[c]	1.19	1.91[i]	DCM	TFAB	*tw*
		0.31[c]	1.01	1.53[i]	DMF	TBAP	*tw*
Py	0.5	0.68[c]	1.32[i]	1.53[i]	DCM	TFAB	*tw*
		0.64[b,c]			DCM/5%Py	TBAP	*tw*
		0.71[c]			Pyridine	TFAB	*tw*
		0.71[b,c]			Py	TBAP	*tw*
		0.70[b,c]	0.88[i]	1.12[i]	DMF/5%Py	TBAP	*tw*
		0.72[b]			Py	TBAP	87
		0.66[b]			Py	TEAP	75
		0.69[c]	0.88		DMA	TPAP	76
		0.69[b]	1.1		Py	TBAP	88
		0.76[c]			Py	TBAP	89
PBu_3	0.58	0.48[c]	1.23	1.71[i]	DCM	TBAP	*tw*
		0.51[c]	1.36		DCM	TFAB	*tw*
		0.52[c]	0.62[j]	1.09[i]	DMF	TBAP	*tw*
cyclo-$C_6H_{11}NC$	0.64	0.64[c]			o-DCB	TBAP	89
PMe_3	0.66	0.54[c]	1.19		DCM	TBAP	*tw*
		0.53[c]	0.64[j]	1.08[i]	DMF	TBAP	*tw*
t-BuNC	0.72	0.47[c]	1.33		DCM	TFAB	69
		0.45[c]	1.32		DCM	TBAP	69
FcNC	0.82	0.51[c]	0.94	1.02	DCM	TBAP	69
		0.51[c]	0.94	1.02	DCM	TFAB	69
$P(OBu)_3$	0.84[a]	0.47[c]	1.23		DCM	TBAP	*tw*
		0.61[c]	1.10[i]		DMF	TBAP	*tw*
DMSO	0.94	0.45[c]	0.87[i]		DMF	TBAP	*tw*
		0.46[b,c]			DMSO	TBAP	*tw*
		0.46[b]			DMSO	TEAP	75
		0.44[b]			DMSO	TBAP	87
		0.48[c]	0.85[i]		Cl-C_6H_5	TBAP	*tw*
n-$BuNH_2$/CO	1.12	0.72[c,i]	0.91[i]		DCM	TBAP	*tw*

[a] Electrolyte concentration is 0.1M unless mentioned in the text and the individual E_L values are provided in Table 8.1; all potentials reported for this work are measured within ±10 mV uncertainty; [b] were measured versus SCE as the reference; [c] were measured versus Fc/Fc^+, Fc^*/Fc^{*+}, or Ag/Ag^+ and adjusted to the SCE scale using known (ref. 78, 81-83) values or those determined in this work; [d] assigned to PcFe(NCO)(DMF) complex; [e] Assigned to $[PcFeCl_2]^{2-}$ complex; [f] Assigned to $[PcFe(DMA)Br]^-$ complex; [g] Assigned to $[PcFe(DMSO)Cl]^-$ complex; [h]

Assigned to $[PcFe(DMSO)Br]^-$ complex; [i] irreversible; [j] Assigned to aggregate species; [k] Cathodic direction scan; [l] Anodic direction scan; *tw* = this work.

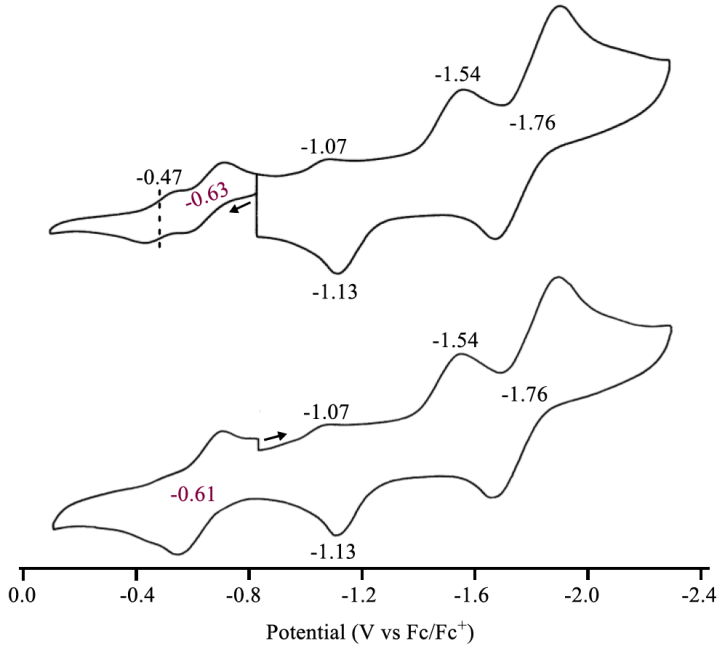

Figure 8.1. Cyclic voltammograms of $[PcFe(NCO)_2]^{2-}$ (**8.1**) complexes in DMF/$KNCO_{(sat.)}$ where the scan starting -0.86 V (vs Fc/Fc^+) was initiated in the anodic direction (top) and cathodic direction (bottom).

Thus, we have conducted cyclic voltammetry (CV) and differential pulse voltammetry (DPV) experiments on the $PcFe^{II}L_2$, $PcFe^{II}L'L''$, and $[PcFe^{II}X_2]^{2-}$ complexes with axial ligands possessing a wide range of E_L parameters (see Table 8.2) in several solvents and electrolytes. These data are discussed in order of increasing $\Sigma E_L(L_{ax})$ parameter starting from four anionic $[PcFe^{II}X_2]^{2-}$ complexes.

Our preliminary electrochemical data on the $[PcFe^{II}(NCO)_2]^{2-}$ (**8.1**) complex ($\Sigma E_L(L_{ax})$ = -0.5V) in DMF/0.1M TBAP/0.005M KNCO system (both $PcFe^{II}$ and **8.1** are not soluble in DCM) was indicative of an equilibrium between several redox-active species. Since some of those species might include $[PcFe^{II/III}(NCO)(ClO_4)]^{n-}$ and $[PcFe^{II/III}(DMF)(ClO_4)]^{n-}$, we have repeated the electrochemical CV and DPV experiments using exclusively saturated in DMF, KNCO as the supporting electrolyte (abbreviated as $DMF/KNCO_{(sat.)}$) to exclude the potential coordination of the other anions to the redox-active phthalocyanine species. Interestingly, in the $DMF/KNCO_{(sat.)}$ system, two closely spaced oxidation processes ($E_{1/2}$ = -0.47 and -0.63 V vs Fc/Fc^+) were observed at very negative potentials when the starting potential was set negative of the first oxidation and the scan was initiated in the anodic direction (top portion of Figure 8.1). A cathodic potential sweep (bottom portion of Figure 8.1) from the same starting potential (-0.86 V vs Fc/Fc^+) resulted in two cathodic peaks at -1.07 and -1.54 V followed by a reversible electron addition at -1.76 V. On the reverse potential sweep, an anodic peak located at -1.13 V was observed followed by one reversible oxidation at -0.61 V where the more positive of the two closely spaced oxidation processes seen in the top of Figure 8.1 is gone. The disappearance of the more positive oxidation wave on the reverse potential sweep and known ligand exchange reactions involving reduced iron phthalocyanines[84] suggest an equilibrium of two different ligated forms of PcFe in solution. Thus, we hypothesize that the two oxidation waves at $E_{1/2}$ = -0.47 and -0.63 V belong to the $[PcFe^{II/III}(NCO)(DMF)]^{n-}$ and $[PcFe^{II/III}(NCO)_2]^{n-}$ species, respectively. This hypothesis correlates well with Lever's proposal on the formation of hexacoordinated $[PcFe^{II/III}(X)(solv)]^{n-}$ and $[PcFe^{II/III}(X)_2]^{n-}$ species during the oxidation of iron(II)

phthalocyanine in organic solvents[75] as well as our spectroelectrochemical data discussed below.

Contrary to complex (**8.1**), the CV and DPV data on the $[PcFe^{II}(Im^{-})_2]^{2-}$ (**8.2**) compound ($\Sigma E_L(L_{ax})$ = -0.46V) collected in DMF shows no equilibrium or sensitivity to the nature of electrolyte as indicated by the two well-resolved reversible oxidation processes (Supporting Information Figure S8.1). These processes, along with the spectroelectrochemical data on this compound, indicate a lack of axial ligand(s) dissociation during the oxidation processes. Interestingly, in the case of the $[PcFe^{II}(Tz^{-})_2]^{2-}$ (**8.3**) complex ($\Sigma E_L(L_{ax})$ = -0.34V), there were three overlapping oxidation processes observed at fairly negative potentials (versus Fc/Fc^{+}) (Supporting Information Figure S8.2). These can be rationalized by the linkage isomerism expected for this compound. Indeed, our DFT calculations discussed below are indicative of close energy 1N and 4N linkage isomers (Chart 8.1) which can co-exist in solution and are responsible for the rather broad quadrupole splitting observed in the Mössbauer spectrum of complex **8.3**.[44] In our case, we speculate that the three overlapping oxidation waves belong to the $[PcFe^{II}(1N\text{-}Tz^{-})_2]^{2-}$, $[PcFe^{II}(4N\text{-}Tz^{-})_2]^{2-}$, and $[PcFe^{II}(1N\text{-}Tz^{-})(4N\text{-}Tz^{-})]^{2-}$ linkage isomers (Chart 8.1). According to the DFT calculations discussed below, the HOMO energy difference between the more thermodynamically stable $[PcFe^{II}(1N\text{-}Tz^{-})_2]^{2-}$ and the less thermodynamically stable $[PcFe^{II}(4N\text{-}Tz^{-})_2]^{2-}$ is ~0.140 eV for all three tested exchange-correlation functionals (Table 8.3). This correlates well with the ~210 mV difference observed between the first and third oxidation waves in complex **8.3** (Table 8.3). Thus, we can tentatively assign the first (lowest potential) oxidation process to the $[PcFe^{II}(1N\text{-}Tz^{-})_2]^{2-}$ isomer, the second oxidation process to the

$[PcFe^{II}(1N\text{-}Tz^{-})(4N\text{-}Tz^{-})]^{2-}$ isomer, and the most positive oxidation process to the $[PcFe^{II}(4N\text{-}Tz^{-})_2]^{2-}$ linkage isomers (Chart 8.1). Since Lever reported[1] the E_L value for $1N\text{-}Tz^{-}$, we used the most negative oxidation potential in the correlation analysis discussed below.

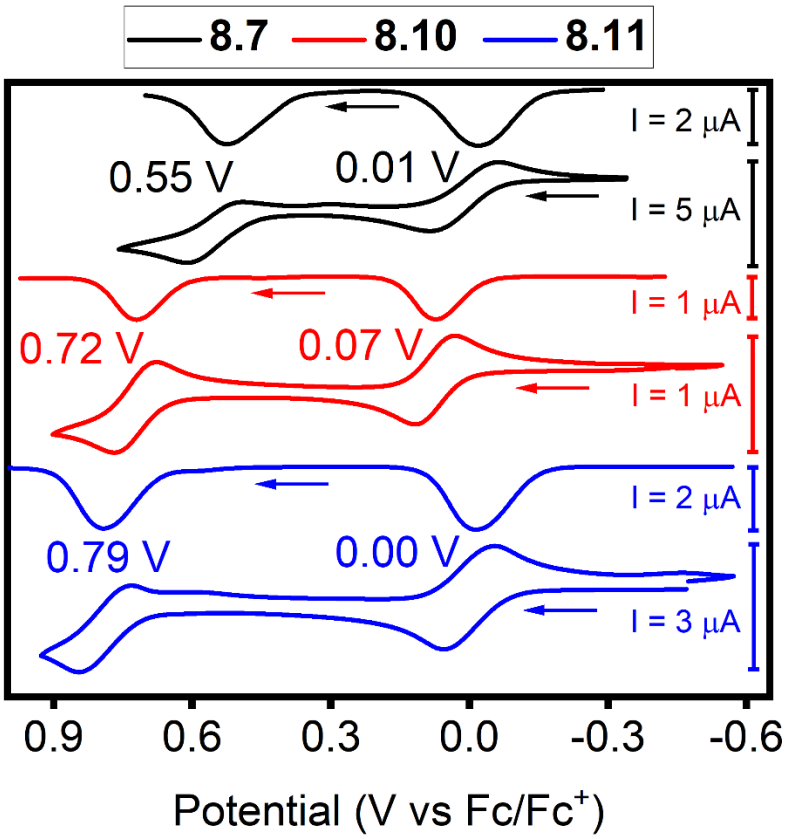

Figure 8.2. CV and DPV data for the **8.7** (top), **8.10** (middle), and **8.11** (bottom) complexes in DCM/0.1M TBAP system.

Similar to complex **8.1**, the electrochemistry of $[PcFe^{II}(NCS)_2]^{2-}$ (**8.4**, $\Sigma E_L(L_{ax})$ = -0.12V) was studied using only 0.1M KNCS as the supporting electrolyte to avoid possible axial coordination of the ClO_4^- anion from TBAP as the NCS^- anion was found to be prone to exchange with the solvent and other anions. While the first oxidation potential at $E_{1/2}$ = 0.20 V was clearly

observed for this complex, further oxidations were not detected due to discharge of the supporting electrolyte (Supporting Information Figure S8.3). Finally, in the case of the $[PcFe^{II}(CN)_2]^{2-}$ (**8.5**) complex ($\Sigma E_L(L_{ax})$ = 0.04V), two clear oxidation processes were observed in the CV and DPV experiments (Supporting Information Figure S8.4) which correlates well with the earlier studies on this compound.[85-87]

Unlike anionic compounds that are only soluble in polar media, the neutral $PcFe^{II}(Im)_2$ (**8.6**, $\Sigma E_L(L_{ax})$ = 0.24V), $PcFe^{II}(n\text{-}BuNH_2)_2$ (**8.7**, $\Sigma E_L(L_{ax})$ = 0.26V), $PcFe^{II}(Py)_2$ (**8.8**, $\Sigma E_L(L_{ax})$ = 0.50V), $PcFe^{II}$(**8.9**, P*n*-$Bu_3)_2$ ($\Sigma E_L(L_{ax})$ = 0.58V), $PcFe^{II}(PMe_3)_2$ (**8.10**, $\Sigma E_L(L_{ax})$ = 0.66V), and $PcFe^{II}$(P(O*n*-$Bu)_3)_2$ (**8.11**, $\Sigma E_L(L_{ax})$ = 0.84V) complexes were studied both in polar and non-polar solvents (Table 8.2 and Figures 8.2 and S8.5-8.7). The first report on the electrochemical oxidation of complex **8.6** was published by Stillman and co-workers in 1986.[76] These authors mentioned two oxidation processes for **8.6** in a DMA/0.1M TPAP (TPAP = tetrapropylammonium perchlorate) system. In agreement with this report, we observed two oxidation processes (one reversible and one irreversible) for **8.6** in a DMF/0.1M TBAP system, although at lower potentials. However, in DCM, three oxidation processes could be observed for this compound (Supporting Information Figure S8.5) with the first two reversible processes being located at $E_{1/2}$ = -0.15 and 0.58 V vs Fc/Fc^+. Similarly, three oxidation processes were observed in both DMF and DCM for complex **8.7** with the two first processes being reversible (Table 8.3 and Figure 8.2). In agreement with the earlier reports,[75,76,88-90] a single reversible oxidation wave for **8.8** was observed in the Py/0.1M TBAP system which has a smaller anodic potential window (Table 8.3 and Supporting Information Figure S8.6). In polar media (DMA/0.1M TPAP system), Stillman and

co-workers observed two oxidation processes for this compound[76] and we observed three oxidation waves (with only the first process being reversible) in a DMF/0.05M TFAB system (Supporting Information Figure S8.6). Two oxidation processes (one reversible and one irreversible) were also observed for **8.8** in a DCM/0.05M TFAB system. For the reasons outlined in the next section, the first oxidation potential for complex **8.8** was also determined in DMF:Py (95:5 v/v) and DCM/Py (95:5 v/v) solvent systems (Supporting Information Figure S8.6) and under each investigated solution condition, in-situ generated **8.8** gave nearly identical first oxidation potentials (see Table 8.3).

Two oxidation processes (one reversible and one irreversible) were observed for **8.9** in a DCM/0.05M TFAB system, while changing the electrolyte to the more common TBAP allowed for the observation of three oxidation processes (two reversible and one irreversible) for this compound (Supporting Information Figure S8.7). Aggregation of the **8.9** complex in a DMF/0.1M TBAP system was confirmed by UV-vis spectroscopy and afforded more complicated current-voltage curves. In particular, three oxidation processes were observed for this compound (Table 8.3). Similar to complex **8.9**, two reversible oxidation processes were observed in a DCM/0.1M TBAP system for compound **8.10**, while an additional aggregation-related oxidation wave was observed in the DMF/0.1 TBAP system (Table 8.3 and Figure 8.2). Two reversible oxidation waves were observed for complex **8.11** in a DCM/0.1M TBAP system, while the second process became irreversible in the DMF/0.1M TBAP system (Table 8.3 and Figure 8.2). In the case of the $PcFe^{II}(DMSO)_2$ complex (**8.12**, $\Sigma E_L(L_{ax})$ = 0.94V), only one oxidation process in the DMSO/0.1M TBAP system was observed due the limited anodic potential window (Supporting Information

Figure S8.8), a result consistent with the previous reports.[75,88] Dissolving the solid sample **8.12**, synthesized according to literature methods,[66] in DMF or chlorobenzene results in the observation of a second irreversible oxidation process at higher potentials (Table 8.3). Based on our spectroelectrochemical data on the first oxidation process, the second process can be assigned either to the $[Pc(1\text{-})Fe^{II}(DMSO)_2]^{+\bullet}/[Pc(1\text{-})Fe^{III}(DMSO)_2]^{2+}$ couple or can be reflective of free DMSO oxidation that dissociates following the equilibrium shown in equation 8.3:

$$[Pc(1\text{-})Fe^{II}(DMSO)_2]^{+\cdot} \rightleftharpoons [Pc(1\text{-})Fe^{II}(DMSO)]^{+\cdot} + DMSO$$

$$DMSO \rightarrow DMSO^{+\cdot} + e^{-} \qquad (8.3)$$

The DMSO ligand is known to be only weakly bound to iron(II) phthalocyanine[91-95] and thus, it is possible to expect the dissociation of ligated DMSO in the other solvent systems upon oxidation of complex **8.12**. For instance, the axial DMSO ligands in **8.12** can be easily replaced by the nitrogen bases.[96] Even the anions such as NCS^- can replace DMSO from complex **8.12**. Indeed, such dissociation was confirmed by NMR spectroscopy upon the addition of KSCN into a $PcFe^{II}(DMSO\text{-}d_6)_2$ solution in DMSO-d_6. Indeed, immediately after addition of KSCN, an additional set of phthalocyanine protons was observed in the NMR spectra, which is indicative of the replacement of axial DMSO molecule(s) with SCN^- anion(s) (Supporting Information Figure S8.25). In his early work,[75] Lever indicated that the first oxidation potential for complex **8.12** differs significantly when recorded in different electrolytes using DMSO as a solvent. The first oxidation potential for this complex was found to be ~60 and ~105 mV lower when recorded using TEABr and LiCl as supporting electrolytes compared to that obtained using more traditional and weakly coordinating TEAP. Based on our NMR and mass spectrometry data, we

speculate that bromide and chloride anions are able to substitute one of the axial DMSO ligands and thus, the reported potentials quite likely belong to the $[PcFe(DMSO)(X)]^-$ complexes (X = Cl^- or Br^-). This hypothesis correlates well with the Ox_1 versus E_L analysis discussed below. Similarly, for the DMA/electrolyte system, Lever reported even larger differences in the observed first oxidation potentials.[75] Indeed, the first oxidation potential is ~110 mV lower in DMA/TEABr and ~ 530 mV (!) in DMA/LiCl system when compared to the data from the more traditional DMA/TEAP system. Although our attempts to study axial substitution for $PcFe(solv.)_2$ by NMR spectroscopy in DMF-d_7 failed because of the low solubility of the iron(II) phthalocyanine in this solvent, the observation of $[PcFeCl_2]^{2-}$ and $[PcFeCl]^-$ anions in the mass spectrum of the PcFe/DMF/LiCl system allows us to propose that $PcFe(DMA)_2$ transforms into $[PcFe(DMA)Br]^-$ and $[PcFeCl_2]^{2-}$ complexes when TEABr and LiCl are used as electrolytes. The closeness of the first oxidation potentials of $[PcFe(NCO)_2]^{2-}$ (**8.1**, $\Sigma E_L(L_{ax})$ = -0.50V) and $[PcFeCl_2]^{2-}$ ($\Sigma E_L(L_{ax})$ = -0.48V) complexes supports this hypothesis.

Finally, formation of the $PcFe^{II}(CO)(n\text{-}BuNH_2)$ complex (**8.13**, $\Sigma E_L(L_{ax})$ = 1.12V) was achieved by bubbling carbon monoxide gas into a DCM/0.1M TBAP solution containing the **8.7** precursor (similar procedure to reported earlier in ref. 47 and 64) and was electrochemically monitored as a function of time (Figure 8.3a). As seen in Figure 8.3b, two irreversible oxidation processes in the freshly prepared **8.13** sample were observed in DCM/0.1M TBAP solution. Similar experiments in DMF/0.1M TBAP failed due to the formation of insoluble precipitate. Overall, where direct comparison is possible, our electrochemical data were found to be in good

agreement with the previously published oxidation potentials for six-coordinate $PcFe^{II}$ complexes.

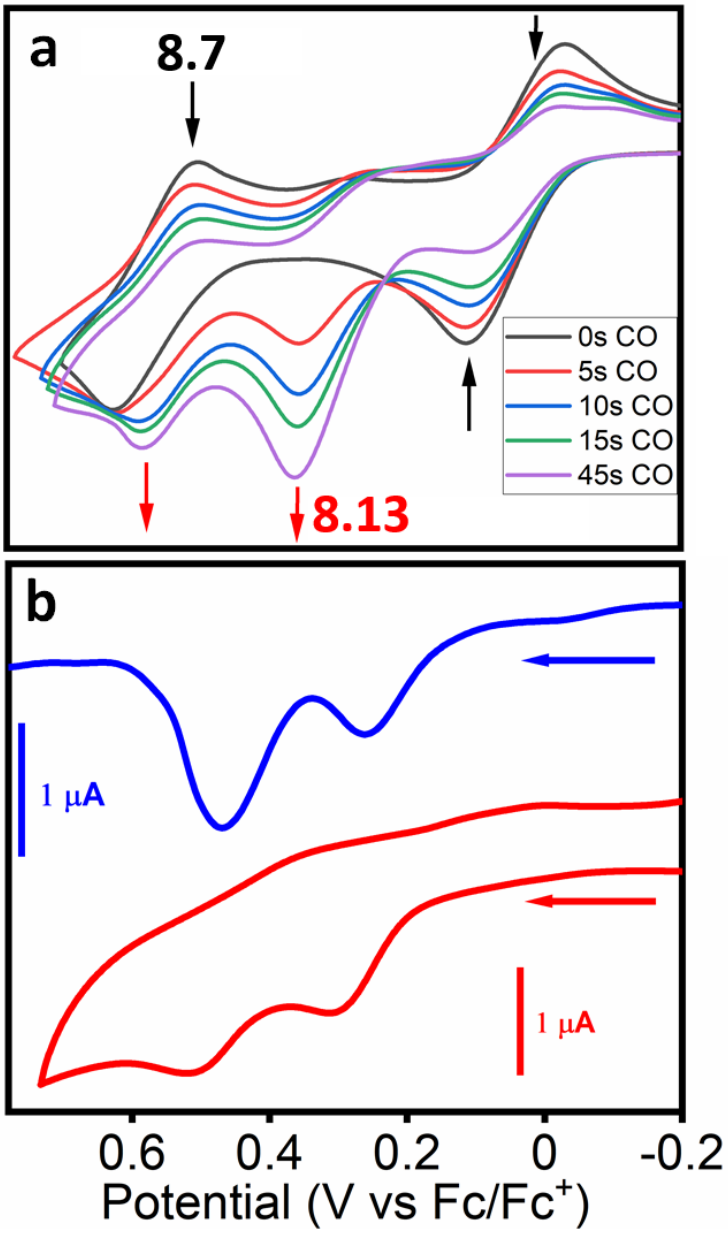

Figure 8.3. (a) Changes in the CV of complex **8.7** upon bubbling of carbon monoxide into the electrochemical cell in a DCM/0.1M TBAP system; (b) CV and DPV of freshly prepared complex **8.13** in a DCM/0.1M TBAP system.

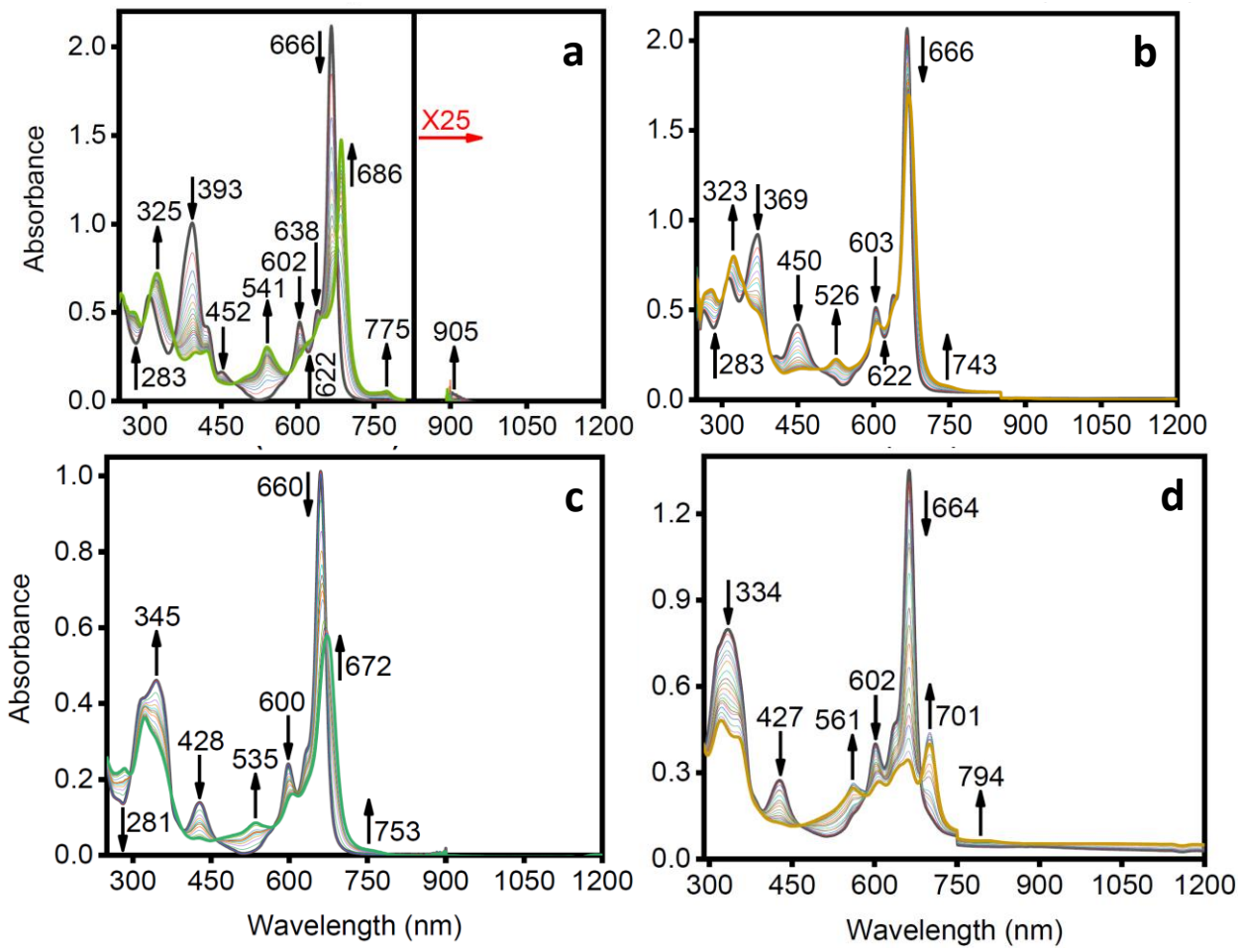

Figure 8.4. UV-vis spectral changes associated with the oxidation of (a) **8.5** in a DMSO/0.3M TBAP system; (b) **8.3** in a DMF/0.3M TBAP system; (c) **8.6** in a DCM/0.3M TBAP system; and (d) **8.7** in a DCM/TBAP system.

8.3.2 Spectroelectrochemistry and chemical oxidation data. In order to probe the nature of the HOMO (*e. g.*, to determine the site of electron abstraction) in the various axially coordinated iron(II) phthalocyanines, we have conducted spectroelectrochemical oxidation experiments on a series of $PcFe^{II}L_2$, $PcFe^{II}L'L''$, and $[PcFe^{II}X_2]^{2-}$ complexes, and complemented those, in some cases, with chemical oxidation or spectroelectrochemical experiments

conducted in various solvents using different electrolytes. First, we will discuss the obvious cases. Oxidation of complex **8.5** under spectroelectrochemical conditions results in the disappearance of the initial *Q*- and MLCT bands at 666 and 452 nm, respectively, and are accompanied by the appearance of transitions at 905, 775, 686, 541, and 325 nm (Figure 8.4a). Such a transformation is in excellent agreement with the chemical oxidation data reported by Ough and Stillman on this compound[97] as well as other spectra reported for the singly oxidized $[PcFe^{III}(CN)_2]^-$ compound.[11,85] The *Q*-band in hexa-coordinated low-spin (s = ½) iron(III) phthalocyanines is known to undergo a low-energy shift and reduction in intensity compared to the respective iron(II) complexes.[11,77,97] In addition, the appearance of a prominent charge-transfer band between ~530 and ~570 nm is also considered to be a spectroscopic signature of hexa-coordinated low-spin (s = ½) iron(III) phthalocyanines,[11,77,97] thus, the first oxidation of **8.5** is assigned to be iron-centered. The $[PcFe^{III}(CN)_2]^-$ complex can be quantitatively reduced back to **8.5** under our spectroelectrochemical conditions (Supporting Information Figure S8.9). Similarly, spectroelectrochemical oxidation of **8.3** results in a red-shifted *Q*-band from 666 to 670 nm, a disappearance of the MLCT band at 450 nm and the appearance of new charge-transfer transitions at 743 and 526 nm (Figure 8.4b). Again, this transformation is fully reversible (Supporting Information Figure S8.10) and indicative of a metal-centered oxidation. In a similar fashion, the spectral changes associated with the oxidation of **8.6** result in a red-shifted *Q*-band from 660 to 672 nm, a disappearance of the MLCT band at 425 nm and the concomitant appearance of new charge-transfer transitions at 753 and 535 nm (Figure 8.4c). Again, this transformation is fully reversible under spectroelectrochemical conditions (Supporting Information Figure S8.11) and is indicative of a Fe^{II}/Fe^{III} oxidation process giving the

$[PcFe^{III}(Im)_2]^+$ compound, an observation in good agreement with the chemical oxidation data discussed by Ough for **8.6**.[77] Oxidation of complex **8.7** under spectroelectrochemical conditions results in the disappearance of the initial *Q*-band and MLCT transition at 427 nm and the appearance of a new *Q*-band at 701 nm with charge-transfer transitions appearing at 794 and 561 nm (Figure 8.4d). The reversibility of this oxidation was found to be ~80% under our spectroelectrochemical conditions (Supporting Information Figure S8.12); however, the final spectra obtained of singly oxidized **8.7** is clearly indicative of a metal-centered electron abstraction affording the $[PcFe^{III}(n\text{-}BuNH_2)_2]^+$ complex.

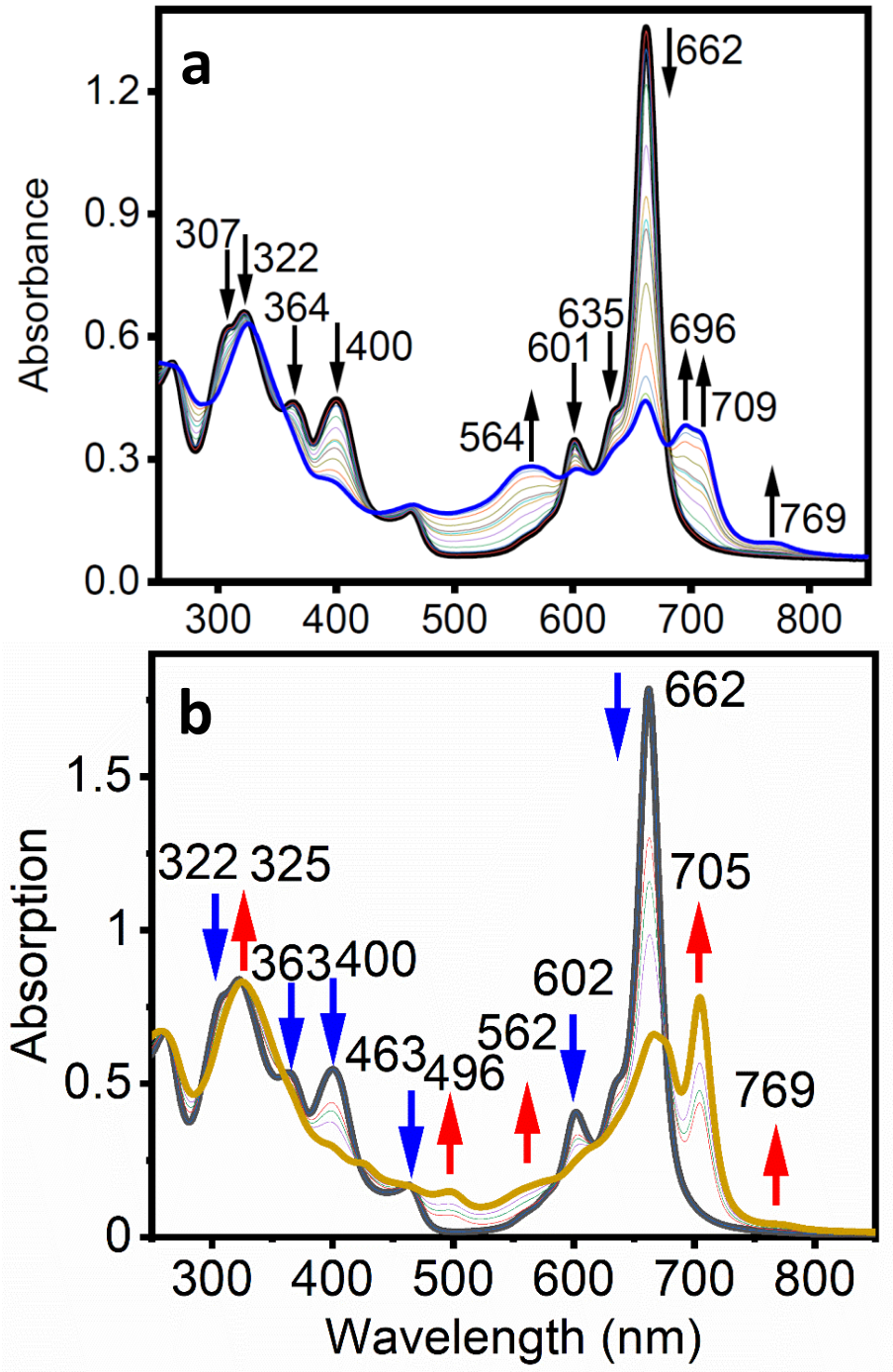

Figure 8.5. UV-vis spectral changes of **8.10** upon (a) electrochemical oxidation in DCM/0.3M TBAP and (b) chemical oxidation by $[NO]^+[BF_4]^-$ in DCM.

Spectral monitoring of the electrochemical or chemical oxidation of the $PcFe^{II}(PR_3)_2$ complexes (R = Me or *n*-Bu; $\Sigma E_L(L_{ax})$ = ~ +0.6) reveals a very similar picture (Figure 8.5 and Supporting Information Figure S8.13). In both cases, the *Q*-band initially observed at 662 (**8.10**) or 668 nm (**8.9**) is reduced in intensity and a new, red-shifted *Q*-band appears in the UV-vis spectra of the oxidized complexes. In addition, new charge-transfer bands at ~770, ~560, and ~470 nm appear upon oxidation of these two complexes, an observation consistent with the formation of low-spin $[PcFe^{III}(PR_3)_2]^+$ complexes. Thus, the first oxidation process in the $PcFe^{II}(PR_3)_2$ complexes is assigned to a Fe^{II}/Fe^{III} oxidation. Oxidation under spectroelectrochemical conditions gives similar spectral results except for the *Q*-band, which appears split by 264 cm^{-1} (Figure 8.5 and Supporting Information Figure S8.13). Again, the generated electrooxidized species could be quantitatively reduced back to the respective $PcFe^{II}(PR_3)_2$ complexes under our spectroelectrochemical conditions (Supporting Information Figures S8.14 and S8.15). The nature of the split *Q*-band in the $[PcFe^{III}(PR_3)_2]^+$ complexes is puzzling as it is expected that unlike in anionic $[PcFe^{II}X_2]^{2-}/[PcFe^{III}X_2]^-$ pairs (X = Cl^-, NCO^-, and NCS^-), dissociation of the axial phosphine ligand should be a highly unfavorable process due to the significant π-accepting properties of the axial PR_3 (R = Me or *n*-Bu) ligands in the $PcFe^{II}(PR_3)_2/[PcFe^{III}(PR_3)_2]^+$ complexes. Indeed, as we recently demonstrated using NMR spectroscopy, the $PcFe^{II}(PR_3)_2$ complexes are stable in solution for prolonged times.[63] In addition, unlike the $[PcFe^{II}X_2]^{2-}$ systems (X = NCO^- and NCS^-), the $PcFe^{II}(PR_3)_2$ complexes are not sensitive toward the nature of supporting electrolyte, which is also indicative of the relatively low mobility of the axial ligands in these systems. The ion-pairing of electrolyte anions to the

cationic $[PcFe^{III}(PR_3)_2]^+$ complexes, which might cause a small splitting of the *Q*-band, is also unlikely as such *Q*-bands were observed in DCM/0.3M TBAP and DCM/0.15M TFAB systems.

The second series of easily interpretable cases belongs to the oxidation of $PcFe^{II}L_2$ complexes (L = *t*-BuNC, FcNC,[69] and $P(OBu)_3$). Indeed, oxidation of these iron(II) phthalocyanines under an applied oxidizing potential or addition of a chemical oxidant results in a disappearance of the initial *Q*-band and appearance of transitions at ~700, ~525, and ~420 nm with the band at ~525 nm being the most intense in the visible region of the spectra (Figure 8.6 and Supporting Information Figure S8.16). The final UV-vis spectral envelopes of these red-colored species are independent of electrolyte (TBAP and TFAB were tested for complex **8.11**) and clearly indicate the formation of well-known phthalocyanine cation-radical species.[69,98-102] The EPR spectra of these oxidized compounds have a very characteristic isotropic signal with the g-value close to that of the free electron and thus, the oxidation of $PcFe^{II}L_2$ (L = *t*-BuNC, FcNC, and $P(OBu)_3$; $\Sigma E_L(L_{ax}) = 0.72 – 0.84$) is assigned to occur at the macrocycle resulting in the formation of a $[Pc(1-)Fe^{II}L_2]^{+\bullet}$ species. In each case, the electrooxidation is fully reversible in both DCM/0.3M TBAP or DCM/0.15M TFAB systems (Supporting Information Figure S8.17). Conversely, oxidation of **8.13** with a chemical oxidant or an applied potential was found to be irreversible (Supporting Information Figure S8.18), a phenomenon which is consistent with the irreversible electrochemical data of this compound (Figure 8.3). Indeed, the reduction of the oxidized species under spectroelectrochemical conditions (Supporting Information Figure S8.19) is indicative of several species present in solution. Although inconclusive, the formation of the red-colored species having absorptions at 714, 522, and 417 nm might suggest an oxidation of

the phthalocyanine macrocycle, which is expected for this complex ($\Sigma E_L(L_{ax})$ = 1.12). We speculate, that the initial oxidation results in the formation of a $[Pc(1-)Fe^{II}(CO)(n\text{-}BuNH_2)]^+$ complex, which is prone to dissociation of one of the axial ligands and dimerization with the formation of the μ-oxo dimer derivatives.[11,103-109]

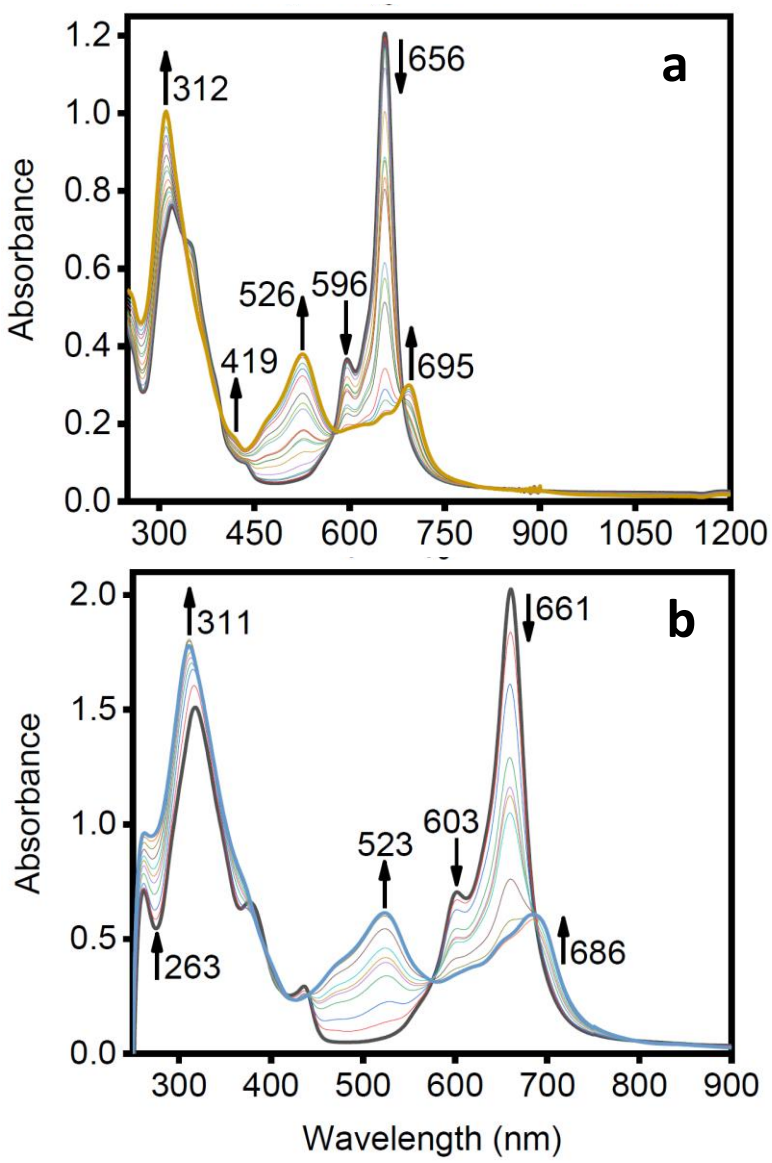

Figure 8.6. UV-vis spectral changes of **8.11** upon (a) electrochemical oxidation in DCM/0.3M TBAP and (b) chemical oxidation by $[NO]^+[BF_4]^-$ in DCM.

Oxidation of complex **8.8** under spectroelectrochemical conditions proved rather interesting and was studied in more detail as compared to the other compounds reported herein. In 1978, Lever mentioned that "an ESR study of an electrochemically oxidized $Fe^{II}Pc/Py$ solution… shows only a weak free-radical g = 2.003 signal".[75] In 1986, Stillman and co-workers reported[76] that oxidation of complex **8.8** in a DCM/0.05M TEAP system (TEAP = tetraethylammonium perchlorate) was indicative of a metal-centered reaction and, thus, formation of a $[PcFe^{III}Py_2]^+$ compound during the first oxidation process. Later, Ough[77] listed the transitions at 791, 688 (*Q*-band), 562, and 324 nm for the singly oxidized product of **8.8** as obtained by the chemical oxidation in *o*-dichlorobenzene. In our hands, when **8.8** was oxidized in a Py/0.1M TBAP or Py/0.15M TFAB system, it was found that the first oxidation process was not fully reversible (Figure 8.7a and Supporting Information Figure S8.20). Nevertheless, the disappearance of the *Q*-band and appearance of new electronic transitions at 1043, 710, 699, and 523 nm along with the observed weak isotropic EPR signal with a g-value close to that of the free electron can be interpreted as macrocycle-centered oxidation and formation of a $[Pc(1-)Fe^{II}Py_2]^+$ species in solution; however, this interpretation should be viewed with some degree of caution due to the lack of reversibility of the process. Indeed, upon reduction, the *Q*-band of the initial **8.8** complex was restored by only 50-60% and the presence of a new intense transition at 624 nm was clearly observed (Supporting Information Figure S8.20). In contrast, the oxidation of *in-situ* generated **8.8** in DMF:Py (95:5 v/v)/0.1M TBAP and DCM:Py (95:5 v/v)/0.1 TBAP systems under spectroelectrochemical conditions was found to be completely reversible (Figure 8.7b,c and Supporting Information Figure S8.20). In both cases, the formation of new bands at 690-695 and 515 nm was observed. The relative intensities of the transitions at 690-695 and 515 nm are,

again, rather suggestive of an electrogenerated phthalocyanine cation-radical species in solution.[69,98-102] In agreement with this, no shift in the first oxidation potential of **8.8** was observed in the Py:DMF/0.1M TBAP system that has the DMF component varied between 0 and 75%, which indicates the relative stability of the Fe-N(Py) bonds under these solution conditions (Supporting Information Figure S8.21). However, when freshly prepared solid **8.8** was dissolved in DMF/0.3M TBAP or was *in-situ* generated using a DCM:Py mixture (consisting of only 2 mol equivalents of pyridine)/0.1M TBAP, the spectral changes associated with electrooxidation were accompanied by the appearance of the 850, 691, 565, and 527 nm bands (Figure 8.7d) for the latter system (*i.e.* DCM with 2 eq. of Py) while a similar picture was observed using DMF/0.3 M TBAP for the solid **8.8** sample. More importantly, the intensity of the band at ~690 nm as well as the presence of the transition at 565 nm could well be indicative of the formation of a $[PcFe^{III}Py_2]^+$ species; however, the reduction of the $[PcFe^{III}Py_2]^+$ species in neat DCM was found to be not fully reversible (likely due to the moderately poor solubility of the neutral species in solution). Thus, our data seems to indicate that the energies of the $[Pc(1\text{-})Fe^{II}Py_2]^{+\bullet}$ and $[PcFe^{III}Py_2]^+$ valence tautomers are close to each other and the equilibrium between them has a clear dependence on the concentration of the pyridine ligand present in solution. This assumption agrees well with the DFT data discussed below.

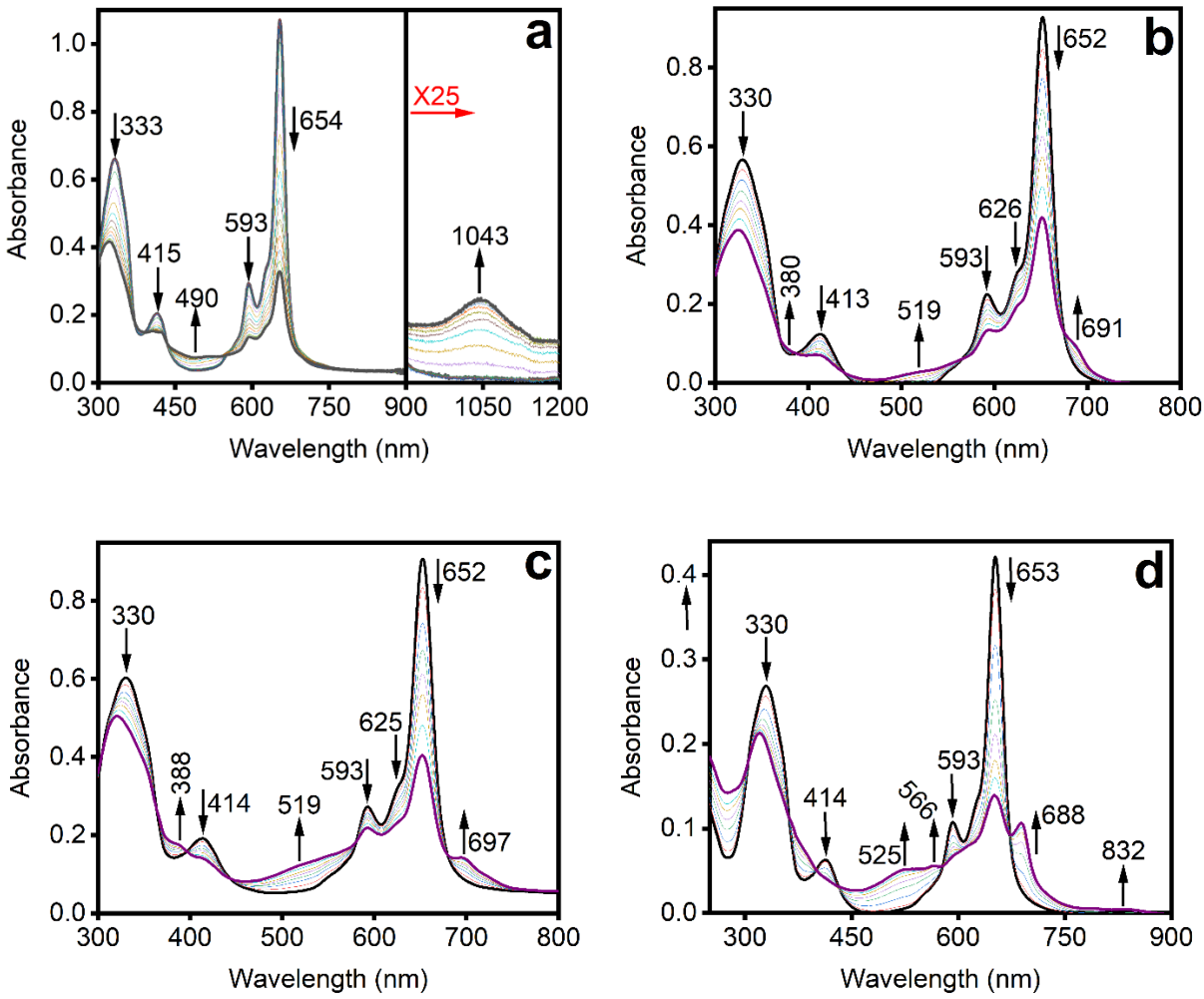

Figure 8.7. UV-vis spectral changes associated with the electrooxidation of **8.8** in (a) Py/0.3M TBAP system (b) DMF:Py (95:5 v/v)/0.1M TBAP system; (c) DCM:Py (95:5 v/v)/0.1M TBAP system; (d) DCM/0.1M TBAP system.

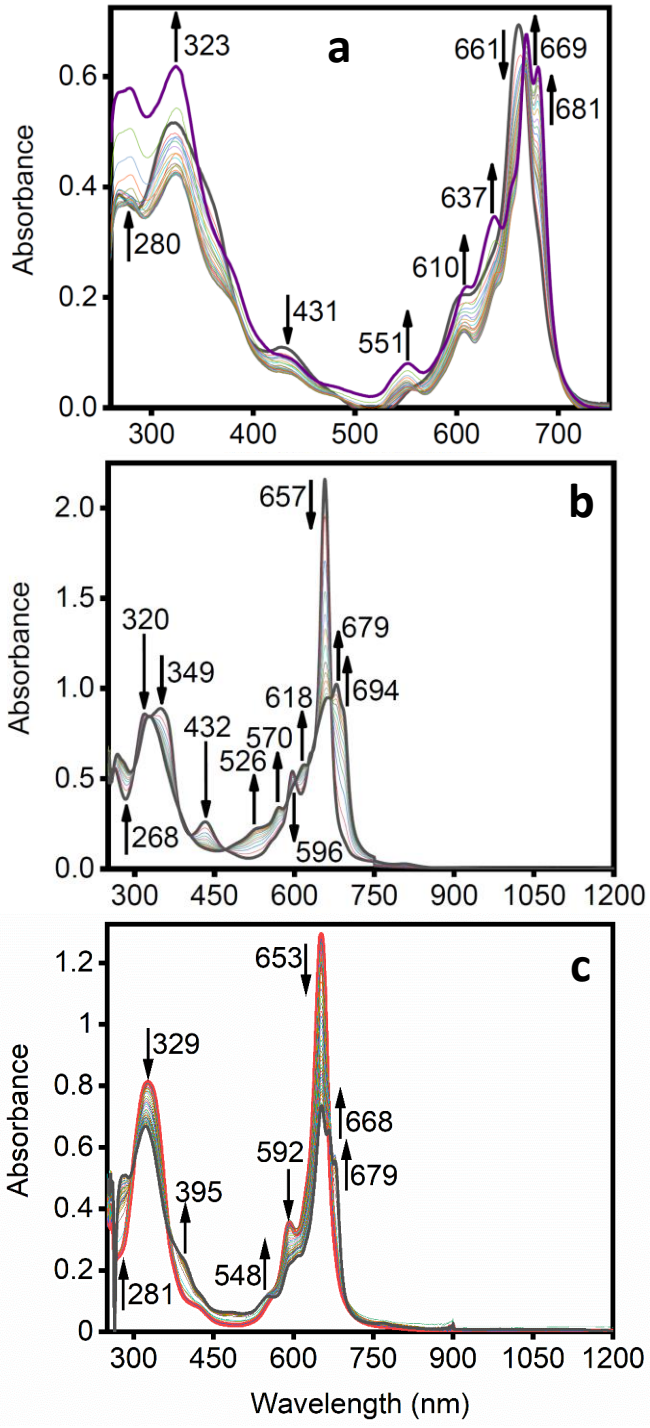

Figure 8.8. UV-vis spectral changes associated with the electrochemical oxidation of (a) **8.1** in DMF/0.3M KNCO, (b) **8.4** in DMF/0.3M KNCS and (c) air-oxidation of $[PcFe^{II}(Cl)_2]^{2-}$ (**8.14**) in a DMF/0.1M LiCl system.

The spectral changes associated with the oxidation of two anionic complexes (**8.1** and **8.4**) are rather interesting and correlate well with the oxidation of the $[PcFeCl_2]^{2-}$ (**8.14**) complex (prepared in a DMA/0.1M LiCl system) reported by Lever in 1978.[75] Both of these complexes have low (negative) first oxidation potentials and possess almost pure σ-donor axial ligands[2,110,111] and thus, the iron-centered occupied d-orbitals should be significantly energetically destabilized as compared to the phthalocyanine-centered a_{1u} molecular orbital. Also, based on the UV-vis spectra discussed below as well as mass spectrometry data, the axial ligands in iron(III) derivatives of these compounds are not strongly bound to the iron center compared to all other complexes discussed in this work.

In the case of complex (**8.1**), both electrooxidation or simple exposure of the initial solution to oxygen results in the decrease of intensity for the initial *Q*-band at 661 nm and the appearance of two intense and narrow transitions at 669 and 681 nm (Figure 8.8a). These transitions, as well as the new bands at 610 and 551 nm, correlate well with the reported spectrum of the metal-centered oxidation product, $[PcFe^{III}(NCO)_2]^-$.[11] When spectroelectrochemical data are considered, this transformation occurs both in DMF/0.15M KNCO and DMF/0.15M TFAB/0.005M KNCO systems. Similarly, oxidation of complex **8.4** under an applied oxidizing potential results in the disappearance of the initial *Q*-band at 657 nm along with new intense transitions at 694, 679, 618, 570, 526, and 328 nm (Figure 8.8b). These changes correlate well with the formation of the earlier reported iron(III) complex, $[PcFe^{III}(NCS)_2]^-$.[11] An explanation for the appearance of two closely spaced (~250-350 cm^{-1}) *Q*-bands in the $[PcFe^{III}X_2]^-$ (X = NCO^- or NCS^-) complexes has yet to be offered in the literature. Moreover, the early oxidation

experiments on "PcFe" in a DMA/0.1M LiCl system (which is effectively complex **8.14**) reported by Lever in 1978,[75] also showed the appearance of two *Q*-bands that are red-shifted compared to the initial Fe^{II} compound. The bands observed by Lever, again, correlate well with the later reported UV-vis spectrum of the $[PcFe^{III}(Cl)_2]^-$ complex[112] as well as our data on the "$PcFe^{II}$" complex dissolved in DMF in the presence of an increasing amount of LiCl (Figure 8.8c). As discussed below, such spectra were only observed for the pure (or almost pure) σ-donor ligands that have low (negative) values of Lever's E_L parameter. There are several explanations for the appearance of two closely spaced *Q*-bands (separated by ~250-350 cm^{-1}) in $[PcFe^{III}X_2]^-$ (X = Cl^-, NCO^-, or NCS^-): (i) the lowest energy band (~680 for X = Cl^- or NCO^- and ~694 nm for NCS^-) belongs to the $Q_{0\text{-}0}$ transition, while the higher energy band (~670 nm for X = Cl^- or NCO^- and ~680 nm for NCS^-) belongs to the $Q_{0\text{-}1}$ transition; (ii) local asymmetry in $[PcFe^{III}X_2]^-$ reduces their effective symmetry from D_{4h} to a two-fold point group and thus, removes the degeneracy of the first excited state; (iii) the lowest energy band belongs to the $Q_{0\text{-}0}$ transition of the $[PcFe^{III}X_2]^-$ complex, while the higher energy band belongs to the $Q_{0\text{-}0}$ transition of the $[PcFe^{III}(X)]$ complex; (iv) the lowest energy band belongs to the $Q_{0\text{-}0}$ transition of the $[PcFe^{III}X_2]^-$ complex, while the higher energy band belongs to the $Q_{0\text{-}0}$ transition of the $[PcFe^{III}(X)(solv)]$ complex. The first hypothesis is highly unlikely because the typical energy difference between the $Q_{0\text{-}0}$ and $Q_{0\text{-}1}$ bands in transition-metal phthalocyanines (including the anionic $[PcFe^{III}(CN)_2]^-$ complex) varies between ~650 and 900 cm^{-1} and the intensity of the $Q_{0\text{-}1}$ band is always significantly (~3 times) lower than that of the $Q_{0\text{-}0}$ band.[11,85,97,113,114] Contrarily, the intensities of the ~690 and ~680 nm bands in the oxidized forms of $[PcFe^{III}X_2]^-$ (X = Cl^-, NCO^-, and NCS^-) have comparable intensities. Similarly, all known $[PcFe^{II/III}L_2]^{n+}$, $[PcFe^{II/III}L'L'']^{n+}$, and $[PcFe^{II/III}X_2]^{n-}$ compounds, even those with

bulky axial ligands of one- or two-fold symmetry (pyridines, azoles, alkylamines, etc.), do not have a split $Q_{0\text{-}0}$ band and thus retain effective degeneracy of the first excited state in solution.[11,47,85] The third and fourth hypotheses were discussed by Lever[75] and Ough[85] and can be summarized by equations. 8.4-8.6:

$$[PcFe^{II}X_2]^{2-} \rightarrow [PcFe^{III}X_2]^{-} + e^{-} \quad (8.4)$$

$$[PcFe^{III}X_2]^{-} \rightleftharpoons PcFe^{III}(X) + X^{-} \quad (8.5)$$

$$PcFe^{III}X + solv. \rightleftharpoons PcFe^{III}(X)(solv.) \quad (8.6)$$

It is known that the spin-admixed (s = 3/2-5/2) penta-coordinated $PcFe^{III}X$ complexes have a *Q*-band between 652 and 657 nm[11,85,114] and thus, observation of their formation might be hindered by the presence of the *Q*-band of the $[PcFe^{II}X_2]^{2-}$ compounds (653-666 nm). Contrarily, low-spin (s = 1/2) hexacoordinated $[PcFe^{III}X_2]^{-}$ complexes are known to possess a *Q*-band in the 670-690 nm region[11,85,114] and thus, our experiments suggests the presence of the singly oxidized hexa-coordinated species of iron(III) phthalocyanine in solution. In 1978,[75] Lever and co-workers indeed observed the characteristic low-spin iron(III) (s = ½) EPR and UV-vis spectra of the $[PcFe^{III}Cl_2]^{-}$ complex which was later independently prepared and characterized by Homborg and co-workers.[112] We speculate that the lowest energy band belongs to the $Q_{0\text{-}0}$ transition of $[PcFe^{III}X_2]^{-}$, while the higher energy band belongs to the $Q_{0\text{-}0}$ transition of the mixed ligand species, $PcFe^{III}(X)(solv)$. Support for the formation of $PcFe^{III}(X)(solv)$ was found in the ESI mass spectrum of complex **8.4** that was incubated in air for 30 minutes prior to injection and displayed m/z values corresponding to $[PcFe^{III}(NCS)_2]^{-}$, $PcFe^{III}(NCS)$, and $PcFe^{III}(NCS)(DMF)$.

Although one might argue that the formation of the $PcFe^{III}(NCS)(DMF)$ complex can originate from $[PcFe^{III}(NCS)_2]^-(solv.)_x$ clusters that are often characteristic for ESI mass spectrometry, no such clusters were observed in the mass spectrum. The facile dissociation of the axial ligand in $[PcFe^{III}X_2]^-$ leading to the formation of $PcFe^{III}X$ was also observed in the ESI mass spectra of $[PcFe^{III}Cl_2]^-$ (Supporting Information Figure S8.22) as well as $[PcFe^{III}(NCO)_2]^-$. The reversibility of the oxidation process for the $[PcFe^{II}X_2]^{2-}$ complexes was demonstrated for the thiocyanate complex, which was reduced from its iron(III) state (mixture of $[PcFe^{III}(NCS)_2]^-$ and $PcFe^{III}(NCS)(DMF)$ species) to an **8.4** complex with ~90% yield under spectroelectrochemical conditions in a DMF/0.1M KSCN system (Supporting Information Figure S8.23). Complete regeneration of complexes **8.14** and **8.1** from their respective iron(III) species has not be achieved. Overall, as expected from Lever's E_L scale[1] and the electronic properties of the axial ligands in $[PcFe^{II}X_2]^{2-}$ ($X = Cl^-$, NCO^-, or NCS^-), the first oxidation process is iron-centered and leads to the formation of hexa-coordinated $[PcFe^{III}X_2]^-$ and $PcFe^{III}(X)(solv.)$ species in solution, while the equilibrium between these species depends on the solvent as well as the nature and concentration of the axial ligand. Our hypothesis on the formation of $[PcFe^{III}X_2]^-$ and $PcFe^{III}(X)(solv.)$ complexes in solution upon oxidation of the $[PcFe^{II}X_2]^{2-}$ compounds does not contradict the earlier data on $[PcFe^{III}X_2]^-$ compounds.[11,115] Indeed, the solid samples of $[PcFe^{III}X_2]^-$ ($X = Cl^-$, N_3^-, NCO^-, and NCS^-) were prepared in the presence of an excess of the axial ligand and thus, it is not surprising that a clear Mössbauer doublet (and in some cases, EPR spectra which are characteristic for low-spin ($s = ½$) iron(III)) were observed for the solid samples as the lack of solvent prohibits axial ligand exchange.[11,115] However, once dissolved in solution, in the absence of excess axial anions, these compounds are able to readily exchange

one of the axial ligands with a solvent molecule whose concentration is in extreme excess, resulting in the observation of a split *Q*-banded UV-vis spectrum.[11,75,115]

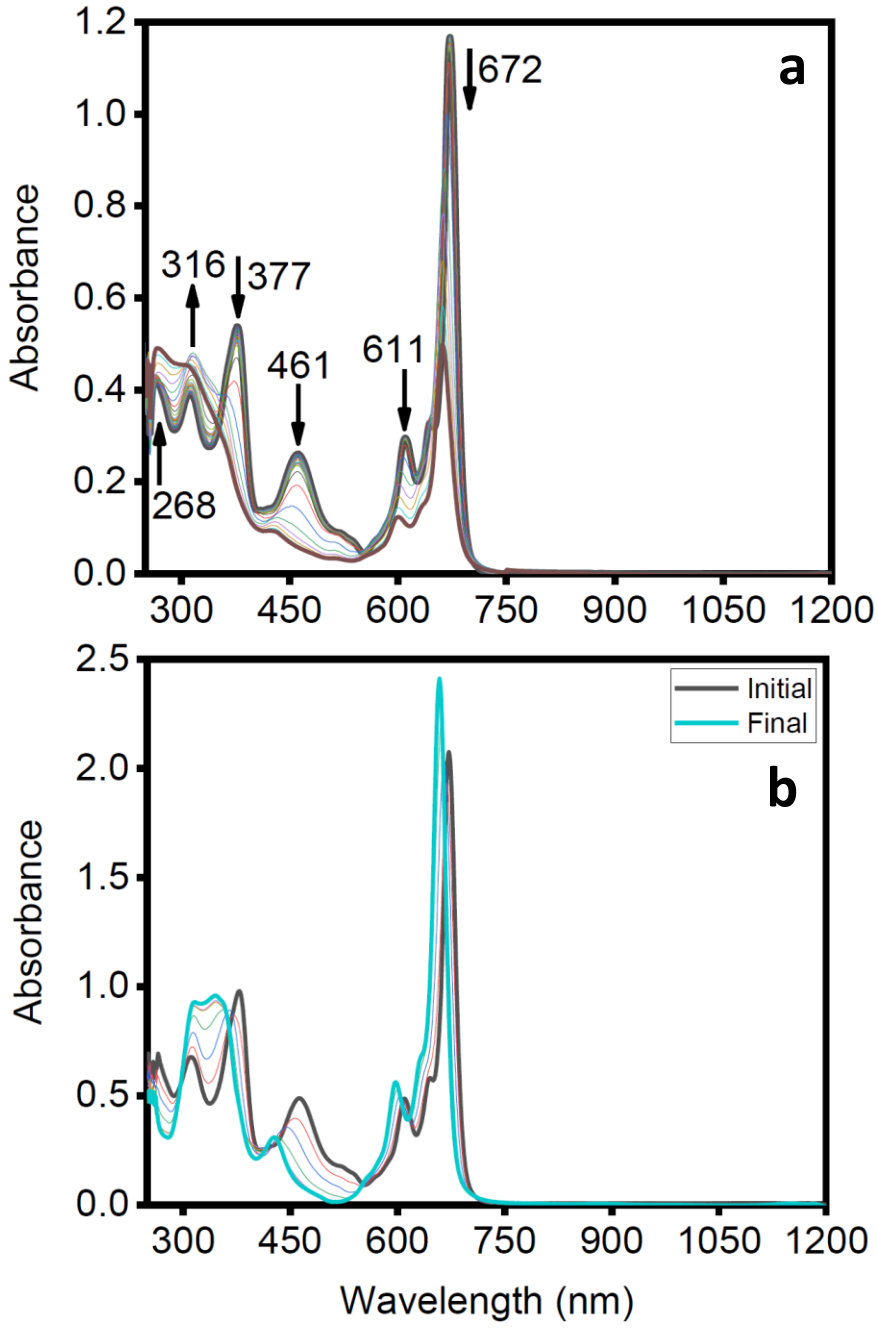

Figure 8.9. UV-Vis spectral changes of **8.2** upon (a) oxidation in DMF/0.3M TBAP and (b) transformation into the corresponding **8.6** via titration of methanol in DMF.

We also attempted to oxidize complex **8.2** ($\Sigma E_L(L_{ax})$ = -0.46) in DMF under the application of a controlled oxidizing potential (Figure 8.9a) or in the presence of a chemical oxidant. Surprisingly, during the first oxidation process in DMF/0.3M TBAP, the initial *Q*-band at 672 nm undergoes a higher-energy shift to 660 nm, while the prominent charge-transfer band at 461 nm shifts to 424 nm. A similar spectroscopic transformation was observed during the titration of **8.2** with water or methanol (Figure 8.9b) and thus, we concluded that upon oxidation to the $[PcFe^{III}(Im^{-})_2]^{-}$ complex, the axial ligands abstract a hydrogen atom from the solvent and form complex **8.6**. The lack of transitions between 500 and 570 nm as well as 680 and 1000 nm exclude the formation of an iron(III) or phthalocyanine cation-radical species.

Finally, the first oxidation process in complex **8.12** is known to be reversible on the electrochemical time-scale[75,88] and our data also supports this conclusion (Supporting Information Figure S8.8); however, the spectroelectrochemical oxidation of this compound in a DMSO/0.1M TBAP or DMSO/0.3M TBAP system (Figure 8.10) was found to be irreversible (and the data from our three separate laboratories correlate well with each other). As seen in Figure 8.10a, upon oxidation of **8.12**, the initial *Q*-band at 653 nm shifts to 647 nm and significantly broadens. In addition, broad bands at ~510 and ~800 nm appear in the spectrum. At first glance, the presence of the low intensity bands at ~510 and ~800 nm appear to indicate formation of a phthalocyanine cation-radical (and our DFT calculations detailed in the following section support this assignment); however, reduction of the electrogenerated species both in slow (40-60 minutes) or fast (40-60 second) spectroelectrochemical cuvettes do not regenerate the initial UV-vis spectrum. Instead, while the bands at ~510 and ~800 nm disappeared, new

bands at 625 and 647 nm appeared in the spectrum (Figure 8.10b). Both of these bands were not observed in the initial UV-vis spectrum of the complex **8.12**.

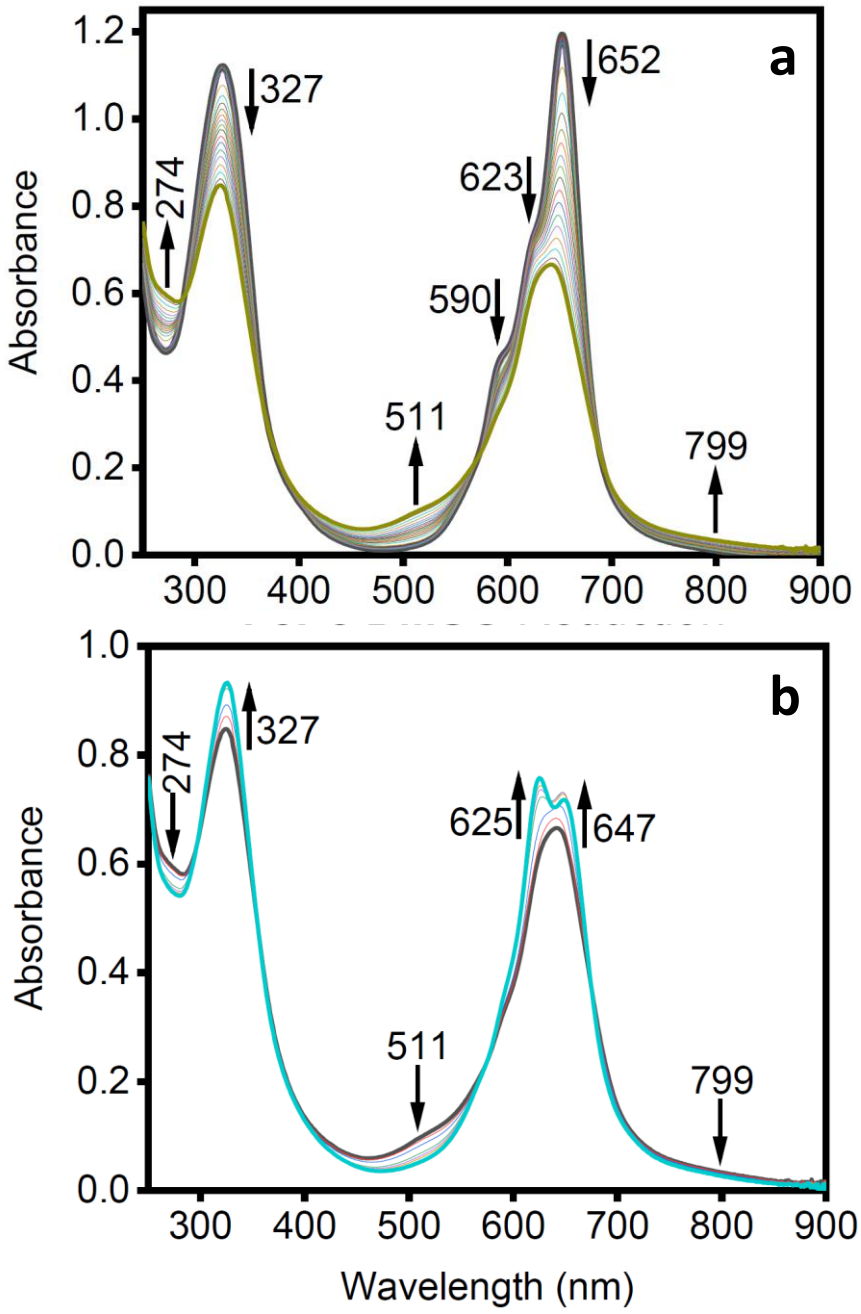

Figure 8.10. UV-Vis spectral changes associated with (a) the electrooxidation and (b) the re-reduction of **8.12** in DMSO/0.3M TBAP.

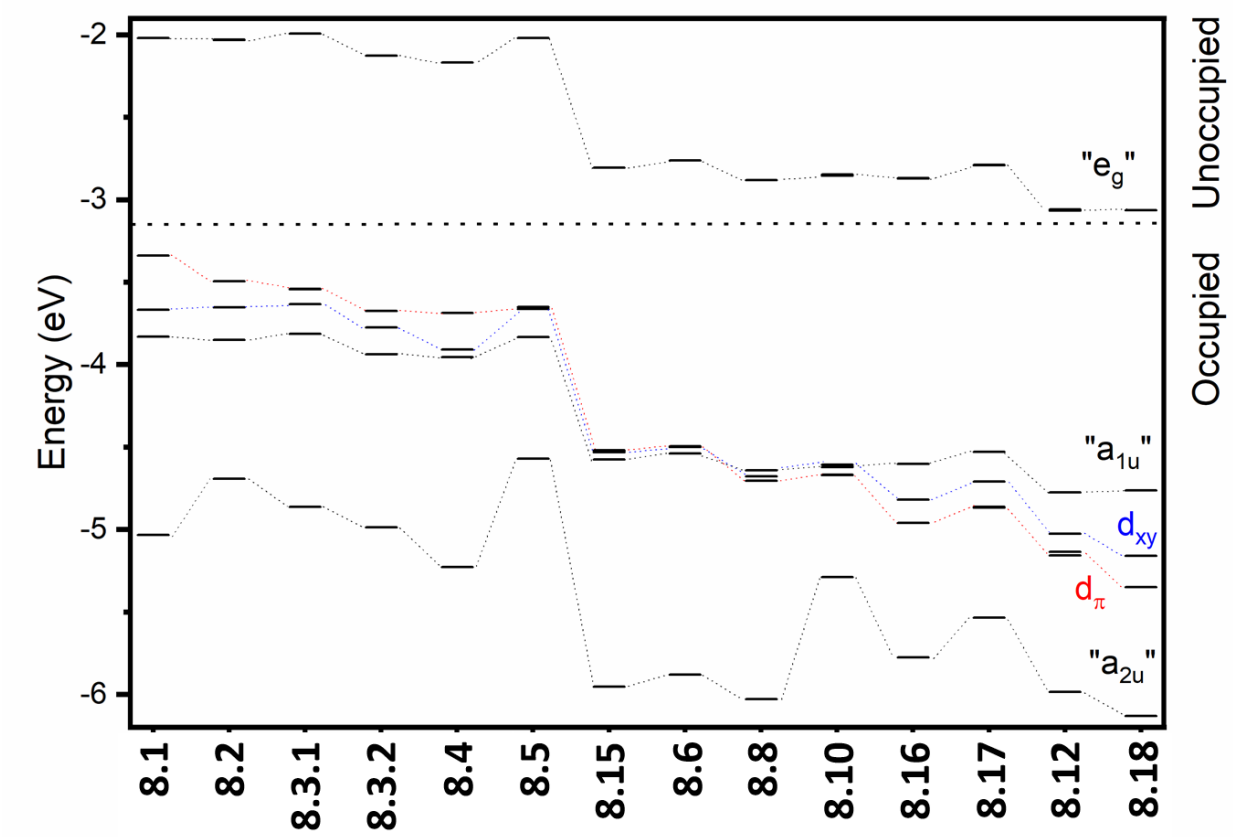

Figure 8.11. DFT-predicted (MPWLYP exchange-correlation functional) energies of the frontier orbitals in iron(II) phthalocyanine complexes. The black dotted lines connect phthalocyanine-centered orbitals, the red dotted lines connect iron(II) d_{xy} orbitals, and the blue dotted lines connect d_{π} orbitals.

8.3.3 DFT Calculations. In order to provide further insight into the electrochemical and spectroelectrochemical data on the $PcFe^{II}L_2$, $PcFe^{II}L'L''$, and $[PcFe^{II}X_2]^{2-}$ complexes as well as their respective one-electron oxidized species described above, their electronic structures were elucidated using DFT calculations. Since it is expected that the relative energies of the metal-centered and phthalocyanine orbitals will have an exchange-correlation functional dependency (and in particular will be sensitive to the amount of Hartree-Fock exchange present in the

specific functional),[42,63,116,117] single point calculations were conducted using MPWLYP (5% of Hartree-Fock exchange), TPSSh (10% of Hartree-Fock exchange), and O3LYP (11.6% of Hartree-Fock exchange) functionals. In our experience, pure DFT functionals are too soft, providing underestimated energies of the transition-metal orbitals with respect to the macrocyclic aromatic chromophores such as phthalocyanines, while more traditional hybrid functionals with 20-25% of Hartree-Fock exchange can lead to some unreliable stabilization of the iron d-orbitals with respect to the π-orbitals of the phthalocyanine core. The DFT-predicted orbital energy diagram for selected compounds and MPWLYP calculations is shown in Figure 8.11 and Supporting Information Figure S8.24 while the energies of the frontier orbitals are listed in Table 8.4.

Table 8.4. Energies (eV) of the frontier occupied molecular orbitals for the $PcFe^{II}L_2$, $PcFe^{II}L'L''$, and $[PcFe^{II}X_2]^{2-}$ complexes calculated using the MPWLYP, TPSSh, and O3LYP functionals with DCM as the solvent.[a]

MO/L/L′/X$^-$	**NH_3/CO**	**DMSO**	**$P(OMe)_3$**	**tBuNC**	**PMe_3**	**Py**	**Im**	**NH_3**	**CN^-**	**NCS^-**	**$1Tz^-$**	**$4Tz^-$**	**Im^-**	**NCO^-**
							MPWLYP							
"a_{1u} (π)"	**-4.764**	**-4.776**	**-4.529**	**-4.603**	-4.622	**-4.642**	-4.540	-4.575	-3.834	-3.954	-3.815	-3.939	-3.850	-3.831
d_{xy}	-5.159	-5.027	-4.709	-4.820	**-4.607**	-4.678	-4.501	-4.531	-3.662	-3.908	-3.630	-3.776	-3.653	-3.667
d_{yz}	-5.349	-5.135	-4.864	-4.960	-4.668	-4.705	**-4.496**	**-4.520**	**-3.651**	**-3.687**	**-3.541**	**-3.675**	**-3.494**	**-3.339**
d_{xz}	-5.349	-5.157	-4.867	-4.960	-4.671	-4.705	-4.496	-4.524	-3.651	-3.687	-3.544	-3.675	-3.494	-3.339
Δ_H[b]	0.395	0.251	0.180	0.217	-0.015	0.036	-0.044	-0.055	-0.183	-0.267	-0.274	-0.264	-0.356	-0.492
Δ_{xy}[c]	0.395	0.251	0.180	0.217	-0.015	0.036	-0.039	-0.044	-0.172	-0.046	-0.185	-0.163	-0.197	-0.164
Δ_π[d]	0.858	0.359	0.335	0.357	0.046	0.063	-0.044	-0.055	-0.183	-0.267	-0.274	-0.264	-0.356	-0.492
							TPSSh							

"a_{1u} (π)"	**-5.018**	**-5.031**	**-4.779**	**-4.860**	**-4.878**	**-4.902**	**-4.804**	**-4.841**	-4.109	-4.223	-4.090	-4.215	-4.128	-4.105
d_{xy}	-5.826	-5.680	-5.360	-5.472	-5.235	-5.279	-5.102	-5.115	-4.295	-4.520	-4.230	-4.377	-4.249	-4.258
d_{yz}	-5.813	-5.606	-5.316	-5.412	-5.096	-5.149	-4.941	-4.963	**-4.078**	**-4.125**	**-3.960**	**-4.105**	**-3.899**	**-3.760**
d_{xz}	-5.813	-5.626	-5.318	-5.412	-5.099	-5.149	-4.941	-4.964	-4.078	-4.125	-3.962	-4.105	-3.900	-3.760
Δ_H[b]	0.795	0.575	0.537	0.552	0.218	0.247	0.137	0.122	-0.031	-0.098	-0.130	-0.110	-0.229	-0.345
Δ_{xy}[c]	0.808	0.649	0.581	0.612	0.357	0.377	0.298	0.274	0.186	0.297	0.140	0.162	0.121	0.153
Δ_π[d]	0.795	0.575	0.537	0.552	0.218	0.247	0.137	0.122	-0.031	-0.098	-0.130	-0.110	-0.229	-0.345
						O3LYP								
"a_{1u} (π)"	**-4.941**	**-4.948**	**-4.703**	**-4.782**	**-4.791**	**-4.823**	**-4.724**	**-4.763**	-4.022	-4.144	-4.005	-4.128	-4.043	-4.023
d_{xy}	-5.706	-5.561	-5.239	-5.344	-5.099	-5.175	-5.000	-5.019	-4.156	-4.418	-4.119	-4.265	-4.140	-4.159
d_{yz}	-5.737	-5.516	-5.233	-5.328	-5.001	-5.058	-4.852	-4.879	**-3.976**	**-4.041**	**-3.866**	**-4.008**	**-3.808**	**-3.675**
d_{xz}	-5.737	-5.533	-5.237	-5.328	-5.004	-5.058	-4.852	-4.880	-3.976	-4.041	-3.868	-4.008	-3.809	-3.675

Δ_H[b]	0.765	0.168	0.530	0.546	0.210	0.235	0.128	0.116	-0.046	-0.103	-0.139	-0.120	-0.235	-0.348
Δ_{xy}[c]	0.765	0.613	0.536	0.562	0.308	0.352	0.276	0.256	0.134	0.274	0.114	0.137	0.097	0.136
Δ_π[d]	0.796	0.168	0.530	0.546	0.210	0.235	0.128	0.116	-0.046	-0.103	-0.139	-0.120	-0.235	-0.348

[a] HOMO is formatted in bold; [b] smallest energy difference between "a_{1u}" and d-orbital, eV; [c] energy difference between "a_{1u}" and d_{xy} orbital; [d] energy difference between "a_{1u}" and d_π orbitals.

In agreement with the spectroelectrochemical and chemical oxidation data (*vide supra*), all three exchange-correlation functionals predict crossover (phthalocyanine-centered "a_{1u}" versus iron(II)-centered d-orbital, similar to the simplified schematic of Scheme 8.1) behavior for the series of selected compounds. As expected, the crossover point predicted for the iron(II) complexes as well as the nature of the redox-active iron(II)-centered orbital depend on the exchange-correlation functional used. In the case of the MPWLYP functional, the predicted nature of the HOMO correlates perfectly well with the spectroelectrochemical and chemical oxidation data used to determine the site of electron abstraction. As depicted in Figure 8.11 (and summarized in bold in Table 8.4) the HOMO of complexes **8.8**, **8.12**, **8.16**, **8.17**, and **8.18** is predicted to be phthalocyanine-centered and thus, the formation of the phthalocyanine cation-radical was expected upon oxidation of these compounds. Conversely, the HOMO of **8.6**, **8.10**, **8.15**, and $[PcFe^{II}X_2]^{2-}$ (X = CN^-, NCS^-, $1Tz^-$, $4Tz^-$, Im^-, and NCO^-) is predicted to be iron(II)-centered and thus, the formation of iron(III) oxidation products is expected for these compounds. The d_{xy} orbital was predicted to be redox-active for the **8.10** complexes, while degenerate (or nearly degenerate) d_π orbitals were predicted to be the redox-active orbitals for the remaining compounds. Both hybrid TPSSh and O3LYP functionals predicted the phthalocyanine-centered "a_{1u}" orbital to be the HOMO for complexes with the $\Sigma E_L(L_{ax})$ between 1.06 and 0.14 V (**8.6**, **8.8**, **8.10**, **8.12**, **8.15**, **8.16**, **8.17**, and **8.18**), while the iron(II)-centered HOMO localized at d_π orbitals were predicted for the remaining compounds with the $\Sigma E_L(L_{ax})$ between 0.04 and -0.50 V (Table 8.4). These results seemingly contradict the experimental data for complexes **8.6**, **8.7**, and **8.10** in which oxidation of the iron(II) center was observed; however, taking into consideration the closeness of the energies of the phthalocyanine-centered "a_{1u}" and iron(II)-centered d-orbitals,

we also optimized geometries and predicted total spin densities of the oxidized $[PcFeL_2]^+$, $[PcFeL'L'']^+$, and $[PcFeX_2]^-$ complexes, which allows for the consideration of potential spin-polarization effects in these species.

The results of four exchange-correlation functionals (we included unrestricted BP86 calculations as the geometries for all complexes were optimized using this exchange-correlation functional and thus data were already available to us) are shown in Figure 8.12 and summarized in Table 8.5 which lists the predicated spin densities at the central iron metal ion for the investigated $[PcFeL_2]^+$, $[PcFeL'L'']^+$, and $[PcFeX_2]^-$ complexes. In agreement with the experimental data, all four tested exchange-correlation functionals predict the formation of a phthalocyanine cation-radical as the singly oxidized product in the case of $[Pc(1-)Fe^{II}(NH_3)(CO)]^{+\bullet}$, $[Pc(1-)Fe^{II}(DMSO)_2]^{+\bullet}$, $[Pc(1-)Fe^{II}(P(OMe)_3)_2]^{+\bullet}$, and $[Pc(1-)Fe^{II}(t\text{-BuNC})_2]^{+\bullet}$ complexes as well as iron(III) species for the $[PcFe^{III}(PMe_3)_2]^+$, $[PcFe^{III}(Im)_2]^+$, $[PcFe^{III}(NH_3)_2]^+$, and $[PcFe^{III}X_2]^-$ ($X = CN^-$, NCS^-, $1Tz^-$, $4Tz^-$, Im^-, and NCO^-) compounds.

The DFT predictions for the $[PcFePy_2]^+$ complex are rather interesting. All four exchange-correlation functionals predicted the preferred formation of $[PcFe^{III}Py_2]^+$ as the singly oxidized product; however, we were able to find a second stable wavefunction solution for the uTPSSh and uMPWLYP calculations which corresponded to the formation of the cation-radical $[Pc(1-)Fe^{II}(Py)_2]^{+\bullet}$ compound (Table 8.5). Wavefunctions for both the $[PcFe^{III}Py_2]^+$ and $[Pc(1-)Fe^{II}(Py)_2]^{+\bullet}$ complexes were found to be stable under perturbation conditions (stable=opt keyword in Gaussian16).[120] The computed energy differences between the $[PcFe^{III}Py_2]^+$ and $[Pc(1-)Fe^{II}(Py)_2]^{+\bullet}$ valence tautomers (0.08 eV for uMPWLYP and 0.15 eV for uTPSSh

calculations) are rather small, a result consistent with the experimentally observed 'dual' behavior of **8.8** upon oxidation where the formation of $[PcFe^{III}Py_2]^+$ or $[Pc(1\text{-})Fe^{II}(Py)_2]^{+\bullet}$ was obtained under certain experimental conditions. When the absolute energies of the frontier occupied orbitals are considered, it is clear that the dianionic $[PcFe^{II}X_2]^{2-}$ and neutral $PcFeL_2$ and PcFeL'L" complexes should be treated separately since uncompensated charge in the former group of compounds destabilizes all orbital energies in a uniform way. Nevertheless, from the data shown in Figure 8.11, it is evident that the energy of the phthalocyanine-centered "a_{1u}" orbital does not vary much as a function of changing the axial ligand, while the energies of iron(II)-centered orbitals have a clear dependence on the axial ligand with the quantitative correlation discussed in the section below.

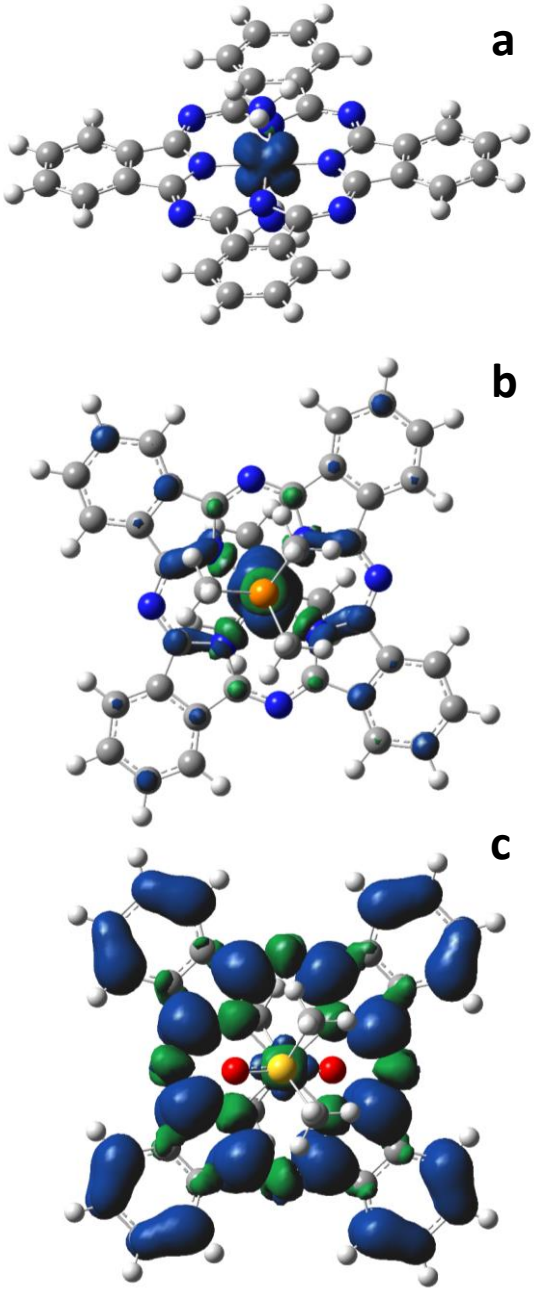

Figure 8.12. DFT-predicted (MPWLYP exchange-correlation functional) total spin densities in (a) $[PcFe^{III}(NH_3)_2]^+$ (example of the $(d_{xy})^2(d_\pi)^3$ electronic configuration), (b) $[PcFe^{III}(PMe_3)_2]^+$ (example of the $(d_{xy})^1(d_\pi)^4$ electronic configuration) and (c) $[Pc(1\text{-})Fe^{II}(DMSO)_2]^{+\bullet}$ (example of the $(a_{1u})^1$ electronic configuration).

Table 8.5. DFT-predicted spin densities at the iron atom in $[PcFeL_2]^+$, $[PcFeL'L'']^+$, and $[PcFeX_2]^-$ complexes.

Compound	uBP86	uMPWLYP	uO3LYP	uTPSSh
$[PcFe(NCO)_2]^-$	0.87	0.9	0.97	0.96
$[PcFe(Im^-)_2]^-$	0.87	0.91	1.2	0.97
$[PcFe(Tz^-)_2]^-$	0.92	0.94	1.19	0.97
$[PcFe(NCS)_2]^-$	0.75	0.8	1.15	0.87
$[PcFe(CN)_2]^-$	0.76	0.99	1.18	1.12
$[PcFe(NH_3)_2]^+$	0.92	0.94	1.14	1.02
$[PcFe(Im)_2]^+$	0.91	0.96	1.14	1.03
$[PcFe(Py)_2]^+$	0.9	0.93 (0.12)[a]	1.14	1.02 (0.15)[a]
$[PcFe(PMe_3)_2]^+$	0.97	0.99	1.1	1.07
$[PcFe(t\text{-}BuNC)_2]^+$	0.18	0.01	0.07	0.08
$[PcFe(P(OMe)_3)_2]^+$	0.24	0.01	0.09	0.1
$[PcFe(DMSO)_2]^+$	0.07	0.02	0.07	0.08
$[PcFe(CO)(NH_3)]^+$	0.01	0.04	0.05	0.06

[a] less energetically favorable valence tautomer. See text for details.

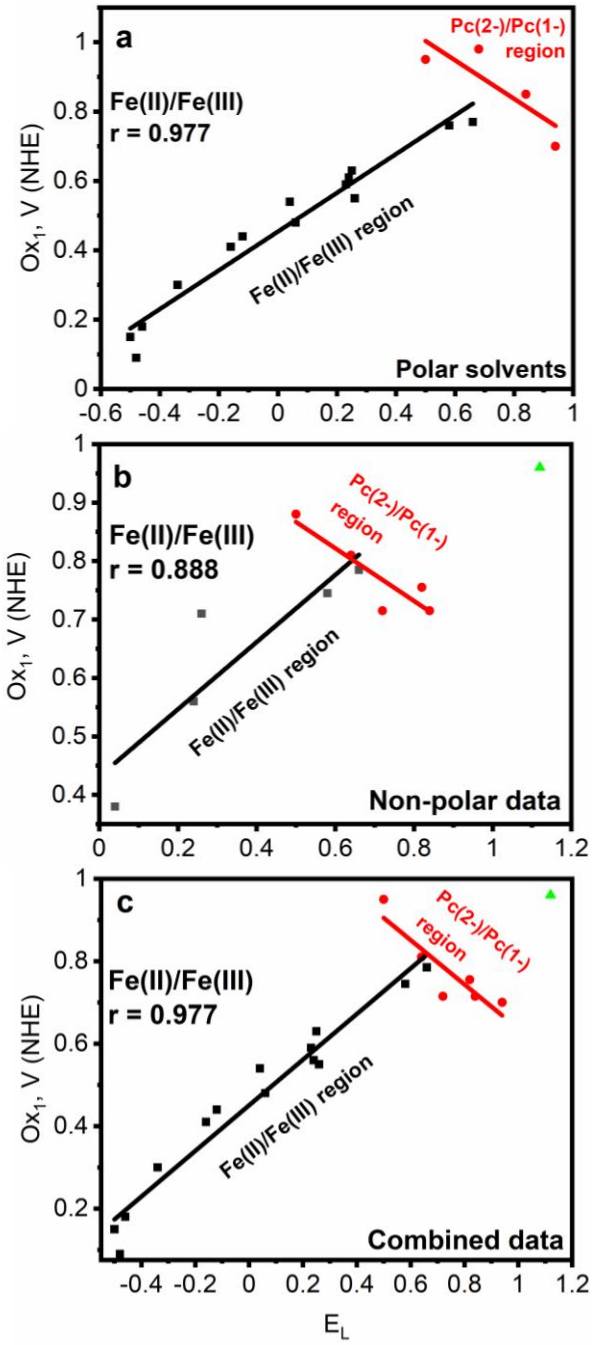

Figure 8.13. Correlation between Lever's $\Sigma E_L(L_{ax})$ values and (a) the first oxidation potential in iron(II) phthalocyanine complexes in polar solvents, (b) the first oxidation potential in iron(II) phthalocyanine complexes in non-polar solvents and (c) the first oxidation potential in iron(II)

phthalocyanine complexes from all data sets. Correlation coefficients for the Fe(II)/Fe(III) couple are listed for each figure. Data for complex **8.13** are shown in green.

8.3.4 Analysis of the redox behavior of $PcFe^{II}L$, $PcFe^{II}L'L''$, and $[PcFe^{II}X_2]^{2-}$ complexes with respect to Lever's E_L scale. After establishing the site of electron abstraction in the first oxidation process of $PcFe^{II}L_2$, $PcFe^{II}L'L''$, and $[PcFe^{II}X_2]^{2-}$ via experimental (spectroelectrochemical and chemical oxidation) and theoretical DFT methods, we then tried to rationalize these findings with respect to the theory behind Lever's E_L scale.[1-3] Assuming that the first oxidation potential belongs to the Fe^{II}/Fe^{III} couple (although we now know it does not in some cases) and the contribution from the phthalocyanine core is considered to be nearly constant,[4] the first oxidation potential in $PcFe^{II}L_2$, $PcFe^{II}L'L''$, and $[PcFe^{II}X_2]^{2-}$ complexes should correlate linearly with the $\Sigma E_L(L_{ax})$ values of the axial ligands given the additive nature of Lever's E_L scale. Comparison of the predicted E_L scale with experimental values indicates that this is not the case (Table 8.3, Figure 8.13). Instead, such a correlation (except for complex **8.13**, which has an iron ion residing outside of the phthalocyanine plane) has a two-slope (or volcano type) profile. Such behavior can only be explained assuming that: (i) the energies of the iron-centered d_{xy} and d_{π} orbitals can intercross; (ii) the energy of the phthalocyanine-centered Gouterman's type[118-120] "a_{1u}" orbital can intercross with the energies of iron-centered orbitals leading to a change in the site of electron transfer. In the former case, the linearity of the Ox_1 versus E_L plot (where Ox_1 is the first oxidation potential) will be lost but since the HOMO is still iron-centered, the oxidation of the $PcFe^{II}L_2$, $PcFe^{II}L'L''$, and $[PcFe^{II}X_2]^{2-}$ complexes should generate low-spin iron(III) compounds. In the latter case, at some point the HOMO will become phthalocyanine-

centered and oxidation of the respective iron(II) complex will lead to the formation of a phthalocyanine cation-radical compound coordinated to the iron(II) center. Since axial ligands with negative E_L values (i.e. strong σ-donors) strongly destabilize occupied iron(II) orbitals, one might expect that such iron/phthalocyanine HOMO intercrossing can only happen with axial ligands which are summed to large positive E_L values (*i.e.* π-acceptors). Numerically, our linear correlation parameters for the polar solvent data set follows the predictions reported by Lever in 2013[4] for all compounds that experimentally and computationally were predicted to form iron(III) species (Figure 8.13a). The correlation coefficient observed for the Fe^{II}/Fe^{III} oxidation potentials versus E_L parameters (r = 0.977) is typical for E_L theory.[1-4] The first oxidation potential for complex **8.13** is an outlier but is also the only complex which should have the iron atom located outside of the phthalocyanine's N4 plane (similar to the crystallographically-characterized PcFe(DMF)(CO) compound). The clear deviation of the first oxidation potential in the **8.8**, $PcFe^{II}(NCR)_2$, $PcFe^{II}[P(OR)_3]_2$, and **8.12** complexes from the expected values is indicative of a change in the site of oxidation at the phthalocyanine macrocycle rather than at the iron center. The correlation coefficient for the Fe(II)/Fe(III) versus E_L relationship in non-polar solvents is not as good (r = 0.888), but only includes five points with a single outlier (complex **8.7**, Figure 8.13b). Finally, the combined dataset (both polar and non-polar solvents) overlays reasonably well and gives $E_{1/2}(NHE) = 0.55\ \Sigma E_L(L_{ax}) + 0.45$ (Figure 8.13c), which is not too far from Lever's report on a limited number of similar compounds ($E_{1/2}(NHE) = 0.76\ \Sigma E_L(L_{ax}) + 0.52$).[4]

Since the DFT-predicted absolute energies of the phthalocyanine-centered "a_{1u}" and iron(II)-centered d_{xy} and d_{π} orbitals are significantly destabilized in dianions due to a lack of charge compensation, no correlation is expected between their energies and Lever's E_L parameter (Supporting Information Figure S8.24); however, as was mentioned above, in agreement with the additive nature of Lever's E_L theory, our DFT calculations are indicative of the low variability of the "a_{1u}" orbital and clear axial ligand dependency of the metal-centered orbitals when subgroups (dianions versus neutral compounds) are considered. Thus, one would expect linear correlations between the DFT-predicted phthalocyanine's "a_{1u}" – iron(II) energy difference ($E_{"a1u"} - E_{dxy}$ and $E_{"a1u"} - E_{d\pi}$) and Lever's E_L parameter. Indeed, such correlations can be clearly seen (Figure 8.14) with correlation coefficients observed between 0.91 and 0.97 for all compounds considered. The observation of such correlations connects Lever's empirically additive E_L theory with DFT calculations and provides additional insight towards the observation of the crossover point of Pc(2-)/Pc(1-) versus Fe(II)/Fe(III) in the series of $PcFe^{II}L_2$, $PcFe^{II}L'L''$, and $[PcFe^{II}X_2]^{2-}$ complexes.

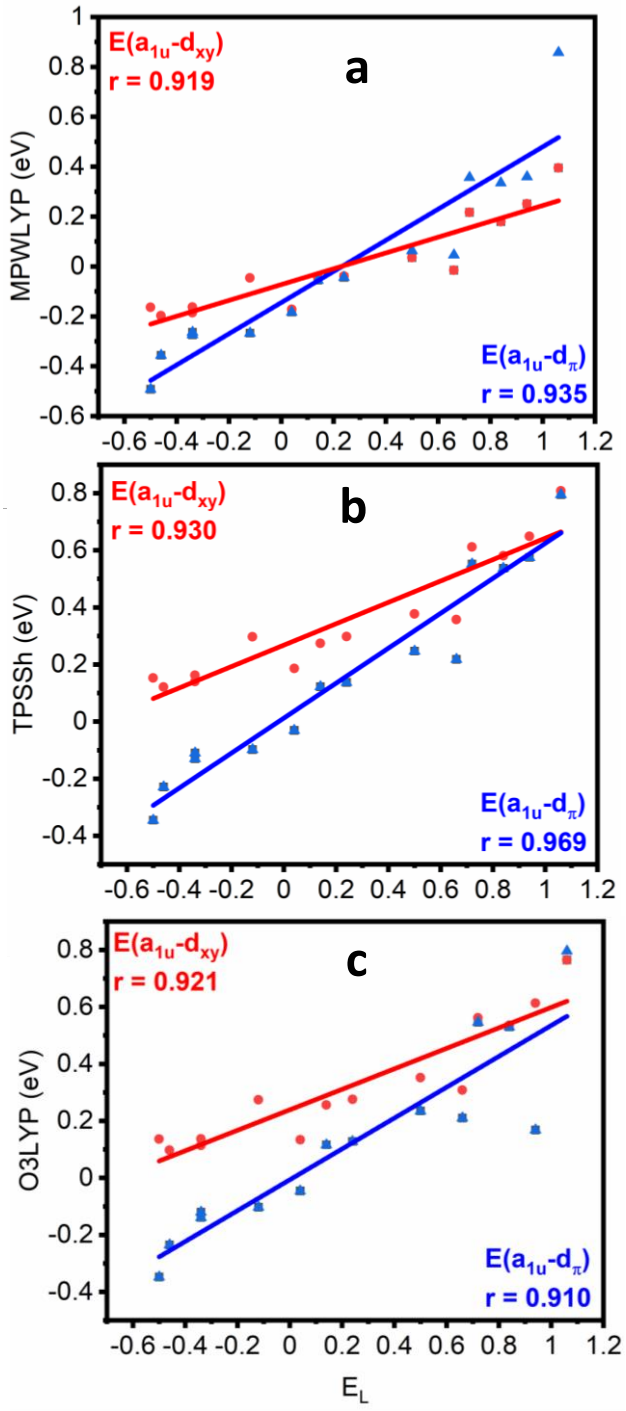

Figure 8.14. Correlation between Lever's $\Sigma E_L(L_{ax})$ values and the energy difference between a_{1u}(Pc) and d_{xy} or d_{π} orbitals predicted using: (a) MPWLYP; (b) TPSSh; and (c) O3LYP exchange-correlation functionals.

8.4 Conclusions

The electronic structures (and in particular, the nature of the HOMO) in a series of $PcFe^{II}L_2$, $PcFe^{II}L'L''$, and $[PcFe^{II}X_2]^{2-}$ complexes were probed by electrochemical, spectroelectrochemical and chemical oxidation as well as theoretical (density functional theory, DFT) studies. Generally, it was found that the energies of the metal-centered occupied orbitals in these various six-coordinate iron phthalocyanines correlate well with Lever's electrochemical parameter, E_L, and intercross the phthalocyanine-centered a_{1u} orbital in several compounds with moderate-to-strong π-accepting axial ligands. In these cases, an oxidation of the phthalocyanine macrocycle (Pc(2-)/Pc(1-) rather than central metal ion (Fe(II)/Fe(III)) was theoretically predicted and experimentally confirmed.

8.5 Experimental Section

8.5.1 Materials. All phthalocyanine complexes were prepared as described previously.[47,63,64,66,72] Tetrabutylammonium tetrakis-(pentafluorophenylborate) (TFAB) electrolyte was prepared following the reported protocol.[121] Dimethyl sulfoxide (DMSO, anhydrous, ≥99.9%), DriSolv anhydrous dichloromethane (DCM, ≥99.8%), pyridine (Py, anhydrous, 99.8%), potassium cyanate (KNCO, 96%) and tetrabutylammonium perchlorate (TBAP, for electrochemical analysis, ≥99.0%) were all purchased from Sigma Aldrich and used as received. N,N-dimethylformamide (DMF, anhydrous, 99.8%) was purchased from Sigma Aldrich and distilled over P_2O_5 prior to use in electrochemical experiments. All other axial ligands were purchased from commercial sources and used as received. Iron phthalocyanine (98%) was

purchased from Aldrich and its quality was assessed and confirmed by Mössbauer spectroscopy.

8.5.2 Spectroscopy and electrochemistry. Electrochemical data were collected using a CH-620 analyzer or an EG&G Princeton Applied Research (PAR) Model 173 potentiostat/galvanostat, paired with an EG&G PAR Model 175 universal programmer and a Houston Instruments Omnigraphic 2000 XY Plotter. Cyclic voltammetric measurements were made using a three-electrode system consisting of a glassy carbon or platinum working electrode, platinum auxiliary electrode, and either a saturated calomel reference electrode (SCE) separated from the bulk of the solution by a fritted solution filled glass bridge of low porosity or a Ag/AgCl wire pseudo-reference electrode. Decamethylferrocene (DmFc) or ferrocene (Fc) was used as an internal standard for the studied complexes and the reported potentials were corrected to the Fc/Fc^+ couple. For consistency purpose, all figures in this work are shown using the Fc/Fc^+ scale. All electrochemical experiments were conducted in either a dichloromethane (DCM), N,N-dimethylformamide (DMF), dimethyl sulfoxide (DMSO), or pyridine/0.1M tetrabutylammonium perchlorate (TBAP) or 0.05M tetrabutylammonium tetrakis(pentafluorophenyl)borate (TFAB) system. Spectroelectrochemical experiments were performed using either a Jasco V-770 UV-vis-NIR spectrophotometer in tandem with a CH Instruments electrochemical analyzer which was operated using the bulk electrolysis mode or a Hewlett-Packard model 8453 diode array paired with an EG&G PAR Model 173 potentiostat/galvanostat used to apply a controlled potential. The data were collected using a custom-made 1 mm cell, a platinum mesh working electrode, platinum auxiliary electrode and either a saturated calomel reference electrode (SCE) separated

from the bulk of the solution by a fritted solution filled glass bridge of low porosity or a Ag/AgCl wire pseudo-reference electrode. Spectroelectrochemical solutions consisted of 0.1, 0.15, or 0.3 M solutions of either TBAP or TFAB in DCM, DMF, DMSO, or pyridine. High-resolution mass spectra were recorded using a Bruker micrOTOF-QIII mass spectrometer. ^{1}H NMR spectra were recorded using Brucker 300 MHz instrument.

8.5.3 Computational details. All calculations were run using Gaussian 16.[122] The BP86[122,123] exchange-correlation functional with Wachters full-electron basis set[124] (Wf) for iron and the 6-311G(d) basis set[125] for the other atoms were used for all calculations. Vibrational frequencies were calculated to ensure all geometries were local minima. Since the nature of the frontier molecular orbitals in the currently investigated complexes are expected to have some dependency on the utilized exchange-correlation functional,[42,63,116,117] single point calculations were conducted using TPSSh,[127,128] O3LYP[129] and MPWLYP[130] exchange-correlation functionals. All computations were solution-phase calculations conducted using the PCM model[131] with dichloromethane (DCM) as the solvent to make an accurate comparison between all complexes. Spin-unrestricted calculations were employed for calculations of the oxidized species. The QMForge program[132] was used for orbital analysis. In order to accelerate the DFT calculations and avoid a conformational search, the *n*-BuNH_2 and P(O*n*-Bu)$_3$ axial ligands were truncated to NH_3 and P(OMe)$_3$ groups, respectively, and the corresponding E_L values were used in the correlation analysis.

8.6 References

1. Lever, A. B. P. "Electrochemical parametrization of metal complex redox potentials, using the ruthenium(III)/ruthenium(II) couple to generate a ligand electrochemical series" *Inorg. Chem.* **1990**, *29*, 1271-1285.
2. Alexiou, C.; Lever, A. B. P. "Tuning metalloporphyrin and metallophthalocyanine redox potentials using ligand electrochemical (E_L) and Hammett (σ_p) parametrization" *Coord. Chem. Rev.* **2001**, *216-217*, 45-54.
3. Lever, A. B. P.; Dodsworth, E. S. in: “Inorganic Electronic Structure and Spectroscopy” Solomon, E. I. and Lever, A. B. P. (Eds.), John Wiley & Sons, Inc., **1999**, *Vol. II*, 227-289.
4. Lever, A. B. P. "The phthalocyanines-molecules of enduring value; a two-dimensional analysis of redox potentials" *J. Porphyrins Phthalocyanines* **1999**, *3*, 488-499.
5. Kepp, K. P.; Dasmeh, P. Effect of Distal Interactions on O_2 Binding to Heme. *J. Phys. Chem. B* **2013**, *117*, 3755-3770.
6. Taube, R. “New aspects of the chemistry of transition metal phthalocyanines” *Pure Appl. Chem.* **1974**, *38*, 427-438.
7. Nemykin, V. N.; Tret'yakova, I. N.; Volkov, S. V.; Li, V. D.; Mekhryakova, N. G.; Kaliya, O. L.; Luk'yanets, E. A. “Synthesis, structure and properties of coordination compounds of iron phthalocyanines and their analogues” *Russ. Chem. Rev.* **2000**, *69*, 325-346.
8. Hanack, M. In Phthalocyanines: Properties and Applications, Eds. Leznoff, C. C. and Lever, A. B. P. VCH, New York, 1989, Vol. 2, pp. 43-96.
9. Ercolani, C.; Floris, B. In Phthalocyanines: Properties and Applications, Eds. Leznoff, C. C. and

Lever, A. B. P. VCH, New York, 1989, Vol. 2, pp. 1-43.

10. Sorokin, A. B. “Phthalocyanine Metal Complexes in Catalysis” *Chem. Rev.* **2013**, *113*, 8152-8191.
11. Kennedy, B. J.; Murray, K. S.; Zwack, P. R.; Homborg, H.; Kalz, W. “Spin states in iron(III) phthalocyanines studied by Moessbauer, magnetic susceptibility, and ESR measurements” *Inorg. Chem.* **1986**, *25*, 2539-2545.
12. Afanasiev, P.; Sorokin, A. B. “μ-Nitrido Diiron Macrocyclic Platform: Particular Structure for Particular Catalysis” *Acc. Chem. Res.* **2016**, *49*, 583-593.
13. Woehrle, D.; Baziakina, N.; Suvorova, O.; Makarov, S.; Kutureva, V.; Schupak, E.; Schnurpfeil, G. “Phthalocyanine coatings on silica and zinc oxide. Synthesis and their activities in the oxidation of sulfide” *J. Porphyrins Phthalocyanines* **2004**, *8*, 1390-1401.
14. Woehrle, D.; Suvorova, O.; Gerdes, R.; Bartels, O.; Lapok, L.; Baziakina, N.; Makarov, S.; Slodek, A. “Efficient oxidations and photooxidations with molecular oxygen using metal phthalocyanines as catalysts and photocatalysts” *J. Porphyrins Phthalocyanines* **2004**, *8*, 1020-1041.
15. Cailler, L. P.; Clemancey, M.; Barilone, J.; Maldivi, P.; Latour, J.-M.; Sorokin, A. B. “Comparative Study of the Electronic Structures of μ-Oxo, μ-Nitrido, and μ-Carbido Diiron Octapropylporphyrazine Complexes and Their Catalytic Activity in Cyclopropanation of Olefins” *Inorg. Chem.* **2020**, *59*, 1104-1116.
16. Colomban, C.; Tobing, A. H.; Mukherjee, G.; Sastri, C. V.; Sorokin, A. B.; de Visser, S. P. “Mechanism of Oxidative Activation of Fluorinated Aromatic Compounds by N-Bridged Diiron-Phthalocyanine: What Determines the Reactivity?” *Chem. Eur. J.* **2019**, *25*, 14320-

14331.

17. Neu, H. M.; Zhdankin, V. V.; Nemykin, V. N. “Binuclear iron(III) phthalocyanine(μ-oxodimer) /tetrabutylammonium oxone: a powerful catalytic system for oxidation of hydrocarbons in organic solution” *Tetrahedron Lett.* **2010**, *51*, 6545-6548.
18. Neu, H. M.; Yusubov, M. S.; Zhdankin, V. V.; Nemykin, V. N. “Binuclear iron(III) phthalocyanine(μ-oxo-dimer)-catalyzed oxygenation of aromatic hydrocarbons with iodosylbenzene sulfate and iodosylbenzene as the oxidants” *Adv. Synth. Catal.* **2009**, *351*, 3168-3174.
19. Geraskin, I. M.; Luedtke, M. W.; Neu, H. M.; Nemykin, V. N.; Zhdankin, V. V. “Organic iodine(V) compounds as terminal oxidants in iron(III) phthalocyanine catalyzed oxidation of alcohols” *Tetrahedron Lett.* **2008**, *49*, 7410-7412.
20. Griffin, J. R.; Wendell, C. I.; Garwin, J. A.; White, M. C. “Catalytic C(sp^3)-H Alkylation via an Iron Carbene Intermediate” *J. Am. Chem. Soc.* **2017**, *139*, 13624-13627.
21. He, C.; Wu, Z.-Y.; Zhao, L.; Ming, M.; Zhang, Y.; Yi, Y.; Hu, J.-S. “Identification of FeN4 as an Efficient Active Site for Electrochemical N_2 Reduction” *ACS Catalysis* **2019**, *9*, 7311-7317.
22. Hu, P.; Tan, M.; Cheng, L.; Zhao, H.; Feng, R.; Gu, W.-J.; Han, W. “Bio-inspired iron-catalyzed oxidation of alkylarenes enables late-stage oxidation of complex methylarenes to arylaldehydes” *Nature Commun.* **2019**, *10*, 1-9.
23. Govan, J.; Abarca, G.; Aliaga, C.; Sanhueza, B.; Orellana, W.; Cardenas-Jiron, G.; Zagal, J. H.; Tasca, F. “Influence of cyano substituents on the electron density and catalytic activity towards the oxygen reduction reaction for iron phthalocyanine. The case for Fe(II) 2,3,9,10, 16,17,23,24-octa(cyano)phthalocyanine” *Electrochem. Commun.* **2020**, *118*, 106784/1-

106784/6.

24. Praats, R.; Kaarik, M.; Kikas, A.; Kisand, V.; Aruvali, J.; Paiste, P.; Merisalu, M.; Leis, J.; Sammelselg, V.; Zagal, J. H. “Electrocatalytic oxygen reduction reaction on iron phthalocyanine-modified carbide-derived carbon/carbon nanotube composite electrocatalysts” *Electrochim. Acta* **2020**, *334*, 135575.
25. Recio, F. J.; Gutierrez, C. A.; Venegas, R.; Linares-Flores, C.; Caro, C. A.; Zagal, J. H. “Optimization of the electrocatalytic activity of MN4-macrocyclics adsorbed on graphite electrodes for the electrochemical oxidation of L-cysteine by tuning the M (II)/(I) formal potential of the catalyst: an overview” *Electrochim. Acta* **2014**, *140*, 482-488.
26. Kuznetsova, N. A.; Kaliya, O. L. “Heterogenized metallophthalocyanines for photodynamic microorganism inactivation: an overview of our experience” *Makrogeterotsikly* **2015**, *8*, 8-19.
27. Gerasimova, G. K.; Yakubovskaya, R. I.; Pankratov, A. A.; Treshchalina, E. M.; Nemtsova, E. R.; Andreeva, T. N.; Venediktova, Yu. B.; Plyutinskaya, A. D.; Bezborodova, O. A.; Sidorova, T. A.; Baryshnikov, A. B.; Kaliya, O. L.; Voroztsov, G. N.; Luzhkov, Yu. M. “Binary catalytic therapy: A new approach to treatment of malignant tumors. Results of pre-clinical and clinical studies” *Russ. J. Gen. Chem.* **2015**, *85*, 289-302.
28. Fitzgerald, J. P.; Lebenson, J. R.; Wang, G.; Yee, G. T.; Noll, B. C.; Sommer, R. D. “Iron Tetraanthracenotetraazaporphyrins: Synthesis, Structural Characterization, Ligand Binding Properties, and Unexpected Selectivity of a Bis-"Bowl" Tetraazaporphyrin” *Inorg. Chem.* **2008**, *47*, 4520-4530.
29. Fitzgerald, J. P.; Haggerty, B. S.; Rheingold, A. L.; May, L.; Brewer, G. A. “Iron

octaethyltetraazaporphyrins: synthesis, characterization, coordination chemistry, and comparisons to related iron porphyrins and phthalocyanines" *Inorg. Chem.* **1992**, *31*, 2006-2013.

30. Ona-Burgos, P.; Casimiro, M.; Fernandez, I.; Navarro, A. V.; Fernandez-Sanchez, J. F.; Carretero, A. S.; Gutierrez, A. F. "Octahedral iron(II) phthalocyanine complexes: multinuclear NMR and relevance as NO_2 chemical sensors" *Dalton Trans.* **2010**, *39*, 6231-6238.
31. Valero-Navarro, A.; Fernandez-Sanchez, J. F.; Segura-Carretero, A.; Spichiger-Keller, U. E.; Fernandez-Gutierrez, A.; Ona, P.; Fernandez, I. "Iron-phthalocyanine complexes immobilized in nanostructured metal oxide as optical sensors of NOx and CO - NMR and photophysical studies" *J. Porphyrins Phthalocyanines* **2009**, *13*, 616-623.
32. Fernandez-Sanchez, J. F.; Fernandez, I.; Steiger, R.; Beer, R.; Cannas, R.; Spichiger-Keller, U. E. "Second-generation nanostructured metal oxide matrices to increase the thermal stability of CO and NO_2 sensing layers based on iron(II) phthalocyanine" *Adv. Functional Mater.* **2007**, *17*, 1188-1198.
33. Nxele, S. R.; Nyokong, T. "Conjugation of Azide-functionalised CdSe/ZnS Quantum Dots with Tetrakis(5-hexyn-oxy) Fe(II) phthalocyanine via Click Chemistry for Electrocatalysis" *Electrochim. Acta* **2016**, *194*, 26-39.
34. Nxele, S. R.; Mashazi, P.; Nyokong, T. "Electrode Modification Using Alkynyl Substituted Fe(II) Phthalocyanine via Electrografting and Click Chemistry for Electrocatalysis" *Electroanalysis* **2015**, *27*, 2468-2478.
35. Maringa, A.; Mashazi, P.; Nyokong, T. "Characterization of electrodes modified by one pot

or step by step electro-click reaction and axial ligation of iron tetracarboxyphthalocyanine" *Electrochim. Acta* **2014**, *145*, 237-244.

36. Coates, M.; Nyokong, T. "Characterization of glassy carbon electrodes modified with carbon nanotubes and iron phthalocyanine through grafting and click chemistry" *Electrochim. Acta* **2013**, *91*, 158-165.
37. Dale, B. W.; Williams, R. J. P.; Edwards, P. R.; Johnson, C. E. "Moessbauer spectra of compounds containing iron(II) in strong-field tetragonal environments" *Trans. Faraday Soc.* **1968**, *64*, 620-629.
38. Dale, B. W.; Williams, R. J. P.; Edwards, P. R.; Johnson, C. E. "Nature of electric field-gradient tensor in strong-field tetragonal and pseudo-tetragonal complexes of divalent iron" *Trans. Faraday Soc.* **1968**, *64*, 3011-3013.
39. Dale, B. W. "Effect of axial ligands on the electronic absorption spectrum of phthalocyanineiron(II)" *Trans. Faraday Soc.* **1969**, *65*, 331-339.
40. Hanack, M.; Hirsch, A. "Synthesis of bridged mixed valence macrocyclic compounds" *Synthetic Metals* **1989**, *29*, F9-F14.
41. Nemykin, V. N.; Polshina, A. E.; Chernii, V. Y.; Polshin, E. V.; Kobayashi, N. "Synthesis, properties and Mossbauer spectra of bisaxially co-ordinated iron(II) phthalocyanine low-spin complexes: the first semi-quantitative explanation of the influence of the character of axial ligands on the spectral parameters" *Dalton* **2000**, 1019-1025.
42. Nemykin, V. N.; Kobayashi, N.; Chernii, V. Y.; Belsky, V. K. "Mossbauer, crystallographic, and density functional theoretical investigation of the electronic structure of bis-ligated low-spin iron(II) phthalocyanines" *Eur. J. Inorg. Chem.* **2001**, 733-743.

43. Fernandez, I.; Pregosin, P. S.; Albinati, A.; Rizzato, S.; Spichiger-Keller, U. E.; Nezel, T.; Fernandez-Sanchez, J. F. “Solution NMR and X-ray structural studies on phthalocyaninatoiron complexes” *Helvetica Chim. Acta* **2006**, *89*, 1485-1496.

44. Nevonen, D. E.; Ferch, L. S.; Chernii, V. Y.; Herbert, D. E.; van Lierop, J.; Nemykin, V. N. “X-Ray structures, Mossbauer hyperfine parameters, and molecular orbital descriptions of the phthalocyaninato iron(II) azole complexes” *J. Porphyrins Phthalocyanines* **2020**, *24*, 894-903.

45. Ettorre, R.; Marton, D.; Russo, U.; Zanonato, P. “Complexes of phthalocyaninatoiron(II) with diazoles” *J. Porphyrins Phthalocyanines* **2001**, *5*, 545-547.

46. Ouedraogo, G. V.; More, C.; Richard, Y.; Benlian, D. “Charge-transfer and Moessbauer spectra of axially substituted iron phthalocyanines” *Inorg. Chem.* **1981**, *20*, 4387-4393.

47. Ough, E. A.; Stillman, M. J. “Analysis of the absorption and magnetic circular dichroism spectra of iron(II) phthalocyanine” *Inorg. Chem.* **1994**, *33*, 573-583.

48. Stillman, M. J.; Thomson, A. J. “Orbital reduction factors in the lowest excited state of the phthalocyanine ring and their measurement by magnetic circular dichroism spectroscopy” *J. Chem. Soc., Faraday Trans. 2,* **1974**, *70*, 805-814.

49. Hanack, M.; Deger, S.; Lange, A. “Bisaxially coordinated macrocyclic transition metal complexes” *Coord. Chem. Rev.* **1988**, *83*, 115-136.

50. Schneider, O.; Hanack, M. “Axially polymerized (phthalocyaninato)iron(II) with pyrazine, 4, 4'-bipyridine, 1,4-diisocyanobenzene, or 1,4-diazabicyclo[2.2.2]octane as bridging ligands; synthesis, characterization, and electrical conductivities” *Chem. Ber.* **1983**, *116*, 2088-2108.

51. Hanack, M.; Hirsch, A.; Lehmann, H. “Soluble oligomeric bridged phthalocyaninatoiron(II) complexes” *Angew. Chem. Int. Ed.* **1990**, *29*, 1467-1468.

52. Hanack, M.; Duerr, K.; Lange, A.; Barcina, J. Osio; Pohmer, J.; Witke, E. “Synthesis of low band gap polymers - a challenge for organic chemists” *Synth. Met.* **1995**, *71*, 2275-2278.

53. Hanack, M. “Intrinsic semiconducting materials on phthalocyanine basis” *Turk. J. Chem.* **1998**, *22*, 13-22.

54. Hanack, M.; Fiedler, M.; Subramanian, L. R. “Phthalocyaninatoiron complexes with tridentate ligands” *Synth. Met.* **1999**, *100*, 123-130.

55. Bayo, K.; Ouedraogo, G. V.; Terzian, G.; Benlian, D. “UV-visible and IR spectra of iron(II) phthalocyanine polymer complexes linked by bis-pyridinato ligands” *Polyhedron* **1990**, *9*, 1087-1090.

56. Ercolani, C.; Monacelli, F.; Dzugan, S.; Goedken, V. L.; Pennesi, G.; Rossi, G. “X-ray crystal structure of μ-oxo-bis[(1-methylimidazole)phthalocyaninatoiron(III)] and comments on the molecular structure and chemistry of oxo-bridged iron phthalocyaninate dimers” *J. Chem. Soc., Dalton Trans.* **1991**, 1309-1315.

57. Janczak, J.; Kubiak, R. “Pyrazine control of the supramolecular chemistry of iron(II) and cobalt (II) phthalocyanines” *CrystEngComm* **2010**, *12*, 3599-3606.

58. Janczak, J.; Kubiak, R. “Synthesis, thermal stability and structural characterization of iron(II) phthalocyanine complex with 4-cyanopyridine” *Polyhedron* **2007**, *26*, 2997-3002.

59. Ohya, T.; Morohoshi, H.; Sato, M. “Preparation and characterization of low-spin iron(II) porphyrin complexes with bis(phosphine) or bis(phosphite) axial ligands” *Inorg. Chem.* **1984**, *23*, 1303-1305.

60. Sweigart, D. A. “Axial ligand substitution in iron(II) phthalocyanine adducts: replacement of tri-n-butyl phosphite by tri-n-butylphosphine” *J. Chem. Soc., Dalton Trans.* **1976**, 1476-1477.

61. Watkins, J. J.; Balch, A. L. “Complexes of ferrous phthalocyanine with aromatic nitroso compounds, isocyanides, and phosphites” *Inorg. Chem.* **1975**, *14*, 2720-2723.

62. Zanguina, A.; Bayo-Bangoura, M.; Bayo, K.; Ouedraogo, G. V. “IR and UV-visible spectra of iron(II) phthalocyanine complexes with phosphine or phosphite” *Bull. Chem. Soc. Ethiopia* **2002**, *16*, 73-79.

63. Nemykin, V. N.; Nevonen, D. E.; Ferch, L. S.; Shepit, M.; Herbert, D. E.; van Lierop, J. “Accurate Prediction of Mössbauer Hyperfine Parameters in Bis-Axially Coordinated Iron(II) Phthalocyanines Using Density Functional Theory Calculations: A Story of a Single Orbital Revealed by Natural Bond Orbital Analysis” *Inorg. Chem.* **2021**, *60*, 3690-3706.

64. Calderazzo, F.; Pampaloni, G.; Vitali, D.; Pelizzi, G.; Collamati, I.; Frediani, S.; Serra, A. M. “Carbonyl derivatives of phthalocyaninatoiron(II), especially those containing Group VI axial donor atoms. Crystal and molecular structure of carbonyl(N,N-dimethylformamide) phthalocyaninatoiron(II) and Moessbauer studies of some of the products” *J. Organomet. Chem.* **1980**, *191*, 217-242.

65. Calderazzo, F.; Frediani, S.; James, B. R.; Pampaloni, G.; Reimer, K. J.; Sams, J. R.; Serra, A. M.; Vitali, D. “Synthesis and Moessbauer spectroscopic studies of carbonyl derivatives of (phthalocyaninato)iron(II)” *Inorg. Chem.* **1982**, *21*, 2302-2306.

66. Calderazzo, F.; Pampaloni, G.; Vitali, D.; Collamati, I.; Dessy, G.; Fares, V. “Bis adducts of phthalocyaninatoiron(II) with Group 6A axial donor atoms. Crystal and molecular structure of sulfur-bonded bis(dimethyl sulfoxide)phthalocyaninatoiron(II)-dimethyl sulfoxide (1/2)” *J. Chem. Soc., Dalton Trans.* **1980**, 1965-1969.

67. Calderazzo, F.; Vitali, D.; Pampaloni, G.; Collamati, I. “Reaction of pentacarbonyliron with

phthalonitrile in dimethylformamide and isolation of carbonyl derivatives of iron(II) phthalocyanine stabilized by group 6 donor atoms" *J. Chem. Soc., Chem. Commun.* **1979**, 221-222.

68. Anderson, D. R.; Solntsev, P. V.; Rhoda, H. M.; Nemykin, V. N. "How big is big? Separation by conventional methods, X-ray and electronic structures of positional isomers of bis-tert-butylisocyano adduct of 2(3),9(10),16(17),23(24)-tetrachloro-3(2),10(9),17(16),24(23)-tetra(2,6-di-iso-propylphenoxy)-phthalocyaninato iron(II) complex" *J. Porphyrins Phthalocyanines* **2016**, *20*, 337-351.
69. Nemykin, V. N.; Purchel, A. A.; Spaeth, A. D.; Barybin, M. V. "Probing the Electronic Properties of a Trinuclear Molecular Wire Involving Isocyanoferrocene and Iron(II) Phthalocyanine Motifs" *Inorg. Chem.* **2013**, *52*, 11004-11012.
70. Hanack, M.; Knecht, S.; Polley, R.; Subramanian, L. R. "Axially 1,4-diisocyanobenzene bridged substituted iron(II) phthalocyanines and 2,3-naphthalocyanines" *Synth. Metals* **1996**, *80*, 183-189.
71. Schmid, G.; Witke, E.; Schlick, U.; Knecht, S.; Hanack, M. "Substituent effects in soluble phthalocyaninatoiron(II) complexes" *J. Mater. Chem.* **1995**, *5*, 855-859.
72. Ryu, H.; Knecht, S.; Subramanian, L. R.; Hanack, M. "Synthesis and properties of bridged phthalocyaninatoiron(II) complexes with bidentate aliphatic isocyanides" *Synth. Metals* **1995**, *72*, 289-296.
73. Hanack, M.; Knecht, S.; Witke, E.; Haisch, P. "Synthesis and properties of soluble metallophthalocyanines" *Synth. Metals* **1993**, *55*, 873-878.
74. Hanack, M.; Lange, A.; Grosshans, R. "Tetrazine-bridged phthalocyaninato-metal complexes

as semiconducting material" *Synth. Metals* **1991**, *45*, 59-70.

75. Lever, A. B. P.; Wilshire, J. P. "Electrochemistry of iron phthalocyanine complexes in nonaqueous solvents and the identification of five-coordinate iron(I) phthalocyanine derivatives" *Inorg. Chem.* **1978**, *17*, 1145-1151
76. Nyokong, T.; Gasyna, Z.; Stillman, M. J. "Photooxidation of phthalocyanines. Photoinduced reactivity of the triplet state" *ACS Symposium Series* **1986**, *321*, 309-327.
77. Ough, E. A. "Metal and ring oxidation in metallophthalocyanines" *Ph.D. Thesis*, University of Western Ontario, Canada, **1993**, pp. 232. https://ir.lib.uwo.ca/cgi/viewcontent.cgi?article=3233&context=digitizedtheses.
78. Holovics, T. C.; Deplazes, S. F.; Toriyama, M.; Powell, D. R.; Lushington, G. H.; Barybin, M. V. "Organometallic Isocyanocyclopentadienides: A Combined Synthetic, Spectroscopic, Structural, Electrochemical, and Theoretical Investigation" *Organometallics* **2004**, *23*, 2927-2938.
79. Mialki, W. S.; Wigley, D. E.; Wood, T. E.; Walton, R. A. "Homoleptic seven- and six-coordinate alkyl isocyanide complexes of chromium: synthesis, characterization and redox and substitution chemistry" *Inorg. Chem.* **1982**, *21*, 480-485.
80. Bullock, J. P.; Mann, K. R. "UV-visible IR thin-layer spectroelectrochemical studies of hexakis(aryl isocyanide)chromium complexes. In situ generation and characterization of four oxidation states" *Inorg. Chem.* **1989**, *28*, 4006-4011.
81. Noviandri, I.; Brown, K. N.; Fleming, D. S.; Gulyas, P. T.; Lay, P. A.; Masters, A. F.; Phillips, L. "The decamethylferrocenium/decamethylferrocene redox couple: A superior redox standard to the ferrocenium/ferrocene redox couple for studying solvent effects on the

thermodynamics of electron transfer" *J. Phys. Chem. B* **1999**, *103*, 6713-6722.

82. Aranzaes, J. R.; Daniel, M.-C.; Astruc, D. "Metallocenes as references for the determination of redox potentials by cyclic voltammetry - Permethylated iron and cobalt sandwich complexes, inhibition by polyamine dendrimers, and the role of hydroxy-containing ferrocenes" *Can. J. Chem.* **2006**, *84*, 288-299.
83. Lever, A. B. P.; Milaeva, E. R.; Speier, G. in: *Phthalocyanines: properties and applications;* C. C. Leznoff and A. B. P. Lever (Eds.), VCH, **1993**, *Vol. 3*, 1-69.
84. Konarev, D. V.; Kuzmin, A. V.; Simonov, S. V.; Khasanov, S. S.; Lyubovskaya, R. N. "Structure and optical properties of fullerene C-60 complex with dipyridinated iron(II) phthalocyanine $[Fe(II)Pc(C_5H_5N)_2]\bullet C\text{-}60\bullet 4C_6H_4Cl_2$. First structure of bisaxially coordinated iron(II) phthalocyanine complex with acetonitrile $Fe(II)Pc(CH_3CN)_2$" *J. Porphyrins Phthalocyanines* **2014**, *18*, 87-93.
85. Behnisch, R.; Hanack, M. "Cyclic voltammetric and electrocrystallization studies of axially substituted dicyano(phthalocyaninato) metal complexes and related compounds" *Synth. Metals* **1990**, *36*, 387-397.
86. Kalz, W.; Homborg, H.; Kueppers, H.; Kennedy, B. J.; Murray, K. S. "Preparation and characterization of dicyano(phthalocyaninato)ferrates(III)" *Z. Natur. B* **1984**, *39B*, 1478-1489.
87. Orihashi, Y.; Ohno, H.; Tsuchida, E.; Matsuda, H.; Nakanishi, H.; Kato, M. "Highly conductive crystals prepared by electrocrystallization of potassium dicyanophthalocyaninatoiron(III)" *Chem. Lett.* **1987**, 601-604.
88. Shao, J.; Richards, K.; Rawlins, D.; Han, B.; Hansen, C. A. "Synthesis, electrochemistry,

spectroelectrochemistry and catalytic properties in DDT reductive dechlorination in of iron(II) phthalocyanine, 2,3- and 3,4-tetrapyridinoporphyrazine complexes" *J. Porphyrins Phthalocyanines* **2013**, *17*, 317-330.

89. Hanack, M.; Lange, A.; Rein, M.; Behnisch, R.; Renz, G.; Leverenz, A. "Bridged macrocyclic transition metal complexes as semiconducting materials" *Synth. Met.* **1989**, *29*, F1-F8.
90. Fukuda, T.; Homma, S.; Kobayashi, N. "A highly deformed iron(II) low-spin phthalocyanine which shows two MLCT transitions beyond the Q-band" *Chem. Commun.* **2003**, 1574-1575.
91. Jones, J. G.; Twigg, M. V. "Reaction of N-substituted imidazoles with ferrous phthalocyanine in dimethylsulfoxide" *Inorg. Chim. Acta* **1975**, *12*, L15.
92. Stynes, D. V. "Complexes of benzyl isocyanide with ferrous phthalocyanine. Model for the heme group and a solar energy storage system" *J. Am. Chem. Soc.* **1974**, *96*, 5942-5943.
93. Stynes, D. V.; James, B. R. "Kinetics and equilibriums for carbon monoxide binding to ferrous phthalocyanine complexes" *J. Am. Chem. Soc.* **1974**, *96*, 2733-2738.
94. Jones, J. G.; Twigg, M. V. "Axial ligand exchange reactions of ferrous phthalocyanine. Exchange of imidazole for dimethyl sulfoxide" *Inorg. Chem.* **1969**, *8*, 2120-2123.
95. Jones, J. G.; Twigg, M. V. "Axial ligand dissociation of phthalocyaninatoiron(II) adducts. Further evidence for a dissociative mechanism of substitution" *J. Chem. Soc., Dalton Trans.* **1978**, 1709-1714.
96. Ascenzi, P.; Ercolani, C.; Monacelli F. “Equilibrium and kinetic study of piperidine binding to phthalocyaninatoiron(II) in dimethylsulfoxide” *Inorg. Chim. Acta* **1994**, *219*, 199-203.
97. Ough, E. A.; Stillman, M. J. "Analysis of the absorption and magnetic circular dichroism spectra of low spin (S = 1/2) iron(III) phthalocyanine" *Inorg. Chem.* **1995**, *34*, 4317-4325.

98. Nevonen, D. E.; Rohde, G. T.; Nemykin, V. N. "New Insight into an Old Problem: Analysis, Interpretation, and Theoretical Modeling of the Absorption and Magnetic Circular Dichroism Spectra of Monomeric and Dimeric Zinc Phthalocyanine Cation Radical" *Inorg. Chem.* **2019**, *58*, 14120-14135.

99. Mack, J.; Stillman, M. J. "Assignment of the optical spectra of metal phthalocyanines through spectral band deconvolution analysis and ZINDO calculations" *Coord. Chem. Rev.* **2001**, *219-221*, 993-1032.

100. Stillman, M. "Formation and electronic properties of ring-oxidized and ring-reduced radical species of the phthalocyanines and porphyrins" *J. Porphyrins Phthalocyanines* **2000**, *4*, 374-376.

101. Ough, E.; Gasyna, Z.; Stillman, M. J. "Photochemical, electrochemical, and chemical formation of the π-cation-radical species of magnesium phthalocyanine. Analysis of the absorption and MCD spectra of $[MgPc(-1)]^{\cdot+}$" *Inorg. Chem.* **1991**, *30*, 2301-2310.

102. Silver, J.; Lukes, P.; Houlton, A.; Howe, S.; Hey, P.; Ahmet, M. T. "Electrochromism in the transition-metal phthalocyanines. Part 3. Molecular organization, reorganization and assembly under the influence of an applied electric field. Response of [Fe(pc)] and [Fe(pc) Cl]" *J. Mater. Chem.* **1992**, *2*, 849-855.

103. Nemykin, V. N.; Chernii, V. Ya.; Volkov, S. V.; Bundina, N. I.; Kaliya, O. L.; Li, V. D.; Lukyanets, E. A. "Further studies on the oxidation state of iron in μ-oxo dimeric phthalocyanine complexes" *J. Porphyrins Phthalocyanines* **1999**, *3*, 87-98.

104. Sorokin, A. B. "Recent progress on exploring μ-oxo bridged binuclear porphyrinoid complexes in catalysis and material science" *Coord. Chem. Rev.* **2019**, *389*, 141-160.

105. Mihara, N.; Yamada, Y.; Takaya, H.; Kitagawa, Y.; Aoyama, S.; Igawa, K.; Tomooka, K.; Tanaka, K. "Oxygen Reduction to Water by a Cofacial Dimer of Iron(III)-Porphyrin and Iron(III)-Phthalocyanine Linked through a Highly Flexible Fourfold Rotaxane" *Chem. Eur. J.* **2017**, *23*, 7508-7514.

106. Colomban, C.; Kudrik, E. V.; Briois, V.; Shwarbrick, J. C.; Sorokin, A. B.; Afanasiev, P. "X-ray Absorption and Emission Spectroscopies of X-Bridged Diiron Phthalocyanine Complexes $(FePc)_2X$ (X = C, N, O) Combined with DFT Study of $(FePc)_2X$ and Their High-Valent Diiron Oxo Complexes" *Inorg. Chem.* **2014**, *53*, 11517-11530.

107. Chen, M. J.; Fremgen, D. E.; Rathke, J. W. "Oxygen atom transfer from μ-Oxobis[1,4,8,11, 15,18,22,25-octakis(trifluoromethyl)phthalocyaninato]diiron(III): Evidence for an FeIV=O intermediate" *J. Porphyrins Phthalocyanines* **1998**, *2*, 473-482.

108. Dieing, R.; Schmid, G.; Witke, E.; Feucht, C.; Dressen, M.; Pohmer, J.; Hanack, M. "Soluble substituted μ-oxo(phthalocyaninato)iron(III) dimers" *Chem. Ber.* **1995**, *128*, 589-598.

109. Ercolani, C.; Monacelli, F.; Dzugan, S.; Goedken, V. L.; Pennesi, G.; Rossi, G. "X-ray crystal structure of μ-oxo-bis[(1-methylimidazole)phthalocyaninatoiron(III)] and comments on the molecular structure and chemistry of oxo-bridged iron phthalocyaninate dimers" *J. Chem. Soc., Dalton Trans.* **1991**, 1309-1315.

110. Kiani, P.; Dodsworth, E. S.; Lever, A. B. P.; Pietro, W. J. "Modeling ligand electrochemical parameters by repulsion-corrected eigenvalues" *J. Comput. Chem.* **2021**, *42*, 1236-1242.

111. Fielder, S. S.; Osborne, M. C.; Lever, A. B. P.; Pietro, W. J. "First-Principles Interpretation of Ligand Electrochemical (EL(L)) Parameters. Factorization of the σ and π Donor and π

Acceptor Capabilities of Ligands" *J. Am. Chem. Soc.* **1995**, *117*, 6990-6993.

112. Sievertsen, S.; Schlehahn, H.; Homborg, H. "Preparation, properties and electronic Raman spectra of bis(chloro)(phthalocyaninato)ferrate(III), -ruthenate(III) and -osmate(III)" *Z. Anorg. Allg. Chem.* **1993**, *619*, 1064-1072.

113. Sievertsen, S.; Grunewald, H.; Homborg, H. "Low spin manganese phthalocyanines: preparation, properties and electronic Raman spectrum of di(cyano) phthalocyaninatomanganate(III) and -(II)" *Z. Anorg. Allg. Chem.* **1993**, *619*, 1729-1737.

114. Kalz, W.; Homborg, H. "Iron(III) phthalocyanines: preparation and spectroscopic characterization of $[Fe(OR)_2Pc(-2)]^-$ (R = hydrogen, methyl, ethyl, isopropyl, and tert-butyl), $(FePc(-2))_2O$ and FeXPc(-2) (X = fluorine, chlorine, bromine, and iodine)" *Z. Naturforsch.* **1983**, *38B*, 470-484.

115. Bakshi, E. N.; Murray, K. S. "Applied field Mössbauer spectra of low-spin mononuclear and binuclear iron(III)-phthalocyanines" *Hyperfine Interactions* **1988**, *40*, 283-286.

116. Nemykin, V. N.; Hadt, R. G. "Influence of Hartree-Fock Exchange on the Calculated Moessbauer Isomer Shifts and Quadrupole Splittings in Ferrocene Derivatives Using Density Functional Theory" *Inorg. Chem.* **2006**, *45*, 8297-8307.

117. Nemykin, V. N.; Basu, P. "Comparative theoretical investigation of the vertical excitation energies and the electronic structure of $[Mo^{V}OCl_4]^-$: influence of basis set and geometry" *Inorg. Chem.* **2003**, *42*, 4046-4056.

118. Zerner, M.; Gouterman, M. Porphyrins. IV. Extended Hueckel Calculations on Transition Metal Complexes. *Theor. Chim. Acta* **1966**, *4*, 44-63.

119. Zerner, M.; Gouterman, M. Porphyrins. V. Extended Hueckel Calculations on Vanadyl (VO2+) and Vanadium(II) Complexes. *Inorg. Chem.* **1966**, *5*, 1699-1706.

120. Zerner, M.; Gouterman, M. Porphyrins. X. Extended Hueckel Calculations on Alkaline Earth Complexes. *Theor. Chim. Acta* **1967**, *8*, 26-34.

121. Barriere, F.; Geiger, W. E. Use of Weakly Coordinating Anions to Develop an Integrated Approach to the Tuning of $\Delta E_{1/2}$ Values by Medium Effects. *J. Am. Chem. Soc.* **2006**, *128*, 3980-3989.

122. Gaussian 16, Revision B.01, Frisch, M. J.; Trucks, G. W.; Schlegel, H. B.; Scuseria, G. E.; Robb, M. A.; Cheeseman, J. R.; Scalmani, G.; Barone, V.; Petersson, G. A.; Nakatsuji, H.; Li, X.; Caricato, M.; Marenich, A. V.; Bloino, J.; Janesko, B. G.; Gomperts, R.; Mennucci, B.; Hratchian, H. P.; Ortiz, J. V.; Izmaylov, A. F.; Sonnenberg, J. L.; Williams-Young, D.; Ding, F.; Lipparini, F.; Egidi, F.; Goings, J.; Peng, B.; Petrone, A.; Henderson, T.; Ranasinghe, D.; Zakrzewski, V. G.; Gao, J.; Rega, N.; Zheng, G.; Liang, W.; Hada, M.; Ehara, M.; Toyota, K.; Fukuda, R.; Hasegawa, J.; Ishida, M.; Nakajima, T.; Honda, Y.; Kitao, O.; Nakai, H.; Vreven, T.; Throssell, K.; Montgomery, J. A., Jr.; Peralta, J. E.; Ogliaro, F.; Bearpark, M. J.; Heyd, J. J.; Brothers, E. N.; Kudin, K. N.; Staroverov, V. N.; Keith, T. A.; Kobayashi, R.; Normand, J.; Raghavachari, K.; Rendell, A. P.; Burant, J. C.; Iyengar, S. S.; Tomasi, J.; Cossi, M.; Millam, J. M.; Klene, M.; Adamo, C.; Cammi, R.; Ochterski, J. W.; Martin, R. L.; Morokuma, K.; Farkas, O.; Foresman, J. B.; Fox, D. J. Gaussian, Inc., Wallingford CT, 2016.

123. Becke, A. D. Density-functional exchange-energy approximation with correct asymptotic behaviour. *Phys. Rev. A*. **1988**, *38*, 3098-3100.

124. Perdew, J. P. Density-functional approximation for the correlation energy of the

inhomogeneous electron gas. *Phys. Rev. B*. **1986**, *33*, 8822-8824.

125. Wachters, A. J. H. Gaussian Basis Set for Molecular Wavefunctions Containing Third-Row Atoms. *J. Chem. Phys.* **1970**, *52*, 1033-1036.

126. McLean, A. D.; Chandler, G. S. Contracted Gaussian basis sets for molecular calculations. 1. Second row atoms, Z = 11-18. *J. Chem. Phys.* **1980**, *72*, 5639-5648.

127. Tao, J. M.; Perdew, J. P.; Staroverov, V. N.; Scuseria, G. E. Climbing the density functional ladder: Nonempirical meta-generalized gradient approximation designed for molecules and solids. *Phys. Rev. Lett.* **2003**, *91*, 146401/1-146401/4.

128. Staroverov, V. N.; Scuseria, G. N.; Tao, J.; Perdew, J. P. Comparative assessment of a new nonempirical density functional: Molecules and hydrogen-bonded complexes. *J. Chem. Phys.* **2003**, *119*, 12129-12137.

129. Cohen, A. J.; Handy, N. C. Dynamic correlation. *Mol. Phys.* **2001**, *99*, 607-15.

130. Schultz, N. E.; Zhao, Y.; Truhlar, D. G. Density functionals for inorganometallic and organometallic chemistry. *J. Phys. Chem. A*. **2005**, *109*, 11127-11143.

131. Tomasi, J.; Mennucci, B.; Cammi, R. Quantum mechanical continuum solvation models. *Chem. Rev.* **2005**, *105*, 2999-3093.

132. Tenderholt, A. L. QMForge, version 2.1; Standord University: Stanford, CA, 2011. https://qmforge.net/.

9. General Trends in Charge-Transfer Spectroscopy of Bisaxially Coordinated Iron(II) Phthalocyanines through the Prism of the Lever's E_L Parameters Scale Determined via Experimental and Theoretical Approaches

9.1 Introduction

Iron phthalocyanine derivatives and their analogues are known for their diversity in oxidation and spin states that range between +1 and +4, and 0 and 5/2, respectively.[1-6] Not surprisingly, such rich electronic structure properties, along with the complex coordination chemistry of iron phthalocyanine, resulted in the usage of these platforms as naked eye detectors of carbon monoxide and NO_x species,[7-11] oxidative catalysts in transformations of organic molecules,[12-22] electrocatalysts,[23-25] reactive oxygen species activators in catalytic cancer therapy,[26,27] and smart electrode materials for the detection of biologically important molecules using electrochemical techniques.[28-31] The ability of the iron(II) phthalocyanine to coordinate two axial ligands such as the isonitriles,[32-38] nitroso compounds,[39] carbon monoxide,[40-42] phosphines and phosphites,[39,43-47] sulfides and sulfoxides,[48-50] and nitrogen bases[51-72] was studied by Mössbauer, NMR, UV-vis, and MCD spectroscopy as well as X-ray crystallography. In 1968, Dale reported the first paper on the UV-vis spectra of the $PcFeL_2$ and $[PcFeX_2]^{2-}$ complexes in which he suggested that the characteristic absorption band observed between 420 and 455 nm has a strong axial ligand dependency and thus can be attributed to the metal-to-ligand (MLCT) trans

ition.[53] The first MCD work on these compounds was reported by Thomson and Stillman in 1974.[62] In their classic 1994 work,[61] Stillman and co-workers studied several $PcFeL_2$, PcFeL'L", and $[PcFeX_2]^{2-}$ complexes (L, = NH_3, piperidine, N-methylimidazole, imidazole, pyridine, 4-methylpyridine; L' = NH_3 and L" = CO; and X = CN^-) using simultaneous band deconvolution analysis of the UV-vis and MCD spectra. Stillman proposed that the first (lowest energy), axial ligand dependent, MCD Faraday *A*-term observed in the 455 – 360 nm region is dominated by the e_g (Fe, d_{xz}/d_{yz}) → $1b_{1u}$ (Pc, π^*) single-electron transition and mostly reflects the relative energy of the iron-centered d_π orbitals (Figure 9.1).

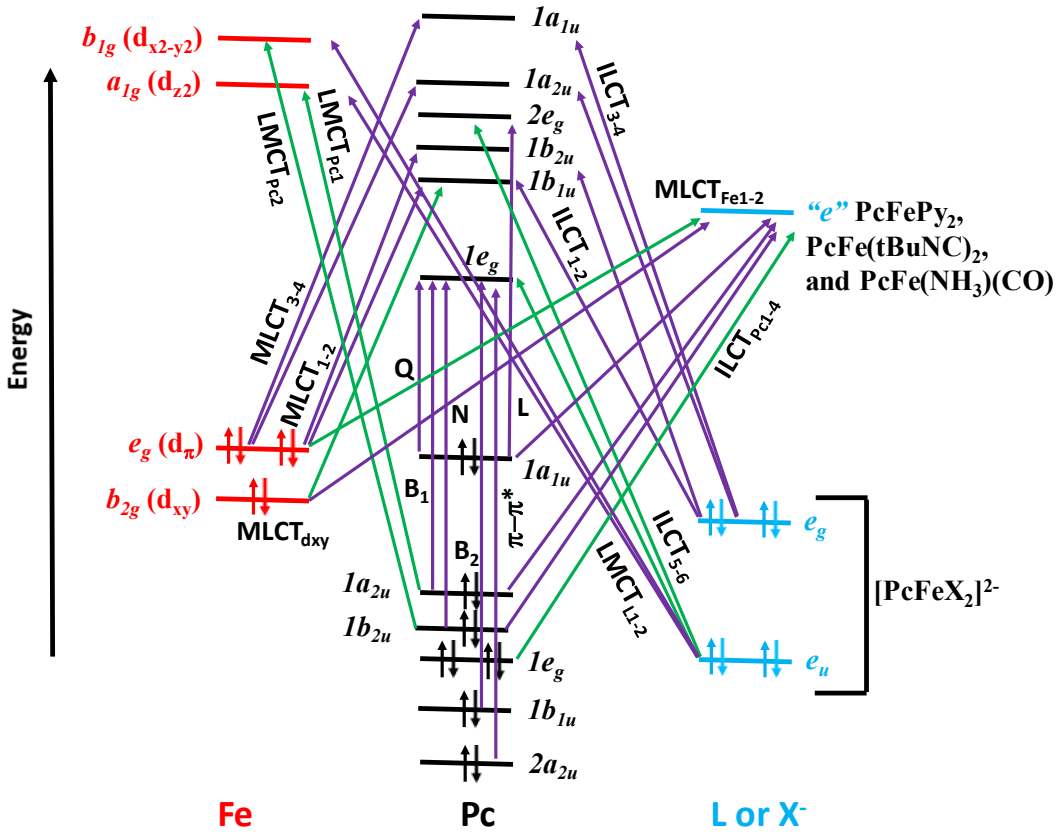

Figure 9.1. Selected arbitrary energy molecular diagram for the $^1A_{1g}$ ground state of $PcFeL_2$, PcFeL'L", or $[PcFeX_2]^{2-}$ complex showing symmetry allowed metal-to-ligand charge-transfer (MLCT), ligand-to-metal charge-transfer (LMCT), phthalocyanine-centered, and inter-ligand charge-transfer (ILCT) transitions. The iron-centered MOs are on the right, phthalocyanine-centered MOs are in the middle, and the axial-ligand MOs are on the left side. All labels except the "*e*" symmetry label for the unoccupied MO in the axial ligands are given for the idealized D_{4h} point group. The "*e*" label reflects the lower DFT symmetry of complexes **8.8**, **8.16**, and **8.18** (Table 8.1). The violet arrows represent XY-polarized transitions that give rise to MCD *A*-terms and green arrows represent Z-polarized transitions that give rise to MCD *B*-terms.

Based on electrochemical, spectroelectrochemical, and chemical oxidation data, we have demonstrated recently that the energies of the iron(II) d_π and d_{xy} orbitals in $PcFeL_2$, PcFeL'L", and $[PcFeX_2]^{2-}$ complexes have clear correlation with Lever's electrochemical E_L parameter.[45] We also have shown that in the case of the axial ligands with moderate to strong π-acceptor character, iron-centered occupied MOs can intercross with the phthalocyanine-centered a_{1u} (in the common Gouterman's notation for the D_{4h} point group) orbital, which leads to the situation when the first oxidation process becomes phthalocyanine-centered.[45] We also observed rather unusual and rich UV-vis spectra for the $PcFeL_2$ complexes coordinated with the phosphine axial ligands. Our previous results pose several interesting questions. If the energy levels of the phthalocyanine ligand are nearly constant, as suggested by Lever's E_L theory,[73-76] will the $[PcFeX_2]^{2-}$ complexes with the axial ligands having large negative E_L values have the most red-shifted MLCT transitions? As of now, there are no reports available on the MCD spectroscopy of the bisaxially coordinated iron(II) phthalocyanines with negative values of the ΣE_L L(ax) which are reflective of strong σ-donor strength of the axial ligands. Next, is the first (the lowest energy) MCD Faraday *A*-term in the 500-350 nm spectral envelope always associated with the e_g (Fe, d_{xz}, d_{yz}) → $1b_{1u}$ (Pc, π^*) MLCT transition that correlates with the Lever's E_L parameters? Finally, although numerical values for the UV-vis spectra of the $PcFeL_2$ complexes with several phosphines and phosphites as the axial ligands were reported in the literature,[43-47] no rational explanation of the nature for the observed transitions between 500 and 450 nm were ever provided and no MCD spectra for these $PcFeL_2$ compounds were ever reported. In order to answer the above mentioned questions, we have conducted a systematic analysis of the UV-vis, MCD, DFT, and TDDFT data on a large range of $PcFeL_2$, PcFeL'L", and $[PcFeX_2]^{2-}$ complexes

(Figure 9.2), which, along with the earlier data from Stillman's and our group, allowed us to rationalize the spectroscopic behavior of these systems with respect to the Lever's E_L ligand's parameter scale.[73-76]

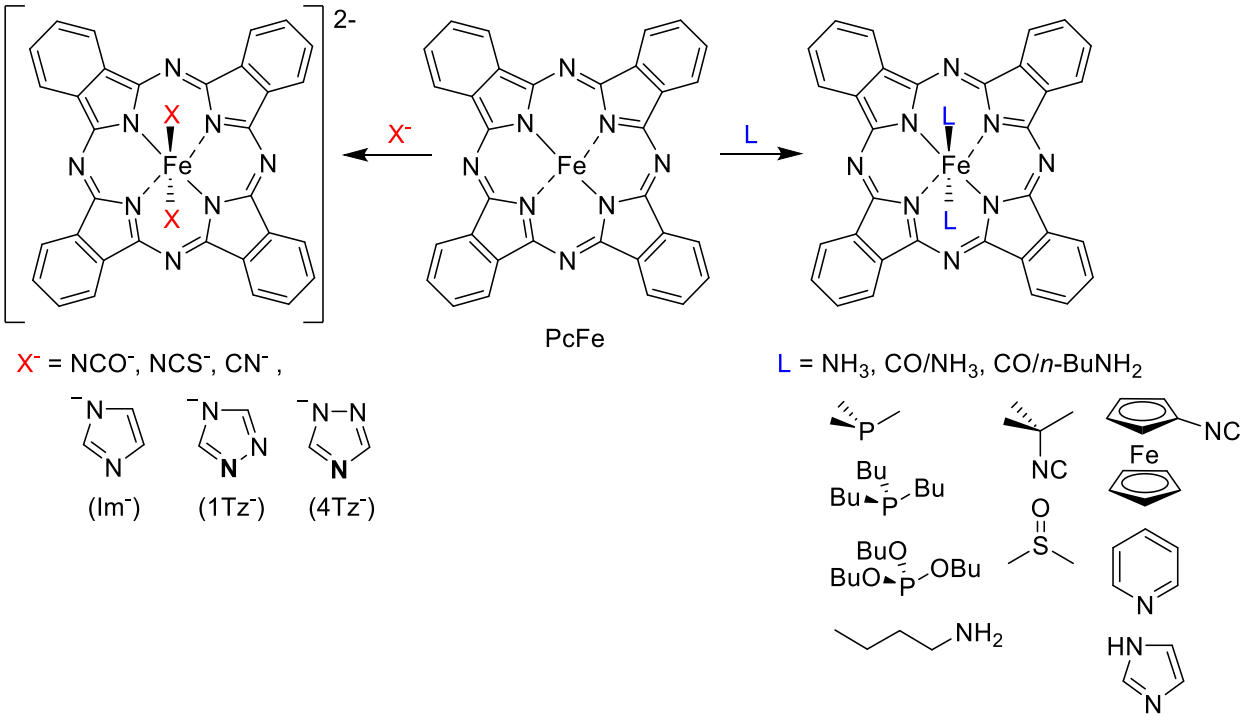

Figure 9.2. Structures of the axially-ligated phthalocyanines featured in this work.

Additive models for the correlation between the charge-transfer transition energies and coordination compound's redox potentials are known for more than a half of century. Early analysis of the relationship between the oxidation potential or the difference of the first oxidation and the first reduction potentials and the energy of the charge-transfer transition was provided by Vlcek, Rabinowitch, Roothaan, Lever, and the other authors.[77-103] In general, such

plots are linear and can be described by the following equation for the series of homogeneous complexes:[75]

$$E_{CT} = F\,(E_{Ox1} - E_{Red1}) + \Sigma a_i = \quad F\,\Delta E + \text{const.} \qquad (9.1)$$

In the case of the lowest energy metal-to-ligand charge-transfer (MLCT) transition that is dominated by the HOMO → LUMO single-electron excitation (i.e. complete absence of small configuration interaction between MLCT and the other states of the same symmetry) without change in the overall spin of the system, ΔE in equation (9.1) represents the difference between the first metal-centered oxidation potential (E_{Ox1}) and the first ligand-centered reduction potential (E_{Red1}) scaled by the factor F, which may be at unity, but usually deviates from unity because of the functional dependence upon the electrochemical potentials. The term Σa_i usually includes molecular and solvent reorganization energies, electrostatic and entropic contributions, as well as other effects. In the case of the $PcFeL_2$, PcFeL'L", and $[PcFeX_2]^{2-}$ complexes, equation (9.1) cannot be used as the lowest energy MLCT band (i.e. e_g (Fe, d_π) → $1e_g$ (Pc, π^*) in the standard notation for D_{4h} point group, Figure 9.1) is symmetry forbidden and was not observed except experimentally in the bisaxially coordinated unsubstituted iron(II) phthalocyanines. Thus, this transition will not be considered here.

Lever also has shown that when the first reduction potential of the ligand is unavailable, equation (9.2) still provides a good linear correlation between the MLCT energies of the ruthenium or iron complexes and the Ru(II)/Ru(III) or Fe(II)/Fe(III) oxidation potential:[75,104]

$$E_{MLCT} = F\,E_{Ox1} + \text{const.} \qquad (9.2)$$

where all variables are the same as for equation (9.1) with constant F being of non-unity value.

Since the Lever's E_L parameters also should directly correlate with the values of E_{Ox1} (i.e. energy of the HOMO in the homogeneous series of the complexes), one would expect that the MLCT energy should also correlate with the E_L values in a linear way:

$$E_{MLCT} = F \Sigma E_L + const. \quad (9.3)$$

Finally, when applied to the homogeneous series of $PcFeL_2$, PcFeL'L", and $[PcFeX_2]^{2-}$ complexes, following Lever's idea outlined earlier,[76] the equation (9.3) can be re-written as:

$$E_{MLCT} = F \Sigma E_L L(ax) + const. \quad (9.4)$$

where $\Sigma E_L L(ax)$ represents the sum of the E_L values of two axial ligands. Equations (9.2) and (9.4) allows for tests of several hypotheses. First, equation (9.2) allows the linear correlation between E_{MLCT} and E_{Ox1} as long as the first oxidation process is metal-centered. As we have shown recently, the first oxidation process in the $PcFeL_2$ and PcFeL'L" complexes with moderate-to-strong π-acceptors as the axial ligands, is phthalocyanine-centered. Thus, significant deviation is expected for these compounds in their E_{MLCT}/E_{Ox1} plot. On the other hand, equation (9.4) can predict the energies of the MLCT transitions in $PcFeL_2$, PcFeL'L", and $[PcFeX_2]^{2-}$ complexes for which the Fe(II)/Fe(III) oxidation potentials are unavailable or hindered by the Pc(2-)/Pc(1-) process. In addition, equation 9.4 can be used in the analysis of the rather complex UV-vis and MCD spectra for $PcFeL_2$ complexes that are axially coordinated with phosphine ligands as well as the spectra of **8.5** as it allows for the estimation of the energy of the e_g (Fe, d_π) → $1b_{1u}$ (Pc, π^*) MLCT band.

9.2 Results

9.2.1 UV-Vis and MCD Spectra. The UV-vis and MCD spectra of 15 compounds discussed in this report are shown in Figure 9.3. When comparison is possible with the MCD spectra of $PcFeL_2$, PcFeL'L", and $[PcFeX_2]^{2-}$ complexes reported earlier by Stillman and co-workers,[61,62] our data were found to be in excellent agreement for compounds **8.5**, **8.6**, **8.8** and **8.12**. In general, all spectra can be roughly partitioned to three spectral envelopes. The first of which is the *Q*-band region (spectral envelope I; 500-750 nm), which for all compounds is dominated by a very intense *Q*-band observed between 653 and 672 nm. The energy of this transition is almost independent of the nature of the axial ligands or solvent (ΔE_Q ~0.05 eV), which is typical for phthalocyanine-centered π-π* transitions with negligible configurational interaction.[105] The energy of the *Q*-band observed in $PcFeL_2$, PcFeL'L", and $[PcFeX_2]^{2-}$ complexes correlates well with the center of the only Faraday MCD *A*-term observed in the *Q*-band region, which confirms the effective four-fold symmetry of the phthalocyanine macrocycle. In addition, two vibronic satellites ($Q_{0\text{-}1}$ and $Q_{0\text{-}2}$) in spectral envelope I were also identified by UV-vis spectroscopy. These are associated with two MCD *B*-terms of positive amplitude and were observed earlier by Stillman and co-workers.[61,62] We assigned spectral envelope II to the 400-500 nm region. This region was traditionally associated with the MLCT (e_g (Fe, d_π) → $1b_{1u}$ (Pc, π*)) transitions.[53,61,62] With respect to spectral envelope II, the $PcFeL_2$, PcFeL'L", and $[PcFeX_2]^{2-}$ complexes reported here can be consolidated into several groups. The group 1 ($PcFeL_2$, L = NH_3, Im, *n*$BuNH_2$, Py, $P(OBu)_3$, and DMSO; $[PcFeX_2]^{2-}$, X = NCO^-, Im^-, Tz^-, NCS^-) complexes have one band in their UV-vis spectrum (often with a shoulder) in this region, which correlates to some extent with a

single MCD *A*-term. Group 2 ($PcFeL_2$, L = PMe_3, PBu_3 and **8.5**) has several observable bands in spectral envelope II in their UV-vis spectra. In the case of the phosphine-coordinated compounds, two MCD *A*-terms can be seen in the experimental MCD spectra, while only one MCD *A*-term can be seen in the experimental MCD spectrum of **8.5** (Figure 9.3). Finally, Group 3 (complexes **8.13** and **8.16**) has no transitions in spectral envelope II. The third spectral envelope in the UV-vis and MCD spectra of the $PcFeL_2$, PcFeL'L", and $[PcFeX_2]^{2-}$ complexes is located in the *B*-band region (250-400 nm). In the majority of cases, two main bands were observed in the UV-vis spectra within the *B*-band region (Figure 9.3). These bands are closely aligned with the two MCD *A*-terms. Again, more rich spectra were observed in the case of the $PcFe(PR_3)_2$ and **8.5** complexes.

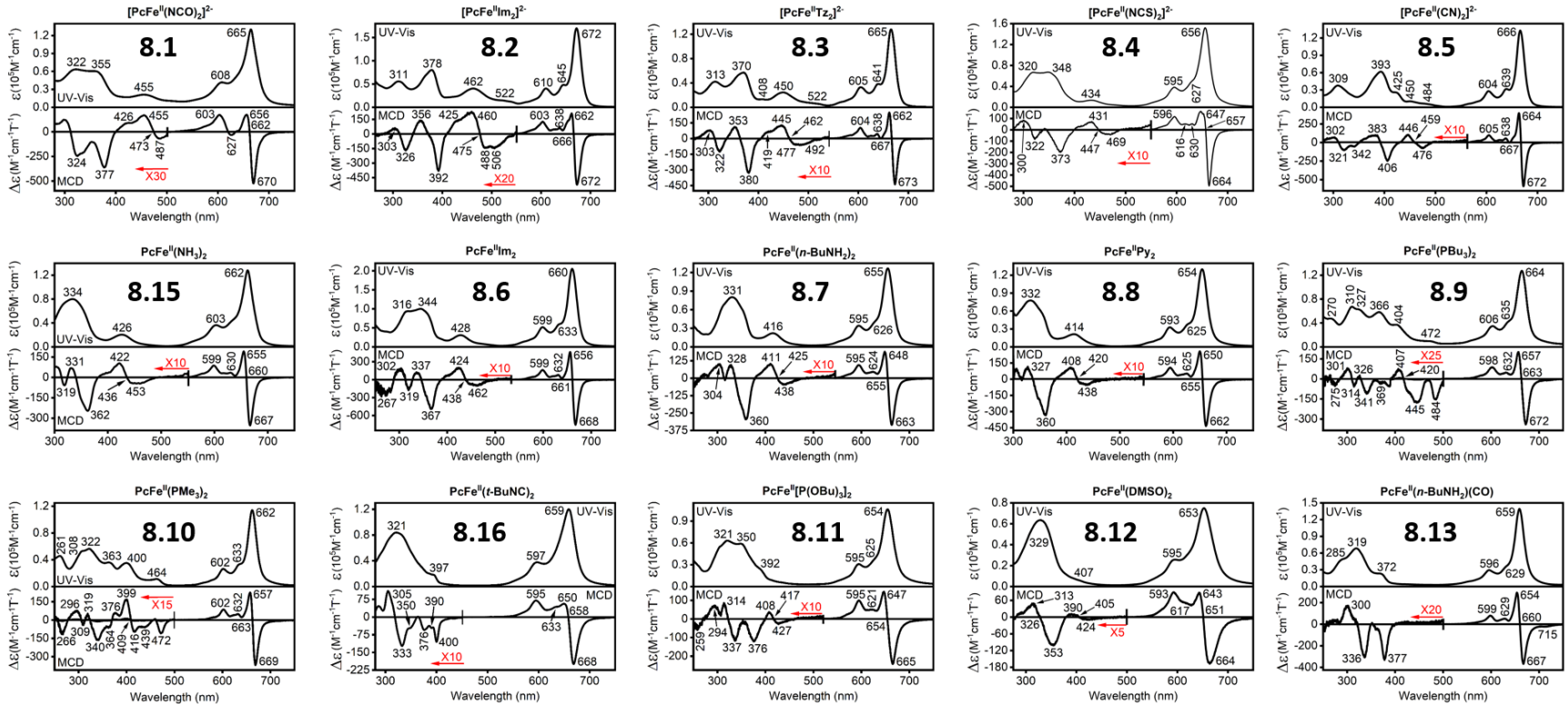

Figure 9.3. Experimental UV-vis and MCD spectra of all compounds evaluated in this work.

9.2.2 Band Deconvolution Analysis. In order to interpret the several overlapping transitions present in their UV-vis and MCD spectra within the higher-energy charge-transfer region, band deconvolution analysis was performed for all compounds. In general, we used the approach similar to that proposed by Stillman and co-workers.[61] Each of the signals in the deconvoluted UV-vis spectrum are energetically aligned with either a corresponding *A*- or *B*-term in the associated MCD spectrum. Sample deconvoluted spectra for complex **8.15** in spectral envelopes II and III are shown in Figure 9.4.

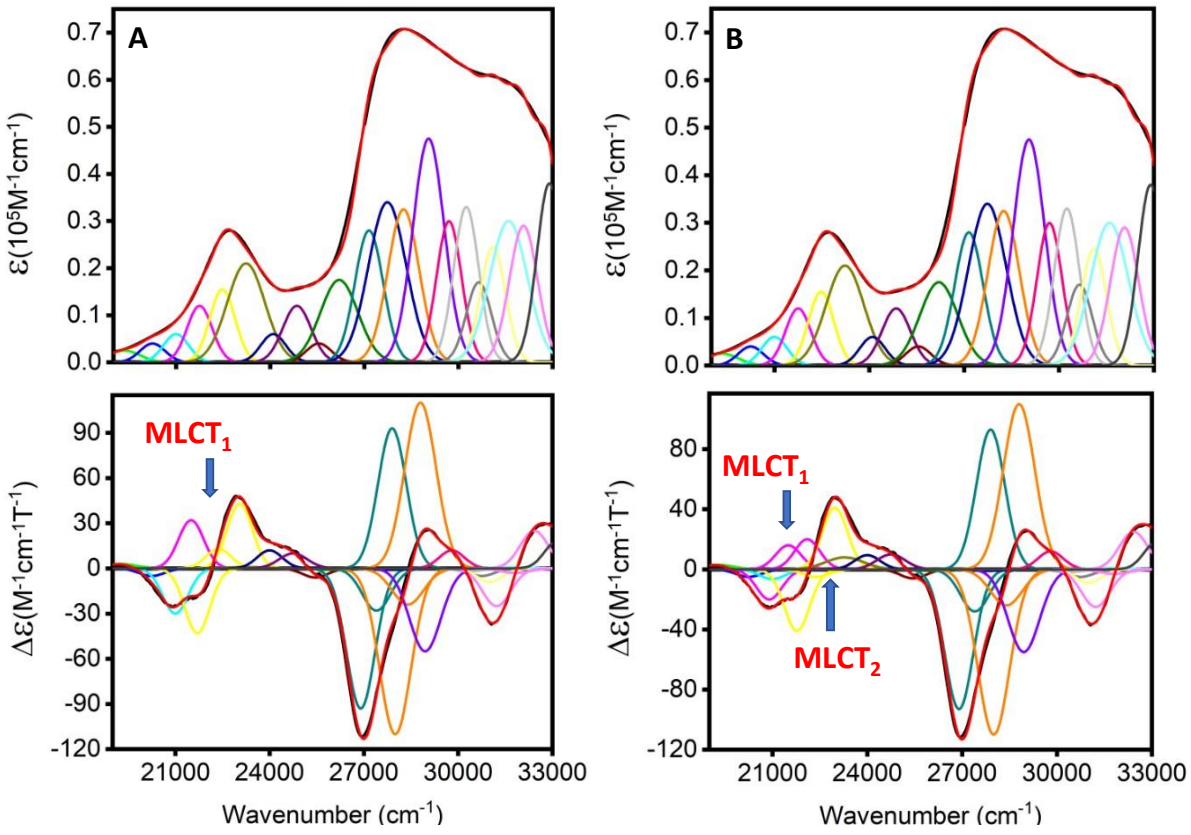

Figure 9.4. Deconvoluted UV-vis (upper) and MCD (lower) spectra for **8.15** using either (A) one *A*-term or (B) two *A*-terms in the MLCT region.

When comparison is possible (with complexes **8.6** and **8.8**), our data are in close agreement with those published by Stillman and co-workers.[61] In the case of complex **8.5**, we used an additional MCD *A*-term at around 425 nm to get a better agreement between theory and experiment. This observation is in agreement with the 1994 paper by Stillman and Ough.[61]

9.2.3 DFT and TDDFT Calculations. For electronic structure elucidation and to substantiate the experimental and deconvoluted UV-vis and MCD spectroscopy data, DFT and TDDFT calculations were performed on ten compounds that have ΔE_L L(ax) values which span between -0.5 and +1.09 V. The relative energies of the phthalocyanine and iron-centered orbitals are expected to be dependent on the exchange-correlation functional used, with particular sensitivity to the magnitude of Hartree-Fock exchange involved in a given functional.[106-109] Therefore, the calculations were performed using the MPWLYP (5% Hartree-Fock exchange), TPSSh (10% Hartree-Fock exchange), and O3LYP (11.6% Hartree-Fock exchange) functionals. Although we focused on the three best performing (for our purpose) exchange-correlation functionals, approximately 25 functionals were initially tested on a limited number of iron(II) phthalocyanine complexes. These functionals were selected for testing based on our experience with similar systems.[108] As expected, the pure DFT functionals have historically underestimated the metal orbital energies in phthalocyanine systems, and hybrid functionals which have 20-42% HF-exchange have been found to unreliably stabilize the d-orbitals of iron relative to the phthalocyanine core orbitals.

The associated DFT-predicted frontier molecular orbital images for selected examples **8.1**, **8.8**, and **8.18** can be found below in Figure 9.5, and the remainder are located in the Supporting

Information Figure S9.1. The DFT-predicted energy-level diagram for all compounds using the MPWLYP exchange correlation functional is presented in Figure 9.6, and those for the TPSSh and O3LYP functionals can be found in the Supporting Information Figure S9.2. Within the energy-level diagram above, the compounds are ordered from low (negative) to high (positive) values of ΣE_L L(ax) going from left to right on the x-axis. In all cases, the phthalocyanine-centered e_g (in the traditional D_{4h} point group notation) orbitals were predicted to be the LUMO and LUMO+1, in agreement with the electrochemical data described earlier. Again, in agreement with the previous electrochemical and spectroelectrochemical data,[45] iron-centered orbitals were predicted to be the HOMO in all complexes except for the cases of **8.8**, **8.12**, **8.17**, and **8.18** in which DFT predicts a phthalocyanine-centered a_{1u} orbital to be the HOMO (Table 9.1). It is important to note (as it will be used in the TDDFT section discussion) that the classic Gouterman's[110-112] phthalocyanine-centered a_{2u} orbital can be mixed with the σ-donor orbital of the axial ligand. As a result, the axial ligand's contribution into this orbital was predicted between 11 and 64% (Supporting Information Table S9.1). For instance, in complexes **8.2**, **8.10**, and **8.12**, the axial ligand contribution to Gouterman's a_{2u} orbital exceeds 50%. Such a large deviation in the axial ligand contribution leads to a significant variation of the Gouterman's a_{2u} orbital energy.

Table 9.1. Energies of the selected frontier MOs in iron(II) phthalocyanine complexes (MPWLYP functional).[a]

MO\L	NCO^- **8.1**	Im^- **8.2**	1-Tz^- **8.3.1**	4-Tz^- **8.3.2**	NCS^- **8.4**	CN^- **8.5**	NH_3 **8.15**	Im **8.6**	Py **8.8**	PMe_3 **8.10**	tBuNC **8.16**	$P(OBu)_3$ **8.11**	DMSO **8.12**	NH_3/CO **8.18**
a_{1g} d_{z2}	-0.296	-0.135	-0.094	-0.285	-0.487	-0.119	-1.432	-1.186	-1.445	-1.376	-1.041	-1.566	-2.328	-1.594
$2e_g$	-0.495	-0.507	-0.481	-0.565	-0.581	-0.494	-1.116	-1.084	-1.153	-1.147	-1.146	-1.107	-1.267	-1.264
$1a_{2u}$	-0.534	-0.549	-0.534	-0.604	-0.615	-0.507	-1.162	-1.123	-1.205	-1.159	-1.141	-1.116	-1.296	-1.210
$1b_{2u}$	-0.739	-0.768	-0.741	-0.835	-0.838	-0.750	-1.430	-1.386	-1.515	-1.479	-1.435	-1.412	-1.616	-1.588
$1b_{1u}$	-0.878	-0.894	-0.861	-0.959	-0.976	-0.878	-1.552	-1.518	-1.604	-1.585	-1.578	-1.515	-1.716	-1.714
$1e_g$	**-2.018**	**-2.030**	**-1.992**	**-2.124**	**-2.169**	**-2.018**	**-2.805**	**-2.763**	**-2.881**	**-2.851**	**-2.871**	**-2.791**	**-3.063**	**-3.064**
e_g d_π	**-3.339**	**-3.494**	**-3.542**	**-3.675**	**-3.687**	**-3.651**	-4.525	**-4.496**	-4.705	-4.670	-4.960	-4.865	-5.146	-5.349
b_{2g} d_{xy}	-3.667	-3.653	-3.629	-3.779	-3.908	-3.662	**-4.524**	-4.501	-4.678	**-4.607**	-4.820	-4.709	-5.027	-5.159
$1a_{1u}$	-3.831	-3.850	-3.815	-3.938	-3.954	-3.834	-4.575	-4.540	**-4.642**	-4.622	**-4.603**	**-4.529**	**-4.776**	**-4.764**
$1a_{2u}$	-5.033	-4.692	-4.863	-4.987	-5.229	-4.570	-5.954	-5.880	-6.028	-5.290	-5.776	-5.535	-5.984	-6.132

[a] All MOs are in traditional D_{4h} point group notation. For low symmetry complexes, the average energies for nearly degenerate "e_g" MOs are shown in the table.

The TDDFT-predicted UV-vis spectra for all compounds using the MPWLYP exchange correlation functional and DCM solvent are shown in Figure 9.7, and those for the TPSSh and O3LYP functionals can be located in the Supporting Information Figure S9.3. In addition, the TDDFT-predicted spectra in DMF versus experimental spectra are also shown in the Supporting Information Figure S9.3. Complexes **8.7**, **8.11**, and **8.13** were not considered as their TDDFT-predicted spectra should be very close to those modeled for **8.15**, **8.10**, and **8.18**, respectively. In each case, when compared to the O3LYP and TPSSh data, the MPWLYP calculations provided a slightly better general agreement with experiment in terms of predicted transition energies, intensities, and overall profile. The TDDFT-predicted properties of the selected excited states for all complexes are listed in Table 9.2, while complete data are present in the Supporting Information Table S9.2.

Table 9.2. Properties of the selected excited states predicted by TDDFT calculations using MPWLYP exchange correlation functional.

Assign.	*E, cm^{-1}*	*λ, nm*	*f*	*Contributions*
8.1				
Q[a]	15635	640	0.506	93.5% H-3 → L/L+1, 2.29% H/H-1 → L+2, 2.12% H-8 → L/L+1
$MLCT_1$[a]	18843	531	0.089	94.3% H/H-1 → L+2, 3.66% HOMO/H-1 → L+3
$MLCT_2$[a]	19995	500	0.202	93.0% HOMO/H-1 → L+3, 2.57% H-1/H → L+2
8.2				
Q	15708	637	0.457	81.6% H-3 → LUMO, 7.44% H-5 → LUMO
Q	15731	636	0.475	78.7% H-3 → L+1, 14.9% H-5 → L+1
$MLCT_1$	19936	502	0.06	91.8% HOMO → L+2, 4.42% H-6 → LUMO, 2.99% H-1 → L+3
$MLCT_1$	19939	501	0.06	91.7% H-1 → L+2, 4.44% H-6 → L+1, 3.03% HOMO → L+3
$MLCT_2$	21291	470	0.339	38.7% HOMO → L+3, 19.7% H-1 → L+3, 15.5% H-6 → L+1, 11.3% H-6 → LUMO, 3.52% H-1 → L+2, 2.08% H-10 → L+1
$MLCT_2$	21291	470	0.339	39.0% H-1 → L+3, 19.6% HOMO → L+3, 15.3% H-6 → LUMO, 11.4% H-6 → L+1, 3.47% HOMO → L+2, 2.06% H-10 → LUMO
8.3.1				
Q	15690	637	0.474	85.0% H-3 → LUMO, 5.59% H-1 → LUMO, 4.10% HOMO → L+1
Q	15722	636	0.513	94.7% H-3 → L+1, 2.07% H-6 → LUMO
$MLCT_1$	20583	486	0.065	93.7% HOMO → L+2, 3.94% H-1 → L+3
$MLCT_1$	20616	485	0.063	93.5% H-1 → L+2, 4.36% HOMO → L+3
$MLCT_2$	21616	463	0.182	86.7% HOMO → L+3, 6.45% H-6 → L+1, 2.58% H-1 → L+2
$MLCT_2$	21636	462	0.178	88.5% H-1 → L+3, 6.96% H-6 → LUMO, 2.32% HOMO → L+2
8.3.2				
Q[a]	15675	638	0.516	95.1% H-3 → LUMO/L+1, 2.18% H-8 → L+1/L
$MLCT_1$[a]	20845	480	0.062	94.1% HOMO/H-1 → L+2, 3.61% H-1/H → L+3
$MLCT_2$[a]	21887	457	0.132	76.5% HOMO/H-1 → L+3, 9.82% H-8 → L+1/L, 9.15% H-1/H → L+7
8.4				
Q[a]	15602	641	0.587	95.3% H-3 → L+1/L, 2.30% H-8 → LUMO/L+1
$MLCT_1$[a]	20820	480	0.061	97.2% HOMO/H-1 → L+2

$MLCT_2$[a]	21967	455	0.149	95.8% H-1/H → L+3
8.5				
Q[a]	15625	640	0.510	93.1% H-3 → L+1/L, 4.86% H-4 → LUMO/L+1
B_1[a]	20511	488	0.066	81.6% H-4 → LUMO/L+1, 11.6% H-1/H → L+2, 2.38% H-3 → L+1/L, 2.11% HOMO/H-1 → L+3
$MLCT_1$[a]	21438	466	0.115	81.1% HOMO/H-1 → L+2, 10.3% H-1/H → L+3, 6.54% H-4 → L+1/L
$MLCT_2$[a]	22646	442	0.459	84.9% HOMO/H-1 → L+3, 5.67% H-1/H → L+2, 3.80% H-4 → LUMO/L+1, 2.14% H-3 → L+1/L
8.15				
Q	15473	646	0.587	96.8% H-3 → LUMO
Q	15478	646	0.587	96.8% H-3 → L+1
$MLCT_1$	22884	437	0.051	95.7% H-1 → L+2
$MLCT_1$	22899	437	0.049	56.2% H-2 → L+2, 39.4% HOMO → L+2, 2.89% H-1 → L+4
$MLCT_2$	23958	417	0.190	91.3% H-1 → L+4, 4.52% H-4 → LUMO
$MLCT_2$	23968	417	0.138	35.3% H-2 → L+4, 32.4% HOMO → L+4, 26.1% H-3 → L+3, 3.25% H-4 → L+1
8.6				
Q	15552	643	0.577	94.3% H-3 → LUMO, 2.23% HOMO → LUMO
Q	15554	643	0.577	94.8% H-3 → L+1
$MLCT_1$	22938	436	0.050	90.5% HOMO → L+2, 4.17% H-1 → L+2
$MLCT_1$	22945	436	0.050	68.7% H-1 → L+2, 24.7% H-2 → L+2, 2.69% HOMO → L+2, 2.06% HOMO → L+3
$MLCT_2$	24032	416	0.119	78.3% HOMO → L+3, 8.33% H-5 → LUMO, 6.66% H-4 → LUMO, 3.23% H-1 → L+3
$MLCT_2$	24039	416	0.117	60.8% H-1 → L+3, 19.2% H-2 → L+3, 7.67% H-4 → L+1, 7.57% H-5 → L+1, 2.04% HOMO → L+3
8.8				
Q[a]	15507	645	0.586	96.9% HOMO → LUMO/L+1
$MLCT_1$[a]	23905	418	0.031	94.9% H-2/H-3 → L+4, 2.88% H-3/H-2 → L+5
$MLCT_2$[a]	24607	406	0.074	83.6% H-3/H-2 → L+5, 9.47% H-4 → LUMO/L+1, 3.68% H-5 → L+1/L
8.10				
Q	15367	651	0.495	92.9% H-1 → LUMO, 5.71% H-4 → L+1

Q	15408	649	0.495	92.7% H-1 → L+1, 5.93% H-4 → LUMO
$L+B_1$	19362	516	0.134	91.7% H-4 → LUMO, 5.00% H-1 → L+1
$L+B_1$	19421	515	0.132	91.8% H-4 → L+1, 4.78% H-1 → LUMO
$MLCT_1$	23823	420	0.052	94.0% H-2 → L+2, 4.30% H-3 → L+3
$MLCT_1$	23852	419	0.049	92.1% H-3 → L+2, 5.27% H-2 → L+3
$MLCT_2$	24835	403	0.264	88.5% H-2 → L+3, 4.79% H-6 → L+1, 3.65% H-3 → L+2
$MLCT_2$	24848	402	0.247	89.7% H-3 → L+3, 4.91% H-6 → LUMO, 3.09% H-2 → L+2
8.16				
Q	15362	651	0.620	95.9% HOMO → LUMO, 2.63% H-4 → L+1
Q	15366	651	0.620	95.9% HOMO → L+1, 2.64% H-4 → LUMO
B_1	23776	421	0.160	84.3% H-4 → LUMO, 5.53% H-6 → LUMO, 4.40% H-5 → L+1
B_1	23778	421	0.160	84.3% H-4 → L+1, 5.49% H-6 → L+1, 4.43% H-5 → LUMO
$MLCT_1$	26166	382	0.006	85.6% H-2 → L+2, 7.10% H-6 → L+1, 3.79% H-3 → L+2, 2.80% H-6 → LUMO
$MLCT_1$	26166	382	0.006	85.5% H-3 → L+2, 7.14% H-6 → LUMO, 3.79% H-2 → L+2, 2.81% H-6 → L+1
$MLCT_2$	26986	371	0.126	37.9% H-2 → L+3, 29.7% H-6 → LUMO, 16.4% H-9 → LUMO, 4.41% H-6 → L+1, 4.28% H-3 → L+2, 2.88% H-5 → L+1
$MLCT_2$	26986	371	0.126	37.9% H-3 → L+3, 29.8% H-6 → L+1, 16.3% H-9 → L+1, 4.46% H-6 → LUMO, 4.24% H-2 → L+2, 2.85% H-5 → LUMO
$MLCT_2$	27904	358	0.955	53.7% H-2 → L+3, 29.6% H-6 → LUMO, 4.44% H-3 → L+2, 3.09% H-4 → LUMO, 2.08% H-6 → L+1
$MLCT_2$	27904	358	0.952	53.5% H-3 → L+3, 29.9% H-6 → L+1, 4.42% H-2 → L+2, 3.11% H-4 → L+1, 2.09% H-6 → LUMO
8.17				
Q	15356	651	0.581	94.1% HOMO → LUMO, 3.05% H-4 → L+1
Q	15361	651	0.569	92.0% HOMO → L+1, 2.99% H-4 → LUMO
B_1+L	22212	450	0.152	88.0% H-4 → LUMO, 3.58% H-4 → L+1, 2.36% H-6 → LUMO, 2.23% HOMO → L+1
B_1+L	22221	450	0.152	87.7% H-4 → L+1, 3.62% H-4 → LUMO, 2.37% H-6 → L+1, 2.20% HOMO → LUMO
$MLCT_1$	25954	385	0.017	84.9% H-2 → L+3, 8.17% H-6 → LUMO, 5.99% H-5 → LUMO

$MLCT_1$	25975	385	0.017	85.6% H-3 → L+3, 8.16% H-6 → L+1, 5.20% H-5 → L+1
$MLCT_2$	26724	374	0.003	66.4% H-2 → L+4, 20.1% H-6 → L+1, 3.89% H-9 → LUMO, 3.51% HOMO → L+6, 3.18% H-5 → L+1
$MLCT_2$	26738	374	0.002	65.1% H-3 → L+4, 21.4% H-6 → LUMO, 4.01% H-9 → L+1, 3.13% HOMO → L+7, 3.10% H-5 → LUMO
8.12				
Q	15220	657	0.597	88.7% HOMO → LUMO, 8.52% HOMO → L+1
Q	15257	655	0.597	88.7% HOMO → L+1, 8.55% HOMO → LUMO
$L+B_1$	22989	435	0.080	87.8% H-4 → LUMO, 3.25% H-4 → L+1, 2.13% H-6 → LUMO
$L+B_1$	23141	432	0.068	87.9% H-4 → L+1, 3.01% H-4 → LUMO, 2.55% H-6 → L+1, 2.30% H-12 → L+1
B_2	26114	383	0.106	45.3% H-6 → LUMO, 22.9% H-2 → L+3, 17.0% H-6 → L+1, 4.95% H-9 → LUMO, 2.82% H-3 → L+4
B_2	26231	381	0.098	48.5% H-6 → L+1, 18.9% H-3 → L+3, 17.1% H-6 → LUMO, 4.02% H-2 → L+4, 3.41% H-9 → L+1, 2.27% H-12 → L+1
$MLCT_1$	26612	376	0.141	66.0% H-2 → L+3, 14.0% H-9 → LUMO, 8.61% H-3 → L+4, 5.37% H-6 → LUMO
$MLCT_1$	26777	373	0.072	68.5% H-3 → L+3, 13.7% H-2 → L+4, 7.25% H-6 → L+1, 3.53% H-9 → L+1, 2.27% H-12 → L+1
$MLCT_2$	27687	361	0.538	73.6% H-2 → L+4, 5.69% H-3 → L+3, 3.91% H-6 → L+1, 3.41% H-9 → L+1, 3.13% H-12 → L+1
$MLCT_2$	27778	360	0.350	74.9% H-3 → L+4, 7.26% HOMO → L+7, 3.27% HOMO → L+6, 3.25% H-12 → LUMO, 2.76% H-6 → LUMO, 2.24% H-2 → L+3
8.18				
Q	15211	657	0.661	97.4% HOMO → LUMO
Q	15213	657	0.659	97.1% HOMO → L+1
B_1	24631	406	0.073	53.7% H-4 → LUMO, 35.7% H-5 → LUMO, 7.28% H-6 → LUMO
B_1	24635	406	0.073	53.6% H-4 → L+1, 35.8% H-5 → L+1, 7.29% H-6 → L+1
N	26669	375	0.419	65.9% H-9 → LUMO, 18.3% H-6 → L+1, 3.91% H-4 → L+1, 2.69% H-3 → L+3, 2.21% HOMO → L+5
N	26670	375	0.423	65.7% H-9 → L+1, 18.6% H-6 → LUMO, 4.01% H-4 → LUMO, 2.52% H-2 → L+3, 2.20% HOMO → L+6

B_2	27095	369	0.244	38.7% H-6 → L+1, 22.3% H-9 → LUMO, 17.0% H-4 → L+1, 7.25% HOMO → L+5, 3.47% H-15 → LUMO, 3.32% H-2 → L+2, 3.13% H-5 → L+1
B_2	27095	369	0.242	38.5% H-6 → LUMO, 22.6% H-9 → L+1, 16.9% H-4 → LUMO, 7.30% HOMO → L+6, 3.46% H-15 → L+1, 3.29% H-3 → L+2, 3.16% H-5 → LUMO
$MLCT_1$	28383	352	0.142	91.0% H-2 → L+2, 2.81% H-3 → L+4, 2.47% H-6 → L+1
$MLCT_1$	28385	352	0.142	91.0% H-3 → L+2, 2.94% H-2 → L+4, 2.46% H-6 → LUMO
$MLCT_2$	29251	342	0.230	49.0% H-2 → L+4, 22.6% H-1 → L+6, 12.8% H-2 → L+7, 8.75% H-1 → L+9
$MLCT_2$	29252	342	0.230	47.5% H-3 → L+4, 22.6% H-1 → L+5, 13.3% H-3 → L+7, 8.71% H-1 → L+10, 3.18% H-3 → L+3

[a] Degenerate state; In all cases, the *Q*-band is dominated by the "a_{1u}" → "e_g", B_1-band is dominated by the "a_{2u}" → "e_g", L+B_1-band is dominated by the "L_{ax}+a_{2u}" → "e_g", $MLCT_1$ is dominated by the "d_π" → "b_{1u}", and $MLCT_2$ is dominated by the "d_π" → "b_{2u}" single-electron excitation.

8.1 $[PcFe^{II}(NCO)_2]^-$

LUMO+11

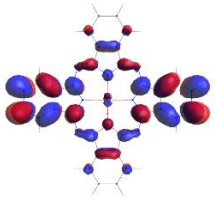

LUMO+10

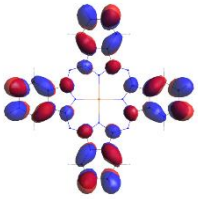

LUMO+9

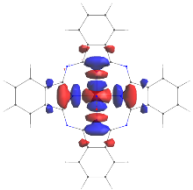

LUMO+8

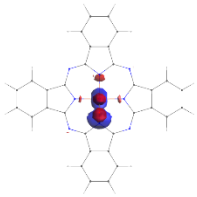

LUMO+7

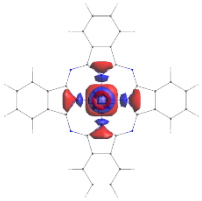

LUMO+6

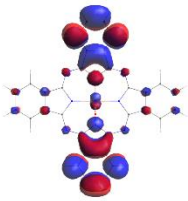

LUMO+5

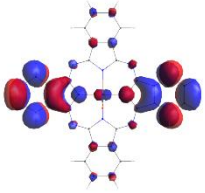

LUMO+4

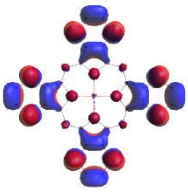

LUMO+3

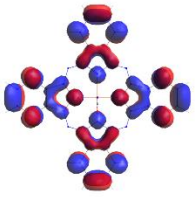

LUMO+2

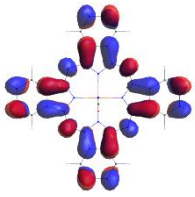

LUMO+1

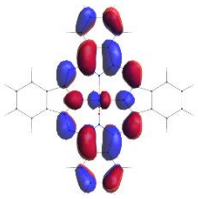

LUMO

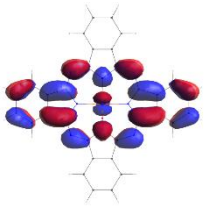

HOMO

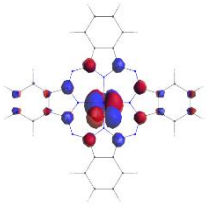

HOMO-1

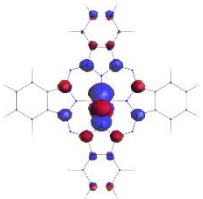

HOMO-2

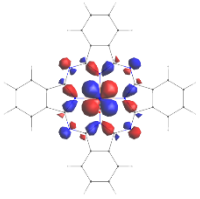

HOMO-3

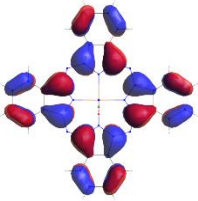

HOMO-4

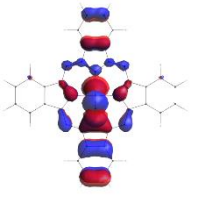

HOMO-5

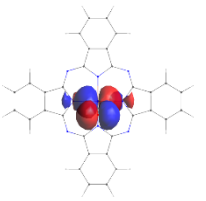

HOMO-6

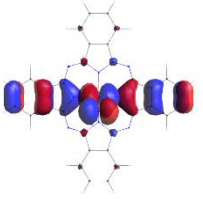

HOMO-7

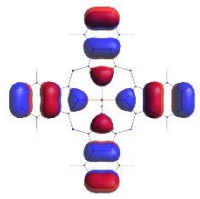

HOMO-8

HOMO-9

HOMO-10

HOMO-11

HOMO-12

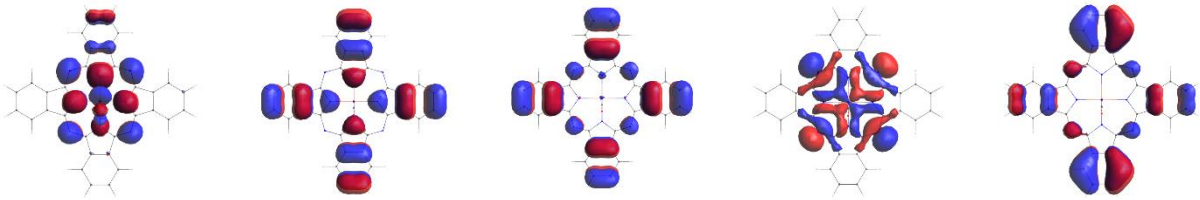

8.8 $PcFe^{II}Py_2$

LUMO+11 LUMO+10 LUMO+9 LUMO+8 LUMO+7

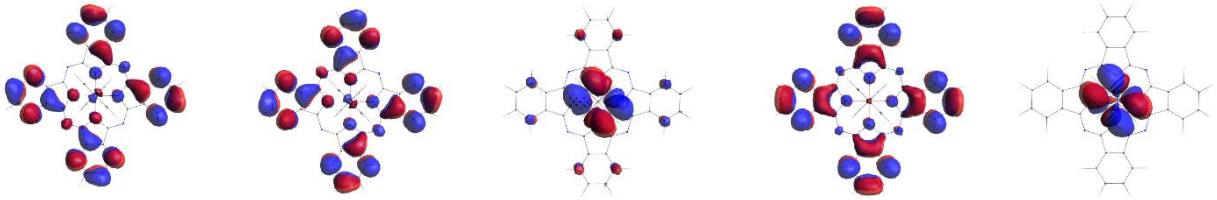

LUMO+6 LUMO+5 LUMO+4 LUMO+3 LUMO+2

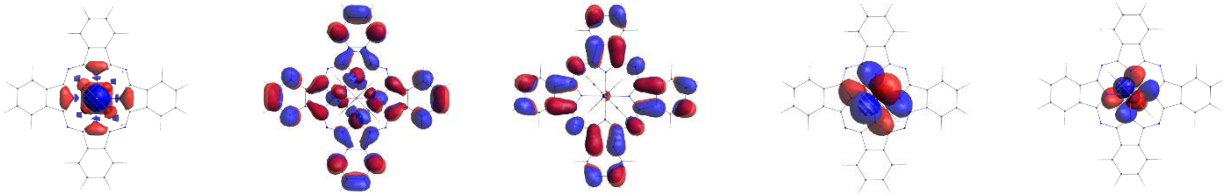

LUMO+1 **LUMO** **HOMO** HOMO-1 HOMO-2

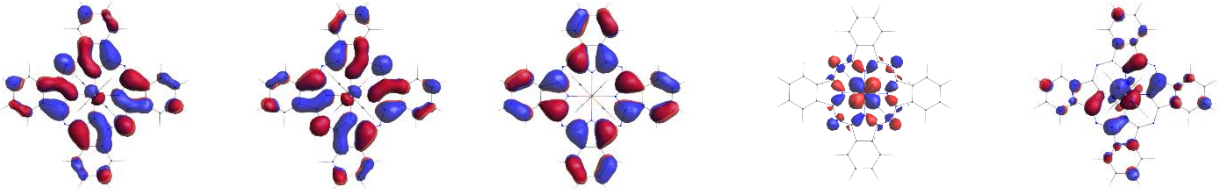

HOMO-3 HOMO-4 HOMO-5 HOMO-6 HOMO-7

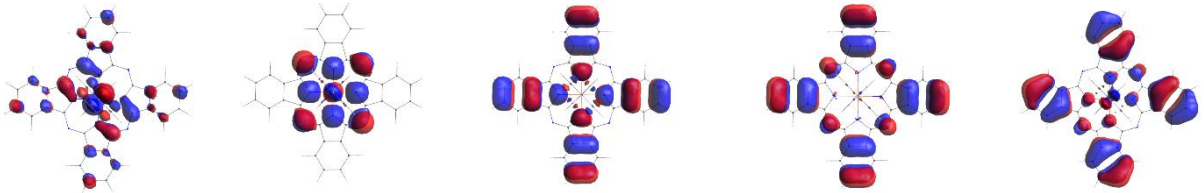

HOMO-8 HOMO-9 HOMO-10 HOMO-11 HOMO-12

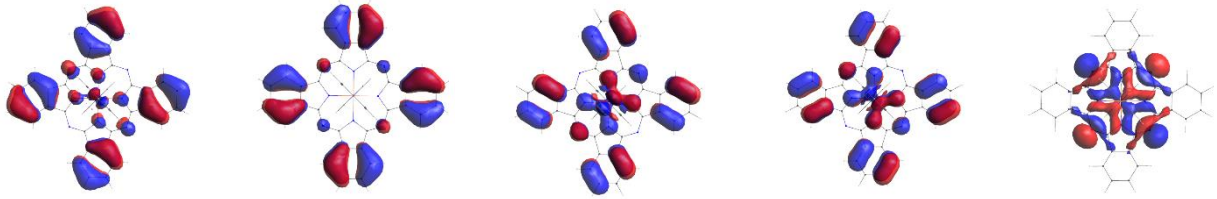

8.18 $PcFe^{II}(NH_3)(CO)$

LUMO+11 LUMO+10 LUMO+9 LUMO+8 LUMO+7

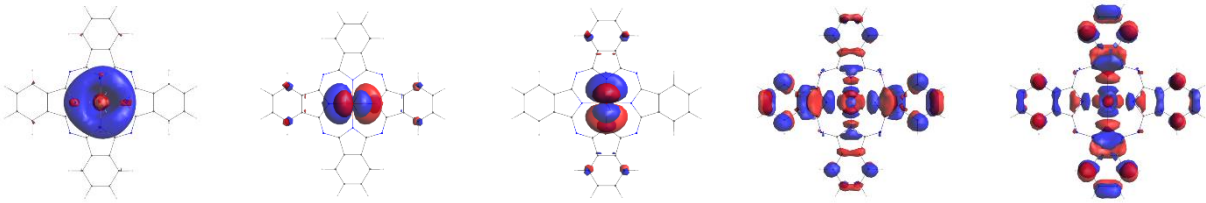

LUMO+6 LUMO+5 LUMO+4 LUMO+3 LUMO+2

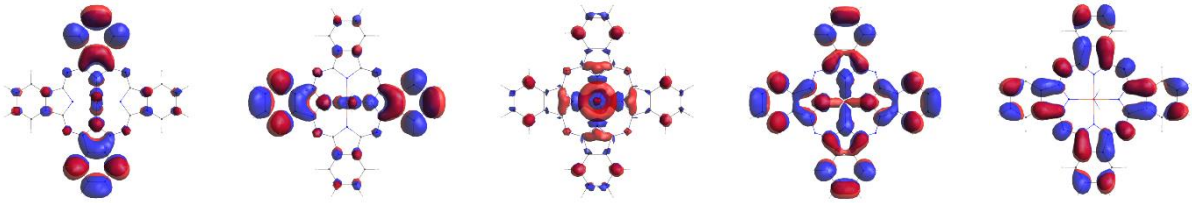

LUMO+1 **LUMO** **HOMO** HOMO-1 HOMO-2

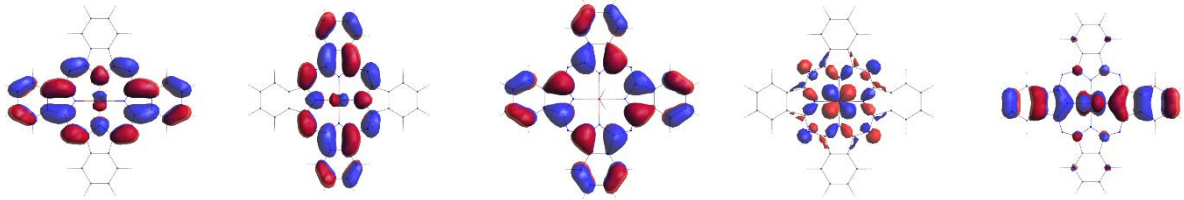

HOMO-3 HOMO-4 HOMO-5 HOMO-6 HOMO-7

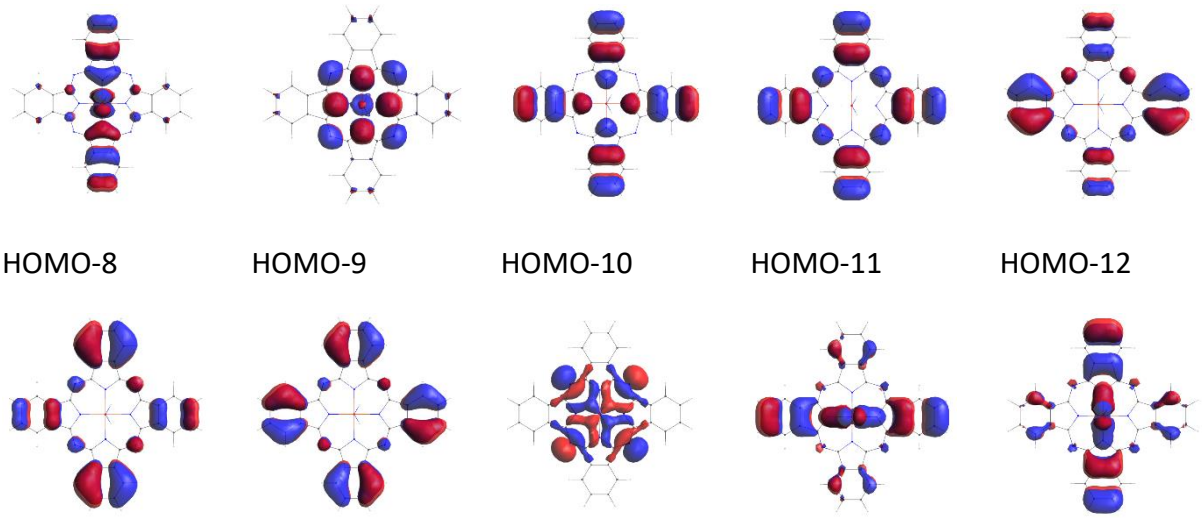

Figure 9.5. Select DFT-predicted frontier molecular orbitals for **8.1**, **8.8**, and **8.18** calculated using the MPWLYP exchange correlation functional.

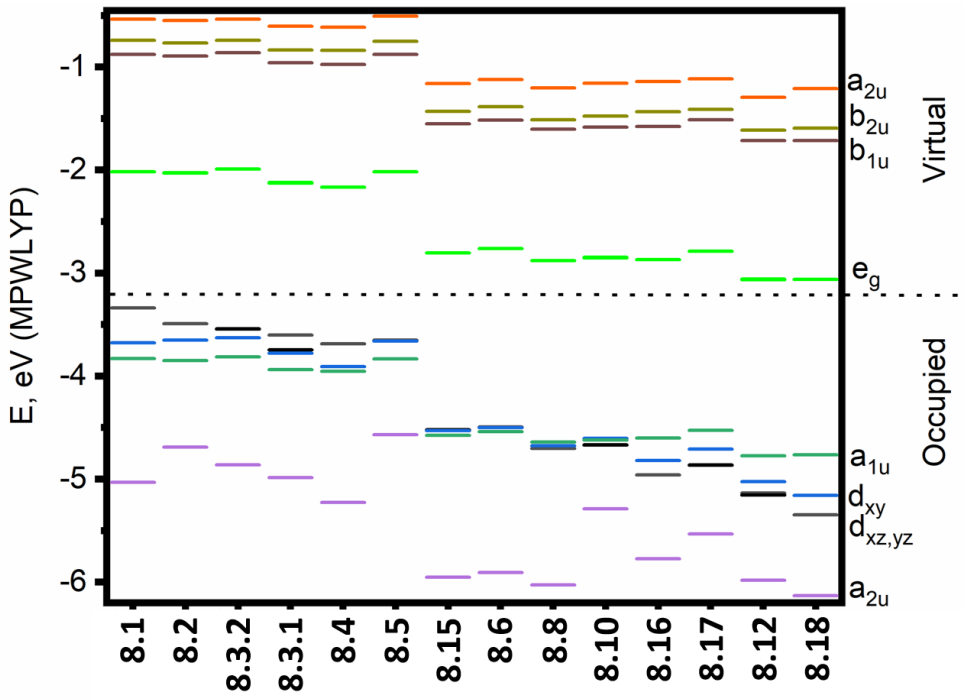

Figure 9.6. DFT-predicted (MPWLYP) energies of the selected orbitals for $PcFeL_2$, PcFeL'L", and $[PcFeX_2]^{2-}$ complexes.

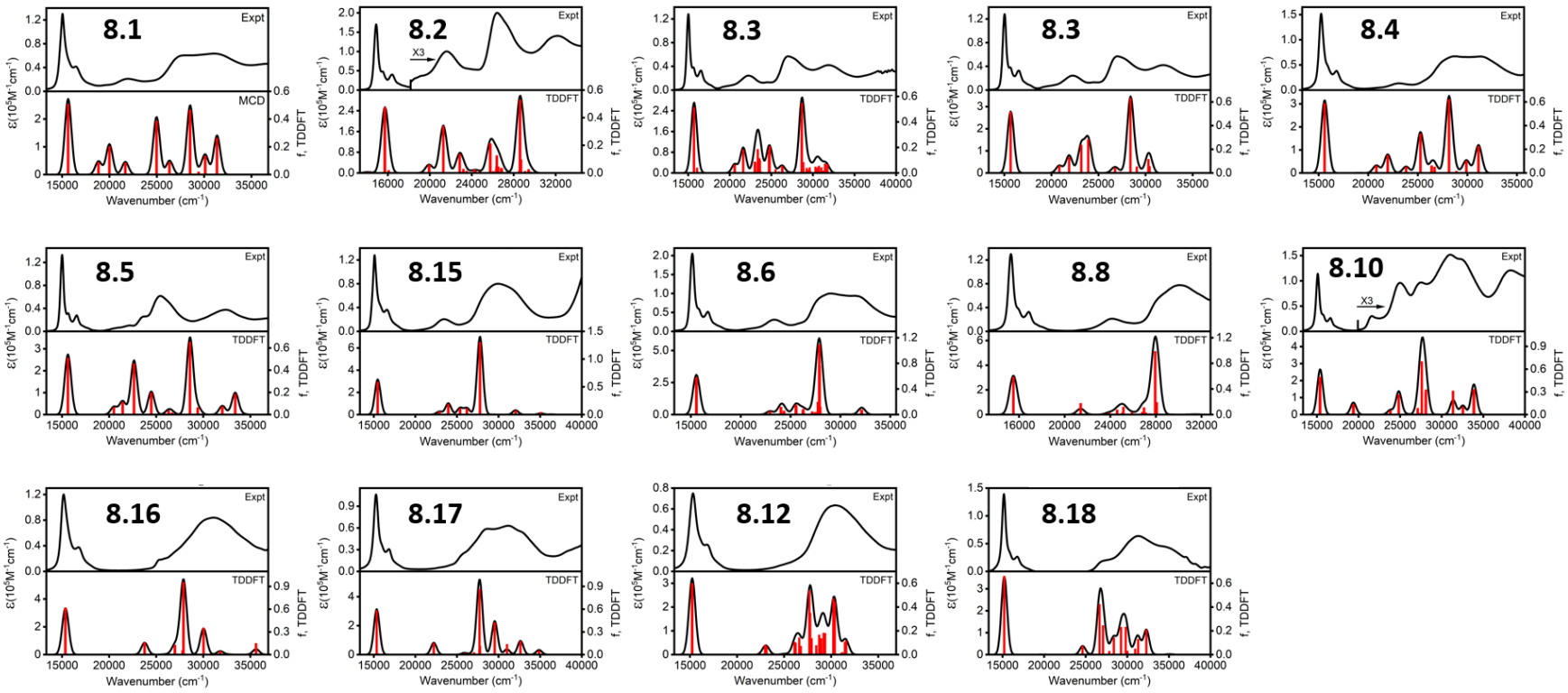

Figure 9.7. Experimental (upper) and TDDFT-predicted (lower) UV-vis spectra of the axially-coordinated phthalocyanines using the MPWLYP exchange correlation functional.

In agreement with the experimental data, the energy deviation of the TDDFT-predicted *Q*-band in the $PcFeL_2$, PcFeL'L", and $[PcFeX_2]^{2-}$ complexes is small (~0.06 eV). Again, TDDFT calculations confirmed that the *Q*-band originates almost entirely from a $1a_{1u}$ (Pc, π) → $1e_g$ (Pc, π*) single-electron transition.[110-112] In agreement with the earlier predictions by Stillman and co-workers,[61] TDDFT calculations identified the $MLCT_1$ and $MLCT_2$ bands as predominantly e_g (Fe, d_π) → $1b_{1u}$ (Pc, π*), and e_g (Fe, d_π) → $1b_{2u}$ (Pc, π*) single-electron excitations in character. The TDDFT-predicted energies of $MLCT_1$ and $MLCT_2$ have clear axial ligand dependency (ΔE = 1.18 and 1.15 eV, respectively). More interestingly, TDDFT calculations predicted that the $MLCT_1$ band in **8.5**, **8.18**, and the $PcFeL_2$ (L= PMe_3, tBuNC, $P(OMe)_3$, and DMSO) complexes has a higher energy than the B_1 band (predominantly $1a_{2u}$ (Pc, π) → $1e_g$ (Pc, π*) in character, Figure 9.1), which was not considered in the previous spectral analyses. Moreover, in the case of complexes **8.12** and **8.18**, the energy of the $MLCT_1$ band was also predicted to be higher than the B_2 and (in the case of the latter compound) N bands.

9.3 Discussion

Before the additive correlations between Lever's electrochemical E_L scale[73,75] and the energy of the MLCT bands can be discussed, we need to accurately interpret the MCD and computational data for the $PcFeL_2$, PcFeL'L", and $[PcFeX_2]^{2-}$ complexes. First, in our hands, the experimentally observed and TDDFT-predicted solvatochromic effect for the $[PcFeX_2]^{2-}$ complexes (X = NCO^-, NCS^-, and CN^-) in DCM, DMF, and DMSO was found to be very small. The $[PcFeX_2]^{2-}$ (X = Im^- or Tz^-), $PcFeL_2$ (L = PR_3, *t*BuNC, $P(OBu)_3$, or DMSO), and **8.13** complexes either have insufficient solubility in counterpart solvents or suffer from aggregation or low-stability

problems in polar or non-polar solvents and thus, solvatochromic effects cannot be measured for these compounds in an accurate way. $PcFeL_2$ (L = NH_3, *n*$BuNH_2$, and Im) have a moderate (~400-1300 cm^{-1} or ~0.05-0.16 eV) solvatochromic effect for the MLCT band observed between 420 and 440 nm (Supporting Information Figure S9.4). Such a solvatochromic effect reflects the formation of the intermolecular hydrogen bond(s) between the axial ligand and the solvent molecules, and will be discussed in detail (on the basis of X-ray, NMR, and Mössbauer spectroscopies) in the follow-up paper. Thus, for the analysis provided below, the only data collected by Stillman's[61,62] and our groups in DCM will be used for all compounds that are soluble and remain monomeric in this solvent. Since $Na_2[PcFeX_2]$ (X = Im^- or Tz^-) complexes are not stable in DCM, we will present data obtained in DMF solutions.

Next, the DFT-predicted energies of the frontier MOs imply that the degenerate, XY-polarized MLCT transitions in $PcFeL_2$, PcFeL'L", and $[PcFeX_2]^{2-}$ complexes can originate from e_g (Fe, d_π) → $1b_{1u}$, $1b_{2u}$, $1a_{2u}$, and $1a_{1u}$ (Pc, π^*) single-electron transitions (in traditional D_{4h} symmetry group notation, Figure 9.1). The bands that predominantly originate from the e_g (Fe, d_π) → $1b_{1u}$ (Pc, π^*) and e_g (Fe, d_π) → $1b_{2u}$ (Pc, π^*) single-electron transitions were labeled as $MLCT_1$ and $MLCT_2$, respectively by Stillman's group.[61] The MLCT band at ~27,000 cm^{-1} that is dominated by the e_g (Fe, d_π) → $1a_{2u}$ (Pc, π^*) single-electron transition was predicted by Sumimoto and co-authors[113] for the $[PcFe(CN)_2]^{2-}$ complex on the basis of TDDFT (B3LYP/6-31G(d)) calculations. The $MLCT_4$ band energy (e_g (Fe, d_π) → $1a_{1u}$ (Pc, π^*)) has not been discussed in the literature. Stillman and Ough used a 0.25 eV energy difference for the e_g (Fe, d_π) → $1b_{1u}$ (Pc, π^*) and e_g (Fe, d_π) → $1b_{2u}$ (Pc, π^*) single-electron transitions as a starting point for their MCD spectral analysis of $PcFeL_2$,

PcFeL'L", and $[PcFeX_2]^{2-}$ complexes (Figure 9.1). This energy difference originates from the MCD data analysis of the $[Pc(-3)Mg]^{-\bullet}$ anion-radical complex conducted by Stillman and co-workers.[114] The discrepancy between this value (0.25 eV or 2050 cm^{-1}) and, proposed on the basis of MCD and UV-vis spectral analysis, the $MLCT_1$-$MLCT_2$ energy gap for $[PcFe(CN)_2]^{2-}$ (~7900 cm^{-1}), $PcFe(NH_3)_2$ (~4300 cm^{-1}), and $PcFe(NH_3)(CO)$ (~1200 cm^{-1}) was attributed to configuration interaction (CI) and the presence of the 3d electrons in the iron compounds.[61] Again, this assumption is a very reasonable starting point. Our DFT calculations using three exchange-correlation functionals (MPWLYP, O3LYP, and TPSSh) as well as the DFT calculations reported by Sumimoto and co-workers[113] using the B3LYP exchange-correlation functional suggest that the energy difference between the $1b_{1u}$ and $1b_{2u}$ MOs is quite small (0.13 – 0.16 eV). Unlike LUMO and LUMO+1 (Pc-centered MOs of e_g symmetry) that have substantial contribution from the iron d-orbitals, the $1b_{1u}$, $1b_{2u}$, and $1a_{2u}$ virtual MOs cannot be mixed with the metal-centered d-orbitals, although the $1a_{2u}$ orbital can mix with the axial ligand's orbitals (Figure 9.1). As a consequence, one might expect that the DFT-predicted energies of the LUMO and LUMO+1 MOs will have a significant dependency on the exchange-correlation functional (and specifically amount of the exact Hartree-Fock exchange present in the functional) used for the calculations, while such dependency should be smaller for the $1b_{1u}$, $1b_{2u}$, and $1a_{2u}$ virtual MOs. Indeed, when the DFT-predicted energy differences between the $1e_g$ and $1b_{1u}$, $1b_{1u}$ and $1b_{2u}$, and $1b_{2u}$ and $1a_{2u}$ MOs are plotted against the amount of exact Hartree-Fock exchange in the functional, it became clear that the above-mentioned argument is correct. For instance, for complex **8.5**, the energy difference between the $1e_g$ and $1b_{1u}$ MOs has a clear functional dependence and varies between 1.09 and 1.72 eV for functionals with 0 to 54% of Hartree-Fock exchange. On the other

hand, it only varies between 0.12 and 0.24 eV for the energy gap between the $1b_{1u}$ and $1b_{2u}$ MOs, while it is nearly constant for the energy difference predicted between the $1b_{2u}$ and $1a_{2u}$ MOs (Supporting Information Figure S9.5). Even when the regular Hartree-Fock calculations for this compound are considered, the $1b_{1u}$-$1b_{2u}$ energy gap remains small (0.34 eV). In addition to a small functional dependency, the DFT-predicted $1b_{1u}$-$1b_{2u}$ energy gap is nearly constant for a given exchange-correlation functional across the E_L axis (Supporting Information Figure S9.5), which (ignoring configurational interactions) implies nearly constant $MLCT_1$-$MLCT_2$ energy gaps in all of the compounds of interest. Our TDDFT calculations with the MPWLYP, O3LYP, and TPSSh functionals predict a 0.10~0.18 eV energy gap between the $MLCT_1$ and $MLCT_2$ states in the $PcFeL_2$, PcFeL'L", and $[PcFeX_2]^{2-}$ complexes, which also correlates well with the 0.16 eV predicted by Sumimoto and co-authors[113] for compound **8.5** and Stillman's estimate of 0.25 eV gained from the spectroscopy of the $[Pc(3-)Mg]^{-\cdot}$ anion-radical.[114] A small $1b_{1u}$-$1b_{2u}$ energy gap leads to the following interesting question. The MCD spectra of the $[PcFeX_2]^{2-}$ (X = NCO^-, Im^-, Tz^-, and NCS^-) and $PcFeL_2$ (L = NH_3, Im, *n*-$BuNH_2$, and Py) compounds in which the 400-450 nm MLCT region is well-separated, are represented by an asymmetric dispersion curve in which the visible MCD *A*-term is located at a higher energy and an additional signal with negative amplitude is located at a lower energy (Figure 9.3). The energy difference between the negative component of the visible *A*-term and lower energy visible *B*-term is close to 0.1 eV in all cases. Similarly, the absorption spectra of these complexes in the same spectral envelope have a visible shoulder at the lower energy side. Again, the energy difference between the shoulder and the main band is about 0.1 eV. In their analysis reported in 1994, Stillman and Ough deconvoluted the MCD spectra of $PcFeL_2$ (L = NH_3, Py, Im, 1-MeIm, 4-MePy, and Pip) in this

region using one MCD *A*-term and one MCD *B*-term of negative amplitude.[61] The nature of this *B*-term has not been discussed in the literature; however, one might argue that it can originate from a Z-polarized b_{2g} (Fe, d_{xy}) → $1b_{1u}$ (Pc, π^*) transition mentioned by Stillman and Ough. In this case, using a simplistic single-electron approximation, the energy of the d_{xy} orbital should be higher than the that of the d_π orbitals and a *B*-term is expected in the MCD spectrum (Supporting Information Figure S9.6). Alternatively, the low-energy signal of negative amplitude can originate from the MCD *A*-term that is closely spaced near the visible *A*-term. In this case, two MCD *A*-terms will represent two closely spaced $MLCT_1$ and $MLCT_2$ excited sates (Supporting Information Figure S9.6). Our TDDFT calculations using three different exchange-correlation functionals suggest that the oscillator strength for the b_{2g} (Fe, d_{xy}) → $1b_{1u}$ (Pc, π^*) transition is very small (f = 0 – 0.002) compared to the predicted oscillator strength of the $MLCT_1$ transition (f = 0.006 – 0.14), which does not support the assignment of these low-energy shoulders as b_{2g} (Fe, d_{xy}) → $1b_{1u}$ (Pc, π^*) in nature. Moreover, TDDFT predicts that in the $[PcFeX_2]^{2-}$ (X = NCO^-, Im^-, Tz^-, and NCS^-) complexes, the energy of the b_{2g} (Fe, d_{xy}) → $1b_{1u}$ (Pc, π^*) transition should be higher in energy compared to the $MLCT_1$. This also agrees well with the MCD spectra assignments of the highly deformed $Pc^{Ph8}FcPy_2$ complex provided by Kobayashi and Fukuda.[155] Indeed, these authors have shown that the MLCT transition originating from the d_{xy} orbital has a higher energy compared to the MLCT transition that originates from the d_π MOs.

Finally, the relative energies of the $MLCT_1$ and $MLCT_2$ transitions with respect to $\pi \rightarrow \pi^*$ transitions originating from the phthalocyanine core should be considered. Historically, it was always assumed that the first higher energy (after the *Q*-band) MCD *A*-term is associated with

the $MLCT_1$ transition.[61,62] However, a previous report by Sumimoto and co-authors[113] as well as our TDDFT calculation suggest that this is not always the case. For instance, TDDFT calculations predict that the B_1 (predominantly $1a_{2u}$ (Pc+L, π) → $1e_g$ (Pc, π^*) single electron transition) band should have a lower energy than $MLCT_1$ in complexes **8.5**, **8.10**, **8.16**, and **8.17**. The B_1 band has XY polarization and is expected to have MCD *A*-term shape. As discussed above, the $1a_{2u}$ orbital can mix with the axial ligands and thus, its energy has a tendency to a fluctuate significantly. As a consequence, the TDDFT-predicted energy of the B_1 band deviates significantly with the nature of the axial ligands. In the case of complexes **8.12** and **8.18**, TDDFT calculations predict several phthalocyanine-centered degenerate π–π^* excited states with energies lower than the $MLCT_1$ transition. Thus, extra care should be taken for the accurate assignments of the charge-transfer bands in the $PcFeL_2$, PcFeL'L", and $[PcFeX_2]^{2-}$ complexes.

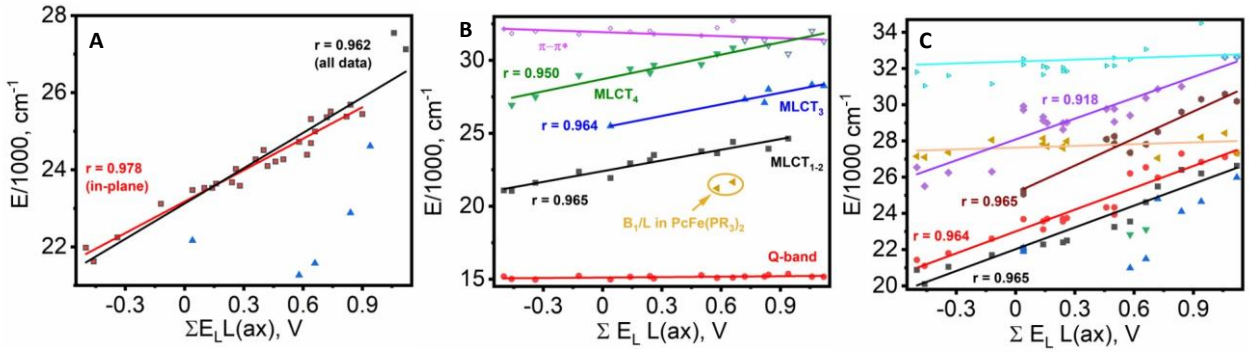

Figure 9.8. Correlation between ΣE_L L(ax) and the MLCT band position in the UV-vis spectra (**A**); ΣE_L L(ax) and the crossing point for the visible MCD *A*-terms (**B**); and ΣE_L L(ax) and the energies of the MCD *A*-terms from the deconvolution analysis (**C**).

When raw data for the main low-energy UV-vis peaks in region II for the $PcFeL_2$, PcFeL'L", and $[PcFeX_2]^{2-}$ complexes are plotted against the ΣE_L L(ax) values to probe the validity of equation 9.4 (Figure 9.8A), one can see five clear outliers coded as blue triangles. These UV-vis bands are associated with the lowest energy (after the *Q*-band) MCD *A*-term and, according to the TDDFT calculations, should be assigned as B_1 ($1a_{2u}$ (Pc, π) → $1e_g$ (Pc, π^*)) phthalocyanine-centered transitions. Once these points are removed from the correlation, the correlation coefficient for the linear regression was found to be 0.962 for all data points or 0.978 for the points in which the central iron ion is located in the plane of the phthalocyanine ligand.

As MCD spectroscopy tends to provide a complimentary resolution of the UV-vis data, we plotted the Y-axis crossing points for the visible *A*-terms observed in the MCD spectra of the $PcFeL_2$, PcFeL'L", and $[PcFeX_2]^{2-}$ complexes against the ΣE_L L(ax) values (Figure 9.8B). It is obvious that the use of the energies of crossing points in the correlation analysis is quite approximate; however, even with such a crude approximation, several trends can be clearly seen. First, the energy of the MCD *A*-term which corresponds to the *Q*-band at ~15,000 cm^{-1} is independent from the ΣE_L L(ax) values. Next, an unique MCD *A*-term at a low energy was observed in the case of the $PcFe(PR_3)_2$ complexes. According to TDDFT calculations, this *A*-term represents the B_1 band, which is dominated by a $1a_{2u}$ (Pc+L, π) → $1e_g$ (Pc, π^*) single-electron contribution. The energy of the $1a_{2u}$ orbital in $PcFe(PR_3)_2$ is highly destabilized because of the large contribution from the lone pair of two phosphine axial ligands. Next, three nearly parallel correlation lines that have clear axial dependency have been observed (Figure 9.8B). All three lines have nearly identical slopes and are separated by 3,000~3,300 cm^{-1} (0.37~0.41 eV) from

each other. We label these correlations as $MLCT_{1\text{-}2}$, $MLCT_3$, and $MLCT_4$ in Figure 9.8B. The rationale for combining the $MLCT_1$ and $MLCT_2$ transitions under the same curve is that TDDFT data from Sumimoto's[113] and our work are suggestive of the $MLCT_1$-$MLCT_2$ gap in the 0.09 – 0.21 eV range (with the majority of those predicted at ~0.15 eV), which is not easy to clearly resolve in the MCD spectra as discussed above. The TDDFT predicted energies of $MLCT_3$ and $MLCT_4$, on the other hand, are better-separated from the energies of $MLCT_1$ and $MLCT_2$ (see discussion below). Obviously, this assumption should be treated with caution and is the main reason why we have deconvoluted the MCD spectra of $PcFeL_2$, PcFeL'L", and $[PcFeX_2]^{2-}$ complexes in two different ways. Another important observation from Figure 9.8B is that the energies of the $MLCT_4$ bands for complexes with high ΣE_L L(ax) values coalesce with the energies of the phthalocyanine-centered $\pi-\pi^*$ transitions observed at ~31,000 cm^{-1}. The latter transition is also almost independent from the nature of the axial ligands, which is a reason for the confident assignment of the last correlation for the phthalocyanine-centered $\pi-\pi^*$ transition. Finally, the correlation results for complex **8.5** implies that the energy of the B_1 and $MLCT_1$ bands should be close to each other, which agrees well with our TDDFT calculations.

Of course, the use of the crossing point of the visible MCD *A*-terms in the correlation analysis is not the best approach in providing a complete picture on the electronic structure and nature of the excited states in $PcFeL_2$, PcFeL'L", and $[PcFeX_2]^{2-}$ complexes because some of the overlapping *A*-terms can visibly appear as a sum of MCD *B*- and *A*-terms (see Supporting Information Figure S9.6 as an example). This is a situation observed for the transitions in $PcFeL_2$, PcFeL'L", and $[PcFeX_2]^{2-}$ complexes in the *B*-band region where a large number of bands are

closely spaced in energy and heavily overlap. In this case, as introduced by Stillman and co-workers for phthalocyanines,[61] simultaneous band deconvolution analysis of UV-vis and MCD spectra is the best alternative for the accurate analysis of the excited states. Since TDDFT predicts that the energy gap between $MLCT_1$ and $MLCT_2$ is rather small, we attempted to accommodate this observation in our analyses (Figure 9.4B); however, we also conducted a more traditional deconvolution analysis, similar to that done by Stillman and co-workers in 1994 (Figure 9.4A).[61] As one can see from Figure 9.4, in the former case, two (closely spaced in energy) *A*-terms were considered in the first MLCT region, while in the latter case, the same region was deconvoluted with a single *A*-term. The energies of the *A*-terms predicted by the deconvolution analysis again correlate well with the ΣE_L L(ax) values (Figure 9.8C and Table 9.3). There are several *A*-terms that were observed with energies that are nearly independent from the nature of the axial ligands. These can be assigned as phthalocyanine-centered excited states. The MLCT transition, on the other hand, has clear axial ligand dependency and correlation coefficients close to those observed with the MCD *A*-terms crossing points.

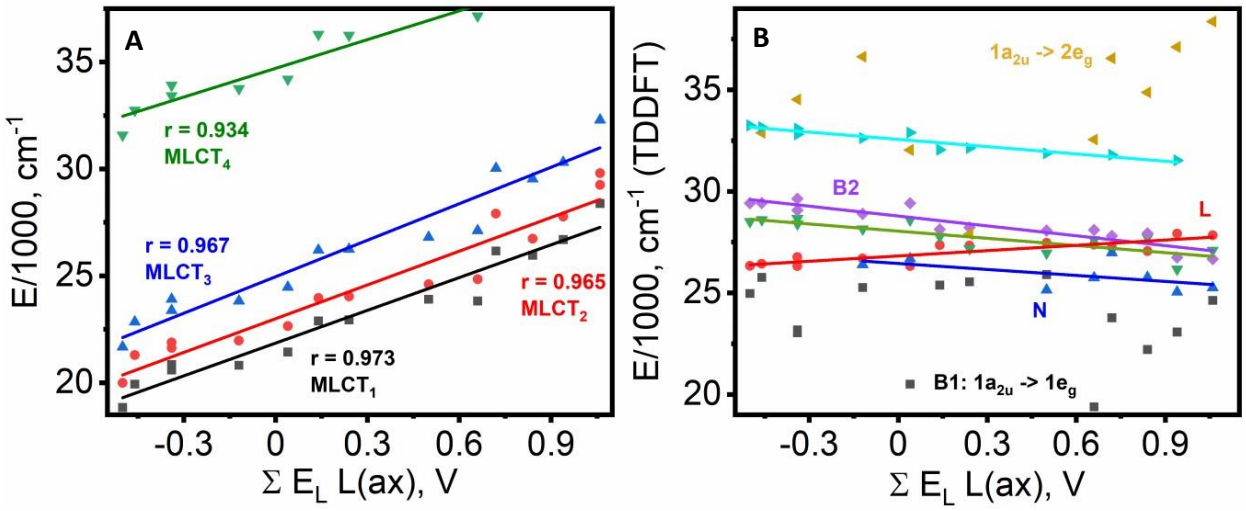

Figure 9.9. Correlation between ΣE_L L(ax) and the TDDFT-predicted MLCT band energies (**A**); ΣE_L L(ax) and the TDDFT-predicted p-p* transitions (**B**).

Table 9.3. MCD *A*-term centers for the degenerate transitions in the $PcFeL_2$, PcFeL'L", and $[PcFeX_2]^{2-}$ complexes in the charge-transfer region (*tw* = this work).

Compound	*Band center/nm*								*Ref.*
8.1	479	465	377	368		314			tw
8.2	498	475	392	369	322	319			tw
8.3	475	459	381	366	316	313			tw
8.4	461	442	372	357	321				tw
8.5	456	422	399	337		310			tw
8.5	453		396	334		307	279	251	61
8.15	449	433	355	343		311			tw
8.15		424	359	341		316	273	253	61
$PcFe(MeIm)_2$		422	361	345		312	271	248	61

8.6	446	425	362	349		314		273			tw
8.6		422	361	345		312		270		248	61
8.7	444	421	357	345		314		277			tw
$PcFe(MePy)_2$		411	356	336		311		277			61
8.8	430	418	359	344	337	307					tw
8.8		411	354	336		311		277			61
8.9	477	438	425	382	366	340	308	266	257	249	tw
8.10	465	433	406	375	360	329	302	262			tw
8.16	403	392	385	370	351	333					tw
8.11	415	379	366	338	323				251		tw
8.12	406	382	373	355	330	290					tw
8.18		369	352	327	307	278					61
8.13	385	376	366	331	307	279					tw

The plot of the energies of the MLCT transitions predicted by TDDFT calculations versus ΣE_L L(ax) values is shown in Figure 9.9A. The correlation coefficients for the TDDFT-predicted $MLCT_{1-3}$ transitions are close to those seen in the MCD plots (Figure 9.8B) and their slopes are close to the slopes observed for the fitted MCD data. One visible discrepancy between the TDDFT calculations and the MCD-based position of its *A*-terms that have a prominent axial ligand dependency is the energy intervals for the MLCT bands. The TDDFT calculations predict that $MLCT_{1-3}$ in the $PcFeL_2$, PcFeL'L", and $[PcFeX_2]^{2-}$ complexes are separated by ~1,000 ($MLCT_{1-2}$) and ~2,000 ($MLCT_{2-3}$) cm^{-1} (Figure 9.8) which correlates very well with the respective

separation of ~1,000 and ~3,000 cm^{-1} predicted by band deconvolution analysis and ~3,000 cm^{-1} interval observed between the first (second for $PcFe(PR_3)_2$ complexes) and the second visible *A*-terms in the experimental spectra of these compounds (Figure 9.3). However, for most of the compounds, it is difficult to derive the experimental position of $MLCT_3$ from the UV-vis and MCD spectra because it heavily overlaps with the other transitions, making proposed assignment quite speculative. In addition, the TDDFT-predicted energy interval between the $MLCT_3$ and $MLCT_4$ bands is ~10,000 cm^{-1}, while ~3,000 cm^{-1} is expected from the MCD band deconvolution analysis. Yet, the TDDFT-predicted energies of the $MLCT_{1-3}$ transitions are well within expectation for TDDFT calculations, being ~0.25 eV (~2,000 cm^{-1}) in uncertainty. They are also lower than the typical uncertainties for the energies of the MLCT transitions in ruthenium(II) and iron(II) complexes predicted using the E_L scale (~0.3 eV).[77]

The MLCT (Fe → Pc) transitions are not the only charge-transfer transitions that are expected in the UV-vis and MCD spectra of the $PcFeL_2$, PcFeL'L", and $[PcFeX_2]^{2-}$ complexes. As was correctly pointed out by Stilman and Ough,[61] two symmetry allowed LMCT (Ligand-to-Metal Charge Transfer) transitions of Pc → Fe character are expected for these compounds in idealized D_{4h} symmetry (Figure 9.1). These are dominated by the $1a_{2u}$ (Pc, π) → a_{1g} (Fe, d_{z2}) and $1b_{2u}$ (Pc, π) → b_{1g} (Fe, d_{x2-y2}) single-electron transitions and are labeled as $LMCT_{Pc1}$ and $LMCT_{Pc2}$ in Figure 1, respectively. Both of these should result in MCD *B*-terms. The $LMCT_{Pc1}$ transitions were predicted between 31,000 and 36,700 cm^{-1} from the TDDFT calculations using the MPWLYP functional. The predicted intensity of this excited state for the axial ligands with ΣE_L L(ax) ≤ 0.5 is rather small, but it is substantial (f > 0.1) for the rest of the tested compounds. The

$LMCT_{Pc2}$ transition was not found in the TDDFT calculations within the 120 lowest energy states and, presumably, appears at higher energy. Next, the electronic structure of the axial ligands should be considered. DFT calculations predict that the negatively charged axial ligands with significant σ- and π-donating properties (NCO^-, Im^-, Tz^-, and NCS^-) should have axial ligand-centered e_g and e_u symmetry orbitals in the HOMO to HOMO-10 region (Table 1). Excited states that are dominated by e_g (X^-, π) → $1b_{1u}$, $1b_{2u}$, $1a_{2u}$, and $1a_{1u}$ (Pc, π∗) single-electron transitions can give rise of four inter-ligand ILCT (X^- → Pc) transitions with MCD *A*-term character that are labeled as $ILCT_{1-4}$ in Figure 9.1. The energies of $ILCT_1$, $ILCT_2$, and $ILCT_3$ were predicted (MPWLYP functional) between 23,300-30,100, 24,500-31,400, and 26,300-33,000 cm^{-1}, respectively. Excited states that are dominated by the e_u (X^-, π) → $1e_g$ and $2e_g$ (Pc, π∗) single-electron transitions can give rise to two ILCT (X^- → Pc) transitions with MCD *B*-term character that are labeled as $ILCT_{5-6}$ in Figure 9.1. The energies of $ILCT_5$ and $ILCT_6$ were predicted (MPWLYP functional) between 26,400 and 32,400 cm^{-1}. Finally, the excited state that is dominated by the e_u (X^-, π) → a_{1g} and b_{1g} (Fe, d_{z2} and d_{x2-y2}) single-electron transitions can give rise to two LMCT (X^- or L → Pc) transitions with MCD *A*-term character that are labeled as $LMCT_{L1-2}$ in Figure 9.1. The energy of $LMCT_{L1}$ was predicted (MPWLYP functional) between 28,900 and 36,700 cm^{-1}, while the energy of the $LMCT_{L2}$ state lies outside of the 120 lowest energy excited states. The increase of the π-accepting character of the cyanide axial ligand results in the stabilization of the occupied, axial ligand-centered e_g and e_u MOs. As a result, the TDDFT-predicted energies of the $ILCT_{1-3}$ bands increased to 35,900-38,800 cm^{-1}. The $PcFeL_2$ and PcFeL'L" complexes in which the axial ligand has a significant π-accepting character (Py, *t*BuNC, and NH_3/CO) have

unoccupied, axial ligand-centered orbitals of *e* symmetry that is reflective of the lowering of their molecular symmetries from the effective D_{4h} to D_{2d}, C_s, and C_i (even the symmetry of complexes **8.16** and **8.18** is C_i or C_s and the axial ligand's MOs that have e_g or e_u symmetries in D_{4h} point group are still nearly degenerate and will be considered below as "*e*" symmetry orbitals). No degenerate or nearly degenerate unoccupied MOs in the LUMO to LUMO+10 energy region were predicted for the $PcFeL_2$ (L = Im, PMe_3, and DMSO) complexes. Similar to the TDDFT calculations of Sumimoto and co-workers,[113] our TDDFT calculations on **8.8** are indicative of XY-polarized (Pc → Py) transitions that originate from $1a_{1u}$, $1a_{2u}$, and $1b_{2u}$ (Pc, π) → *e* (Py, π*) single-electron excitations and one Z-polarized transition dominated by the $1e_g$ (Pc, π) → *e* (Py, π*) single-electron excitation (here we use D_{4h} point group notation for the phthalocyanine and metal-centered orbitals in order to be consistent with the previous discussion and Figure 9.1). These transitions are labeled as $ILCT_{Pc1-4}$ in Figure 9.1 and were predicted at 20,100, 32,000, 33,000, and 34,900 cm^{-1}, respectively. In addition, two MLCT (Fe → Py) transitions labeled as $MLCT_{Fe1-2}$ in Figure 9.1 that originate from e_g (Fe, d_π) → "*e*" (Py, π*) and b_{2g} (Fe, d_{xy}) → "*e*" (Py, π*) single-electron transitions have Z- and XY-polarizations, respectively. According to TDDFT calculations both of these transitions have small intensities. No Pc → *t*BuNC ILCT transitions were predicted by TDDFT calculations within the lowest energy 210 excited states; however, $MLCT_{Fe1-2}$ transitions were predicted at 35,600 (*f* = 0.15) and 32,600 (*f* = 0.004) cm^{-1}. Finally, the $ILCT_{Pc1}$ transition was predicted at 30,000 cm^{-1} with reasonable intensity (*f* = 0.03) for **8.18**, while $MLCT_{Fe1-2}$ transitions in the 33,300 – 34,800 cm^{-1} window were predicted to have zero intensities. Overall, our TDDFT calculations indicate that

the axial ligands can contribute to the UV-vis and MCD spectra of $PcFeL_2$ and PcFeL'L" complexes via MLCT, ILCT, and LMCT mechanisms.

9.4 Conclusions

The energy of the experimentally observed (in the UV-vis and MCD spectra) low-energy metal-to-ligand charge-transfer (MLCT) band in the low-spin iron(II) phthalocyanine complexes of general formula $PcFeL_2$, PcFeL'L", and $[PcFeX_2]^{2-}$ complexes (L, L', or L" are neutral and X- is an anionic axial ligand) was correlated with Lever's electrochemical E_L scale. The TDDFT-predicted UV-vis spectra are in very good agreement with the experimental data for all complexes. In the majority of compounds, TDDFT predicts that the first degenerate MLCT band that correlates with the MCD *A*-term observed between 360 and 480 nm is dominated by an e_g (Fe, d_π) → $1b_{1u}$ (Pc, π^*) single-electron excitation (in traditional D_{4h} point group notation) and agrees well with the previous assignment discussed by Stillman and co-workers. The TDDFT calculations are also suggestive of small $1b_{1u}/1b_{2u}$ (Pc, π^*) orbital splitting and closeness of the $MLCT_1$ and $MLCT_2$ transitions. In the case of the $PcFeL_2$ complexes with phosphines as the axial ligands, additional degenerate charge-transfer transitions were observed between 450 and 500 nm. These transitions are dominated by a_{2u}/PR_3 (Pc, π) → $1e_g$ (Pc, π^*) single-electron excitations and are unique for the bisaxially coordinated iron(II) phthalocyanines. In addition, the L/X^- → Pc, Pc → L, X^- → Fe, and Fe → L charge-transfer transitions were predicted by TDDFT calculations in specific cases.

For the hard chromophoric $PcFe^{II}L_2$, $PcFe^{II}L'L''$, and $[PcFe^{II}X_2]^{2-}$ systems explored in these last two chapters (8 and 9), the general effect on the electronic structures that the structural

modifications via axial ligation had were restricted to manipulation of the energies of the metal d_{xz} and d_{yz} orbitals which were dependent on the electronic nature of the ligand. Specifically, for σ-donating axial ligands, the energies of d_{xz} and d_{yz} increased with magnitudes depending on σ-donating strength, and for π-accepting axial ligands, the d_{xz} and d_{yz} energies decreased. Generally, the energies of the phthalocyanine core orbitals decreased as $\Sigma E_L(L_{ax})$ increased; however, the frontier Pc orbitals experienced a similar decrease in energy as $\Sigma E_L(L_{ax})$ increased and were only slightly shifted relative to each other. Therefore, this particular structural approach (of axial ligation) was not suitable for manipulation of the energies of these frontier Pc core orbitals and these compounds possess a ΔHOMO > ΔLUMO relationship which indicates an electronic structure that can be generally classified as synthetic.

9.5 Experimental Section

9.5.1 Materials. Dichloromethane solvent was purchased from commercial sources and distilled over sodium hydride to eliminated moisture and acid contamination. Tetrabutylammonium perchlorate (TBAP, for electrochemical analysis, ≥99.0%) was purchased from Sigma Aldrich and recrystallized prior to use. All compounds were prepared as described previously.[45,61]

9.5.2 UV-Vis and MCD Spectroscopy. All UV-vis spectra were collected on a Jasco V-770 spectrophotometer and MCD spectra were measured with a Jasco J-1500 CD spectrometer using a Jasco MCD-581 electromagnet operated at 1.0 T. The completed MCD spectra were measured at 10 °C in parallel and antiparallel orientations with respect to the magnetic field.

The MCD spectra were recorded in terms of mDeg = [θ] on the y-axis and were converted to molar ellipticity via Δε = θ/(32980*Blc*), where *B* is the magnetic field, *l* is the path length (cm), and *c* is the concentration (M).[116]

9.5.3 Computational Aspects. All calculations were run using Gaussian 16.[117] BP86[118,119] with Wachter's full-electron basis set[120] (Wf) for iron and the 6-311G(d) basis set[121] for the other atoms was used for all geometry optimizations. Similar to our previous report,[45] two geometries of the **8.3** were considered in the calculations (Figure 9.2). Vibrational frequencies were calculated to ensure all geometries were local minima. Time-dependent density functional theory (TD-DFT) with TPSSh,[122,123] O3LYP[124] and MPWLYP[125] was used to calculate the first eighty excited states of each molecule. In addition, BP86, B3LYP,[126] PBE0,[127] M05,[128] M06,[129] M11,[130] MN12SX,[131] SOGGA11X,[132] wB97X,[133] TPSS/KCIS,[134] MPWKCIS,[135] X3LYP,[136] M11L,[137] wB97XD,[138] tHCTHThyb,[139] MN15,[140] HISSPBE,[141] CAM-B3LYP,[142] HSE0,[143] and LC-wHPBE[144] functionals were tested on a small group of compounds. The same basis sets as for the geometry optimizations were used for the TD-DFT calculations. Single point calculations using the same parameters as the TD-DFT calculations were also performed. All calculations were run in solution using the PCM model,[145] with dichloromethane (DCM) or dimethylformamide (DMF) as the solvents. DCM was used with TPSSh, O3LYP and MPWLYP, while DMF was only tested with MPWLYP. The compounds with butyl alkyl groups were shortened to methyl groups to minimize computational cost; so, **8.9** was not calculated and **8.17** was calculated instead of **8.11**. QMForge[146] was used for the molecular orbital composition analyses.

9.6 References

1 Nemykin, V. N.; Tret'yakova, I. N.; Volkov, S. V.; Li, V. D.; Mekhryakova, N. G.; Kaliya, O. L.; Luk'yanets, E. A. "Synthesis, structure and properties of coordination compounds of iron phthalocyanines and their analogues" *Russ. Chem. Rev.* **2000**, *69*, 325-346.

2 Hanack, M. In Phthalocyanines: Properties and Applications, Eds. Leznoff, C. C. and Lever, A. B. P. VCH, New York, 1989, Vol. 2, pp. 43-96.

3 Ercolani, C.; Floris, B. In Phthalocyanines: Properties and Applications, Eds. Leznoff, C. C. and Lever, A. B. P. VCH, New York, 1989, Vol. 2, pp. 1-43.

4 Taube, R. "New aspects of the chemistry of transition metal phthalocyanines" *Pure Appl. Chem.* **1974**, *38*, 427-438.

5 Sorokin, A. B. "Phthalocyanine Metal Complexes in Catalysis" *Chem. Rev.* **2013**, *113*, 8152-8191.

6 Kennedy, B. J.; Murray, K. S.; Zwack, P. R.; Homborg, H.; Kalz, W. "Spin states in iron(III) phthalocyanines studied by Moessbauer, magnetic susceptibility, and ESR measurements" *Inorg. Chem.* **1986**, *25*, 2539-2545.

7 Fitzgerald, J. P.; Lebenson, J. R.; Wang, G.; Yee, G. T.; Noll, B. C.; Sommer, R. D. "Iron Tetraanthracenotetraazaporphyrins: Synthesis, Structural Characterization, Ligand Binding Properties, and Unexpected Selectivity of a Bis-"Bowl" Tetraazaporphyrin" *Inorg. Chem.* **2008**, *47*, 4520-4530.

8 Fitzgerald, J. P.; Haggerty, B. S.; Rheingold, A. L.; May, L.; Brewer, G. A. "Iron octaethyltetraazaporphyrins: synthesis, characterization, coordination chemistry, and

comparisons to related iron porphyrins and phthalocyanines" *Inorg. Chem.* **1992**, *31*, 2006-2013.

9 Ona-Burgos, P.; Casimiro, M.; Fernandez, I.; Navarro, A. V.; Fernandez-Sanchez, J. F.; Carretero, A. S.; Gutierrez, A. F. "Octahedral iron(II) phthalocyanine complexes: multinuclear NMR and relevance as NO_2 chemical sensors" *Dalton Trans.* **2010**, *39*, 6231-6238.

10 Valero-Navarro, A.; Fernandez-Sanchez, J. F.; Segura-Carretero, A.; Spichiger-Keller, U. E.; Fernandez-Gutierrez, A.; Ona, P.; Fernandez, I. "Iron-phthalocyanine complexes immobilized in nanostructured metal oxide as optical sensors of NOx and CO - NMR and photophysical studies" *J. Porphyrins Phthalocyanines* **2009**, *13*, 616-623.

11 Fernandez-Sanchez, J. F.; Fernandez, I.; Steiger, R.; Beer, R.; Cannas, R.; Spichiger-Keller, U. E. "Second-generation nanostructured metal oxide matrices to increase the thermal stability of CO and NO_2 sensing layers based on iron(II) phthalocyanine" *Adv. Functional Mater.* **2007**, *17*, 1188-1198.

12 Afanasiev, P.; Sorokin, A. B. "μ-Nitrido Diiron Macrocyclic Platform: Particular Structure for Particular Catalysis" *Acc. Chem. Res.* **2016**, *49*, 583-593.

13 Woehrle, D.; Baziakina, N.; Suvorova, O.; Makarov, S.; Kutureva, V.; Schupak, E.; Schnurpfeil, G. "Phthalocyanine coatings on silica and zinc oxide. Synthesis and their activities in the oxidation of sulfide" *J. Porphyrins Phthalocyanines* **2004**, *8*, 1390-1401.

14 Woehrle, D.; Suvorova, O.; Gerdes, R.; Bartels, O.; Lapok, L.; Baziakina, N.; Makarov, S.; Slodek, A. "Efficient oxidations and photooxidations with molecular oxygen using metal

phthalocyanines as catalysts and photocatalysts" *J. Porphyrins Phthalocyanines* **2004**, *8*, 1020-1041.

15 Cailler, L. P.; Clemancey, M.; Barilone, J.; Maldivi, P.; Latour, J.-M.; Sorokin, A. B. "Comparative Study of the Electronic Structures of μ-Oxo, μ-Nitrido, and μ-Carbido Diiron Octapropylporphyrazine Complexes and Their Catalytic Activity in Cyclopropanation of Olefins" *Inorg. Chem.* **2020**, *59*, 1104-1116.

16 Colomban, C.; Tobing, A. H.; Mukherjee, G.; Sastri, C. V.; Sorokin, A. B.; de Visser, S. P. "Mechanism of Oxidative Activation of Fluorinated Aromatic Compounds by N-Bridged Diiron-Phthalocyanine: What Determines the Reactivity?" *Chem. Eur. J.* **2019**, *25*, 14320-14331.

17 Neu, H. M.; Zhdankin, V. V.; Nemykin, V. N. "Binuclear iron(III) phthalocyanine(μ-oxodimer)/tetrabutylammonium oxone: a powerful catalytic system for oxidation of hydrocarbons in organic solution" *Tetrahedron Lett.* **2010**, *51*, 6545-6548.

18 Neu, H. M.; Yusubov, M. S.; Zhdankin, V. V.; Nemykin, V. N. "Binuclear iron(III) phthalocyanine(μ-oxo-dimer)-catalyzed oxygenation of aromatic hydrocarbons with iodosylbenzene sulfate and iodosylbenzene as the oxidants" *Adv. Synth. Catal.* **2009**, *351*, 3168-3174.

19 Geraskin, I. M.; Luedtke, M. W.; Neu, H. M.; Nemykin, V. N.; Zhdankin, V. V. "Organic iodine(V) compounds as terminal oxidants in iron(III) phthalocyanine catalyzed oxidation of alcohols" *Tetrahedron Lett.* **2008**, *49*, 7410-7412.

20 Griffin, J. R.; Wendell, C. I.; Garwin, J. A.; White, M. C. "Catalytic C(sp^3)-H Alkylation via an Iron Carbene Intermediate" *J. Am. Chem. Soc.* **2017**, *139*, 13624-13627.

21 He, C.; Wu, Z.-Y.; Zhao, L.; Ming, M.; Zhang, Y.; Yi, Y.; Hu, J.-S. “Identification of FeN4 as an Efficient Active Site for Electrochemical N_2 Reduction” *ACS Catalysis* **2019**, *9*, 7311-7317.

22 Hu, P.; Tan, M.; Cheng, L.; Zhao, H.; Feng, R.; Gu, W.-J.; Han, W. “Bio-inspired iron-catalyzed oxidation of alkylarenes enables late-stage oxidation of complex methylarenes to arylaldehydes” *Nature Commun.* **2019**, *10*, 1-9.

23 Govan, J.; Abarca, G.; Aliaga, C.; Sanhueza, B.; Orellana, W.; Cardenas-Jiron, G.; Zagal, J. H.; Tasca, F. “Influence of cyano substituents on the electron density and catalytic activity towards the oxygen reduction reaction for iron phthalocyanine. The case for Fe(II) 2,3,9,10,16,17,23,24-octa(cyano)phthalocyanine” *Electrochem. Commun.* **2020**, *118*, 106784.

24 Praats, R.; Kaarik, M.; Kikas, A.; Kisand, V.; Aruvali, J.; Paiste, P.; Merisalu, M.; Leis, J.; Sammelselg, V.; Zagal, J. H. “Electrocatalytic oxygen reduction reaction on iron phthalocyanine-modified carbide-derived carbon/carbon nanotube composite electrocatalysts” *Electrochim. Acta* **2020**, *334*, 135575.

25 Recio, F. J.; Gutierrez, C. A.; Venegas, R.; Linares-Flores, C.; Caro, C. A.; Zagal, J. H. “Optimization of the electrocatalytic activity of MN4-macrocyclics adsorbed on graphite electrodes for the electrochemical oxidation of L-cysteine by tuning the M (II)/(I) formal potential of the catalyst: an overview” *Electrochim. Acta* **2014**, *140*, 482-488.

26 Kuznetsova, N. A.; Kaliya, O. L. “Heterogenized metallophthalocyanines for photodynamic microorganism inactivation: an overview of our experience” *Makrogeterotsikly* **2015**, *8*, 8-19.

27 Gerasimova, G. K.; Yakubovskaya, R. I.; Pankratov, A. A.; Treshchalina, E. M.; Nemtsova, E. R.; Andreeva, T. N.; Venediktova, Yu. B.; Plyutinskaya, A. D.; Bezborodova, O. A.; Sidorova, T. A.; Baryshnikov, A. B.; Kaliya, O. L.; Voroztsov, G. N.; Luzhkov, Yu. M. "Binary catalytic therapy: A new approach to treatment of malignant tumors. Results of pre-clinical and clinical studies" *Russ. J. Gen. Chem.* **2015**, *85*, 289-302.

28 Nxele, S. R.; Nyokong, T. "Conjugation of Azide-functionalised CdSe/ZnS Quantum Dots with Tetrakis(5-hexyn-oxy) Fe(II) phthalocyanine via Click Chemistry for Electrocatalysis" *Electrochim. Acta* **2016**, *194*, 26-39.

29 Nxele, S. R.; Mashazi, P.; Nyokong, T. "Electrode Modification Using Alkynyl Substituted Fe(II) Phthalocyanine via Electrografting and Click Chemistry for Electrocatalysis" *Electroanalysis* **2015**, *27*, 2468-2478.

30 Maringa, A.; Mashazi, P.; Nyokong, T. "Characterization of electrodes modified by one pot or step by step electro-click reaction and axial ligation of iron tetracarboxyphthalocyanine" *Electrochim. Acta* **2014**, *145*, 237-244.

31 Coates, M.; Nyokong, T. "Characterization of glassy carbon electrodes modified with carbon nanotubes and iron phthalocyanine through grafting and click chemistry" *Electrochim. Acta* **2013**, *91*, 158-165.

32 Anderson, D. R.; Solntsev, P. V.; Rhoda, H. M.; Nemykin, V. N. "How big is big? Separation by conventional methods, X-ray and electronic structures of positional isomers of bis-tert-butylisocyano adduct of 2(3),9(10),16(17),23(24)-tetrachloro-3(2), 10(9),17(16),24(23)-tetra(2,6-di-iso-propylphenoxy)-phthalocyaninato iron(II) complex" *J. Porphyrins Phthalocyanines* **2016**, *20*, 337-351.

33 Nemykin, V. N.; Purchel, A. A.; Spaeth, A. D.; Barybin, M. V. “Probing the Electronic Properties of a Trinuclear Molecular Wire Involving Isocyanoferrocene and Iron(II) Phthalocyanine Motifs” *Inorg. Chem.* **2013**, *52*, 11004-11012.

34 Hanack, M.; Knecht, S.; Polley, R.; Subramanian, L. R. “Axially 1,4-diisocyanobenzene bridged substituted iron(II) phthalocyanines and 2,3-naphthalocyanines” *Synth. Metals* **1996**, *80*, 183-189.

35 Schmid, G.; Witke, E.; Schlick, U.; Knecht, S.; Hanack, M. “Substituent effects in soluble phthalocyaninatoiron(II) complexes” *J. Mater. Chem.* **1995**, *5*, 855-859.

36 Ryu, H.; Knecht, S.; Subramanian, L. R.; Hanack, M. “Synthesis and properties of bridged phthalocyaninatoiron(II) complexes with bidentate aliphatic isocyanides” *Synth. Metals* **1995**, *72*, 289-296.

37 Hanack, M.; Knecht, S.; Witke, E.; Haisch, P. “Synthesis and properties of soluble metallophthalocyanines” *Synth. Metals* **1993**, *55*, 873-878.

38 Hanack, M.; Lange, A.; Grosshans, R. “Tetrazine-bridged phthalocyaninato-metal complexes as semiconducting material” *Synth. Metals* **1991**, *45*, 59-70.

39 Watkins, J. J.; Balch, A. L. “Complexes of ferrous phthalocyanine with aromatic nitroso compounds, isocyanides, and phosphites” *Inorg. Chem.* **1975**, *14*, 2720-2723.

40 Calderazzo, F.; Frediani, S.; James, B. R.; Pampaloni, G.; Reimer, K. J.; Sams, J. R.; Serra, A. M.; Vitali, D. “Synthesis and Moessbauer spectroscopic studies of carbonyl derivatives of (phthalocyaninato)iron(II)” *Inorg. Chem.* **1982**, *21*, 2302-2306.

41 Calderazzo, F.; Pampaloni, G.; Vitali, D.; Collamati, I.; Dessy, G.; Fares, V. “Bis adducts of phthalocyaninatoiron(II) with Group 6A axial donor atoms. Crystal and molecular

structure of sulfur-bonded bis(dimethyl sulfoxide)phthalocyaninatoiron(II)-dimethyl sulfoxide (1/2)" *J. Chem. Soc., Dalton Trans.* **1980**, 1965-1969.

42 Calderazzo, F.; Vitali, D.; Pampaloni, G.; Collamati, I. "Reaction of pentacarbonyliron with phthalonitrile in dimethylformamide and isolation of carbonyl derivatives of iron(II) phthalocyanine stabilized by group 6 donor atoms" *J. Chem. Soc., Chem. Commun.* **1979**, 221-222.

43 Ohya, T.; Morohoshi, H.; Sato, M. "Preparation and characterization of low-spin iron(II) porphyrin complexes with bis(phosphine) or bis(phosphite) axial ligands" *Inorg. Chem.* **1984**, *23*, 1303-1305.

44 Sweigart, D. A. "Axial ligand substitution in iron(II) phthalocyanine adducts: replacement of tri-n-butyl phosphite by tri-n-butylphosphine" *J. Chem. Soc., Dalton Trans.* **1976**, 1476-1477.

45 Nemykin, V. N.; Nevonen, D. E.; Osterloh, W. R.; Ferch, L. S.; Harrison, L. A.; Marx, B. S.; Kadish, K. M. "Application of Lever's E_L Parameter Scale toward Fe(II)/Fe(III) versus Pc(2-)/Pc(1-) Oxidation Process Crossover Point in Axially Coordinated Iron(II) Phthalocyanine Complexes" *Inorg. Chem.* **2021**, *60*, 16626-16644.

46 Zanguina, A.; Bayo-Bangoura, M.; Bayo, K.; Ouedraogo, G. V. "IR and UV-visible spectra of iron(II) phthalocyanine complexes with phosphine or phosphite" *Bull. Chem. Soc. Ethiopia* **2002**, *16*, 73-79.

47 Nemykin, V. N.; Nevonen, D. E.; Ferch, L. S.; Shepit, M.; Herbert, D. E.; van Lierop, J. "Accurate Prediction of Mössbauer Hyperfine Parameters in Bis-Axially Coordinated

Iron(II) Phthalocyanines Using Density Functional Theory Calculations: A Story of a Single Orbital Revealed by Natural Bond Orbital Analysis" *Inorg. Chem.* **2021**, *60*, 3690-3706.

48 Calderazzo, F.; Pampaloni, G.; Vitali, D.; Pelizzi, G.; Collamati, I.; Frediani, S.; Serra, A. M. "Carbonyl derivatives of phthalocyaninatoiron(II), especially those containing Group VI axial donor atoms. Crystal and molecular structure of carbonyl(N,N-dimethylformamide) phthalocyaninatoiron(II) and Moessbauer studies of some of the products" *J. Organomet. Chem.* **1980**, *191*, 217-242.

49 Lever, A. B. P.; Wilshire, J. P. "Electrochemistry of iron phthalocyanine complexes in nonaqueous solvents and the identification of five-coordinate iron(I) phthalocyanine derivatives" *Inorg. Chem.* **1978**, *17*, 1145-1151.

50 Jones, J. G.; Twigg, M. V. "Axial ligand dissociation of phthalocyaninatoiron(II) adducts. Further evidence for a dissociative mechanism of substitution" *J. Chem. Soc., Dalton Trans.* **1978**, 1709-1714.

51 Dale, B. W.; Williams, R. J. P.; Edwards, P. R.; Johnson, C. E. "Moessbauer spectra of compounds containing iron(II) in strong-field tetragonal environments" *Trans. Faraday Soc.* **1968**, *64*, 620-629.

52 Dale, B. W.; Williams, R. J. P.; Edwards, P. R.; Johnson, C. E. "Nature of electric field-gradient tensor in strong-field tetragonal and pseudo-tetragonal complexes of divalent iron" *Trans. Faraday Soc.* **1968**, *64*, 3011-3013.

53 Dale, B. W. "Effect of axial ligands on the electronic absorption spectrum of phthalocyanineiron(II)" *Trans. Faraday Soc.* **1969**, *65*, 331-339.

54 Hanack, M.; Hirsch, A. “Synthesis of bridged mixed valence macrocyclic compounds” *Synthetic Metals* **1989**, *29*, F9-F14.

55 Nemykin, V. N.; Polshina, A. E.; Chernii, V. Y.; Polshin, E. V.; Kobayashi, N. “Synthesis, properties and Mossbauer spectra of bisaxially co-ordinated iron(II) phthalocyanine low-spin complexes: the first semi-quantitative explanation of the influence of the character of axial ligands on the spectral parameters” *Dalton* **2000**, 1019-1025.

56 Nemykin, V. N.; Kobayashi, N.; Chernii, V. Y.; Belsky, V. K. “Mossbauer, crystallographic, and density functional theoretical investigation of the electronic structure of bis-ligated low-spin iron(II) phthalocyanines” *Eur. J. Inorg. Chem.* **2001**, 733-743. DOI: 10.1002/1099-0682(200103)2001:3<733::AID-EJIC733>3.0.CO;2-2

57 Fernandez, I.; Pregosin, P. S.; Albinati, A.; Rizzato, S.; Spichiger-Keller, U. E.; Nezel, T.; Fernandez-Sanchez, J. F. “Solution NMR and X-ray structural studies on phthalocyaninatoiron complexes” *Helvetica Chim. Acta* **2006**, *89*, 1485-1496.

58 Nevonen, D. E.; Ferch, L. S.; Chernii, V. Y.; Herbert, D. E.; van Lierop, J.; Nemykin, V. N. “X-Ray structures, Mossbauer hyperfine parameters, and molecular orbital descriptions of the phthalocyaninato iron(II) azole complexes” *J. Porphyrins Phthalocyanines* **2020**, *24*, 894-903.

59 Ettorre, R.; Marton, D.; Russo, U.; Zanonato, P. “Complexes of phthalocyaninatoiron(II) with diazoles” *J. Porphyrins Phthalocyanines* **2001**, *5*, 545-547.

60 Ouedraogo, G. V.; More, C.; Richard, Y.; Benlian, D. “Charge-transfer and Moessbauer spectra of axially substituted iron phthalocyanines” *Inorg. Chem.* **1981**, *20*, 4387-4393.

61 Ough, E. A.; Stillman, M. J. “Analysis of the absorption and magnetic circular dichroism spectra of iron(II) phthalocyanine” *Inorg. Chem.* **1994**, *33*, 573-583.

62 Stillman, M. J.; Thomson, A. J. “Orbital reduction factors in the lowest excited state of the phthalocyanine ring and their measurement by magnetic circular dichroism spectroscopy” *J. Chem. Soc., Faraday Trans. 2,* **1974**, *70*, 805-814.

63 Hanack, M.; Deger, S.; Lange, A. “Bisaxially coordinated macrocyclic transition metal complexes” *Coord. Chem. Rev.* **1988**, *83*, 115-136.

64 Schneider, O.; Hanack, M. “Axially polymerized (phthalocyaninato)iron(II) with pyrazine, 4,4'-bipyridine, 1,4-diisocyanobenzene, or 1,4-diazabicyclo[2.2.2]octane as bridging ligands; synthesis, characterization, and electrical conductivities” *Chem. Ber.* **1983**, *116*, 2088-2108.

65 Hanack, M.; Hirsch, A.; Lehmann, H. “Soluble oligomeric bridged phthalocyaninatoiron(II) complexes” *Angew. Chem. Int. Ed.* **1990**, *29*, 1467-1468.

66 Hanack, M.; Duerr, K.; Lange, A.; Barcina, J. Osio; Pohmer, J.; Witke, E. “Synthesis of low band gap polymers - a challenge for organic chemists” *Synth. Met.* **1995**, *71*, 2275-2278.

67 Hanack, M. “Intrinsic semiconducting materials on phthalocyanine basis” *Turk. J. Chem.* **1998**, *22*, 13-22.

68 Hanack, M.; Fiedler, M.; Subramanian, L. R. “Phthalocyaninatoiron complexes with tridentate ligands” *Synth. Met.* **1999**, *100*, 123-130.

69 Bayo, K.; Ouedraogo, G. V.; Terzian, G.; Benlian, D. “UV-visible and IR spectra of iron(II) phthalocyanine polymer complexes linked by bis-pyridinato ligands” *Polyhedron* **1990**, *9*, 1087-1090.

70 Ercolani, C.; Monacelli, F.; Dzugan, S.; Goedken, V. L.; Pennesi, G.; Rossi, G. “X-ray crystal structure of μ-oxo-bis[(1-methylimidazole)phthalocyaninatoiron(III)] and comments on the molecular structure and chemistry of oxo-bridged iron phthalocyaninate dimers” *J. Chem. Soc., Dalton Trans.* **1991**, 1309-1315.

71 Janczak, J.; Kubiak, R. “Pyrazine control of the supramolecular chemistry of iron(II) and cobalt (II) phthalocyanines” *CrystEngComm* **2010**, *12*, 3599-3606.

72 Janczak, J.; Kubiak, R. “Synthesis, thermal stability and structural characterization of iron(II) phthalocyanine complex with 4-cyanopyridine” *Polyhedron* **2007**, *26*, 2997-3002.

73 Lever, A. B. P. "Electrochemical parametrization of metal complex redox potentials, using the ruthenium(III)/ruthenium(II) couple to generate a ligand electrochemical series" *Inorg. Chem.* **1990**, *29*, 1271-1285.

74 Alexiou, C.; Lever, A. B. P. "Tuning metalloporphyrin and metallophthalocyanine redox potentials using ligand electrochemical (E_L) and Hammett (σ_p) parametrization" *Coord. Chem. Rev.* **2001**, *216-217*, 45-54.

75 Lever, A. B. P.; Dodsworth, E. S. in: “Inorganic Electronic Structure and Spectroscopy” Solomon, E. I. and Lever, A. B. P. (Eds.), John Wiley & Sons, Inc., **1999**, *Vol. II*, 227-289.

76 Lever, A. B. P. "The phthalocyanines-molecules of enduring value; a two-dimensional analysis of redox potentials" *J. Porphyrins Phthalocyanines* **1999**, *3*, 488-499.

77 Vlcek, A. A. Relation between spectral and redox properties of coordination compounds. *Electrochim. Acta*, **1968**, *13*, 1063-1078.

78 Goswami, S.; Chakravarty, A. R.; Chakravorty, A. Chemistry of ruthenium. 5. Reaction of trans-dihalobis[2-(arylazo)pyridine]ruthenium(II) with tertiary phosphines: chemical,

spectroelectrochemical, and mechanistic characterization of geometrically isomerized substitution products. *Inorg. Chem.* **1982**, *21*, 2737-2742.

79 Chakravarty, A. R.; Chakravorty, A. Chemistry of ruthenium. Part 6. Bis(2,2'-bipyridine)(isonitrosoketonato)ruthenium(II) perchlorate monohydrate. Synthesis, spectra, and electrochemistry. *J. Chem. Soc., Dalton Trans.* **1982**, *9*, 1765-1771.

80 Matsubara, T.; Ford, P. C. Some applications of cyclic voltammetry to the reactions and properties of ruthenium ammine complexes. Reduction potentials and rate studies. *Inorg. Chem.* 1976, *15*, 1107-1110.

81 Day, P.; Sanders, N. Spectra of complexes of conjugated lignads. I. Charge-transfer in phenanthroline complexes: energy shift on substitution. *J. Chem. Soc. A* **1967**, *10*, 1530-1536.

82 Toma, H. E. Ion association and charge-transfer excitation between N-heterocyclic cations and cyanoiron complexes. *Can. J. Chem.* **1979**, *57*(16), 2079-2084.

83 Pombeiro, A. J. L.; Richards, R. L. The chemical oxidation and electronic spectra of the trans-bis[bis(diphenylphosphino)ethane]bis(substituted isonitrile) metal complexes trans-[M(CNR)2(Ph2PCH2CH2PPh2)2] (M = molybdenum or tungsten) *J. Organomet. Chem.* **1979**, *179*, 459-477.

84 Brisset, J. L.; Biquard, M. Pentacyano(pyridine)ferrates(II) and –(III) and related compounds. *Inorg. Chim. Acta* **1981**, *53*, L125-L128.

85 Shriver, D. F.; Posner, J. Bridge addition compounds. III. The influence of boron containing Lewis acids on electronic spectra, vibrational spectra, and oxidation potentials of some iron-cyanide complexes. *J. Am. Chem. Soc.* **1966**, *88*, 1672-1677.

86 Dart, J. W.; Lloyd, M. K.; Mason, R.; McCleverty, J. A.; Williams, J. Properties of isocyanide ligands in metal complexes. Characterization and voltametric properties of bis(tertiary phosphine)tris(isonitrile) cobalt(I) complexes. *J. Chem. Soc., Dalton Trans.* **1973**, *17*, 1747-1751.

87 Rillema, D. P.; Mack, K. B. The low-lying excited state in ligand π-donor complexes of ruthenium(II): mononuclear and binuclear species. *Inorg. Chem.* **1982**, *21*, 3849-3854.

88 Ford, P. C.; Rudd, D. P.; Gaunder, R.; Taube, H. Synthesis and properties of pentaamminepyridineruthenium(II) and related pentaammineruthenium complexes of aromatic nitrogen heterocycles. *J. Am. Chem. Soc.* **1968**, *90*, 1187-1194.

89 Johnson, C. R.; Shepherd, R. E. Metal-to-ligand charge-transfer spectra of pentacyanoruthenate(II) complexes of aromatic nitrogen heterocycles. *Inorg. Chem.* **1983**, *22*, 2439-2444.

90 Ghosh, P.; Chakravorty, A. Hydroxamates of bis(2,2'-bipyridine)ruthenium: synthesis, protic, redox, and electroprotic equilibria, spectra, and spectroelectrochemical correlations. *Inorg. Chem.* **1984**, *23*, 2242-2248.

91 Goswami, S.; Mukherjee, R.; Chakravorty, A. Chemistry of ruthenium. 12. Reactions of bidentate ligands with diaquabis[2-(arylazo)pyridine]ruthenium(II) cation. Stereoretentive synthesis and tris chelates and their characterization: metal oxidation, ligand reduction, and spectroelectrochemical correlation. *Inorg. Chem.* **1983**, *22*, 2825-2832.

92 Sullivan, B. P.; Caspar, J. V.; Meyer, T. J. Hydrido carbonyl complexes of osmium(II) and ruthenium(II) containing polypyridyl ligands. *Organometallics* **1984**, *3*, 1241-1251.

93 Saji, T.; Aoyagui, S. Polarographic studies on bipyridine complexes. II. Correlation between charge-transfer frequencies and oxidation potentials of tris(2,2'-bipyridine) complexes of iron, ruthenium, osmium, cobalt, and chromium. *J. Electroanal. Chem. Interfacial Electrochem.* **1975**, *60*, 1-10.

94 Curtis, J. C.; Sullivan, B P.; Meyer, T. J. Hydrogen-bonding-induced solvatochromism in the charge-transfer transitions of ruthenium(II) and ruthenium(III) ammine complexes. *Inorg. Chem.* **1983**, *22*, 224-236.

95 Ohsawa, Y.; Hanck, K. W.; DeArmond, M. K. A systematic electrochemical and spectroscopic study of mixed-ligand ruthenium(II) 2,2'-bipyridine complexes [Ru(bpy)3-nLn]2+ (n = 0, 1, 2, and 3). *J. Electroanal. Chem. Interfacial Electrochem.* **1984**, *175*, 229-240.

96 Toma, H. E. Intervalence transfer in outer-sphere hexaammineruthenium(III)pentacyanoferrate(II) complexes. *J. Chem. Soc. Dalton Trans.* **1980**, *3*, 471-475.

97 Curtis, J. C.; Meyer, T. J. Outer-sphere intervalence transfer. *J. Am. Chem. Soc.* **1978**, *100*, 6284-6286.

98 Hennig, H.; Rehorek, A.; Ackerman, M.; Rehorek, D.; Thomas, P. Photocatalytic systems. XLIV. Intervalence charge transfer behavior of ion pair associates of octacyanomolybdate. *Z. Anorg. Allg. Chem.* **1983**, *496*, 186-196.

99 Dodsworth, E. S.; Lever, A. B. P. Correlation of electronic charge transfer transitions and electrochemical potentials. The bipyrazine(tetracarbonyl) molybdenum(O) system in various solvents. *Chem. Phys. Lett.* **1984**, *112*, 567-570.

100 Dodsworth, E. S.; Lever, A. B. P. Relationships between electronic spectroscopy and electrochemistry. A probe of reorganization energies. *Chem. Phys. Lett.* **1985**, *119*(1), 61-66.

101 Lever, A. B. P.; Pickens, S. R.; Minor, P. C.; Licoccia, S.; Ramaswamy, B. S.; Magnell, K. Charge-transfer spectra of metallophthalocyanines: correlation with electrode potentials. *J. Am. Chem. Soc.* **1981**, *103*, 6800-6806.

102 Vlcek, A. A.; Dodsworth, E. S.; Pietro, W. J.; Lever, A. B. P. "Excited State Redox Potentials of Ruthenium Diimine Complexes; Correlations with Ground State Redox Potentials and Ligand Parameters" *Inorg. Chem.* **1995**, *34*, 1906-1913.

103 Allard, M. M.; Odongo, O. S.; Lee, M. M.; Chen, Y.-J.; Endicott, J. F.; Schlegel, H. B. "Effects of Electronic Mixing in Ruthenium(II) Complexes with Two Equivalent Acceptor Ligands. Spectroscopic, Electrochemical, and Computational Studies" *Inorg. Chem.* **2010**, *49*, 6840-6852.

104 Dodsworth, E. S.; Lever, A. B. P. "Correlations between electrochemical potentials and optical charge transfer energies in ruthenium bipyridine derivatives" *Chem. Phys. Lett.* **1986**, *124*, 152-158.

105 V. N. Nemykin and E. A. Lukyanets, "The key role of the peripheral substituents in the chemistry of phthalocyanines", in: *Handbook of Porphyrin Science*, K. M. Kadish, K. M. Smith and R. Guilard (Eds.); World Scientific: Singapore, **2010**, *Vol 3*., pp 1 - 323.

106 Nemykin, V. N.; Hadt, R. G. "Influence of Hartree-Fock Exchange on the Calculated Moessbauer Isomer Shifts and Quadrupole Splittings in Ferrocene Derivatives Using Density Functional Theory" *Inorg. Chem.* **2006**, *45*, 8297-8307.

107 Nemykin, V. N.; Basu, P. "Comparative theoretical investigation of the vertical excitation energies and the electronic structure of $[Mo^{V}OCl_4]^-$: influence of basis set and geometry" *Inorg. Chem.* **2003**, *42*, 4046-4056.

108 Belosludov, R. V.; Nevonen, D.; Rhoda, H. M.; Sabin, J. R.; Nemykin, V. N. Simultaneous Prediction of the Energies of Qx and Qy Bands and Intramolecular Charge-Transfer Transitions in Benzoannulated and Non-Peripherally Substituted Metal-Free Phthalocyanines and Their Analogues: No Standard TDDFT Silver Bullet Yet. *J. Phys. Chem. A* **2019**, *123*, 132-152.

109 Martynov, A. G.; Mack, J.; May, A. K.; Nyokong, T.; Gorbunova, Y. G.; Tsivadze, A. Yu Methodological Survey of Simplified TD-DFT Methods for Fast and Accurate Interpretation of UV-Vis-NIR Spectra of Phthalocyanines. *ACS Omega* **2019**, *4*, 7265-7284.

110 Zerner, M.; Gouterman, M. Porphyrins. IV. Extended Hueckel Calculations on Transition Metal Complexes. *Theor. Chim. Acta* **1966**, *4*, 44-63.

111 Zerner, M.; Gouterman, M. Porphyrins. V. Extended Hueckel Calculations on Vanadyl (VO2+) and Vanadium(II) Complexes. *Inorg. Chem.* **1966**, *5*, 1699-1706.

112 Zerner, M.; Gouterman, M. Porphyrins. X. Extended Hueckel Calculations on Alkaline Earth Complexes. *Theor. Chim. Acta* **1967**, *8*, 26-34.

113 Sumimoto, M.; Kawashima, Y.; Hori, K.; Fujimoto, H. "Theoretical investigation of the molecular and electronic structures and excitation spectra of iron phthalocyanine and its derivatives, FePc and FePcLn (L = Py, CN-; n = 1, 2)" *Dalton Trans.* **2009**, 5737-5746.

114 Ough, E.; Gasyna, Z.; Stillman, M. J. "Photochemical, electrochemical, and chemical formation of the π-cation-radical species of magnesium phthalocyanine. Analysis of the absorption and MCD spectra of [MgPc(-1)]$^{\cdot+}$" *Inorg. Chem.* **1991**, *30*, 2301-2310.

115 Fukuda, T.; Homma, S.; Kobayashi, N. "A highly deformed iron(II) low-spin phthalocyanine which shows two MLCT transitions beyond the Q-band" *Chem. Commun.* **2003**, 1574–1575.

116 Galinato, M. G. I.; Spolitak, T.; Ballou, D. P.; Lehnert, N. Elucidating the Role of the Proximal Cysteine Hydrogen-Bonding Network in Ferric Cytochrome P450cam and Corresponding Mutants Using Magnetic Circular Dichroism Spectroscopy. *Biochemistry* **2011**, *50*(6), 1053-1069.

117 Gaussian 16, Revision B.01, Frisch, M. J.; Trucks, G. W.; Schlegel, H. B.; Scuseria, G. E.; Robb, M. A.; Cheeseman, J. R.; Scalmani, G.; Barone, V.; Petersson, G. A.; Nakatsuji, H.; Li, X.; Caricato, M.; Marenich, A. V.; Bloino, J.; Janesko, B. G.; Gomperts, R.; Mennucci, B.; Hratchian, H. P.; Ortiz, J. V.; Izmaylov, A. F.; Sonnenberg, J. L.; Williams-Young, D.; Ding, F.; Lipparini, F.; Egidi, F.; Goings, J.; Peng, B.; Petrone, A.; Henderson, T.; Ranasinghe, D.; Zakrzewski, V. G.; Gao, J.; Rega, N.; Zheng, G.; Liang, W.; Hada, M.; Ehara, M.; Toyota, K.; Fukuda, R.; Hasegawa, J.; Ishida, M.; Nakajima, T.; Honda, Y.; Kitao, O.; Nakai, H.; Vreven, T.; Throssell, K.; Montgomery, J. A., Jr.; Peralta, J. E.; Ogliaro, F.; Bearpark, M. J.; Heyd, J. J.; Brothers, E. N.; Kudin, K. N.; Staroverov, V. N.; Keith, T. A.; Kobayashi, R.; Normand, J.; Raghavachari, K.; Rendell, A. P.; Burant, J. C.; Iyengar, S. S.; Tomasi, J.; Cossi, M.; Millam, J. M.; Klene, M.; Adamo, C.; Cammi, R.; Ochterski, J. W.;

Martin, R. L.; Morokuma, K.; Farkas, O.; Foresman, J. B.; Fox, D. J. Gaussian, Inc., Wallingford CT, 2016.

118 Becke, A. D. Density-functional exchange-energy approximation with correct asymptotic behaviour. *Phys. Rev. A*. **1988**, *38*, 3098-3100.

119 Perdew, J. P. Density-functional approximation for the correlation energy of the inhomogeneous electron gas. *Phys. Rev. B*. **1986**, *33*, 8822-8824.

120 Wachters, A. J. H. Gaussian Basis Set for Molecular Wavefunctions Containing Third-Row Atoms. *J. Chem. Phys.* **1970**, *52*, 1033-1036.

121 McLean, A. D.; Chandler, G. S. Contracted Gaussian basis sets for molecular calculations. 1. Second row atoms, Z = 11-18. *J. Chem. Phys.* **1980**, *72*, 5639-5648.

122 Staroverov, V. N.; Scuseria, G. N.; Tao, J.; Perdew, J. P. "Comparative assessment of a new nonempirical density functional: Molecules and hydrogen-bonded complexes" *J. Chem. Phys.* **2003**, *119*, 12129-12137.

123 Tao, J. M.; Perdew, J. P.; Staroverov, V. N.; Scuseria, G. E. Climbing the density functional ladder: Nonempirical meta-generalized gradient approximation designed for molecules and solids. *Phys. Rev. Lett.* **2003**, *91*, 146401.

124 Cohen, A. J.; Handy, N. C. Dynamic correlation. *Mol. Phys.* **2001**, *99*, 607-615.

125 Schultz, N. E.; Zhao, Y.; Truhlar, D. G. Density functionals for inorganometallic and organometallic chemistry. *J. Phys. Chem. A*. **2005**, *109*, 11127-11143.

126 Becke, A. D. "Density-functional thermochemistry. III. The role of exact exchange" *J. Chem. Phys.* **1993**, *98*, 5648-5652.

127 Ernzerhof, M.; Perdew, J. P. “Generalized gradient approximation to the angle- and system-averaged exchange hole” *J. Chem. Phys.* **1998**, *109*, 3313-3320.

128 Zhao, Y.; Schultz, N. E.; Truhlar, D. G. Exchange-correlation functionals with broad accuracy for metallic and nonmetallic compounds, kinetics, and noncovalent interactions. *J. Chem. Phys.* **2005**, *123*, 161103/1-161103/4.

129 Zhao, Y.; Truhlar, D. G. The M06 suite of density functionals for main group thermochemistry, thermochemical kinetics, noncovalent interactions, excited states, and transition elements: two new functionals and systematic testing of four M06 functionals and twelve other functionals. *Theor. Chem. Acc.* **2008**, *120*, 215-241.

130 Peverati, R.; Truhlar, D. G. Improving the accuracy of hybrid meta-GGA density functionals by range separation. *J. Phys. Chem. Lett.* **2011**, *2*, 2810-2817.

131 Peverati, R.; Truhlar, D. G. Screened-exchange density functionals with broad accuracy for chemistry and solid-state physics. *Phys. Chem. Chem. Phys.* **2012**, *14*, 16187-16191.

132 Peverati, R.; Zhao, Y.; Truhlar, D. G. “Generalized Gradient Approximation that Recovers the Second-Order Density-Gradient Expansion with Optimized Across-the-board Performance” *J. Phys. Chem. Lett.* **2011**, *2*, 1991-1997.

133 Chai, J. D.; Head-Gordon, M. Systematic optimization of long-range corrected hybrid density functionals. *J. Chem. Phys.* **2008**, *128*, 084106/1-084106/15.

134 Zhao, Y.; Lynch, B. J.; Truhlar, D. G. Multi-coefficient extrapolated density functional theory for thermochemistry and thermochemical kinetics. *Phys. Chem. Chem. Phys.* **2005**, *7*, 43-52.

135 Zhao, Y.; González-García, N.; Truhlar, D. G. Benchmark database of barrier heights for heavy atom transfer, nucleophilic substitution, association, and unimolecular reactions and their use to test density functional theory. *J. Phys. Chem. A* **2005**, *109*, 2012-2018.

136 Xu, X.; Goddard, W. A. III. The X3LYP extended density functional for accurate descriptions of nonbond interactions, spin states, and thermochemical properties. *Proc. Natl. Acad. Sci. USA*, **2004**, *101*, 2673-77.

137 Peverati, R.; Truhlar, D. G. M11-L: A local density functional that provides improved accuracy for electronic structure calculations in chemistry and physics. *J. Phys. Chem. Lett.* **2011**, *3*, 117-124.

138 Chai, J. D.; Head-Gordon, M. Long-range corrected hybrid density functionals with damped atom-atom dispersion corrections *Phys. Chem. Chem. Phys.* **2008**, *10*, 6615-6620.

139 Boese, A. D.; Martin, J. M. L. Development of density functionals for thermochemical kinetics. *J. Chem. Phys.* **2004**, *121*, 3405-3416.

140 Yu, H. S.; He, X.; Li, S.; Truhlar, D. G. MN15: A Kohn-Sham global-hybrid exchange-correlation density functional with broad accuracy for multi-reference and single-reference systems and noncovalent interactions. *Chem. Sci.* **2016**, *7*, 5032-5051.

141 Heyd, J.; Scuseria, G. Efficient hybrid density functional calculations in solids: The HS-Ernzerhof screened Coulomb hybrid functional. *J. Chem. Phys.* **2004**, *121*, 1187-1192.

142 Yanai, T.; Tew, D.; Handy, N. A new hybrid exchange-correlation functional using the Coulomb-attenuating method (CAM-B3LYP). *Chem. Phys. Lett.* **2004**, *393*, 51-57.

143 Heyd, J.; Scuseria, G. E.; Ernzerhof, M. Hybrid functionals based on a screened Coulomb potential. *J. Chem. Phys.* **2003**, *118*, 8207-8215.

144 Vydrov, O. A.; Scuseria, G. E. Assessment of a long range corrected hybrid functional. *J. Chem. Phys.* **2006**, *125*, 234109/1-234109/9.

145 Tomasi, J.; Mennucci, B.; Cammi, R. Quantum mechanical continuum solvation models. *Chem. Rev.* **2005**, *105*, 2999-3093.

146 Tenderholt, A. L. QMForge, version 2.1; Standord University: Stanford, CA, 2011. https://qmforge.net/.

10. Conclusions

10.1 Summary

Throughout this thesis, the electronic structures of several soft and hard chromophoric porphyrin, phthalocyanine, and triazacorrole systems were examined. These featured molecules were subjected to structural manipulations which had an effect on their optical absorption spectra. The origin of these predictable changes in their absorption spectra lies in the energies of the frontier molecular orbitals and excited states involved. Therefore, the imparted structural modifications were employed in a manner which exploited known effects on these frontier orbitals. Although each chapter featured a unique and substantial evaluation of these electronic structures, the unifying goal here was to impart structural modifications on these macrocycles in a way that flipped the typically encountered (for synthetically prepared molecules) ΔHOMO > ΔLUMO relationship to the reverse case of

ΔHOMO < ΔLUMO, which has historically been restricted to naturally occurring reduced porphyrinoid systems. Primarily, this targeted ordering and energetic sequencing of the Gouterman's four frontier orbitals was chosen to demonstrate how specific orbital manipulations could be achieved through structural modification without any guesswork. This focal point was secondarily justified as an effort to promote these samples in their various applications as being either potentially "biologically cohesive" or "more natural" in terms of electronic structure which is becoming an increasingly important consideration of modern consumers; however, it should be noted that, for example, the therapeutic effectiveness of such a synthetically created macrocyclic compound with a "natural" ΔHOMO < ΔLUMO relationship wouldn't be expected to perform any differently than a similarly structured alternative with a traditional "synthetic" electronic structure.

Chapters two through five featured various porphyrin systems which are examples of soft chromophores which possess frontier orbitals that can be easily manipulated through structural modification. Since the goal was to impart structural modifications on these porphyrins in a manner which resulted in a ΔHOMO < ΔLUMO relationship, several attempts were made at increasing the energy (destabilizing) of the porphyrin e_{gy} frontier orbital.

The first attempt (chapter two) extended the π-system in a single direction (in the y-direction) using two different pentacene-derived moieties. It was hypothesized that once the π-system was extended in the y-direction, the e_{gy} orbital would be destabilized which would increase the value of ΔLUMO. Surely enough, ΔLUMO was increased by default since fusion of the pentacene moiety onto the previously symmetric porphyrin scaffold removed the degeneracy from the system, thereby eliminating the occurrence of any doubly

degenerate e_g orbitals; however, these structural manipulations were not enough for ΔLUMO to overcome the magnitude of ΔHOMO, and these pentacene-fused porphyrin systems possessed electronic structures that are common for other synthetically-prepared macrocycles.

There were a total of six pentacene-fused porphyrin samples that were analyzed which contained either a nickel, zinc, or metal-free center and one of two pentacene moieties where one pentacene moiety possessed two phenylacetylene units and the other possessed two ketone groups on the central extended ring. These pentacene-fused porphyrins possessed a rich UV-vis spectrum in the 250-700 nm region and an MCD spectrum with relatively strong signals exclusively comprised of Faraday *B*-terms. For all compounds, the electrochemical experiments uncovered two to three oxidation events and three to four reduction processes with varying reversibility. All compounds were fully reversible under spectroelectrochemical conditions and, for the "dioxo-pentacene" samples, possible cationic radical formation was observed at 900 nm and longer. Interestingly, the spectroelectrochemical experiments performed on the "diphenylacetylene-pentacene" compounds revealed an intense and very broad signal at ~2000 nm which represented either the spectroscopic signature of radical species delocalization over the extended π-system or a mixed valence electron hole. The UV-vis spectra were accurately simulated using the B3LYP and M06 exchange correlation functionals. Finally, the DFT-predicted energy-level diagrams displayed a larger band gap for the "dioxo-pentacene" samples compared to the "diphenylacetylene-pentacene" compounds.

The work involving the pentacene-fused porphyrin systems (Ch. 2) demonstrated that addition of a chromophoric pentacene substituent onto the porphyrin core substantially increased the richness of the optical absorption spectral profile which consisted of a combination of signals from both the porphyrin and pentacene chromophores. Extension of the π-system in a single direction (the arbitrary y-direction) removed the degeneracy from the previously symmetric system and destabilized the e_{gy} orbital which increased the magnitude of ΔLUMO; however, this increase was not enough to overcome ΔHOMO and these pentacene-fused porphyrin systems possess electronic structures that are generally characteristic of other synthetically prepared macrocycles as dictated by their observed ΔHOMO > ΔLUMO relationship.

Following the electronic structure evaluation of the pentacene-fused porphyrins, the porphyrin tape systems were examined from a theoretical standpoint. This work (featured in chapter three) improved upon the previously reported PPP SCI[1] and ZINDO/S[2] calculations by employing modern DFT/TDDFT methods to fully analyze this novel system. Specifically, the improvements gained by the DFT/TDDFT calculations over previous reports include a substantial improvement in the accuracy of the predicted spectra with respect to the simulated energies and intensities of the bands, as well as a closer reproduction of the experimental UV-vis and MCD spectra. Therefore, our revised and improved assessment of the band assignments can be considered as the most accurate report available to date. This includes the assignment of the lower energy (mid to near infrared) spectral region to HOMO→LUMO dominated excitations, the most intense signals in the "central energy region" were largely assigned as x-polarized Soret-type transitions, and the most intense

peaks in the higher energy (UV) region were dominated by y-polarized Soret-type transitions. Also correctly predicted by TDDFT were the linear relationships between the TDDFT-predicted vs. experimentally obtained λ_{max} band energies and the λ_{max} band wavelength vs. number of units in the chain. Exponential decay behavior for the λ_{max} band energy vs. number of units in the chain was also simulated and accurately reflects what was observed with the experimental data. Lastly, DFT predicted an increase in the band gap as the length of the porphyrin tape was increased, which was experimentally confirmed via evaluation of the experimentally obtained λ_{max} band energies as the porphyrin chain is lengthened.

Building on what was gained from the work involving the pentacene-fused porphyrins, this porphyrin tapes (chapter three) body of work expanded upon the notion of extending the π-system along the y-axis. Specifically, the π-system of the starting zinc-centered *meso*-tetraphenylporphyrin molecules was extended in both directions (along the y-axis) to form these planar triply-linked porphyrin tapes. This π-system extension of the porphyrin tapes had a similar effect to that of the pentacene-fused porphyrin systems where the e_{gy} orbital was destabilized and ΔLUMO was increased. In fact, this increase in ΔLUMO was so substantial that it was able to overcome the magnitude of ΔHOMO with the dimer and longer porphyrin tapes. Therefore, these synthetically prepared porphyrin tape systems possess a very rare (for synthetic molecules) ΔHOMO < ΔLUMO relationship that can be generally classified as “natural” as it resembles the electronic structure of naturally occurring reduced porphyrin systems. This success was due in large part not only by the substantial destabilization of the e_{gy} orbital, but also by the rigid triple-linkages that

prevented these porphyrin tapes from undergoing significant twisting which would have a negative effect on the absorption profile of these systems. Nonetheless, negligible twisting of the longer porphyrin tapes (octamer and larger) was observed through simulation.

Following our success in replicating the electronic structures of naturally occurring reduced porphyrinoids with the porphyrin tapes, we then applied this same methodology to a similar system: the twin porphyrins (chapter four). This series of compounds featured porphyrin cores with phenyl groups at the *meso* positions and the macrocyclic centers were either metal-free or contained either one or two group ten transition metal atom/s. These novel twin porphyrins were fused to each other through a total of two linkages which allowed for the accommodation of a second metal center due to the presence of a large central cavity within the macrocycle. These twin porphyrins possessed several quasi-reversible oxidation and reduction processes that were electrochemically observed. Between compounds, these redox processes only varied subtly suggesting that they largely occur over the macrocyclic core. The optical absorption spectra of these twin porphyrins were quite distinct from each other which indicated mixing of the metal-centered d-orbitals with the macrocyclic π-system. In general, the MCD signals for the metalated twin porphyrins were quite strong; however, they were weak for the metal-free compound **4.1** which suggested the absence of a strong macrocyclic ring current. This finding essentially confirmed that these twin porphyrins don't actually possess macrocyclic aromatic character, but rather two nearly independent conjugated π-systems (one on each porphyrin) which are separated by the two central pyrazole units. From the DFT/TDDFT calculations, it was discovered that the frontier MOs associated with the lowest energy excitations were largely

confined to the pyrrolic fragments of the macrocyclic core and only small contributions were made by the pyrazole units (< 25%) and metal centers (< 10%). Interestingly, the frontier orbitals were predicted to extend over the entire macrocycle for the twin porphyrins that contained two metal-centers; however, for the monometallic twin porphyrins, the electron density on the HOMO was confined to the metalated half while the LUMO was confined to the metal-free side.

These twin porphyrin systems provided an important insight into the spectroscopic and electronic effects of extension of the π-system along the arbitrary y-axis. The specific rational behind this type of structural manipulation was to destabilize the e_{gy} orbital which would increase the value of ΔLUMO, hopefully to the extent that its magnitude would overtake ΔHOMO. The double-linkages that these twin porphyrins possess enabled the incorporation of two metal-centers into the structure; however, they did not provide the structural support that is necessary to avoid significant twisting of the twin porphyrin. As a result, instead of a single strong macrocyclic ring current that cycles around the structural perimeter like most porphyrinoids, the significant twisting that these twin porphyrins endure results in a disturbance of this aromatic ring current which is actually separated into two nearly independent conjugated π-systems with one on each half of the twin porphyrin. In addition to this twisting, the MCD spectra demonstrated a negative-to-positive sign sequence (in ascending energy) of the major bands which indicate a ΔHOMO > ΔLUMO relationship and an electronic structure that can generally be described as synthetic.

Chapters 2 through 4 featured soft chromophoric porphyrin systems with manipulated structures where the π-systems were extended in various ways. The following chapter (five)

also featured soft-chromophoric porphyrins with extended π-systems; however, the extension of the π-systems in this chapter was far more dramatic in terms of the approach and outcome. The self-assembly of chiral porphyrin-based microscale architectures, which are driven by non-covalent aggregation, have been extensively studied in organic solvents[3-6] and more recently, in aqueous systems[7-9]. Due to the common use of porphyrins as agents for treating cancer via photodynamic therapy[10-18], the encapsulation of a co-drug into a supramolecular "porphyrin cage" as a prospective next-generation alternative to current formulations may be advantageous. In this study (featured in chapter five), microscale architectures were assembled using a water-soluble, tetraphenyl sulfonated tetracationic N-confused porphyrin and the formation of chiral nanoparticles was induced by the addition of L- or D-tartaric acid. The electronic and physical structure of this supramolecular system was studied using UV-vis, circular dichroism (CD), and MCD spectroscopies, DFT/TDDFT, and dynamic light scattering (DLS). The CD data indicated the formation of chiral particles which were visible in solution without magnification and were determined from DLS to have hydrodynamic radii ranging in size from 1-10 μm. The TDDFT calculations run on the monomeric and dimeric scaffolds provided simulated spectra which were compared with experimental data in order to determine the nature and type of aggregation. In addition to UV-vis, the TDDFT data uncovered J-type aggregation behaviour and reasonable correlation with experimental data was achieved.

The effect of rotating a single pyrrole ring in porphyrin to form an N-confused porphyrin results in more stabilized a_{1u} orbital and a more destabilized a_{2u}, which leads to an increase in ΔHOMO. For this work involved in chapter five, the goal was to extend the π-system and

evaluate the resulting electronic structure regardless of the outcome. Through DLS and even visual inspection, it was clear that the π-system had become significantly extended through aggregation and the J-type stacking that was observed was facilitated by tartaric acid, which provided order to the system. Since the MCD spectra possessed a negative-to-positive sign sequence (in ascending energy) of the major signals, a ΔHOMO > ΔLUMO relationship is indicated and these systems also possess electronic structures that can be generally classified as synthetic.

The work involving the soft chromophoric systems of chapters two through five demonstrated how the energies of the frontier molecular orbitals can be manipulated through specific types of structural modification with the focal point of design for those chapters being various types of π-system extension. Conversely, the hard chromophoric systems featured in chapters six through eight possess frontier orbitals which are difficult to manipulate through structural modification and this difficulty stems from the characteristically very large ΔHOMO value that they possess. Nonetheless, a few hard chromophoric systems were structurally manipulated in an effort to decrease the magnitude of ΔHOMO to the point where it is overtaken by that of ΔLUMO. The first of these attempts was documented in chapter six with the triazatetrabenzcorrole (TBC) systems.

These hard chromophoric TBC systems included a total of two samples: one with octacarbazole (**6.1**) and the other with tetra-*tert* butyl (**6.2**) peripheral substituents. The UV-vis spectrum for **6.1** was quite rich with several transitions occupying the UV-region and also the spectral window between the *B*- and *Q*-bands; however, the UV-vis spectrum of **6.2**

was largely limited to the *B*- and *Q*-bands without many supplementary signals, indicating that the carbazole substituents contribute to the absorption profile. For both compounds, the MCD spectra were dominated by quasi *A*-terms which were associated with the *B*- and *Q*-bands. The electrochemical data for **6.1** showed two reversible oxidation processes: a carbazole-oriented multielectron process at lower potential and a single-electron process at higher potential originating from the TBC core. For **6.2**, the electrochemical results show no reversibility and only a single irreversible reduction process indicating that the carbazole substituents contribute significantly to the observed redox processes of **6.1**. The results of the spectroelectrochemical experiments also varied dramatically between compounds as the recorded spectra of **6.1** were fully reversible and demonstrated a broad signal at 946 nm which was assigned to cationic radical formation. For **6.2**, the spectroelectrochemical experiment was irreversible with no sign of cationic radical formation. An accurate TDDFT-based simulation of the UV-vis spectra for both compounds was achieved using the B3LYP exchange correlation functional, although several methods were tested before arriving at this conclusion. If was determined from the DFT calculations that for **6.1**, HOMO to LUMO+4 had electron density almost exclusively confined to the macrocycle but for HOMO-1 to HOMO-10, the electron density was located over the octacarbazole fragments. Due to the lack of chromophoric substituents, the DFT-predicted frontier MOs of **6.2** were confined to the TBC core. Finally, the DFT-predicted energy level diagram for both compounds revealed that the frontier MOs of **6.1** were more energetically compressed than they were for **6.2**.

This triazatetrabenzcorrole system can be envisioned as a phthalocyanine which has been structurally manipulated so that one *meso*-nitrogen atom is removed from the framework.

The rationale behind this structural manipulation was that omission of one of the *meso*-nitrogen atoms would destabilize the a_{2u} orbital which would lead to a decrease in ΔHOMO. Although we were successful in lowering the energy of a_{2u}, it was not enough to decrease ΔHOMO to a point where it was less than ΔLUMO. This was experimentally determined through examination of the MCD spectra for both compounds, which possessed a negative to positive sign sequence (in ascending energy), and also theoretically confirmed by examination of the DFT-predicted energy levels which suggested a ΔHOMO > ΔLUMO relationship. Therefore, these synthetic TBC systems possess electronic structures that can generally be described as synthetic.

Since the electronic structures of the triazatetrabenzcorroles of chapter six were quite similar to those typically encountered in phthalocyanines, an entirely different approach to the structural modification of metalated phthalocyanines to dramatically manipulate the electronic structures was envisioned; however, in order to better understand the hypothesized results, a preliminary project was utilized which provided substantial insights, and this was the cationic zinc phthalocyanine radical system of chapter seven. This report featured a tetra-*tert*-butylated zinc-centered phthalocyanine which was oxidized both chemically and spectroelectrochemically using an applied potential to the solution containing electrolyte. It was determined via MCD spectroscopy that the NIR band observed at ~1000 nm for the $[\mathbf{7.1}]_2^{2+}$ dimer originated from transitions involving non-degenerate orbitals. Also of interest was an observed temperature dependence of the monomer-dimer equilibrium of the oxidized species. In regards to the DFT/TDDFT calculations, 16 different exchange correlation functionals were tested in an effort to achieve the most accurate

spectral simulation where the band energies, intensities, and overall UV-vis and MCD signal profile were the focal points of this target of accuracy. The M05 exchange correlation functional provided the best results for both the monomer and the antiferromagnetically coupled dimer. In addition to providing a correct description of the experimentally observed MCD *B*-term in the fingerprint region, the TDDFT calculations also correctly predicted the antiferromagnetic coupling between the two singly oxidized phthalocyanine macrocycles.

The work performed on the cationic zinc phthalocyanine radical system provided us with insight into what to spectroscopically expect when a cationic radical species is encountered. This includes the broad signal between the *B*- and *Q*-bands (at ~530 nm) as well as the broad signal observed at ~1025 nm in the UV-vis spectrum of the oxidized phthalocyanine.

In addition to the oxidation of Fe(II) to Fe(III), the formation of a cationic radical species was hypothesized to occur for the axially coordinated iron phthalocyanine systems described in chapter eight. These systems featured a variety of axial ligands with a large range of electronic and steric properties. The axial ligands featured in chapter eight also possessed a range of E_L values which are assigned based on σ-donor strength, π-acceptor strength, and steric bulk[19-22]. The nature of the HOMO was investigated using spectroelectrochemical and chemical oxidation techniques using several different solvents and electrolytes. The energies of the metal-centered occupied orbitals were found to correlate well with the E_L parameter values of the coordinated ligands. The DFT calculations, which were in line with the experimental data, indicated that an increase in the π-accepting strength of the axial ligands results in a decrease of the energy gap between the iron-centered HOMO and the Pc-centered HOMO-*n* (a_{1u}) orbitals. In several compounds, these

orbitals were found to intercross with the moderate-to-strong π-accepting axial ligands. In these cases, the phthalocyanine macrocycle (Pc^{2-}/Pc^{1-}) was oxidized instead of the central iron atom, which was predicted by DFT/TDDFT and experimentally confirmed. The data collected for this project can be used to supplement Lever's previous related reports[19-22] and to explain inconsistencies between the first oxidation potential and the $\Sigma E_L(L_{ax})$ values.

The axially coordinated iron phthalocyanine systems featured in chapters eight and nine were designed to influence the frontier core orbitals of the phthalocyanine. By increasing the iron phthalocyanine from four- to six-coordinate via axial ligation, the iron d-orbitals were mixed with the phthalocyanine core orbitals and the resulting spectral profiles of each compound were different based on the electronic and steric nature of the axial ligands. Due to geometric restrictions, the axial ligands of these compounds influence the metal d_{xz} and d_{yz} orbitals. For the compounds containing axial ligands thatx are strong σ-donors, the d_{xz} and d_{yz} orbitals increased in energy depending on the magnitude of the σ-donating strength. Conversely, strong π-accepting ligands decrease the energies of the d_{xz} and d_{yz} orbitals; the magnitude of which is dependent on the π-accepting strength of the coordinated ligand. It was generally observed that the energies of the Pc core orbitals decreased with increasing $\Sigma E_L(L_{ax})$. Based on the DFT-predicted energy-level diagram and the MCD spectra for all compounds, these axially coordinated iron phthalocyanines possess a ΔHOMO > ΔLUMO relationship which is typical for synthetically prepared macrocycles.

Overall, the work described in this thesis provides several examples of how structural manipulation can affect the electronic structures and corresponding absorption spectra of porphyrins and phthalocyanines. Rather than providing an example of each possible type of

structural manipulation that could influence the electronic structures, we set a goal to manipulate the samples in a way that resulted in a ΔHOMO < ΔLUMO relationship, which is observed in most naturally occurring reduced porphyrinoid species. The structural modifications described herein involved various degrees of π-system extension, elimination of a *meso*-nitrogen, and axial coordination. The soft chromophoric systems of chapters 2-5 demonstrated how the structural manipulations employed were able to dramatically influence the energies of the frontier molecular orbitals; however, only the porphyrin tapes system (Ch. 3) resulted in the targeted ΔHOMO < ΔLUMO relationship. This was due to the rigidness that the triple-linkages provided. We found that if only double linkages are used, such as in the twin porphyrins of chapter four, the structure dramatically flexes which disrupts the overall aromatic character of the macrocycle. For the hard chromophoric systems of chapters 6-8, the a_{2u} frontier orbital was at such a low energy compared to the other three Gouterman's frontier orbitals, that neither omission of a single meso-nitrogen atom nor axial ligation with various ligands was enough to decrease the ΔHOMO value to a point where it was lower than ΔLUMO.

10.2 Outlook

The compound sets featured in this thesis possessed either a porphyrin, phthalocyanine, or triazacorrole core which had been structurally modified in some fashion. The goal with the structural modifications was to perturb the electronic structure in a specific way in the hope of imparting these systems with the characteristic ΔHOMO < ΔLUMO relationship that naturally occurring reduced porphyrins possess. This target was selected based on the

trends of modern consumers who currently show in increasing enthusiasm for products that are either natural or designed after nature. This research represents a small part of the growing collective of scientists who are seeking to understand how porphyrins and phthalocyanines can be structurally modified in order to tune their electronic properties to best suit a targeted application.

In terms of the possibilities for structural modification, there is a limited number of modifications that can be performed on porphyrins, phthalocyanines, and related macrocycles. These include the incorporation of electron-donating, electron-withdrawing, and/or bulky substituents onto the α-, β-, or *meso*-positions, or coordinating various ligands to the central metal. There also exist other outside-the-box types of structural modifications such as “macrocyclic fusion” (Ch. 4) or self-assembly (Ch. 5).

Given the fact that traditional modifications of porphyrins and phthalocyanines and their resultant perturbations on their electronic structures are well-understood at this point, a logical future direction of this research would be to apply the concepts included herein and elsewhere to develop useful functional materials for certain targeted applications such as PDT of cancer or solar cells. The UV-vis spectra of the pentacene-fused porphyrin samples of chapter two indicate that when two conjugated substrates are bound to each other, the resulting spectral profile consists of overlapping spectra of each of the two substrates. Certainly, solar cell materials could be designed in this way which have strong optical absorption activity present throughout the entire UV-vis-NIR window, thereby increasing efficiency.

Given the success of the porphyrin tapes of chapter three in replicating the electronic structure, or at least the ΔHOMO < ΔLUMO relationship, of naturally occurring reduced porphyrinoids, the same chemistry could be applied to other systems. This could include porphyrin tapes with different metal centers or porphyrin tapes with different *meso*-capping groups such as methyl, ethyl, butyl, or other cyclic species. Although the *meso*-nitrogen atoms of phthalocyanines would increase the difficulty, perhaps a phthalocyanine tape could be formed and compared. After a rich history, the future is still bright for porphyrin and phthalocyanine research following our now complete understanding of how structural modifications affect their corresponding electronic structures.

10.3 References

1. Cho, H. S.; Jeong, D. H.; Cho, S.; Kim, D.; Matsuzaki, Y.; Tanaka, K.; Tsuda, A.; Osuka, A. Photophysical Properties of Porphyrin Tapes. *J. Am. Chem. Soc.* **2002**, *124*, 14642-14654.
2. Muranaka, A.; Yokoyama, M.; Matsumoto, Y.; Uchiyama, M.; Tsuda, A.; Osuka, A.; Kobayashi, N. Magnetic Circular Dichroism Study of Directly Fused Porphyrins. *ChemPhysChem* **2005**, *6*, 171-179.
3. Kumar, M.; Jonnalagadda, N.; George, S. J. Molecular Recognition Driven Self-Assembly and Chiral Induction in Naphthalene Diimide Amphiphiles. *Chem. Commun.* **2012**, *48* (89), 10948-10950.
4. George, S. J.; de Bruijn, R.; Tomovic, Z. E.; Van Averbeke, B.; Beljonne, D.; Lazzaroni, R.; Schenning, A. P. H. J.; Meijer, E. Asymmetric Noncovalent Synthesis of Self-Assembled

One-Dimensional Stacks by a Chiral Supramolecular Auxiliary Approach. *J. Am. Chem. Soc.* **2012**, *134* (42), 17789-17796.

5. Sobczuk, A. A.; Tsuchiya, Y.; Shiraki, T.; Tamaru, S. I.; Shinkai, S. Creation of Chiral Thixotropic Gels Through a Crown-Ammonium Interaction and Their Application to a Memory-Erasing Recycle System. *Chem.-Eur. J.* **2012**, *18* (10), 2832-2838.

6. Yashima, E.; Ousaka, N.; Taura, D.; Shimomura, K.; Ikai, T.; Maeda, K. Supramolecular Helical Systems: Helical Assemblies of Small Molecules, Foldamers, and Polymers with Chiral Amplification and Their Functions. *Chem. Rev.* **2016**, *116* (22), 13752-13990.

7. Kumar, M.; Brocorens, P.; Tonnele, C.; Beljonne, D.; Surin, M.; George, S. J. A Dynamic Supramolecular Polymer with Stimuli-Responsive Handedness for *in situ* Probing of Enzymatic ATP Hydrolysis. *Nat. Commun.* **2014**, *5*, 5793/1-5793/8.

8. Dhiman, S.; Jain, A.; George, S. J.; Transient Helicity: Fuel-Driven Temporal Control Over Conformational Switching in a Supramolecular Polymer. *Angew. Chem., Int. Ed.* **2017**, *56* (5), 1329-1333.

9. Dhiman, S.; Jain, A.; Kumar, M.; George, S. J. Adenosine-Phosphate-Fueled, Temporally Programed Supramolecular Polymers with Multiple Transient States. *J. Am. Chem. Soc.* **2017**, *139* (46), 16568-16575.

10. McRae, E. K. S.; Nevonen, D. E.; McKenna, S. A.; Nemykin, V. N. Binding and Photodynamic Action of the Cationic Zinc Phthalocyanines with Different Types of DNA

Toward Understanding of their Cancer Therapy Activity. *J. Inorg. Biochem.* **2019**, *199*, 110793/1-110793/9.

11. Agostinis, P.; Berg, K.; Cengel, K. A.; Foster, T. H.; Girotti, A. W.; Gollnick, S. O.; Hahn, S. M.; Hamblin, M. R.; Juzeniene, A.; Kessel, D.; Korbelik, M.; Moan, J.; Mroz, P.; Nowis, D.; Piette, J.; Wilson, B. C.; Golab, J. Photodynamic Therapy of Cancer: An Update. *Ca-Cancer J. Clin.* **2011**, *61*, 250– 281.

12. Ethirajan, M.; Chen, Y.; Joshi, P.; Pandey, R. K. The Role of Porphyrin Chemistry in Tumor Imaging and Photodynamic Therapy. *Chem. Soc. Rev.* **2011**, *40*, 340–362.

13. Singh, S.; Aggarwal, A.; Bhupathiraju, N. D. K.; Arianna, G.; Tiwari, K.; Drain, C. M. Glycosylated Porphyrins, Phthalocyanines, and Other Porphyrinoids for Diagnostics and Therapeutics. *Chem. Rev.* **2015**, *115*, 10261–10306.

14. Ziessel, R.; Hissler, M.; El-Ghayoury, A.; Harriman, A. Multifunctional Transition Metal Complexes: Information Transfer at the Molecular Level. *Coord. Chem. Rev.* **1998**, *178*, 1251–1298.

15. Li, X.; Zheng, B.-D.; Peng, X.-H.; Li, S.-Z.; Ying, J.-W.; Zhao, Y.; Huang, J.-D.; Yoon, J. Phthalocyanines as Medicinal Photosensitizers: Developments in the Last Five Years. *Coord. Chem. Rev.* **2019**, *379*, 147–160.

16. Li, X.; Lee, S.; Yoon, J. Supramolecular Photosensitizers Rejuvenate Photodynamic Therapy. *Chem. Soc. Rev.* **2018**, *47*, 1174–1188.

17. Vakrat-Haglili, Y.; Weiner, L.; Brumfeld, V.; Brandis, A.; Salomon, Y.; McLlroy, B.; Wilson, B. C.; Pawlak, A.; Rozanowska, M.; Sarna, T.; Scherz, A., The microenvironment effect on the generation of reactive oxygen species by Pd-bacteriopheophorbide. *J. Am. Chem. Soc.* **2005,** *127* (17), 6487–6497.

18. Huang, Y.-Y.; Balasubramanian, T.; Yang, E.; Luo, D.; Diers, J. R.; Bocian, D. F.; Lindsey, J. S.; Holten, D.; Hamblin, M. R., Stable synthetic bacteriochlorins for photodynamic therapy: Role of dicyano peripheral groups, central metal substitution (2H, Zn, Pd), and Cremophor EL delivery. *ChemMedChem.* **2012,** *7* (12), 2155–2167.

19. Lever, A. B. P. "Electrochemical parametrization of metal complex redox potentials, using the ruthenium(III)/ruthenium(II) couple to generate a ligand electrochemical series" *Inorg. Chem.* **1990**, *29*, 1271-1285.

20. Alexiou, C.; Lever, A. B. P. "Tuning metalloporphyrin and metallophthalocyanine redox potentials using ligand electrochemical (E_L) and Hammett (σ_p) parametrization" *Coord. Chem. Rev.* **2001**, *216-217*, 45-54.

21. Lever, A. B. P.; Dodsworth, E. S. in: “Inorganic Electronic Structure and Spectroscopy” Solomon, E. I. and Lever, A. B. P. (Eds.), John Wiley & Sons, Inc., **1999**, *Vol. II*, 227-289.

22. Lever, A. B. P. "The phthalocyanines-molecules of enduring value; a two-dimensional analysis of redox potentials" *J. Porphyrins Phthalocyanines* **1999**, *3*, 488-499.